An experimental investigation into the use of vortex generators to improve the performance of a high lift system

by

Fraser Innes

Thesis submitted as part of the requirements for the degree of Doctor of Philosophy

Centre for Aeronautics
School of Mechanical Engineering and Aeronautics

June 1995

Abstract

Windtunnel tests have been conducted on a two-dimensional model of a three element high lift system in a take-off configuration in City University's T2 low speed windtunnel. The high lift system was mounted between endplates and consisted of a leading edge Handley Page slat and a trailing edge Fowler flap. Endplate boundary layer control ensured two-dimensional conditions up to and beyond the stall incidence of the high lift system and was provided by blowing through two near tangential slots located flush in each endplate adjacent to the main wing element. The windtunnel tests involved:

◆ monitoring the pressure distribution around each element of the multiple element aerofoil

◆ investigating the structure of the shear layers above the main wing and flap elements of the high lift system.

Boundary layer separation was first seen at the trailing edge of the main wing and developed steadily with incidence. The stall of the high lift system coincided with the rapid divergence of the static pressure at the trailing edge of the flap. However, the stall was preceded by a loss of load at the rear of the main wing attributable to the adverse viscous effects of the confluency of the main wing upper surface boundary layer and the slat wake, resulting in a substantial growth in the thickness of the shear layers above the main wing and the appearance of separated flow on this element first.

Various vane vortex generator configurations were tested on the upper surface of the main wing of the high lift system. Each configuration had a favourable influence on the suppression of separation at the rear of the main wing. However, for all configurations the generators had an adverse effect on the normal force coefficient generated by the high lift system at incidences below the stall incidence of the cleanfoil, resulting from an increased displacement effect of the shear layers above the upper surface of the main wing.

A system of co-rotating airjet vortex generators installed in the main wing and utilizing a constant blowing pressure of 60% above freestream stagnation pressure significantly increased the maximum total normal force coefficient of the high lift system. The high lift system also exhibited an increase in total normal force coefficient at all incidences below the stall incidence of the cleanfoil, resulting from a reduced displacement effect of the shear layers above the upper surface of the main wing. A reduction in the profile drag of the high lift system can be inferred from a lower value of momentum defect in the shear layers above the flap at all incidences.

The improvements achieved by the airjets were significantly greater than those produced with the various vane vortex generator configurations and cannot be attributed to just the suppression of boundary layer separation at the rear of the main wing. The airjets and associated vortices which they generate promote enhanced mixing and momentum transfer across the complex shear layers above the main wing in ways which cannot be achieved with vane generated vortices.

It is felt the low Reynolds number and Mach number of the tests do not detract from the fundamental fluid processes at work and hence the applicability of airjets to high lift systems. However, further work needs to be done to establish the balance between aerodynamic benefit and the performance cost of installing and driving the jets.

Contents

List of Figures

Nomenclature

α	angle of incidence (°)
δ	shear layer thickness (mm)
δ^*	displacement thickness of shear layers (mm)
θ	momentum thickness of shear layers (mm)
ρ	density (kgm^{-3})
ajvg	airjet vortex generator
c	retracted chord length (500mm)
c_f	skin friction coefficient
C_L	lift coefficient
C_n	normal force coefficient, based on retracted wing chord of 0.5m
C_p	pressure coefficient
d	length of longest side of airjet (mm)
D	distance between airjet vortex generators (mm)
D/d	Initial lateral spacing between vortices from a divergent pair of vanes (see figure 2.8)
f	distance between co-rotating vane vortex generators (multiple of height in mm)
h	height of vane vortex generator (mm)
H	shape factor of shear layers
H	total pressure (Nm^{-2})
K	numerical constant
M	Freestream Mach number
P	pressure (Nm^{-2})
Re	Freestream Reynolds number
u	streamwise velocity in shear layers (ms^{-1})
U	velocity in freestream (ms^{-1})
vvg	vane vortex generator
x/c	chordwise position
y/c	distance through shear layers perpendicular to surface
z/c	spanwise distance

subscipts

1	upstream location in tunnel contraction
2	downstream location in tunnel contraction
3	location in centre of working section
atmos	atmosphere
b	plenum pressure
e	value in freestream adjacent to shear layer
o	freestream stagnation
∞	freestream static

Declaration

'I grant powers of discretion to the university librarian to allow this thesis to be copied in whole or in part without further reference to me. This permission only covers single copies made for study purposes, subject to normal conditions of acknowledgement.'

Acknowledgements

This thesis is proof enough of the infinite patience and constant encouragement that I have received from so many quarters.

I would especially like to thank Prof. H.H.Pearcey to whom I am greatly indebted for his invaluable guidance during the course of this work.

Thanks are due to Mr. D.M.Sykes, Mr. M.Smith, Mr. C.Barber and Mr. K.Harvey for giving their advice, time and effort into the design and manufacture of the windtunnel models.

Above all, I would like to thank my parents for teaching me the basic skills which have helped me to achieve so much.

1. Introduction

1.1 Overview

The research described in this thesis was carried out at City University between 1989 and 1993, for the early part in collaboration with British Aerospace (Kingston). The work originated out of an underlying interest from within British Aerospace into the limitations of aiming for high agility (ie. high rate of turn) as a main project design criterion with considerations such as speed and G limits taking lower priority.

British Aerospace is responsible for the design and manufacture of the complete wing of the Airbus A320 (the Weybridge conceived W6-4 wing). The aerodynamic configuration of this wing was the first to be devised jointly utilizing the many years of research and design experience gained through the U.K. "National High Lift Programme" (1970-1978) and the computational fluid dynamic code "VGK" (a full potential inviscid theory incorporating an interactive boundary layer solution). The associated high lift system, designed within the constraints of the high speed cruise and low speed landing and take-off requirements, proved to be highly efficient in terms of parameters such as L/D and C_{Lmax}. It consists of a near full span leading edge over wing Handley Page slat and a trailing edge Fowler flap system. Its physical lightness and simplicity contribute to the Airbus A320's success.

City University has a successful history of research into boundary layer flow separation control. This is best shown in the work recently completed by Rao (1988) into the use of vortex generators to control shock induced boundary layer separation. Rao produced a steady shock wave on half bump aerofoil models of varying thickness in City University's transonic windtunnel. Various vane vortex generator configurations were attached to the surface of the model. The criterion used to judge their effectiveness in controlling shock induced boundary layer separation was the improvement in static pressure recovery seen towards the trailing edge of the model. Several airjet vortex generator configurations were also tested in the same manner. In conclusion, Rao found the beneficial effects of airjet vortex generators to be at least comparable to those seen with the more conventional vane vortex generators.

Use of vane vortex generators as part of the original design concept is the design philosophy at Boeing. Vane vortex generators have been used for stall control, e.g. to eliminate wing rock on the Harrier. However, others look upon vane vortex generators as an "aerodynamic fix" installed only when the need arises, for example where flow control problems not seen at the design stage appear during airworthiness trials. They have several advantages when used in this manner. They are simple and easily installed, rugged and inexpensive. However, they cannot be used in "active" stall control, that is they may have detrimental effects in other regions of the flight envelope such as producing parasitic drag in flow situations where stall suppression or flow control is not required (ie. steady cruise). However, careful design of the generators can usually reduce this to a minimum.

Airjet vortex generators obviate both of these disadvantages. Vortices generated by airjets lend themselves well to 'active' stall control since the jet strength may be altered

according to the demands made upon the system. For flow situations where flow control is not needed, the airjets avoid the generation of parasitic drag losses by easily being turned off (assuming cavities would be removed through a well thought out deployment system). The potential applications of airjet vortex generator systems are numerous for external flows over aircraft and missiles. Internal flows like those seen in jet engine inlets and subsonic diffusers could be improved in terms of reduced energy losses. Yet the advantages that airjet vortex generators have can only be exploited if they are accepted as an integral part of aerodynamic design.

Active stall control is a technology which is now being developed for highly manoeuvrable aircraft and commercial aircraft. For the former, higher lift coefficients reduce manoeuvre times increasing the aircraft's level of agility and hence improving battlefield survivability. In the latter, the profit margin per aircraft flight depends upon the payload capacity and performance at take-off and ultimately the maximum C_L at take-off and climb-out. There are limitations to the ability to engineer variable geometry high lift devices which deal with critical areas of the wing. It is here that active boundary layer control could be an effective way of dealing with localised problems. Such a control system could greatly diminish the need for stall fixing and its associated loss of maximum lift.

An experimental investigation has been undertaken into the use of vortex generators to control boundary layer separation on a high lift system (similar to that seen on the Airbus A320). A two-dimensional model was installed in City University's T2 lowspeed windtunnel (0-45ms^{-1}). Various vortex generator configurations were tested and detailed boundary layer measurements were carried out on the main wing and flap upper surfaces. Airjet vortex generators improved the characteristics of the high lift system over and above the suppression of boundary layer separation; they seem to offer possibilities for a novel approach towards increasing the efficiency of high lift systems (ie. in terms of increased C_{Lmax}). Discussion of this is an important part of this thesis. The work necessitated the assembly of a data acquisition system and details of this are included along with the control software.

1.2 Review of previous work

The time honoured high lift design and optimization procedure which relied largely on an iterative wind tunnel testing process, with extrapolation of results to full scale conditions based on experimental data from past aircraft of similar type, has become inadequate. The role of the wind tunnel has changed as computational methods of increasing power become more readily available. Much routine parametric evaluation can now be conducted systematically without the need for extensive testing of simplified models which is both time-consuming and expensive. Theoretical methods and experimental techniques are now seen as a necessary complementary pair.

This section summarizes research undertaken to date on high lift systems and vortex generators in their capacity as boundary layer control devices. It does not seek to be an exhaustive reference list to publications on each subject. Instead, it should be used as a guide to the more important articles available to the reader in each area.

1.2.1 High lift systems

In aircraft design, the constraints between the high speed cruise and the low speed take-off and landing conditions force the designer to incorporate some form of high lift device to improve lift at low speed. Most aircraft, be they civil or military, have some form of high lift device that is normally used exclusively during take-off and landing (fig. 1.1). The device usually involves some form of mechanical alteration to the wing section. The chordwise extent of any high lift device is largely governed by the positions of the main structural elements of the wing, namely the front and rear spars which form the main wing box. High lift devices can occupy the area in front and behind these stations which are typically at 15 and 65% of wing chord. They act to increase the lift of the wing by effectively increasing the extent of one or more of the following 1) chord, 2) positive camber or 3) boundary layer control.

Various examples of different types of leading edge high lift devices can be found on a large range of aircraft. The *F16 & F18* have a rotatable nose flap which simply increases leading edge positive camber to reduce tip stall effects at low speed. Krueger leading edge flaps can be found on the inboard wing sections of the *Tornado (IDS variant)* and increase lift by effectively increasing wing area and positive camber. The slotted slat acts by increasing all three parameters mentioned in the previous paragraph and can be found on the *A320, B747 and F14.* For the latter aircraft favourable effects are also seen on lateral/directional qualities in addition to solely increasing lift.

High lift trailing edge devices, more commonly termed flaps can be found in several different disguises. Split flaps can be seen on *A4 Skyhawks* while Fowler flaps are present on the *Alphajet, TU-22 and F-111* aircraft. The *AV-8A* variant of the Harrier (non-supercritical wing) relied upon increased lift at low speed by use of a plain flap while the uprated *AV-8B* (supercritical wing) has a slotted flap as do the *Tornado, Jaguar, F-14 and F-18.*

1.2.1.1 Theoretical

The flow about a two-dimensional multi-element aerofoil at high lift is one of the most complex flows to be modelled by theoretical methods. The problem is to calculate as accurately and as quickly as possible the basic mean flow properties - pressure, velocity,

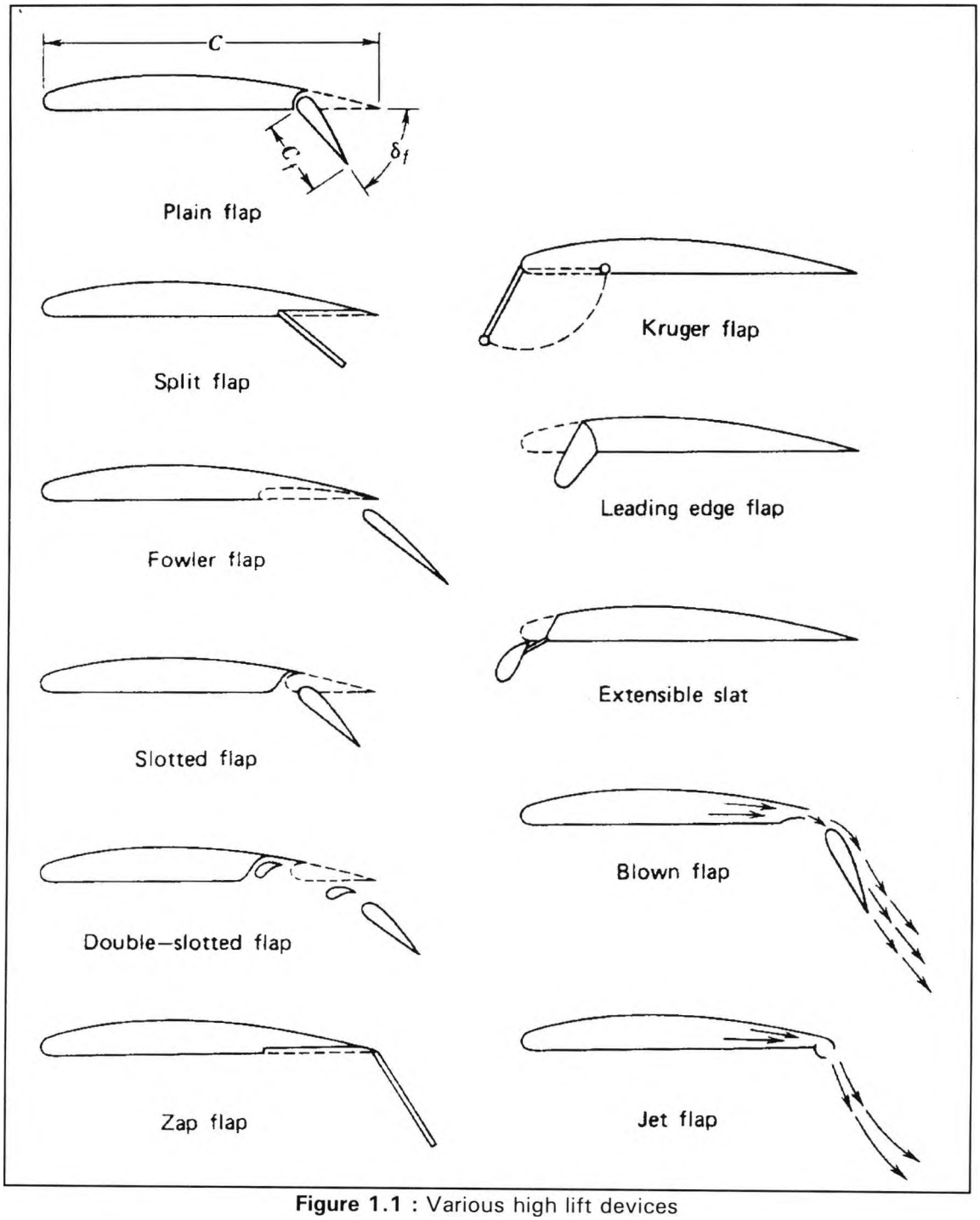

Figure 1.1 : Various high lift devices

temperature, skin friction and overall forces, for example, on and near the surface of what is invariably an extremely complicated shape. The flow field contains several complicating features not found for an isolated aerofoil (fig. 1.2). These include:

(a) the region of the flow is multiply connected, which makes even the calculation of the inviscid flow difficult.

(b) the wakes from upstream elements interact with boundary layers on downstream elements forming confluent boundary layers.

(c) upstream elements shed wakes which develop in the strong pressure gradients produced by downstream elements.

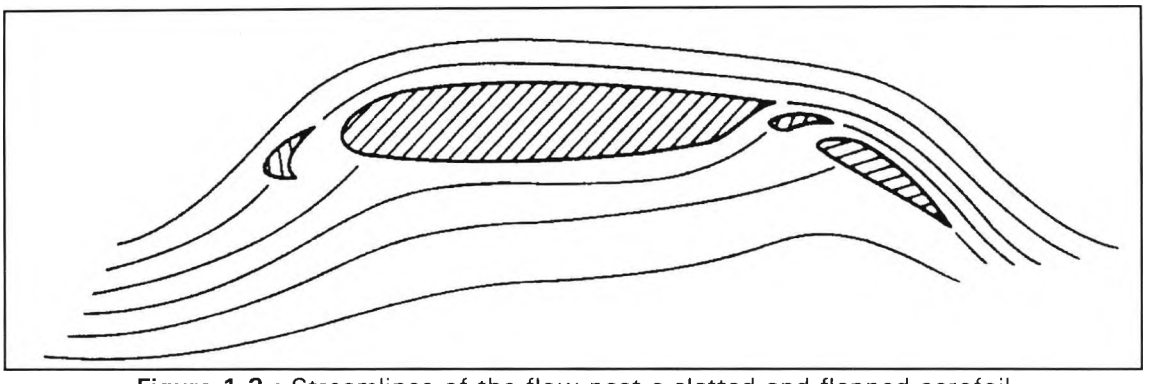

Figure 1.2 : Streamlines of the flow past a slatted and flapped aerofoil

(d) the viscous flow region above the flap is very thick and highly curved producing significant static pressure gradients normal to the plane of the layer.

(e) slat and flap devices must retract to form the cruise aerofoil resulting in the presence of coves on the lower surfaces of all upstream elements. Here the flow will separate from the sharp edge of the cove and re-attach before the trailing edge of the element is reached.

(f) if the angle of deflection of the flap is sufficiently large the flow will separate from the upper surface of the flap although the aerofoil as a whole may not necessarily stall. This condition can be present throughout the incidence range.

(g) at high incidences the high lift coefficients generated can lead to a small region of supersonic flow on the upper surface of the slat which may be terminated by a shock wave. This in turn may cause the laminar boundary layer to separate and re-attach in turbulent form or cause more severe separation and even trigger the stall.

Since air is a viscous compressible fluid the equations that we have to solve and which capture all the features of the flow are those of *Navier and Stokes*. Reynolds numbers associated with high lift systems results in large regions of turbulent flow so that some form of turbulence modelling is inevitable. The equations are impossible to solve with present mathematical techniques because the boundary conditions become randomly time dependent at high Reynolds numbers (disturbance sensitive). For flows which are steady; that is ones in which we can average out the turbulence (so the boundary conditions become independent of time) the N-S equations yield themselves amenable to solution - although the computational problems are still formidable. With the latest generation of supercomputers, very accurate solutions have been obtained for two-dimensional laminar flow with relatively simple geometries. With sufficient boundary conditions, the three-dimensional laminar flow equations can also be solved numerically. Numerical solutions for two-dimensional turbulent flows have been obtained but these involve empirical modelling for phenomena such as transition, Reynolds stresses and the flow features mentioned previously. This approach has great promise as the computational time needed to solve for the compressible viscous flow over multi-element aerofoils is dropping continuously. However, the over-simplification of the turbulence modelling techniques remains prohibitive particularly in abilities of codes to accurately predict C_{lmax}.

Fortunately the effects of viscosity and turbulence are confined to shear layers in the immediate vicinity of each element of the high lift system. Outside these regions the inviscid Euler equations are applicable to a high degree of accuracy. It is therefore advantageous to use a technique known as *Viscous-inviscid interaction (VII)*, whereby separate calculation methods for the external inviscid flow and the viscous shear layers are combined interactively and iteratively to provide a composite solution to the problem. Different approaches to the convergence of a solution within VII techniques have been identified and are known as the 'Direct', 'Semi-inverse' and 'Quasi-simultaneous' methods.

VII techniques for calculating the flow about multi-element aerofoils have been under development in the UK for the last 15 years after a gradual unification of theoretical models of various physical flow phenomena provided the necessary computational tools for flow analysis.

Williams (1971) calculated the inviscid plane potential flow about two adjacent lifting aerofoils. The potential flow about two lifting circles is calculated by the method of images. The two circles are then mapped conformally on to two aerofoils by a double application of the *Karman-Trefftz* transformation. He thereby obtains an exact solution for the inviscid flow about the lifting aerofoils. Two particular cases were examined known as Williams configurations A and B. These serve as important test cases against which to assess other numerical inviscid incompressible flow methods. Williams himself compared the exact solutions for each case against the solutions obtained by the numerical method of Smith (1966) which uses a distribution of sources over each aerofoil. The agreement was found to be very good, validating Smith's method.

The complexity of the geometry of multi-element aerofoils has forced many researchers to use surface singularity methods although it is possible to use a field method. Hall et al (1984) through subsequent transformations map two aerofoils onto two concentric circles. The annular region between the circles represents the external region about the aerofoils. Such a transformation was first introduced by Ives (1976). In a similar manner Grossman et al (1976) solved the inviscid compressible transonic potential flow about two aerofoils. However a direct extension of the Hall et al method to three element aerofoils (ie. mapping onto three concentric circles) is not possible since the multiple connectivity of the flow in the physical domain is not modelled after transformation. Halsey (1979) suggested a conformal mapping process to overcome this which was used by Hall et al (1984) in a modified form to ensure a correct grid density in regions where the elements overlapped. Alas, due to increased short comings with a greater number of elements present multi-element aerofoil analysis by this method has serious drawbacks.

Callaghan et al (1972) adopted the classic panel method devised by Smith et al (1966), the so-called *'Douglas-Neumann'* method, to calculate the inviscid potential flow field about a multi-element aerofoil. This method made it possible for the first time to analyze flows past bodies of realistic geometry and is especially well suited for interference problems like those seen about a multi-element aerofoil. By suitably refining the method the solution can be made as accurate as desired and is consequently thought of as an exact method.

The chordwise profile of each element of the multi-element aerofoil can be approximated by a closed polygon of N planar panels. Source and vortex singularities are distributed over the body surface so as to make the total field tangent to the body at the mid-point of each panel. After employing this flow condition the potential flow becomes unique if the circulation is specified, which is the net vortex strength. Following Smith et al (1966), the source strength is taken as constant on each panel but variable from one panel to the next. Hence there are N source strengths to be determined and the vortex strength. The integral flow equation defining the velocity potential at any point in the flow yields N simultaneous equations. By imposing the Kutta condition in the form in which we equate the tangential velocity components on the panels adjacent to the trailing edge we obtain the final necessary equation to solve for the $N+1$ unknowns. Once solved the tangential velocity at the mid-point of each panel can be calculated and hence C_p. Lift and pitching moment are estimated by assuming C_p is constant over each panel.

A dominant factor in determining the aerodynamic performance of a multi-element aerofoil is the presence of viscous boundary layers and more importantly their behaviour with increasing incidence. Mavriplis (1971) concluded that confluent boundary layers were largely responsible for the discrepancies between inviscid potential flow theory and experiment. The theoretical codes of Stevens et al (1971) and Callaghan et al (1972) represent early attempts at modelling viscous flow about two-dimensional multi-element aerofoils. Continued usage of the Stevens et al (1971) program has resulted in improved versions and Brune et al (1978) detail modifications undertaken on the original code. These include the method by which the outer potential flow is affected by the viscous flow over the aerofoil surfaces. Previously the displacement thickness of the boundary layer was added directly to the aerofoil geometry to form a new 'equivalent' body. This was replaced by an equivalent distribution of sources along the aerofoil contours and wake centre lines which simulates the growth of the boundary layers and wakes. The method is called the surface transpiration technique and the source strengths are proportional to

$$\frac{d}{ds}(\delta^* u) \qquad (1\text{-}1)$$

u is the inviscid flow velocity that would be seen at the aerofoil surface in the absence of viscosity.

The properties of turbulent wakes are analyzed with the lag-entrainment method of Green et al (1973). The method is formulated in terms of the momentum integral equation (Von Karman, 1921), the lag-entrainment equation and an empirical equation for the streamwise rate of change of the entrainment coefficient. The entrainment equation is derived from the definition of the entrainment coefficient which represents the non-dimensional rate at which fluid enters the boundary layer from the external inviscid flow. Drag prediction is achieved using the method of Squire & Young (1937). The program computes confluent boundary layer development with the model of Goradia (1971), whereby development is divided into three regions. In the first, turbulent mixing of wake and boundary layer is

incomplete. In the second, the effect of the wake is no longer visible in the mean velocity profile which is similar to that of a wall jet. Finally, the confluent boundary layer degenerates into an ordinary boundary layer.

The calculation of lift is primarily an inviscid problem requiring only a viscous correction for boundary layer displacement and entrainment effects. In contrast the prediction of drag with comparable accuracy is more formidable because aerofoil drag, a result of viscous phenomena, depends on the accurate prediction of the details of the laminar and turbulent viscous flow and the interaction of the viscous flow with the inviscid flow. Brune et al (1978) found that a direct extension of the method of Squire & Young to calculate drag on multi-element aerofoils does not produce acceptable results. This is because the technique uses a generalised parametric formula for the pressure distribution in the wake which was derived from data from one single element aerofoil.

The analysis of conventional boundary layers assumes that static pressure across the layer is constant (neglecting the effects of curvature). The static pressure gradient at the upper edge of the wake is not necessarily equal to that at the lower edge. This effect is more pronounced as the curvature of the wake increases. Olson et al (1978) calculate the drag from the momentum defect in the wake at a distance of 0.5 to 2.0 chords downstream of the aerofoil trailing edge by assuming that the static pressure varies linearly between the potential flow pressure at the lower and upper edge of the wake. The magnitudes of the velocity defects present in the confluent boundary layers and wakes are dependant upon an accurate eddy-viscosity model for both regions of the viscous flow. The code accurately predicted the $dC_L/d\alpha$ curve between -5° and +10° of a two element aerofoil (NACA 4412 with single slotted flap deflected 10°) although drag prediction was somewhat less accurate. They conclude that future efforts should consider high incidences and flap loadings in configurations where wake/boundary layer merging is more significant.

Oskam et al (1984) deal with two aspects of the computational fluid dynamic problems that are associated with high lift systems, one which Oskam raised himself (Oskam, 1980) being the computation of turbulent wakes in adverse pressure gradients. This flow process is unique to multi-component aerofoils and occurs where a trailing edge static pressure is less than the free stream value. A large amplification is seen to occur in the displacement thickness of the wake due to interaction between the viscous and inviscid flow. In extreme cases it is possible to have flow reversal towards the centre line of the wake. By analysing a turbulent wake and employing classic boundary layer assumptions it is found that in general a turbulent boundary layer separates at approximately $H = 2.35$ while turbulent wakes exhibit reversed flow when $H > 4$. More importantly by modelling more accurately the behaviour of a wing wake in an adverse pressure gradient it was found that the wing wake displacement development with incidence had an equivalent inviscid effect on the flap surface pressures.

In the UK, collaboration between BAe and RAE produced a method, called *MAVIS*, for calculating the flow about two-dimensional high lift systems (Williams & Butter, 1980). The inviscid incompressible potential flow solution at the heart of the scheme was developed

by Newling (1977) and solves the standard Laplace equation by using the external Neumann boundary conditions as employed by Smith et al (1966). However, instead of arbitrarily choosing either the source or vortex distribution on the surface of the aerofoil, the method solves for both as unknowns. For computing reasons they employ a constant source strength at each panel mid-point and a linear vorticity distribution defined at the panel edges. The Kutta condition in its implicit form is employed at the trailing edge by equating the vortex strengths on the upper and lower surfaces to zero. This is done to prevent a poorly conditioned matrix from forming if the geometry is such that the trailing edge is cusped. Normal matrix algebra is used to solve for all the unknowns.

The viscous calculation uses integral methods to predict the development of the shear layers once the inviscid potential pressure distribution is known. Finite difference methods would be more accurate (if higher order terms are included) but to do this correctly demands something approaching a solution of the full time-averaged N-S equations. A small loss in accuracy is accepted in order to obtain a sufficiently fast solution. The laminar portion of the boundary layer is calculated by the method due to Thwaites (1960). Transition is predicted by the empirical correlation of Granville (1953) and if laminar separation occurs upstream of natural transition the semi-empirical method of Horton (1967) is used to predict the development of the separation bubble. Turbulent boundary layer growth is calculated by the lag-entrainment method of Green et al (1973) which is also applied to predict wake development downstream of the trailing edges of each element. The interaction between the wake and boundary layer is calculated by the integral method due to Irwin (1974) in which an algebraic expression containing 6 unknowns is used to describe the velocity profile of the boundary layer and a single wake. This method can only model a single wake, but it is a reasonable approximation to add the slat and wing wakes to form a single wake which then interacts with the flap boundary layer.

Agreement between the theoretical code and experiment is good for single element aerofoils at incidences below the stall although the theoretical method does not predict sufficient load at the trailing edge. The interesting test case of a three element aerofoil at a moderate incidence to which MAVIS was applied revealed several short comings. At the heart of the code is the solution of the incompressible potential equations. The panel method has been extended to predict subcritical flows by using the Prandtl-Glauert transformation but again this is essentially a scaling factor. Consequently the method cannot handle shock waves and peak suctions seen on the upper surface of the slat element tend to be over estimated. On the flap, MAVIS predicted a separation about 3/4 of the chord back from the leading edge although this was not seen during experiments. The trailing edge parameters were then in error giving rise to the incorrectly predicted C_D particularly at high lift coefficients.

The performance of a multi-element aerofoil (as are all aerofoils) is limited by the stall. An aerofoil designer needs to predict with confidence the angle of incidence at which the stall occurs and the lift and drag coefficients at and beyond the stall. In effect a designer would like to predict the viscous effects for both attached and separated flow.

Williams (1985) extends VII techniques for use with separated flows. When integral methods are used to calculate the shear layers present close to the surface of an aerofoil several obstacles occur to the mathematical process when separation appears. Firstly an integral of the boundary layer equations with a specified pressure distribution will encounter a singularity at the point of separation. The second obstacle is the integration of the boundary layer equations through the separated region in which the velocity profile has reversed flow. Le Balleur (1981) has developed empirical two parameter velocity profile families which can be used to describe both attached and separated flows. These can be included in the integral boundary layer method to give satisfactory predictions of separated flow. The third obstacle is concerned with matching of the outer inviscid flow and a separated boundary layer which no longer obeys classical approximations. This difficulty is overcome by extending the inviscid flow calculation through the shear layer to the aerofoil surface and a convenient inviscid streamline in the wake, subject to real viscous flow boundary conditions. The final obstacle is concerned with obtaining convergence in the matching of the outer inviscid flow and the inner shear layer. It is found that the direct scheme is generally unstable for separated flows. The fully inverse method is stable for separated flows but the relaxation factor (a numerical parameter associated with the convergence rate in the mathematical techniques) is inversely proportional to the size of the computational domain resulting in slow convergence for external aerodynamics. The semi-inverse scheme is stable for separated flows and allows the relaxation factor to take different values at different locations along the aerofoil surface depending upon the state of the boundary layer. With a semi-inverse scheme a direct inviscid calculation is matched (ie. pressure calculation from specified shape) with an inverse shear layer calculation (pressure gradient found from boundary layer development). In the inverse boundary layer calculation an estimate of the normalised transpiration velocity provides an estimate of the tangential velocity at the surface (U_{iw}) in the equivalent inviscid flow The estimated normalised transpiration is then used as a boundary condition in the direct inviscid method to yield another estimate of U_{iw} in the equivalent inviscid flow. The difference between the two estimates of U_{iw} is used to correct the normalised transpiration velocity and the two simultaneous calculations are then repeated.

Detailed measurements of the separated flow on a single element NACA 4412 aerofoil at two different Reynolds numbers are compared with results obtained using both the semi-inverse method and the direct method noting here that the boundary layer calculations are done by the same methods as employed in MAVIS. The direct method of coupling is shown to produce results which disagree with experimental values as soon as there is a significant region of separated flow on the aerofoil. The semi-inverse method adequately predicts the lift up to and beyond stall although there are detailed differences in the surface pressure distribution. A good estimate of the drag for separated flows cannot be made until the boundary layer method includes second order terms which are felt to be significant in separated flow. No universal correlation for normal stress in terms of integral parameters of the boundary layer for separating flows has yet been established. The method ignores the effect of wake curvature which would be significant for a multi-element aerofoil.

Lock and Williams (1987) recognised that VII techniques had reached an advanced state of development and so undertook an extensive review of the subject. This timely paper provides a physical background to the subject and covers the basic theoretical principles of interactive methods for two dimensions. An account is given of the corresponding treatment in three dimensions and mathematical coupling techniques are discussed in detail. A number of recent VII methods are reviewed and their results compared with experimental data. The interested reader is guided towards this paper if more information is required as it covers single and multi-element aerofoils in low speed and transonic flow.

King and Williams (1988) summarize recent developments in computational methods for high lift aerofoils. As discussed previously, codes such as MAVIS and HILDA give reasonable predictions of lift for viscous attached flow but fail to give an estimate of C_{Lmax} and associated flow separations. Improvements will be seen if the following are modelled i) compressible inviscid flow, ii) curved wakes in an adverse pressure gradient and their confluence with boundary layers and iii) a method of coupling inviscid and viscous flows which will allow the calculation of separated flow in cove regions and at trailing edges.

For incompressible flow linear surface-singularity methods have proved to be very popular for high lift calculations in two and three dimensions since a computational mesh is not required in the field. Several attempts have been made to build the effects of compressibility into linear incompressible surface-singularity methods but the methods are restricted to subcritical flow. The complex geometry associated with high lift aerofoils makes the calculation of compressible flow difficult but necessary.

Hall et al (1984) use a finite difference technique to solve the non-linear compressible potential equations with the grid produced by conformal mapping but as mentioned previously this method is restricted to two element aerofoils. Oskam (1983) and Hill et al (1986) both generate boundary conforming grids in regions where compressibility effects are likely to be significant. The full potential equations within the grids are solved by a variety of field methods (finite difference, finite volume) with the boundary conditions on three sides of the grid provided by linear surface-singularity methods whilst the fourth is the aerofoil surface. Both methods suffer the disadvantage that regions in which compressibility effects are important must be known in advance - relatively easy for two dimensions but very difficult for a three dimensional layout.

With direct coupling schemes discontinuities in surface slopes must be faired in by some convenient curve which should represent the displacement effect of the separation bubble. Direct coupling schemes are unable to calculate separated flow in these regions. If supersonic flow at the slat leading edge produces separation and turbulent re-attachment direct coupling schemes will be unable to model this underestimating lift and drag.

If an integral method is used to calculate the development of the boundary layer it can be shown (Lock and Williams, 1987) for attached flow

$$\frac{d}{dS}\left(\frac{dU}{ds}\right)<0 \qquad \text{(1-2)}$$

for separating flow

$$\frac{d}{dS}\left(\frac{dU}{ds}\right)=0 \quad \ldots\ldots\ldots\ldots\ldots\ldots\ldots\ldots \quad (1\text{-}3)$$

and for separated flow

$$\frac{d}{dS}\left(\frac{dU}{ds}\right)>0 \quad \ldots\ldots\ldots\ldots\ldots\ldots\ldots\ldots \quad (1\text{-}4)$$

Here, dU/ds is the streamwise velocity gradient along the surface of the aerofoil and S is the non-dimensional source strength. These equations summarise some of the known characteristics of boundary layers developing in adverse pressure gradients. For attached flow the slope of the viscous curve is large and negative; for separating flow the slope is zero; whilst for separated flow the slope is positive and small. Considering the case for attached flow an initial guess for the non-dimensional source strength S in a direct coupling scheme leads to a first approximation to the velocity gradient dU/ds from a solution to the inviscid equation. This estimate of the velocity gradient is used to calculate the develpment of the boundary layer which gives a new estimate for the rate of growth of the boundary layer. This new estimate is used to recalculate the inviscid flow and the process is repeated until convergence is achieved.

The local shape of the viscous and inviscid curves determines the convergence characteristics of a solution method. An ability to predict separation using the semi-inverse scheme is achieved through a thorough analysis of the coupling nature between viscous and inviscid solutions. The basic feature of this method is that two estimates of the velocity gradient are given by solutions of the direct inviscid method and inverse viscous method. The difference in the velocity gradients is used in a correction formula to improve the viscous and inviscid calculations. However, the method does not include an allowance for the confluence of the wake and boundary layer over the flap as no inverse procedure exists for such a calculation. Hence flap separation is unlikely to be modelled correctly.

The quasi-simultaneous coupling scheme uses both estimates of velocity gradient obtained from the viscous and inviscid solutions in a closer coupling technique which results in a scheme which is faster to converge than the semi-inverse method. The viscous flow equations are essentially solved in the direct mode and Oskam et al (1984) employed the technique for calculating the wake development above the flap in a high lift system. For a comprehensive explanation to coupling techniques and convergence characteristics of Viscous-Inviscid Interaction methods the reader is guided to Lock and Williams (1987).

FELMA represents a compressible finite element method for calculating the flow about multi-element aerofoils. It was developed by King et al (1988) and obtains its viscous solution from the method developed by Butter et al (1980) in MAVIS/HILDA. The governing flow equations of compressible inviscid flow are discretised on a grid surrounding the high lift system. This grid must possess certain properties to ensure that the numerical solution is accurate and consistent. The grid mesh should be orthogonal and the cell aspect ratio close

to one in regions where the velocity gradients are likely to be high. Boundary conditions are more easily applied if the grid is aligned to the geometric surfaces. These properties are obtained by defining a flow grid based on incompressible potential flow streamlines and equi-potentials for each setting of the separate high lift elements. Shock waves, if present, should be represented by the inviscid method. However, since the supersonic flow is a local feature, it should be adequate to solve the transonic potential equation rather than the full Euler equations. A finite element method discretises the governing equation and the problem posed in an integral form. A compressible version of Thwaites laminar boundary layer model is used for the laminar portion of the boundary layer. Transition and turbulent boundary layers are modelled in the same ways as found in MAVIS. The second order terms for longitudinal curvature of the displacement surface are included but not those for normal stress or normal pressure gradient. Currently there is no explicit modelling of the interaction between the wake from one component and the boundary layer on the upper surface of a downstream element. A single wake calculation is performed at the flap trailing edge by combining the flow properties for the upper and lower surfaces at the trailing edge.

The coupling between the viscous flow and the outer equivalent inviscid flow can be performed in a variety of ways within FELMA. A semi-inverse coupling can be used but in practice this approach has difficulties operating in a steep favourable pressure gradient. Therefore either a mix of direct and semi-inverse coupling is used or alternatively the quasi-simultaneous approach is employed which has the added advantage of converging faster. The method accurately predicts C_{Lmax} and gives reasonable values of drag for a simple two-element configuration. It has demonstrated its ability to predict flow separation on various components of a multi-element aerofoil and shock waves on slats. Despite the fact that there are several enhancements that could yet be made to the viscous method, FELMA offers a standard of flow prediction not previously available to the high lift designer.

Closing remarks: Although the results achieved by VII techniques like FELMA are impressive there are some areas of the flow which may require a solution of the time-averaged N-S equations if they are to be described adequately. This is no more evident than in regions where wake/boundary layer interactions occur. A future crucial ingredient in any theoretical method will be its ability to address wake development in the pressure field of a downstream element. The resulting wake curvature has a significant effect upon the turbulent structure within the wake. The large pressure gradients existing across the wake call into question the classical boundary layer approximations. Initial calculations indicate that the inclusion of the longitudinal strain rate term in any turbulence model has a significant effect upon the predicted lift and drag.

Even with the advent of supercomputers, most N-S methods are severely limited by (a) excessively long computing times as the grid is refined close to the surface and (b) inadequacies in turbulence modelling. These problems can be overcome by a zonal approach in which the N-S equations are solved in zones close to the aerofoil and the Euler equations solved in the remaining flow field. Flores et al (1986) use a zonal approach for the flow past a transonic wing. This scheme suggests a mechanism by which a N-S solution for the flow

over the flap of a multi-element aerofoil could be coupled to a solution of the inviscid and boundary layer equations for the rest of the aerofoil. Such a method would have the potential of producing more accurate predictions of lift and drag up to stall within a timescale suitable for the aircraft designer.

1.2.1.2 Experimental

Nearly all of the basic principles for influencing a flow to develop high lift have been known from the very early days of the aeroplane. The ancestry of flaps can be traced back to ARC R&M 110 (1914) which details experiments carried out on a RAF 9 aerofoil having a 0.385c plain flap. Slats were first conceived to eliminate leading edge stall on thin biplane wings during the first world war. Handley Page in his lecture to the *Royal Aeronautical Society* on February 17th 1921 described ten years of work on aerofoils that had slots. One of his extreme aerofoils (fig. 1.3) investigates the effect on lift by heavily modifying a RAF 19 section into an eight element aerofoil (see below).

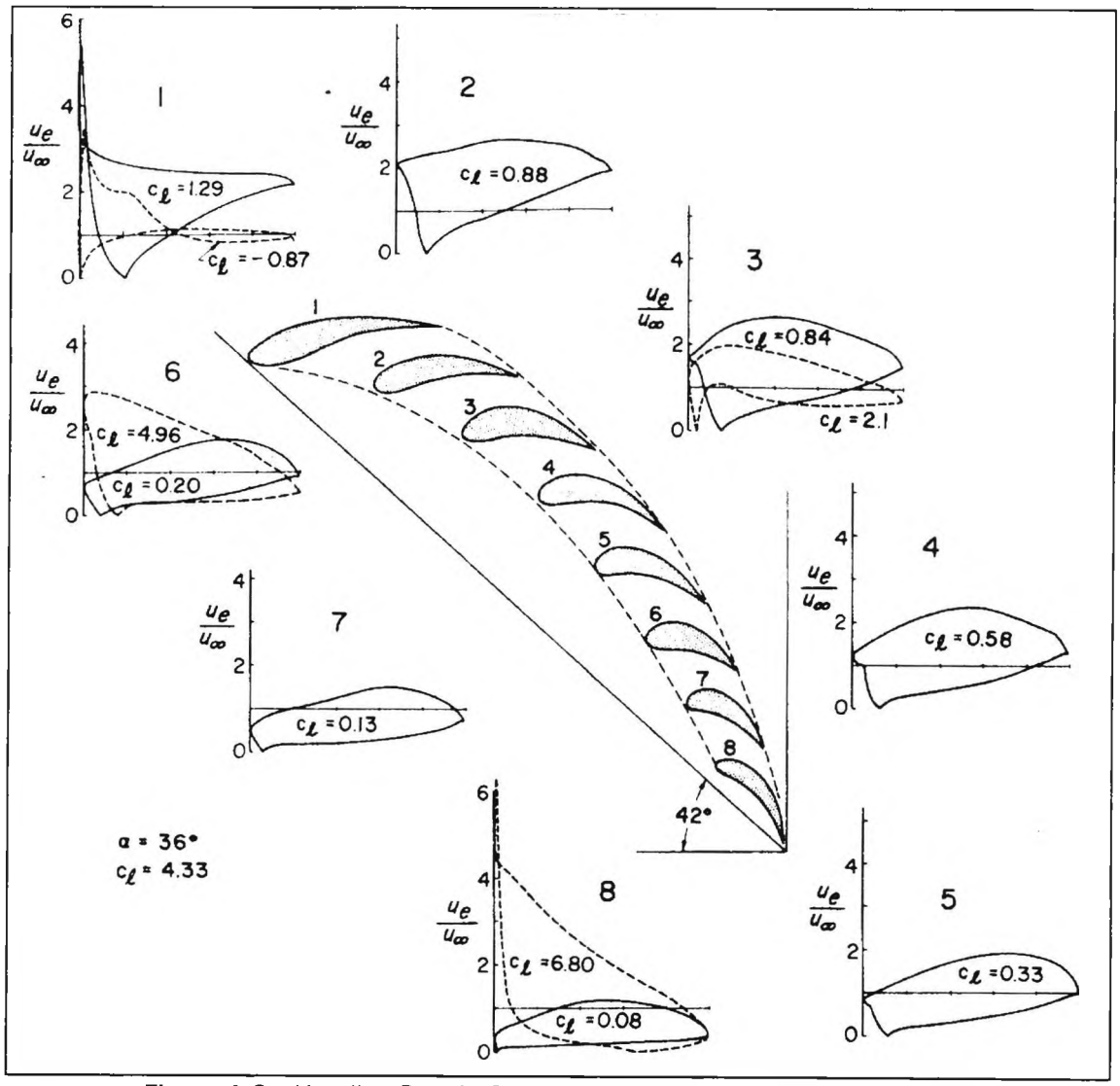

Figure 1.3 : Handley Page's 8 element aerofoil, α = 42°, C_L = 4.33

The flap became a device of practical importance in the 1930's and 1940's after successful concerted efforts were made to reduce profile drag and increase wing loadings of wartime aircraft. As a consequence gliding angles decreased and take off and landing speeds

increased until landing and take-off difficulties threatened to offset further aerodynamic advantages. The flap was then adopted as the obvious solution as it provided lift to reduce stalling speed and drag to increase the glide angle. The demands of the Fleet Air Arm hastened flap development with its stringent landing and take-off requirements. Alston (1935), Duddy (1949) and Young (1947) all examine the basic characteristics of various flap configurations.

Abbott et al (1949) quote a maximum lift coefficient of 2.6 for a wing with a double slotted flap and a leading edge slat. During the 1950's and 1960's a large amount of work was done on two-dimensional high lift research and by the early seventies the figure of 2.6 had risen to over 5 for a similar configuration. However the research often involved boundary layer control in the form of jet flaps or boundary layer suction slots. Relatively little attention was paid to increasing the efficiency of mechanical devices probably due to an under estimation of their high lift potential. Consequently high lift wing design became a heuristic process heavily dependant upon experimental data obtained previously with improvements tending to be small. The *Airbus A300B* high lift system was developed from the *Trident 1E* system. It became apparent that fundamental work on high lift systems was necessary, independent of the pressure of project time constraints.

Between 1970 and 1978 an extensive programme of high lift research undertaken on both 2 -dimensional aerofoils and 3-dimensional wings led to the design and testing of a large number of different high lift devices as part of the UK government funded *National High Lift Programme*. The origins of the *A320* high lift system are to be found in this work.

Foster et al (1970) describe experimental measurements and a theoretical analysis of the flow around a wing with a single slotted flap. They found that flap gap variation resulted in much larger changes of lift than variation of overlap. In addition, the lift generated by the flap was seen to vary in a manner similar to that predicted by inviscid potential theory. This was the case only if a region of flow with freestream total pressure separated the main wing wake and flap upper surface boundary layer.

Ljungstrom (1972) carried out boundary layer studies on a 2-dimensional wing model equipped with a leading edge slat and a trailing edge flap. He found that the downwash efficiency of the wing and flap flow was sensitive to the mixing time history of the slat wake and the main wing upper surface boundary layer. Increasing the slat gap size was found to increase the skin friction values seen at the main wing trailing edge. A similar effect was found if boundary layer suction was applied at the trailing edge of the slat upper surface. Less mixing seemed to create a more stable boundary layer and hence delay separation. Quinn (1947) carried out similar tests on a NACA 64A212 aerofoil achieving a C_{Lmax} of 3.86 with boundary layer suction at 40% chord on the main wing. He also found that the combination of leading edge slat and double slotted flap with boundary layer suction was insensitive to scale effect.

Due to the multiply connected nature of the flow about a high lift system, slats or trailing edge flaps cannot be treated separately when seeking an optimised profile for the multi-element aerofoil. Often, the slat position has a substantial viscous effect on the flow

over the main wing and flap elements while the flap primarily has an inviscid effect on the flow about the slat (the degree of these effects obviously depends on the relative spacing between the sections involved, particulalrly the slat gap/lap). The competing effects of favourable inviscid interaction (ultimately limited by compressibility effects) and adverse viscous effects (contamination of downstream boundary layers by upstream wakes) leads to the existence of an optimum position for each element of the high lift system. McRae (1973) illustrated that one device design optimisation exercise involves the angle, gap and lap of the slat, flap and if appropriate the tab as well. Each individual optimisation will cover about three variables with four or five values of each. This totals about 100 runs for each device before considering the variables of Reynolds number and Mach number. Butter (1984) outlines methods for reducing the cost and timescale that a programme of such size would entail but justifies optimisation procedures through the improvements that would result. A 5% improvement in take-off C_{Lmax} enables a 12-15% increase in payload. A 5% improvement in take-off L/D allows a 20% increase in payload while a 5% improvement in landing C_{Lmax} would lead to a 25% increase in payload. Ljungstrom (1974) surmises that the lift generated by a multi-element aerofoil is more sensitive to the optimisation of gap and angle parameters than the overlap values of each element.

Van den Berg (1979) undertook surface pressure measurements, boundary layer/wake traverses and surface flow visualizations on a two element high lift system at three angles of attack using two different flap gap settings. Although the work is useful to the theoretician, direct information on the viscous effects was not available.

The transport of energy and momentum by turbulence that is present in the flow around a multi-element aerofoil can have a dominant role determining its performance. The optimisation of multi-element aerofoils is dependant on sufficient knowledge and understanding of these turbulent transport processes. Olson (1981) investigates the structure of the attached flow in the vicinity of a NACA 4412 aerofoil equipped with a NACA 4415 single slotted flap. Detailed measurements of the mean velocity flow field and of the second order Reynolds stresses in the boundary layers, wakes and merging shear layers were carried out to provide information useful for the development of improved turbulence models that are needed for analysis of multi-element aerofoil configurations.

Similar measurements by Nakayama et al (1990) on a three element aerofoil reveal considerable static pressure gradients exist in the thick shear layers above the flap. With considerable flap deflections curvature effects may be so strong that flow reversal in the near wake is feasible. Overall the data indicates that the shear flows are very different from classical shear layers.

A viscous interaction occurs when the boundary layer on the upper surface of the flap becomes confluent with the main wing wake prior to reaching the trailing edge of the flap. Moser et al (1973) also show that where potential flow is present between the main wing wake and flap boundary layer (ie. viscous stresses caused by wake in flap boundary layer are absent) a loss of flap lift still occurs. That is, the presence of the main wing wake has an inviscid effect on the lift of the flap. This can be beneficial in that the onset of flow separation

on the flap can be delayed, possibly resulting in a favourable development of the stall and a better maximum lift.

Both Fiddes et al (1984) and Thain (1973) investigate the effects of scale and compressibility on the lift and drag of high lift aerofoils. At freestream Mach numbers as low as 0.2, sonic flow on the upper surface of the slat can be terminated by a small local shock which in turn can induce local separation of the boundary layer. If this occurs the boundary layer will thicken rapidly as it progresses over the wing upper surface with a consequent degradation in the flow over the flap. The resulting decrease in circulation causes loss of lift and often determines C_{Lmax}. Alleviating this effect either by increasing the angle of rotation of the slat or moving it away from the main wing will reduce favourable inviscid interaction and hence raise the suction peak on the main wing, until it in turn suffers compressibility effects or premature separation. Hence at constant Reynolds number high lift aerofoils are adversely sensitive to Mach number effects as supercritical flow is approached over the slat or main wing. Increasing Reynolds number at a constant Mach number is seen to allow the slat to move nearer to the main wing. This is consistent with thinner shear layers allowing more movement towards the main wing before adverse boundary layer interaction occurs although the effect is not as marked as that seen with Mach number variation. With boundary layer control a high lift system would be expected to be less sensitive to Reynolds number effects as the boundary layer itself would be more tolerant to its own mixing time history as confirmed by Quinn (1947).

Butter (1984) and Ljungstrom (1972) believe that although progress will still be made in the understanding of high lift flows there will remain a margin of improvement which will only be achieved with the use of active boundary layer control. This is due to practical limitations on the ability to engineer variable geometry aerofoils. Aircraft through conforming with airworthiness requirements must provide protection against atmospheric disturbances and engine failures. Consequently high lift devices are deployed to larger deflection angles than are often required generating unnecessary drag which would not be the case if these margins did not have to be permanently provided. This could be avoided if active boundary layer control were available when required allowing rapid demand and employment with little effect on engine and thrust performance. Take-off and landing manoeuvres could be programmed to be controlled in the most efficient manner in parallel with the use of the mechanical high lift devices to minimise drag and the demands made on the active control system. Extending this to c.g. control and relaxed stability result in powerful ways of improving high lift performance.

1.2.2 Vortex generators

Until very recently computational fluid dynamic techniques have been unable to predict the effect of a streamwise vortex on the characteristics of a two-dimensional turbulent boundary layer in an adverse pressure gradient. Consequently the vast majority of work undertaken on vortex generators has been experimental in nature.

Vane vortex generators have found applications in areas such as the improvement of aircraft buffet boundaries as a result of postponing shock-induced separation, low Reynolds

number aerofoils, inlets and diffusers, aircraft stall/spin control and drag reduction. Vortex production in a turbulent boundary layer is also of interest in areas such as noise reduction and heat transfer.

The principle of boundary layer control by vortex generators in the form that we now know them was first conceived by Bruynes and Taylor of the United Aircraft Corporation in 1950. Pearcey (1961) presented an extensive review of measurements for a wide range of vortex generator arrays. Using measurements of mean axial velocity he tracked the locations of the vortices and determined the extent of boundary layer modification due to their presence. He developed empirical rules for the design of vane vortex generator arrays to forestall boundary layer separation. Spangler and Wells (1964) concluded that vortices substantially increase the skin friction in downwash regions where the boundary layer is thinned. Mehta (1983) provides a detailed set of data at a single streamwise location for each of two embedded vortex pairs. The focus of the work was on the turbulent structure in the disturbed boundary layer. Westphal et al (1985) examined the development of single vortices in a zero and small adverse pressure gradient. Pauley et al (1988) extend Westphal's work to 16 different vortex pairs and two regular arrays embedded in a zero pressure gradient turbulent boundary layer. In general the study of the development of streamwise vortices embedded in a turbulent boundary layer has been carried out in conditions with zero or little adverse pressure gradient (ie. flat plate or windtunnel wall).

Fixed solid vane vortex generators suffer from the penalty of producing parasitic drag in flow situations where flow separation control is unnecessary. The increased drag results from a combination of higher levels of skin friction drag and induced drag.

Rao et al (1988) investigate the ability of submerged vortex generators to alleviate separation in a turbulent boundary layer encountering a two-dimensional adverse pressure gradient of sufficient severity to ensure complete separation (on the flat plate) in the absence of boundary layer control. The vortices were generated from crest-line separations on cylindrical rods of semi-circular cross-section, or from the sharp trailing edges of concave slats. The vortex generators were immersed within the boundary layer (62.5% or less of δ), fixed on the plate obliquely to the freestream and arranged in parallel or vee configurations. The results of the investigation show that an optimum arrangement of the concave slat vortex generator has the potential to perform as well as conventional vane type vortex generators. Moreover, due to their reduced scale this can be done with reduced parasitic drag at optimum design conditions. Lin et al (1990) investigate the Wheeler doublet and wishbone type submerged vortex generators. They find that device drag increases exponentially with device height with the wishbone vortex generators enhancing separation at a device height of the order of 5% of δ (ie. functioning more as surface roughness elements rather than boundary layer control devices). At or above a height of 8% of δ they became effective in controlling the boundary layer separation. This figure coincides with the termination of the inner (log) region of the boundary layer giving what appears to be a lower limit to the height of these devices.

Jets of air issuing through small holes in a flow surface have proven effective in the control of turbulent boundary layer separation. The method was first examined by Wallis (1952) to eliminate laminar separation at the leading edges of thin wings after Fage et al (1944) used the method to fix boundary layer transition.

When an airjet issues into a stream normal to the flow direction two counter-rotating vortices are formed, one on each spanwise edge of the jet. Wallis (1956) found that by skewing the jet and thereby introducing some degree of cross-flow component, each jet produced a single persistent vortex. Wallis et al (1958) and Pearcey (1961) examine the possibility of using airjets to alleviate shock induced separation. A continuation of this work by Rao (1988) revealed (i) the physical mechanism of vortex production by an airjet and (ii) the performance of an optimum arrangement of airjets to be comparable to that of a system of conventional vane vortex generators in their ability to prevent this type of separation.

Zhang et al (1987) and Compton et al (1992) investigate the effect of a simple round airjet on the characteristics of an oncoming turbulent boundary layer in a zero adverse pressure gradient.

A parametric study by Selby et al (1992) found that when compared to slot blowing, circular airjet vortex generators provided an equivalent level of flow control over a two-dimensional rearward facing ramp. With jet exit area and speed also taken into account the circular airjets were found to be effective over a larger spanwise region.

Johnston et al (1989) use adaptive wall technology to impose a strong adverse pressure gradient upon the opposite flat wall of a low speed wind tunnel in which are embedded various arrays of circular airjets. By comparing skin friction measurements with those generated by Pauley et al (1988) using vane vortex generators, Johnston surmises that airjets generate vortices of similar strength to those shed from vane vortex generators. More specifically it was shown that a substantial reduction in the size of the stall region occurs for airjet velocities above 80% of local velocity, although an assumption is made that an improvement in the control of flow separation would not be seen if this figure is increased above 100%!

More recently work by Akanni et al (1994) has shown that it is possible to model numerically the three-dimensional flowfield created by pitched and skewed airjets issuing into an otherwise undisturbed incompressible turbulent boundary layer. It was demonstrated that each airjet produces a single strong longitudinal vortex and that the strength of this vortex was influenced by pitch and skew angles, exit velocity and downstream distance in ways which accord with published experimental results.

With the present interest in high lift systems and the current emphasis on increased performance near stall there may be considerable benefits to be gained if airjet vortex generators are applied to high lift aerofoils.

1.3 Objectives

Firstly, a representative high lift system had to be chosen and it was decided through consultations with British Aerospace that a system similar to that found on the Airbus A320 would be suitable for the current work. It would consist of a Handley Page leading edge slat

and a trailing edge Fowler flap. The fundamental nature of the work was such that two-dimensional testing was felt to be of more benefit than a three-dimensional half model swept wing.

Although the ultimate objective of the work was to examine the possibility of improving the performance of high lift systems through the use of airjet vortex generators, early work was to be conducted using vane vortex generators. This was done for comparative reasons. Previous work established that the effects of vanes are near enough analogous to airjets and therefore a broad survey of the possibilities and prospects of these would be obtained by the initial use of vanes.

Approaching the problem from this point of view would allow a model to be constructed from three solid elements ie. without the provision for ducting air to airjet vortex generators. This would minimise the initial model manufacturing time and cost and an early assessment could be made of the effects of various vane vortex generator configurations on the two-dimensional stalling characteristics of the high lift system. Any flow problems which might become apparent during initial testing could then be tackled in the design of the second model which would be specifically for airjets.

The effect of airjet vortex generators on the stall of the high lift system would be investigated in detail and an evaluation made of their potential for use in active stall control.

Running parallel with the initial testing phase would be the commissioning of a new data acquisition system to be ready for use in tests involving airjet vortex generators.

2. Theory

2.1 High lift systems

The problem of obtaining high lift is that of developing the lift in the presence of boundary layers - getting all the lift possible without causing separation. Provided that boundary layer control is not used, our only means of obtaining more lift is to modify the geometry of the aerofoil. For a single element aerofoil there are several means for improvement - changed leading edge radius, a flap, changed camber, a nose flap, a variable camber leading edge and changes in the detailed shape of the pressure distribution.

If more lift is to be generated the circulation around the aerofoil section must be increased, or equivalently, the velocity over the upper surface must be increased relative to the velocity over the lower surface. However, the Kutta condition at the trailing edge requires the upper surface and lower surface velocities assume an equal value. When higher velocities over the upper surface of the aerofoil are produced in order to get more lift, larger pressure gradients are required to decelerate the flow from the maximum velocity to the trailing edge velocity. Again, if this process of deceleration is too severe, separation occurs.

There appear to be five primary mechanisms which enable high lift systems to generate the necessary lift while simultaneously minimizing boundary layer separation. Following the pioneering work of Smith (1975), these are:

(i) Downstream effect - to a first approximation an upstream element can be modelled as a point vortex of strength K in inviscid flow. The flow field produced by a point vortex contains streamlines which are concentric circles. The velocity at any point in the flow is tangential to a streamline and of magnitude $K/2\pi r$ where r is the radial distance from the origin of the point vortex. Consequently, the velocity experienced at any point on the downstream element will be a result of a vectorial sum of the velocity associated with the point vortex and the velocity field associated with the downstream element. The velocities in the vicinity of the leading edge of the downstream element are considerably reduced (and hence the magnitude of the peak suction). In turn the boundary layer on the downstream element negotiates a less severe adverse pressure gradient than that which would be experienced in the absence of the point vortex. The downstream effect decreases in magnitude as one progresses further aft over the downstream element with the pressure distribution tending to that seen in the absence of the point vortex.

(ii) Circulation effect - the corollary of the downstream effect is that the trailing edge of the upstream element is in a region of flow of considerably higher velocity than that seen in the freestream. Since the vortex can now be used to model the circulation on the downstream element it can be placed close to the trailing edge of the upstream element. The velocity field of the point vortex now effectively locates the trailing edge of the upstream element at a high angle of attack. However, reality dictates that the Kutta condition must be met at the trailing edge (ie. tangential flow condition) and so the circulation on the upstream element increases until this condition is satisfied. Unlike the downstream effect where the influence was

localised to the leading edge of the downstream element (in terms of significant magnitude) the circulation effect is felt over the entire surface of the upstream element.

(iii) Dumping effect - this is related to the circulation effect and can be defined as the ratio $(u_{t.e}/u_{max})^2$ where $u_{t.e}$ is the velocity at the trailing edge of the upstream element and u_{max} is the maximum local velocity experienced on the same element. The closer this ratio is to unity implies the boundary layer has experienced a reduced pressure rise thus alleviating potential separation problems which may have arisen otherwise. This is peculiar to the trailing edge region and is strictly only applicable to inviscid flow.

(iv) Off-the-surface pressure recovery - the upper surface boundary layer from the upstream element is shed into the wake at a static pressure significantly lower than freestream static pressure. The recovery to freestream static pressure is achieved out of contact with a surface (ie. zero adverse skin friction forces present) and the dispersion by turbulent mixing of the associated momentum defect is achieved more rapidly since full potential flow is present above and below the wake (initially anyway).

(v) Fresh boundary layer effect - new boundary layers grow from the leading edge of each successive element. Each new boundary layer will have an associated transition region (however small) and will be thinner as it approaches the adverse pressure gradient behind the associated peak suction for the element in question. Thinner that is than had a single boundary negotiated the previous adverse pressure gradients on upstream elements. Thinner boundary layers are better able to withstand strong adverse pressure gradients without incurring separation problems.

2.2 Separation and stall

For many high Reynolds number flows, the flow field may be divided into two regions: (i) a viscous boundary layer adjacent to the surface of the aerofoil and (ii) the essentially inviscid flow outside the boundary layer. The velocity of the fluid particles increases from a value of zero (no-slip) at the wall (body fixed coordinates) to a value which corresponds to the external 'frictionless' flow outside the boundary layer (fig. 2.1). As a result of these velocity gradients, shear forces are relatively large within the boundary layer. Outside the boundary layer, the velocity gradients become so small that the shear stresses acting on a fluid element are negligible. The effect of viscous terms may then be ignored for the flow field external to the boundary layer.

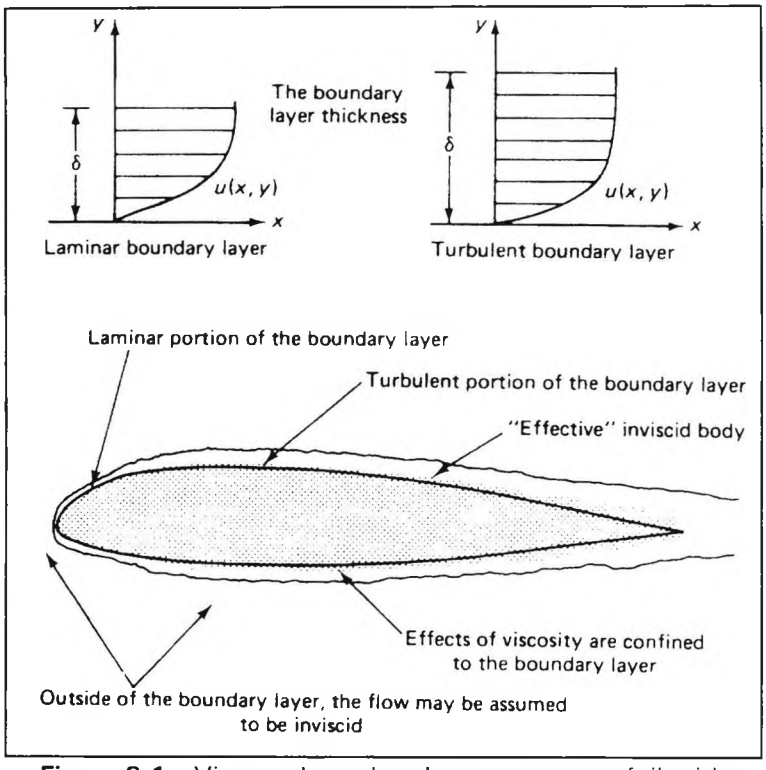

Figure 2.1 : Viscous boundary layer on an aerofoil with attached flow

The loss of lift due to viscosity is comparatively small when viscous effects are confined to thin attached boundary layers. When a boundary layer becomes detached from the surface without re-attachment occurring, very large losses of lift will result with a corresponding increase in drag.

Shear forces and pressure forces act to retard the motion of the flow within a boundary layer. Consequently, continuity of mass flow dictates that the boundary layer will increase in thickness. The slower parts of the flow (near the aerofoil surface) will decelerate to zero speed sooner than will the flow in the outer regions of the boundary layer. Hence, there will appear a locus of points within the boundary layer where u = 0 originating from the aerofoil surface (fig. 2.2).

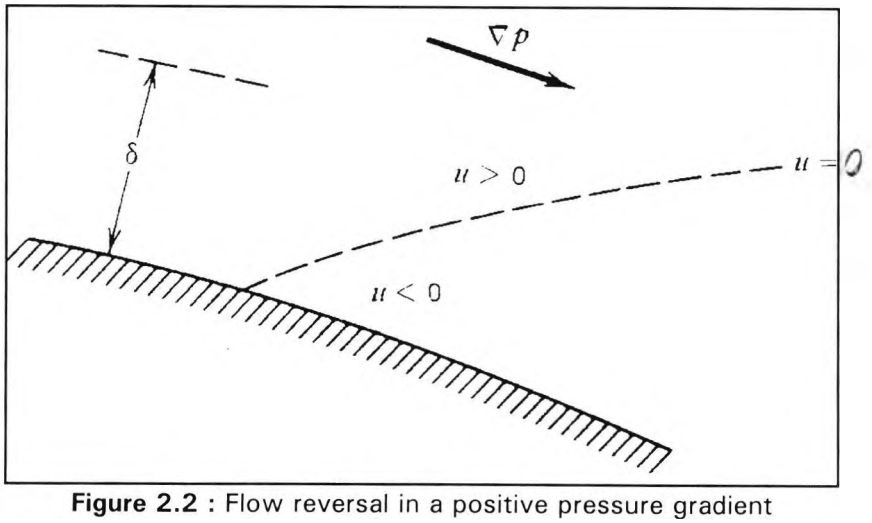

Figure 2.2 : Flow reversal in a positive pressure gradient

With further deceleration u < 0 on the downstream side of the locus and the streamline pattern will be as in figure 2.3. In particular, there must be one streamline which separates streamlines that reverse their direction at the u = 0 locus from those that start further upstream. The origin of this streamline coincides with the point on the aerofoil surface at which u = 0, the separation point, and the flow is said to have separated from the surface as the streamlines no longer follow the surface.

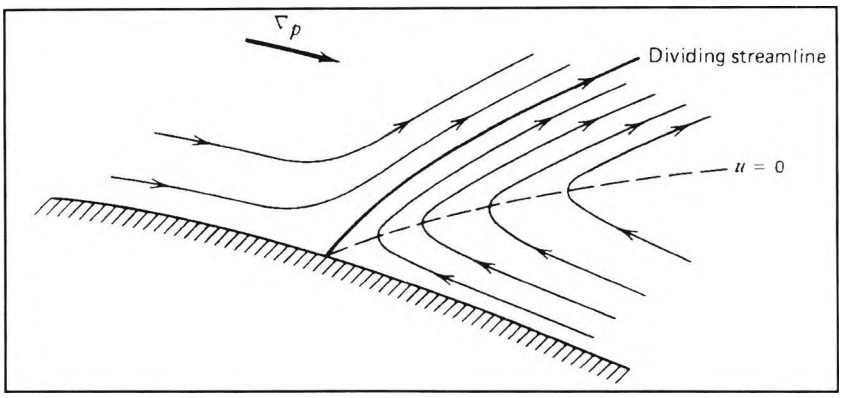

Figure 2.3 : Boundary layer separation in a positive pressure gradient

There are two distinct types of boundary layer flow, laminar and turbulent, the transition process from laminar to turbulent flow occurring over a finite distance known as the transition zone. In the case of flow past an aerofoil, the boundary layer starts as laminar at the stagnation point with a finite thickness. Eventually all laminar boundary layers become unstable and any small disturbance triggers transition to the erratic unsteady condition known as turbulent. Transition starts at a particular value of the Reynolds number based on the distance from the origin of the boundary layer. For a boundary layer on a smooth flat plate, the critical value of the Reynolds number is approximately 2,800,000 depending upon the turbulence in the onset flow. Transition is hastened (ie. the transition Reynolds number is lowered) by many parameters such as surface roughness, surface temperature, positive pressure gradient and Mach number. A turbulent boundary layer may revert back to a laminar boundary layer if the pressure gradient it experiences becomes favourable once again.

When the boundary layer is laminar, a transverse exchange of momentum takes place on a microscopic scale. As a result slower moving particles from the lower layers (laminii) of fluid move upward, conversely faster moving particles from the upper layers migrate downwards tending to accelerate the

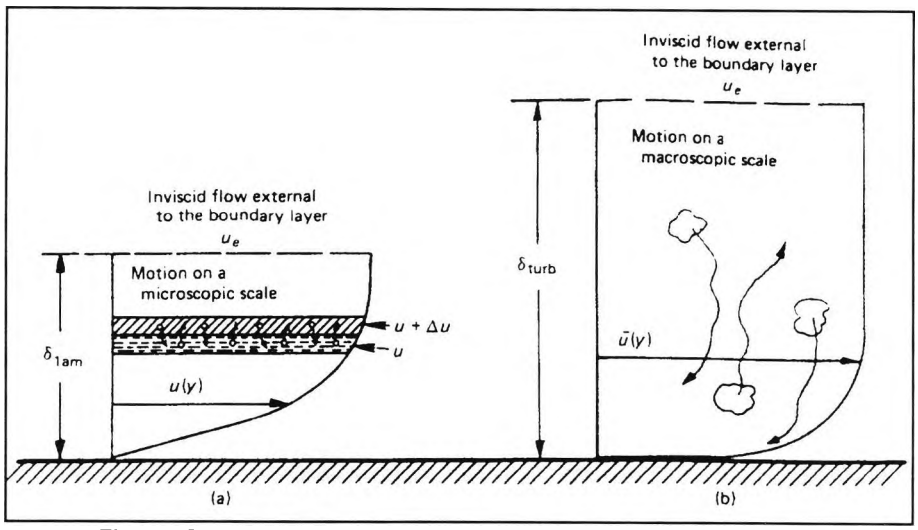

Figure 2.4 : Momentum transport models (a) laminar & (b) turbulent

fluid particles closer to the surface. The laminar boundary layer tends to be relatively thin with limited mass transfer and hence relatively low velocity and pressure gradients exist near the surface with low skin friction (fig. 2.4).

A turbulent boundary layer exhibits a macroscopic transport of fluid particles. Thus in addition to the laminar shear stress there is an effective turbulent shear stress that is due to the transverse transport of momentum. The slower moving particles close to the surface are moved well upward being replaced by relatively high velocity fluid particles from the outer boundary layer. This creates relatively higher shear stresses at the wall than that for a laminar boundary layer. Thus the turbulent boundary layer is thicker with considerably more mass transport. However, the higher velocities near the surface of the aerofoil give rise to higher skin friction.

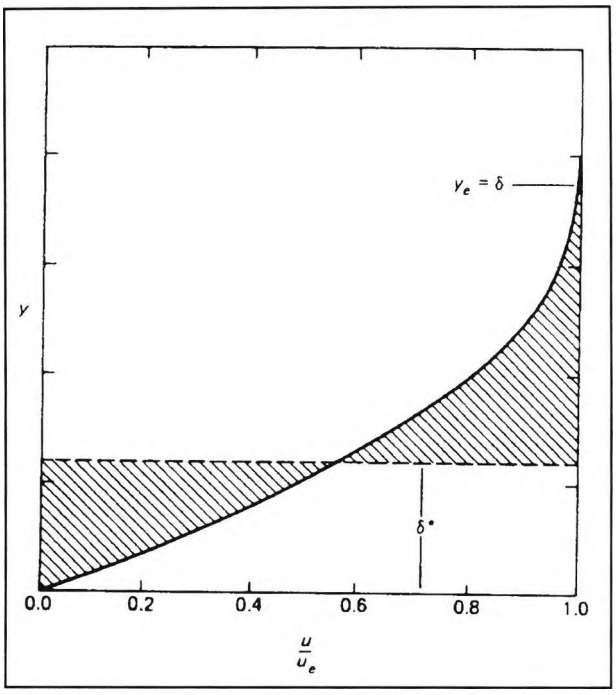

Figure 2.5 : Velocity profile of a boundary layer on a flat plate illustrating the relationship between δ and δ^*

A boundary layer in an adverse pressure gradient will resist separation in proportion to its ability to transfer momentum from its outer regions to the slower ("tired") flow regions closer to the surface. Thus a turbulent boundary layer with its higher rate of momentum transport can survive a higher adverse pressure gradient without separating than can a laminar boundary layer. Yet the thicker the turbulent boundary layer the harder it is to achieve effective momentum transfer and hence the more easily the boundary layer becomes detached from the surface of the aerofoil.

Several parameters are used to describe the state of a boundary layer at a given distance from its origin. The criteria used to define the edge of the boundary layer and thereby its thickness δ is the height at which $u/U_e = 0.995$. A more significant parameter is the displacement thickness of the boundary layer given by

$$\delta^* = \int_0^{\delta} \left(1 - \frac{u}{U_e}\right) dy \cdot \cdots \cdots \cdots \cdots \cdots \cdots \cdots \cdots \quad (2\text{-}1)$$

where U_e = local velocity outside the boundary layer, which can be derived by considering conservation of mass. The source of this name is in fact that it is the distance the external flow streamlines are displaced by the boundary layer. The relationship between δ and δ^* is shown in figure 2.5. By applying the conservation of momentum at the boundary layer origin and at a distance x downstream yields a defining relation for another parameter, the momentum thickness Θ given by

$$\theta = \int_0^{\delta} \frac{u}{U_e}\left(1 - \frac{u}{U_e}\right) dy \quad \ldots\ldots\ldots\ldots\ldots\ldots \quad (2\text{-}2)$$

This indicates the thickness that a layer of external inviscid flow would need to be to carry a momentum flow rate equal to the deficit in momentum caused by the presence of the boundary layer.

These parameters form the key to any boundary layer analysis and are all related to one another by the Von Karman momentum integral equation which can be derived using the continuity equation and the conservation of momentum in the streamwise direction. It has the form

$$\frac{d}{dx}(\theta) + \frac{\theta}{U_e}(2 + H)\frac{dU_e}{dx} = \frac{1}{2}c_f \quad \ldots\ldots\ldots\ldots\ldots\ldots \quad (2\text{-}3)$$

where

$$H = \frac{\delta^*}{\theta} \quad \ldots\ldots\ldots\ldots\ldots\ldots \quad (2\text{-}4)$$

called the shape factor, and c_f is the skin friction coefficient. These definitions hold true for any steady incompressible flow, whether laminar or turbulent, constant or variable pressure, constant or variable temperature.

Modern high lift systems achieve high lift curve slopes while tolerating a small degree of flow separation ie. cove separation, separation bubbles and small amounts of trailing edge separation. However, if the extent of separation increases to a point where the gross character of the flow changes, restricting the lift coefficient to an upper maximum this is termed flow breakdown. Beyond this, massive separation causes a decrease in lift with increasing incidence and the aerofoil is said to be have stalled.

As a basis for the discussion of the mechanism of the stall of aerofoil sections with high lift devices, the classical classifications of the single aerofoil stall will be discussed briefly first. When the incidence of an aerofoil is increased towards that of maximum lift, regions of separated flow are formed whose position and development determine both C_{Lmax} and the post stall behaviour of the aerofoil. These regions are usually situated near the leading or trailing edges and it is convenient to categorise the behaviour of single element aerofoils into one of three basic types (fig. 2.6 & 2.7).

Trailing edge stall: Identified by movement of the turbulent separation point forward from the trailing edge with increasing incidence. This is characteristic of most thick aerofoil sections with the lift curve peak usually being rounded and loss of lift after stall gradual. The rate with which separation moves forward from the trailing edge is dependant upon the shape of the pressure recovery curve. A concave upper surface leads to values of the shape parameter H which can be large over much of the rear of the aerofoil and separation may spread forward very rapidly. Conversely, convex surfaces can produce low values of H except near the trailing edge and hence can accelerate stall onset. However, the separation point will move more

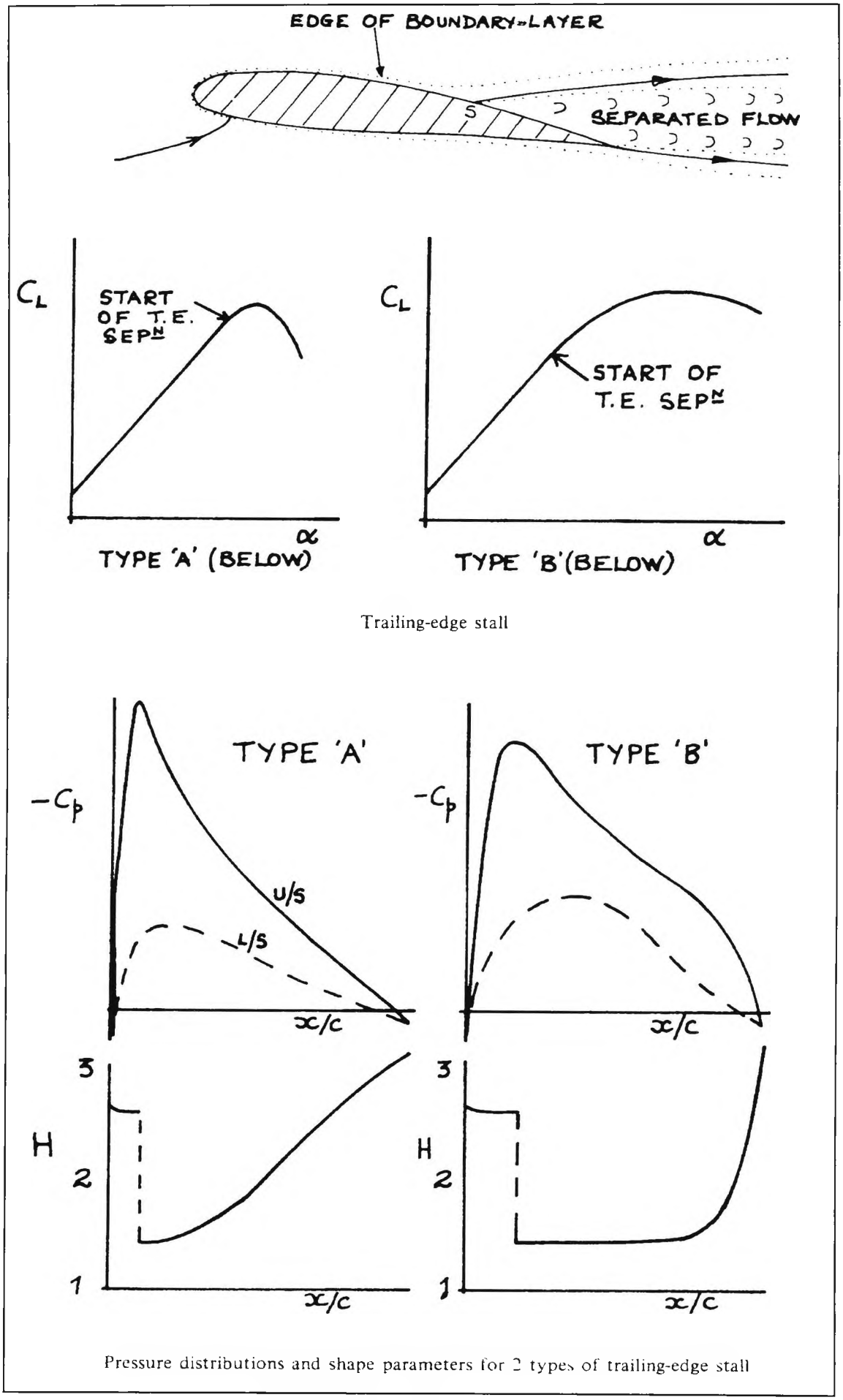

Trailing-edge stall

Pressure distributions and shape parameters for 2 types of trailing-edge stall

Figure 2.6 : Trailing edge stalls

gradually and the loss of lift will be less sudden.

Leading edge stall: Caused by sudden flow separation without re-attachment and is associated with the existence of a small region of separated flow near the leading edge of the aerofoil. Often exhibited by moderately thick sections little rounding is seen in the lift curve before stall. The laminar boundary layer separates with transition occurring in the separated boundary layer. The turbulent boundary layer re-attaches to form a short bubble. With increasing incidence the bubble shortens until at some critical lift coefficient the turbulent boundary layer fails to re-attach forming a large separated region over most of the aerofoil or alternatively, the reattachment is quickly followed by a further separation of the turbulent boundary layer, both giving rise to a sudden stall.

Thin aerofoil stall: Characterised by flow separation close to leading edge with re-attachment at a point which moves progressively rearward with increasing incidence. This stall occurs on all sharp edged aerofoils and on thin aerofoils with rounded leading edges. In the case of sharp edged aerofoils the re-attachment point moves progressively rearwards until at approximately maximum lift it reaches the trailing edge after which the stall occurs. On thin rounded leading edge aerofoils the short bubble which forms at low incidence bursts into a long (2-3% chord) bubble resulting in the characteristic kink in the lift curve slope. With increasing incidence the bubble again extends rearwards until it reaches the trailing edge. During this process $dC_L/d\alpha$ decreases steadily and a smooth maximum results.

An aerofoil can exhibit different stalling behaviours at different Reynolds numbers and a combination of stalling characteristics can occur simultaneously at the same Reynolds number. The addition of camber can significantly alter the stalling behaviour of an aerofoil.

With a little thought we may apply the empirical guide lines above to high lift systems and possibly anticipate how these systems may stall. In attempting to do this we assume that the position of the separate elements is such as to produce optimum aerodynamic performance for the system as a whole. Experiments have shown that for an aerofoil having a plain leading edge and deployed trailing edge, the pressure distribution over the flap varies little with incidence (Foster et al, 1970). Hence under conditions of weak interference from the main wing wake the flap upper surface boundary layer development might therefore be expected to be almost invariant with incidence. Flap deployment significantly increases the trailing edge camber of an aerofoil. This significantly increases the adverse pressure gradient just downstream of the main wing leading edge and hence it is reasonable to expect a flapped aerofoil section (in the absence of any leading edge devices) to experience a leading edge stall unless the profile shape is designed with prevention of this possibility in mind.

A wing with a slat may stall either as a result of flow breakdown on the upper surface of the slat or main wing. The surface on which the breakdown occurs is determined by the geometric position of the slat relative to the main wing. Experiments have shown that for a high angle of rotation of the slat relative to the main wing chordline the adverse pressure gradient on the slat upper surface is comparatively mild at the expense of the pressure gradient at the main wing leading edge. The reverse is true if the slat angle is low and in these circumstances the slat will suffer a leading edge stall, shedding an unsteady wake which in

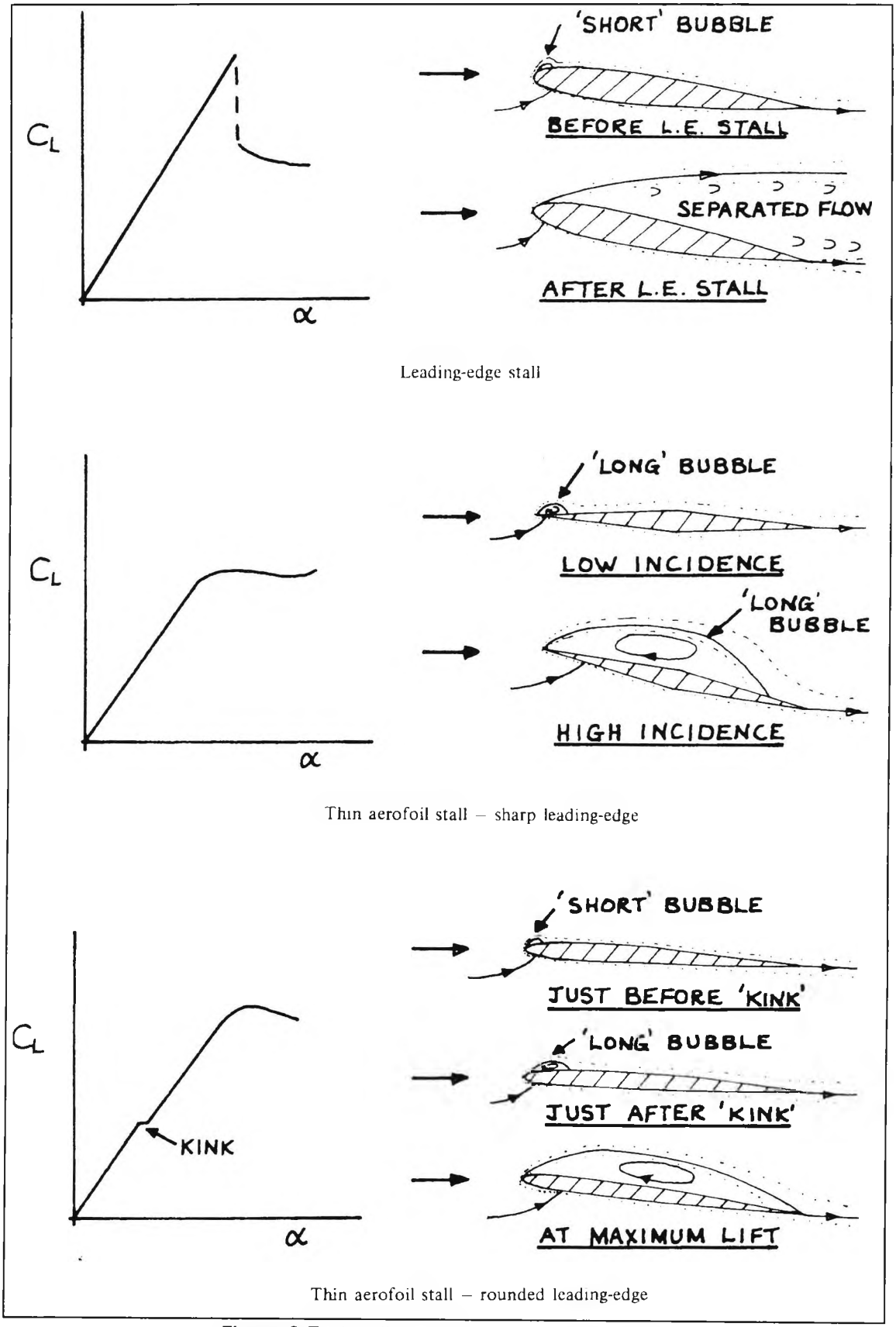

Figure 2.7 : Leading edge & thin aerofoil stalls

turn would probably cause a premature separation on the downstream elements. Turning to the main wing, Foster et al (1970) found that the mere presence of a turbulent wake may induce early transition of a laminar boundary layer on a downstream element and hence reduce the possibility of a leading edge stall.

2.3 Vortex generators

Any technique that can enhance the momentum transfer processes which occur naturally within a boundary layer will inevitably delay separation. A commonly utilised method for flow separation control employs small vane vortex generators embedded in a turbulent boundary layer ahead of a line of flow separation. Their use relies on the increased mixing between the external stream and the boundary layer that is promoted by streamwise vortices shed from the vanes trailing longitudinally over the surface, adjacent to the edge of the boundary layer. Fluid particles with high streamwise momentum are swept in along helical paths towards the surface, mixing with and to an extent replacing retarded fluid particles close to the surface. The mean streamwise momentum of the fluid particles in the boundary layer is thereby increased. This process continues for as long as the vortices remain strong enough to impose a helical motion on the fluid particles. The motion provides a continuous source of re-energization to the boundary layer, countering the effects of adverse pressure gradients and surface skin friction.

In their simplest form vane vortex generators consist of a row of small flat plates which project perpendicular to the surface of interest (fig. 2.8). Each is set at an angle of incidence to the local flow direction to produce a single trailing vortex. Co-rotating vortices are obtained by setting all the vanes (usually equally spaced) to the same angle of incidence, producing vortices of similar strength at the same height above the surface. Counter-rotating vortices are generated by alternately setting the vanes at positive and negative angles. They are equally spaced in pairs only but again usually set to produce vortices of equal strength at the same height. Other devices producing vortex action are leading-edge and trailing-edge fences and leading-edge discontinuities.

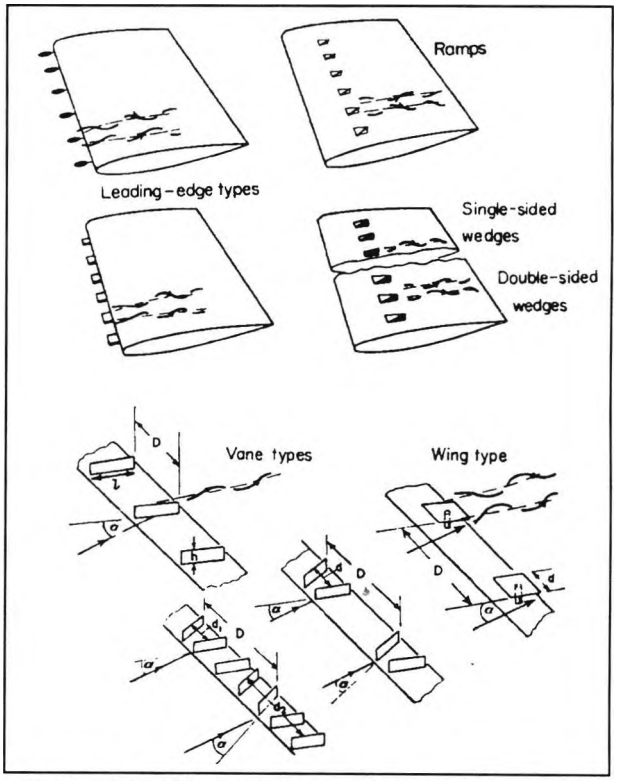

Figure 2.8 : Various types of vortex generator (Pearcey, 1961)

The most important single factor in establishing an effective co-rotating vortex pattern is the need to keep the spacing of adjacent vortices above a certain minimum value. An effective co-rotating vortex pattern is one which contains strong discrete vortices lying close to the surface, but which are far enough apart to prevent the low momentum air that is being swept out on one side of each vortex from being swept in to the surface again by an adjacent vortex, ie. to prevent mutual viscous interaction. This is achieved only if the initial spacing of the vortices is greater than about four times their height ($D/h > 4$). For a smaller

spacing than this the co-rotating vortices tend to damp one another, failing to maintain high momentum air at the surface at any point in the cross-section of the boundary layer (fig. 2.9). Until this point was appreciated the performance of co-rotating vane vortex generators compared unfavourably with that of counter-rotating types. Once the spacing is well above this minimum value their effectiveness falls only slowly with further increases in spacing (provided the vortices are themselves strong). Systems with $5 \leq d/h \leq 8$ are frequently used in practice.

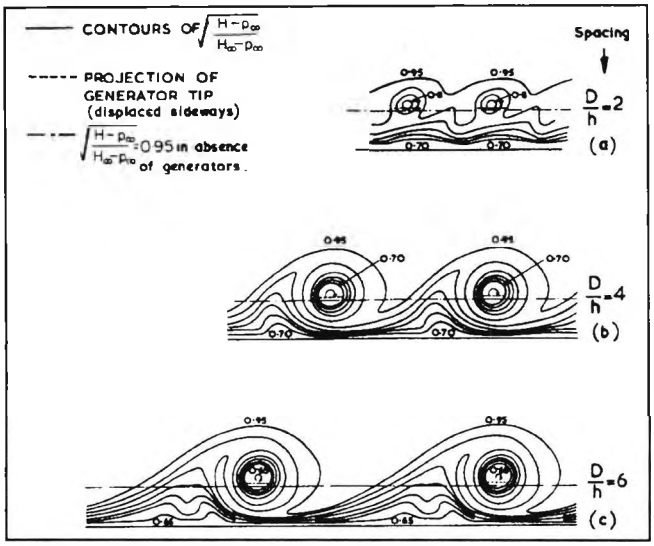

Figure 2.9 : Pitot pressure contours for co-rotating vortices at a fixed distance downstream of generators (Pearcey, 1961)

Counter-rotating vortices are effective in delaying separation when they are arranged as shown in figure 2.10. This shows extensive regions where the boundary layer is kept thin between alternate pairs of vortices. However, this favourable vortex arrangement is not maintained as the downstream distance increases. The centres of the vortices move closer together in pairs and further away from the surface until the vortices eventually become damped out.

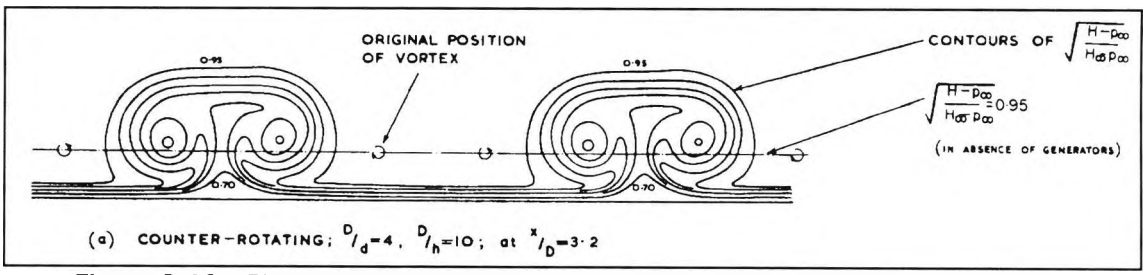

Figure 2.10 : Pitot pressure contours for a typical counter-rotating configuration (Pearcey, 1961)

Each vortex in a system of vortices cannot be considered in isolation. Velocities are induced on any one vortex by its neighbours located on either side. Considering first a system of co-rotating vortices where the individual vortices are all of the same strength and height above the surface. We can see that the induced velocities on any one vortex due to its neighbours cancel out (fig. 2.11). However the vortex is displaced laterally under the velocity induced by the images in the surface. This is the same for all vortices in an infinite row and the system is displaced bodily in a lateral direction. It is these induced velocities which are responsible for the vortices in a co-rotating system i) maintaining a constant height above the surface and ii) retaining their effectiveness for up to 100 generator heights downstream of their origin.

The induced velocities for counter-rotating systems causes the array of vortices to change substantially as it moves downstream. The consideration of vortex paths then

becomes vital in the design of these systems. Considering a system in which all the vortices are equally spaced the resultant induced velocity at the centre of any one vortex will be parallel to the surface (as in a co-rotating system). However, the lateral induced velocity is in opposite directions for adjacent vortices causing them to move together in pairs. Once pairing has begun to occur the induced velocity vector rapidly rotates in a direction away from the surface. This movement of the vortices limits the range of effectiveness for vortices which are originally equally spaced to about 20 generator heights downstream from their origin. However, the downstream range of effectiveness can be controlled to a significant degree by the choice of original arrangement (fig. 2.12).

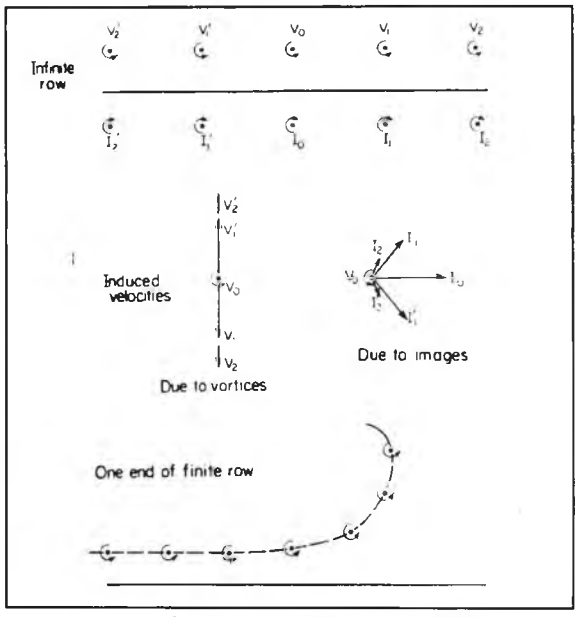

Figure 2.11 : Co-rotating vortices (Pearcey, 1961)

There is a net penalty drag associated with the use of vane vortex generators although the magnitude of this penalty varies widely with each application. Positive contributions to the drag include: the drag of the blades themselves of which the major portion is the induced drag associated with the vortices; and the increased skin friction on the wing surface due to the vortex action. These contributions are to an extent offset by the reduction in form drag of the wing that follows from the reduction in boundary layer displacement thickness. The net penalty drag is a balance between these opposing contributions and is generally very small. Examples of the types of change that can be made to a system of co-rotating vortex generators to reduce its drag can be found in figure 2.13.

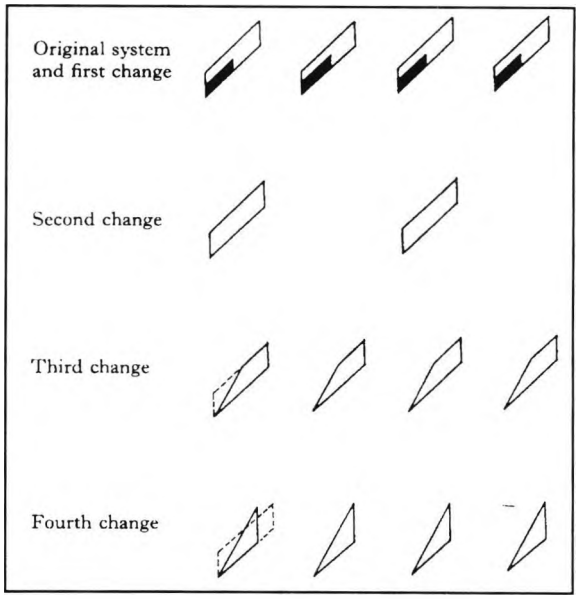

Figure 2.13 : Changes to a system of co-rotating vortex generators which will reduce its drag (Pearcey, 1961)

The fluid issuing from a jet normal to the surface into a confined cross-flow is characterised by a highly complex flow field that includes a primary vortex located in the wake region of the jet, secondary counter-rotating vortices located in the side regions of the jet and a horseshoe vortex located along the circumference of the jet. The primary and secondary vortices are both helical vortices. The horseshoe vortex is a ring of reversed flow and is generated by the strong adverse pressure gradient in the near upstream vicinity of the jet. The secondary vortices are

generated by the severe shearing forces exerted by the jet flow.

If the jet is inclined to the flow to give both streamwise and spanwise velocity components on exit, one member of the pair of secondary vortices is strengthened significantly (fig. 2.14). The action of the vortex from the inclined jet is similar to that of the vortex from an inclined vane with the advantage that at cruise conditions when no separation is present the jet can be switched off to avoid the undesirable drag penalties associated with vane vortex generators.

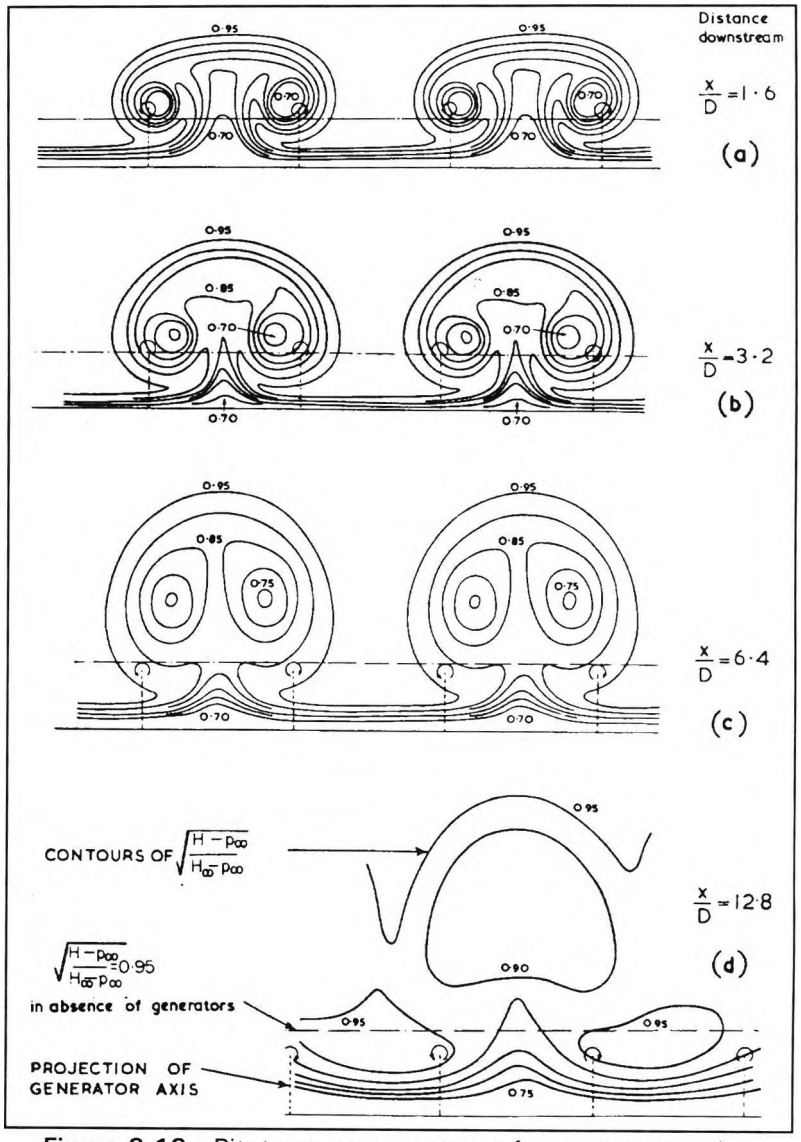

Figure 2.12 : Pitot pressure contours for counter-rotating vortices that are initially equally spaced (Pearcey, 1961)

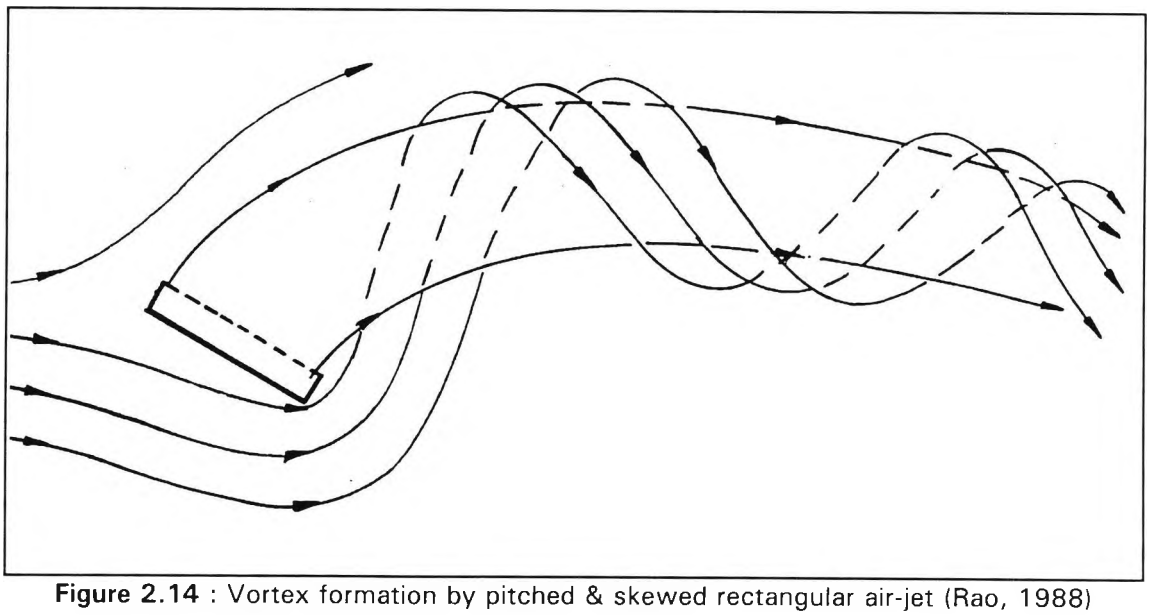

Figure 2.14 : Vortex formation by pitched & skewed rectangular air-jet (Rao, 1988)

3. Experimental Techniques

3.1 Windtunnel

The work was conducted in City University's T2 lowspeed windtunnel which has a Reynolds number capability of 3.1 million per metre (0-45ms^{-1}). It is of the closed circuit type and has a working section size 0.81*1.12m with corner fillets and a length of 1.68m. The working section is vented to atmosphere at the rear and the turbulence level is below 0.7%.

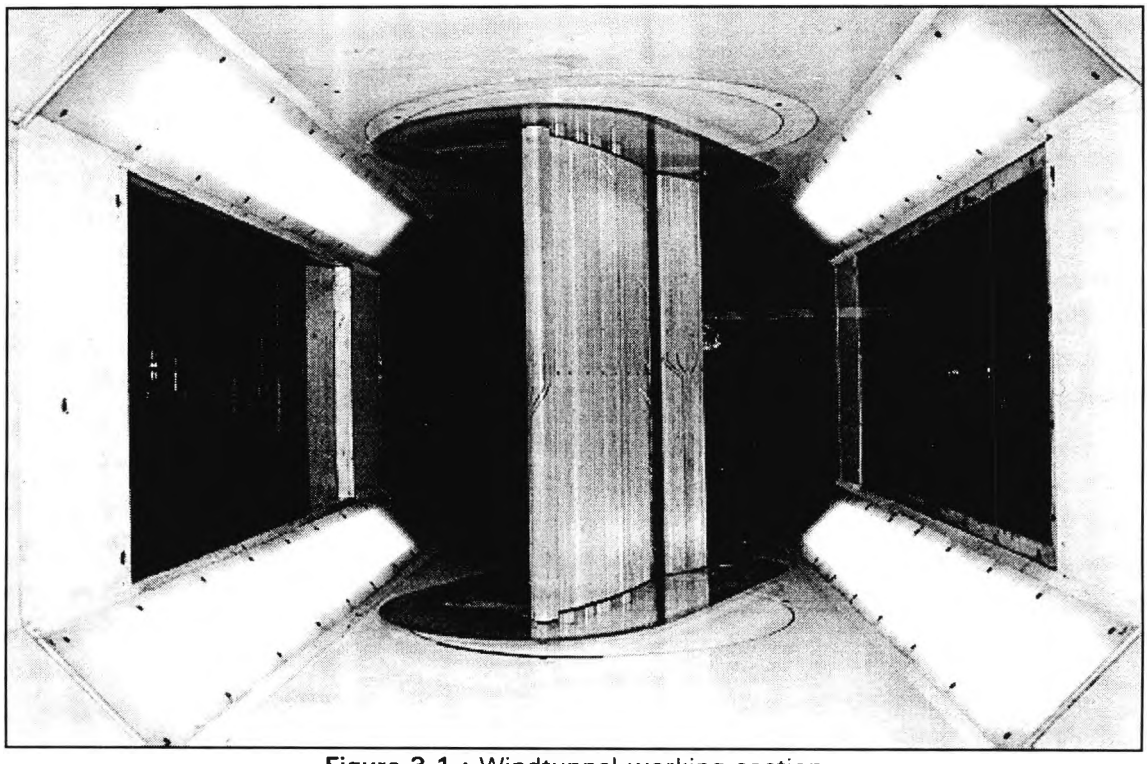

Figure 3.1 : Windtunnel working section

3.2 Two-dimensional model

3.2.1 Aerofoil

Each element of the high lift system was constructed from laminated African mahogany using a glue of low moisture content (Cascophen) to minimise movement on completion. The wooden slat was later replaced by a much stiffer one piece aluminium slat which eliminated the need for mounting brackets to support the slat via the main wing at selected points along its span. The chordwise profile of the high lift system can be seen in figure 3.2. The lap and gap distances and angles for the slat and flap elements were those shown in figure 3.3.

Harpoon bolts secured the slat and main wing elements of the high lift system to endplates. The flap element was secured to two moveable aluminium plates which in turn were also countersunk into each endplate. Although the flap could not be fully retracted the aluminium plates allowed for considerable variation in setting the flap gap, lap and angle parameters independently (fig. 3.4).

Located at the mid-span of the slat, main wing and flap were twelve, thirty-one and fourteen pressure tappings respectively. Normal force coefficients for each element were derived from these tappings. A retracted chord length of 500mm was used to calculate their

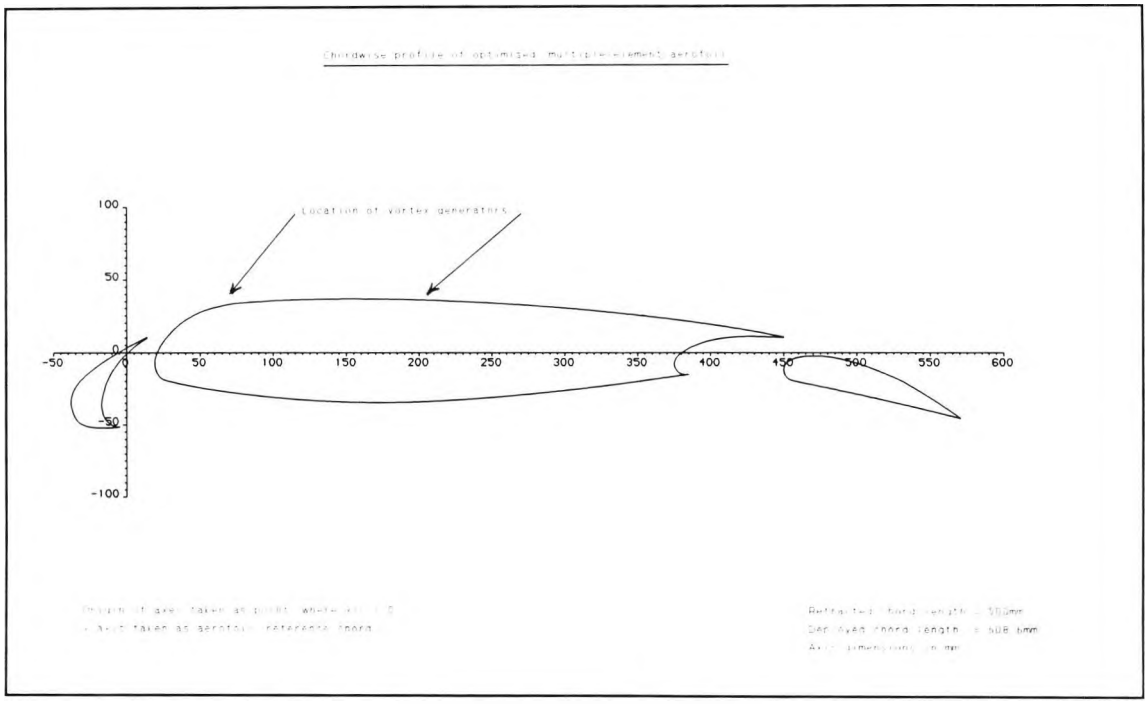

Figure 3.2 : High lift system

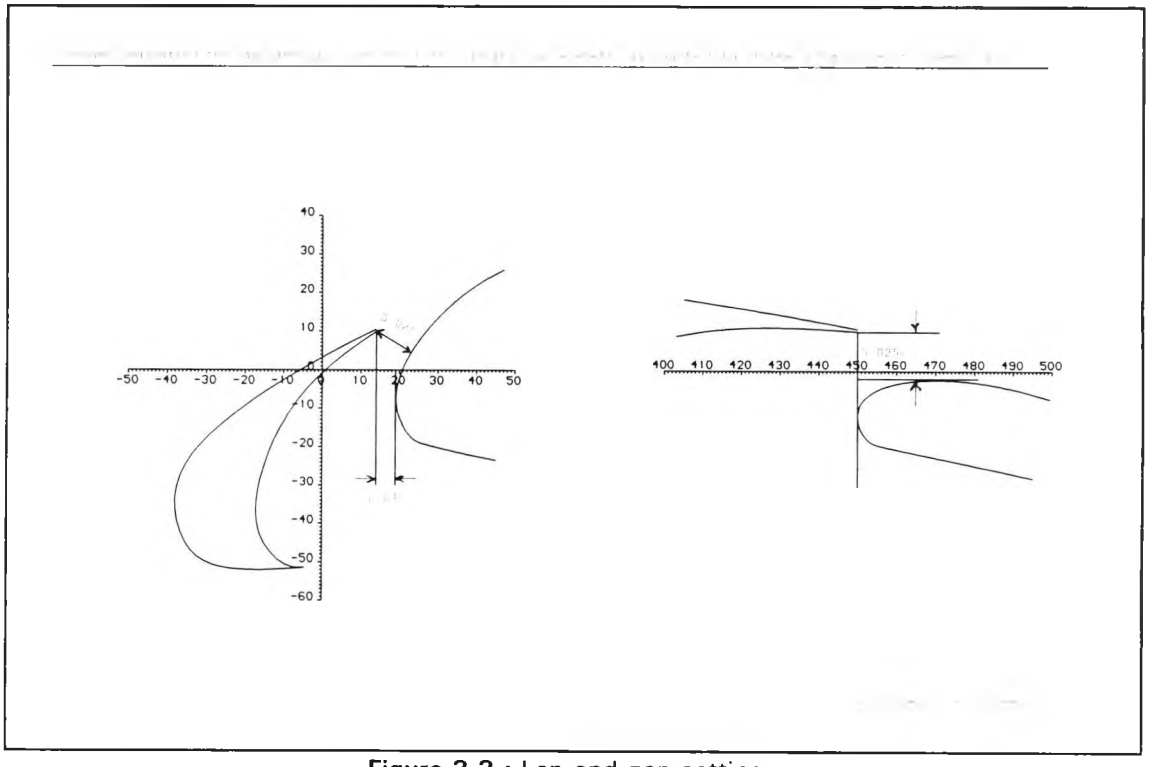

Figure 3.3 : Lap and gap settings

x/c values with the model having span and deployed chord lengths of 740mm and 608.6mm respectively. Tables 1 to 3 in Appendix D contain the surface coordinates for each element.

The load path to carry aerodynamic forces out of the complete structure consisted of two aluminium spindles 40mm in diameter securely attached to large aluminium plates countersunk into the main wing at each spanwise extremity. The spindles passed through the windtunnel roof and floor to sit neatly into two sets of thrust and roller bearings conveniently located in steel cross members attached to the working section support structure (fig. 3.5). The overall effect was to have the aerofoil mounted vertically on the thrust bearings allowing

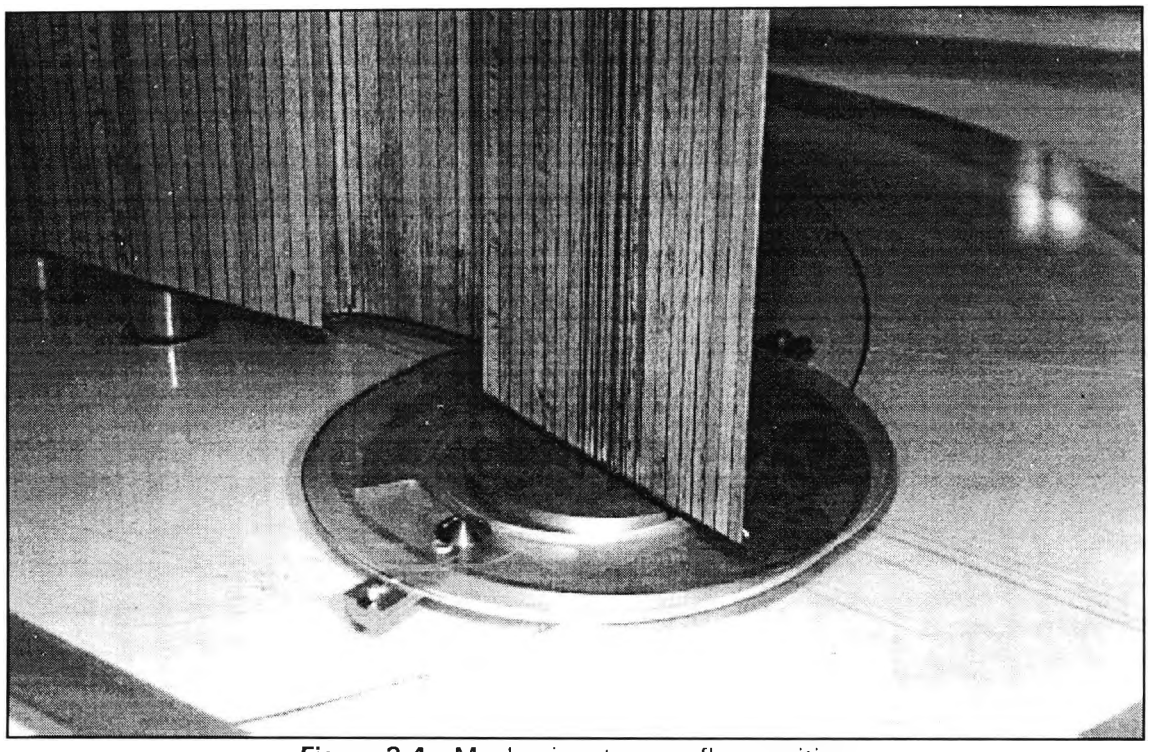

Figure 3.4 : Mechanism to vary flap position

it to rotate freely about an axis through the spindles.

3.2.2 Endplates

These were manufactured from transparent perspex 9.5mm thick with their height and length as shown in figure 3.6. Preliminary calculations on the tunnel wall boundary layer thickness indicated that the minimum distance required between the tunnel walls and endplates for these to be effective in preventing boundary layer spillage was 17mm. The actual value used was 25mm.

It was essential to maintain an airtight seal at the junctions between each endplate and the individual elements of the high lift system. Rubber foam was cut to the shape of each element using aluminium templates. During model assembly the foam was then inserted between the endplates and the spanwise extremities of each element. Tightening the harpoon bolts ensured the rubber foam compressed sufficiently to guarantee no leakage of flow from the lower surface to the upper surface.

Provision for boundary layer control on the endplates was made through the use of aluminium plates countersunk into each endplate at three different chordwise positions (0.16, 0.30 and 0.612) adjacent to the main wing (fig. 3.7). Into these could be inserted airjet vortex generators or lateral slots through which compressed air could be supplied at varying pressure. The plates could be extracted/inserted without the need for removing the entire model from the working section.

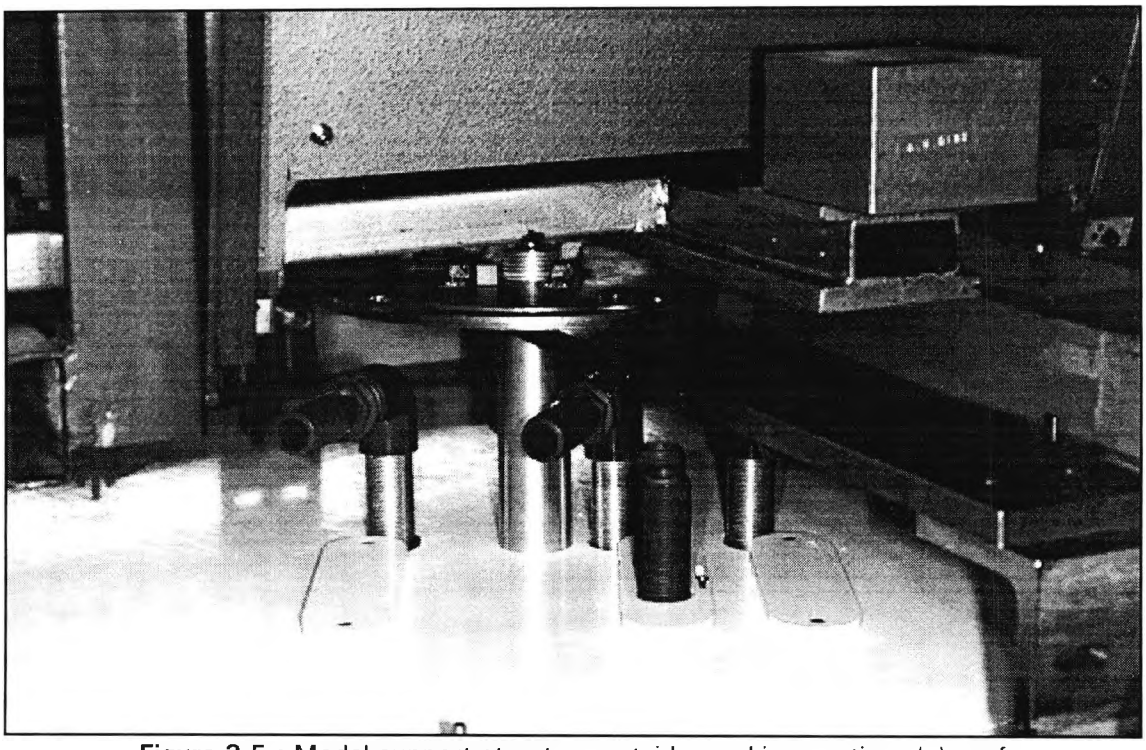

Figure 3.5 : Model support structure outside working section: (a) roof

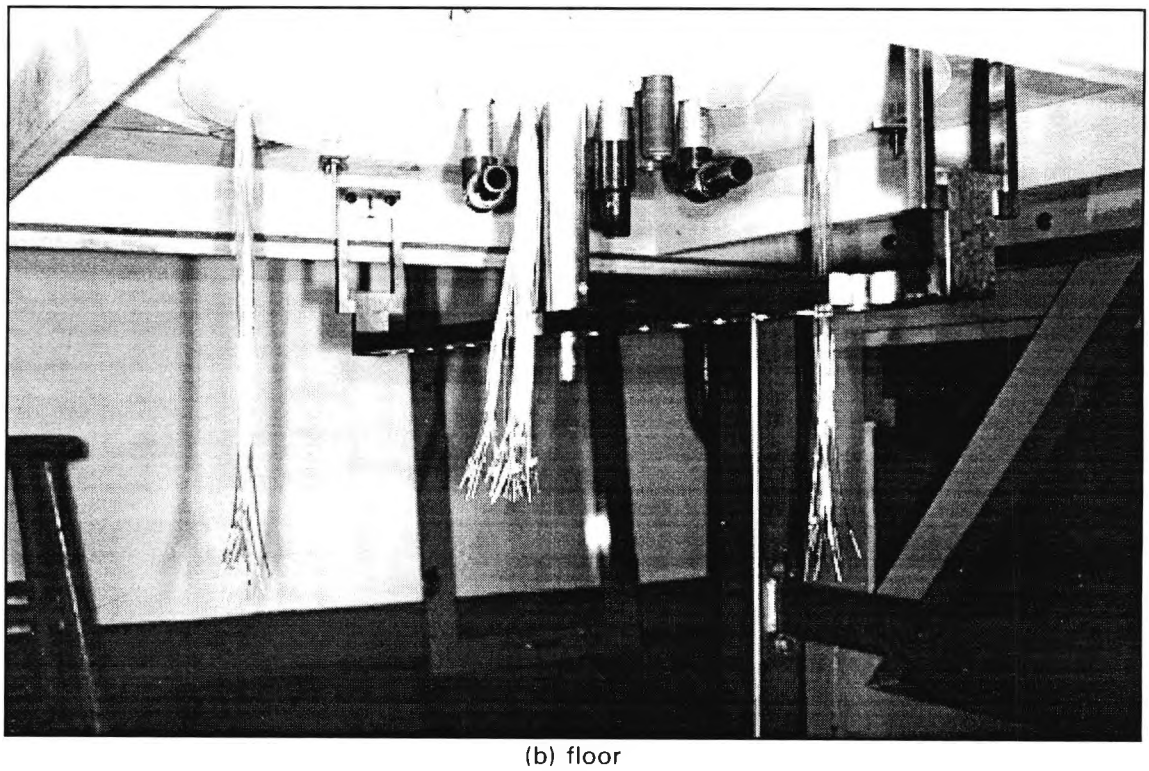

(b) floor

3.3 Vane vortex generator design

The emphasis in choosing the arrangement for vane vortex generators was on producing an array of vortices that would be effective for separation positions over most of the upper surface of the main wing. This would enable possibilities to be explored broadly, in a preliminary way, and provide useful guide lines for the development of more sophisticated and finely tuned airjet systems. The first requirement, therefore, was a co-rotating system to ensure that the vortices remained close to the surface. The vanes were positioned at x/c = 0.14 where the local velocities would ensure that the vortices were strong and generated well

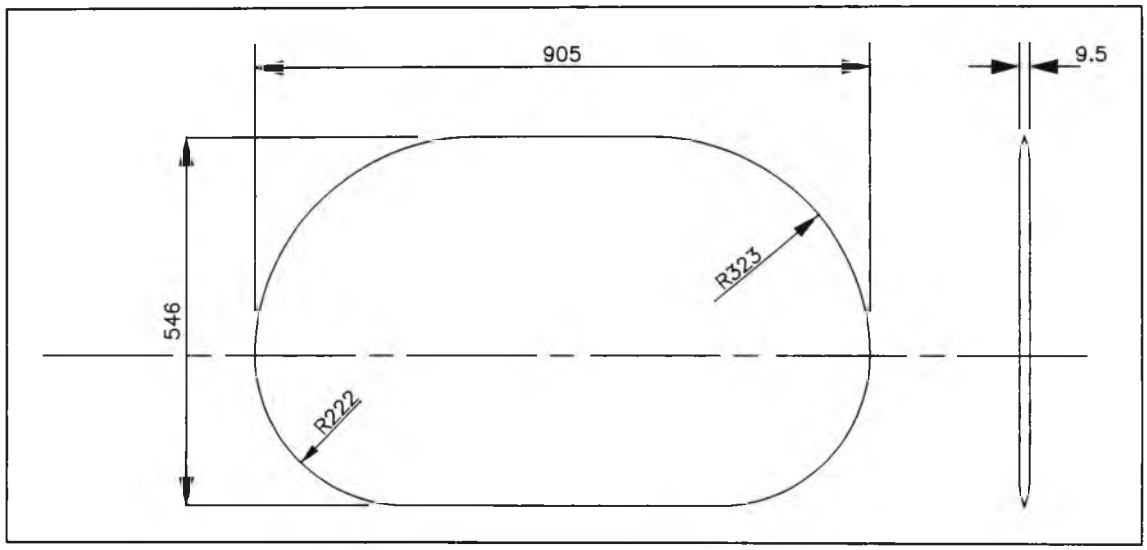

Figure 3.6 : Dimensions of endplate (mm)

upstream of any likely separation positions. Other details of the configuration were based on recommendations given by Pearcey (1961). The vanes were of cropped delta form with 60° leading-edge sweep, height 7.5mm with root and tip chords of 30 and 17mm respectively. A spacing of 60mm apart (8*height) allowed for 11 vanes along the span of the model. The vanes were set at 20° to the undisturbed stream (fig. 3.8).

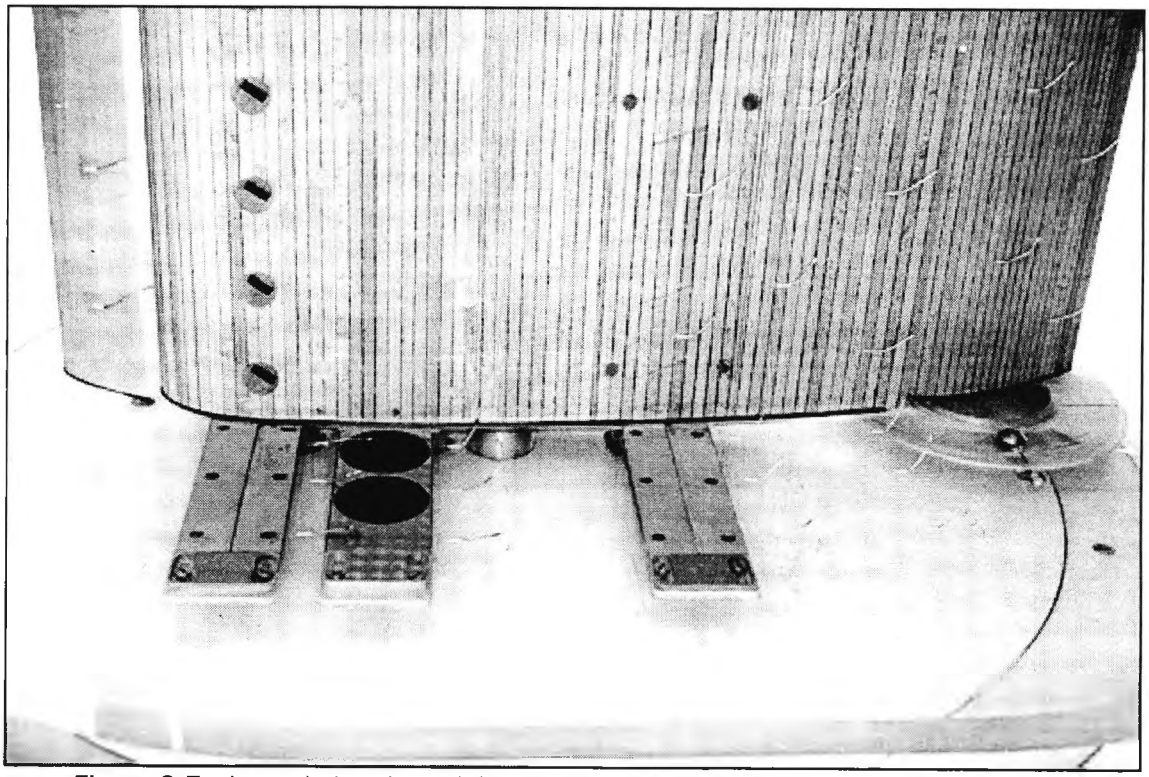

Figure 3.7 : Lateral slots in endplate to facilitate endplate boundary layer control

Counter-rotating vane vortex generator configurations were tested at two positions, x/c = 0.14 and x/c = 0.4, using the same vane design. The vanes were grouped in pairs 148mm apart, the vanes in each pair being 37mm apart (ie. D/d = 4). The vanes were again set at 20° to the undisturbed stream. The vanes were manufactured from thin Brass sheeting and pressed so that each vane had a small flat surface protruding horizontally from its root

chord. This allowed each vane to be secured to the model by double-sided sticky tape which proved adequate for all test conditions.

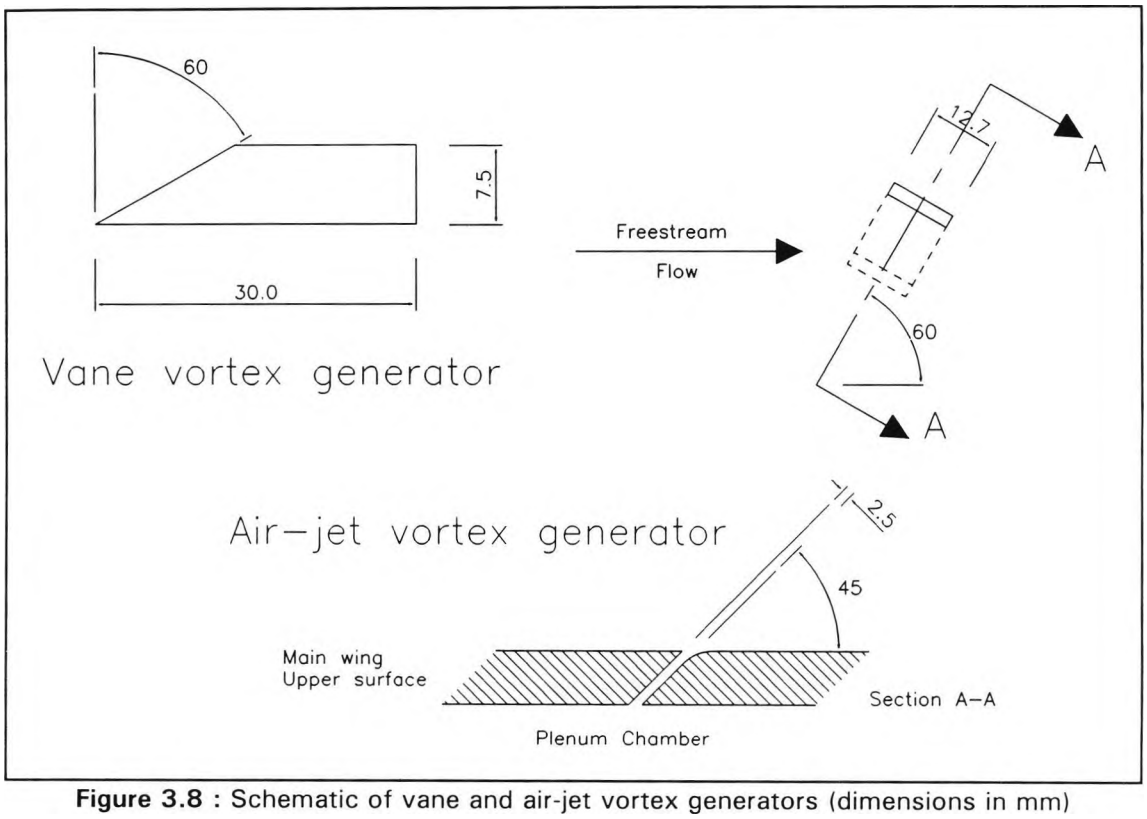

Figure 3.8 : Schematic of vane and air-jet vortex generators (dimensions in mm)

3.4 Airjet vortex generator design

3.4.1 Ducting

Facilities were available which allowed for the storage of up to 15.2 m^3 of dry air at a maximum pressure of 45 bar. A high pressure air line was constructed, which when finished, enabled air from this source to be available from an outlet close to the working section of the windtunnel. This 'primary' air line consisted of approximately 35m of 50.8/38 mm (OD/ID) reinforced vinyl tubing capable of supplying air at a maximum pressure of five bar.

In the vicinity of the working section the primary air line divided equally into two separate lines, each supplying air to a large steel plenum chamber. One plenum chamber was allocated for supplying air solely to the endplate boundary layer control slots, while the second provided air for the airjet vortex generators in the model. A maximum of four secondary air lines 38/25 mm could be attached to each plenum chamber while a system of orifice plates within each plenum chamber ensured an equal distribution of air to each secondary air line.

A lever operated ball valve (Crane D191, 38mm ID) could be used to isolate the ducting system from the storage facility while a similar second valve could isolate the plenum chamber supplying air to the airjet vortex generators from the endplate ducting. A pressure regulating valve (Hale Hamilton PL5M) enabled the delivery pressure from the storage facility to be varied according to the demands of the system at any one time.

During windtunnel operation, endplate boundary layer control was always used at a constant blowing pressure which was determined from previous tests to ensure two-

dimensional conditions up to and beyond the stall of the clean aerofoil. With the implementation of endplate boundary layer control at two chordwise positions on each endplate, full use was then made of the maximum possible number of four secondary air lines from the endplate steel plenum chamber.

Practical limitations on the design of the model prevented each airjet from having an individual air supply. As a result, compressed air from the steel plenum chamber supplying air to the airjets passed into subsidiary plenum chambers located inside the main wing of the model. In total, four such plenum chambers (two per model semi-span) were integrated into the design of the main wing at two chordwise locations (fig. 3.9). The chordwise extent of each plenum chamber was large enough so that a degree of flexibility could be accommodated for in the location of the airjet vortex generator configurations. The leading-edge plenum chamber extended from 0.1 to 0.22 x/c while the trailing-edge plenum chamber was located between 0.56 and 0.69 x/c. A smaller plenum chamber situated behind each leading-edge plenum chamber was incorporated into the design in anticipation for the need to control corner flow at the junction of the main wing and each endplate. In the event, this chamber was never needed and remained sealed for the entire duration of the tests. Air entered all plenum chambers from above and below the working section. Channels passing under the pressure tapping locations linked plenum chambers adjacent to one another either side of the model centre line. Orifice plates within the plenum chambers provided an adequate distribution of air throughout each chamber (fig. 3.10). In order to incorporate tests at all incidences the ducting system to the model had to be flexible and not interfere with the balance mechanism which is present above the working section.

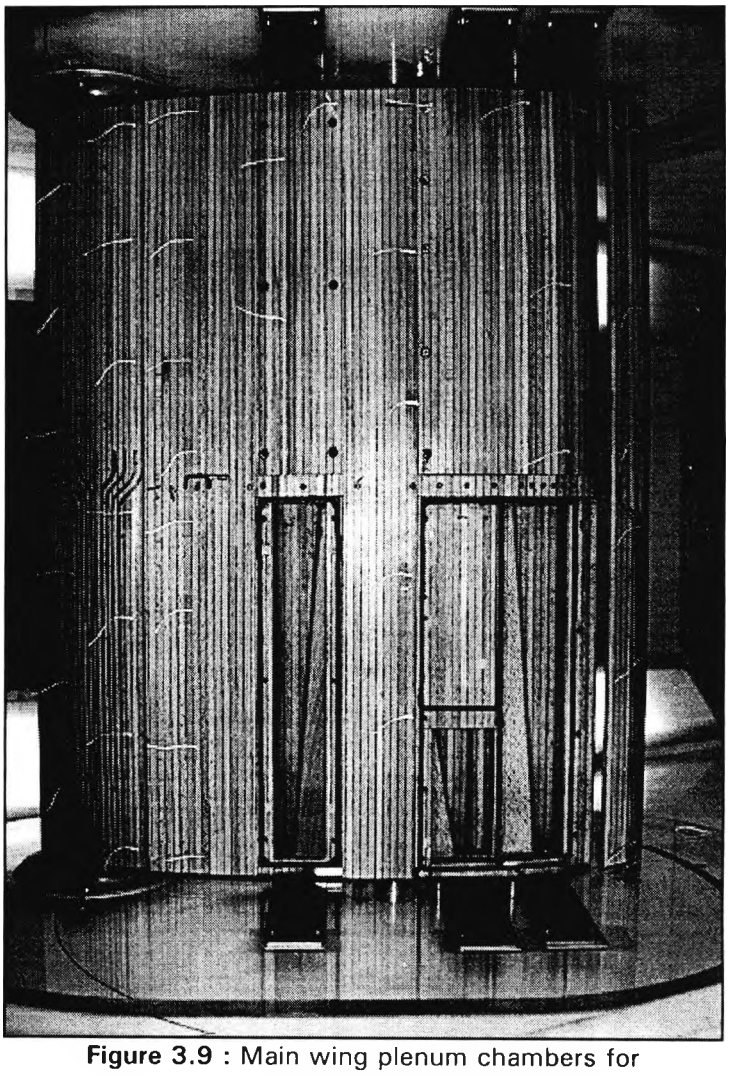

Figure 3.9 : Main wing plenum chambers for lower semi-span

Two static pressure tappings monitored the pressure in each plenum chamber within the model. To complete the main wing upper surface profile, wooden lids for each plenum chamber shaped to the local profile of the main wing upper surface were fitted into place and

secured tightly using wood screws. An air-tight seal was ensured along the join by compression of a rubber O-ring gasket. Testing with no boundary layer control was achieved by merely testing with lids manufactured with no airjet provision. The model was designed so that an exchange of lids could occur without having to remove the model from the working section.

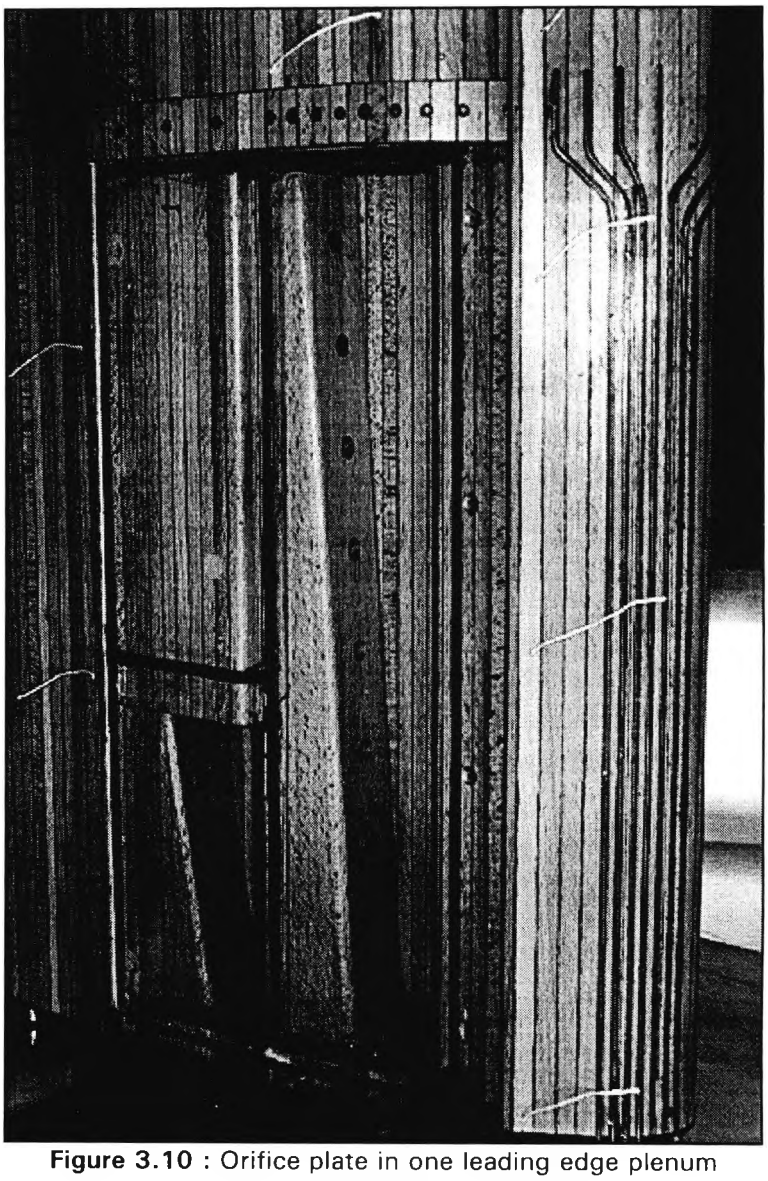

Figure 3.10 : Orifice plate in one leading edge plenum chamber

3.4.2 Airjet vortex generator

Whereas guide lines similar to those described by Pearcey (1961) aid the designer in the installation of a vane vortex generator system, similar empirical rules do not exist for guidance in the installation of an airjet vortex generator system. The over-riding concern governing the current work was that the vortices generated by airjets would be far enough apart so as to prevent low energy air that is being swept out on one side of each vortex from being swept into the surface again by an adjacent vortex. The work deals only with airjets having a rectangular cross-section as Freestone (1985) showed that the vorticity generated by such a jet is greater than that from a circular jet having a similar cross-sectional area.

Following recommendations by Rao (1988), each rectangular airjet had an aspect ratio of five and was vectored 60° from the freestream direction. An inclination angle of 45° to the local surface tangent was chosen to ensure adequate penetration of the jet through the multiple shear layers where vortex formation could then occur (fig. 3.8). Three pairs of matching lids with provision for airjets were produced, in addition to blank lids, for the leading edge plenum chambers. The rear plenum chambers were left with blank lids inserted for the present time. Each pair of lids contained a different airjet vortex generator configuration with each system positioned symmetrically about the model centre line. The first contained a co-rotating system at $x/c = 0.14$ with the centre of each jet spaced 53mm apart (fig. 3.11). The second and third pairs contained counter-rotating systems (also at $x/c = 0.14$); in the event

the improved performance of the high lift system with the co-rotating airjet vortex generators installed at $x/c = 0.14$ merited detailed study of the shear layers above the high lift system. With the co-rotating system it was inevitable that one airjet adjacent to an endplate would produce vorticity which would be detrimental to the corner flow and as a result this airjet was excluded from the design.

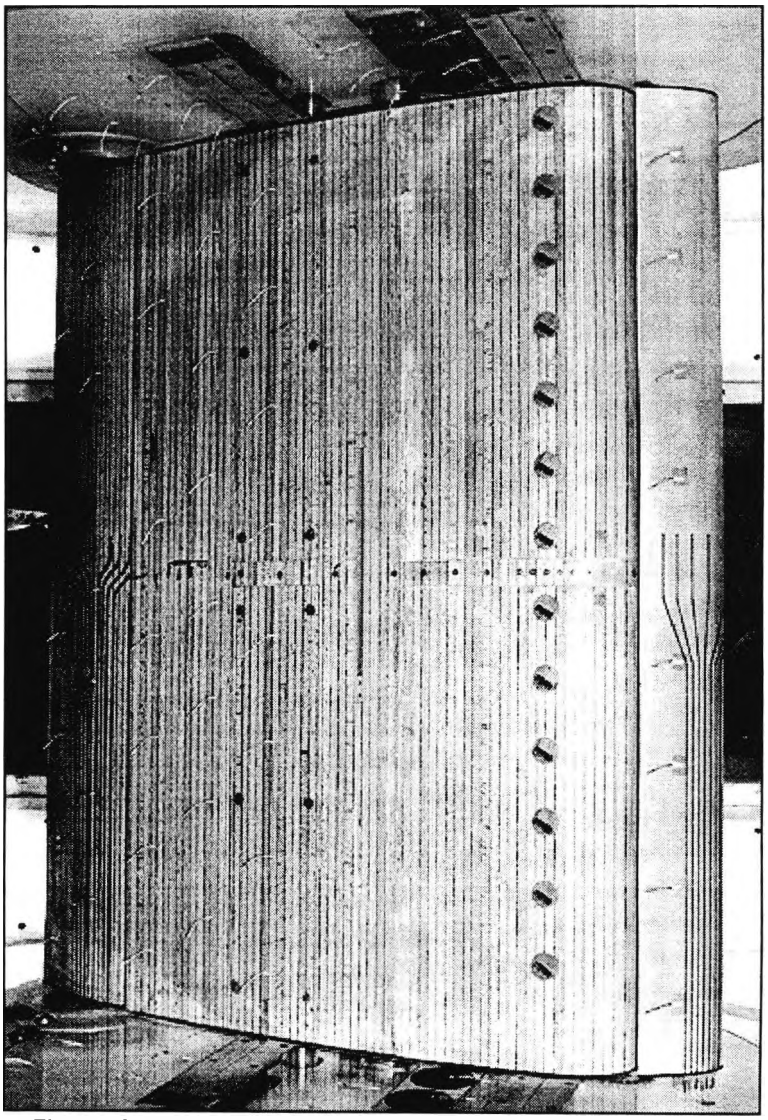

Figure 3.11 : Co-rotating air-jet vortex generator system

The rectangular slot for each airjet (12.5 x 2.5mm) was milled into a solid wooden plug (25mm diameter and 14mm thick). Each airjet vortex generator plug was then inserted into the wooden lid at the appropriate location and glued into place. Tests conducted prior to lid manufacture revealed that shearing forces in the region of 0.18 imperial tons were required to cause failure of the plugs when inserted into a wooden plate having the same thickness to the lids sealing the leading edge plenum chambers. The total pressure needed in each plenum chamber to subject a similar shear force was calculated to be far in excess of that to be used in tests.

3.5 Shear layer rakes

3.5.1 Pitot

In anticipation of examining shear layers which may have a total thickness in excess of 15% of the aerofoil chord length, it was decided to construct two pitot rakes to be used at different chordwise locations on the upper surface of the aerofoil depending upon the model incidence. This would prevent flow information from being lost, which can occur when using too small a rake towards the trailing edge of the aerofoil at high incidence or too large a rake towards the leading edge of the aerofoil at low incidence.

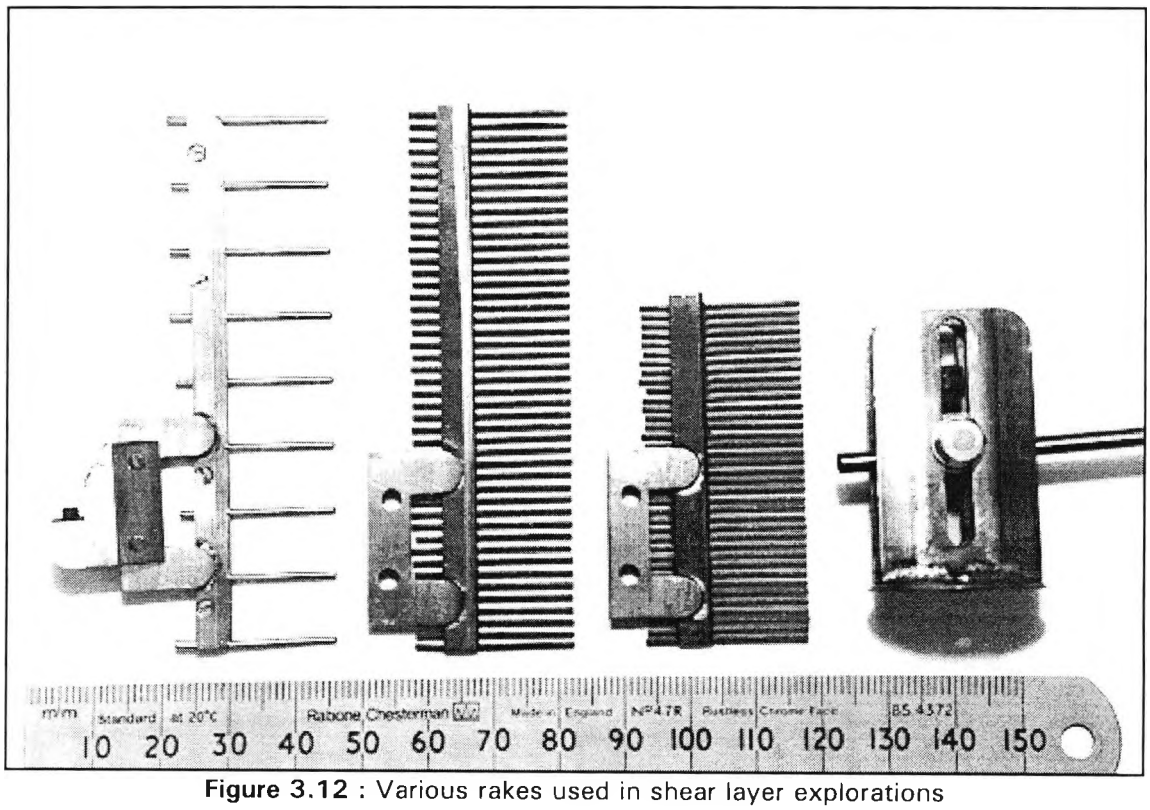

Figure 3.12 : Various rakes used in shear layer explorations

Both rakes were constructed using stainless steel tubing 0.7112/0.4064 mm (OD/ID) connected to vinyl tubing 1.4/0.63 mm (OD/ID). The larger rake consisted of 45 tubes approximately 1.9mm between centre lines rising to a height of 83.53mm above the model surface. The smaller rake contained 37 tubes approximately 1.5mm apart rising to a height of 52.11mm above the model surface. After manufacture a travelling microscope was used to locate the position of each tube in each rake to within 1×10^{-2}mm (fig. 3.12).

Explorations with the pitot rakes were carried out at 0.354 x/c, 0.9 x/c and 1.0 x/c. At each chordwise position a rake would provide data at nine spanwise locations 10mm apart for a given incidence and configuration, enabling a three-dimensional image to be derived of the shear layer structure.

3.5.2 Static rake

The static rake was manufactured from slightly larger thin walled stainless steel tubing 0.8128/0.635 mm (OD/ID). Nine tubes were used at 10mm intervals covering a total length of 80mm (fig. 3.12). In the event this rake was used only once to give some indication as to the whereabouts of the vortices formed by the airjet vortex generators. It was never

calibrated and the data it provided can only be treated as relative rather than absolute in magnitude.

3.5.3 Rake support

Two possibilities were available for providing a solution as to how to fix the various rakes in place above the aerofoil surface. Attaching the rakes to the end of a long sting extending upstream from beyond the trailing edge of the aerofoil was ruled unsatisfactory due to the excessive movement which would be seen at the rake position. There remained only one other solution whereby the rakes would be fixed in place by attachment to the model upper surface.

Dovetailed slots were machined into two aluminium bars. These were countersunk in a spanwise orientation into the upper surfaces of the main wing and flap. Two tapped runners were allowed to travel along the length of each dovetailed slot. A stiff streamlined structure was secured to the two runners by two small threaded bolts (fig. 3.12). The rakes in turn were then secured to the streamline structure by a stainless steel rod 0.125" in diameter. This method of securing the rakes into place allowed movement in the chordwise and spanwise directions and, as will be seen later, proved very effective as a means of examining the shear layer structure above the aerofoil. A sting extending upstream from beyond the trailing edge of the aerofoil provided the means for removing the vinyl tubing associated with the rakes away from the close vicinity of the aerofoil. The alignment of each rake with the streamwise direction was achieved using a combination of several precision made squares.

3.6 Data error assessment

All data accumulated from experimental sources carries with it an intrinsic error of some degree. The validity of the data may be open to doubt if the degree of error is unacceptably large. All necessary steps must then be taken to minimise this error.

3.6.1 Aerofoil

After the manufacture of the model was completed, a vernier travelling microscope confirmed the positions of the chordwise static pressure tappings to within 0.01mm and that specified model dimensions were correct to within 0.5mm. Periodically, through movement of the wood used to construct the model, the brass static tappings would gradually protrude from the wooden surface, necessitating removal through gentle filing.

The model incidence was measured by two separate methods relative to the tunnel centre line. The endplate adjacent to the windtunnel floor had the chord line of the aerofoil scored along its entire length. A brass arc (radius of curvature 325mm) was inscribed with an incidence scale between 0° and 45° and countersunk into the windtunnel floor. As the model rotated the leading edge of the endplate passed over the scale measuring the aerofoil incidence to ± 0.125°. The chord line marked on the lower endplate also enabled the zero incidence setting to be repeated to within ± 0.03°. A second pointer (radius 412mm) was attached to one of the 40mm diameter spindles about which the model rotated and which passed through the windtunnel roof. This pointer measured the incidence of the model from a second scale to an accuracy of ± 0.06°. The test procedure was to first allow the tunnel

to settle at the required Reynolds number and then increase the model incidence to the value sought. This allows the vortices to be interacting with the boundary layer before the cleanfoil stall incidence is reached. This is beneficial in that at an incidence above the cleanfoil stall incidence the vortex generators will be preventing the boundary layer from separating; rather than first having to attach it after which attachment must then be maintained. This also prevents measured pressures from suffering hysteresis effects.

3.6.2 Pressure measurement

Due to the type of aerofoil under test and the need to monitor pressures in regions where access with brass tubing proved to be difficult, the output from the pressure transducers was initially fed into an oscilloscope to determine the response rate of the pneumatic vinyl tubing/pressure transducer combinations. This in turn provided an indication of the maximum possible scanning rate which could be used when using the data acquisition system.

A procedure was developed which allowed the C_p's to be calculated from a derivation of the standard equation:

$$C_p = \frac{(P - P_{static})}{\frac{1}{2}\rho U_\infty^2} \quad \ldots\ldots\ldots\ldots\ldots\ldots \quad (3\text{-}1)$$

giving

$$C_p = \frac{(P - P_{atmos}) - (P_{static} - P_{atmos})}{\frac{1}{2}\rho U_\infty^2} \quad \ldots\ldots\ldots\ldots\ldots\ldots \quad (3\text{-}2)$$

Assuming

$$\begin{aligned} \tfrac{1}{2}\rho U_\infty^2 &= K_1(P_1 - P_2) \\ (P_1 - P_3) &= K_2(P_1 - P_2) \\ (P_2 - P_3) &= K_3(P_1 - P_2) \end{aligned} \quad \ldots\ldots\ldots\ldots\ldots\ldots \quad (3\text{-}3)$$

where P_1-P_2 is the static pressure drop along the tunnel contraction and P_3 is the static pressure in the centre of the working section, gives

$$C_p = \frac{(P - P_{atmos}) - (P_2 - P_{atmos})}{K_1(P_1 - P_2)} + \frac{K_3}{K_1} \quad \ldots\ldots\ldots\ldots\ldots\ldots \quad (3\text{-}4)$$

By calibrating the tunnel we obtain K_1, K_2 and K_3. It was found that $K_1 = 1.073$, $K_2 = 1.0368$ and $K_3 = 0.03675$ so that

$$C_p = \frac{(P - P_{atmos}) - (P_2 - P_{atmos})}{1.073(P_1 - P_2)} + 0.034 \quad \ldots\ldots\ldots\ldots\ldots\ldots \quad (3\text{-}5)$$

This is line 370 to 372 in the software listing shown chapter 4.

Using this method to calculate C_p's eliminates the need for an absolute calibration of the pressure transducers. Instead, so long as their output is proportional to their input within the range used, C_p's can be derived from voltage units alone. The method requires certain ports on each scanivalve to be reserved for the pressure differences which need to be known. These were chosen as port 0 (windoff), 24 (P_1-P_{atmos}) and 25 (P_2-P_{atmos}) with each other port monitoring (P-P_{atmos}). Equation 3.5 was modified further to account for the small changes in tunnel speed which occur in the time period between measurement of (P-P_{atmos}), (P_1-P_{atmos}) and (P_2-P_{atmos}). The accuracy which could be achieved in the measurement of C_p's depends on the capability of the ADC's present in the CED1401. Each ADC can only resolve to ± ½ a bit. All voltage signals (± 5 volt range) were handled to 12 bit accuracy ie. ± 2.4

mV. A constant tunnel speed of 40 ms^{-1} gave a pressure difference for (P_1-P_2) equal to 950 mV and hence a resolution in excess of ± 0.25% could be achieved in the value of C_p. Periodic checking of the calibration for each ADC was carried out by applying a known voltage (accurate to 4 d.p.s.) to each and ensuring that the CED1401 correctly converted the known voltage to its equivalent bit designation.

3.6.3 Windtunnel corrections

With reference to Pankhurst & Holder (1952), a wing of maximum thickness t symmetrically placed between the roof and floor of a closed working section of height h and completely spanning the breadth b has an associated degree of solid blockage ϵ_s in two-dimensional flow given by the expression:

$$\epsilon_s = \tau\lambda\left(\frac{t}{h}\right)^2 \quad \text{(3-6)}$$

where

$$\tau = \frac{\pi^2}{12} \quad \text{(3-7)}$$

The wake blockage (ϵ_w) in two-dimensional flow is given by

$$\epsilon_w = \frac{1}{4}\frac{c}{h}C_{DT} \quad \text{(3-8)}$$

where C_{DT} is the measured drag coefficient. The effective increase in camber (γ_F-γ_T), the induced upwash w and increase of incidence (α_T-α_F) at the half chord point are given by:

$$\gamma_F - \gamma_T = \frac{\pi}{192}\left(\frac{c}{h}\right)^2 C_{LT} \quad \text{(3-9)}$$

$$\alpha_F - \alpha_T = \frac{w}{U} = \frac{\pi}{96}\left(\frac{c}{h}\right)^2 (C_{LT} + 4C_{MT}) \quad \text{(3-10)}$$

where subscripts T and F refer to the measured tunnel values and the corresponding free-air values respectively. These formulae apply to thin (t/c ≤ 12%), lightly loaded aerofoils having moderate camber distribution and a small chord length (t/h ≤ 15%). The high lift system in question is highly cambered and loaded and has a t/h ratio of 0.45. At high incidences the magnitude of the wake and solid blockage corrections would be very large and incorrectly calculated by the above formulae. Application of the above correction techniques would be unjustifiable on these grounds and produce incorrect free air results.

The only method of which the author is aware, which could correct the windtunnel results for interference effects and produce equivalent free air data, is the method of Ashill & Weeks (1982). However, the objective of the work is not to produce absolute design data, rather it is to undertake comparative testing.

4. Data acquisition system

With the emphasis in computer technology moving away from the BBC Master computer to IBM PC's having the 386/486 series processor chips and their associated DOS operating environments, it was felt that the current work provided an ideal opportunity to update the Department's data acquisition techniques. Problems were being anticipated in future data transfer processes between BBC Master computers and networked PC/UNIX systems, the latter providing greater opportunities to use advanced software.

At the heart of the new system is the use of a PC in conjunction with the Cambridge Electronic Design (CED) 1401. This is an 'intelligent' computer peripheral that contains a 65C02 microprocessor, 64 Kbytes of memory, software in ROM, an interface to the host computer and a wide range of input/output hardware. It can be used to generate and receive waveform, digital and timing signals. Using its own processors, clocks and memory, under control of the host computer, it makes complex real world tasks easy to control.

4.1 CED 1401

The 1401 is a multi-tasking system. This means that the operating system is designed to allow more than one process to be carried out at any one time. When this occurs, the main activity of the 1401 carries on as normal, but it is interrupted at intervals by hardware, causing the processor to execute a different program for a while before returning to the main activity exactly where it left off. There are two types of 1401 commands that do not use multi-tasking, but simply execute when invoked. The first of these is the dedicated type in which for maximum speed, all other processor tasks are suppressed while ie. an ADC is sampled at the fastest possible rate. The second is more tolerant and can run in the background while an interrupt driven command also runs. Typical of these are the arithmetic commands. Communication between the PC and the 1401 is achieved using an interface card installed on the hosts mother board. A 37 pin serial line control lead connects the interface card to the 1401.

4.1.1 Fundamentals of 1401 use

The computer communicates with the 1401 through the operating system which must be DOS 2.0 or later. The 1401 can be driven as if it were a printer and any language that is able to read and write text strings can be used to control its behaviour. The 1401 monitor software interprets each text string and invokes the appropriate code which carries out the actual task requested. An error will be generated if the code for the requested command was not present in the 1401 memory, if the command parameters were incorrect or if there was an error during execution.

A 1401 command consists of a list of ASCII characters terminated by a semicolon or RETURN character. The command string can be split into separate items separated by commas. An item could be a number, a character, a list of numbers separated by spaces or a string of characters. How many items are present depends on the command. Some typical commands are:

ERR; DAC,0,1024; ADC,0 1 2 3,2;

1401 commands obey a number of conventions. The most fundamental is that the first item in the command string is the command name, a text string containing up to seven characters. The rest of the items in the command string are command parameters specifying precisely the action requested by the user.

4.1.2 Memory

The 1401 contains both ROM and RAM chips. The software contained in ROM includes self-test programs which are executed on power-up (indicated by illumination of the red LED on the front panel), a small monitor or operating system and a number of commands referred to as "built-in" commands. Other 1401 commands to carry out different data acquisition tasks must be loaded prior to use in the 1401 RAM memory. By doing this, 1401 memory is only used to store commands that are wanted for the current application and the maximum amount of memory is left free for data storage. The code for most commands is under 1000 bytes and seldom more than 5 commands are loaded at any one time. The FFT command is the largest at 2.5 Kbytes.

The 1401 user memory starts at address zero and continues up to a variable top position; as commands are loaded the ceiling moves downwards. Consequently the memory available to the user for data storage in the standard unit is approximately 50 Kbytes. Some applications need to capture larger amounts of data at fast rates so an optional upgrade is available to 2 or 8 Mbytes of RAM.

4.1.3 Hardware settings

The standard 1401 handles all voltage signals to 12 bit accuracy, that is 1 part in 4096. Some applications do not need this resolution and you can save memory space and get faster performance by choosing to use only the top 8 bits, giving a resolution of 1 in 256. ADC readings cannot resolve to better than ± ½ a bit, so conversion of a steady signal may fluctuate by 16 or 256 units. The data representation is justified to fill the 16 bit (2 byte) range as follows:

Bits in word	-ve full scale	step size	+ve full scale
12	-32768	16	+32752
	-5 volts	2.4 mV	4.9976 volts
8	-128	1	+127
	-5 volts	39 mV	+4.961

The standard 1401 has a full scale voltage range for the ADC's of ±5 volts. This may be readily altered to ±10 volts, the safe limit being ±25 volts although no two inputs should differ by more than 20 volts. Signals should be amplified so that the expected maximum amplitude is between half and full scale or potential resolution will be lost. The input impedance of the ADC's is approximately 1Mohm. The full scale output voltages (DAC's) are similarly ±5 volts or ±10 volts. They are capable of driving 600 ohms to 5 volts. They are

not meant to be power drivers however and their settling time deteriorates with load impedances below 2 Kohms. The DAC's are short circuit proof.

4.2 Electrical Instrumentation

The data acquisition system is composed of two separate electrical circuits; the pressure measurement circuit and the Scanivalve control circuit.

4.2.1 Pressure measurement circuit

The Druck pressure transducer PDCR22 is a special purpose transducer designed specifically for scanning applications. It features excellent linearity, negligible hysteresis and a very low volume allowing fast scanning rates. It is designed to fit neatly into the main body of a Scanivalve. A pressure difference applied across the single crystal silicon diaphragm contained within the transducer causes deflection of the diaphragm . The diaphragm forms an integral part of a strain gauge bridge and the consequent strain caused by movement of the diaphragm is seen as a change in potential across the bridge circuit.

The excitation voltage for the pressure transducer is supplied by a Fylde FE-492-BBS bridge conditioning unit. This is a combined bridge/dc power supply unit and can provide energization and balance facilities for 1,2 or 4 active arm transducers of Wheatstone bridge form. Front panel controls allow for bridge supply voltage variation, zeroing of bridge by trim potentiometer and adjustment of bridge offset by ten-turn potentiometer. When used in conjunction with the PDCR22 pressure transducer the unit is configured for full bridge, constant voltage operation.

The output signals usually associated with dc bridge transducers are in the microvolt or millivolt range. To avoid losing resolution of the signal and hence accuracy, the signal must be amplified prior to input into a 1401 ADC channel. The Fydle FE-254-GA differential dc pre-

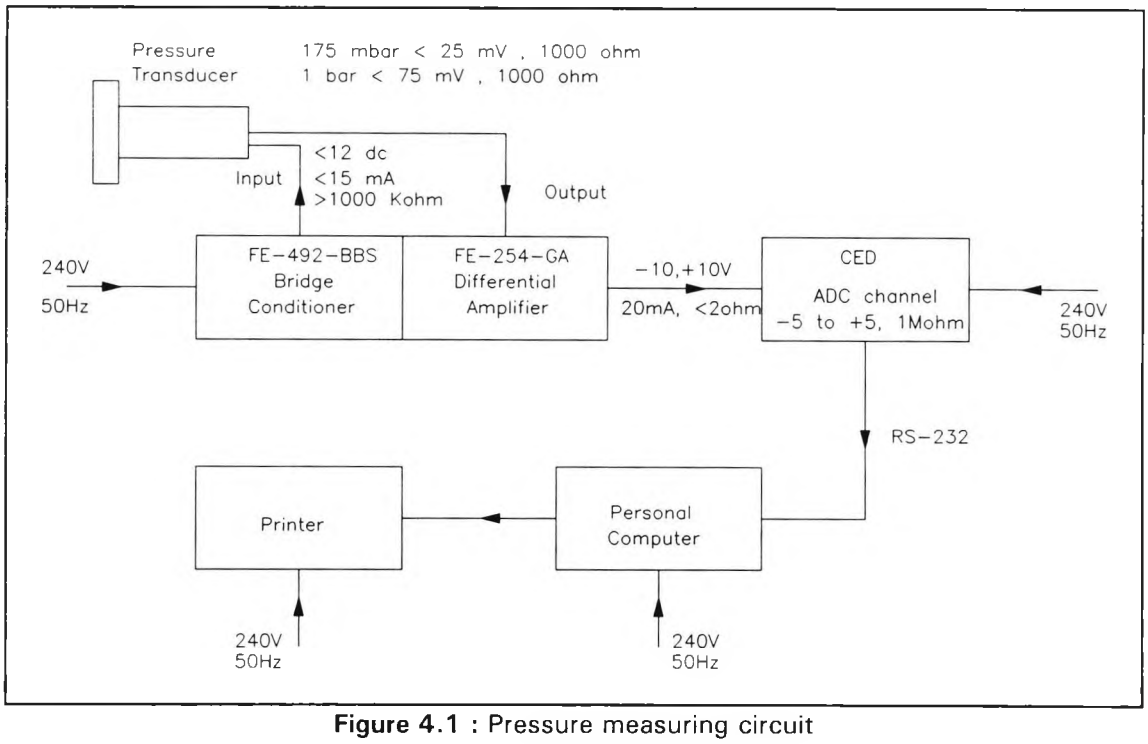

Figure 4.1 : Pressure measuring circuit

amplifier is used for this purpose. Using the amplifier with a particular source, knowledge of

the maximum expected output from the source (say 10mV) enables a gain to be selected (say x200) to obtain a useful output (2 volts) which into a load of 10Kohms will give 200 μA. Variable gain from x20 to x1000 can be selected while a 30 turn trim potentiometer gives a shift capability over the full voltage output range. Different sensitivities were employed for each transducer according to the magnitude of the pressure coefficients each was allocated to monitor. The pressure measuring electrical circuit is shown in figure 4.1.

4.2.2 Scanivalve control circuit

The common Scanivalve present in most Aeronautical engineering laboratories is a scanning type pressure sampling scanner capable of measuring multiple pressures. The Scanivalve enables one integral pressure transducer and its associated circuitry undertake the work of up to 48 transducers sampling 48 different pressures. A Scanivalve is composed of several individual modules each with their own particular task. The solenoid drive (as used in the current work) provides sequential connection of each of the 48 ports to the integral pressure transducer. A position transmitter electrically indicates port number being measured and the scanner which forms the main body of the Scanivalve contains the integral ducting necessary to allow each port access to the pressure transducer. Finally, the pneumatic connection which attaches to the scanner at one end provides the means for simple connection of pressure lines to the Scanivalve.

The standard 1401 has 32 bits controlling 32 digital input and output lines which are situated at the extreme right on the front panel of the 1401. Eight of these bits are permanently assigned to input and eight as output. The remaining eight bits for each input and output port may be assigned individually by the user as either for use as input or output lines. The permanently assigned bits appear to the user as the high byte of the digital input/output word (8-15), the user assignable bits appearing as the low byte (0-7). Only the digital output port is used for the current application.

Two bits (ie. lines) are required to control each Scanivalve (1 for home and 1 for step). By setting the direction of the user-assignable bits (0-7) to output the user has the possibility of controlling up to eight Scanivalves (16 bits) although in its present form the software can control a maximum of four. In the high state (+5 volts) the permanently assigned outputs will supply 15mA while the user-assignable outputs can only supply 200 micro-amps.

Each Scanivalve requires 2 amps from a regulated voltage supply. Consequently it is not possible to connect the Scanivalves directly to the digital output port. A succession of relays, each with its own power supply must be inserted between the digital output port and the Scanivalve. This allows the user to control Scanivalve behaviour while also satisfying their power demands. A schematic of the Scanivalve control circuit for each output line (ie. bit) is shown in figure 4.2. The diodes are present to prevent back e.m.f's from the inductance coils spiking the 1401 causing a hardware reset every time an output line is sunk to a low state (0 volts). The regulated voltage supplies are from transformers connected to the mains ac supply.

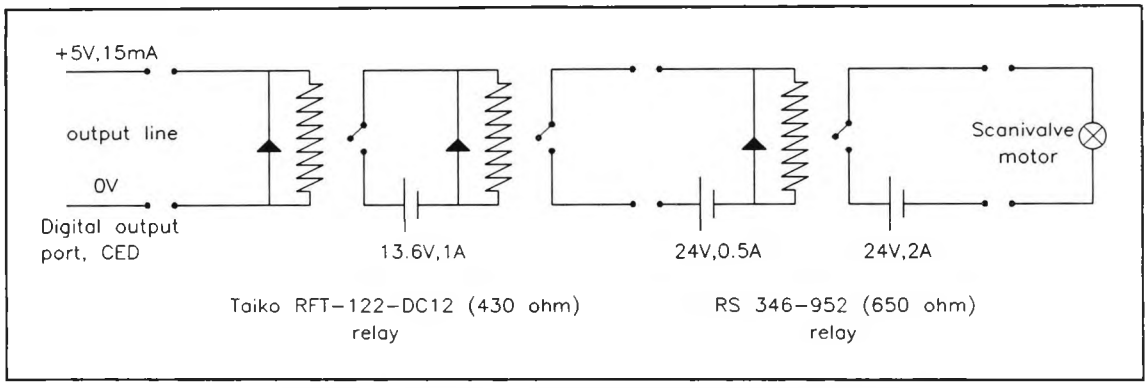

Figure 4.2 : Electrical circuit to control each scanivalve

4.3 Data acquisition software

The software has been written in Ryan-McFarland Professional Fortran. This is not the best language for writing user friendly software. However, Fortran is used widely in the scientific community and is ideally suited for handling large amounts of data. Ryan-McFarland Fortran does not contain code idiosyncrasies which are common in packages such as Microsoft Fortran. A detailed discussion of the software (listed in Appendix D) and a representative flow chart now follow.

The software comprises 452 lines of code: lines 4-149 form the main program; and lines 152-452 contain 14 subroutines.

lines 4-20: standard fortran variable definition procedures. All the variables used in the main program and those used in more than one subroutine must be defined here. By default all data sent to or from the 1401 must be in 2 byte, 16 bit integer form (really 12 bit as only the top 12 bits are used). Fortran can handle 2 byte integer variables if they are defined as integer*2. Real variables are never passed to the 1401.

lines 24-29: these lines clear the monitor screen and introduce the software to the current user. By default fortran unit numbers for the screen and keyboard are 6 and 5 respectively.

lines 35-54: the user is prompted for a title to head the printout that can be produced simultaneously while code execution is in hand. The title may have up to a maximum of 12 characters. The user is also asked if he/she wishes to store the data on disk and if so is asked to provide a filename for the data file. Two data files are in fact created, filename and filename.raw. Filename.raw contains the raw voltages (minus zero readings) as seen at the front panel of the 1401. This file aids location of i)possible hardware faults, ii)voltages which go out of range, and other problems which will result in errors appearing in the processed data held in filename.

lines 58-63: allow the user to specify the number of Scanivalves to be used in the text. Subroutine "Scanval" assigns odd numbered relays as step relays and even numbered relays as home relays. For example if one Scanivalve is to be used relays 1 & 2 are the step and home relays respectively for only this Scanivalve. The software calculations depend on each Scanivalve having three of its 48 ports monitoring specific pressures. Port zero is open to the atmosphere, port 24 is connected to the upstream contraction static and port 25 is connected to the downstream contraction static. If a Scanivalve is homed no pressure difference will act

across the integral pressure transducer. (P_{24}-P_{atm}) and (P_{25}-P_{atm}) give wind tunnel speed by a simple arithmetic relation.

lines 67-69: after the program has been successfully compiled it must be linked with the object file LABPRO.OBJ which CED supply for users writing software in professional fortran. This file assists in reading responses from the 1401, loading commands and transferring data blocks between the 1401 and the host. It holds the subroutines and functions essential for smooth communication with the 1401. Output can be sent to the 1401 either by writing text strings to a unit number or by calling the subroutine LABSTR(chars). This routine will send the text string associated with the character variable chars to the 1401. This routine is much faster than using WRITE statements. However it has the disadvantage that if the character string contains any variables (ie. numbers) these must first be converted to text strings before LABSTR can be used. The author selected the former method since speed was not an essential criteria for the work. To open a file for output on unit one we have OPEN(1,file = 'Labo'). Labo is a character device supporting all the character output functions contained in LABPRO.OBJ. The function LABGO must then be called before any other library routines (in LABPRO.OBJ) are used. It opens the file LABI for input and sets the character device driver to a ready condition. The integer*2 value returned on calling LABGO must be zero otherwise an error has occurred in the procedure.

lines 73-78: record the current ambient test conditions and model angle of attack.

line 82: homes all the Scanivalves under 1401 control. All the home relays are even numbered (lines 58-63) and these relays are controlled by the odd numbered bits 9-15 (pins 4-1 in the 1401 digital output port). Setting their state high (+5 volts) ensures the Scanivalves home to port zero. Bits 9-15 are then returned to their low state (+0 volts).

lines 83-85: the response characteristic of each transducer and the length of pneumatic tubing connecting the pressure measurement location to the Scanivalve determines the settling time of the pressure transducer output voltage. Therefore the scanning rate for each Scanivalve must be flexible and the software is written with this in mind. If the integer value which controls the scanning rate is increased from 2 to 4 the scanning rate will be halved.

lines 89-95: the pressure transducer output voltages (via the Fylde amplifier) can be connected to one of 16 different ADC inputs on the front panel of the 1401. The user is therefore asked to indicate which ADC inputs are in use.

lines 99-112: T2 can be run for extended periods of time. It is possible to record several data sets with each use of the tunnel. The user is asked for the current run number and prior to each run wind off or zero voltage readings are taken for the pressure transducers and manometer. These values are echoed to the screen for the user to check before continuing.

line 113: The Scanivalves can be plumbed in as the user so wishes (except ports 0,24 & 25). Subroutine STRTSCAN allows the user to locate the Scanivalve at any port prior to scanning the remaining ports. By plumbing backwards (ie. 47 downwards) the user can avoid unnecessary scanning of unused ports. Step control to each Scanivalve is achieved in the same way as homing except the step relays (odd numbered) are controlled by the even bits between 8-14 in the digital output port (pins 17-14).

lines 119-121: the Scanivalves do not scan the remaining ports until the user indicates that he/she is ready to do so.

lines 122-123: call the STEPSCAN subroutine. This routine is at the heart of the software. Each Scanivalve is dealt with in turn. The output voltages from the appropriate pressure transducer and manometer are digitised simultaneously. An average value is calculated after this is repeated 50 times. The same procedure is repeated after the Scanivalve is stepped forward one port. After the first Scanivalve reaches port 0 control is switched to the next Scanivalve and the procedure repeated. Eventually all Scanivalves are located at their individual zero numbered ports. The Scanivalves are then homed. If any Scanivalve responds to this command an error has occurred in the run procedure. Wind off readings are again recorded for the pressure transducers and the manometer.

lines 127-130: call the subroutine CPCALC. This routine converts the voltage data into static pressure coefficients. If a boundary layer profile is required, the results are processed further to reveal the variation of u/U_e (subroutine BDLYCALC) noting that the first port scanned must be the static port in the surface at the boundary layer rake location.

lines 131-132: call the subroutine CPPRINT. This subroutine controls the format with which the results are presented on the monitor (and consequently on the printout). The data file filename is also opened and the processed results stored in a similar format.

lines 136-137: the subroutine RAWDATA opens the data file filename.raw and records the unprocessed voltage readings which are invaluable in diagnosing faults.

lines 138-149: clear the monitor screen, reset the appropriate variables to zero and prompt the user to end the session or repeat the entire procedure.

4.3.1 Software particulars

The subroutine CONVERT (lines 152-157) contains the arithmetic relation which converts integer values representing voltages seen at the front end of the 1401 into their voltage equivalent. The arithmetic equation (line 155) depends on the hardware setting of the 1401 ADC's having a full scale range of ± 5 volts. If this is altered, for example to ± 10 volts the equation must reflect the new hardware setup bearing in mind that resolution will be halved.

Every time the program is executed a file called FORT3 is created in the same directory as that containing the software. This file (opened on unit 3) contains carriage returns (ie. blank lines). It arises from fortrans inability to allow a timed pause to occur during program execution. This is overcome by the software entering a null do loop a predetermined number of times (lines 172-186). This file is harmless and can be removed by the user in the normal manner.

Fortran is a language suited to processing numbers. Prompts to the user which inevitably lead to a reply in the form of a character string are not handled easily. They must be converted to their ASCII equivalent before the software can decide the course of action to take. Subroutine ANSWER (lines 164-170) carries out this task.

Output to the 1401 (contained in WRITE statements) is buffered and to be sure that any command has actually been sent to the 1401 the output buffer should be flushed with a REWIND statement. Any text strings will then be sent forceably to the 1401.

All input from the 1401 is in the form of integers separated by commas with a carriage return at the end of each input line. The LABNUM routine reads an entire line from the 1401 (knowing how many integers to look for) and is one of the subroutines supported by LABPRO.OBJ.

The tunnel calibration factor for T2 is incorporated into the calculations within the subroutine CPCALC. The software calculations must be amended if the calibration alters or the software is used in tests which are carried out in a tunnel other than T2.

The boundary layer calculations in subroutine BDLYCALC rely on the first scanned port monitoring the static pressure acting at the boundary layer rake location.

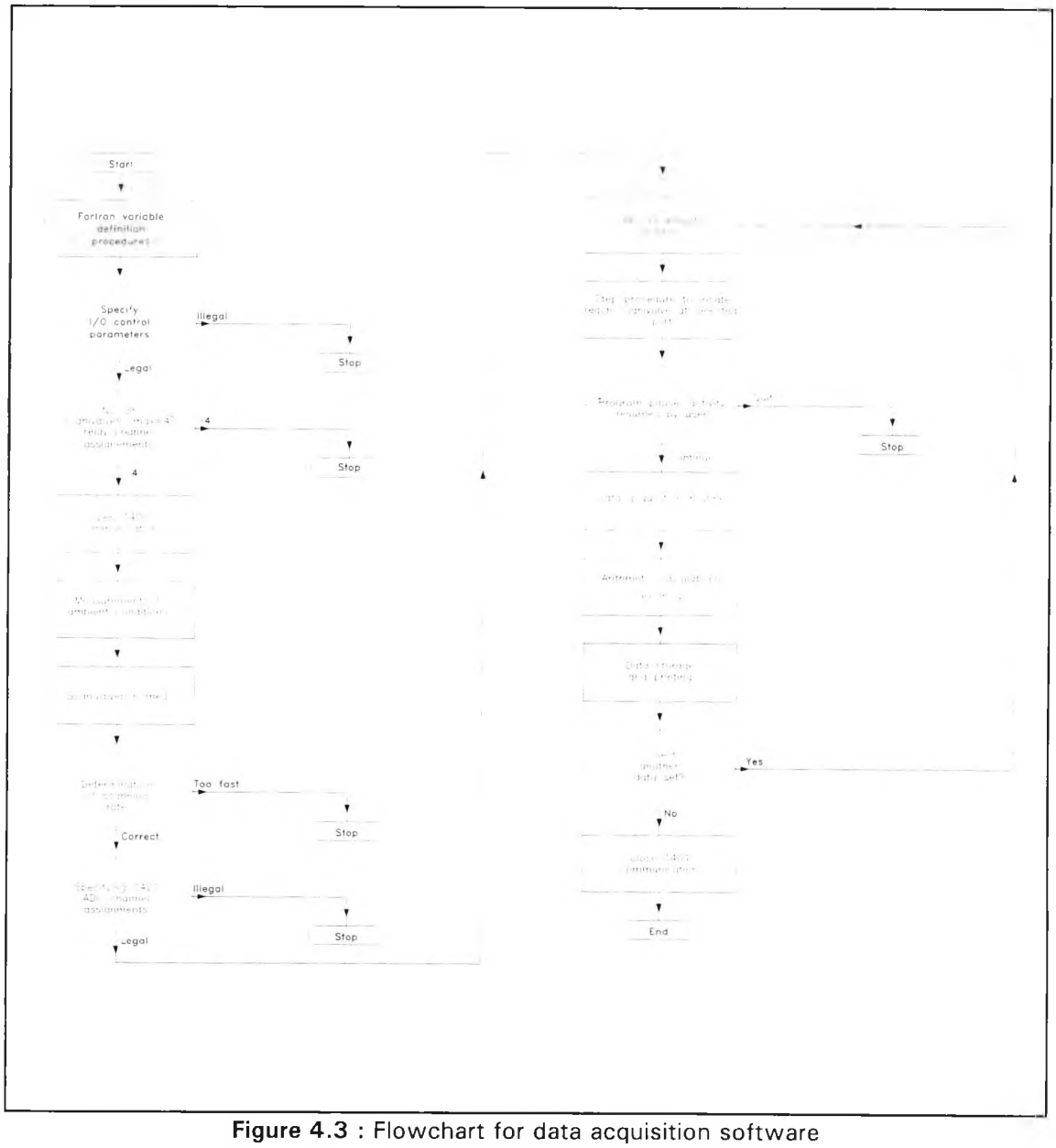

Figure 4.3 : Flowchart for data acquisition software

5. Cleanfoil

5.1 Background to tests

Though two-dimensional flows never really exist on aircraft wings, two-dimensional windtunnel tests on aerofoils with high lift devices can be very instructive, since the essential features of the three-dimensional wing usually are well represented by the two-dimensional flow (wake/boundary layer mixing, gap and lap sizes). Wing flow, however, is very much three dimensional in nature and hence stall and post-stall behaviour will be different. Windtunnel tests of high lift systems presents problems which are particular to this class of aerofoil, first by the high aerodynamic loads and secondly, by the complexity of the models. Unfortunately, during the early part of the work problems associated with conducting experiments of this kind were significantly underestimated. The main problems the author encountered are detailed below.

5.1.1 Contamination

In the early stages of the project it was discovered during inspection that the fine mesh gauze upstream of the working section was dirty. In particular a large percentage of the lower half of the screen was found to be coated in a thick layer of glycerine (from previous experiments), rending this region of the gauze effectively impervious to the flow in the windtunnel. Thorough cleaning of the mesh gauze undertaken while the tunnel underwent a process of dismantling, relocation and re-assembly will undoubtedly have reduced the general level of turbulence in the freestream and hence reduced boundary layer thickness on both the model and endplates. The model characteristics certainly changed - this view arising from the more predictable and symmetric behaviour of the flow over the endplates: flow separation moving forward with increasing incidence rather than a sudden severe separation occurring seemingly randomly on either endplate.

5.1.2 Leakage

This problem, common to both the wall-to-wall model and the endplate model, originates from the high aerodynamic loads which are carried particularly by the slat and main wing elements of the high lift system. A two-dimensional test set-up is obtained by placing a model of finite span between reflection planes. These may be the walls of the windtunnel or endplates. Nevertheless, at the junction of these reflection planes and the model spanwise extremities it is essential that no leakage of flow occurs from the lower surface of the aerofoil to the upper surface. Rubber gaskets shaped to the chordwise profile of each (individual) element were incorporated into the model design. These were inserted between the model ends and each endplate to ensure that an airtight seal was present at this junction.

5.1.3 Construction

Difficulties can occur with the construction of leading edge slats since these elements of high lift systems are thin and the loads are high (often $C_{n\ max} > 1.0$). A construction with an acceptable stiffness must be obtained. The first slat used for testing was of a laminated wooden construction, made in two equal ½ spanwise lengths (for ease of pressure tapping). These were joined together by glue to form the full length slat. Added

stiffness came in the form of two slat brackets, each located equidistant from one endplate and the model centre line. However, the condition of this first slat deteriorated with time. The trailing edge began to break simply because of its inherent thinness. Significant deflections began to occur under load, distorting the geometry of the slat gap and hence the flow through the leading edge slot.

It became clear that a second slat had to be manufactured but not from wood. Aluminium was the material finally chosen and the end product proved a success in three respects: i) because of its one piece construction and inherent stiffness qualities it had little deflection under load; ii) removal of the spanwise supporting brackets allowed for greater uniformity in the flow through the slot; iii) greater precision in manufacture eliminated local flow separation cells which were present on the wooden slat once its surface began to deteriorate.

The manufacture of the slat from Aluminium was a decision which was not taken lightly as it was the first aerofoil to be made entirely from this material in the workshops. It also proved rather costly in terms of the number of cutters which were used during the milling process.

5.1.4 Endplate boundary layer control

The interference effects of reflection planes perpendicular to the model are almost entirely due to the boundary layer on these walls. The boundary layer at the model/endplate junction is subjected to the same adverse pressure gradient as that on the aerofoil. However, it does not benefit from the fresh boundary layer effect (Smith, 1975) and separation inevitably occurs at the model/endplate junctions prior to being seen on the model. Although

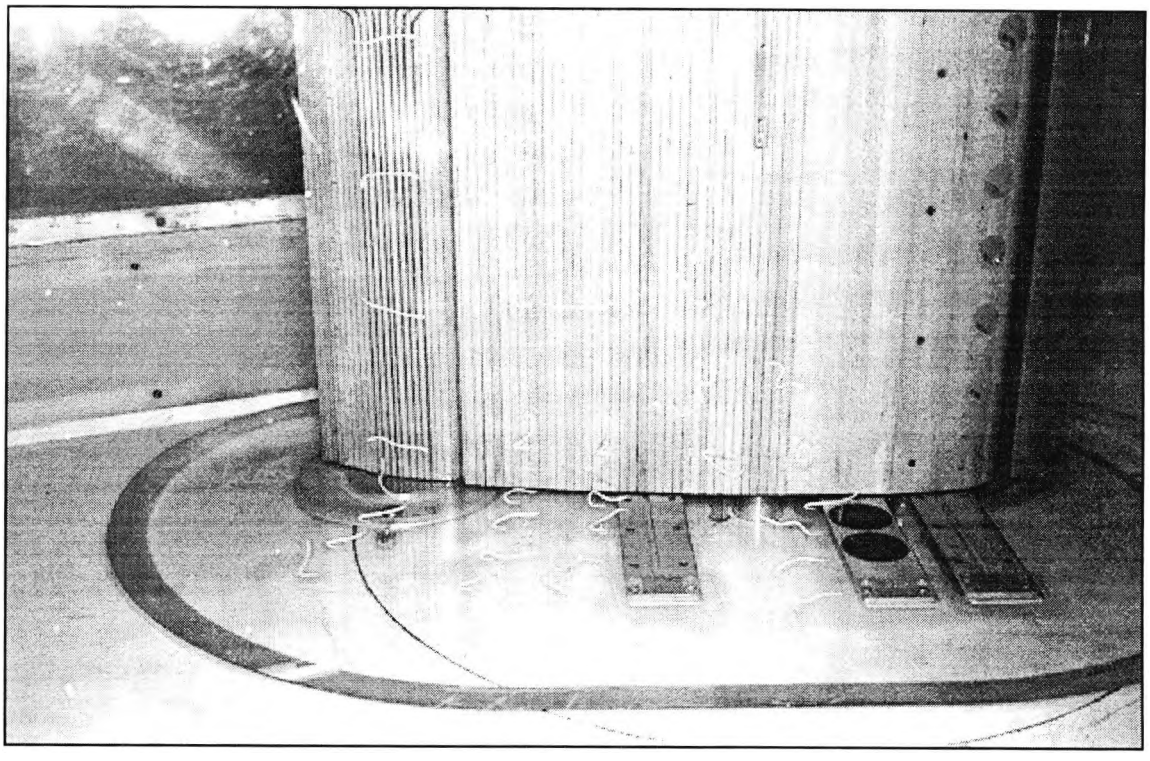

Figure 5.1 : The effects of separated flow on an endplate

the boundary layers on the endplates are thinner than those on the tunnel walls (and hence can withstand greater adverse pressure gradients before separating), wall interference effects can be severe. The regions of separated flow spread spanwise (fig. 5.1) in triangular wedges with an angle of approximately 45°. Consequently for a model with a geometric aspect ratio less than two (we have 1.4) flow separations can exist at the model centre line which have originated at the endplates. Large local lift losses will be associated with the separated flow regions, reducing the effective aspect ratio of the system and introducing discrepancies into the relationship between the geometric and effective incidence of the model.

The behaviour of the flow on both endplates was repeatable and consistent with each another, with separation of the boundary layer moving forward with increasing incidence from a position adjacent to the main wing trailing edge. By 20° control of endplate boundary layer separation was essential if two-dimensional conditions (as indicated by tufts) were to prevail on the high lift system. Initial attempts to control the separation using vane vortex generators proved marginally successful in that the maximum incidence available for testing was increased to above 25°. A second method involving the use of a circular jet blowing arrangement, whereby compressed air was blown tangentially across the main wing/ endplate junctions to re-energize the boundary layer in this region further increased the maximum incidence to 28°. However this method was often inconsistent and introduced repeatability errors into the results.

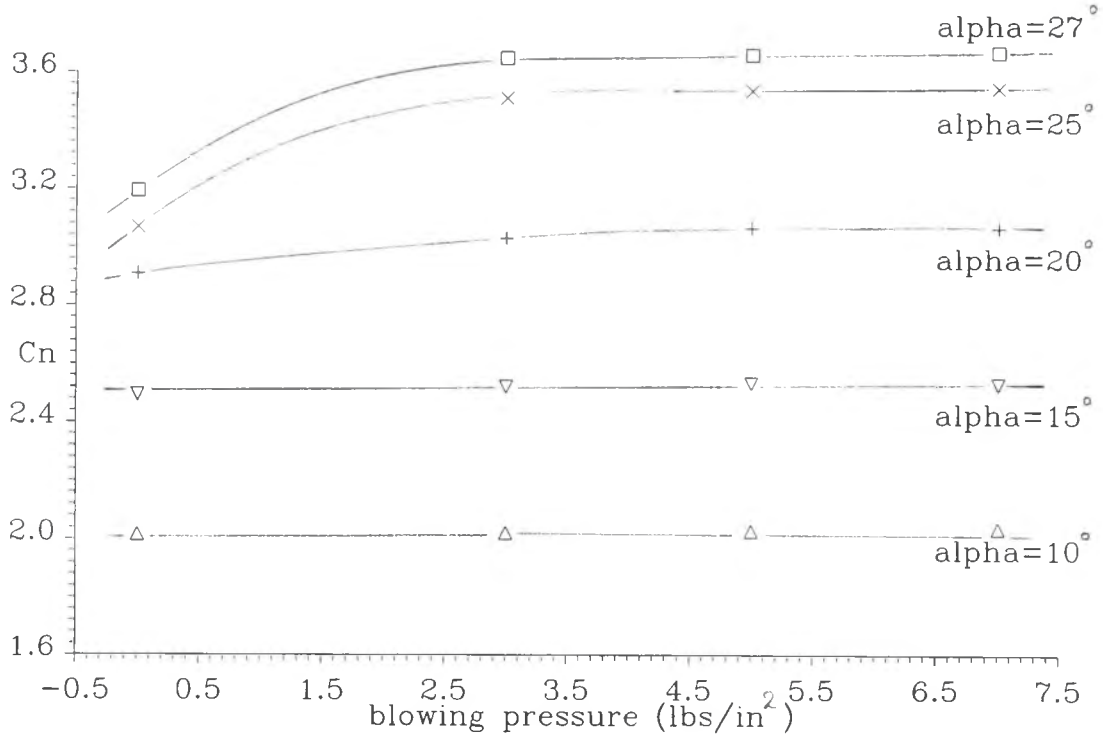

Figure 5.2 : The effect of endplate blowing on total normal force coefficient

A more acceptable solution was sought in the from of blowing slots installed flush into each endplate. Two slots at x/c = 0.14 and x/c = 0.612 of the retracted chord were found to be sufficient (provision was made for a third, intermediate one, but not used). These slots allowed compressed air to be blown tangentially over the endplate surfaces parallel to the

chord of the aerofoil. Each slot was 1mm wide, inclined at 15° to the surface of the endplate and each extended a distance of x/c = 0.3 out from the endplate/main wing junction. Their downstream face was faired to promote their tangential blowing qualities and shallow plenum chambers slightly less deep than the thickness of each endplate ensured a uniform jet per unit length of slot without creating additional local blockage between each endplate and the adjacent tunnel wall.

Figure 5.2 presents the variation of total C_n with slot blowing pressure at several geometric incidences for the high lift system. It is apparent that the total C_n initially increases rapidly with increasing blowing pressure for incidences above 20°, but that above a slot blowing pressure of approximately 3 psi the total C_n at any given angle of incidence remains constant within the experimental scatter. Furthermore , for incidences up to 15° when the adverse pressure gradient along each endplate is not sufficient to cause large local regions of separated flow at the endplate/ main wing junctions, the pressure tappings at mid-span are insensitive to needless endplate boundary layer control by slot blowing.

Evidently, the effect of blowing on the endplates is small as soon as the blowing quantity exceeds the amount needed to avoid the onset of flow separation occurring prior to the flow reaching the endplate trailing edge. In addition the insensitivity of the system to excessive blowing negates the necessity for adjustment of the blowing quantity required to achieve the best two-dimensional stall pattern. So long as a level of blowing is selected which exceeds the minimum value necessary to ensure that early flow separations do not originate from the endplate main wing junctions, it can be assumed two-dimensional flow conditions will prevail over the whole incidence range. Consequently, the author selected a blowing level of 4½/5 psi for each slot which was used for all tests up to and beyond the stall incidence of the high lift system. Figure 5.3 illustrates the effect of slot blowing on the endplates.

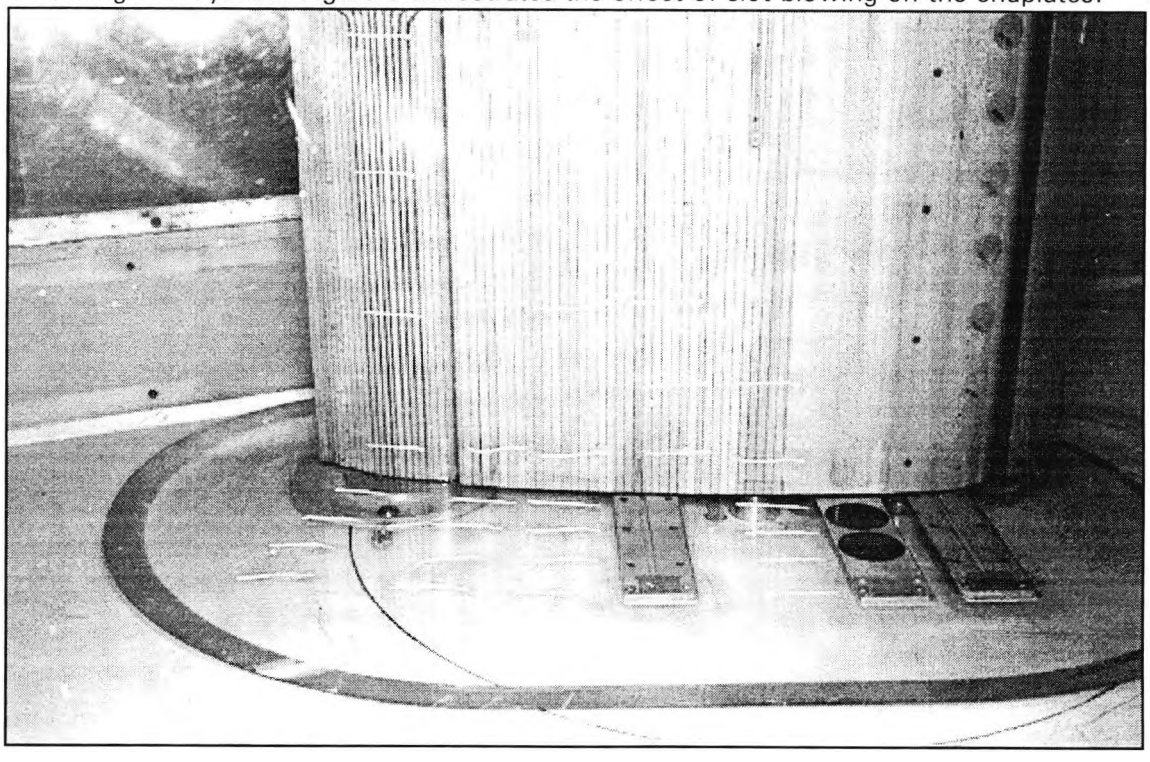

Figure 5.3 : The effects of slot blowing on the endplate boundary layer

5.2 Format to the discussion of results

The following chapters discuss those results obtained from tests undertaken with the model at various angles of attack with and without the use of boundary layer control. The present chapter deals with the cleanfoil case while tests with vanes and airjets are discussed in subsequent chapters. The tests involved:

(i) monitoring the pressure distribution around each element of the multiple element aerofoil

(ii) investigating the structure of the shear layers above the main wing and flap elements of the high lift system.

Simpsons rule is used to calculate the normal force coefficient generated by each element of the high lift system. For the flap and main wing elements of the high lift system the integration starts on the lower surface of each element at the tapping adjacent to the trailing edge, proceeds forward around the leading edge and over the upper surface of each element. In this way the normal force coefficient for the flap and main wing elements will be underestimated by a small but consistent amount since i) the contribution from the loading in the flap cove on the lower surface of the main wing beyond $x/c = 0.82$ and ii) the loading on the flap between the trailing edge and the first tapping on the lower surface are both neglected. The loading carried by the upper surface of the slat is first calculated and then added to that carried by the lower surface. The slat had no trailing edge pressure tapping at $x/c = 0.03$ and so a linear extrapolation of the loading on the upper surface of the slat was assumed beyond $x/c = 0.0$. This was also the case for the lower surface. The total load carried by the slat will be underestimated as Simpsons rule cannot account for the slat peak suction seen between the tappings located at $x/c = -0.08$ and $x/c = -0.06$. The areas referred to in this paragraph are shaded in Figure 5.13. Normal force coefficients are always calculated using the reference chord length (500mm).

The variation with incidence of the peak suctions on the slat and main wing elements have been chosen as being represented by the pressure experienced at a particular port on each of these elements. For the slat this is the pressure tapping located at $x/c = -0.08$ and for the main wing it is the pressure tapping at $x/c = 0.1$. The results presented in each of the figures contained in the appendices are derived from at least two separate tests thereby ensuring the validity of the results.

The shear layers adjacent to the upper surface of the high lift system were examined at various locations along the chord of the aerofoil. In the case of the cleanfoil configuration investigations took place at (% x/c) 14.2%, 20.3%, 25.3%, 35.4% and 90% (trailing edge) on the main wing, and on the flap at 100% (just beyond the location of maximum thickness). Tests undertaken with co-rotating vanes and airjets positioned on the main wing at 14% chord produce a shear layer structure which is three-dimensional in nature and has a characteristic spanwise periodicity. Within the limited time available, explorations of these shear layers were restricted to those chordwise positions which were anticipated as having a greater bearing on the understanding of the fluid mechanics at work. Thus shear layer explorations in the presence of co-rotating vanes and airjets were undertaken at 35.4% and 90% x/c on the main wing and at 100% x/c on the flap. The shear layer information is presented in contour plot

form, with two figures (at two different incidences) on the same page. Occasionally data is also presented in a three-dimensional surface plot form alongside the relevant contour plot. The following table is included as a quick reference guide to the more **important** shear layer explorations which were undertaken above the high lift system.

α x/c	0°	5°	10°	15°	20°	25°	26°	27°	28°	30°	32°
35.4	1	1	1,2,3	1	1,2,3	1,2,3			1,2	3	
90	1	1	1,3	1	1,3	1,2,3	1	1	2	2,3	2
100	1,2,3	1	1,2,3	1	1,2,3	1,2	1	1	2	2,3	2,3

Key: 1 - Cleanfoil, 2 - Co-rot. vvg's, 3 - Co-rot. ajvg's

The parameters δ^*, θ, and H used to describe a shear layer (equ. 2.1 - 2.4) are calculated for each shear layer exploration carried out above the cleanfoil and presented below the relevant figure. **Mean** values of these parameters calculated while employing co-rotating vane vortex generators or co-rotating airjet vortex generators observe an upper limit of δ = 0.995; that is they do not include the high momentum air of the airjet cores which can be seen in the shear layer presentations included in subsequent chapters. The use of pitot rakes in the vortex flows anticipated can be justified as the crossflow component of the vortex induced velocity was not expected to be greater than approximately 15% of the total velocity vector except near the vortex cores and the surface. The effects of yaw on pitot readings should therefore not have been large in general.

The results presented seem to indicate the principle that enhanced mixing promoted by airjet vortex generators can lead to significant improvements in the lift and reduction in the profile drag of a high lift system above and beyond that achieved by vane vortex generators. It is felt the flow processes involved are of a fundamental nature and are unlikely to be influenced in their applicability by the low Re. number or Mach number of the tests, or by the effects of windtunnel wall interference. The object of the tests is not to produce absolute design data.

5.3 Reynolds number effects (fig. 5.4)

Figure 5.4 shows the effect of Reynolds number variation on the normal force coefficient generated by the main wing of the high lift system at various angles of incidence up to the stall incidence of the cleanfoil. For incidences below the stall the effect of increasing Reynolds number within the range available is negligible. For incidences close to the stall ($\alpha \geq 25°$) Reynolds number effects are present although only to a slight degree. All tests discussed in this report were carried out at a Reynolds number of 1.3 million which is close to the maximum for this combination of model geometry and tunnel size.

5.4 Pressure distribution measurements (fig. 5.6 to 5.22, Appendix A)

At zero degrees incidence the flap normal force coefficient is approximately four times as large as that of the slat (fig. 5.17). The peak suction generated at the leading edge

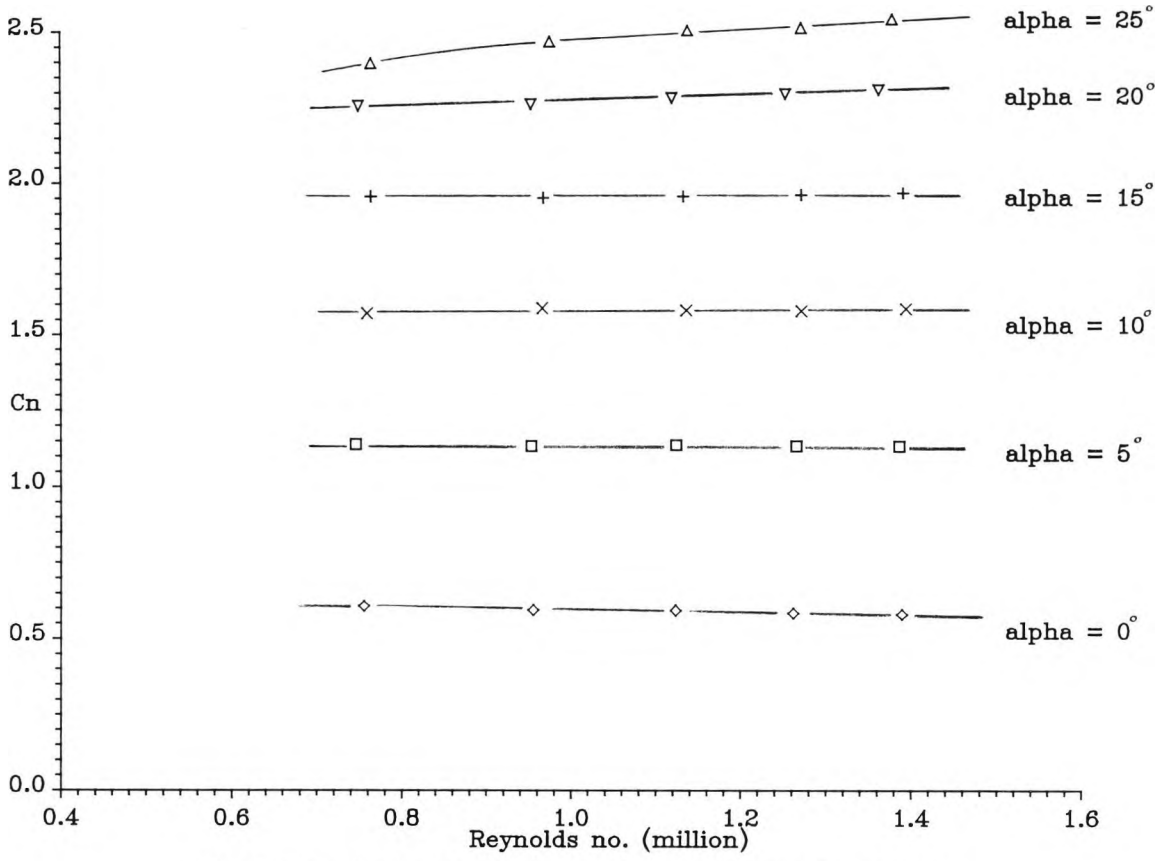

Figure 5.4 : Variation of main wing C_n with Reynolds number

of all three elements is of the same magnitude at -1.25 (fig. 5.6). The total normal force coefficient generated by the three element system is 0.9 (fig. 5.20). The characteristic flatness seen in the pressure distribution associated with the slat cove at all angles of attack is indicative of a separation bubble in this region. The flow will separate from the sharp edge of the cove and re-attach close to the trailing edge of the lower surface of the slat in accordance with the local Kutta condition. The re-circulation velocity is low in such a bubble which gives rise to a nearly constant static pressure throughout the slat cove. This is a good example of the small amount of separation which must be tolerated by a high lift system, which has to have been designed within the constraints of the cruise aerofoil configuration, so that it achieves a high lift curve slope. The size and shape of the separation bubble will vary with incidence, although re-attachment will occur sooner at high incidences through movement of the stagnation point towards the sharp leading edge of the cove.

Close examination of the pressure distributions in figure 5.6 reveal that although the slat has a stagnation point at its most negative chordwise extremity, the main wing is devoid of a leading edge stagnation point at this incidence (0°). Further more, a large proportion of the leading of the main wing is subject to the same slightly negative level of pressure as the lower surface of the slat (slat cove). As the flow accelerates around the leading edge of the slat it separates from the sharp leading edge of the slat cove and re-attaches on the lower surface of the main wing beyond approximately 20% x/c. On the upper surface of the slat the flow leaves the trailing edge smoothly and re-attaches on the upper surface of the main wing at approximately 5% x/c. Thus a large proportion of the main wing leading edge is in the

separation bubble produced by the slat cove. Consequently, there is no slot flow through the slat gap at this incidence.

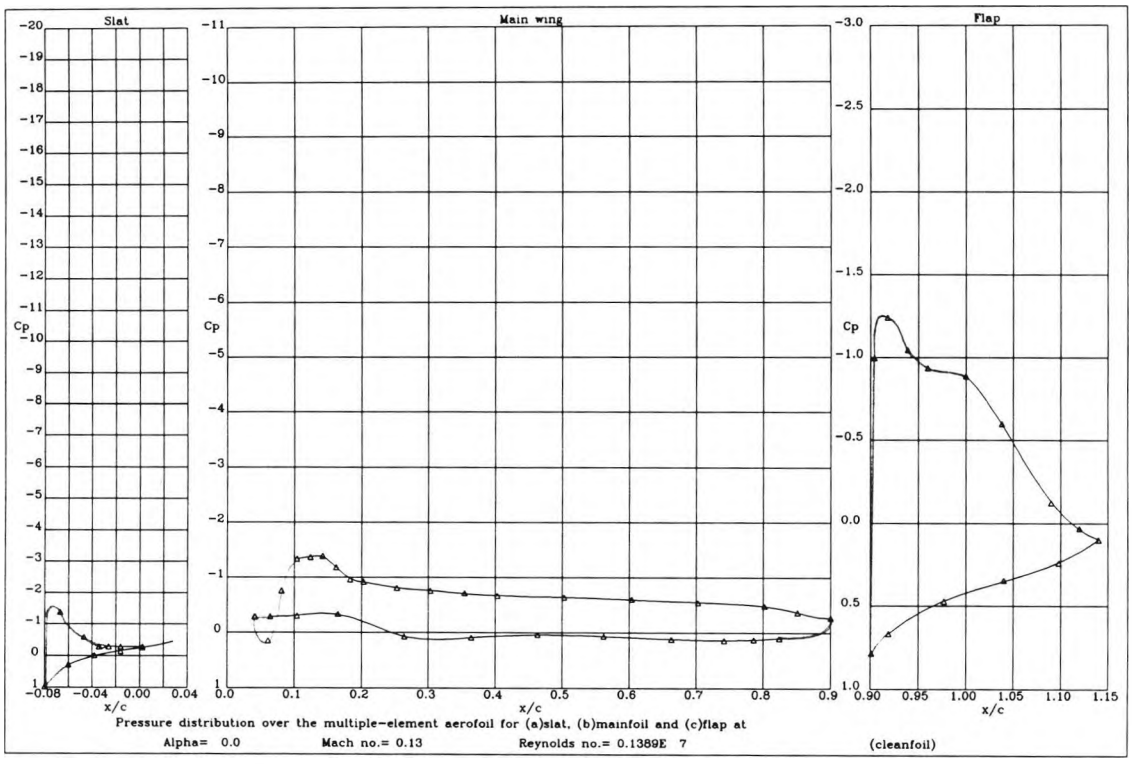

Figure 5.6 : Pressure distribution over the high lift system at 0°

By 5° the main wing has a lower surface stagnation point at x/c = 0.1. However the close proximity of the slat still influences the pressure distribution at the main wing leading edge (figure 5.7) in a manner which continues to incidences in excess of 10° (fig. 5.8). Initially, the flow (and hence the flow in the boundary layer) experiences a favourable pressure gradient as it travels from the main wing stagnation point towards the leading edge of the main wing. The pressure gradient then becomes adverse for a finite length before returning to a favourable condition to beyond the location of the main wing peak suction. The changing nature of the pressure gradient to which the main wing boundary layer is subjected is again associated with the separation bubble of the slat cove. Either the separation bubble of the slat lower surface is continuing to impinge on the leading edge of the main wing or alternatively the two streamlines defining the limits of the separation bubble and the boundary layer at the leading edge of the main wing form a convergent-divergent 'nozzle', through which passes the potential flow of the freestream. The exit plane of this convergent-divergent 'nozzle' will be defined by the perpendicular drawn from the main wing leading edge which intercepts the slat trailing edge. From this point the pressure gradient will once again become favourable until the location of the main wing peak suction. The pressure distributions (fig. 5.6 to 5.8) cannot tell us what effect this has on the local boundary layer but transition (in the absence of attachment line transition) may occur sooner than otherwise expected with re-laminarization also a possibility.

The dumping effect referred to in section 2.1 can be clearly seen in action on both the slat and main wing elements throughout all the figures (fig. 5.6 - 5.16). The magnitude

of the effect is greater at the trailing edge of the slat at high incidences where the local velocity exceeds twice the freestream velocity (fig. 5.13). The static pressure at the trailing edge of the flap exhibits the Kutta condition in its more familiar form (ie. similar to that seen on single element aerofoils) in that the local velocity is seen to be lower than that in the freestream.

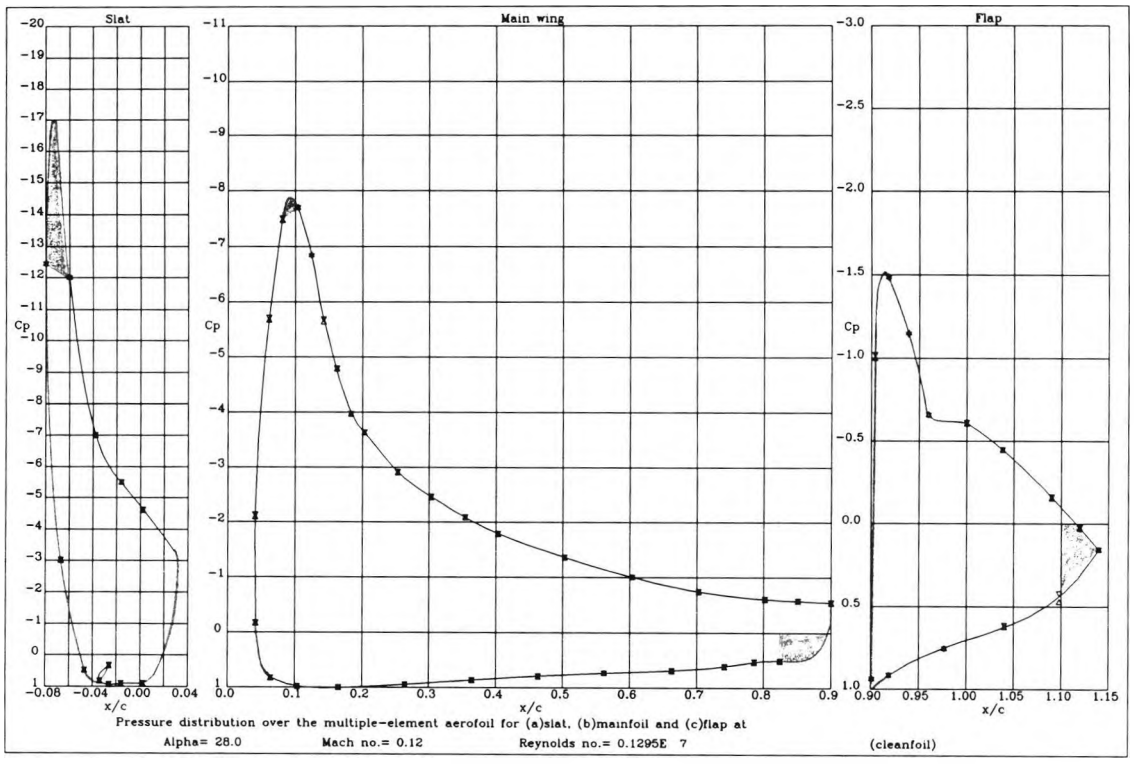

Figure 5.13 : Pressure distribution over the high lift system at 28°

The slat pressure distribution changes rapidly with increasing incidence below 10° (fig. 5.6 to 5.8) and provides only a limited contribution to the lift generated by the high lift system at these incidences. By 15° however, the slat pressure distribution has taken on a more familiar form and the C_n of the slat and flap are equal at 0.28 (fig. 5.17). The location of the stagnation point at the leading edge of the slat at low incidences (-0.08 x/c) quickly becomes the location close to where the slat peak suction occurs at high incidences. As the stall incidence of the high lift system is approached (fig. 5.13 & 5.17), the slat is seen to generate a normal force coefficient of 0.9. The severe adverse pressure gradient which exists over a large proportion of the slat upper surface by 15° will force rapid transition of the boundary layer. Flow visualization techniques were employed to detect this physical phenomena. A turpentine solution containing fluorescent chalk powder held in suspension was applied to the upper surface of the slat and the windtunnel quickly run up to the full test Reynolds number. The results did indeed show that the boundary layer on the upper surface of the slat was turbulent prior to separation from its trailing edge (fig. 5.5). However, it could not be ascertained whether this was as a consequence of natural transition or whether a laminar separation bubble exists on the upper surface of the slat after which the boundary layer reattaches in turbulent form. Unfortunately the slat is inadequately pressure tapped for this to be seen in the pressure distributions relating to this element. The small degree of

curvature seen in the streamlines was present as the problem of endplate boundary layer separation had yet to be solved at that time.

The precise location of the stagnation point on the lower surface of the main wing at high incidences is unclear since as much as 10% of the main wing chord on the lower surface experiences a static pressure close to the total pressure of the freestream (fig. 5.10 to 5.18). Unlike single element aerofoils, where the boundary layer on the lower surface experiences a large favourable pressure gradient over a considerable distance behind the leading edge stagnation point, the boundary layer on the lower surface of the main wing experiences a much smaller favourable gradient which is continuous to the sharp edge of the main wing cove. If transition occurs in this boundary layer before it reaches the main wing cove, the length of the boundary layer transition region will be a significant percentage of the wing chord.

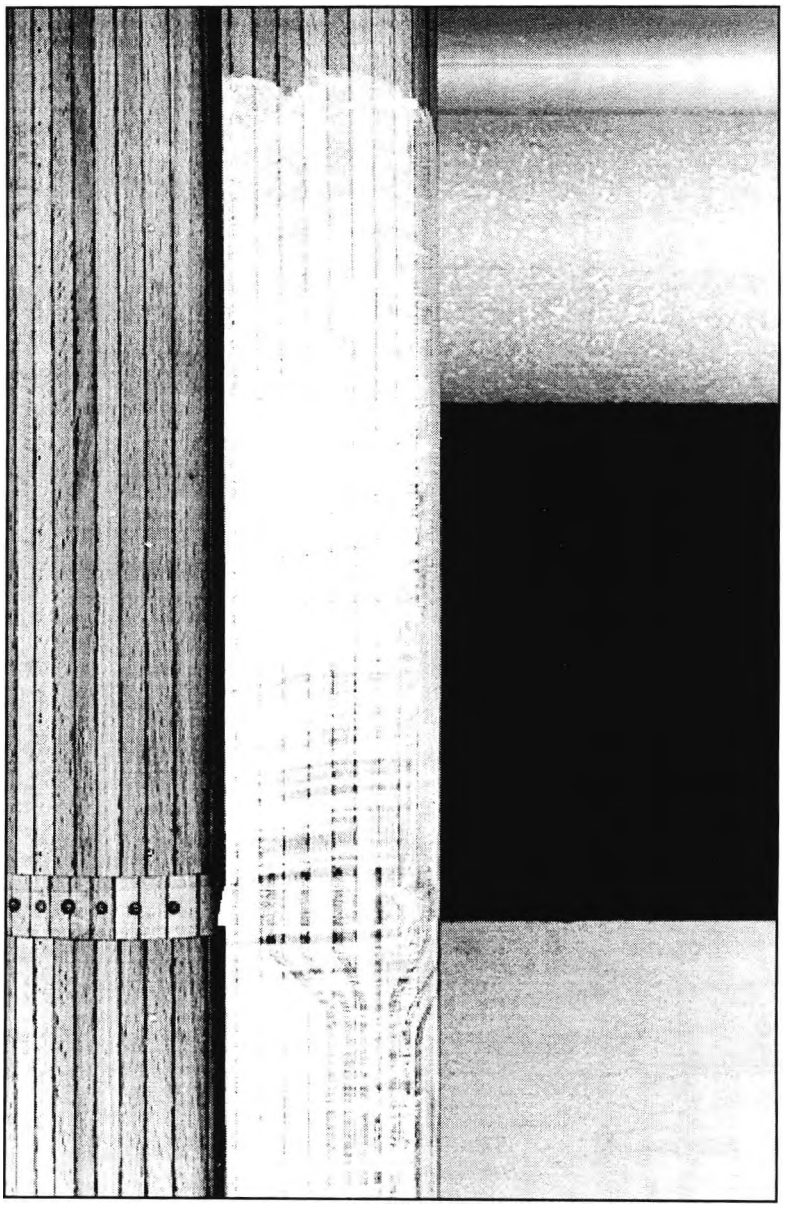

Figure 5.5 : Transition in slat upper surface boundary layer

Although the slat and circulation effects (section 2.1) are always present on a high lift system, their effect can be more easily seen in figures 5.10 to 5.12. The main wing peak suction increases by -1.5 between 20° and 27°. Through the same incidence range the slat peak suction increases by -5.5. The rate at which the slat peak suction increases is seen to accelerate through the low incidence range whereupon at 20° and above the rate of increase becomes linear (fig. 5.19). The rate of increase seen in the main wing peak suction remains constant throughout the incidence range (fig. 5.19). If the peak suction experienced by the slat at 25° (fig. 5.11) was experienced at the leading edge of the main wing in isolation the main wing would almost certainly exhibit large regions of separated flow.

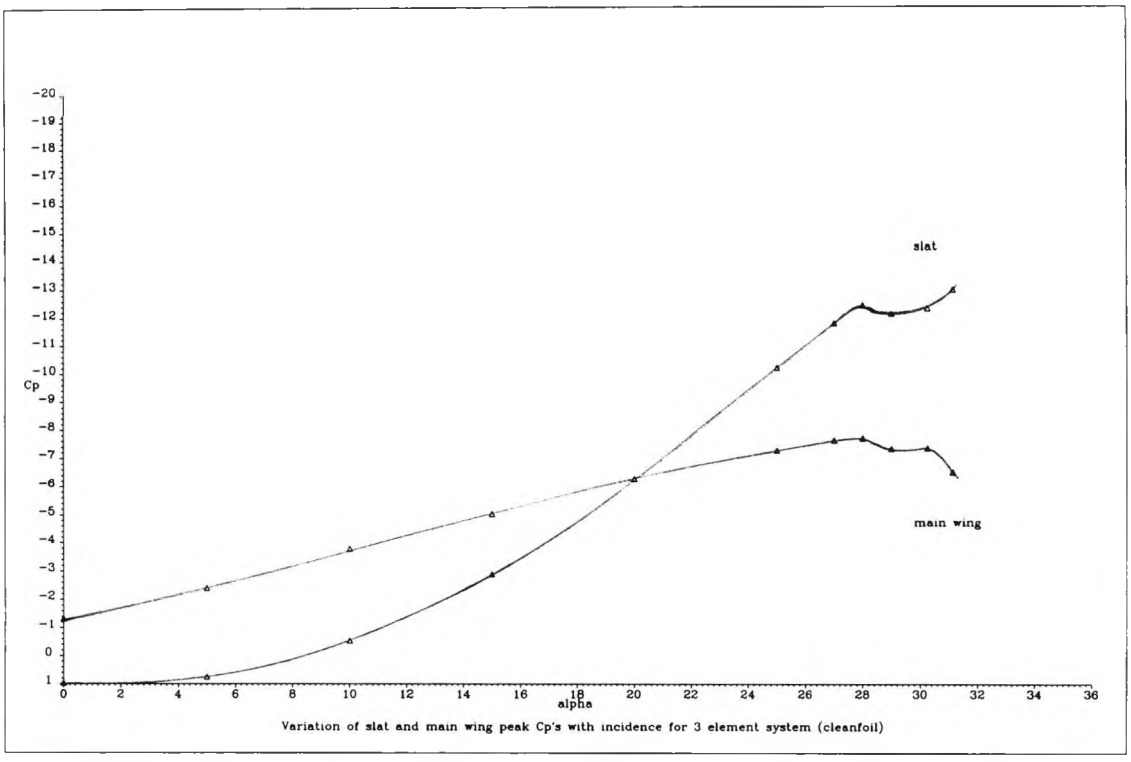

Figure 5.19 : Variation of slat & main wing peak C_p's with α for the cleanfoil

The characteristic linear increase with incidence usually seen in the normal force coefficient generated by single element aerofoils is also present for the high lift system between 5° and 20° (fig. 5.18). Above 20° however, the linearity in this curve is lost for the high lift system. This coincides with the locus of the main wing trailing edge pressure (at x/c = 0.9) beginning to level out prior to divergence (fig. 5.20 & fig. 5.21). Further examination reveals that by 20° and as far forward as x/c = 0.6 from the main wing trailing edge the static pressures acting on the upper surface of the main wing have either reached a minimum or have begun to rise (fig. 5.22). This feature is most marked at 80% x/c where by 15° the local static pressure has already reached a minimum. Since separation is not present on the main wing at this incidence the gradual development of this loss of load at the rear of this element must be due to the adverse viscous shear introduced into the main wing boundary layer by confluency with the slat wake, increasing the displacement effect of the shear layers at the rear of the main wing (fig. 5.25 to 5.28). The variation of C_p at this location on the main wing follows the characteristic variation of pressure seen at a fixed point well forward of the trailing edge on a single element aerofoil as a rear separation moves forward over it. Inevitably, the normal force generated by the main wing is adversely affected which accounts for the loss of linearity in the variation of C_n with incidence from 20° (fig. 5.18).

Throughout all tests, cotton tufts were present on the upper surfaces of all elements. By combining this technique of flow visualization with the pressure distribution information we see that the main wing element experiences flow separation close to its trailing edge by 27° (fig. 5.12). This is accompanied by a reduction in the pressure recovery at the trailing edge of the flap (fig. 5.21), presumably because of the increased overall thickness of the

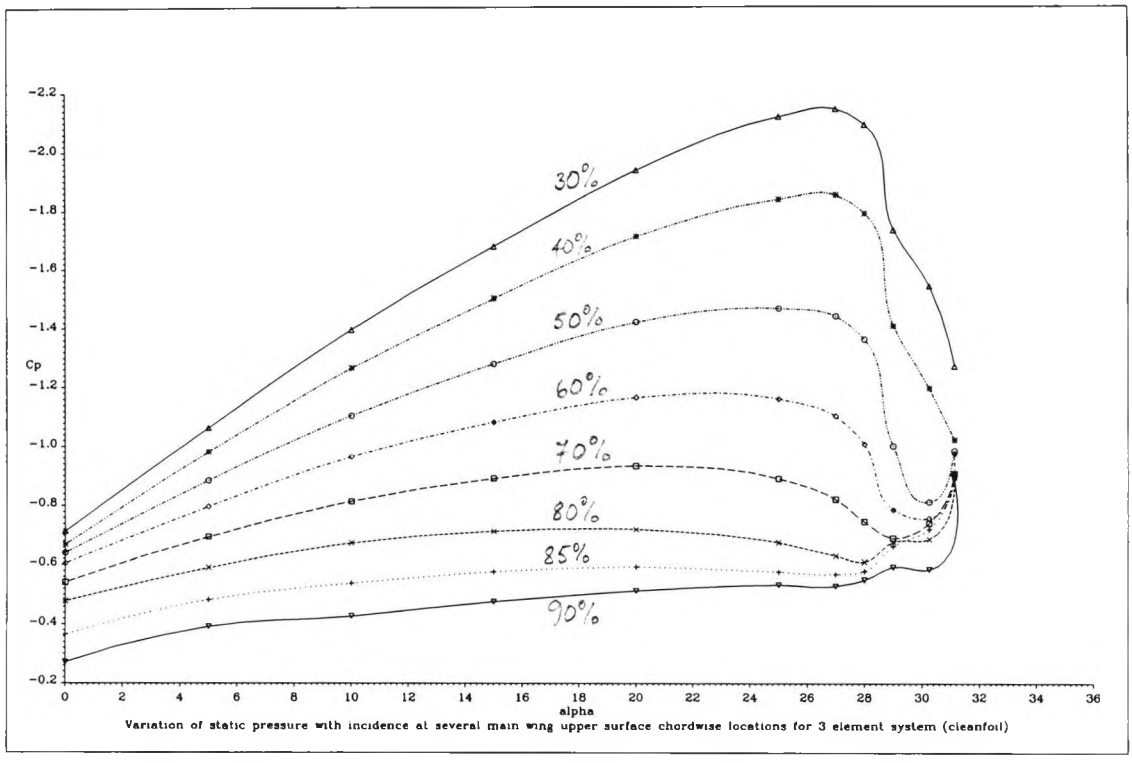

Figure 5.22 : Variation of static C_p with incidence at several x/c positions on the main wing upper surface

shear layers at this location (fig. 5.35 & 5.36). The boundary layer separation on the main wing develops slowly as does the fall in the pressure at the trailing edge of the flap, although the classic trailing edge divergence behaviour seen on single aerofoils is not clearly defined at the main wing trailing edge until above 30° (fig. 5.20). The total C_n for the system as a whole reaches a maximum (3.662) at 28° (fig. 5.13 & 5.18), largely due to the slat contribution continuing to increase beyond 27° (fig. 5.17). By 29° the flow has collapsed on the flap (fig. 5.14), accompanied by a significant fall in the pressure recovery at the trailing edge of the flap, resulting in a reduction in the overall circulation of the high lift system - total C_n falls as does the slat peak suction and C_n. The boundary layer separation on the main wing continues to develop steadily with incidence, moving forward to x/c = 0.4 by 31° (fig. 5.16).

The question raised is whether the mechanism of the stall of the high lift system arises from the continual development of one event, namely the rear separation on the main wing triggering the collapse of the flow on the flap and hence the overall stall; or whether there are two events, more independent, namely the slowly developing rear separation on the main wing which is overtaken by the collapse of the flow on the flap and which dominates the mechanism of the stall of the high lift system. As results in later chapters with vortex generators will demonstrate, when separation at the rear of the main wing is delayed the separation on the flap is also delayed. Hence, the level of circulation which the high lift system generates up to and through stall is determined by the satisfaction of the Kutta condition at the trailing edge of the **flap**.

By five degrees incidence the pressure distribution over the flap has adopted a form which changes little with further increases in incidence through to the stall incidence of the

high lift system (fig. 5.13). Consequently, the normal force coefficient generated by the flap also remains approximately constant with incidence (fig. 5.17). Under conditions of weak interference from the wake of the main wing and slat, the development of the boundary layer on the upper surface of the flap would then also be expected to be almost invariant with incidence. From this position we could then argue that the **initial** onset of stall will not occur as a result of the viscous development of the boundary layer on the upper surface of the flap. This is indeed the case as we have already seen that events which occur towards the trailing edge of the main wing produce a localised boundary layer separation in that region.

The behaviour of the static pressure at the trailing edge of the flap (figs. 5.20 & 5.21) is particularly interesting. For incidences up to approximately 13° a progressive increase can be seen in the pressure recovery achieved at the flap trailing edge. However, between 13° and 20° the static pressure remains constant before rising sharply once again for incidences between 20° and 25°. The pressure distributions associated with the flap element clearly show that a small region of separated flow is established between x/c = 1.12 and x/c = 1.14 by 13° on the flap upper surface (fig. 5.9). By 20° the feature is at its most prominent (fig. 5.10). With further increases in incidence up to 25° the flow is seen to re-attach (fig. 5.11) and the pressure recovery at the flap trailing edge improves (fig. 5.20 & fig. 5.21).

A discontinuity can be seen in the main wing upper surface pressure distribution at x/c = 0.14 (fig. 5.6 to 5.9). The feature gradually disappears by 20° at this location (fig. 5.10) and is associated with the presence of the slat wake above the main wing upper surface. A similar feature can be seen in the pressure distribution over the upper surface of the flap between x/c = 0.96 and x/c = 1.0. The feature is particularly marked at 0° but decreases in severity with increasing incidence up to 10°. Above this incidence the severity of the feature gradually returns until at 28° only a very small adverse pressure gradient exists in this region on the upper surface of the flap. It is interesting to note that when the feature is very prominent the boundary layer separation at the flap trailing edge is absent with the converse also being true. Another point of interest is that as the stall incidence of the high lift system is approached the concave pressure distribution over the flap upper surface beyond 100% x/c gradually becomes convex in nature.

5.5 Shear layer measurements (fig. 5.23 to 5.40, Appendix A)

Figure 5.23 presents the change in the profile of the shear layers between x/c = 0.14 and x/c = 0.9 above the upper surface of the main wing at 0°. The absence of any slat wake confirms that while the slat produces little usable lift at this incidence (fig. 5.17) it also produces little drag ($\theta_{slat} \approx 0$). The total thickness of the boundary layer at x/c = 0.142 is 3.5mm. The chordwise location of this boundary layer measurement is also seen to coincide with the chordwise limit of the favourable pressure gradient at the leading edge of the main wing for this incidence (fig. 5.6). The slight adverse pressure gradient which exists between x/c = 0.142 and x/c = 0.354 is seen to increase the thickness of the boundary layer by only 1mm (fig. 5.23 & 5.34). However, the magnitude of u/U_e measured at the lowest pitot station

in the rake above the main wing exhibits a large reduction (and hence by inference kinetic energy), leading to a higher velocity gradient within the boundary layer at x/c = 0.203. By x/c = 0.9 (main wing trailing edge) the thickness of the boundary layer has increased to 11.75mm with the velocity measured by the pitot tube closest to the surface of the main wing being less than 50% of that outside the boundary layer. There is no evidence of any slot flow at this incidence confirming the separation bubble associated with the slat cove impinges on the main wing leading edge.

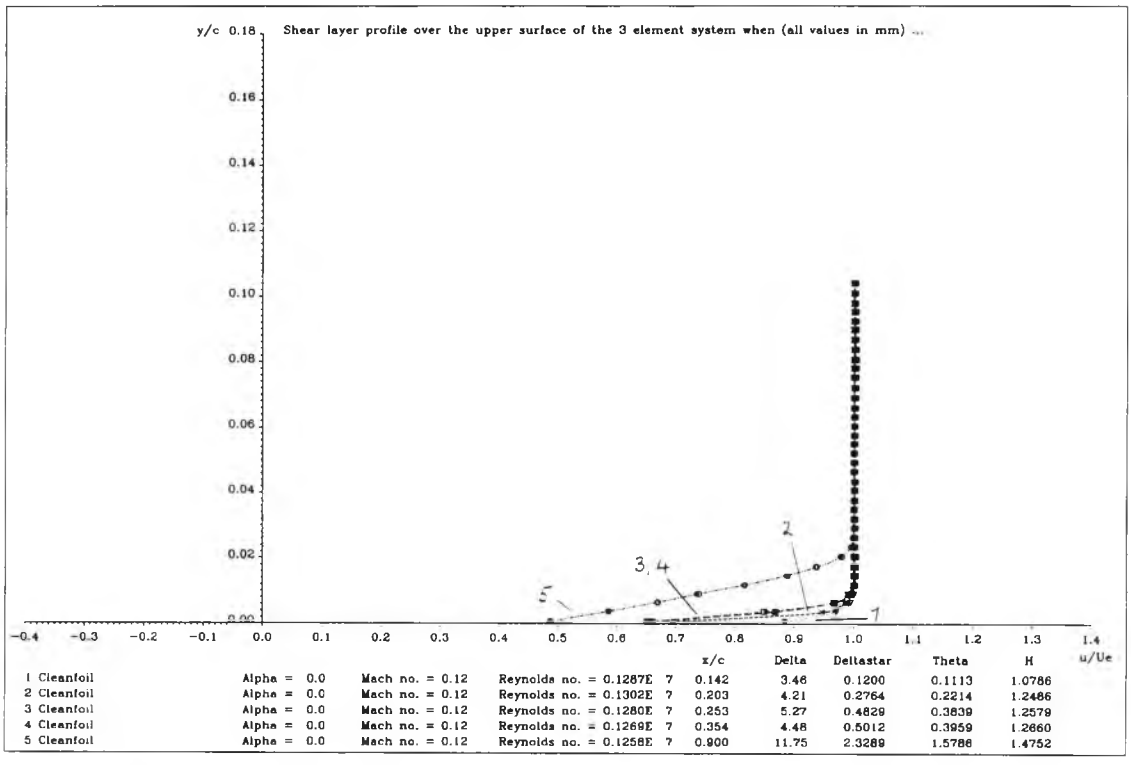

Figure 5.23 : Shear layer development over the main wing of the high lift system at 0°

The mean velocity profile of the shear layer above the flap at x/c = 1.0 and 0° incidence is presented in figure 5.30. The flap upper surface boundary layer is seen to be confluent with the wake from the main wing at this incidence. Hence freestream pitot pressure is not reached anywhere in the flow through the gap which will have a detrimental effect on the boundary layer thickness at the trailing edge of this element and in turn the pressure recovery (fig. 5.20). Inevitably, the inviscid effect (section 2.1) which the flap has on the slat and main wing elements is reduced, giving rise to the non-linearity seen in the C_n curve for the high lift system at low incidences (fig 5.18). By 5° the flap upper surface boundary layer is not confluent with the wake of the main wing and slat at x/c = 1.0. Freestream pitot pressure is reached in the flow through the flap gap and the loading on the flap is seen to increase (fig. 5.7). In general, the total lift of the high lift system will vary with flap position in a manner similar to that predicted by inviscid theory so long as streamlines having freestream pitot pressure separate the flap upper surface boundary layer from the viscous shear layers shed by the main wing.

Figures 5.30 to 5.33 show that from 5° to above the stall incidence of the main wing element of the high lift system (27°, fig 5.17) flow having freestream pitot pressure

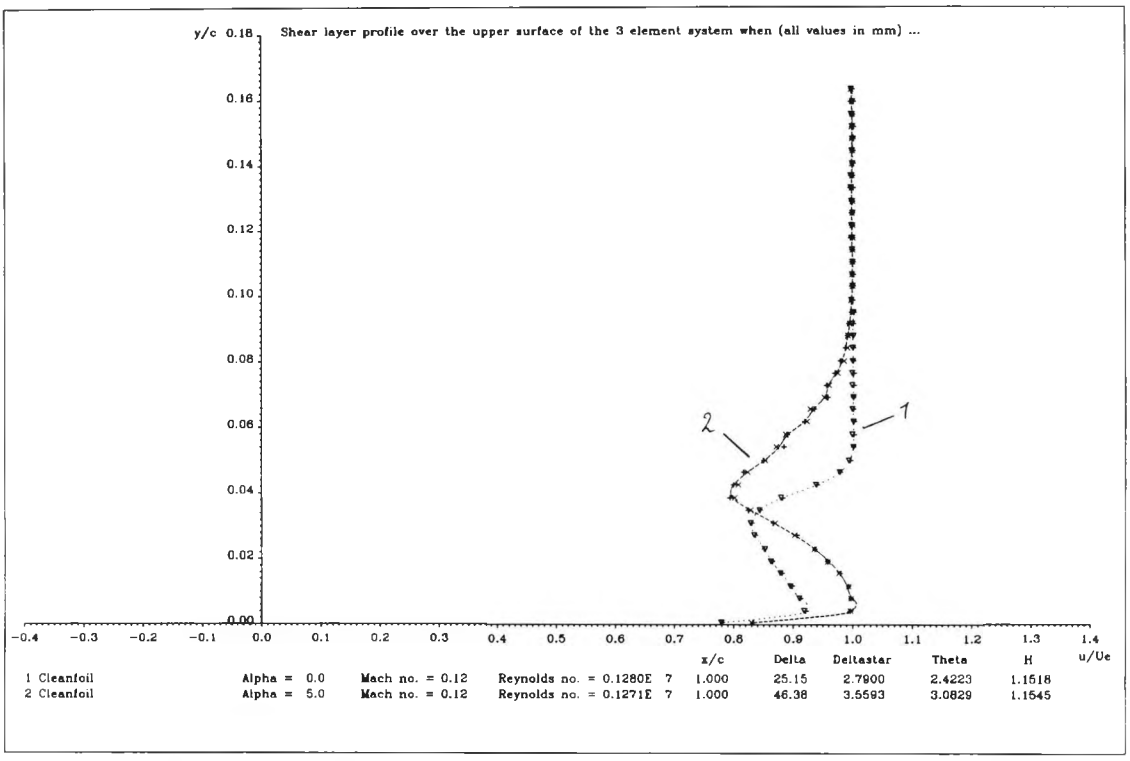

Figure 5.30 : Shear layer profiles over flap of the high lift system at 0° & 5°

always separates the boundary layer on the upper surface of the flap from the confluent wake of the main wing and slat at x/c = 1.0. Further, the height to which this slot flow extends to above the surface of the flap nearly doubles between 5° and 27° (4.5mm to 8.5mm). Figures 5.30 to 5.33 also show that the flap upper surface boundary layer changes very little with incidence as suggested, confirming the **initial** onset of stall for the high lift system originates towards the trailing edge of the main wing.

Figure 5.39 illustrates the effect which the momentum thickness of the shear layers above the flap has on the flap peak suction. The initial stepwise behaviour is due to the confluency of the flap upper surface boundary layer and main wing wake at 0°. When calculating the various values of θ at x/c = 1.0 the contributions from the momentum defect due to the flap upper surface boundary layer alone can be assumed to be approximately constant because little change is seen in both the pressure distribution over the flap for and in the boundary layer on its upper surface. Hence figure 5.39 illustrates the effect which the momentum thickness of the confluent main wing and slat shear layers have on the flap peak suction (through the mechanism discussed by Moser and Schollenberger, 1973). It must be noted here that between 5° and 27° incidence the location of the flap leading edge stagnation point moves only by 0.02 x/c and in a manner which would otherwise try to increase the loading on the flap. A smaller confluent main wing and slat wake is seen to improve the flow over the flap and hence increase the flap loading. The associated increased pressure rise behind the flap peak suction may in turn be responsible for the flap trailing edge separation seen at x/c = 1.12 to 1.14 (fig. 5.6 - 5.10).

At 5° (fig 5.24) the mean velocity profiles towards the leading edge of the main wing begin to show the presence of a slat wake. By comparing the profile obtained at the

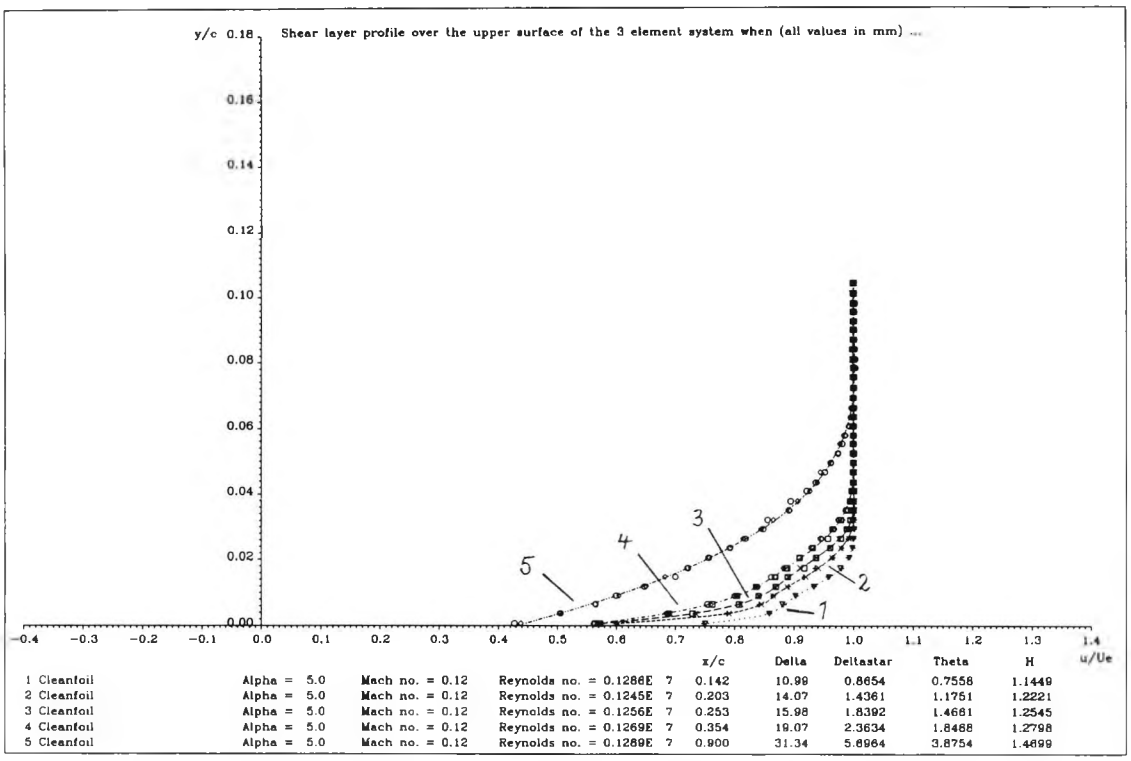

Figure 5.24 : Shear layer development over the main wing of the high lift system at 5°

same location on the main wing for 0° and 5° it can be seen that a large increase has occurred in the thickness of the shear layers (as much as 450% at x/c=0.354). The shear layer profiles measured between x/c=0.142 and x/c=0.354 inclusive also show a high degree of similarity in their general shape. This is due to the dominant influence of the slat wake and that the shear layers at these locations at 5° are now all subjected to an adverse pressure gradient as the location of the peak suction has moved forward to x/c=0.1. By x/c=0.9 the slat wake and main wing upper surface boundary layer have completely merged (through turbulent mixing) to form a confluent boundary layer with a velocity profile which conceals its multi-source origin. At 20° (fig. 5.27) the streamwise distance over the upper surface of the main wing is not sufficient for the two shear layers to completely merge and the shear layer profile at the main wing trailing edge then shows two distinct regions.

The most striking development at 10° (fig 5.25) is that at all chordwise locations on the main wing and flap the high lift system experiences a reduction in the total thickness of the shear layers over that seen at 5° (fig. 5.25 & fig 5.34). The effect is greatest at x/c=0.354 and derives from the movement of the leading edge stagnation point on the slat towards to the sharp leading edge of the slat cove. The increased circulation around this element allows the slat to generate a normal force coefficient equal to that of the flap (fig. 5.17), while at the same time its particular shape achieves this by encouraging earlier re-attachment of the separated flow in the slat cove. This is consistent with the near disappearance of the unusual pressure distribution which dominates the region around the leading edge of the main wing element below 10°. Further, figure 5.40 shows the high lift system produces its maximum L/D ratio at approximately 12° as a direct result of these developments.

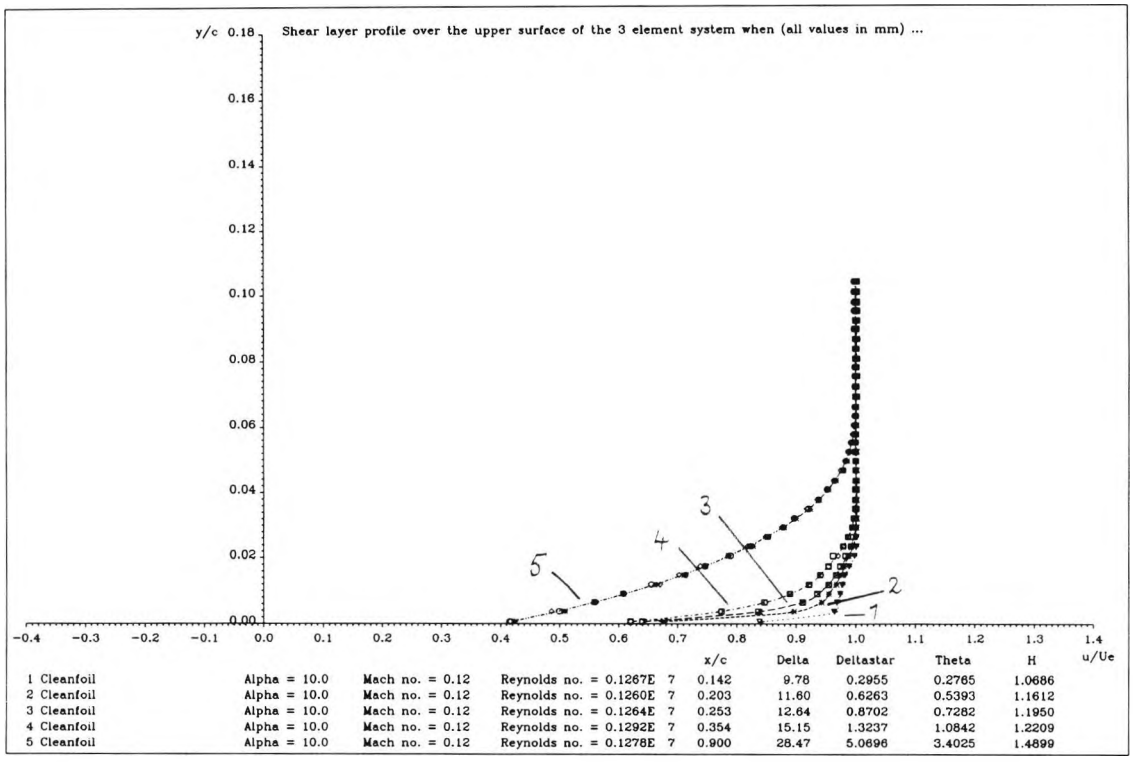

Figure 5.25 : Shear layer development over the main wing of the high lift system at 10°

Although the total thickness of the shear layers at any location above the main wing or flap show little overall increase between 5° and 15°, detailed changes in the shape and structure of the shear layers do take place. The gradual emergence of flow through the slat gap with near total pressure can be seen in the shear layer profiles shown in figures 5.26 - 5.28. The appearance of the slot flow, which with incidence, increasingly delays the start of confluency between the slat wake and main wing boundary layer, improves both δ^* and θ at the locations x/c = 0.142 to x/c = 0.354 inclusive (fig. 5.35 and 5.36). In fact both δ^* and θ at these chordwise positions do not again reach the peak values which they obtained at 5° until incidences in excess of the stall incidence of the high lift system. The local skin friction coefficients in the chordwise region between x/c = 0.142 and x/c = 0.253 on the main wing probably increase through the delayed merge of the main wing boundary layer with the slat wake. This is because the pitot measurements adjacent to the main wing surface show a consistent increase in the value of u/U_e and by also delaying the merge momentum energy which otherwise would be lost as unrecoverable turbulence is retained. These events coincide with the gradual disappearance at this location of the discontinuity which is evident in the main wing pressure distributions.

However, the thickness of the shear layers above the main wing trailing edge gradually increases with increasing incidence (figs. 5.23 to 5.29, except fig. 5.25). The slat wake is dumped at velocities appreciably greater than freestream velocity. The deceleration to freestream conditions is accompanied by a large increase in the thickness of the slat wake which in turn is responsible for the mixing of this wake with the main wing boundary layer. A level of turbulence associated with the slat wake will be introduced into the main wing boundary layer which further promotes the mixing of these two shear layer regions. The main

wing boundary layer will thicken significantly, impeding its ability to withstand adverse pressure gradients. Figures 5.23 to 5.29 show that u/U_e measured at the lowest pitot station above the main wing trailing edge consistently decreases with increasing incidence. At 27° (fig. 5.29) the pitot rake detects separated flow (by registering a negative reading as well as intercepting the y/c axis some considerable height above y/c = 0) confirming the indications already given by the tufts and the pressure distributions (fig. 5.12 and 5.20).

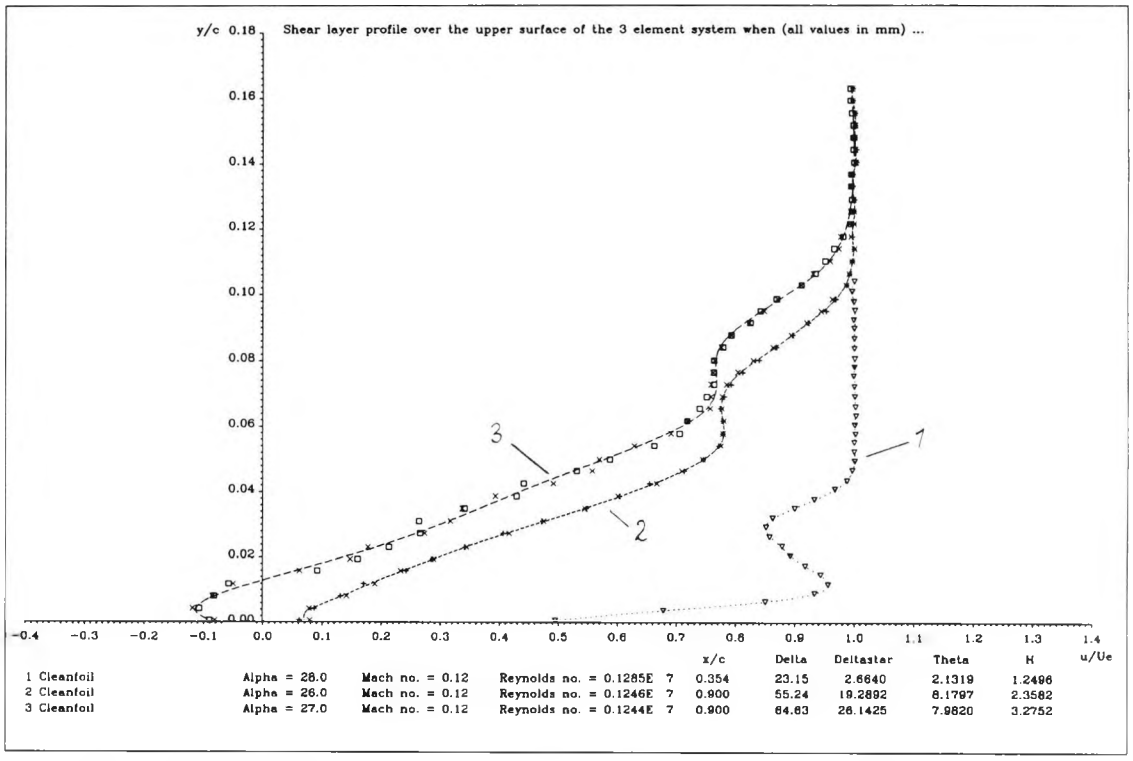

Figure 5.29 : Shear layer development over the main wing of the high lift system at 26° & 27° (x/c = 0.9) & 28° (x/c = 0.354)

Although wakes undergoing deceleration to freestream velocities away from contact with a surface enable the recovery from high negative C_p values to be made in a much shorter distance than when the deceleration is in contact with a surface, flow reversal in the wake can still occur before separation is present on the surface (Smith, 1972). Even after undergoing its most severe deceleration at 27° (fig. 5.29) it is clear the slat wake does not suffer this phenomena (as $u/U_e \geq 0.7$).

A careful examination of figures 5.32 and 5.33 will show the reader that as the incidence increases from 26.3° to 27°, the height of the layer of potential flow above the flap has decreased slightly (since curve 2 lies closer to y/c = 0 for any given value of u/U_e). This is in marked contrast to the behaviour of this region of flow between 5° and 26° (figs. 5.30 to 5.33, see before). The author regrets not having recorded the shear layer profile above the flap at 28°. However, the author believes this reduction occurs as a direct result of the appearance of separated flow at the main wing trailing edge. As the separation moves forward from the trailing edge (fig. 5.13), increasing in severity, the re-circulation in the main wing wake probably penetrates into the flow above the flap which results in the collapse of the flap peak suction at 29° (fig. 5.14).

6. Vane Vortex Generators

For clarity this section discusses solely those measurements which were obtained when vane vortex generators were present on the upper surface of the main wing at either x/c = 0.14 or x/c = 0.403. In all cases the generators were positioned symmetrically about the centre line of the model to ensure the centre line pressure tappings were equidistant between two adjacent generators.

The various vane vortex generator configurations tested on the high lift system were selected for their well known effectiveness at suppressing straightforward boundary layer separation (Pearcey 1961). In the event each configuration tested on the main wing had a favourable influence on the suppression of separation which develops at the rear of the main wing. However, in all cases the generators had an adverse effect on the normal force coefficient generated by the high lift system at incidences below the stall of the cleanfoil.

6.1 Pressure distribution measurements (fig. 6.1 to fig. 6.35, Appendix B)

6.1.1 Co-rotating vane vortex generators at x/c = 0.14, f = 8 (fig. 6.1 - fig. 6.7, Appendix B)

Initially, it was believed the pressure distributions had changed very little when comparing, for example, figures 6.1 - 6.3 with figures 5.10 - 5.12. However, on closer examination it can be seen that subtle changes have occurred in the shape of the pressure distributions. Figures 6.20 - 6.22 compare the pressure distributions obtained with and without co-rot. vane vortex generators at x/c = 0.14 for selected incidences.

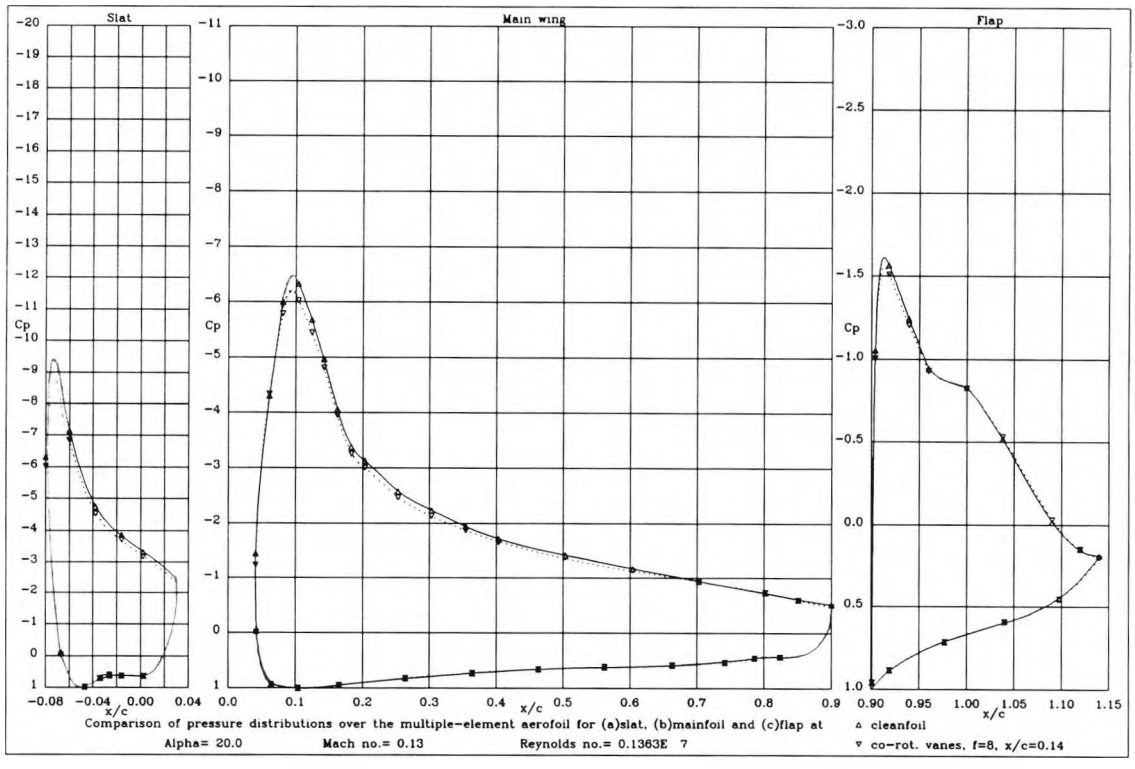

Figure 6.20 : Comparison of pressure distributions at $\alpha = 20°$ obtained with and without co-rot. vanes at x/c = 0.14

At 20° (fig. 6.20) the co-rot. vane vortex generators have reduced the peak suctions on all elements to levels slightly below those seen on the cleanfoil. More specifically the co-

rot. vane vortex generators have reduced the upper surface loading on both the slat and main wing, while the lower surface pressure distributions remain unchanged when compared with the cleanfoil case. As a consequence the C_n coefficient of these two elements is reduced (fig. 6.29) which in turn reduces the total C_n of the high lift system (fig. 6.30). Although the co-rot. vane vortex generators were located on the main wing of the high lift system and affected locally the loading on this element, they also have had a detrimental effect on the circulation generated on the slat. This can be explained through their adverse influence on the circulation effect (section 2.1) which determines in part the level of circulation on the forward element.

With hindsight the choice of vanes with a height of $y/c = 0.015$ was a good compromise between maximizing the possible strength of the vortices and minimizing the drag penalties associated with the generator height. At 0° (fig. 5.23) and $x/c = 0.14$ the thickness of the shear layers is 0.007 y/c so the generators could be said to be a little large. However, by 25° the tips of the generators are immersed in the wake of the slat in a region where $u/U_e = 0.94$. Hence the strength of the vortices will be only marginally reduced by the lower flow velocity.

The flap pressure distribution (fig. 6.20) behind the peak suction on this element remains unchanged by the presence of vortex generators at the leading edge of the main wing. In particular the small region of separated flow present towards the trailing edge of the flap ($x/c = 1.12$ to 1.14) persists. Both the main wing and flap trailing edge pressures show little difference over that measured on the cleanfoil at this incidence (fig. 6.32).

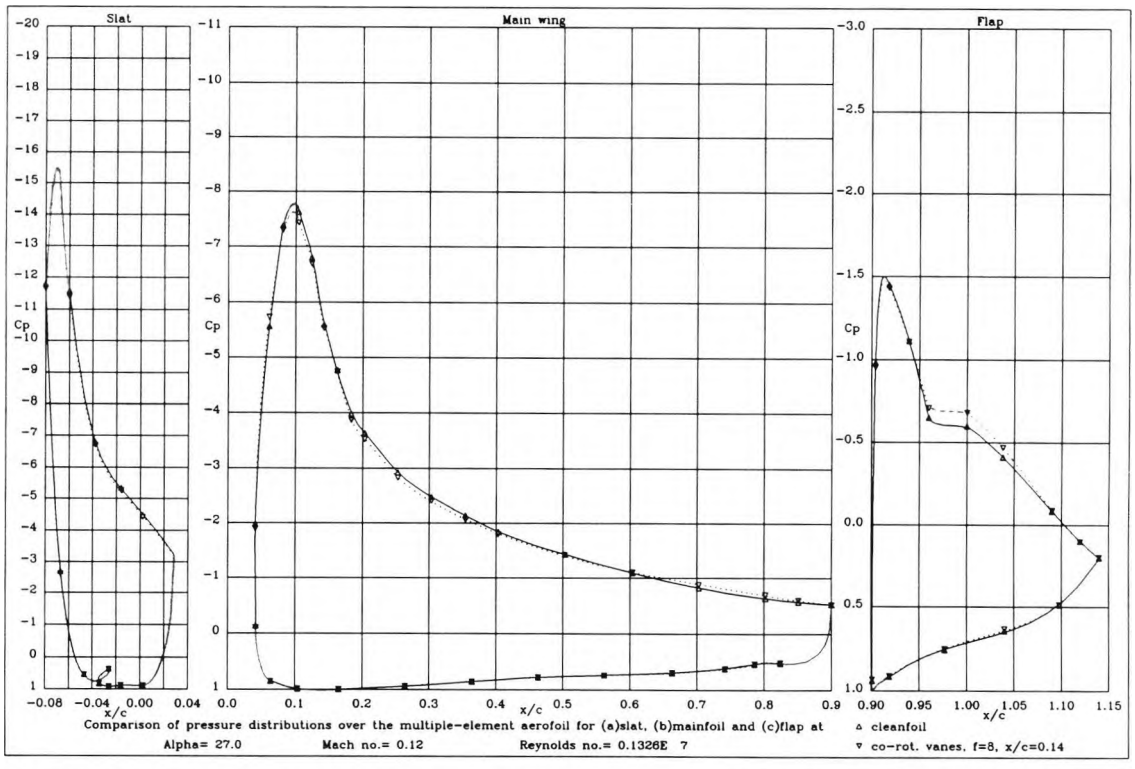

Figure 6.21 : Comparison of pressure distributions at $\alpha = 27°$ obtained with and without co-rot. vanes at $x/c = 0.14$

By 27° the adverse influence which the co-rotating vane vortex generators have on the total normal force coefficient of the high lift system has reduced significantly when

compared with the cleanfoil case (fig. 6.30). Figure 6.29 also shows that the individual C_n's for both the slat and main wing are comparable with that measured in the cleanfoil condition. However figure 6.21 illustrates these improvements do not stem entirely from the co-rot. vane vortex generators no longer having an adverse influence on the pressure distribution acting towards the leading edge of the main wing when compared with the cleanfoil case. This influence is still present, however, figure 6.21 shows the co-rot. vane vortex generators have reduced the extent of the loss of load towards the trailing edge of this element beyond $x/c = 0.6$. The vane vortex generators are therefore alleviating the adverse influences which are exerted on the main wing boundary layer through confluency with the slat wake. The overall circulation generated on the main wing element then approximates to that which it generates in the cleanfoil condition (fig. 6.29). The slat has all but lost the small deficit in circulation which existed at lower incidences when compared with the cleanfoil case.

The suppression of separation at the trailing edge of the main wing at 27° by the co-rot. vane vortex generators has had a noticeable effect on the pressure distribution on the upper surface of the flap (fig. 6.21) in that the generators enable a slightly higher level of loading to exist behind the flap peak suction.

The co-rot. vane vortex generators increase the stall incidence of the high lift system to above 32° by delaying the boundary layer separation which develops at the trailing edge of the main wing (fig. 6.22). The most striking feature is that by delaying the appearance of boundary layer separation at the trailing edge of the main wing the vane vortex generators have prevented the sudden collapse of the flow over the flap. The character of the stall is less abrupt than seen in the cleanfoil case and the maximum total normal force coefficient increases by 5% from 3.662 to 3.842 (fig. 6.30). Figure 6.29 shows that this increase comes almost entirely from a substantial increase in the normal force coefficient of the slat element of the high lift system. Although the co-rot. vane vortex generators are able to delay the loss of loading which occurs towards the trailing edge of the main wing from 27° to above 31° (figs. 6.3 - 6.5 & fig. 6.33), the main wing peak suction increases by only -0.5 (fig. 6.31). This in turn is reflected in the rather small increase measured in the main wing normal force coefficient (fig. 6.29). Nevertheless, by delaying the abrupt divergence of the flap trailing edge pressure (fig. 6.32), the co-rot. vane vortex generators enable the overall circulation generated by the high lift system and in particular the load on the slat element to increase significantly with increasing incidence beyond 28° (fig. 6.29). The magnitude of the slat peak suction increases substantially from -12.5 to in excess of -16 (fig. 6.31) and although beyond 31° the main wing C_n gradually decreases (fig. 6.29) the slat peak suction and normal force coefficient continue to increase with incidence (fig. 6.29 & fig. 6.31).

The flap trailing edge pressure diverges from 25° (fig. 6.32) as was the case for the cleanfoil. However, the divergence is of a more gradual nature and the characteristic convex shape which the flap upper surface pressure distribution adopts in the cleanfoil case at 28° (fig. 5.13) becomes more accentuated (fig. 6.4 - fig. 6.7) with increasing incidence. The flap peak suction does not collapse abruptly even though by 34° (fig. 6.7) boundary layer separation on the main wing upper surface is evident from $x/c = 0.6$.

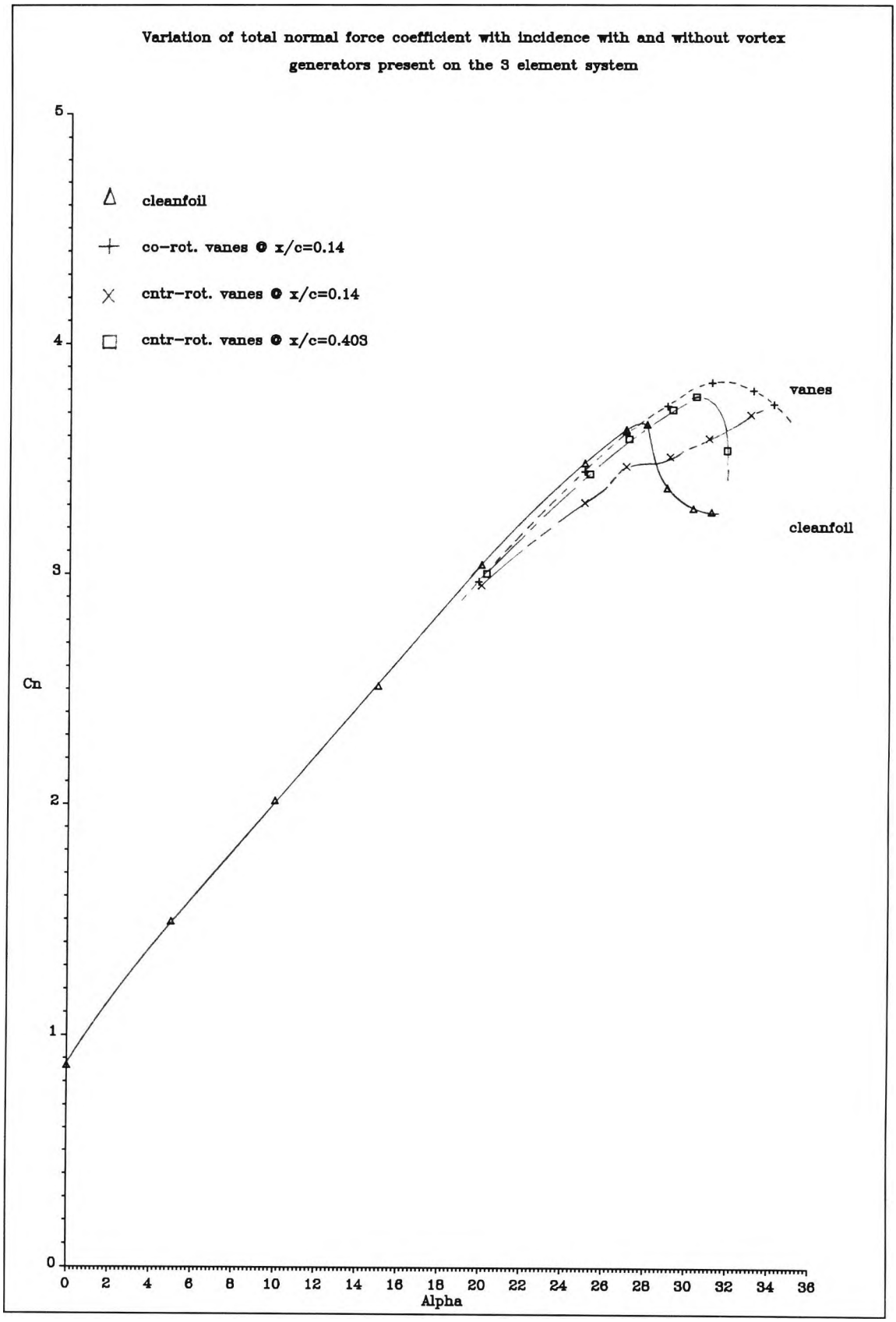

Figure 6.30 : Variation of total C_n with α with and without vane vortex generators present on the 3 element system

The variation of static pressure at the main wing trailing edge exhibits the same plateau as that seen in the cleanfoil tests between 25° and 27° (fig. 6.32). The co-rot. vane vortex generators extend this to approximately 29° after which a gradual divergence behaviour occurs when compared with the cleanfoil case. Figure 6.33 illustrates the effect which the co-rotating vane vortex generators have on several upper surface static pressures acting towards the rear of the main wing. It is clear that the co-rot. vane vortex generators delay the loss of loading towards the rear of the main wing and the forward movement of the boundary layer separation which originates from this region of the main wing upper surface.

6.1.2 Cntr-rotating vane vortex generators at x/c = 0.14, D/d = 4 (fig. 6.8 - fig. 6.13, Appendix B)

Figure 6.29 illustrates that this configuration of vane vortex generators has the greatest adverse effect on the main wing C_n and indeed for the high lift system as a whole at incidences below the stall when compared to the cleanfoil case (fig. 6.30). At 20° total C_n is reduced by 0.1 but by 27° this has increased to 0.2. Their influence is not restricted to the main wing and slat. At 20° (fig. 6.23) the vortex generators have changed the pressure distribution over the upper surface of the flap. Although the flap peak suction is reduced the vortex generators increase the loading towards the trailing edge of this element and have eliminated the small region of separated flow beyond x/c = 1.12. This was not the case with co-rot. vane vortex generators (fig. 6.20). Their net effect, however, is minimal on the flap normal force coefficient.

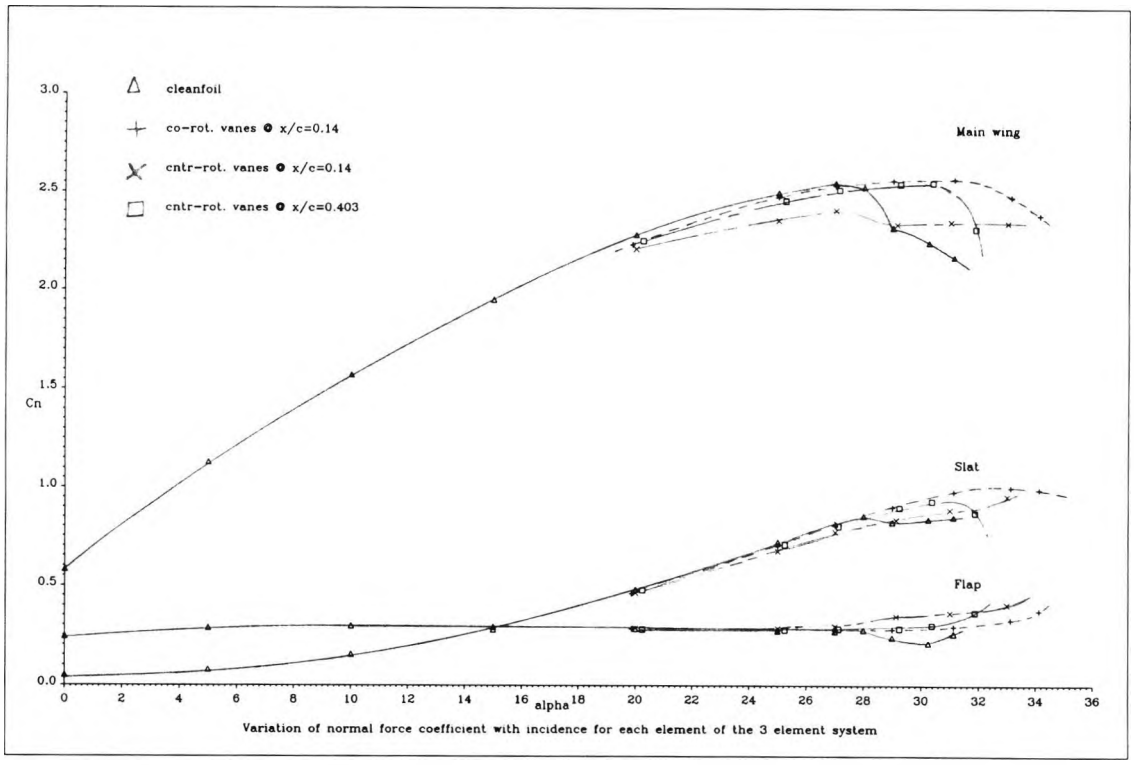

Figure 6.29 : Variation of C_n with α for each element of the 3 element system with and without vane vortex generators

At 25° (fig. 6.9) the main wing upper surface pressure distribution at x/c=0.8 shows an uncharacteristic change in slope which is not present on the cleanfoil. By 27° (fig. 6.10 & fig. 6.24) the feature has moved forward to x/c=0.7. The vortices shed from this configuration of vanes will tend to move towards each other in pairs and away from the surface of the main wing. The author believes the sudden change of slope in the pressure distribution towards the main wing trailing edge is associated with this known behaviour of cntr-rot. vane vortex generators. It may be that as the vortices travel away from the main wing surface the displacement effect of the vortex cores and the shear layers is diminished giving rise to the slightly elevated level of loading beyond x/c=0.65 (fig. 6.24).

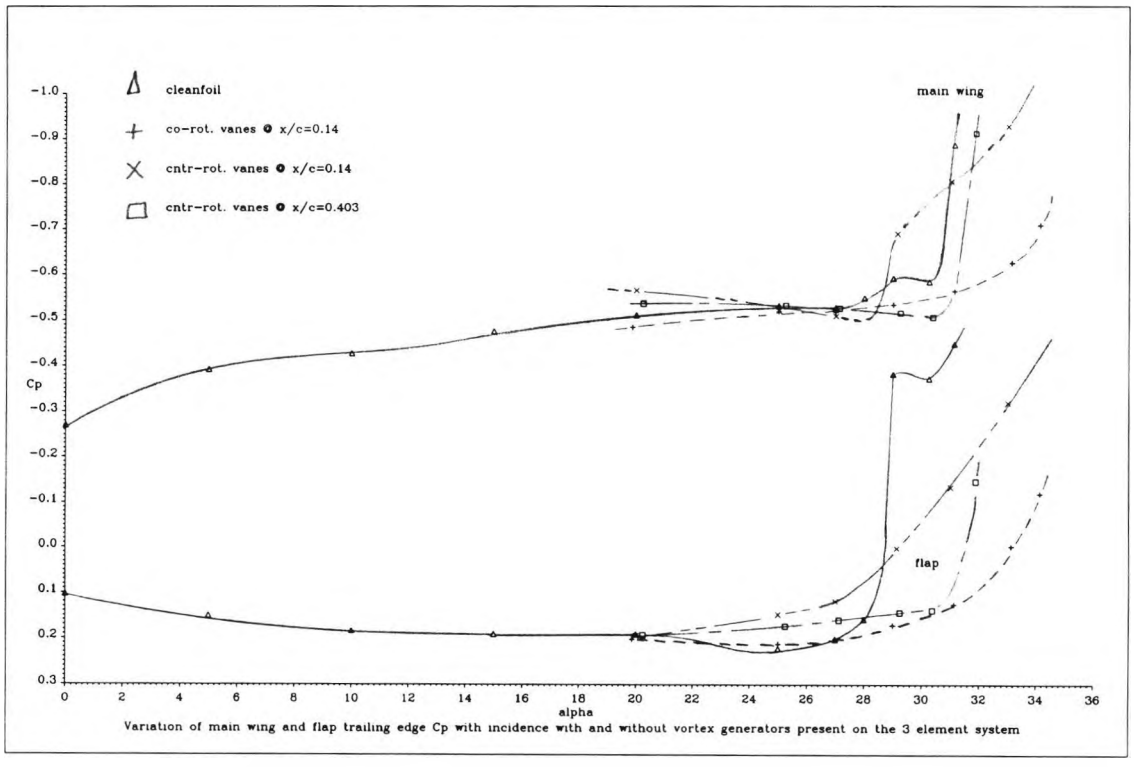

Figure 6.32 : Variation of main wing & flap trailing edge C_p's with α with and without vane vortex generators present on the 3 element system

The most worrying development with this configuration of vane vortex generators is the gradual divergence (ie. tendency to become more negative with increasing incidence) of the flap trailing edge pressure from 20° (fig. 6.32), 5° before it occurs in the cleanfoil case or with co-rot. vane vortex generators at x/c=0.14. Comparing figure 5.11 (cleanfoil, 25°), figure 6.2 (co-rot. vanes, 25°) and figure 6.9 (cntr-rot. vanes, 25°), we see that the level of pressure at x/c=1.0 on the upper surface of the flap is approximately the same in all three cases (as is the main wing trailing edge pressure, fig. 6.32). The only thing which differs in each case is the structure of the wake shed from the main wing. In particular, the thickness and curvature of this wake and the displacement effect of the vortex cores shed from the vanes will have both a viscous (if merging) and an inviscid (separated by potential flow) influence on the pressure distribution over the upper surface of the flap. The pressure recovery achieved at the flap trailing edge depends on the thickness of the shear layers entering the wake and therefore partly on the characteristics of the main wing wake. A thicker

main wing wake will act to suppress the flap peak suction for example (fig. 5.39) and reduce the pressure recovery achieved at the trailing edge of this element. Once the flap trailing edge pressure begins to diverge the pressure distribution over the flap between $x/c = 1.0$ and $x/c = 1.14$ acquires a convex shape - which occurs rather earlier with cntr-rot. vane vortex generators at $x/c = 0.14$ (fig. 6.9). By virtue of the divergence of the flap trailing edge pressure (albeit gradual, fig. 6.32) from 20°, the high lift system will show an increase in profile drag from this incidence over that which would otherwise be seen in the absence of cntr-rot. vane vortex generators at $x/c = 0.14$.

Within the range of incidence tested no definitive stall incidence was found for the high lift system when cntr-rot. vane vortex generators were present at $x/c = 0.14$. Instead the total C_n increased steadily up to 33° (the maximum incidence tested) improving total C_n from 3.662 to 3.704 (1.15%, fig. 6.30). This improvement, although small, largely originates from the effect of increasing incidence upon the slat circulation (fig. 6.29 & fig. 6.31), through the delay in the collapse of the flow over the flap (flow separation was present but intermittent on this element at 33°). The main wing C_n peaks between 27° and 29° (fig. 6.29) and by 29° the main wing is showing a large region of separated flow from $x/c = 0.7$ comparable in size to that seen in the cleanfoil case (fig. 6.25 and fig. 6.34). This has moved forward to $x/c = 0.5$ by 33° (fig. 6.13 & fig. 6.34). It is interesting to note that although the main wing is showing a significant amount of separated flow by 29° the flap peak suction has not collapsed as was the case for the cleanfoil. This may be due to the tendency for the counter-rotating vortex cores to move away from the main wing surface, taking with them the main wing wake and reducing the adverse viscous interaction with the flow over the flap.

If the cntr-rot. vane vortex generators are to have a greater influence on the main wing trailing edge separation they may have to be closer to the main wing trailing edge.

6.1.3 Cntr-rotating vane vortex generators at $x/c = 0.403$, $D/d = 4$ (fig. 6.14 - fig. 6.19, Appendix B)

By moving the vanes to a location further aft we immediately suffer a reduction in the strength of the vortices shed from the vanes (Pearcey, 1961), since one would expect the tips of the generators to be immersed in a region of lower flow velocity. However, there is a balance to be made between the height of the vanes, the thickness of the confluent boundary layer and the reduced distance from the generator location to the main wing trailing edge (so that the vortices reach this before they migrate away from the main wing surface). For the vanes to be most effective their tips should preferably be at a height where the magnitude of the velocity in the boundary layer is comparable to the local velocity in the freestream. With these factors in mind the author chose $x/c = 0.403$ as a suitable location. Figure 5.27 reveals with hindsight that at $x/c = 0.4$ and 20° the vortex generators (of height $y/c = 0.015$) have their tips in a region of the slat wake which has u/U_e approximately 0.95 which is a good compromise between the factors discussed above.

Figure 6.30 illustrates the C_n of the high lift system compares more favourably with the cleanfoil case for incidences below the stall incidence of the cleanfoil. The deficit in C_n has

been reduced from 0.1 to 0.05 which remains constant up to the stall incidence of the cleanfoil (28°). As before the deficit is in the main wing C_n, the slat element showing a very small change from the cleanfoil case (fig. 6.29). Changes have occurred to the flap upper surface pressure distribution which are similar to those seen when the vortex generators were at the forward location of x/c = 0.14 (cf. fig 6.23 & fig. 6.26), although their beneficial effect on the small region of separated flow beyond x/c = 1.12 has diminished slightly.

The pressure distribution over the rear portion of the main wing shows no abrupt change of slope similar to that which occurred when the generators were at x/c = 0.14. In fact figure 6.35 shows that between x/c = 0.8 and x/c = 0.9 and from 20° the pressure distribution in this region on the main wing remains unusually constant with incidence. Consequently the main wing trailing edge pressure shows no tendency to diverge, instead it is the flap trailing edge pressure which diverges from 29°, albeit more slowly than when the vortex generators were farther forward (fig. 6.32). The convex shape associated with the pressure distribution over the upper surface of the flap from x/c = 1.0 is sustained from 25° to in excess of 30° (fig. 6.15 to fig. 6.18), when the flap then begins to show signs of intermittent boundary layer separation (fig. 6.18 & tuft information).

The cntr- rot. vane vortex generators at x/c = 0.403 delay the stall of the high lift system to approximately 31°, increasing the total C_n from 3.662 to 3.781 (3.25%, fig. 6.30). The increase is largely confined to the slat (from .856 to.931) although the main wing shows a very small increase (up from 2.528 to 2.549, fig. 6.29). The stall itself is very abrupt (fig. 6.35) with the main wing upper surface pressures only showing signs of its impending occurrence forward of x/c = 0.8 by the rise in static pressure similar to that seen on the cleanfoil. Separated flow is then present on the main wing as far forward as x/c = 0.6 (fig.6.18 and fig. 6.19).

6.2 Shear layer measurements (fig. 6.36 to fig. 6.73, Appendix B)

6.2.1 Contour plots (fig. 6.36 - fig. 6.43, Appendix B)

With the application of vane vortex generators the shear layer structure above the high lift system acquires a periodicity corresponding to the distance between two vane vortex generators. Consequently, both chordwise and spanwise shear layer traverses are required to reveal the behaviour of the modified structure of the viscous layers. From this it is hoped to be able to explain the altered characteristics of the high lift system and in particular the increase in $C_{n\,max}$ and reduction in lift curve slope below the stall incidence. It was decided to study the modified structure of the shear layers associated with the application of **co-rot. vane vortex generators** at x/c = 0.14 as this configuration produced the greatest increase in $C_{n\,max}$.

Figures 6.36 and figure 6.37 clearly show the spanwise periodicity which exists between 10°and 28° at x/c = 0.354. In particular, the figures show an encouraging resemblance to data produced by Pearcey (1961). At this location and incidence (x/c = 0.354, α = 10° fig. 6.36) the vortex cores have maintained the initial separation distance of 60mm and are located a distance of 0.02 y/c above the surface (ie. 0.005 y/c higher than at their origin, the origin being the height of the vanes). By 28° (fig. 6.37) this height has increased

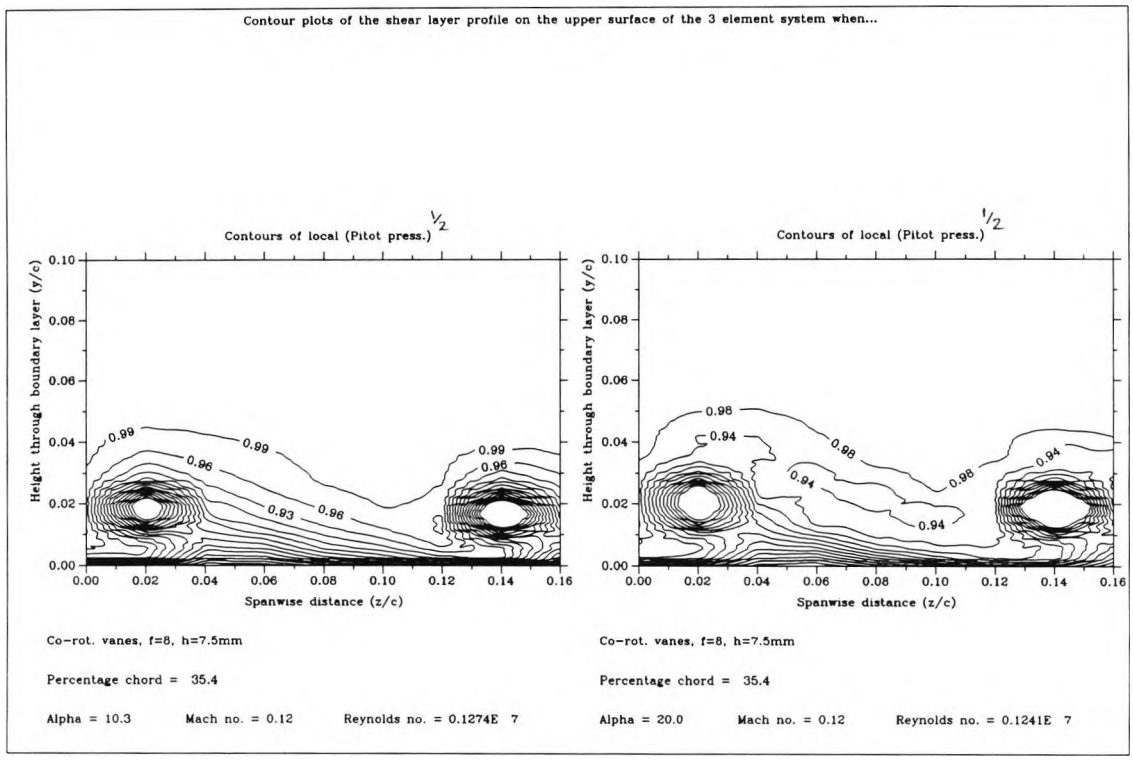

Figure 6.36 : Contour plots of the shear layer structure above the main wing at x/c = 0.354 for $\alpha = 10°$ & 20° when co-rot. vvg's are at x/c = 0.14

by only a further 0.005 y/c. The downwash region to the left of each vortex core (the vortices have an anticlockwise sense as one looks at the paper) has reduced the thickness of the shear layers in figure 6.36 between z/c = 0.08 and z/c = 0.12. Over the remaining spanwise region the shear layers experience an increase in thickness. In particular the main wing boundary layer in the upwash region of the vortex (z/c = 0.04 to z/c = 0.06) has significantly increased in thickness. The region of high shear can also be clearly seen directly below each vortex core. The contour plots suggest that at x/c = 0.354 the vortex cores have yet to burst.

At 10° the wake from the slat, although wide, has little momentum defect. It is already confluent with the main wing boundary layer by x/c = 0.142 (fig. 5.25) and by x/c = 0.354 the slat wake has little in the way of a separate identity. Consequently, in figure 6.36 at 10° it is hard to locate this shear layer structure. However, the story is very different at 20° (fig. 6.36). The slat is producing a considerable amount of lift and is shedding a wake both significant in size and in momentum defect (fig. 5.27). It is apparent that the vortex cores are located between the main wing boundary layer and the slat wake (fig. 6.36 & fig. 6.37). The segment of the slat wake which would otherwise be confluent with the main wing boundary layer at x/c = 0.354 in the absence of the vortices has found itself above the vortex core structure under the influence of the upwash velocity of the vortex. The remainder of the slat wake is located between each vortex core and remains relatively undisturbed structurally, except that its height varies across the span depending on whether it is located in the upwash or downwash regions of the adjacent vortices. Very little mixing has occurred to this section of the slat wake since its maximum momentum defect is comparable to that measured in the absence of the vortices (cf. fig. 5.27 - fig. 5.29 with fig. 6.36 and 6.37). The spanwise length

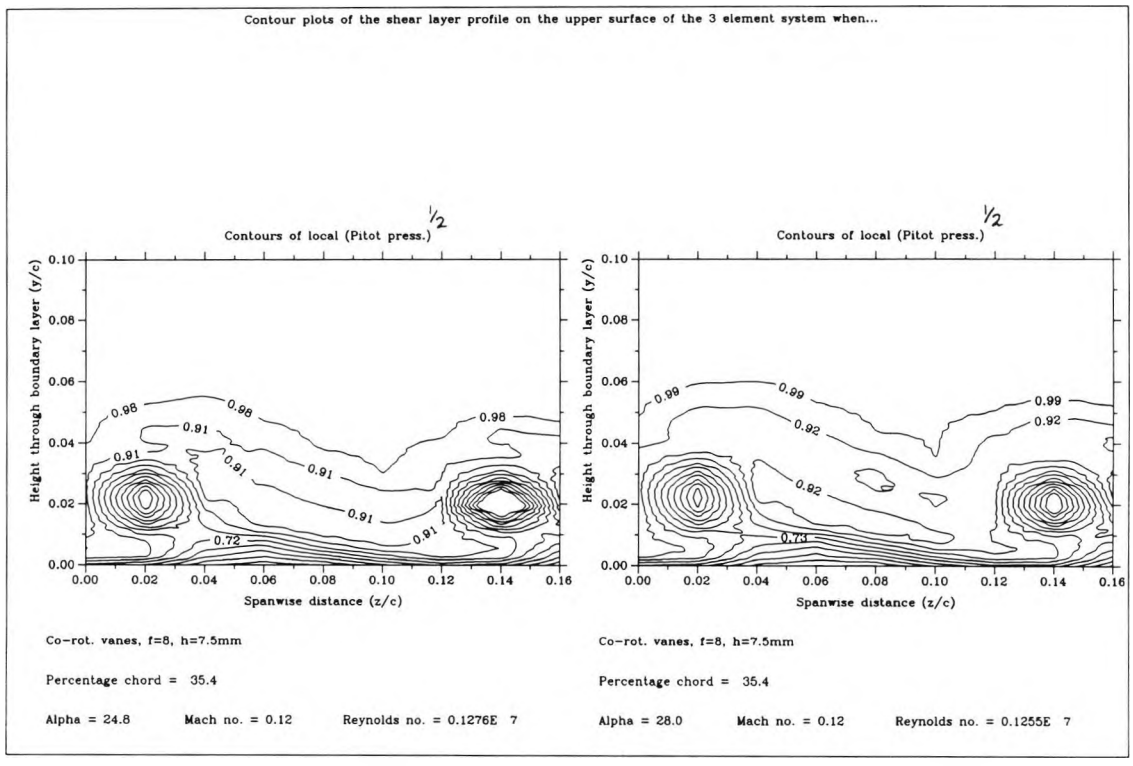

Figure 6.37 : Contour plots of the shear layer structure above the main wing at x/c = 0.354 for $\alpha = 25°$ & 28° when co-rot. vvg's are at x/c = 0.14

in which the shear layer thickness is less than that seen in the absence of the vortices gradually reduces in size with increasing incidence until by 28° at x/c = 0.354 (fig. 6.37) this region occupies the region between z/c = 0.08 and z/c = 0.1 only. It is apparent when comparing figure 6.36 and figure 6.37 that at x/c = 0.354 the vortex cores are formed within the shear layer structure (not at the periphery) and have only a localised mixing effect on the shear layers at this chordwise position.

Figures 6.38 and 6.39 reveal the shear layer structure at the main wing trailing edge and how this changes as the incidence is increased from 25° to above 32°. The adverse gradient through which the vortices have had to travel, from their origin at x/c = 0.14 to the main wing trailing edge (x/c = 0.9), has caused a marked increase in their size, with a corresponding displacement of their centres to y/c = 0.055 at 25°. As the incidence is increased to above 32° the effects of an increasing adverse pressure gradient and viscous dissipation act to damp out the vortices in this region on the main wing (cf. fig 6.38 and fig. 6.39). The slat wake can no longer be easily identified in the shear layer structure implying that much mixing has occurred between x/c = 0.354 and x/c = 0.9. As at x/c = 0.354 the region of relatively high shear close to the main wing upper surface can still be found directly below the vortex cores.

A feature which first appears at the main wing trailing edge at 25° (fig. 6.38) and which becomes more prominent with increasing incidence is an apparent region of separated flow adjacent to the main wing upper surface at z/c = 0.12. This is unusual in that the flow appears to be separated at an incidence below that at which it first appears in the cleanfoil case (27°, fig. 5.29). Furthermore the pressure distribution data (fig. 6.2) suggests a good

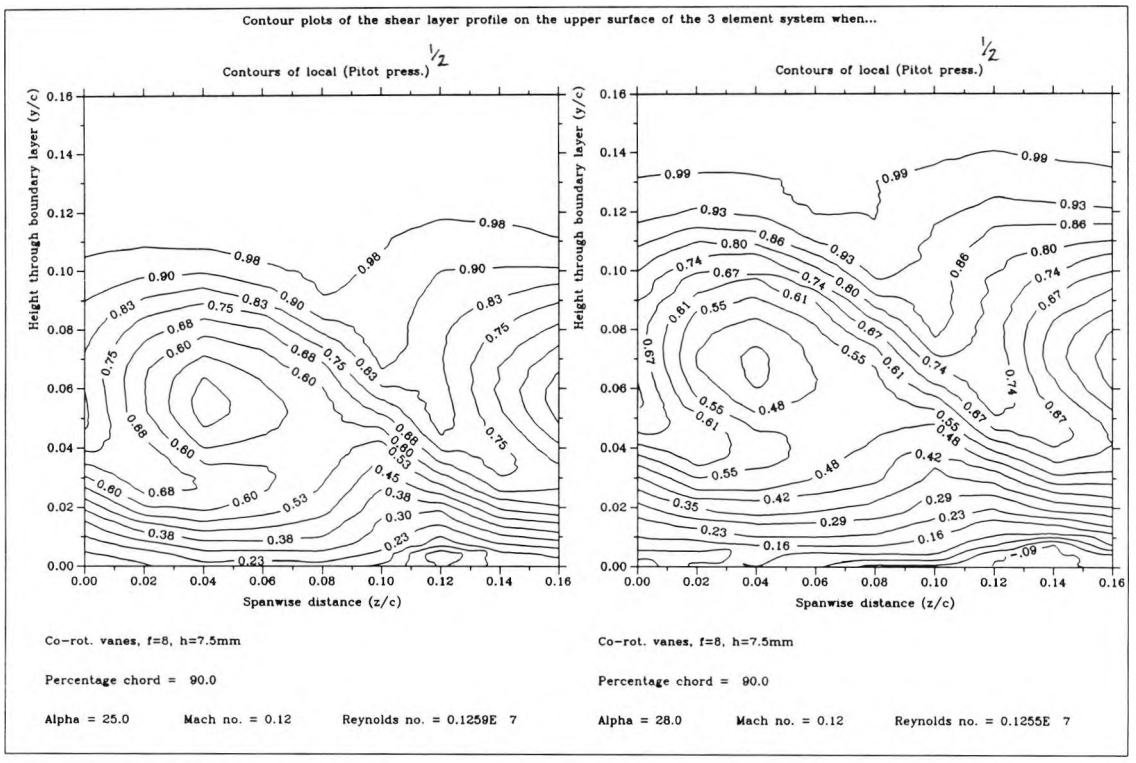

Figure 6.38 : Contour plots of the shear layer structure above the main wing at x/c = 0.9 for $\alpha = 25°$ & 28° when co-rot. vvg's are at x/c = 0.14

pressure recovery is achieved towards the trailing edge on the main wing at this incidence. There is no reason to question the validity of the reading of the centreline pressure tapping at the trailing edge of the main wing. Any significant spanwise variation in static pressure caused by the presence of the co-rotating vane vortex generators would have manifest itself as a pressure discontinuity upstream of the trailing edge in the measured pressure distributions (fig. 6.1 - 6.7). This is not observed and so the measured pressure can be felt to be a good indication of the static pressure at the trailng edge of the main wing. In fact separation at the main wing trailing edge does not appear until above 31° (cf. fig. 6.5, fig. 6.6 and fig. 6.33). It is known that errors greater than 1% of dynamic pressure will arise when the local flow is yawed to a pitot tube at angles larger than approximately 20°. The author believes the negative values of pitot pressure in figure 6.38 are the result of locally highly yawed flow which manifests itself as an apparent region of reversed flow. However, in fig. 6.39 at 32.3° the negative pitot readings adjacent to the main wing surface are probably regions of separated flow as the pressure distribution data suggests.

A somewhat unusual and interesting series of contour plots were recorded over the upper surface of the flap at x/c = 1.0 for incidences between 0° and 32° (fig. 6.40 - fig. 6.43). The damped vortices generated by the vanes can be clearly seen in the shear layer structure above the upper surface of the flap. However, the contour plots also reveal a region of low streamwise pitot pressure below and to the right of each vortex generated by the vanes on the main wing. The size of this region is smaller than that associated with the vane generated vortex. It persists with incidence and is located in a region between the potential flow passing through the slot and the vortices embedded in the shear layer structure of the

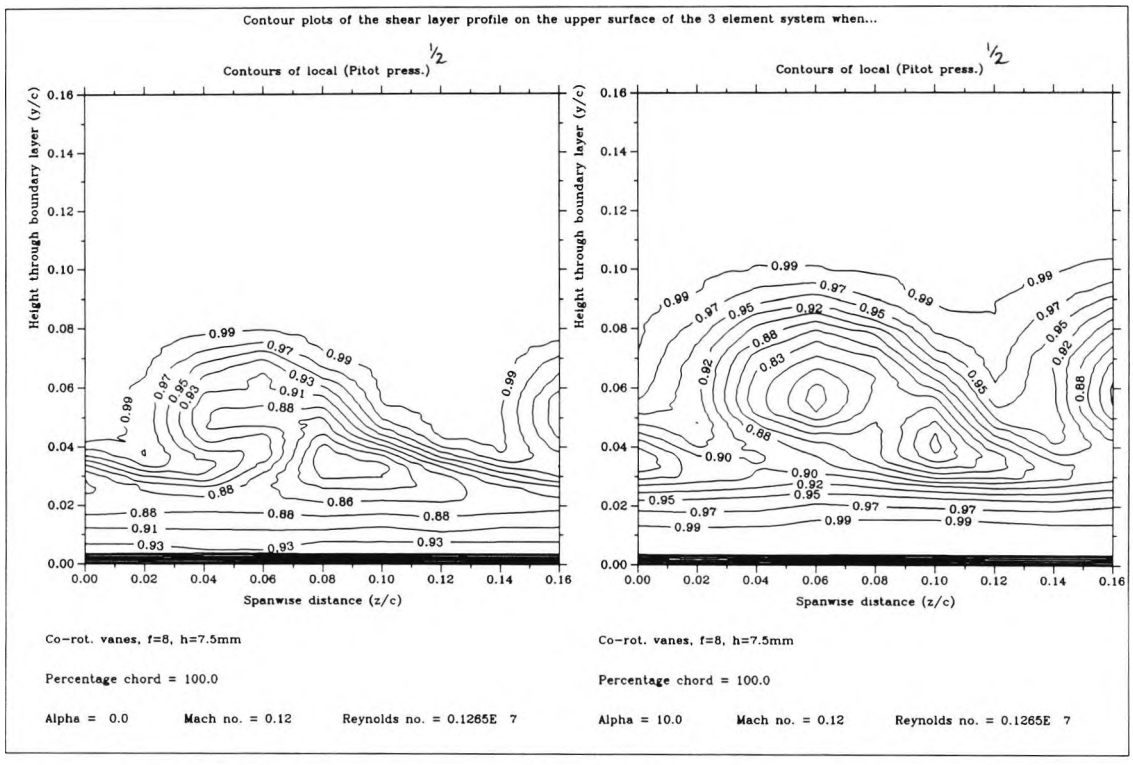

Figure 6.40 : Contour plots of the shear layer structure above the flap at x/c = 1.0 for $\alpha = 0°$ & 10° when co-rot. vvg's are at x/c = 0.14

main wing upper surface boundary layer. The exception to this occurs at 0° (fig. 6.40) when it must be remembered that the main wing wake and flap upper surface boundary layer are confluent by x/c = 1.0. Consequently no slot flow can be seen in the contour plot. The author suggests the unusual feature may well be a weak vortex of opposite sense to that produced by the vanes on the main wing, which is formed by the viscous interaction of the highly yawed and sheared flow of the main vortex with the flow shed from the cove region on the lower surface of the main wing. Its location is insensitive to incidence which the slot flow is not.

6.2.2 Detailed comparison of shear layer profiles at x/c = 0.354 (fig. 6.44 - fig. 6.51, Appendix B)

The figures to be discussed in the following sections of Appendix B are grouped into pairs. The first figure compares the cleanfoil shear layer profile at a given location and incidence with the corresponding **mean** profile when co-rotating vane vortex generators are at x/c = 0.14. The second figure in each pair (and following) compares selected profiles, used in the calculation of the mean profile, with the cleanfoil case to give a further insight into what is happening locally between vortices across the span. Mean profiles were obtained by selecting six successive pitot rake profiles (remembering measurments were recorded at 9 spanwise stations spaced 10mm apart in order to capture the full picture between adjacent vanes), allocating equal weight to data values at the same height in each profile and from this calculating a numerical mean profile. Six stations are chosen as this gives an adequate

representation across the span without i) placing unwanted numerical weighting to any one station when more than six are used or ii) inadequate representation if less than six are used.

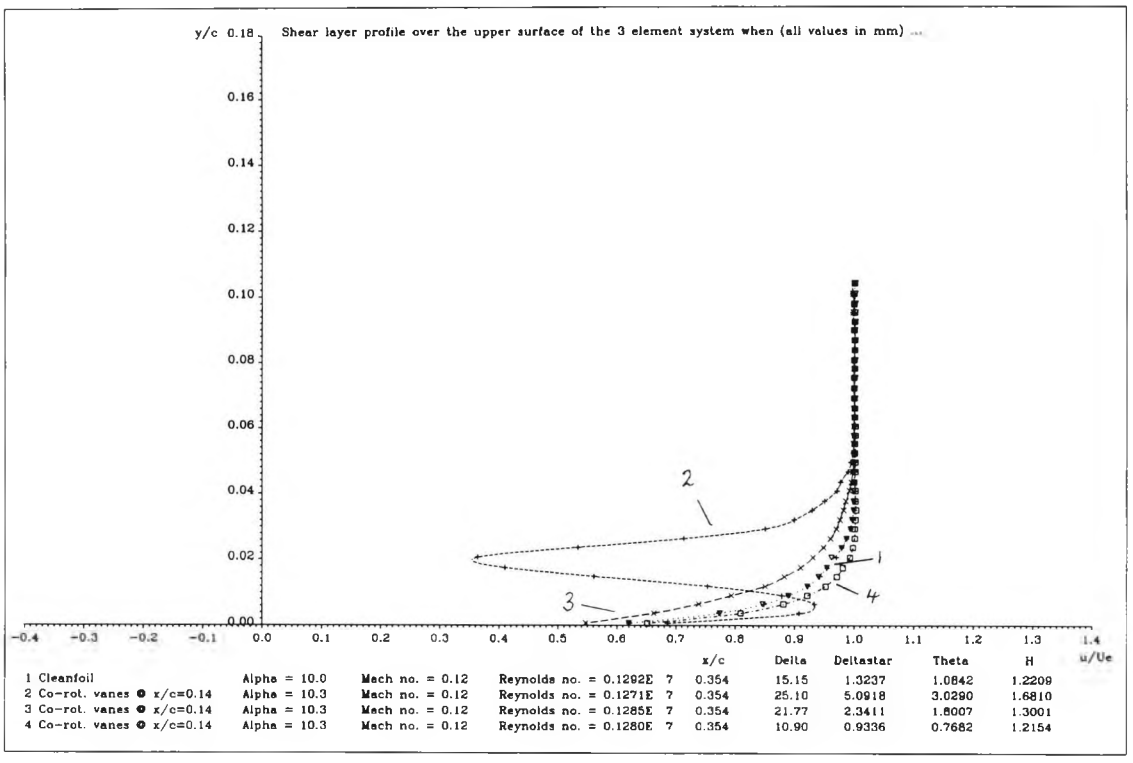

Figure 6.45 : Spanwise variation of shear layer profile at x/c = 0.354, $\alpha = 10°$, obtained when co-rot. vanes are at x/c = 0.14

At 10° a comparison of the mean shear layer profiles at x/c = 0.354 obtained with and without co-rot. vane vortex generators at x/c = 0.14 show only small differences towards the inner region of the shear layer above the main wing (fig. 6.44). In the outer region of the mean shear layer profile associated with vanes a feature can be seen which is suggestive of the presence of a slat wake, although one would not expect this to be prominent at this incidence. The feature is due to the strong influence which the low streamwise dynamic pressure region of the vortex core (although only measured at one spanwise location) has on the final shape of the mean profile. Figure 6.44 **suggests** the vanes have transferred little, if any, fluid particles with relatively high momentum into the inner regions of the shear layer. Instead the situation **seems** to be worsened with both mean δ, δ^* and θ values having increased significantly. Fortunately, figure 6.45 shows this is not the case. Shear layer profiles at three equispaced spanwise locations between two adjacent generators are compared with the cleanfoil case. The curve labelled 2 illustrates the very low streamwise u/U_e region associated with the strong vortex core. Although for this curve δ and δ^* are larger than in the cleanfoil case (66% and 285% respectively) the region of high shear below the vortex core is easily seen and has a fuller profile when compared with the cleanfoil profile as does curve 4. The vanes have transferred high momentum fluid into the inner region of the shear layers which mixes and to an extent replaces retarded air adjacent to the surface of the main wing (curves 2 & 4, figs. 6.45, 6.47, 6.49 & 6.51).

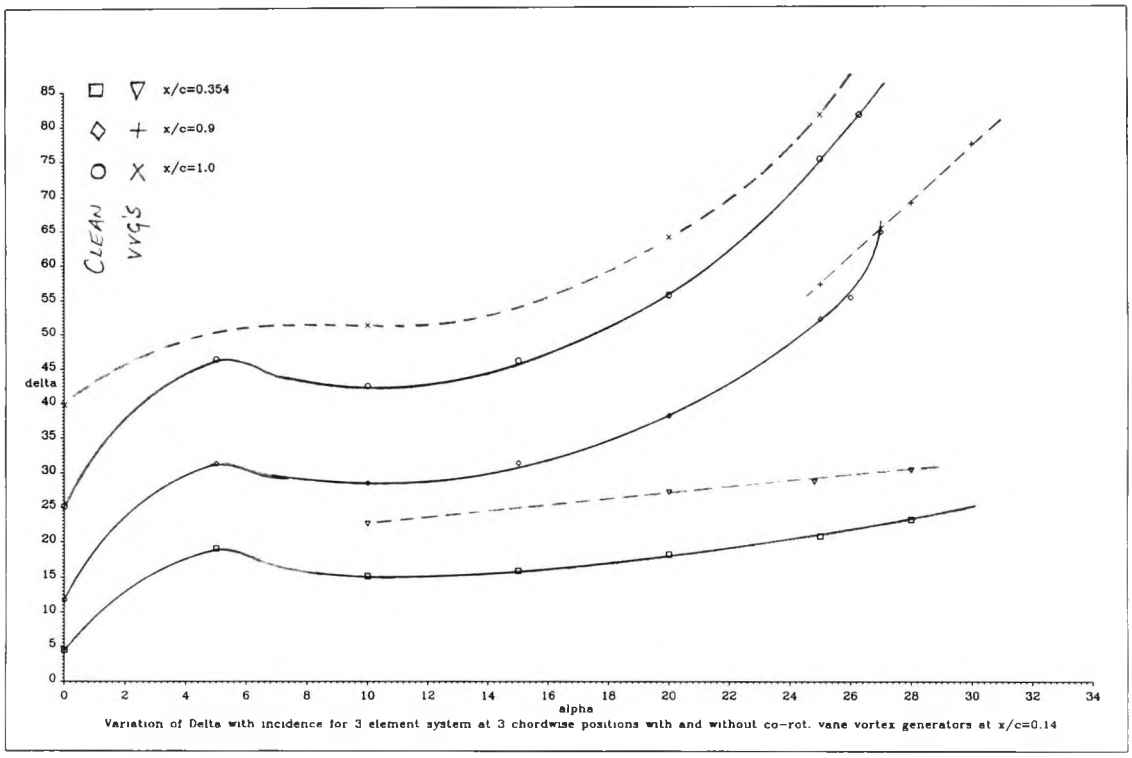

Figure 6.69 : Variation of δ (in mm) with α at 3 chordwise locations, with and without co-rot. vane vortex generators at x/c = 0.14

As the incidence is increased several patterns emerge in the shear layer structure at this location on the main wing with vanes at x/c = 0.14. The mean shear layer profile comparison with the cleanfoil case becomes increasingly worse for values of y/c < 0.01 although the agreement for the mean u/U_e at the wall remains remarkably consistent (figs. 6.44, 6.46, 6.48 & 6.50). The non-dimensionalised velocity ratio within the vortex core remains approximately constant (0.3) considering the large change in the shear layer structure which occurs at the location of the vanes (again figs. 6.45, 6.47, 6.49 & 6.51). The breadth of the vortex core increases slightly as viscous damping and adverse pressure gradients increase with incidence ahead of x/c = 0.354. The mean shear layer thickness δ at x/c = 0.354 shows an increase over the cleanfoil case throughout the incidence range (fig. 6.69) as do δ^* (fig. 6.70) and θ (fig. 6.71). As the percentage increments in these parameters are proportionally the same H shows little change with and without vanes at x/c = 0.14 (fig. 6.72).

6.2.3 Detailed comparison of shear layer profiles at x/c = 0.9 (fig. 6.52 - fig. 6.58, Appendix B)

The favourable influence which the co-rotating vortices have had on the shear layer structure of the high lift system is immediately apparent in figure 6.52. Unlike at x/c = 0.354 the mean shear layer profile at 25° shows an improvement in u/U_e for values of y/c < 0.03 when compared with the cleanfoil case. The benefit is illustrated further in figures 6.54 and 6.56 when it is realised that the comparisons are not made at the same incidence (cleanfoil 27°, vanes 26°, 30° and 32.3°). The remains of the slat wake and vortex cores can be clearly seen in these figures. At the expense of transferring streamwise momentum into the

inner shear layers adjacent to the main wing however, the co-rotating vortices have greatly increased the mean θ deficit associated with the outer regions of the shear layers (figs. 6.52, 6.54 and 6.56). If the mean profile associated with the vanes (ie. fig. 6.52) is separated into its constituent parts (fig. 6.53) curves 2 & 3 show large increases in u/U_e for $y/c < 0.03$ when compared with the cleanfoil case (curve 1). Only curve 4 compares unfavourably with the cleanfoil case for $y/c < 0.03$ although in turn this same curve compares favourably for $y/c > 0.04$ against the cleanfoil case. Much can be gleamed from these figures.

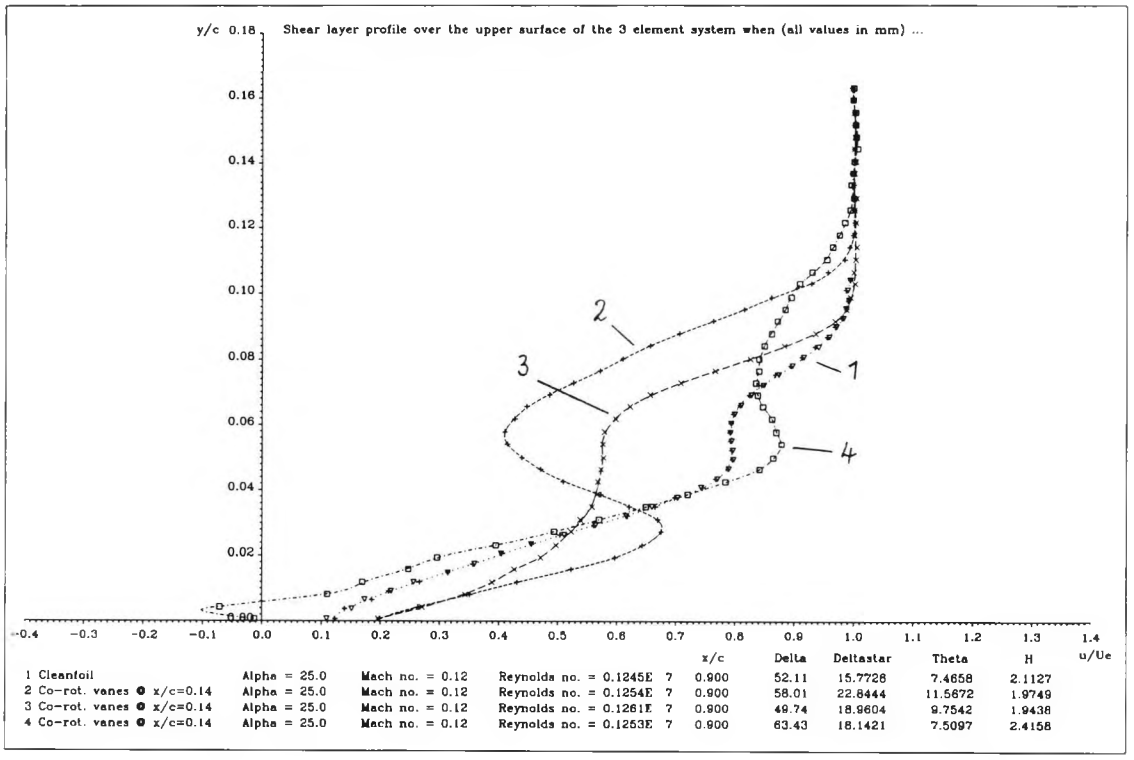

Figure 6.53 : Spanwise variation of shear layer profile at $x/c = 0.9$, $\alpha = 25°$, obtained when co-rot. vanes are at $x/c = 0.14$

The flow in the shear layers is moving more slowly than in the adjacent potential flow, ie. the streamlines in the shear layers are further apart than in the 'inviscid flow'. Streamlines outside a shear layer are shifted outwards by the displacement thickness of the shear layer. As the trailing edge of an aerofoil is approached δ^* increases rapidly and the trailing edge is effectively thickened. The shift upwards of the mean line of the aerofoil and wake corresponds to an increase in thickness of the aerofoil and an addition of negative camber. At the expense of increasing u/U_e in the inner regions of the shear layers the co-rotating vortices increase mean δ and δ^* over the upper surface of the main wing at incidences below the stall incidence of the cleanfoil (fig. 6.52), leading to a loss of load on this element and a reduction in $dC_n/d\alpha$ (fig. 6.29). This in turn effects the circulation on the slat by virtue of the circulation effect (section 2.1) and a small reduction is also seen in the $dC_n/d\alpha$ for this element (fig. 6.20). Consequently the overall $dC_n/d\alpha$ for the high lift system is reduced for incidences below the stall incidence of the cleanfoil (fig. 6.30). The effect can be further appreciated by examining figure 6.53. The displacement thickness at all spanwise stations with vanes present is greater than for the cleanfoil case. The reverse is true for incidences

above the stall incidence of the cleanfoil because of the large increase in the wake and shear layer thicknesses when separated flow is present (fig. 6.55). Judging by the data in figure 6.29 one can probably say the effect is more severe in the cases where cntr-rot. vane vortex generators were placed on the main wing at $x/c = 0.14$, the effect being reduced if the cntr-rot. vortex generators are placed further aft on the main wing.

Some of the shear layer profiles show an abrupt reduction in slope in the inner region of the profile (ie. curves 3 & 4, figs. 6.53 & 6.55). This is the misleading effect of high yaw angles on the lowest pitot tubes and one would be better to maintain a constant slope through to the main wing upper surface at $y/c = 0$. The mean shear layer profile obtained at $x/c = 0.9$ at 32.3° (fig. 6.56), the data from which it was obtained (fig. 6.58) and the values of δ, δ^*, θ and H are subject to errors as the height of the shear layer structure exceeded the height of the pitot rake! Consequently, these values are not included in figures 6.69 to 6.73. Fluctuations associated with unsteady separated flow are apparent in shear layer profile 3, figure 6.58. Momentum thickness at the trailing edge of the main wing shows a relatively large increase over that measured in the cleanfoil case for incidences approaching the stall incidence (fig. 6.71). The only parameter to show a reduction with co-rotating vane vortex generators in use is H (fig. 6.72).

6.2.4 Detailed comparison of shear layer profiles at $x/c = 1.0$ (fig. 6.59 - fig. 6.68, Appendix B)

At 0° the co-rot. vortices are seen to have reduced the mean momentum defect in the shear layers above the flap at heights below $y/c < 0.04$. But again this is at the expense of increasing the mean thickness significantly from 25mm to nearly 40mm (fig. 6.59). The value of u/U_e measured by the lowest pitot tube above the flap shows little variation along the span and indicates the mixing process which the vortices encourage is weak at this low height in the shear layers over the flap (fig. 6.60). This is further emphasised in figure 6.61 and figure 6.62 where the appearance of potential flow through the slot isolates the boundary layer on the flap from the vortex induced mixing at work in the main wing and slat wakes above. This is the reason why the pressure distribution over the upper surface of the flap shows only small changes from the cleanfoil case and which are probably inviscid in origin.

The large variation of u/U_e (min) across the span which was evident at $x/c = 0.354$ at 20° (approx. 0.7, fig. 6.47) has given way to a smaller variation in the shear layers above the span of the flap (0.05, figs. 6.64 & 6.66). The separate identities of the main wing and slat wakes have all but been lost in the mixing process and have been replaced in the mean shear layer profiles by a region where u/U_e is approximately constant for a considerable height through the shear layers (fig. 6.63, 6.65 & 6.67). Figure 6.67 compares the variation of the mean shear profile above the flap with increasing incidence for co-rotating vanes at $x/c = 0.14$ with the cleanfoil case measured at 27° (just prior to stall). It is interesting to note that the value of u/U_e (min) at $y/c = 0.06$ in the mean profiles tends to the value measured in the cleanfoil case! It is all the more interesting when one realises that at 32.3° little variation in u/U_e (min) is seen across the span above the flap (fig. 6.68) and which is close to the stall

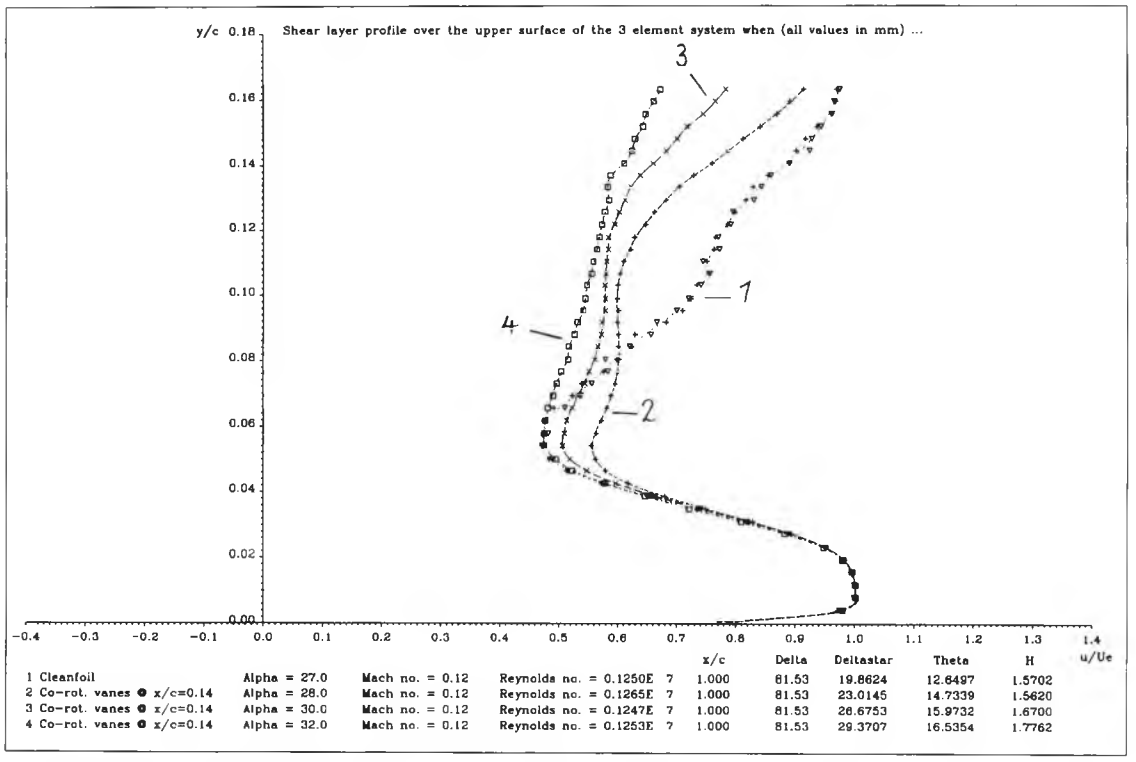

Figure 6.67 : Comparison of mean shear layer profiles at x/c = 1.0, $\alpha = 27°$ (cleanfoil), 28°, 30° & 32° (co-rot. vanes at x/c = 0.14)

incidence when co-rot. vane vortex generators are present on the main wing at x/c = 0.14 (fig. 6.30). Is there possibly a minimum threshold value to u/U_e below which the high lift system stalls. This aspect of the shear layer data is not easily seen in similar figures for the chordwise position x/c = 0.9 (fig. 6.52 - fig 6.58) because of the effect of high yaw on the pitot data in the inner regions of some shear layer profiles. The large increase in θ above the flap at all incidences when compared with the cleanfoil case (fig. 6.71) indicates the profile drag of the high lift system will be increased with the addition of vanes at x/c = 0.14 except possibly below 5°.

7. Airjet Vortex Generators

This section discusses those measurements which were obtained when a system of co-rotating airjet vortex generators were present on the upper surface of the main wing at $x/c = 0.14$ utilizing a constant blowing pressure of 60% above freestream stagnation pressure. As with vane vortex generators the airjets were positioned symmetrically about the centre line of the model to ensure the centre line pressure tappings were equidistant between two adjacent generators.

The configuration of airjet vortex generators selected for installation in the main wing of the high lift system was arrived at on the basis of previous work by Rao (1988). Rao found that the particular array of airjets produced a degree of boundary layer control comparable with that achieved by an optimised array of vanes in the suppression of shock-induced boundary layer separation. It is possible (and probable) that this configuration is not the optimum configuration for airjets in use in suppressing boundary layer separation in subsonic flow. However no guidelines exist for the use of airjets in subsonic flow at this point in time.

In the event, the improvements achieved by the airjets were significantly greater than those produced with the various vane vortex generator configurations and cannot be attributed to just the suppression of boundary layer separation at the rear of the main wing. The airjets and associated vortices which they generate promote enhanced mixing and momentum transfer across the complex shear layers above the main wing in ways which cannot be achieved with vanes.

7.1 Pressure distribution measurements (fig. 7.1 to fig. 7.24, Appendix C)

The variation of pressure over the high lift system at 0° with airjets in use at $x/c = 0.14$ is presented in figure 7.1 and its comparison with the cleanfoil case is shown in figure 7.15. The most obvious difference when the airjets are in use is the appearance of two areas of lowered pressure on the upper surface of the main wing at $x/c = 0.2$ and a more broader region at $x/c = 0.3$ when compared with the cleanfoil pressure distribution. These features are caused by the close proximity to the pressure tappings of one or possibly two airjets (depending on their angle of yaw) as they pass over the centre line of the model. Between these two prominent features the static pressure is seen to return to that seen in the cleanfoil pressure distribution at the same incidence (figs. 7.15 - 7.18). The airjets are not choked so the static pressure in the exit plane of the airjets is the local static pressure acting at $x/c = 0.14$ on the main wing. Rao (1988) found that the core of the airjet passes through the centre of the vortex. Consequently at 0° the author suggests the raised level of suction at $x/c = 0.2$ and $x/c = 0.3$ results from vortex induced velocities. The flow accelerates as it passes under the airjet resulting in a lower static pressure reading. These features combined with a slightly greater flap peak suction (fig. 7.1) and an increased level of loading over the main wing downstream of the location of the airjets allows the high lift system to show an improvement in total normal force coefficient at 0° (fig. 7.21).

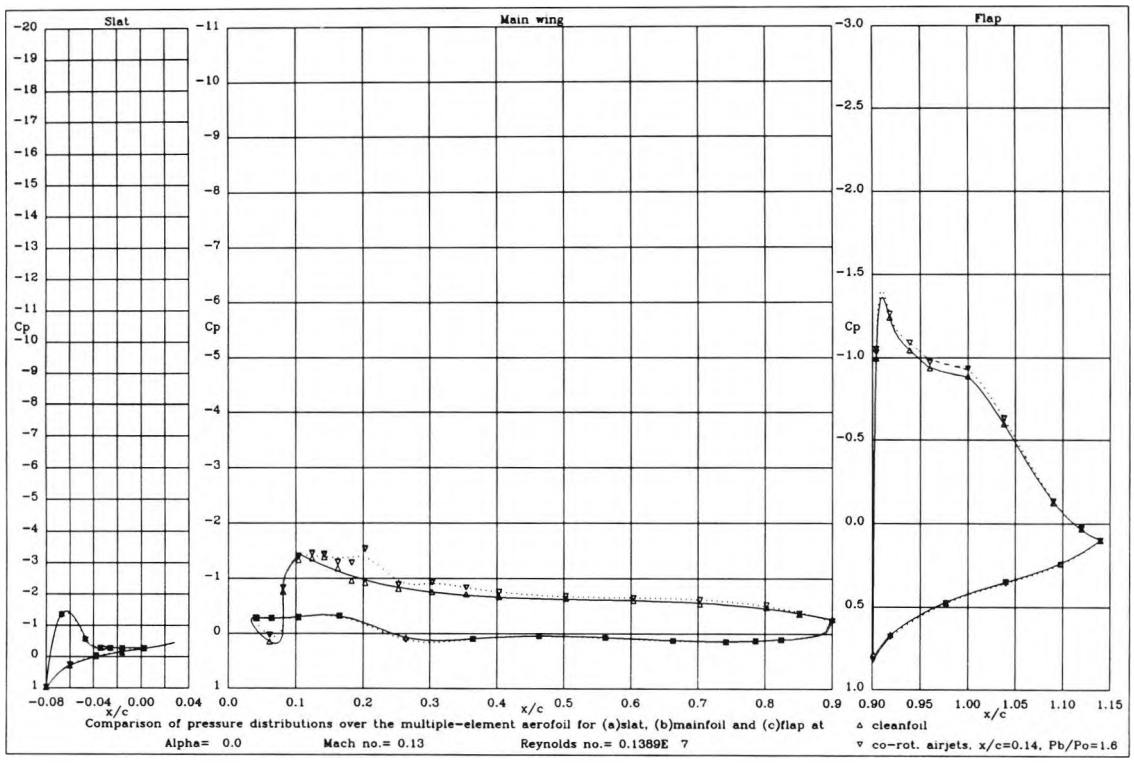

Figure 7.15 : Comparison of pressure distributions at $\alpha = 0°$ obtained with and without co-rot. airjets at x/c = 0.14

The airjets are seen to have a relatively large favourable interaction with the shear layers above the main wing of the high lift system at 5°, as the pressure recovery at the trailing edge of this element is significantly higher than that achieved in the cleanfoil case (fig. 7.23). This is because they probably alleviate the adverse influence, in the form of alternating pressure gradients, which the slat has on the boundary layer at the leading edge of the main wing at this incidence (see section 5.4).

At 10° both the pressure 'peaks' discussed above are still visible in the upper surface pressure distribution for the main wing (fig. 7.3). However, it is apparent the small but significant increment in loading which the airjets produced at 0° continues to persist over the upper surface of the main wing from x/c = 0.18 to the trailing edge of this element (fig. 7.16). This small increase in loading over the upper surface of the main wing suggests the airjets are reducing the displacement effect of the shear layers above this surface, contrasting with the effect which the co-rotating vane vortex generators had on the same surface. The main wing shows an increased C_n (fig. 7.20) although the pressure distributions over the lower surface of this element and over the slat show negligible changes from that seen in the cleanfoil case. In particular the main wing and slat peak C_p's show no change from the cleanfoil condition (fig. 7.22).

Figure 7.23 reveals the static pressure at the trailing edge of the main wing at 10° is unchanged from that seen in the absence of the airjets (and remains so until above 20°, fig. 7.24) but the pressure recovery at the flap trailing edge is slightly higher giving rise to the changed pressure distribution over this element (fig. 7.16) but negligible change in flap C_n (fig. 7.20). The small region of separation which is present towards the trailing edge of the flap

in the cleanfoil tests for incidences between 13° and 20° is absent with airjets in use at x/c=0.14 (fig. 7.3 - fig. 7.5). Consequently, the airjets are seen to improve the pressure recovery at the flap trailing edge steadily between 10° and 20° (fig. 7.23).

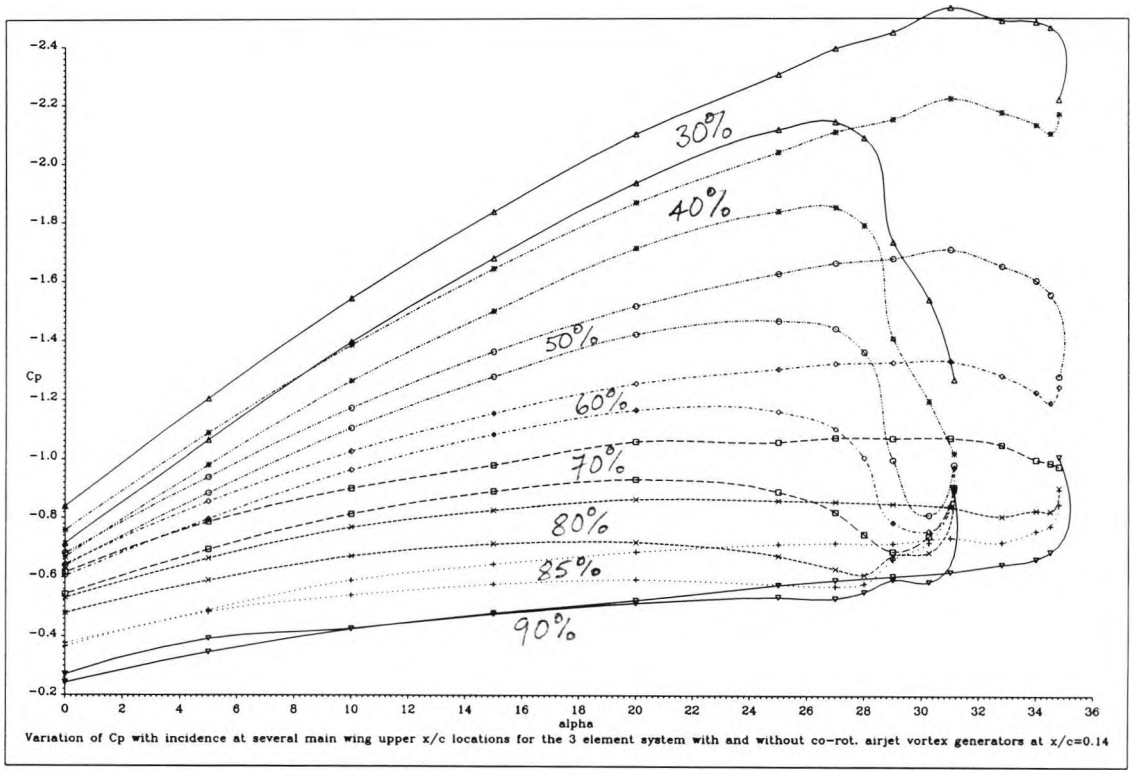

Figure 7.24 : Variation of static C_p with incidence at several x/c positions on the main wing upper surface with and without co-rot. airjet vortex generators at x/c=0.14

The loss of loading which occurred towards the rear of the main wing in the cleanfoil condition, and which was emphasised no more so than by the static pressure variation with incidence at 80% x/c reaching a minimum value at 15°, is delayed by the use of the airjets (fig. 7.24). Instead, the static C_p at 80% x/c is seen to fall steadily with increasing incidence beyond 15° and reach a minimum at approximately 22°. From this position it rises only slightly as stall approaches which is in marked contrast to its behaviour in the cleanfoil tests. The increased loading at the rear of the main wing with airjet vortex generators is accompanied by a progressive increase in the main wing C_n with incidence above 20° (fig. 7.20). Although the co-rotating vane vortex generators also delayed the loss of loading at the rear of the main wing, they were not able to increase the load on this element to levels above that seen in the cleanfoil tests at incidences below the stall incidence of the cleanfoil. The improved flow over the main wing is also reflected in the extended linear variation of the static pressure at the trailing edge of this element with incidence (fig. 7.23).

The improvement in total normal force coefficient above 20° now increasingly embraces that generated by the slat (fig. 7.20). The increased load on the main wing and slat both follow from the increased overall circulation and which in turn derives from the higher pressure recovery at the flap trailing edge (fig. 7.23). Figure 7.18 clearly illustrates the increased circulation generated by the high lift system at 27° with airjets in use, and the

effect which this has on the load carried by both the slat and the main wing. This contrasts with that achieved with co-rotating vane vortex generators at the same incidence (fig. 6.24).

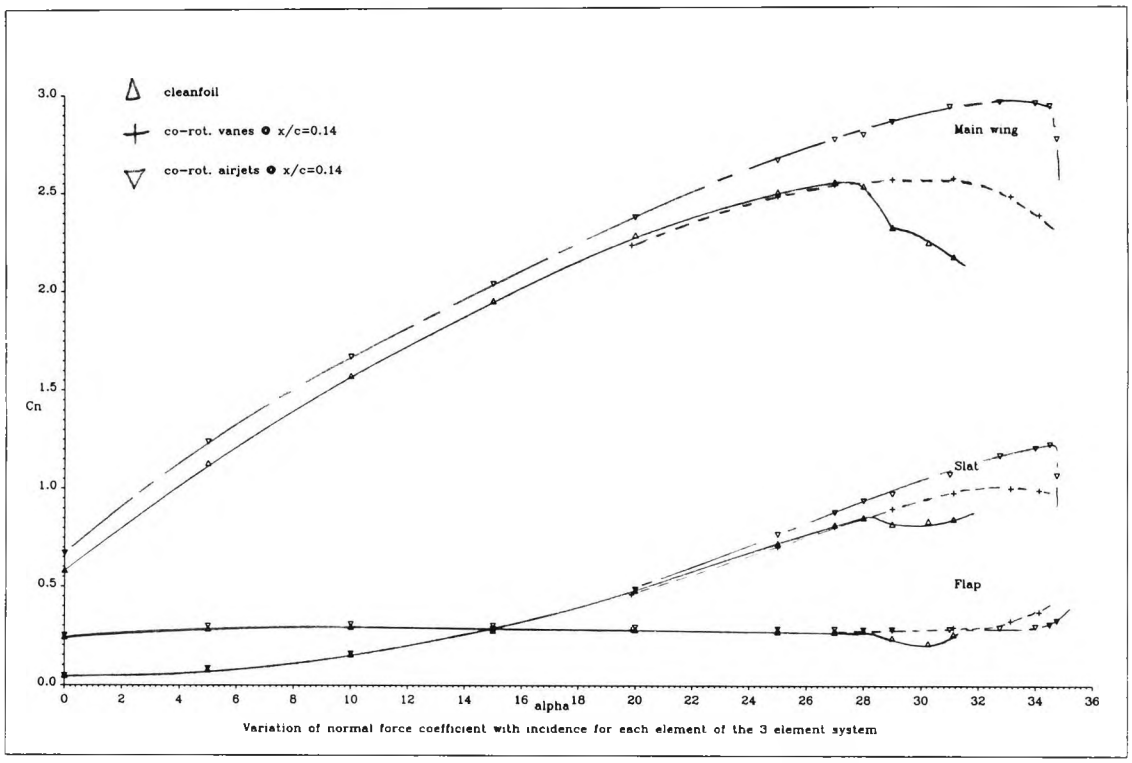

Figure 7.20 : Variation of C_n with α for each element of the high lift system when co-rot. airjet vortex generators are at x/c = 0.14

The co-rotating airjet vortex generators increase the stall incidence of the high lift system by 6.5° from 28° to 34.5° (fig. 7.21). The character of the stall is very abrupt and the maximum total normal force coefficient is increased by 22% from 3.662 to 4.468. This figure comprises a slat C_n of 1.225 (an increase of 40%) and a main wing maximum C_n of 2.935 (an increase of 16%). The increased incidence range through which the slat C_n increases linearly with incidence (fig. 7.20) sees the slat peak C_p increase from -12½ to nearly -20 (fig. 7.22). Figure 7.19 shows how typically for the cleanfoil at 31.1° the flow is separated from x/c = 0.4 on the main wing and over the flap and the adverse effect which its presence has on the load carried by the slat. In contrast, the airjet vortex generators ensure attached flow to the trailing edge of the main wing and increasing normal force coefficients up to the stall incidence. The static pressure at the trailing edge of the flap with airjets in use begins to diverge from approximately 31°, nearly 2° earlier than that at the trailing edge of the main wing (≈32.8°, fig. 7.23). Previously, the divergence of the static pressure at the flap trailing edge has been accompanied by the gradual development of a pressure recovery over the flap upper surface beyond x/c = 1.0 which is convex in nature (fig. 5.12 - cleanfoil, figs. 6.7, 6.10 & 6.17 - vane vortex generators). However, this is not seen with airjets in use at x/c = 0.14; instead the concave pressure recovery beyond x/c = 1.0 adopts a linear form (fig. 7.13). Figure 7.24 illustrates the loading at the trailing edge of the main wing with airjets in use is maintained at an almost constant level beyond x/c = 0.7 for incidences above 27°. Static pressures towards the leading edge (ahead of x/c = 0.6) of the main wing are seen to

rise (in particular at x/c = 0.6) from 31°. Consequently, the mechanism of the stall is not quite so clear as it was on the cleanfoil or in the presence of vane vortex generators. The peak suction on the main wing is held beyond $C_{n\,max}$ and the slat peak suction falls - both indicators of a loss of overall circulation following from a much thickened wake - a rear stall from the main wing trailing edge? The divergence of the static pressure at the trailing edge of the flap (fig. 7.23) may however indicate the stall arises from a sudden collapse of the flow over the flap.

The increased C_{lmax} of the high lift system with airjet vortex generators installed at x/c = 0.14 on the main wing together with the increased lift generated at incidences below the stall, particularly when compared with that obtained when co-rotating vane vortex generators are installed at the same location, suggests the airjet vortex generators are achieving more than just suppression of boundary layer separation at the rear of the main wing.

7.2 Shear layer measurements (fig. 7.25 to fig. 7.61, Appendix C)

7.2.1 Contour plots (fig. 7.25 - fig. 7.31, Appendix C)

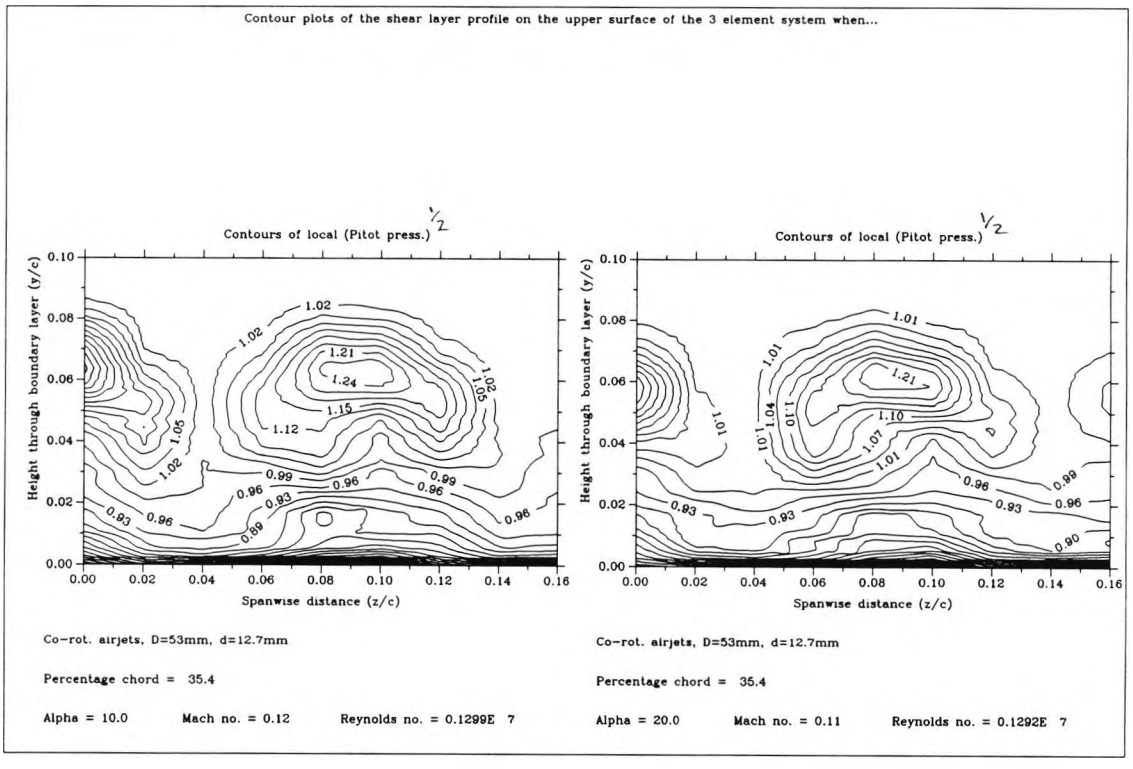

Figure 7.25 : Contour plots of the shear layer structure above the main wing at x/c = 0.354 for $\alpha = 10°$ & 20° when co-rot. ajvg's are at x/c = 0.14

Figures 7.25 and 7.26 present the results of spanwise pitot rake surveys carried out at x/c = 0.354 for incidences between 10° and 30°. Again the characteristic spanwise periodicity produced by the airjets is evident in the shear layers above the main wing as was the case with vane vortex generators. The core flow of each airjet has penetrated the thick shear layers above the main wing to form a region of high velocity flow located in the adjacent freestream. Each of these flow structures form the core region of an associated primary vortex (Rao, 1988), the sense of each vortex is anticlockwise as one looks at the paper.

At 10° at x/c = 0.354 each discrete jet is separated by a region of potential flow (fig. 7.25) which quadruples in size by 30° (fig. 7.26) as the jet core shrinks significantly in size in the upwash region of the vortex with increasing incidence. It is clear the shape of the jet changes with incidence - at 10° the jet is approximately symmetric about a vertical plane through its core - but by 30° presumably under the persistent influence of the vortex-induced cross-flow and hence vorticity, the jet becomes markedly thicker in the downwash region of the vortex. The emergence of the entrained cross-flow from under the jet which forms the upwash region of the vortex and which is responsible for the distinctive kidney shape of the jet, produces a marked thickening in the shear layers in this region when compared with the downwash region. Here we see the the mechanism which produces the enhanced mixing of the shear layers above the high lift system - high momentum air is displaced towards the surface of the main wing in the downwash region of the vortex and low momentum air is swept away from the surface in the upwash region of the vortex.

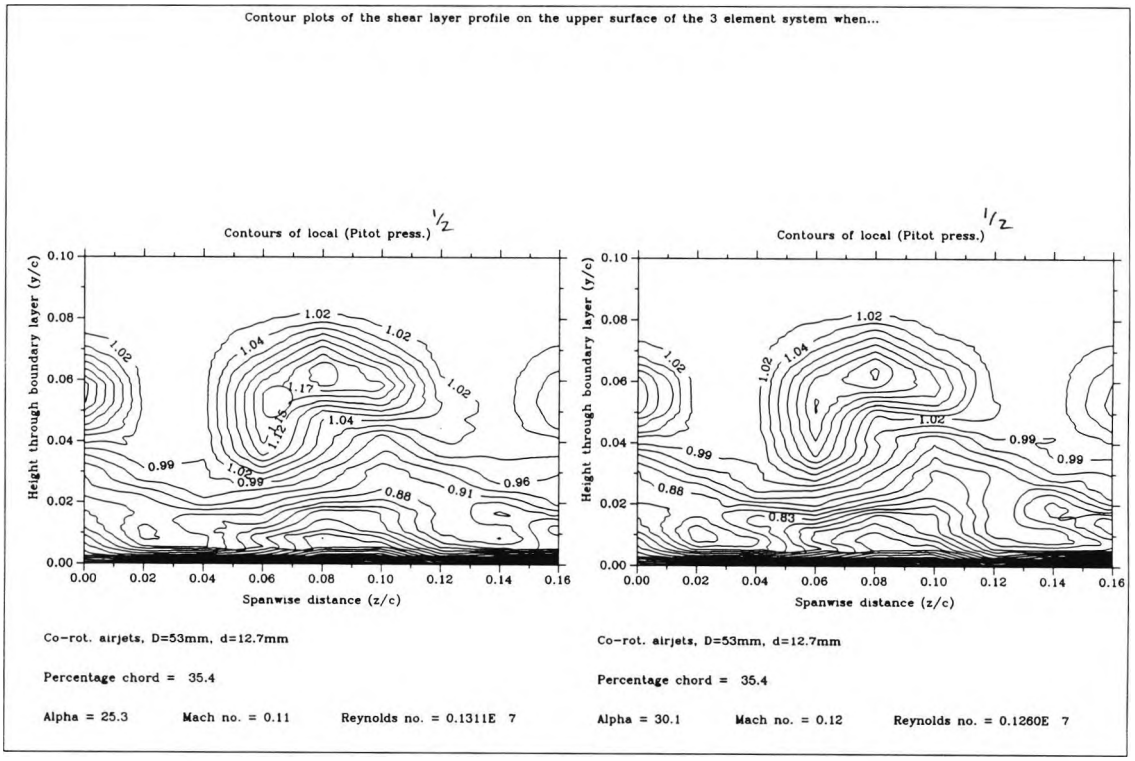

Figure 7.26 : Contour plots of the shear layer structure above the main wing at x/c = 0.354 for $\alpha = 25°$ & 30° when co-rot. ajvg's are at x/c = 0.14

The height of the jet at this chordwise location (x/c = 0.354) remains approximately constant with incidence as does its spanwise location. The most striking difference between these contour plots (figs. 7.25 & 7.26) and the corresponding plots with vane vortex generators (figs. 6.36 & 6.37) is the difficulty in establishing the location of the slat wake.

The high momentum cores of adjacent airjets have expanded and partly merged at the main wing trailing edge (x/c = 0.9) at 10° (fig. 7.27). This situation does not change significantly with incidence, except only in that the height of the jet cores above the main wing surface increases from 0.11 y/c at 10° (fig. 7.27) to 0.14 y/c at 30° (fig. 7.28) under the action of the increasing adverse pressure gradient on the shear layers beneath. It is

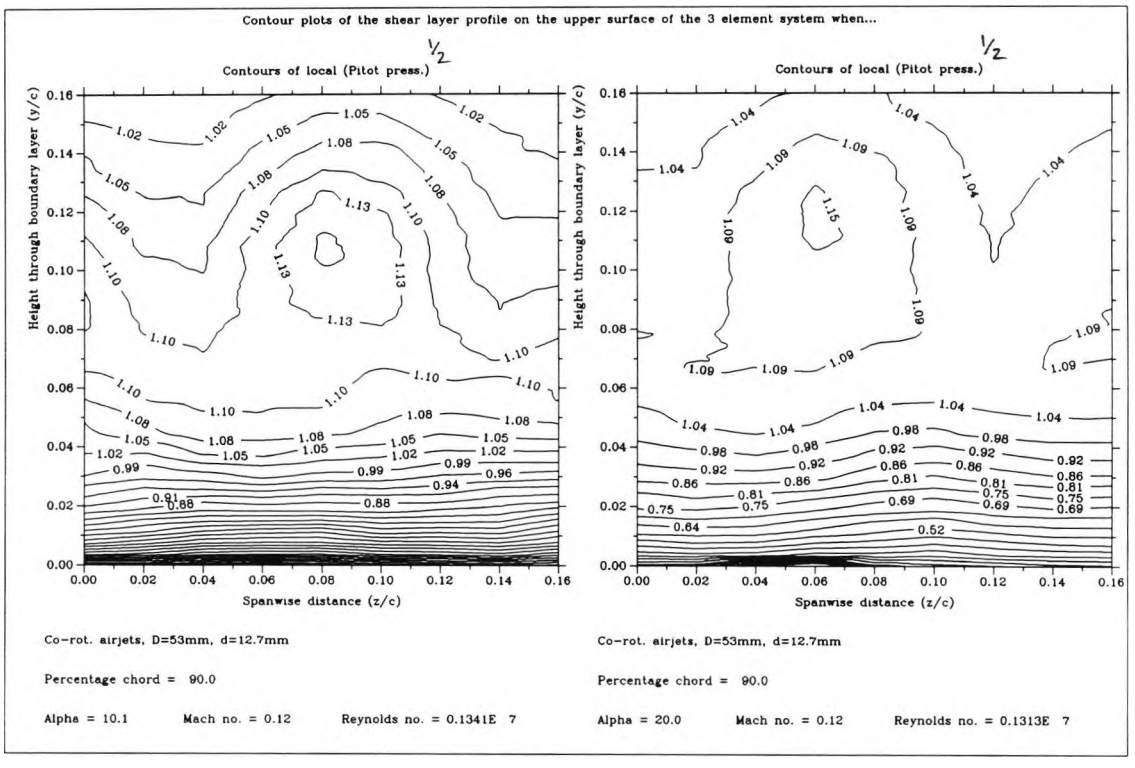

Figure 7.27 : Contour plots of the shear layer structure above the main wing at x/c = 0.9 for $\alpha = 10°$ & 20° when co-rot. ajvg's are at x/c = 0.14

probable the vortices have burst (large increase in core size and the jet cores have merged - the associated vortices would then tend to rapdily damp one another out) by this chordwise location but their action has left a shear layer structure which is surprisingly uniform in the spanwise direction through most of its height. However, below y/c = 0.1 at 10° and at z/c = 0.06 (fig. 7.27) a region of highly sheared flow appears whose extent develops with incidence until by 30° (fig. 7.28) separated flow appears to be present across the whole spanwise region monitored, although pressure distribution data suggests otherwise (figs. 7.10 & 7.23). This is discussed further in section 7.2.3 and is believed to be due to the effect of high yaw on these particular pitot tubes. The magnitude of the pitot readings in the centre of the core region of the jets above the main wing does not drop significantly ($\approx 1.15\ u/U_e$) with incidence between 10° and 30° (figs. 7.27 & 7.28). This suggests the enhanced mixing produced by the vortices has not penetrated to the centre of each airjet in the chordwise distance over which the vortex was able to persist.

A similar story can be told for the shear layers above the flap between 0° and 32° (figs. 7.29 - 7.31). Again the core flow of the jets moves away from the upper surface of the flap with incidence and eventually out of reach of the pitot rake! The slot flow above the flap seems to be unaffected by the airjets but the uniformity in the shear layers at low incidence (fig. 7.29) diminishes with incidence and at 30° (fig. 7.30) a definite variation in the thickness of the shear layers above the flap is evident above 0.1 y/c (as much as 0.02 y/c). In fact this feature is present in the shear layers at the main wing trailing edge but is not so marked (≈ 0.01 y/c).

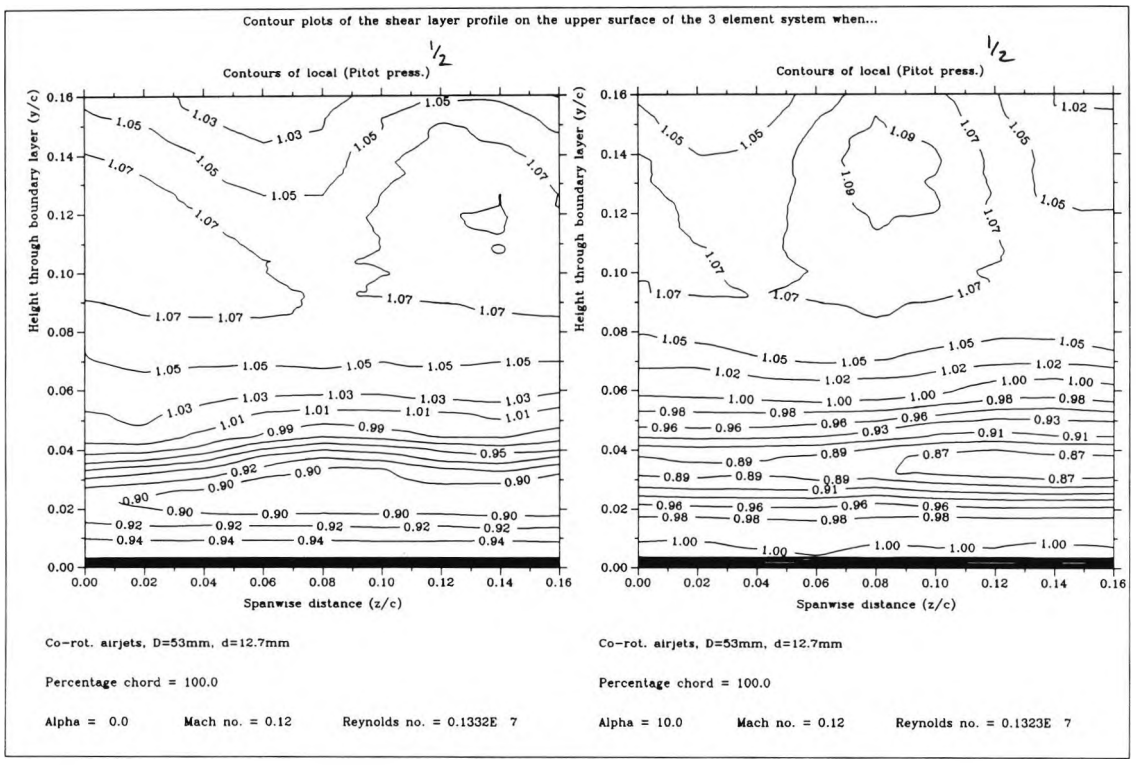

Figure 7.29 : Contour plots of the shear layer structure above the flap at x/c = 1.0 for $\alpha = 0°$ & 10° when co-rot. ajvg's are at x/c = 0.14

7.2.2 Detailed comparison of shear layer profiles at x/c = 0.354 (fig. 7.32 - fig. 7.39, Appendix C)

As explained in the equivalent section for vane vortex generators (section 6.2.2) the figures referenced in this and subsequent sections are grouped into pairs. The first figure in each pair compares the cleanfoil shear layer profile at a given chordwise location and incidence with the corresponding mean profile when co-rotating airjet vortex generators are at x/c = 0.14. The second figure (following directly on) compares selected profiles across the span between airjets with the cleanfoil profile. For most of the figures the two selected profiles which were compared with cleanfoil shear layer profile were those which either passed directly through the jet core or through the shear layer between airjets. Mean profiles were obtained by selecting five successive pitot rake profiles as the jets were 53 mm apart.

Figure 7.32 compares the mean shear layer profile at x/c = 0.354 at 10° with the cleanfoil shear layer structure at the same location. There are small differences between the profiles particularly the shear measured by the lowest pitot tube above the main wing surface where u/U_e is reduced by 10% in the mean profile for airjets. The figure clearly shows the flow in the jet and the height to which this reaches at this chordwise location. The mean shear layer thickness is unchanged but both momentum thickness and displacement thickness show small increases with airjets in use. If the mean profile is now represented by two constituent profiles (figure 7.33) the strength of the jet flow is more apparent at a height of $\approx 2\frac{1}{2}$ times the shear layer thickness. The thickness of the shear layer below this structure remains comparable with the cleanfoil case (curve 3) but between the jets the shear layer profile is much improved (curve 2). It is also noticeable that streamwise u/U_e is constant (≈ 0.78) for

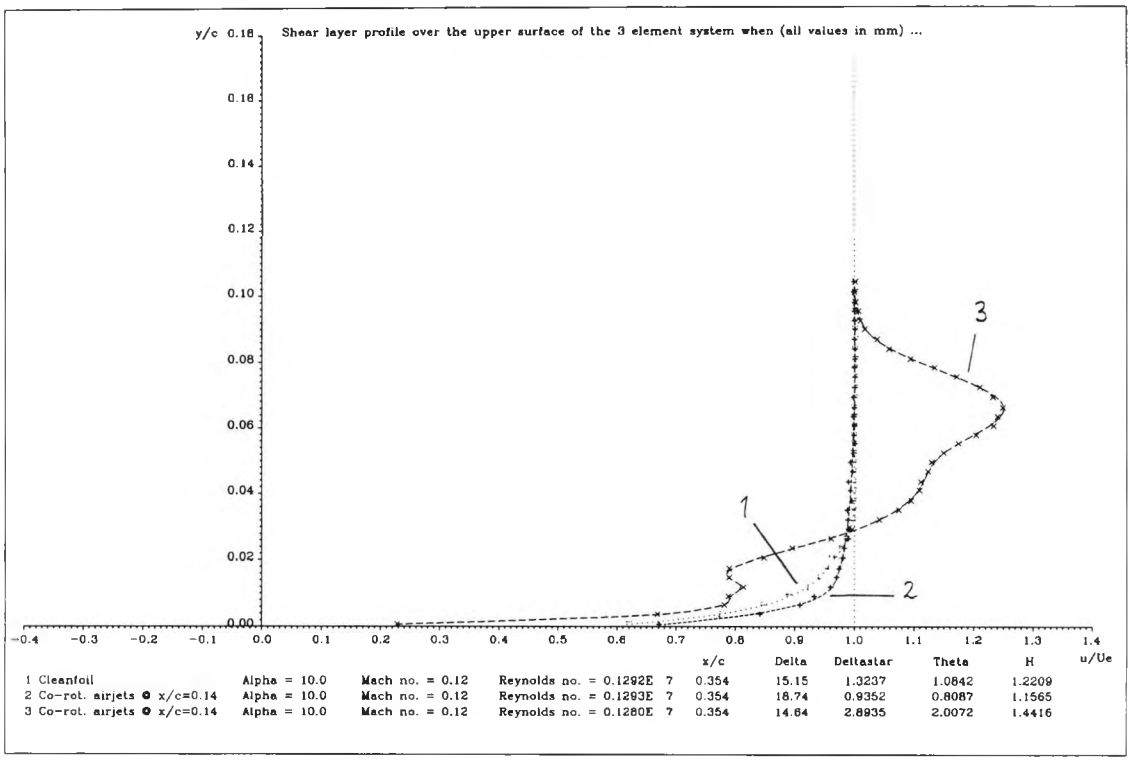

Figure 7.33 : Spanwise variation of shear layer profile at x/c = 0.354, $\alpha = 10°$, obtained when co-rot. airjets are at x/c = 0.14

a considerable height under the jet and the shear measured by the lowest pitot tube has dropped to only 0.23, far lower than seen with vane vortex generators for the corresponding case (fig. 6.45).

At higher incidences (figs. 7.34, 7.36 and 7.38) the slat wake, its partial confluency with the main wing boundary layer and the remnants of the slot flow appear in the cleanfoil shear layer profile. The mean profiles with airjets now show smaller changes in u/U_e measured at the lowest pitot station above the main wing when compared with the equivalent cleanfoil case but the slot flow feature and its associated relatively high velocities at $\approx$ 0.01 y/c are seemingly dispersed, the more so as incidence increases from 20° to 30°. Additionally the separate identity of the slat wake is reduced and is replaced in the mean shear layer profiles with jets by a region of steadily increasing shear which has a fuller profile between 0.02 y/c and 0.04 y/c. This contributes to the mean shear layer profiles with jets now also showing a consistent reduction in shear layer thickness.

Figures 7.35, 7.37 and 7.39 again show in more detail the effect which the airjets have on the shear layers between 20°and 30°at x/c = 0.354. The core jet height is invariant with incidence and the shear layer profiles between adjacent jets (curve 2 in each figure) show only small changes when compared with cleanfoil profile below y/c = 0.01. The profiles depicted by the curve 2 are located in the downward region of the vortex associated with each airjet (ie. not influenced directly by the jet) and consequently the increased momentum transfer into this region is solely attributable to the vortex action which results in a consistent fuller profile for the shear layers at this point in the span and higher shear at the main wing surface. The high velocities associated with the slot flow have been reduced and there is little

sign of a slat wake. Curve 3 represents profiles directly below and through the jet core. High velocity gradients exist at heights below 0.01 y/c and between 0.01 y/c and 0.02 y/c u/U_e again remains constant. There is no sign of the slot flow in these profiles and the slat wake has been partially absorbed into a region of higher shear at the base of the core flow of each jet.

Evidently, the jets are producing very high cross-flow velocities in the lower regions of the shear layer directly below the jet (hence $u/U_e \approx 0.2$) far larger than that seen with co-rotating vane vortex generators. The region where shear remains $\approx$ constant between 0.01 y/c and 0.02 y/c is the entrained cross-flow depicted by figure 2.14 (Rao, 1988). The enhanced mixing produced by the jets and their associated vortices has resulted in the slot flow being absorbed into the surrounding shear layers and the reduced identity of the slat wake as it is swept up in the mixing process. This is in contrast to the spanwise shear layer structure produced by the co-rotating vane vortex generators at $x/c = 0.354$ (fig. 6.63 and 6.37) where the slat wake was clearly identifiable between adjacent vortices.

7.2.3 Detailed comparison of shear layer profiles at x/c = 0.9 (fig. 7.40 - fig. 7.47, Appendix C)

Figures 7.40, 7.42, 7.44 and 7.46 compare the cleanfoil shear layer profile with the mean shear layer profile obtained with airjets at the main wing trailing edge ($x/c = 0.9$) for incidences between 10° and 30°. At 10° (fig. 7.40) the mean shear layer profile with airjets in use shows considerable differences when compared with the cleanfoil shear layer profile obtained at the same incidence. As incidence is increased these differences become more marked. By 20° (fig. 7.42) the gradient of the shear layer profile close to the wall is below that measured in the cleanfoil case. Again as with vanes at this incidence no separation was evident in surface tufts. The strong cross flow generated by the vortices will in the region of low streamwise velocity adjacent to the surface of the main wing lead to high values of yaw locally and false readings in the pitot tubes at these low heights within the shear layer. For figures fig. 7.40 to fig. 7.47 the reader would gain a better impression of the shear layer profile by the gradient of shear further out and extrapolate this to the main wing surface. The fact that the misleading pitot readings are present right across the span between two airjets by 25° (fig. 7.45) is indicative of the strength of the cross-flow and which is greater than that produced by the co-rotating vane vortex generators (compare fig. 6.53 with fig. 7.45).

Figures 7.40 to 7.44 inclusive illustrate that the airjets at low incidences have been able to reduce the thickness of the shear layers (defined by the region in which $u/U_e \leq 0.995$) at the trailing edge of the main wing by nearly 50% (fig. 7.57). In addition displacement thickness also shows a marked reduction at $x/c = 0.9$ with airjets in use, the actual reduction probably being greater than that indicated by the data below the figures (and fig. 7.58), since we know the shear at low values of y/c to be subject to errors due to high yaw locally. Here we have the reason why with airjets at $x/c = 0.14$ on the main wing the high lift system is able to generate a slightly higher normal force coefficient at low incidences. The reduction of displacement thickness at the trailing edge of the main wing corresponds to a reduction in the

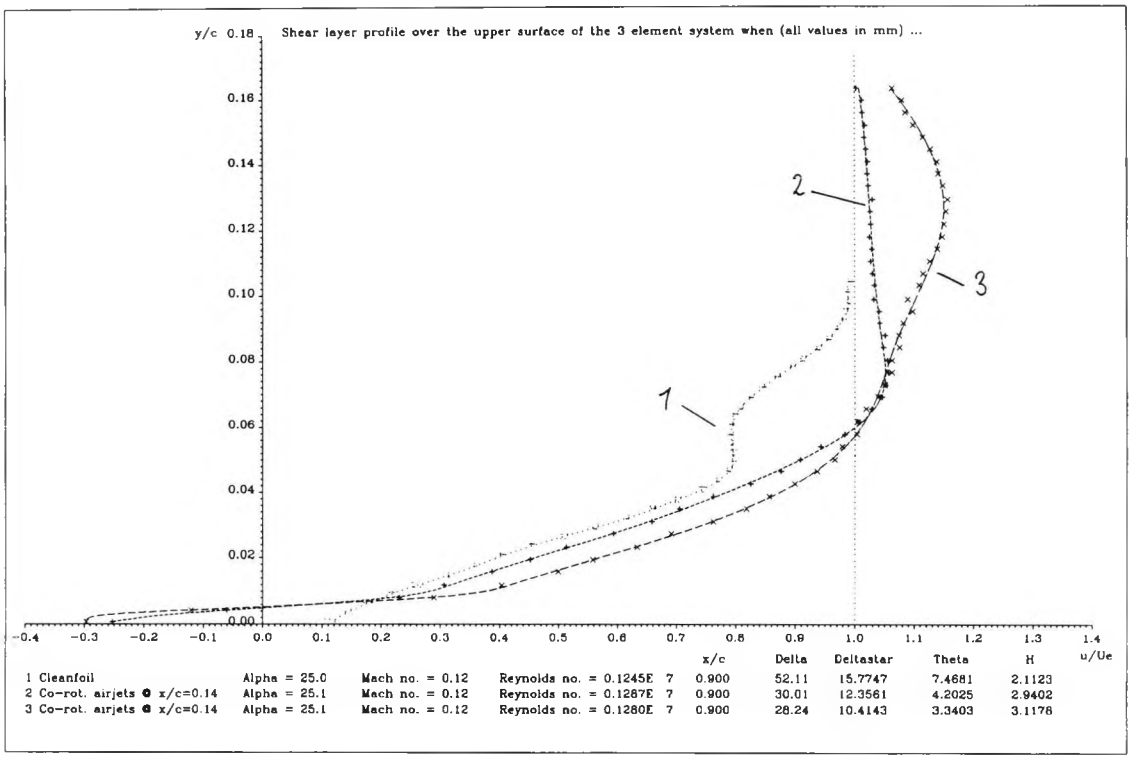

Figure 7.45 : Spanwise variation of shear layer profile at x/c = 0.9, $\alpha = 25°$, obtained when co-rot. airjets are at x/c = 0.14

thickness effect of the boundary layer and a reduction of negative camber. This is precisely opposite to the effect which vane vortex generators have on the shear layers at the trailing edge of the main wing at low incidence (see section 6.2.3).

Figures 7.42 to 7.47 illustrate how well the slat wake has been completely absorbed into a region of higher shear by x/c = 0.9 under the action of the airjets and associated vortices. This remains true both in a spanwise direction and with increasing incidence. The remains of the expanded jet cores are clearly visible high above the main wing surface. Figures 7.41 and 7.43 reveal how small the variation is in the profile of the shear layers across the span at low incidences, but some spanwise differences do appear at high incidences (fig. 7.45 and fig. 7.47). The improved shear layer profile at the trailing edge of the main wing at all incidences with airjets in use at x/c = 0.14 must be directly attributable to the enhanced mixing produce by the airjets and their associated vortices. This is particularly emphasised by figures 7.46 and 7.47 when one realises the comparison is not made at the same incidence. All the measured shear layer profiles obtained at the trailing edge of the main wing and referenced in this section convey a common message; it seems probable the level of blowing used for the airjet vortex generators is rather too large since most of the high momentum flow is present high above the main wing. The energy in this flow will not be transferred by viscous shear and vortex induced mixing to the lower regions of the shear layers where it would be of the most benefit. This excess energy is interpretated as an additional drag penalty for the high lift system. However a lower blowing pressure will with the same configuration of airjet vortex generators probably generate a lower strength of cross-flow and hence vorticity. Obviously an optimum must exist.

7.2.4 Detailed comparison of shear layer profiles at x/c = 1.0 (fig. 7.48 - fig. 7.56, Appendix C)

Bearing in mind the main wing and flap shear layers are confluent by x/c = 1.0 at 0° any improvement in structure of the shear layers shed by the main wing will inevitably have a favourable influence on the shear layers above the flap at this incidence. The airjets do reduce the adverse effects of confluency in the shear layers above the flap at 0° (fig. 7.48 and fig 7.49). The measured value of u/U_e at the lowest pitot station in the rake above the flap is increased, the flap upper surface boundary layer is significantly fuller and the overall thickness of the shear layer structure is reduced slightly.

Above 0° the flap upper surface boundary layer is not confluent with the main wing wake at x/c = 1.0 and so u/U_e at the lowest point in the pitot rake above the flap upper surface remains unchanged with airjet vortex generators at x/c = 0.14 on the main wing (figs. 7.50 - 7.56). The same figures show how at any incidence the velocity defect associated with the main wing / slat wake structure above the flap is significantly reduced on comparison with the cleanfoil case. There is no sign of the slat wake and the jet has almost dispersed high above the flap upper surface. The spanwise variation in the structure of the main wing / slat wake above the flap has almost disappeared except above y/c = 0.1 (figs. 7.49, 7.51, 7.55 and 7.56). The exception to this is at 20° (fig. 7.53) which the author is at a loss as to explain why, since at the main wing trailing edge little variation could be seen in the shear layer structure across the span (fig. 7.43).

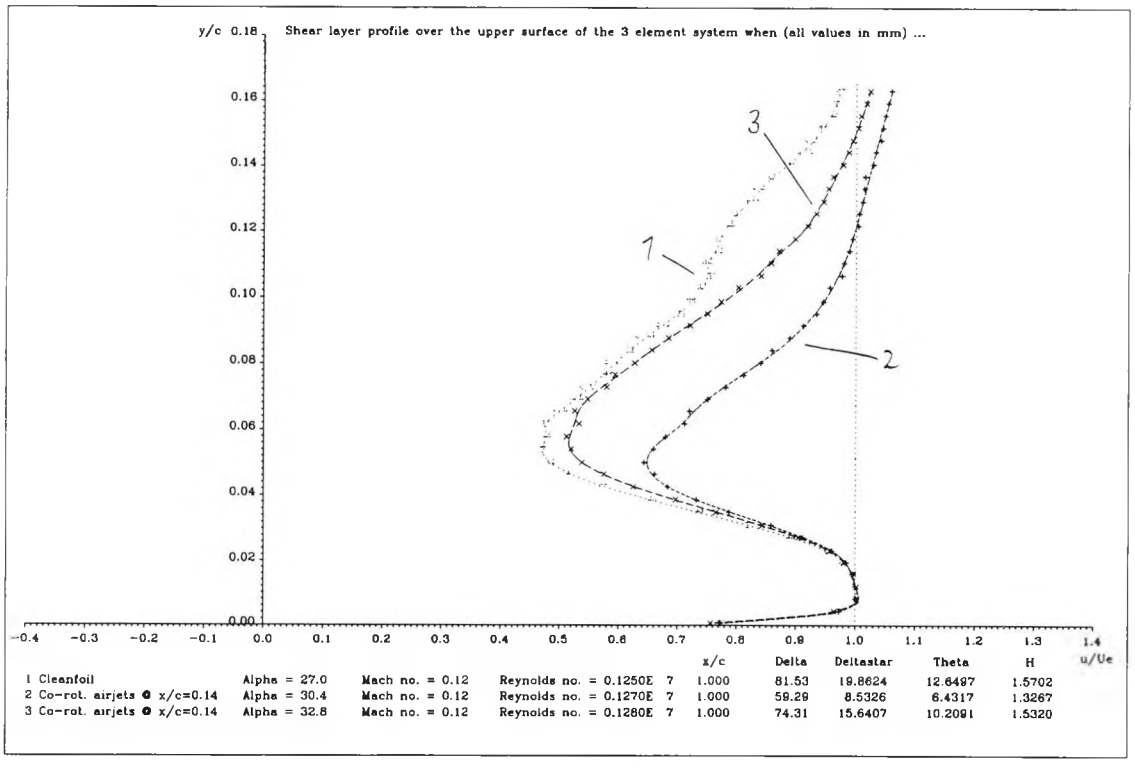

Figure 7.54 : Comparison of mean shear layer profiles at x/c = 1.0, $\alpha = 27°$ (cleanfoil), 30° and 32.8° (co-rot. airjets at x/c = 0.14)

The extent of the flow through the slot remains unchanged with airjet vortex generators on the main wing.

Figure 7.54 once again raises an issue which was mentioned previously in section 6.2.4 in relation to vane vortex generators, in that the minimum value of u/U_e in the main wing / slat wake structure above the flap with airjet vortex generators is seen to tend towards that value seen in the cleanfoil case at 27° (just prior to stall).

At all incidences momentum thickness is significantly reduced in the shear layers above the flap when compared with the cleanfoil case (fig. 7.59). By inference the high lift system will exhibit a reduction in profile drag at all incidences.

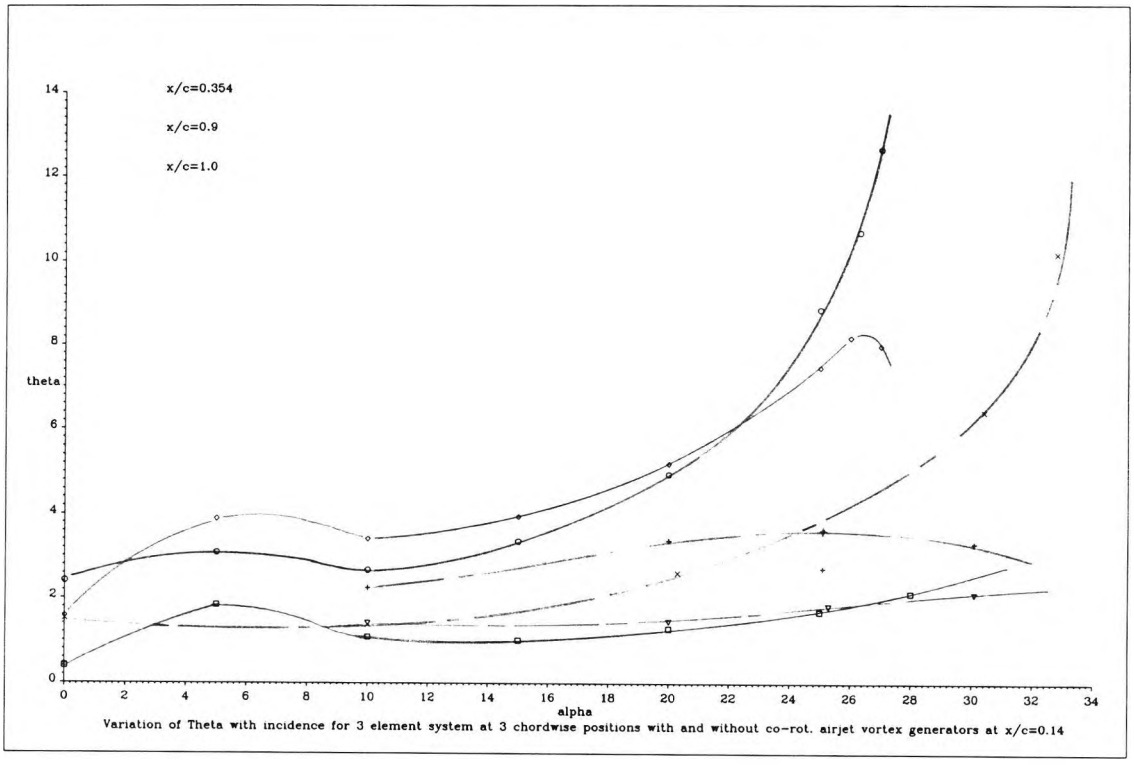

Figure 7.59 : Variation of θ (in mm) with α at 3 chordwise locations, with and without co-rot. airjet vortex generators at x/c = 0.14

8. Summary and Conclusions

Windtunnel tests have been conducted on a two-dimensional model of a three element high lift system in a take-off configuration in City University's T2 low speed windtunnel. The high lift system was mounted between endplates and consisted of a leading edge Handley Page slat and a trailing edge Fowler flap. Endplate boundary layer control ensured two-dimensional conditions up to and beyond stall and was provided by blowing through two near tangential slots located flush in each endplate adjacent to the main wing element. The windtunnel tests involved monitoring the pressure distribution around each element of the high lift system and investigating the structure of the shear layers above the main wing and flap elements.

Without any form of additional boundary layer control the high lift system (or cleanfoil) generated a maximum total normal force coefficient of 3.662 at 28°. Boundary layer separation was first seen at the trailing edge of the main wing at 27° and developed steadily with incidence moving forward to $x/c = 0.4$ by 31°. The stall of the high lift system coincided with the rapid divergence of the static pressure at the trailing edge of the flap. However the stall was preceded by a loss of load at the rear of the main wing attributable to the adverse viscous effects of the confluency of the main wing upper surface boundary layer and the slat wake, resulting in a substantial growth in the thickness of the shear layers at the rear of the main wing and the appearance of the separated flow in this region.

Various vane vortex generator configurations were located on the upper surface of the main wing at $x/c = 0.14$ and $x/c = 0.403$. For every configuration tested the high lift system exhibited a reduction in total normal force coefficient at incidences below the stall incidence of the cleanfoil, resulting from an increased displacement effect of the shear layers above the upper surface of the main wing. The most beneficial configuration was a system of co-rotating vane vortex generators at $x/c = 0.14$ which increased the stall incidence by more than 4° and produced an improvement in maximum total normal force coefficient of 5% (up to 3.842). Although the co-rotating vane vortex generators delayed the loss of loading which was seen to develop at the rear of the main wing in the cleanfoil condition (by alleviating the adverse effects of confluency of the main wing with the slat wake) the maximum normal force coefficient of the main wing did not increase significantly. Instead, the greater part of the improvement in maximum total normal force coefficient resulted from increased loading of the slat at incidences above the stall incidence of the cleanfoil. The co-rotating vane vortex generators delay the separation which develops at the rear of the main wing in their absence at 27°, increasing the trailing edge pressure recovery on the flap and hence overall circulation. A mean value of momentum thickness for the shear layers above the flap at 100% x/c reveals the high lift system exhibits an increase in profile drag with co-rotating vane vortex generators at $x/c = 0.14$ for all incidences except possibly close to 0°.

A system of co-rotating airjet vortex generators installed at $x/c = 0.14$ on the main wing and utilizing a constant blowing pressure of 60% above freestream stagnation pressure increased the stall incidence of the high lift system by 6½° and the maximum total normal

force coefficient by 22% (to 4.468). The high lift system exhibited an increase in total normal force coefficient at all incidences below the stall incidence of the cleanfoil (28°). The improved characteristics which the high lift system exhibits with the application of airjet vortex generators cannot be solely due to the suppression of boundary layer separation at the trailing edge of the main wing. For incidences up to 20° these improvements result from a reduced displacement effect of the shear layers above the main wing. For incidences between 20° and 28° the co-rotating airjet vortex generators allow the load on the main wing to increase progressively with incidence. In addition the improvement in total normal force coefficient now also embraces that generated by the slat. The overall circulation of the high lift system which derives from the increased pressure recovery at the flap trailing edge is better sustained with airjets. Above 28° attached flow on both the main wing and flap contribute to developing circulation and increased normal force coefficients. A reduction in the profile drag of the high lift system can be inferred from a lower value of momentum defect in the shear layers above the flap at all incidences. The abrupt stall characteristics of the high lift system when airjets are in use may be due to the airjets improving the flow over the main wing to such a degree that the onset of stall shifts to the flap. If a lower blowing pressure is utilized for the airjets this may not be the case as the vortices will reduce in strength and the onset of stall may return to the main wing in which case the abruptness of the stall may be alleviated somewhat.

The core flow from an airjet vortex generator is capable of penetrating the thick shear layers which exist above the main wing of a high lift system to form a vortex which promotes enhanced mixing (and hence momentum transfer) that embraces all constituent elements which make up the shear layer structure - the main wing upper surface boundary layer, the potential flow through the slot, the slat wake and the external flow of the freestream as well as the momentum of the jet itself. Unless a vane vortex generator is unpractically large it is unable to achieve the same degree of enhanced mixing.

The results indicate that airjet vortex generators may offer a new approach to the design of high lift systems since the benefits they provide are superior to those offered by vane vortex generators but can only be obtained if they are considered as a integral part of the aerodynamic design of the high lift system. In particular, the competing effects of favourable inviscid interaction and adverse viscous effects leads to the existence of an optimum position for each element of the high lift system. By alleviating the adverse effects of the contamination of the main wing boundary layer by the wake from the slat, the airjets offer a further degree of flexibility in gap settings between the slat and main wing or alternatively between the main wing and flap which will allow for further exploitation of the mutual inviscid potential flow effects. Alternatively they could be used to prevent tip stall so avoiding the need for stall fixing through the deliberate degradation of the flow over wing inboard leading edges.

9. Further Work

It must be emphasised that only one configuration of airjet vortex generators has been tested at one constant blowing pressure. The most pressing work which needs to be done is to investigate the performance of the same installation with various blowing pressures before the effect of other parameters are examined such as chordwise location, spacing and jet exit shape.

A drag/thrust audit is also required to ascertain whether the measured reduction in profile drag of the high lift system is more than offset by an allowance for the jet momentum. Inevitably a performance penalty will be associated with the system since not all of the kinetic energy in the jet flow will be transferred to the shear layers (not an ideal process). Work needs to be done to reveal the fundamental fluid dynamic processes at work which would lead to an optimised system and the best balance between performance gains and installation penalties.

References

Abbott, I.H. and von Doenoff, A.E. (1949)
"Theory of wing sections."
McGraw Hill & Dover Publications, New York.

Akanni, S. and Henry, F.S. (1995)
"Numerical calculations of airjet vortex generators in turbulent boundary layers."
CEAS European Forum on High Lift & Separation Control, paper 16.

Alston, R.P. (1935)
"Wing flaps and other devices as aids to landing."
Journal of the Royal Aeronautical Society (39), pp637-650.

Ashill, P.R. and Weeks, D.J. (1982)
"A method for determining wall interference corrections in solid wall tunnels from measurements of static pressure at the walls."
AGARD-CP-335, paper 1.

Berg, B. van den (1979)
"Boundary layer measurements on a two-dimensional wing with flap."
NLR TR 79009U.

Brune, G.W. and Manke, J.W. (1978)
"Upgraded viscous flow analysis of multi-element aerofoils."
AIAA 11th Fluid and Plasma Dynamics Conference, AIAA-78-1224.

Bruynes, H. and Taylor H.D. (1950)
"Summary report on vortex generators."
United Aircraft Research Department R-05280-9.

Butter, D.J. and Williams, B.R. (1980)
"The development and application of a method for calculating the viscous flow about high lift aerofoils."
AGARD-CP-291, paper 25.

Butter, D.J. (1984)
"Recent progress on development and understanding of high lift systems."
AGARD-CP-365, paper 1.

Callaghan, J.G. and Beatty, T.D. (1972)
"A theoretical method for the analysis and design of multi-element aerofoils."
Journal of Aircraft (9), no.12, pp844-848.

Compton, D.A. and Johnston, J.P. (1992)
"Streamwise vortex production by pitched and skewed jets in a turbulent boundary layer."
AIAA(30), no.3, March 1992.

Duddy, R.R. (1949)
"High lift devices and their uses."
Aeronautical Journal (53), pp860-883.

Fage, A. and Sargent, R.F. (1944)
"The air-injection method of fixing transition for laminar to turbulent flow in a boundary layer."
ARC R&M 2106.

Fiddes, S.P. , Kirby, D.A. , Woodward, D.S. and Peckham, D.H. (1984)
"Investigations into the effects of scale and compressibility on the lift and drag in the RAE 5m pressurised low speed wind tunnel."
AGARD-CP-365, paper 2.

Flores, J. , Holst, T.L. , Gundy, K.L. and Chaderjin, N. (1986)
"Transonic Navier-Stokes wing solution using a zonal approach."
AGARD-CP-412, paper 30.

Foster, D.N. (1971)
"The flow around wing sections with high lift devices."
AIAA-71-0096.

Foster, D.N. , Irwin, H.P.A.H. and Williams, B.R. (1970)
"The two-dimensional flow around a slotted flap."
ARC R&M 3681.

Foster, D.N. (1971)
"Some comments on characteristics of high lift wings."
AGARD LS 43, paper 13.

Freestone, M.M. (1985)
"Preliminary tests at low speed on vorticity produced by air-jet vortex generators."
RM 85/1 City University, London.

Freestone, M.M. (1995)
"Inviscid theory applied to vortex-induced mixing."
CEAS European Forum on High Lift & Separation Control, paper 15.

Goradia, S.H. (1971)
"Confluent boundary layers flow development with arbitrary pressure distribution."
PhD Thesis, Georgia Institute of Technology.

Granville, P.S. (1953)
"The calculation of viscous drag of bodies of revolution."
David Taylor Model Basin, Report 849.

Green, J.E. , Weeks, D.G. and Brooman, J.W.F (1973)
"Prediction of turbulent boundary layers and wakes in compressible flow by a lag-entrainment method."
ARC R&M 3791

Grossman, B. and Melnik, R.E. (1976)
"The numerical computation of the transonic flow over two element aerofoil systems."
Fifth conference on Numerical Methods in Fluid Dynamics. Enschede, Netherlands.

Hall, I.M. and Suddhoo, A. (1984)
"Inviscid compressible flow past a multi-element aerofoil."
AGARD-CP-365, paper 5.

Halsey, N.D. (1979)
"Potential flow analysis of multi-element aerofoils using conformal mapping."
AIAA (17), no.12, pp1281-1287.

Henry, F.S. and Pearcey, H.H. (1994)
"Numerical model of boundary layer control using airjet generated vortices."
AIAA(32), no.12, pp2415-2425.

Hill, M.G. and Riley, N.A. (1986)
"A hybrid method for transonic flow past multi-element aerofoils."
Journal of Fluid Mechanics (170), pp253-264.

Horton, H.P. (1967)
"A semi-empirical theory for the growth and bursting of laminar separation bubbles."
ARC CP 1073.

Irwin. H.P.A.H (1974)
"A calculation method for the two dimensional turbulent flow over a slotted flap."
ARC CP 1267.

Ives, D.C. (1976)
"A modern look at conformal mapping including multiply connected regions."
AIAA (14), pp1006-1011.

Johnston, J. and Nishi, M. (1989)
"Vortex generator jets - a means for passive and active control of boundary layer separation."
AIAA-89-0564.

King, D.A. and Williams, B.R. (1988)
"Developments in computational methods for high lift aerodynamics."
Aeronautical Journal, Aug/Sept 1988, pp265-289.

Le Balleur, J.C. (1981)
"Strong matching method for computing transonic viscous flows including wakes and separations."
La Recherche Aerospatiale (3), pp21-45.

Lin, J.C. , Howard, F.G. , Bushnell, D.M. and Selby, G.V. (1990)
"Investigation of several passive and active methods for turbulent flow separation control."
AIAA-90-1598

Ljungstrom, B.L.G. (1972)
"Boundary layer studies on a two-dimensional high lift wing."
FFA report AU 862.

Lock, R.C. and Williams, B.R. (1987)
"Viscous-inviscid interactions in external aerodynamics."
Progress in Aerospace Sciences (24), pp51-171.

Mavriplis, F. (1971)
"Aerodynamics research on high lift systems."
AGARD LS43, paper 15.

McRae, D.M. (1973)
"The aerodynamic development of the wing of the A300B."
Aeronautical Journal, July 1973, pp367-379.

Mehta, R.D. ,Shabaka I.M.M.A, Shibl, A. and Bradshaw, P. (1983)
"Longitudinal vortices imbedded in turbulent boundary layers."
AIAA paper 83-0378, January 1983.

Moser, A. and Shollenberger, C.A. (1973)
"Inviscid wake aerofoil interaction on multi-element high lift systems."
Journal of Aircraft (10), no.12, pp765-767.

Nakayama, A. , Kreplin, H.P. and Morgan, H.L. (1990)
"Experimental investigation of flowfield about a multi-element aerofoil."
AIAA (28), no.1, pp14-21.

Newling, J.C. (1977)
"An improved two dimensional multi-aerofoil program."
HSA-MAE-R-FDM-0007.

Olson, L.E. and Orloff, K.L. (1981)
"On the structure of turbulent wakes and merging shear layers of multi-element aerofoils."
AIAA-81-1238.

Olson, L.E. , James, W.D. and McGowan, P.R. (1978)
"Theoretical and experimental study of the drag of multi-element aerofoils."
AIAA 11th Fluid and Plasma Dynamics Conference, AIAA-78-1223.

Oskam, B. (1980)
"Computational aspects and results of low speed viscous flow about multi-component aerofoils."
AGARD-CP-291, paper 19.

Oskam, B. (1983)
"Transonic panel method for the full potential equation applied to multi-component aerofoils."
AIAA-83-1855.

Oskam, B., Laan, D.J. and Volkers, D.F. (1984)
"Recent advances in computational methods to solve the high lift multi-component aerofoil problem."
AGARD-CP-365, paper 3.

Pankhurst, R.C. and Holder, D.W. (1952)
"Wind-tunnel technique."
Published by Issac Pitman & Sons, London.

Pauley, W.R. and Eaton, J.K. (1988)
"Experimental study of the development of longitudinal vortex pairs embedded in a turbulent boundary layer."
AIAA(26), no.7, July 1988.

Pearcey, H.H., Rao, K. and Sykes, D.M. (1993)
"Inclined airjets used as vortex generators to suppress shock-induced separation."
AGARD-CP-534, paper40.

Pearcey, H.H. (1961)
"Shock induced separation and its prevention by design and boundary layer control."
Boundary layer and flow separation control, Pergamon Press, pp1166-1344.

Quinn, J.H. (1947)
"Tests of the NACA 64_1A212 aerofoil section with a slat, a double slotted flap and boundary layer control by suction."
NACA-TN-1293.

Rao, D.M. and Kariya, T.T (1988)
"Boundary layer submerged vortex generators for separation control - an exploratory study."
AIAA-88-3546

Rao, K. (1988)
"Use of air-jet vortex generators to control shock induced boundary layer separation."
PhD Thesis, City University, London.

Selby, G.V. , Lin, J.C. and Howard, F.G. (1992)
"Control of low speed turbulent separated flow using jet vortex generators"
Experiments in Fluids, vol.12, no.6, pp394-400.

Smith, A.M.O. and Hess, J.L. (1966)
"Calculation of potential flow about arbitrary bodies."
Progress in Aeronautical Sciences (8), pp1-139, Pergamon Press.

Smith, A.M.O. (1972)
"Aerodynamics of high lift aerofoil systems."
AGARD-CP-102, paper 10.

Smith, A.M.O. (1975)
"High lift aerodynamics."
Journal of Aircraft (12), no.6, pp501-530.

Spangler, J.G. and Wells, C.S. (1964)
"Effects of longitudinal vortices on turbulent boundary layer skin friction."
NASA CR-145, December 1964.

Stevens, W.A. , Goradia, S.H. and Braden, J.A. (1971)
"Mathematical model for two-dimensional multi-component aerofoils in viscous flow."
NASA CR-1843.

Thain, J.A. (1973)
"Reynolds number effects at low speeds on the maximum lift of two-dimensional aerofoil sections equipped with mechanical high lift devices."
Report DM/NAE (3), Quarterly Bulletin, National Aeronautical Establishment, Canada.

Thwaites, B. (1960)
"Incompressible aerodynamics."
Fluid motion memoirs, Claredon Press, Oxford.

Von Karman, Th. v. (1921)
"Uber laminare und turbulente Reilung."
Z. angew. Math. Mech., vol. 1, pp233-252

Wallis, R.A. (1952)
"The use of airjets for boundary layer control."
Appendum to Aero. Technical Note no.110 (N-34736)
Aeronautical Research Laboratories, Australia.

Wallis, R.A. (1956)
"A preliminary note on a modified type of airjet for boundary layer control."
CP 513, Aerodynamics Research Laboratories, Australia.

Wallis, R.A. and Stuart, C.M. (1958)
"On the control of shock-induced boundary layer separation with discrete airjets."
A.R.C. Report no. 19865

Westphal, R.V. , Eaton, J.K. and Pauley, W.R. (1985)
"Interaction between a vortex and a turbulent boundary layer in a streamwise pressure gradient."
Turbulent Shear Flows edited by Durst, Launder, Schmidt and Whitelaw,
Springer Verlag, New York, pp 266-277.

Williams, B.R. (1985)
"The prediction of separated flow using a viscous-inviscid interaction method."
Aeronautical Journal (89), no.885, pp185-197.

Williams, B.R. (1971)
"An exact test case for the plane potential flow about two adjacent lifting aerofoils."
ARC R&M 3717.

Young, A.D. (1947)
"The aerodynamic characteristics of flaps."
ARC R&M 2622.

Zhang, S. and Fan, L. (1987)
"Experiments about the airjet vortex generator."
Proceedings of the 8th Institute of Aeronautics & Astronautics Conference, Cincinnati, Ohio, pp513-516.

Bibliograph

"BAe shows SABA alternative."
Flight International, 12/12/87.

Back, R.F. and Wedderspoon, J.R. (1986)
"The A320 wing - designing for commercial success."
Aerospace Journal, January 1986, pp12-19.

Berg, B. van den (1971)
"Some notes on two-dimensional high lift tests in windtunnels."
AGARD LS 43, paper 5.

Bertin, J.J. and Smith, M.L. (1989)
"Aerodynamics for Engineers." 2nd Edition
Prentice-Hall Inc., Englewood Cliffs, New Jersey 07632.

Brune, G.W. , Sikavi, D.A. , Tran, E.T. and Doerzbacher, R.P. (1982)
"Boundary layer instrumentation for high lift aerofoil models."
AIAA-82-0592.

Delery, J. , Horowitz, E. , Leuchter, O. and Solignac, J.L. (1984)
"Fundamental studies on vortex flows."
LA Recherche Aerospatiale 1984-2.

Disimile, P.J. , Dimicco, R.G. , Toy, N. and Savory, E. (1990)
"The development of twin jets issuing into a crossflow."
Proc. of 12th Biennial Symp. on Turbulence, Univ. of Missouri-Rolla, Sept. 1990.

Flaig, A. and Hilbig, R. (1993)
"High lift design for large civil aircraft."
AGARD-CP-515, paper 31.

Foster, D.N. (1972)
"The low speed stalling of wings with high lift devices."
AGARD-CP-102, paper 11.

Hastings, R.C. and Williams, B.R. (1987)
"Studies of the flow field near a NACA 4412 aerofoil at maximum lift."
Aeronautical Journal, Jan 1987.

Horton, H.P. (1971)
"Fundamental aspects of flow separation under high lift conditions."
AGARD LS 43, paper 4.

Innes, F. and Pearcey, H.H. (1994)
"An experimental investigation into the use of vortex generators to enhance the performance of a high lift system."
Report no. 193, June 1994, School of Mechanical & Aeronautical Engineering, City University, London.

Johnston, J.P. and Nishi, M. (1990)
"Vortex generator jets - means for flow separation control."
AIAA(28), no.6, June 1990.

Kim, S.W. and Benson, T.J. (1993)
"Fluid flow of a row of jets in crossflow - a numerical study."
AIAA (31), no.5, pp806-811.

Liebeck, R.H. (1973)
"A class of aerofoils designed for high lift in incompressible flow."
Journal of Aircraft (10), no.10, pp610-617.

Lin. J.C. , Howard, F.G. and Selby, G.V. (1989)
"Turbulent flow separation control through passive techniques."
AIAA-89-0976.

Ljungstrom, B.L.G. (1974)
"Experimental high lift optimization of multi-element aerofoils."
AGARD-CP-143, paper 13.

Mahgoub, H.E.H and Bradshaw, P. (1979)
"Calculation of turbulent inviscid flow interactions with large normal pressure gradients."
AIAA Journal (17), no.10, pp1025-1029.

McMasters, J.H. and Henderson, M.L. (1981)
"Some recent applications of high lift computational methods at Boeing."
AIAA-81-1657.

McRae, D.M. (1971)
"Aerodynamics of mechanical high lift devices."
AGARD LS 43, paper 1.

Moran, J. (1984)
"An introduction to theoretical and computational aerodynamics." 1st Edition
John Wiley & Sons Inc., 605 3rd Avenue, New York 10158.

Moses, H.L. , Jones, R.R. and O'Brien, W.F. (1978)
"Simultaneous solution of the boundary layer and freestream with separated flow."
AIAA Journal (16), no.1, pp61-66.

Nark, T.C. (1993)
"Design, development and flight evaluation of the Boeing YC-14."
AGARD-CP-515, paper 30.

Smith, A.M.O. (1975)
"Remarks on fluid mechanics of the stall."
AGARD LS 74, paper 2.

Squire, H.B. and Young, A.D. (1937)
"The calculation of the profile drag of aerofoils."
ARC R&M 1838.

White, F.M. (1974)
"Viscous fluid flow." 1st Edition
McGraw-Hill Inc., 1221 Avenue of the Americas, New York 10020.

Woodward, D.S. and Lean, D.E. (1993)
"Where is high lift today? - a review of past UK research programmes."
AGARD-CP-515, paper 1.

Wortmann, F.X. (1972)
"Design of aerofoils with high lift at low and medium subsonic mach numbers."
AGARD-CP-102, paper 7.

Zhang, X. (1993)
"Interaction between a turbulent boundary layer and elliptic and rectangular jets."
Second International Symposium on Engineering Turbulence Modelling & Measurements,
Florence, Italy, June 1993.

Appendix A - Windtunnel test results with the cleanfoil

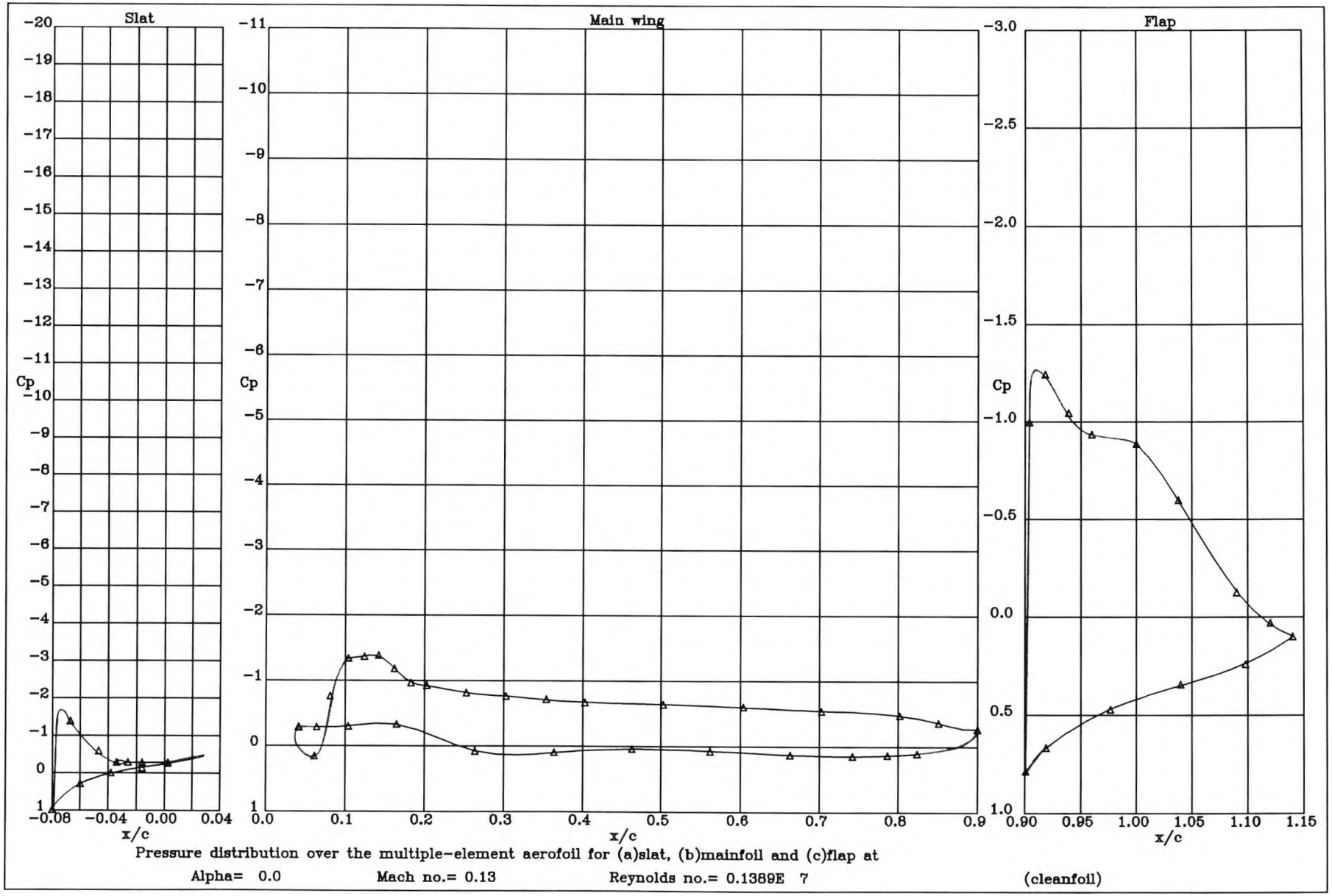

Pressure distribution over the multiple-element aerofoil for (a)slat, (b)mainfoil and (c)flap at

Alpha= 0.0 Mach no.= 0.13 Reynolds no.= 0.1389E 7 (cleanfoil)

Figure 5.6 : Pressure distribution over the high lift system at 0°

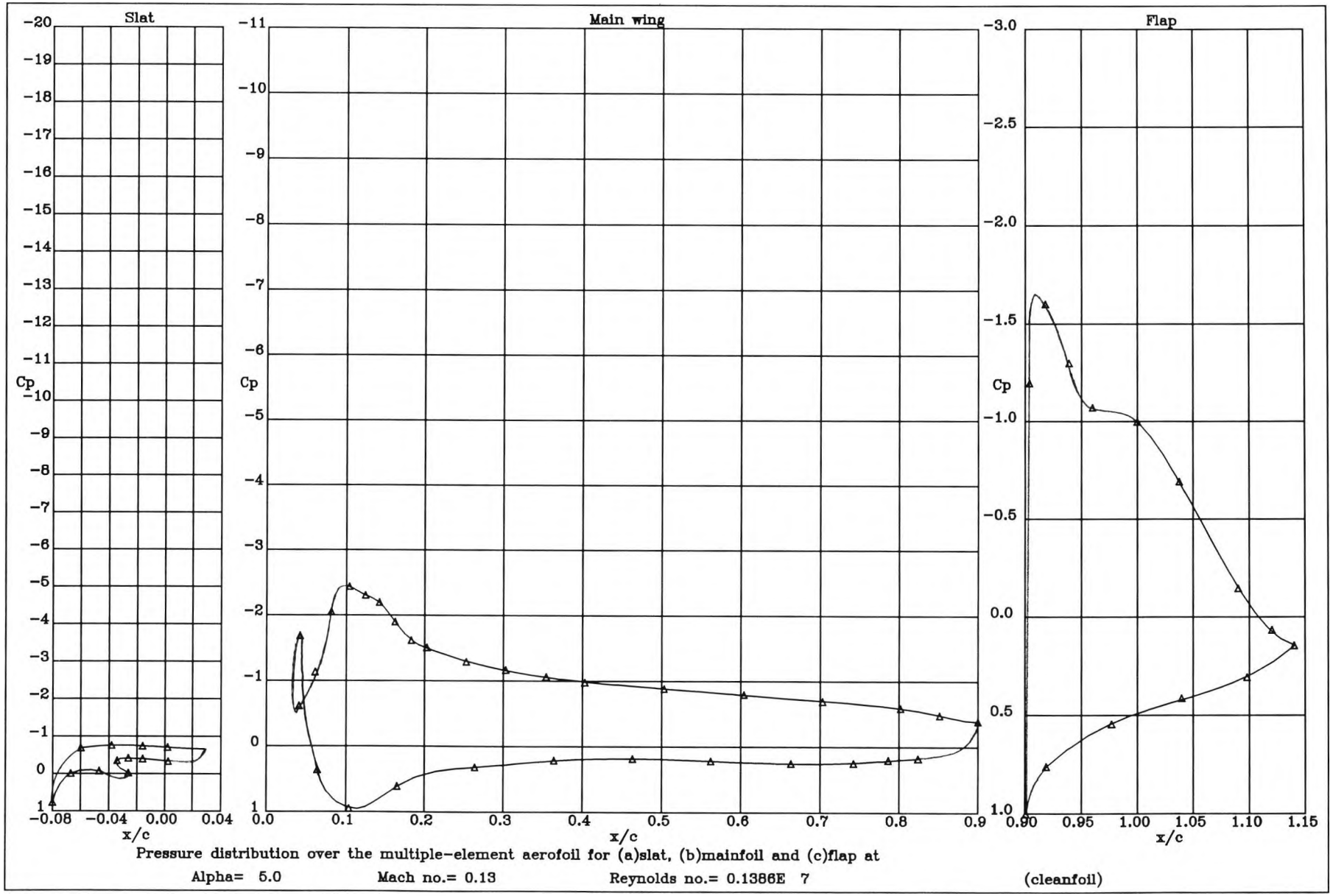

Figure 5.7 : Pressure distribution over the high lift system at 5°

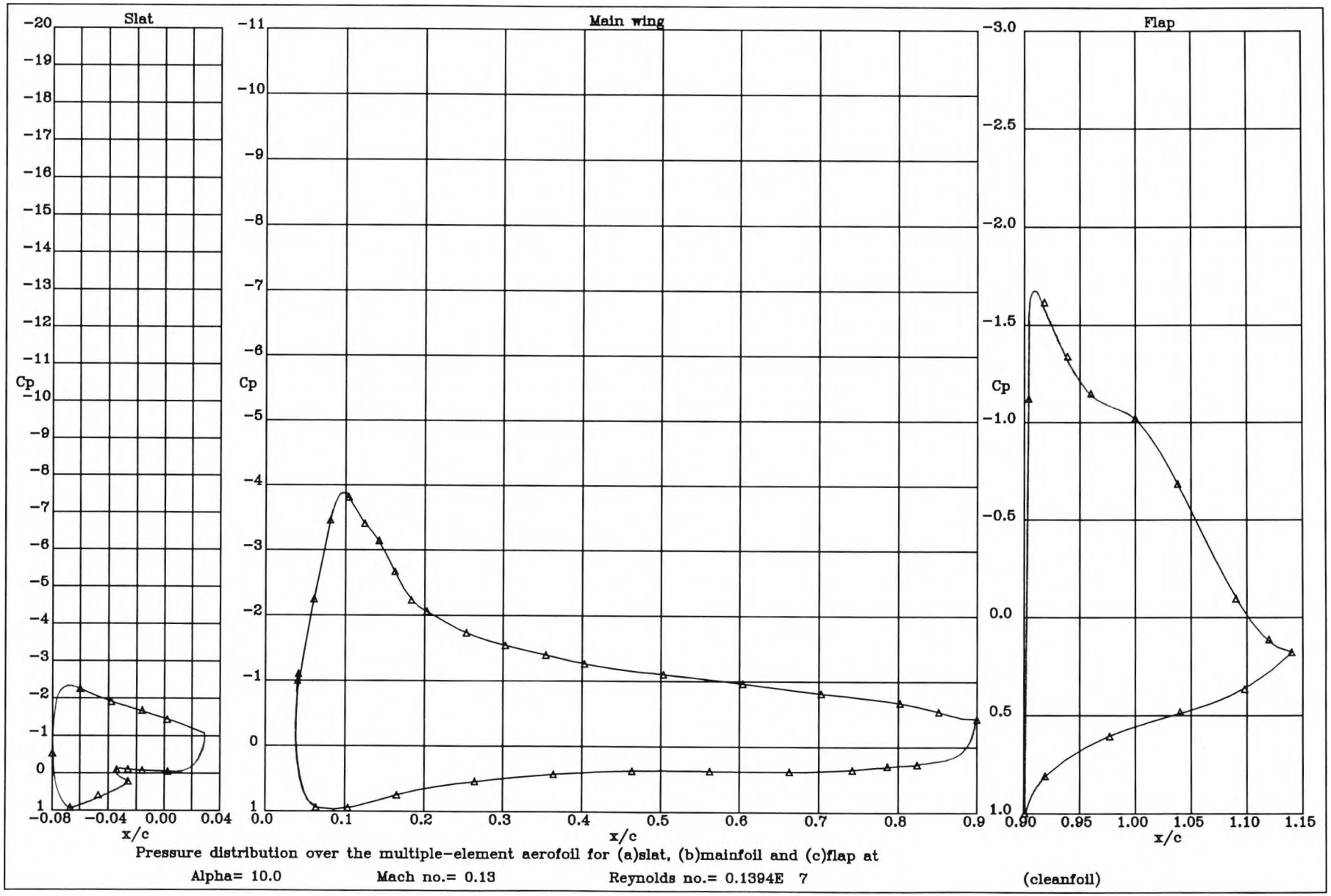

Figure 5.8 : Pressure distribution over the high lift system at 10°

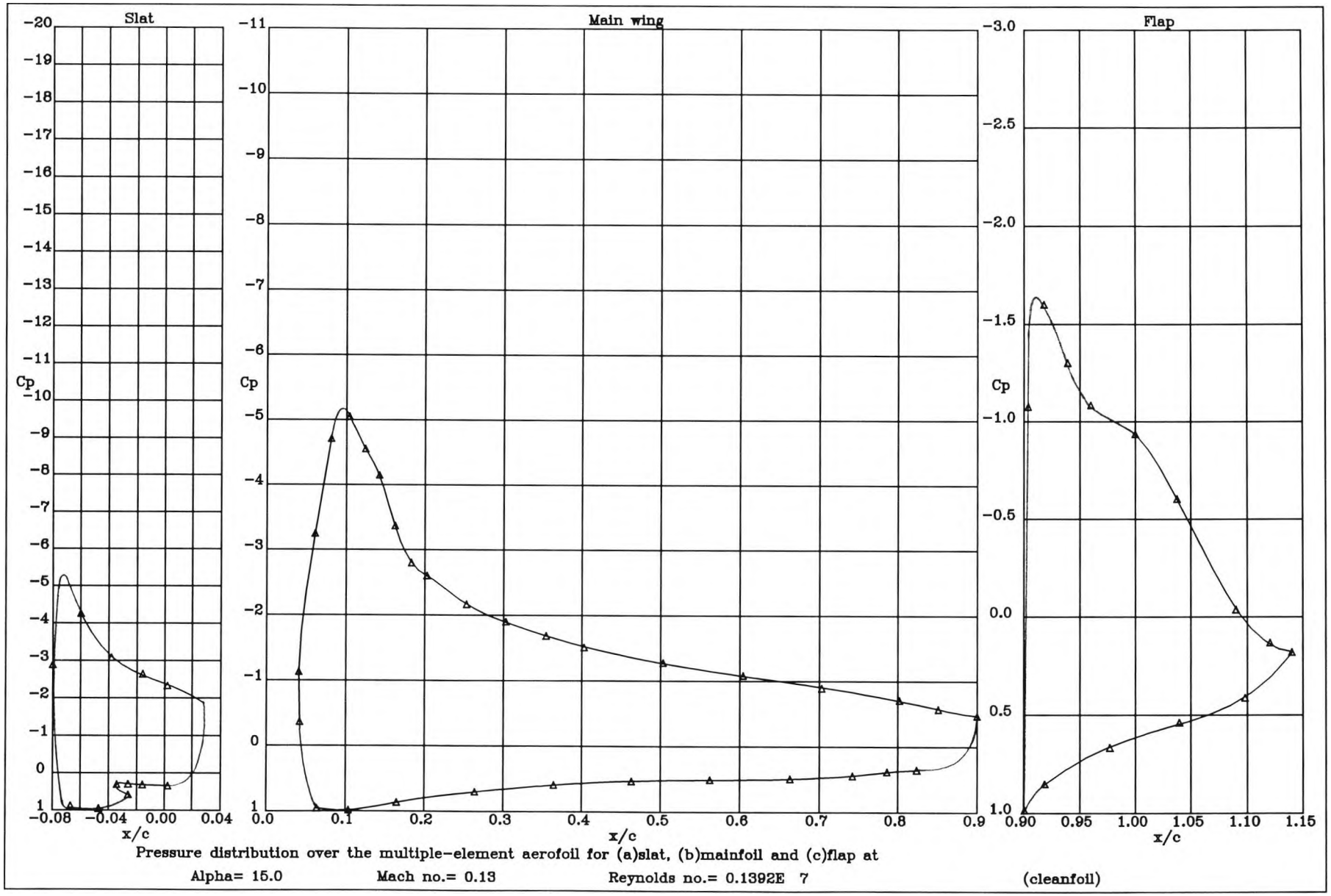

Figure 5.9 : Pressure distribution over the high lift system at 15°

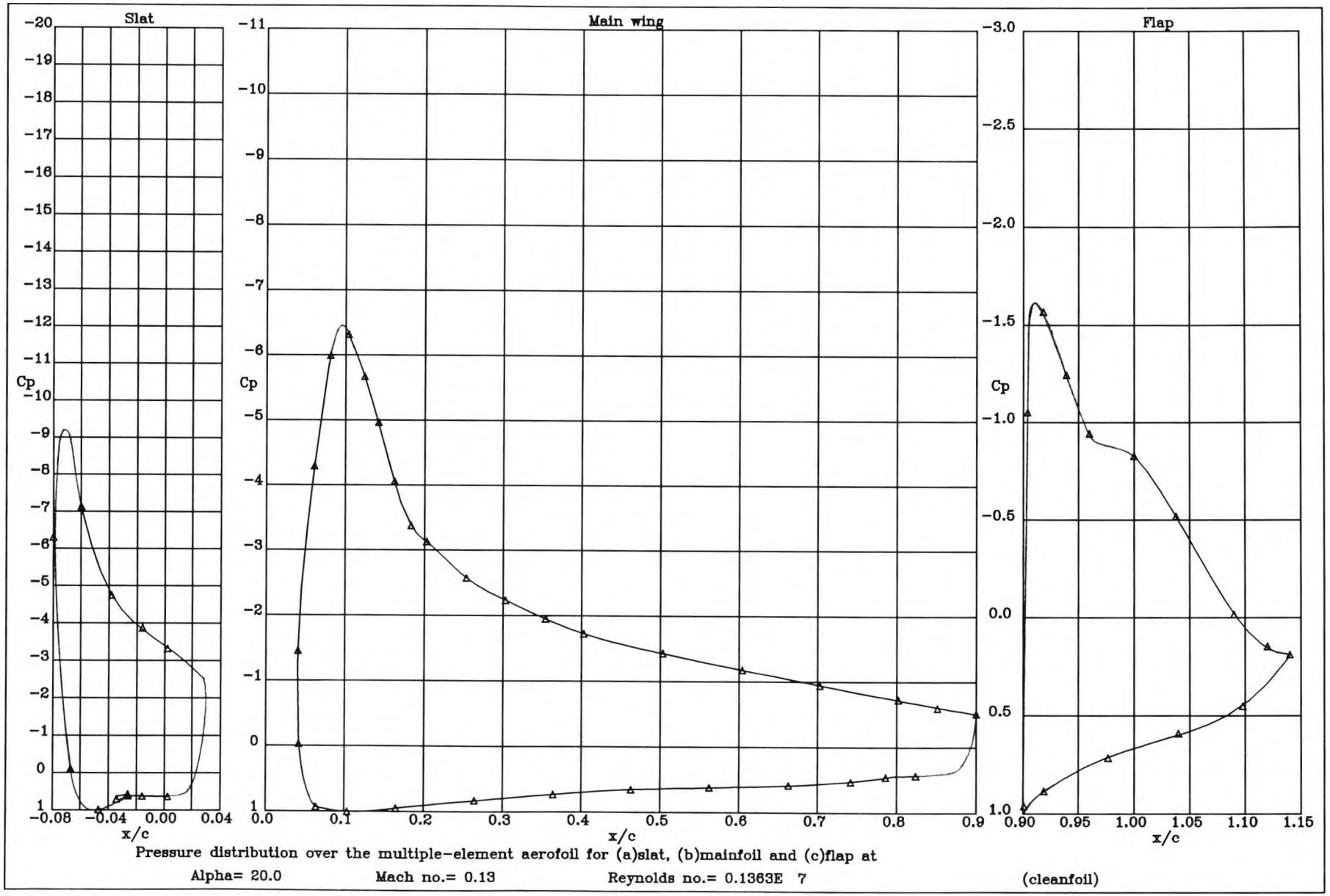

Figure 5.10 : Pressure distribution over the high lift system at 20°

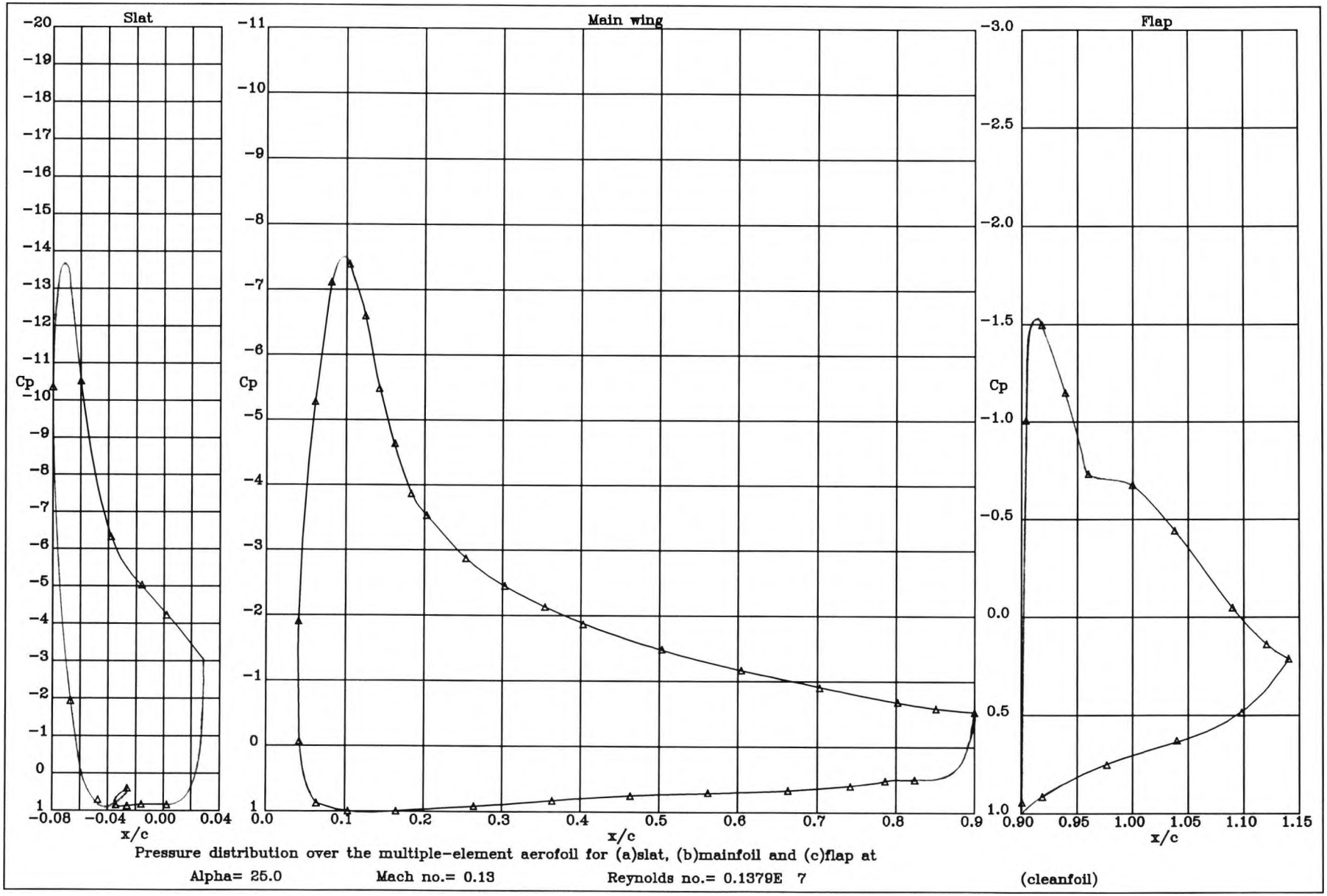

Figure 5.11 : Pressure distribution over the high lift system at 25°

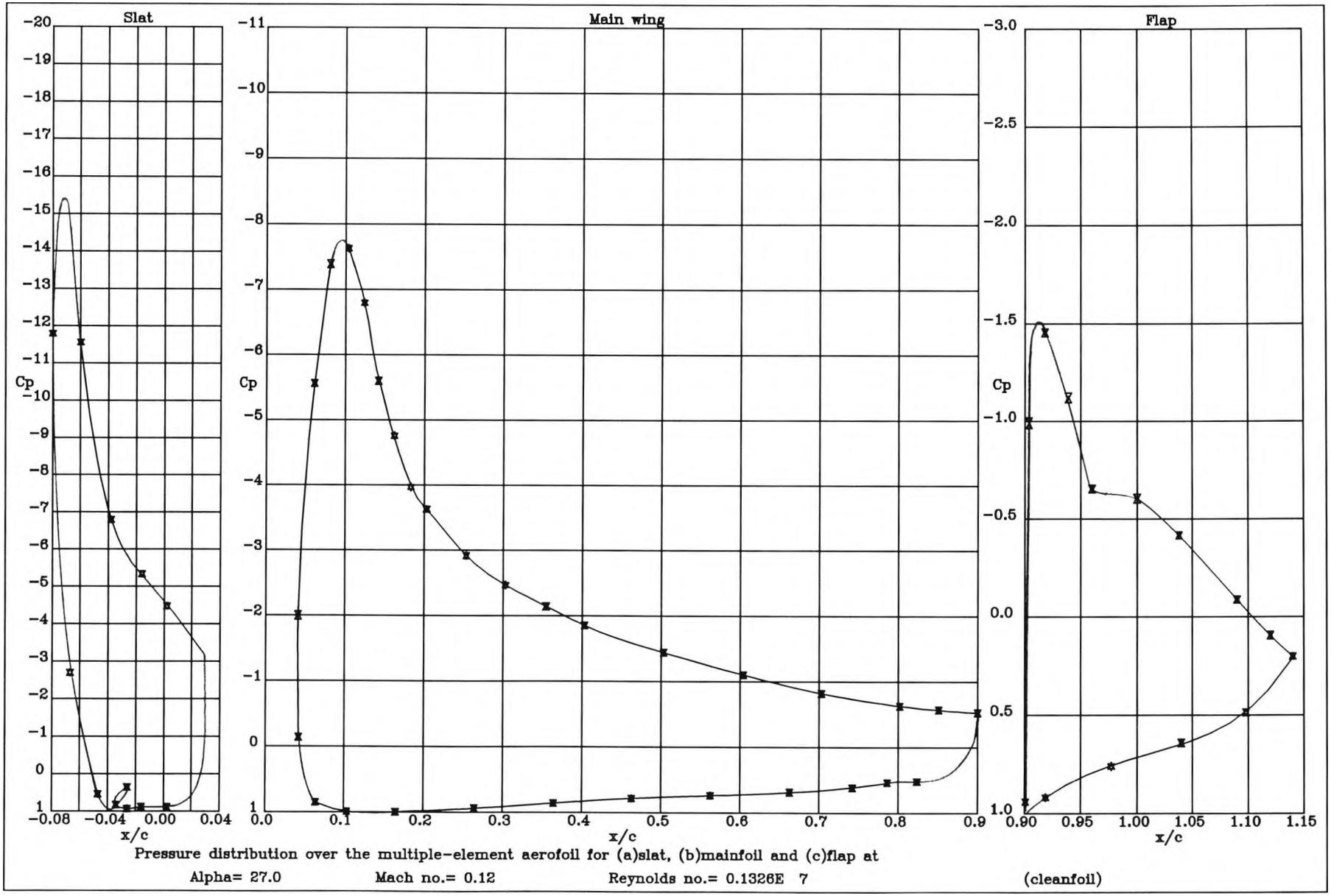

Figure 5.12 : Pressure distribution over the high lift system at 27°

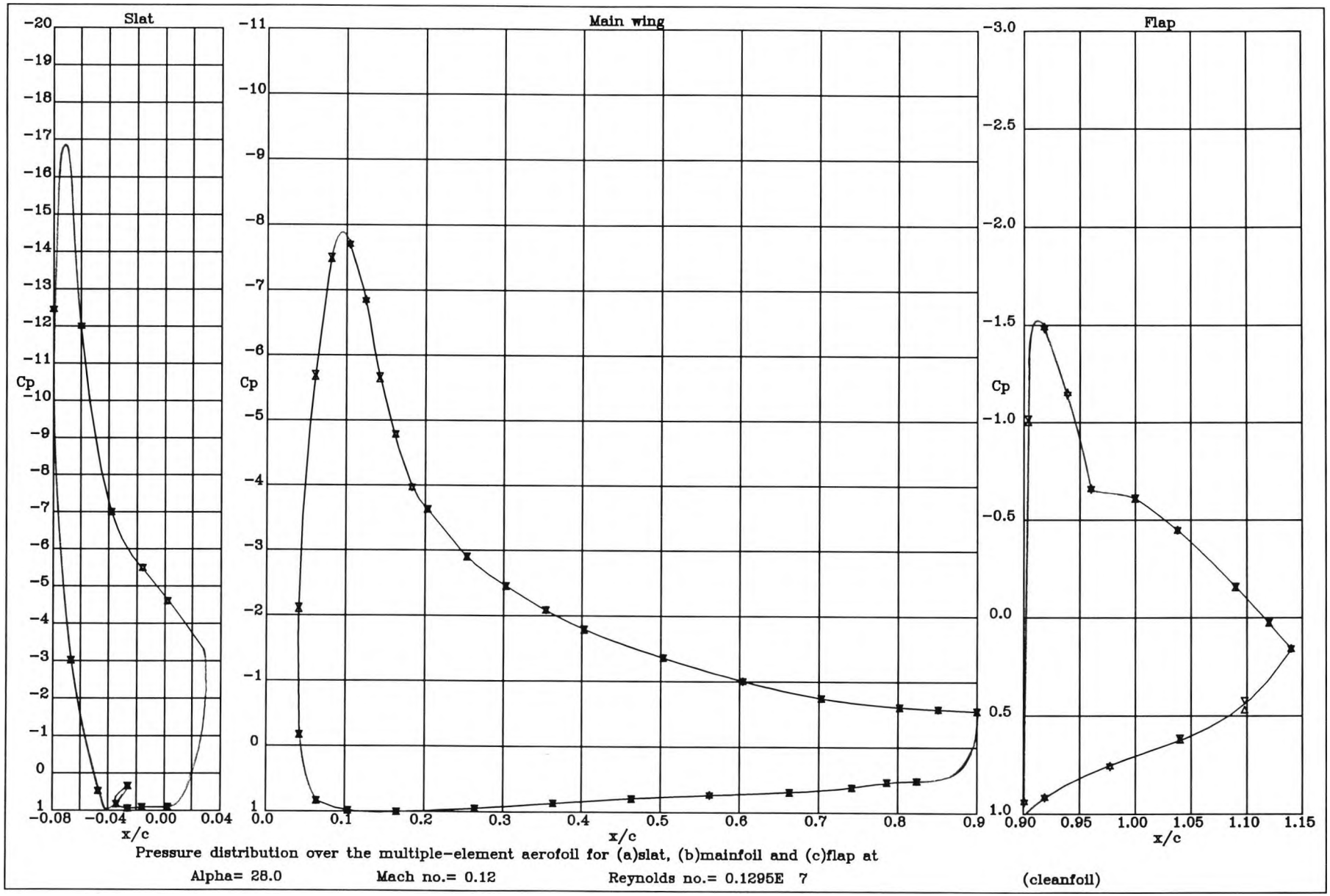

Figure 5.13 : Pressure distribution over the high lift system at 28°

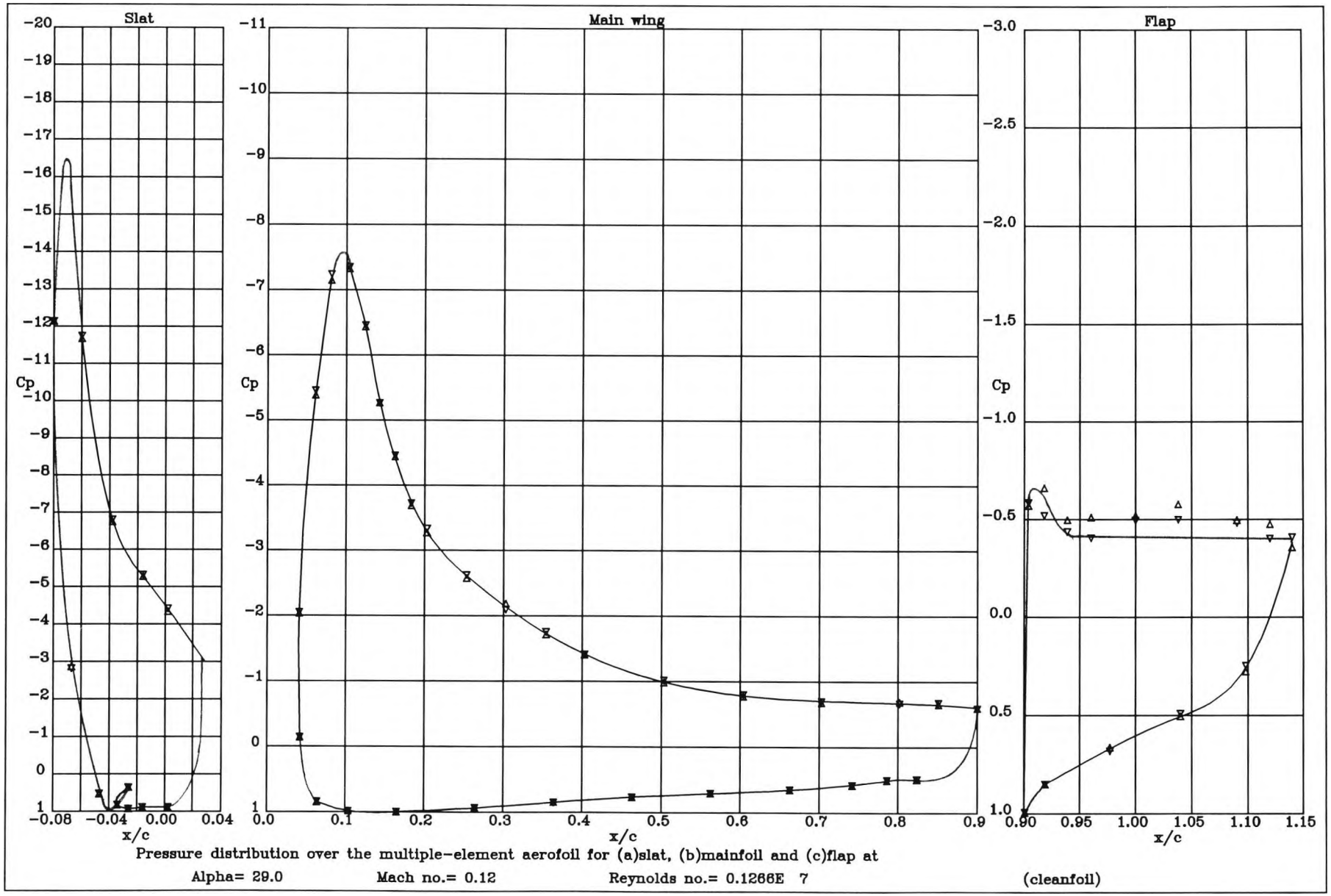

Figure 5.14 : Pressure distribution over the high lift system at 29°

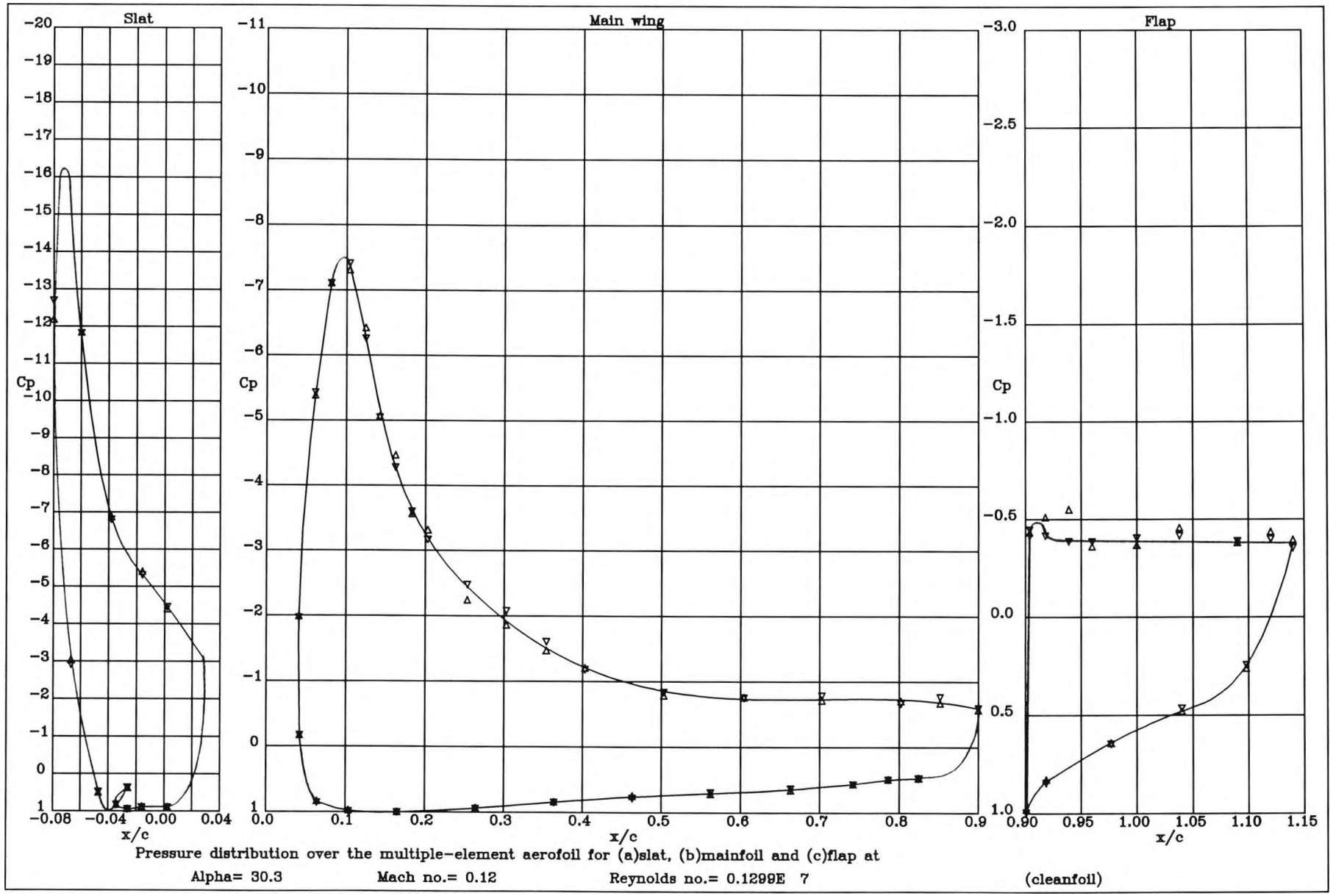

Figure 5.15 : Pressure distribution over the high lift system at 30.3°

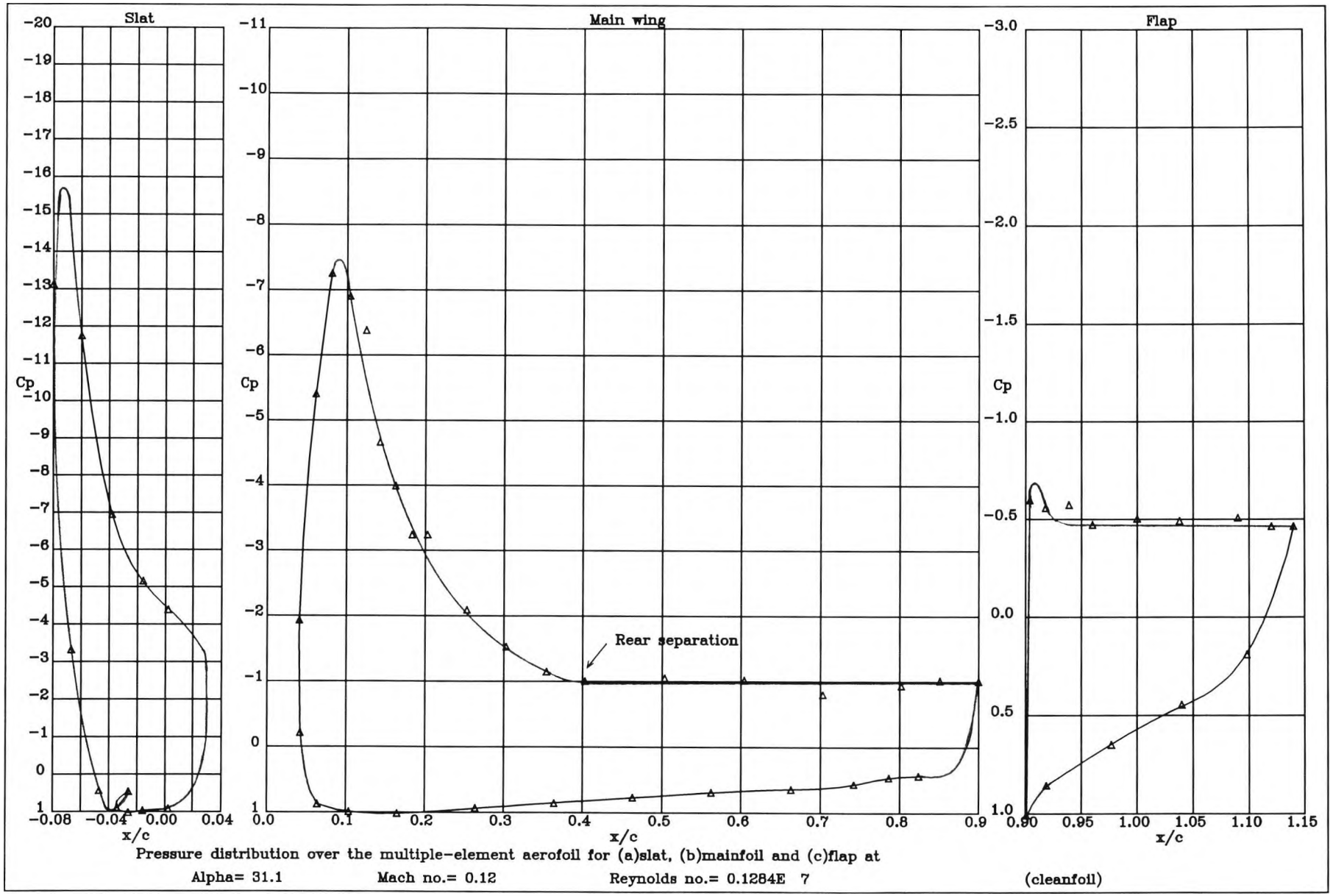

Figure 5.16 : Pressure distribution over the high lift system at 31.1°

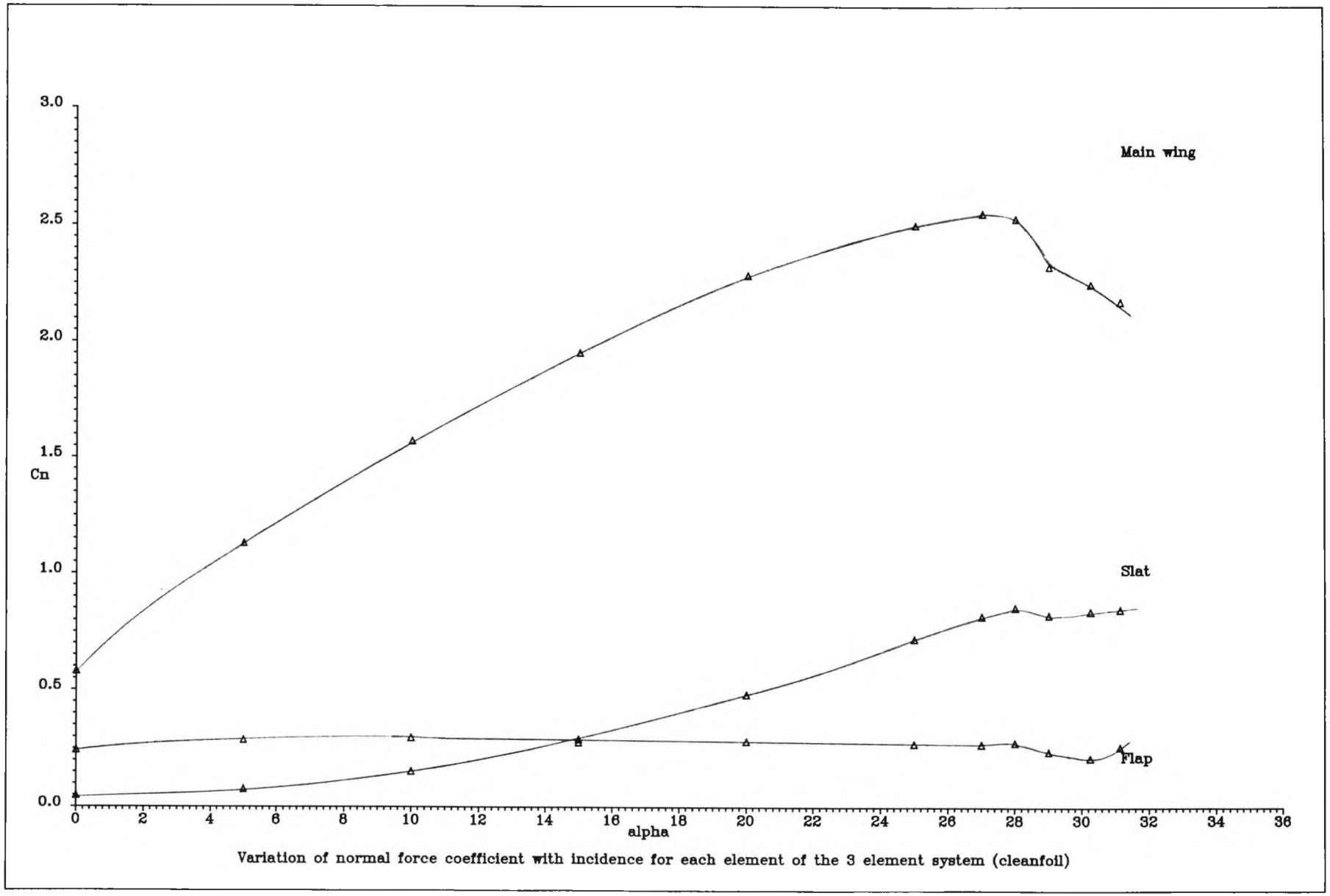

Figure 5.17 : Variation of C_n with α for each element of the cleanfoil

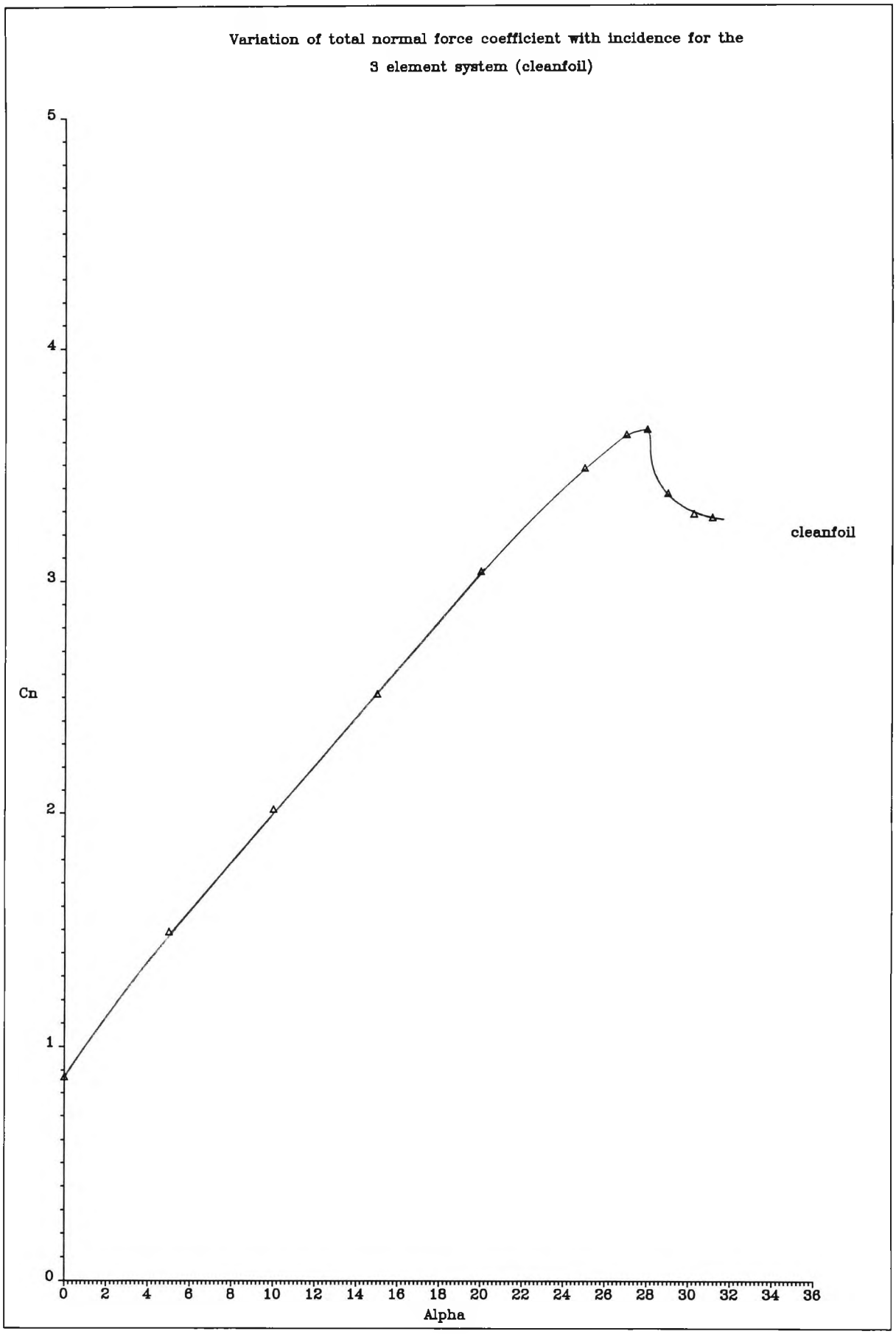

Figure 5.18 : Variation of total C_n with α for the cleanfoil

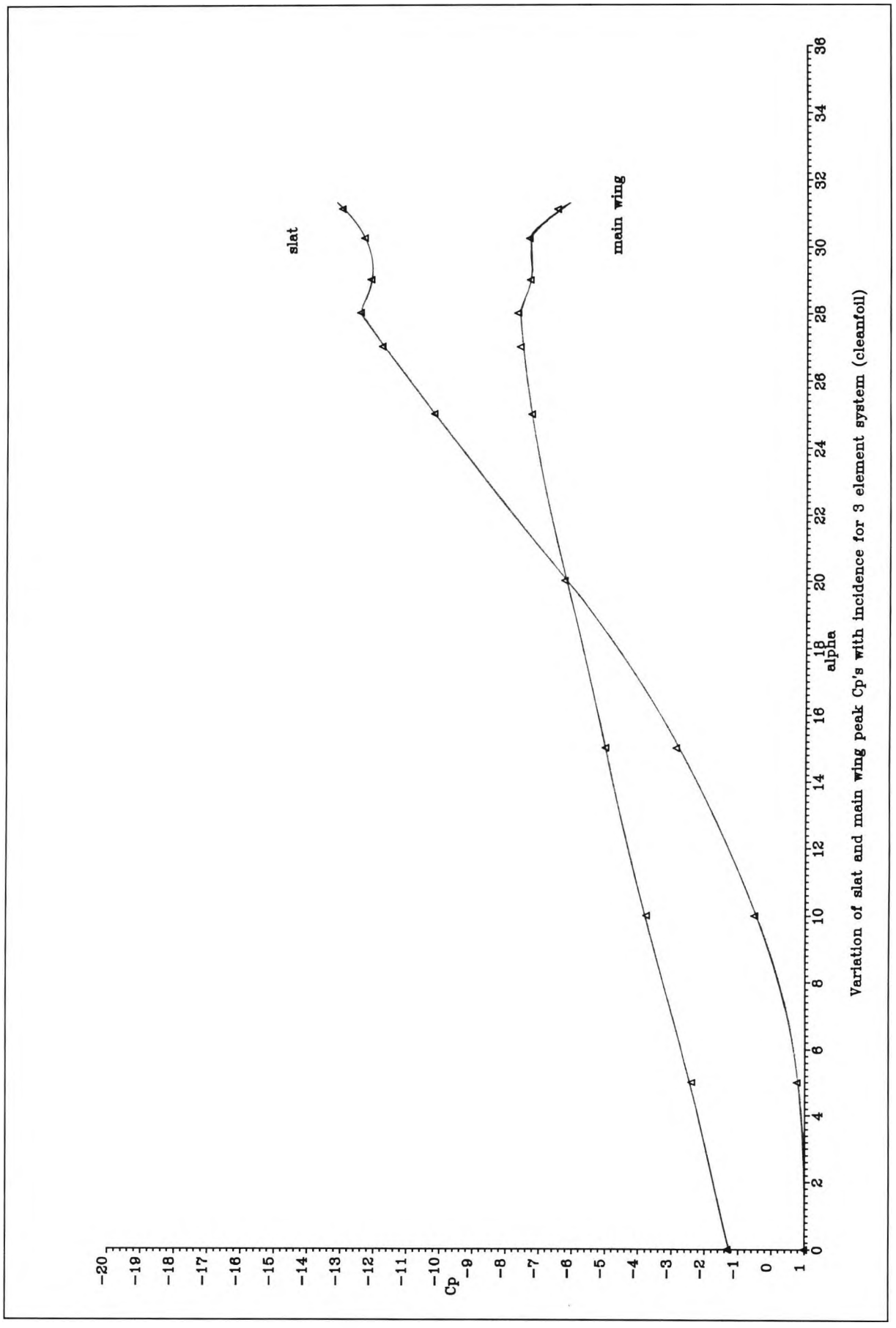

Figure 5.19 : Variation of slat & main wing peak C_p's with α for the cleanfoil

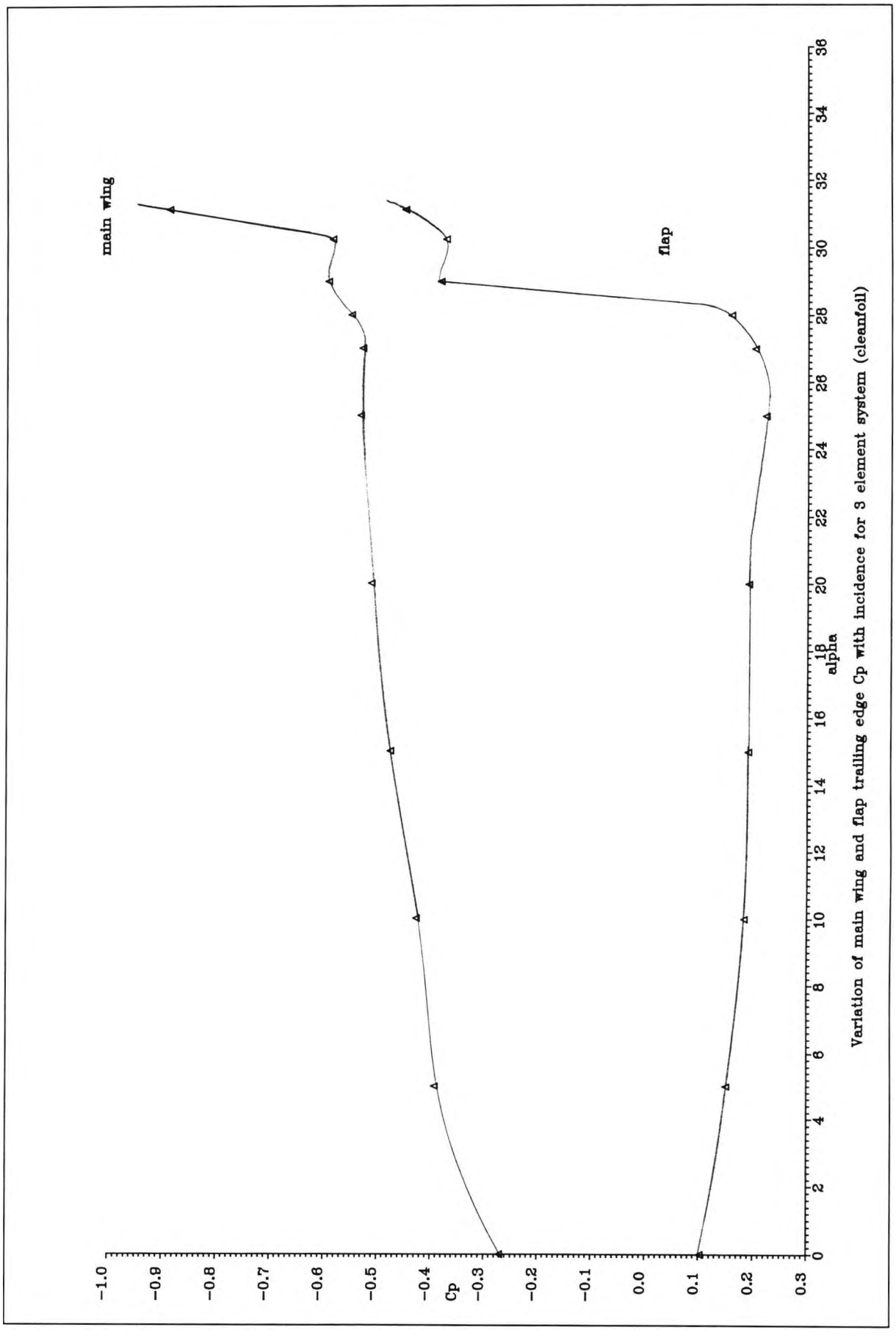

Figure 5.20 : Variation of main wing & flap trailing edge C_p's with α for the cleanfoil

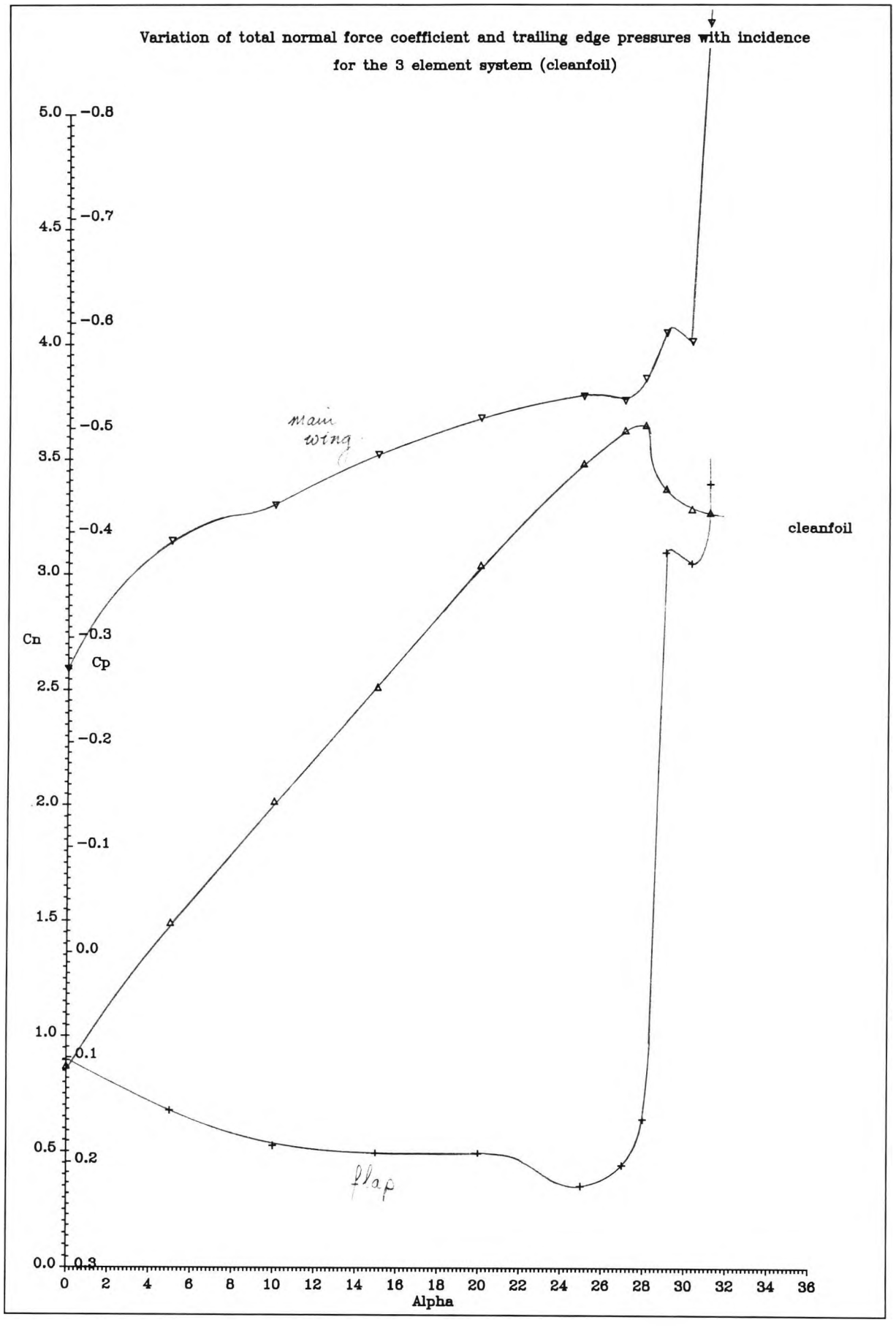

Figure 5.21 : Relationship between total C_n coefficient and main wing & flap trailing edge C_p's

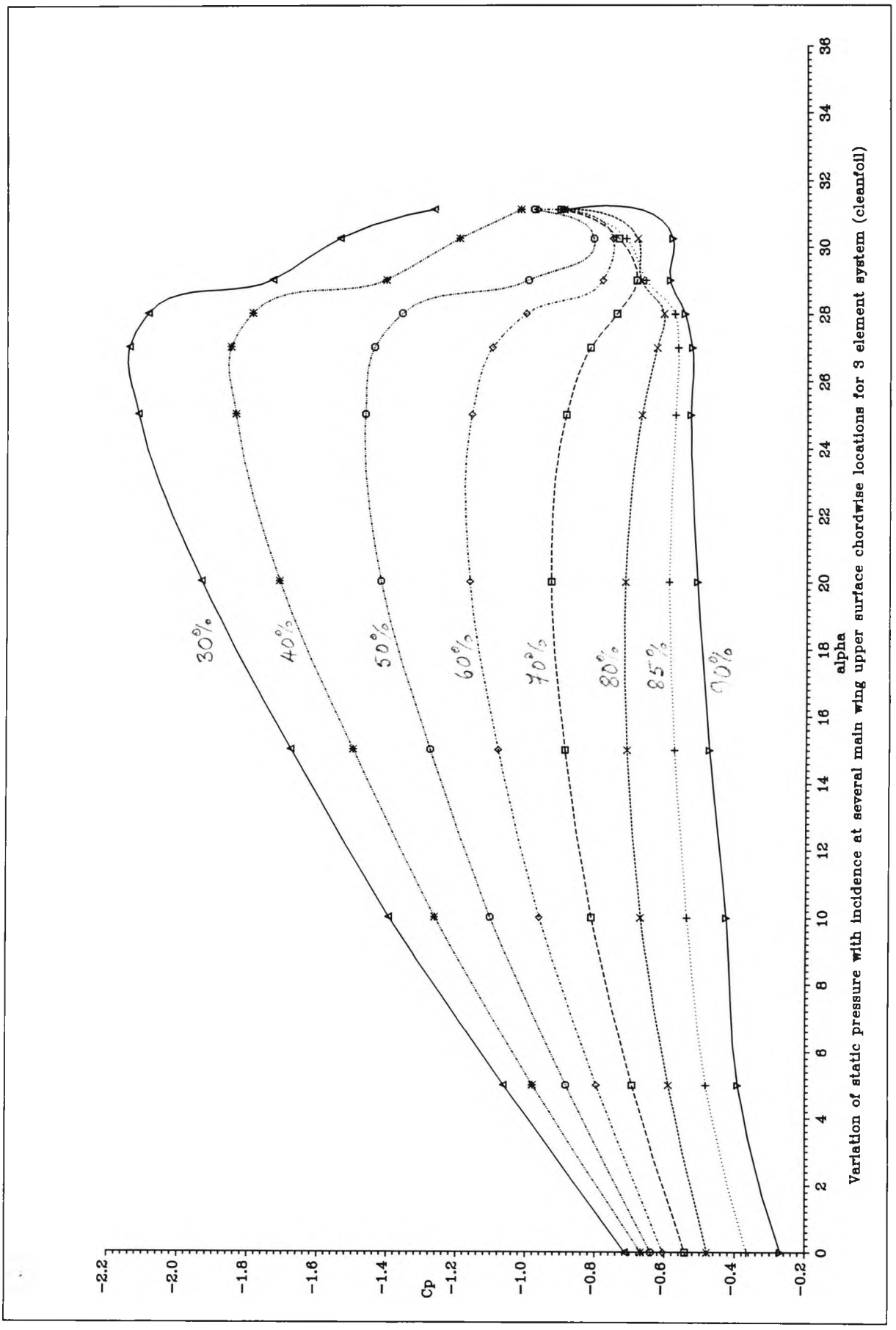

Figure 5.22 : Variation of static C_p with incidence at several x/c positions on the main wing upper surface

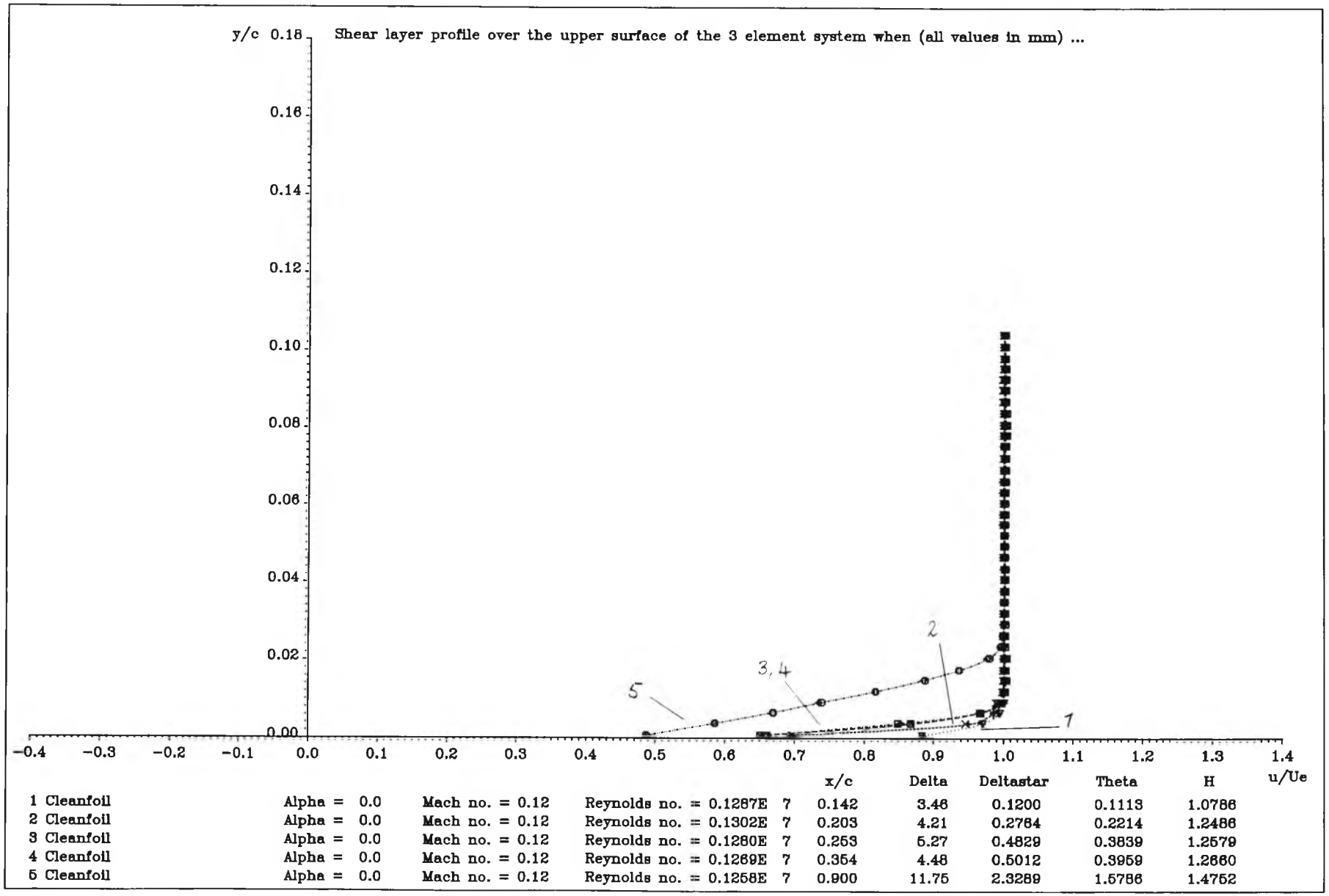

Figure 5.23 : Shear layer development over the main wing of the high lift system at 0°

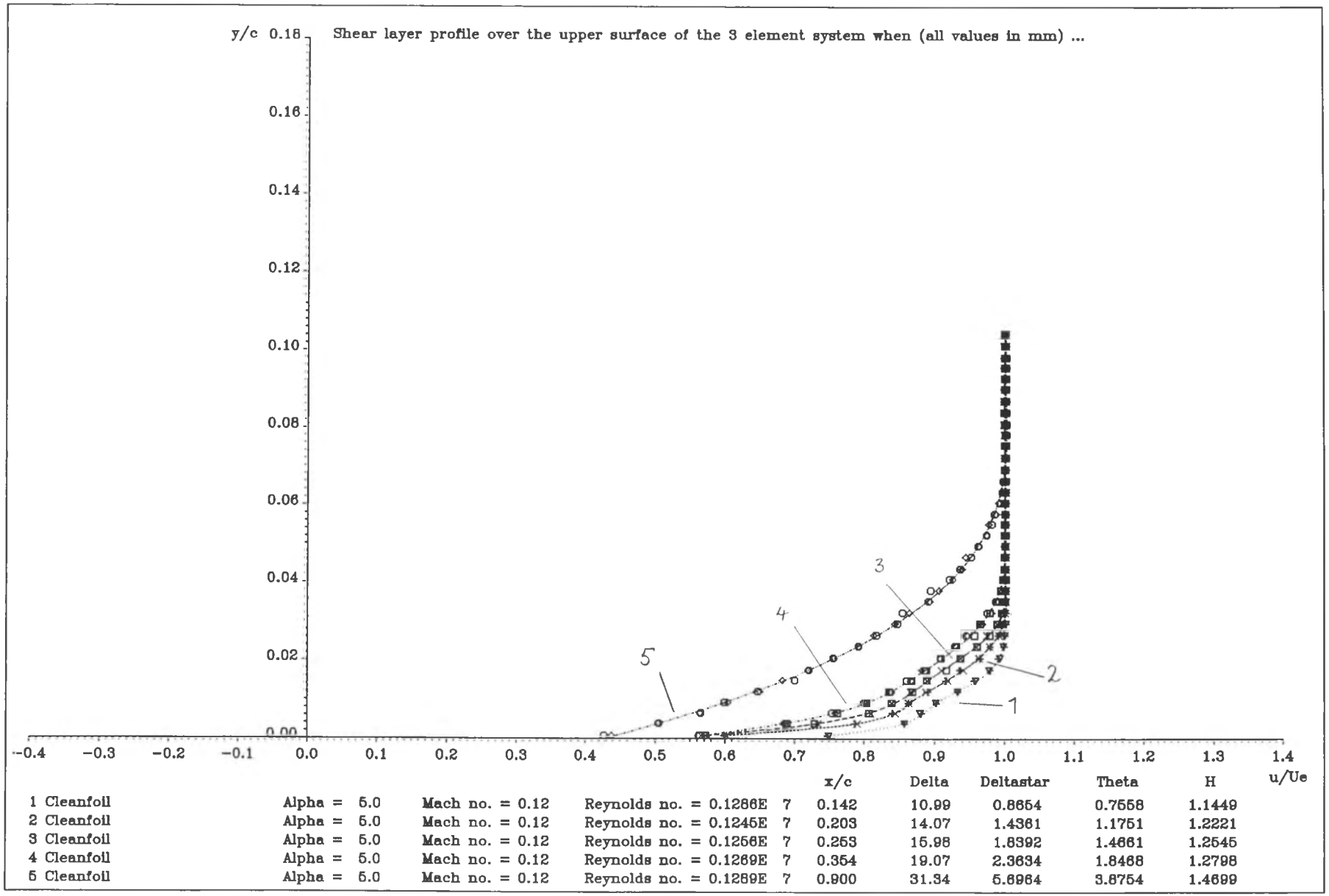

				x/c	Delta	Deltastar	Theta	H
1 Cleanfoil	Alpha = 5.0	Mach no. = 0.12	Reynolds no. = 0.1286E 7	0.142	10.99	0.8654	0.7558	1.1449
2 Cleanfoil	Alpha = 5.0	Mach no. = 0.12	Reynolds no. = 0.1245E 7	0.203	14.07	1.4361	1.1751	1.2221
3 Cleanfoil	Alpha = 5.0	Mach no. = 0.12	Reynolds no. = 0.1256E 7	0.253	16.98	1.8392	1.4661	1.2545
4 Cleanfoil	Alpha = 5.0	Mach no. = 0.12	Reynolds no. = 0.1269E 7	0.354	19.07	2.3634	1.8468	1.2798
5 Cleanfoil	Alpha = 5.0	Mach no. = 0.12	Reynolds no. = 0.1289E 7	0.900	31.34	5.6964	3.8754	1.4699

Figure 5.24 : Shear layer development over the main wing of the high lift system at 5°

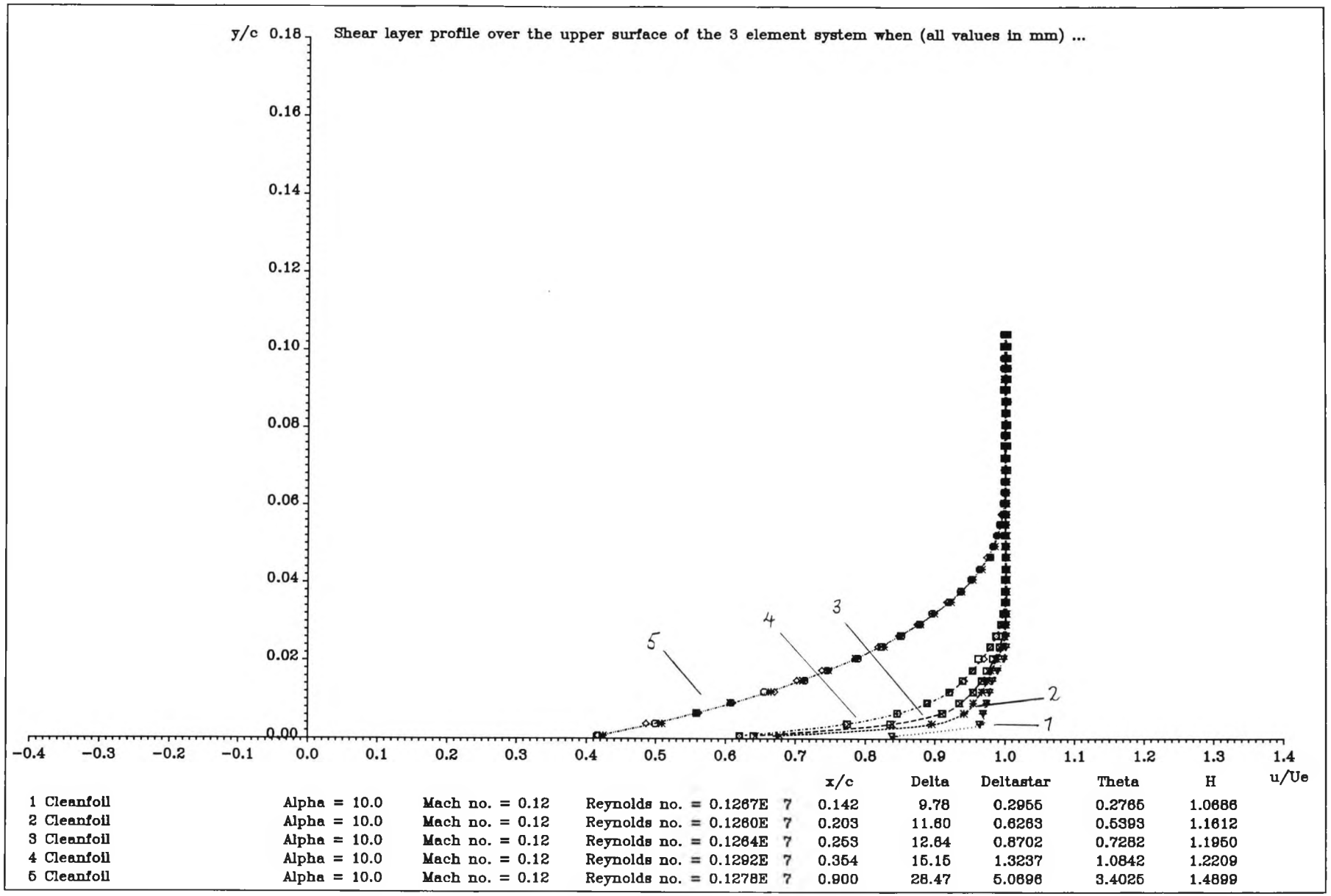

Figure 5.25 : Shear layer development over the main wing of the high lift system at 10°

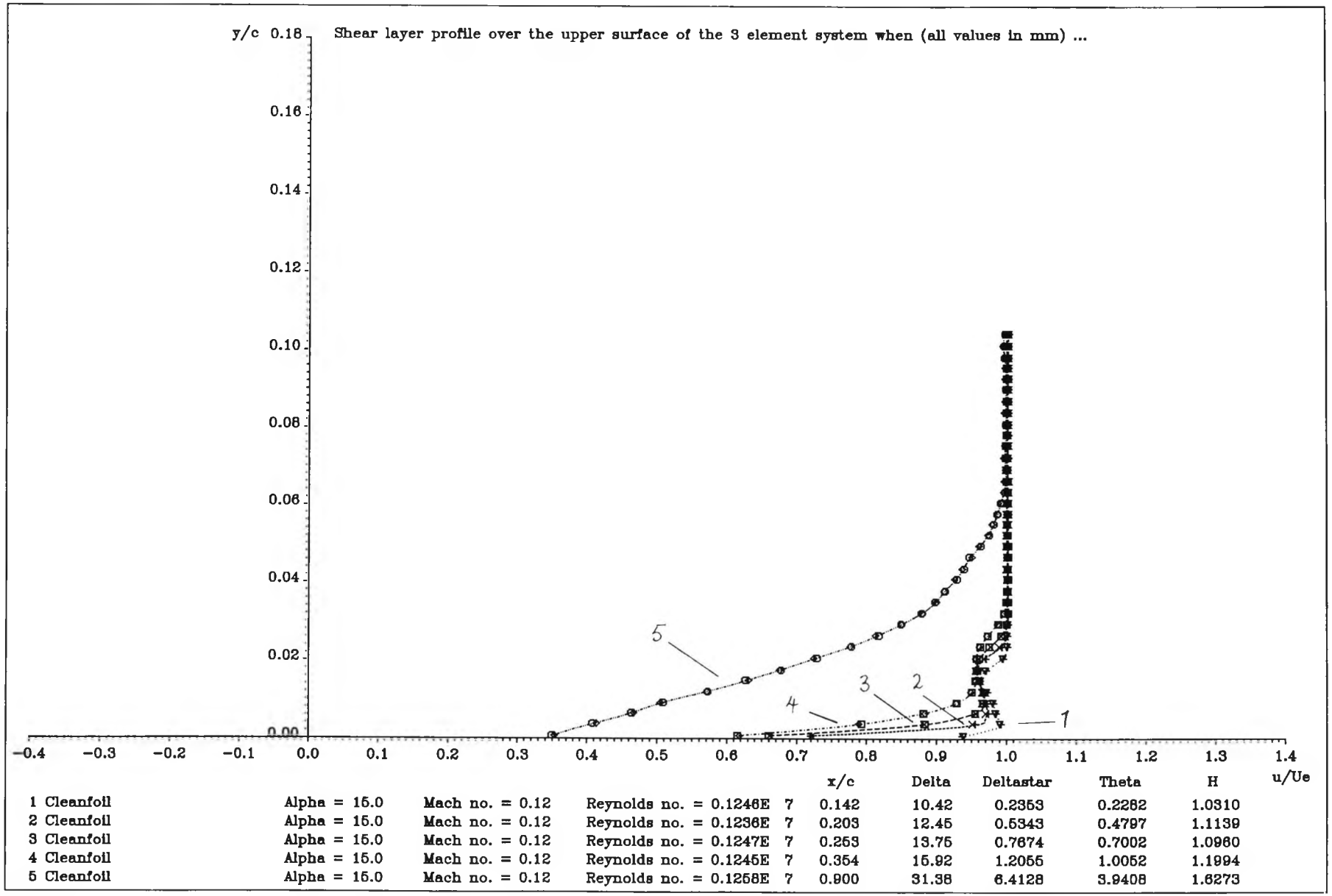

Figure 5.26 : Shear layer development over the main wing of the high lift system at 15°

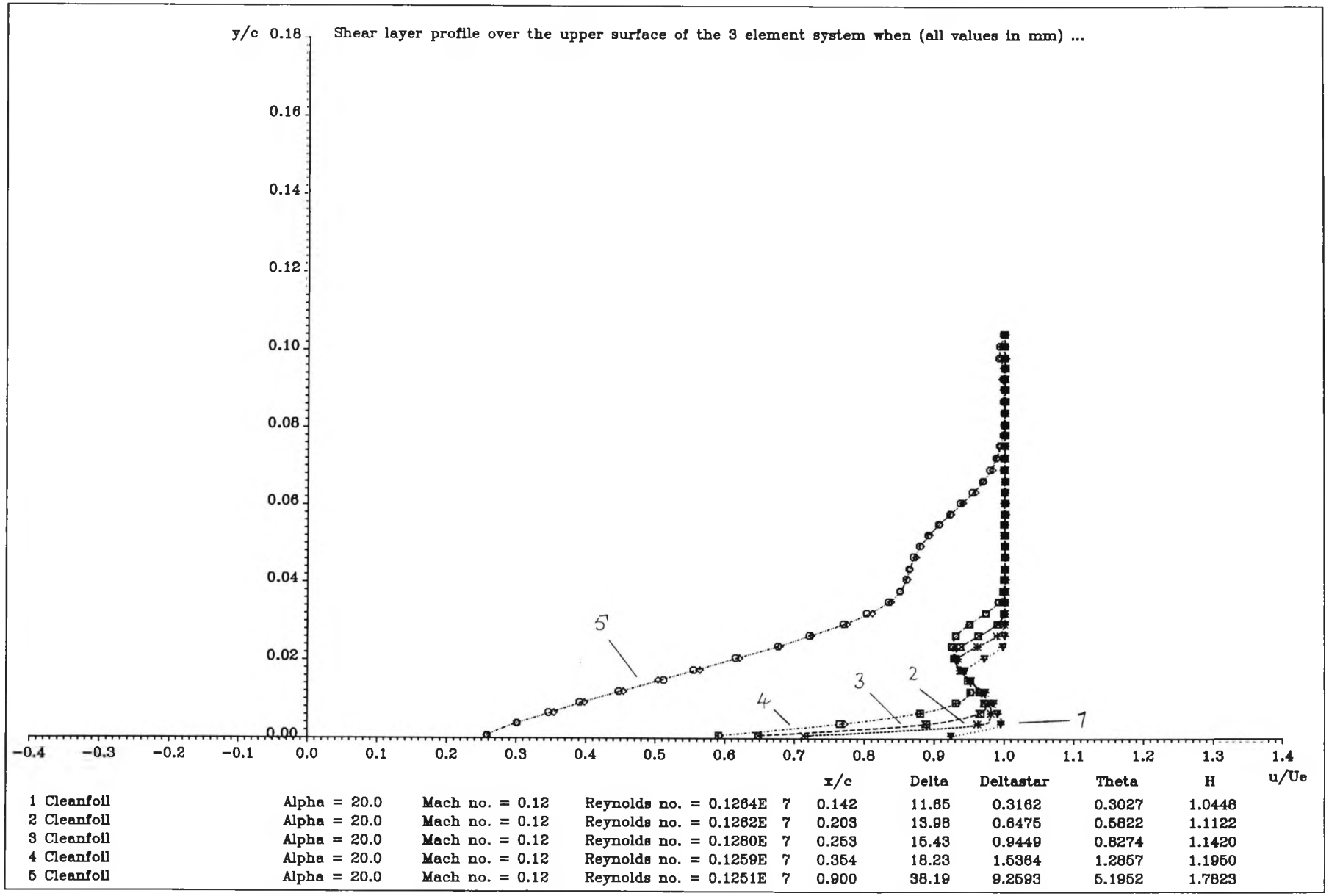

Figure 5.27 : Shear layer development over the main wing of the high lift system at 20°

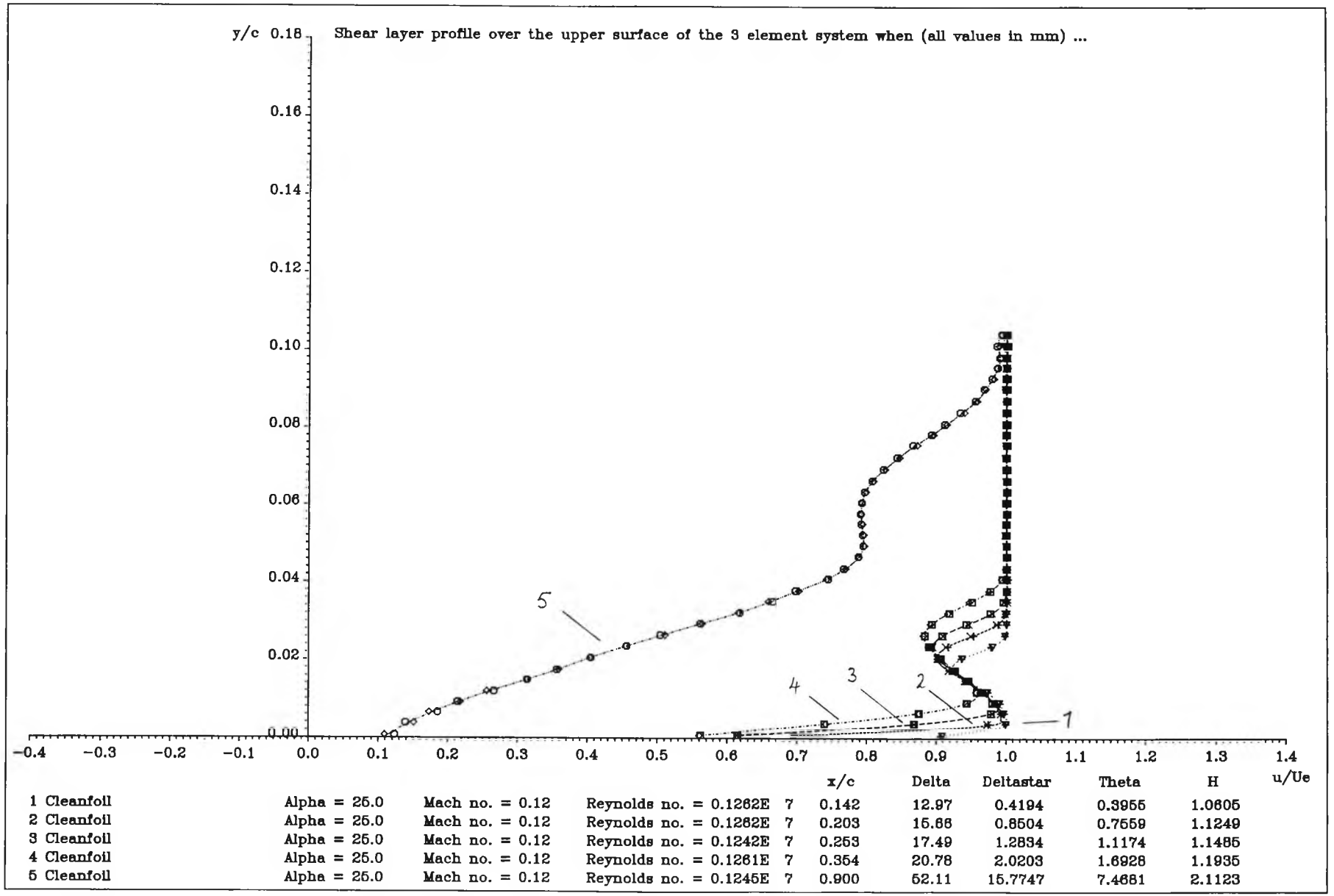

				x/c	Delta	Deltastar	Theta	H
1 Cleanfoil	Alpha = 25.0	Mach no. = 0.12	Reynolds no. = 0.1262E 7	0.142	12.97	0.4194	0.3955	1.0605
2 Cleanfoil	Alpha = 25.0	Mach no. = 0.12	Reynolds no. = 0.1262E 7	0.203	15.66	0.8504	0.7559	1.1249
3 Cleanfoil	Alpha = 25.0	Mach no. = 0.12	Reynolds no. = 0.1242E 7	0.253	17.49	1.2834	1.1174	1.1485
4 Cleanfoil	Alpha = 25.0	Mach no. = 0.12	Reynolds no. = 0.1261E 7	0.354	20.78	2.0203	1.6928	1.1935
5 Cleanfoil	Alpha = 25.0	Mach no. = 0.12	Reynolds no. = 0.1245E 7	0.900	52.11	15.7747	7.4681	2.1123

Figure 5.28 : Shear layer development over the main wing of the high lift system at 25°

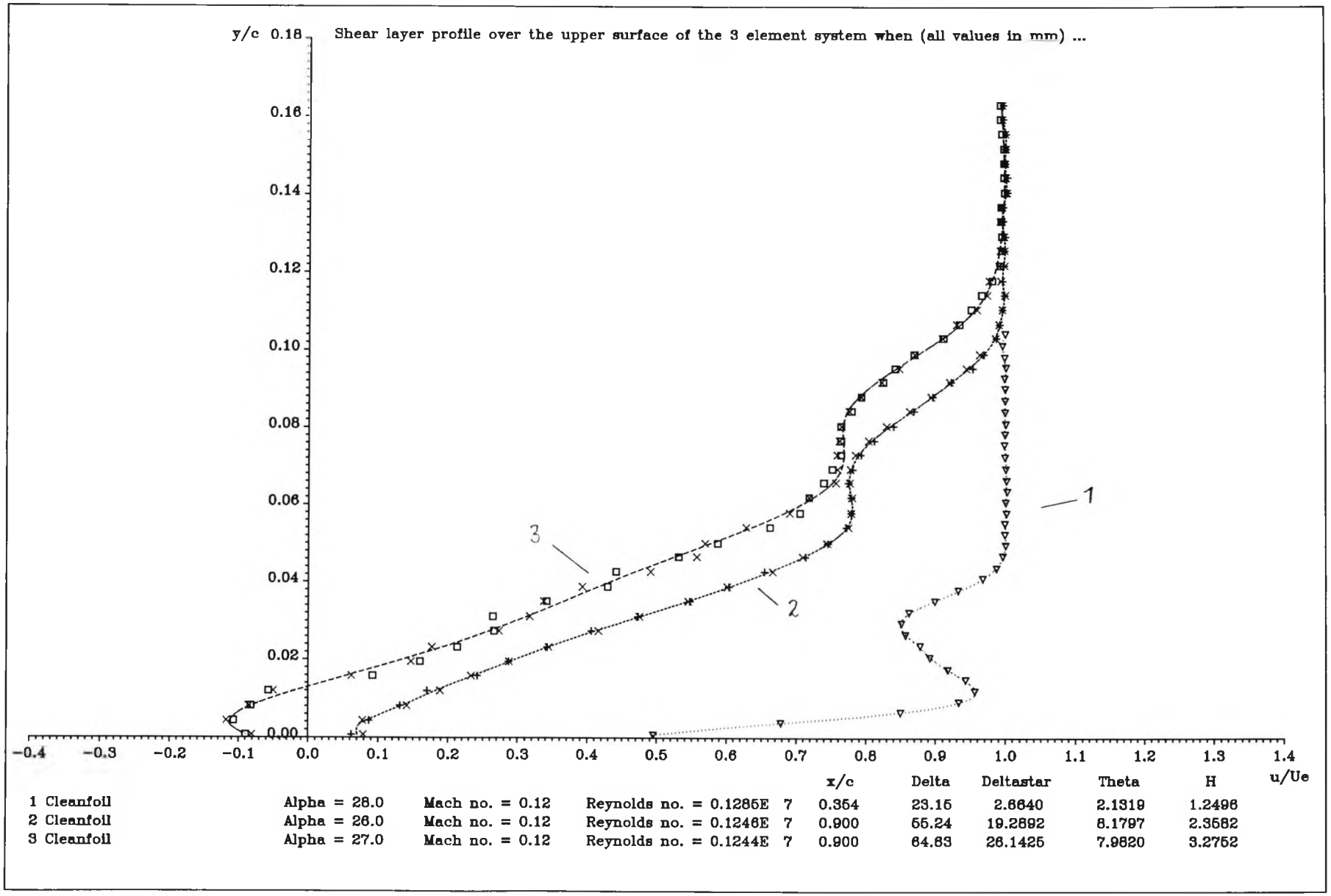

Figure 5.29 : Shear layer development over the main wing of the high lift system at 26° & 27° (x/c = 0.9) & 28° (x/c = 0.354)

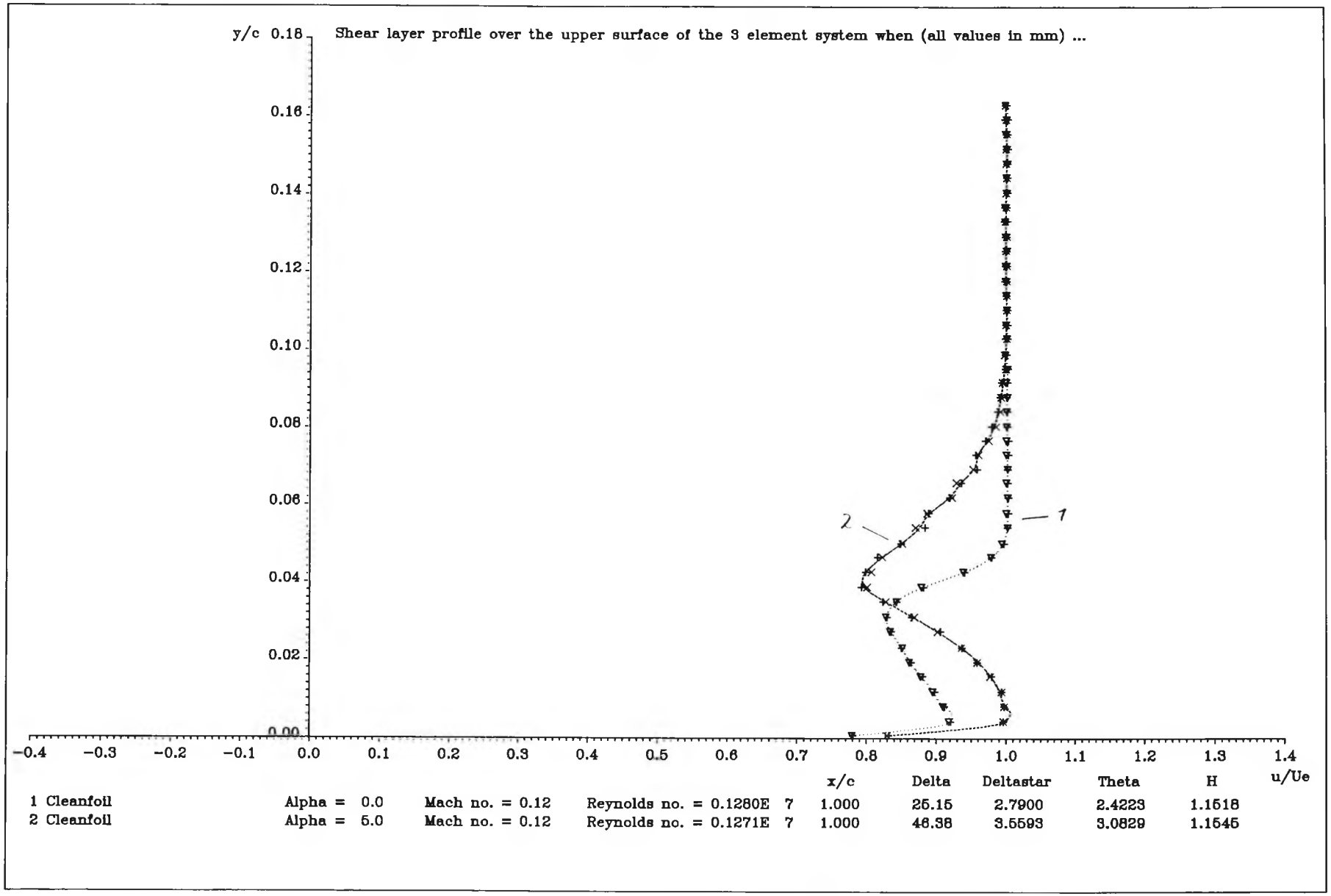

Figure 5.30 : Shear layer profiles over flap of the high lift system at 0° & 5°

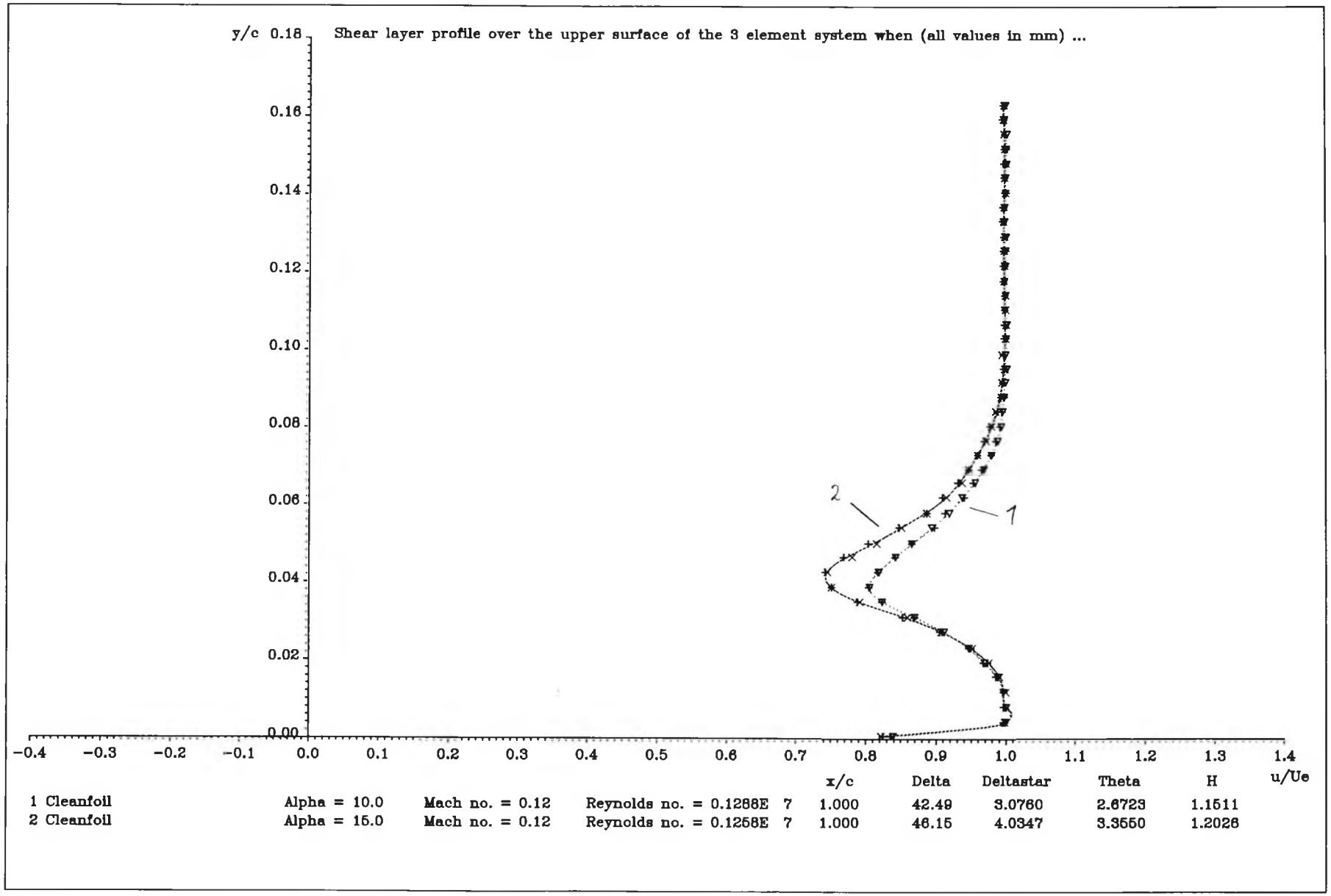

Figure 5.31 : Shear layer profiles over flap of the high lift system at 10° & 15°

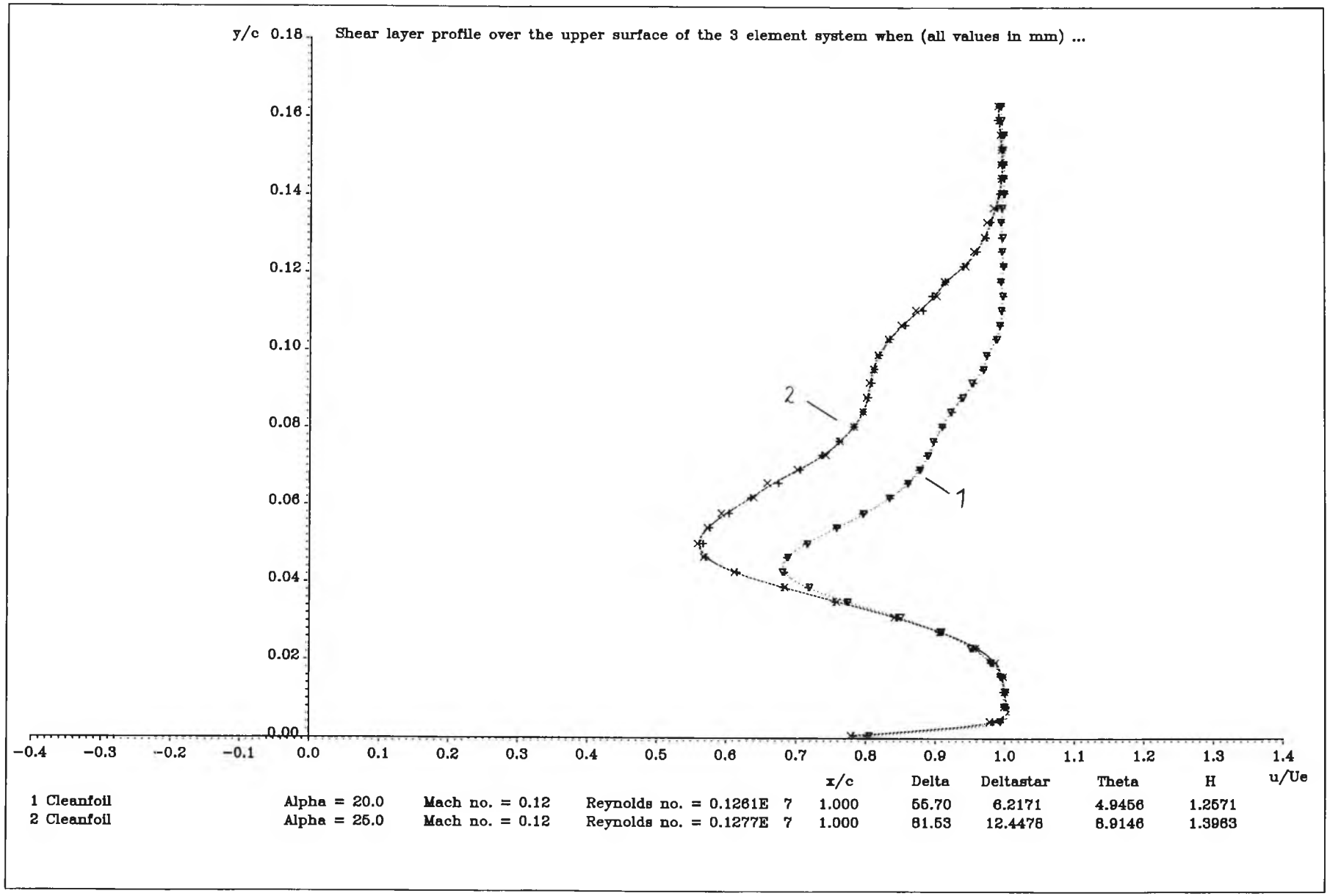

Figure 5.32 : Shear layer profiles over flap of the high lift system at 20° & 25°

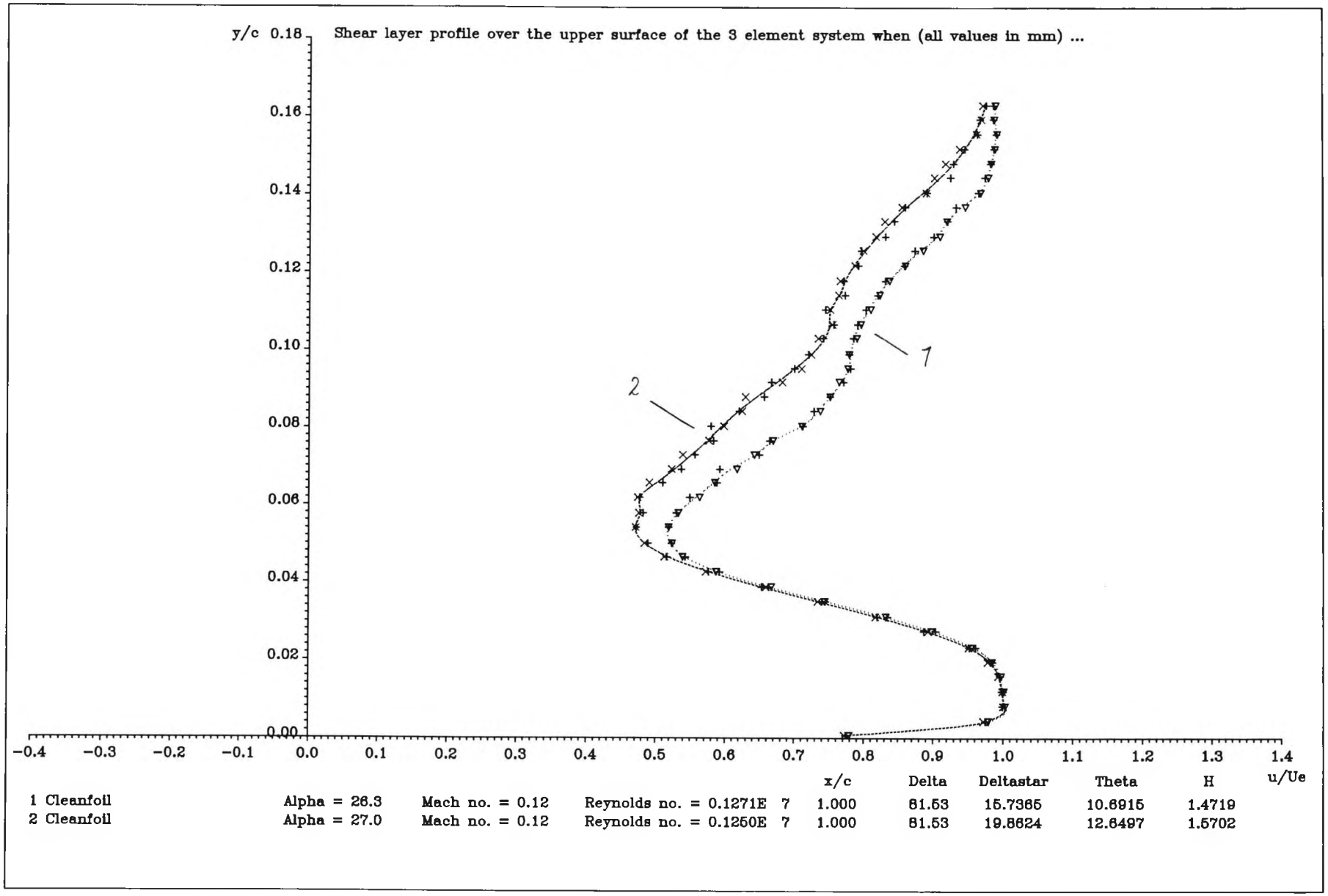

Figure 5.33 : Shear layer profiles over flap of the high lift system at 26° & 27°

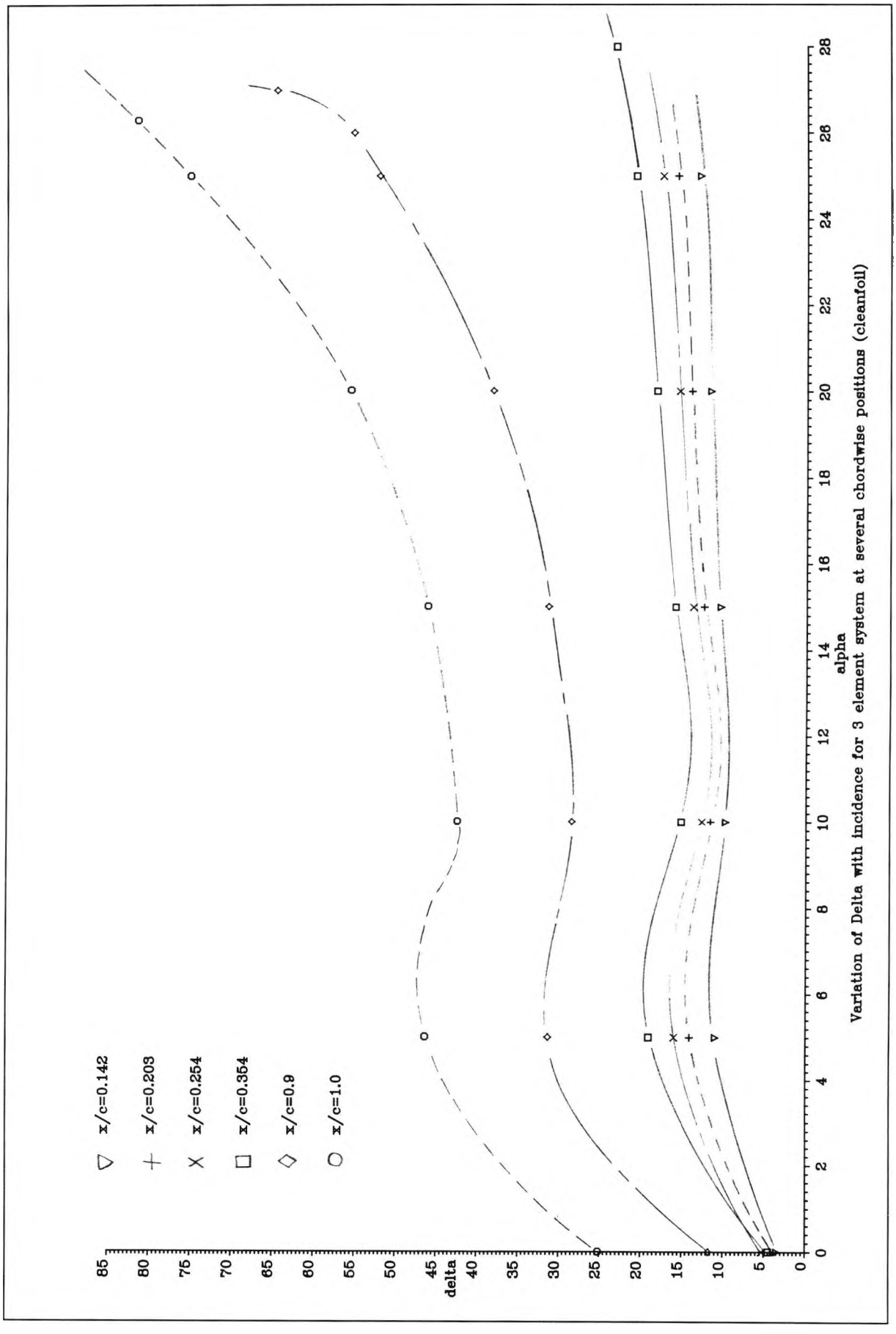

Figure 5.34 : Variation of δ (in mm) with α at several x/c positions on the cleanfoil

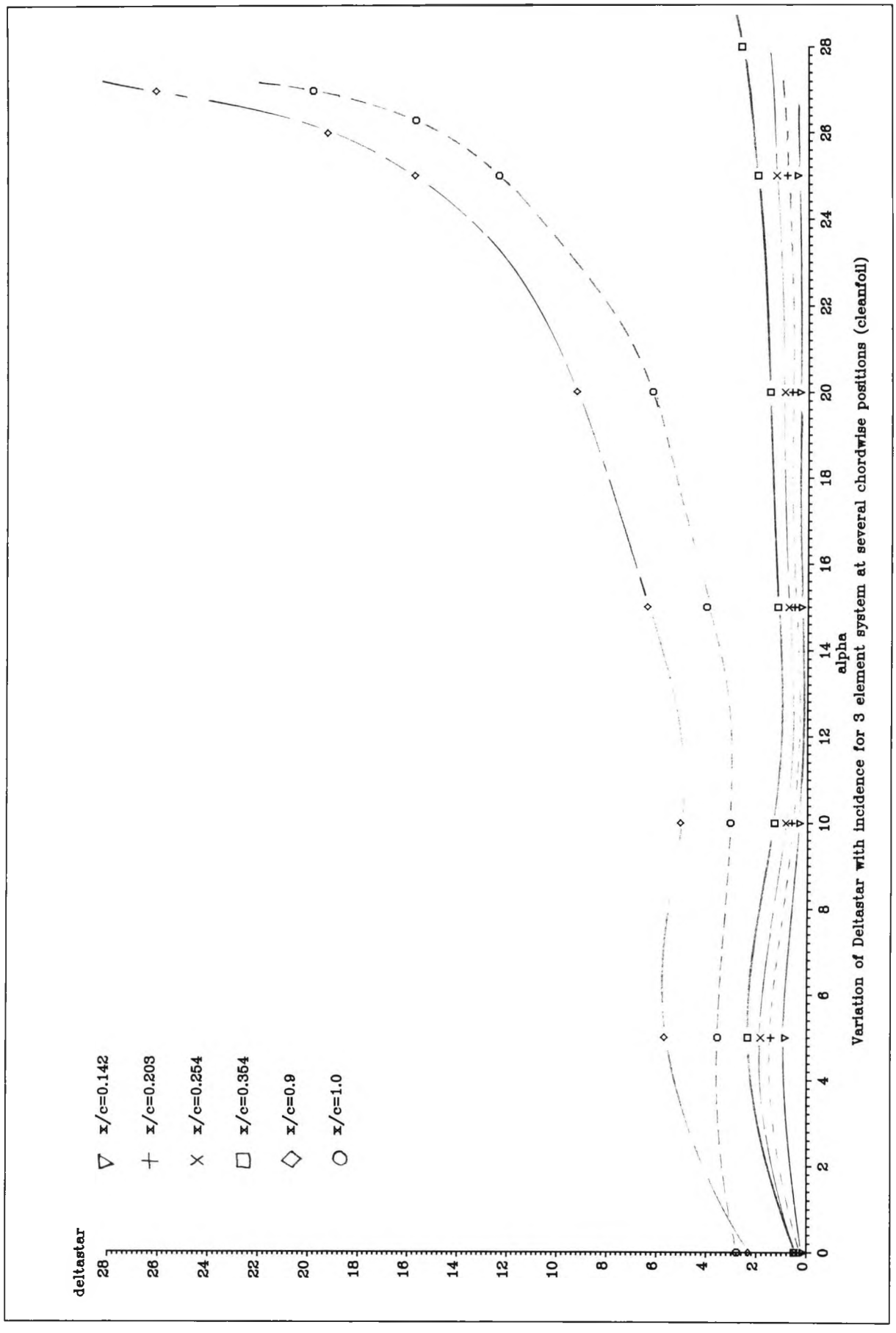

Figure 5.35 : Variation of δ^* (in mm) with α at several x/c positions on the cleanfoil

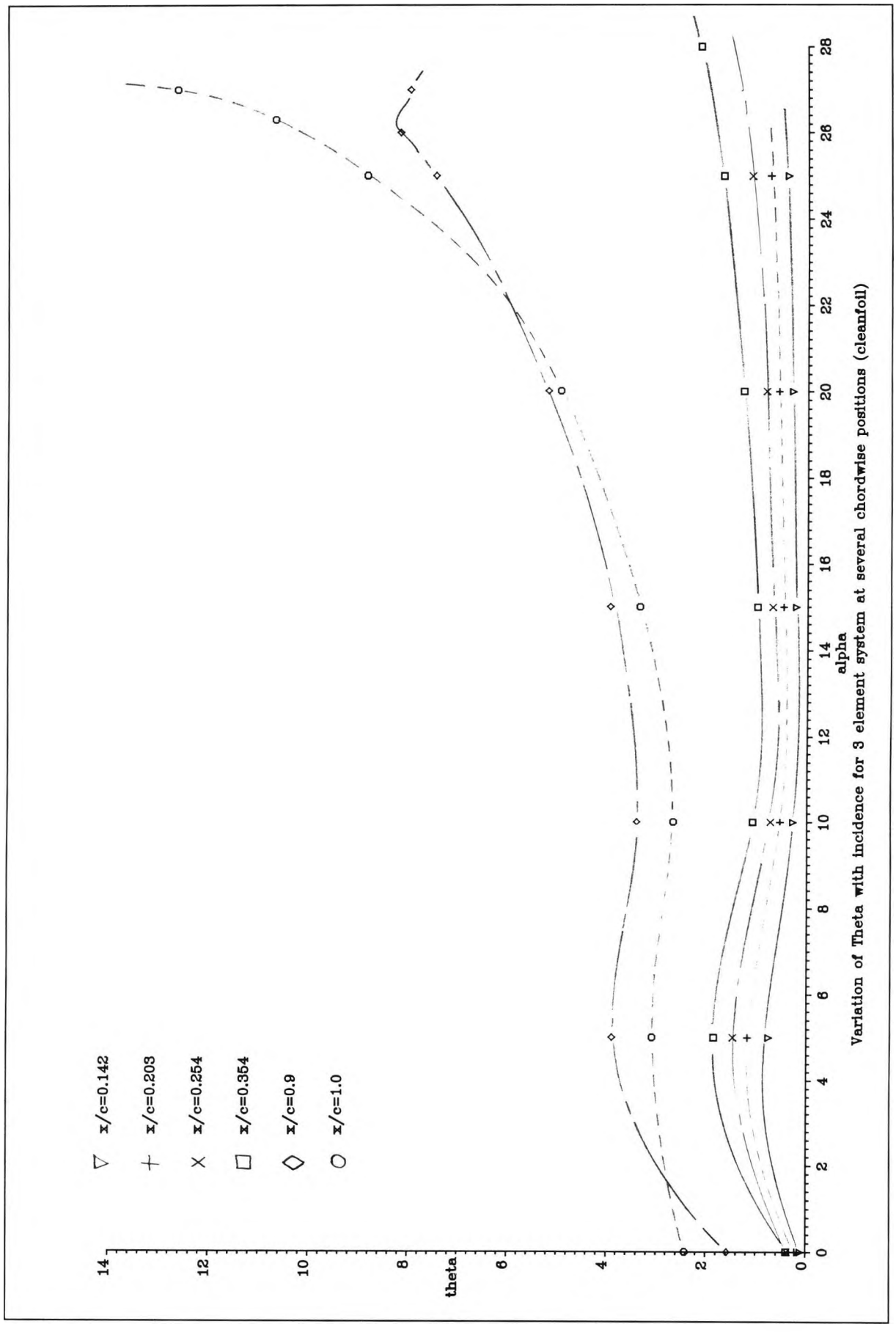

Figure 5.36 : Variation of θ (in mm) with α for several x/c positions on the cleanfoil

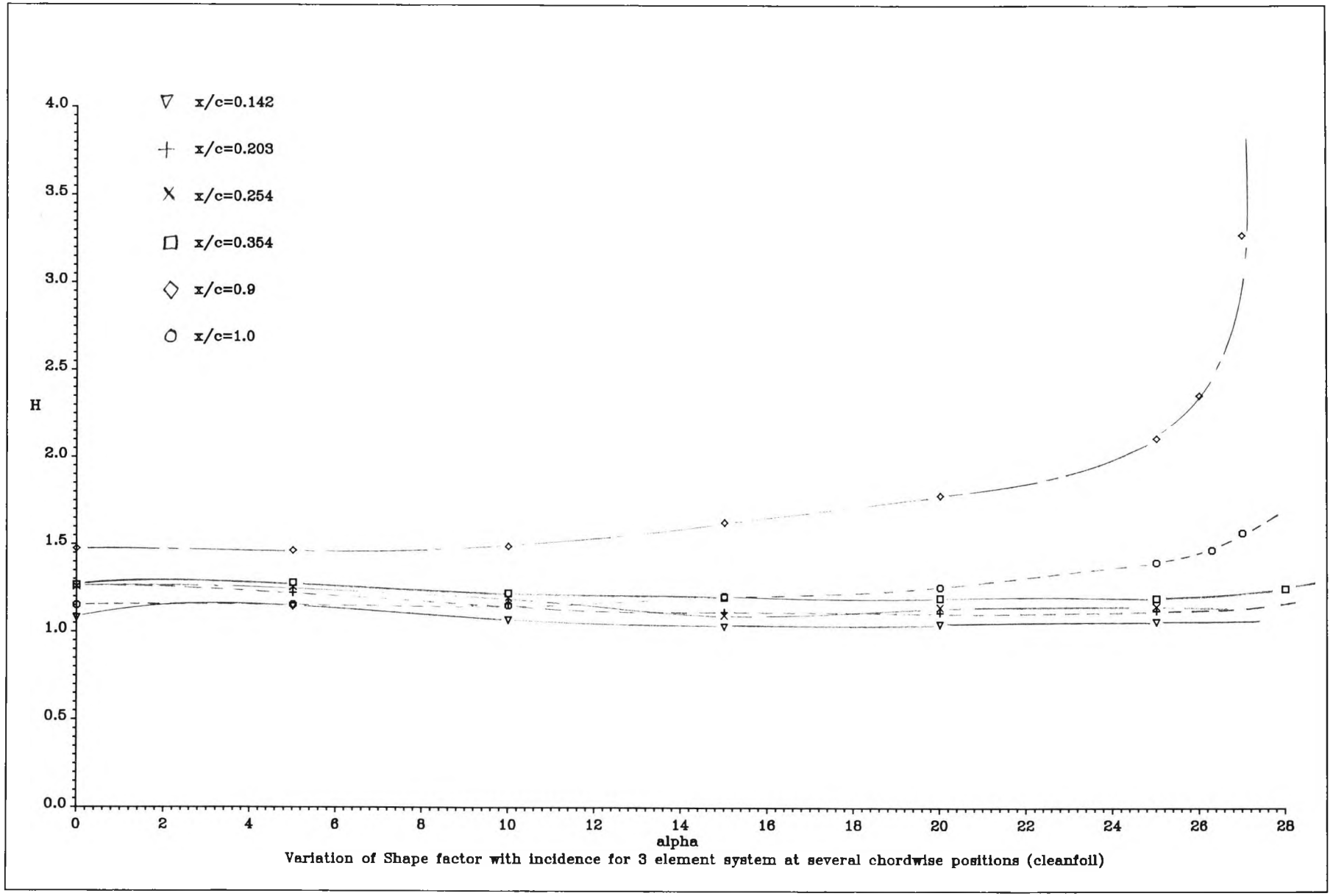

Figure 5.37 : Variation of H (in mm) with α for several chordwise positions on the cleanfoil

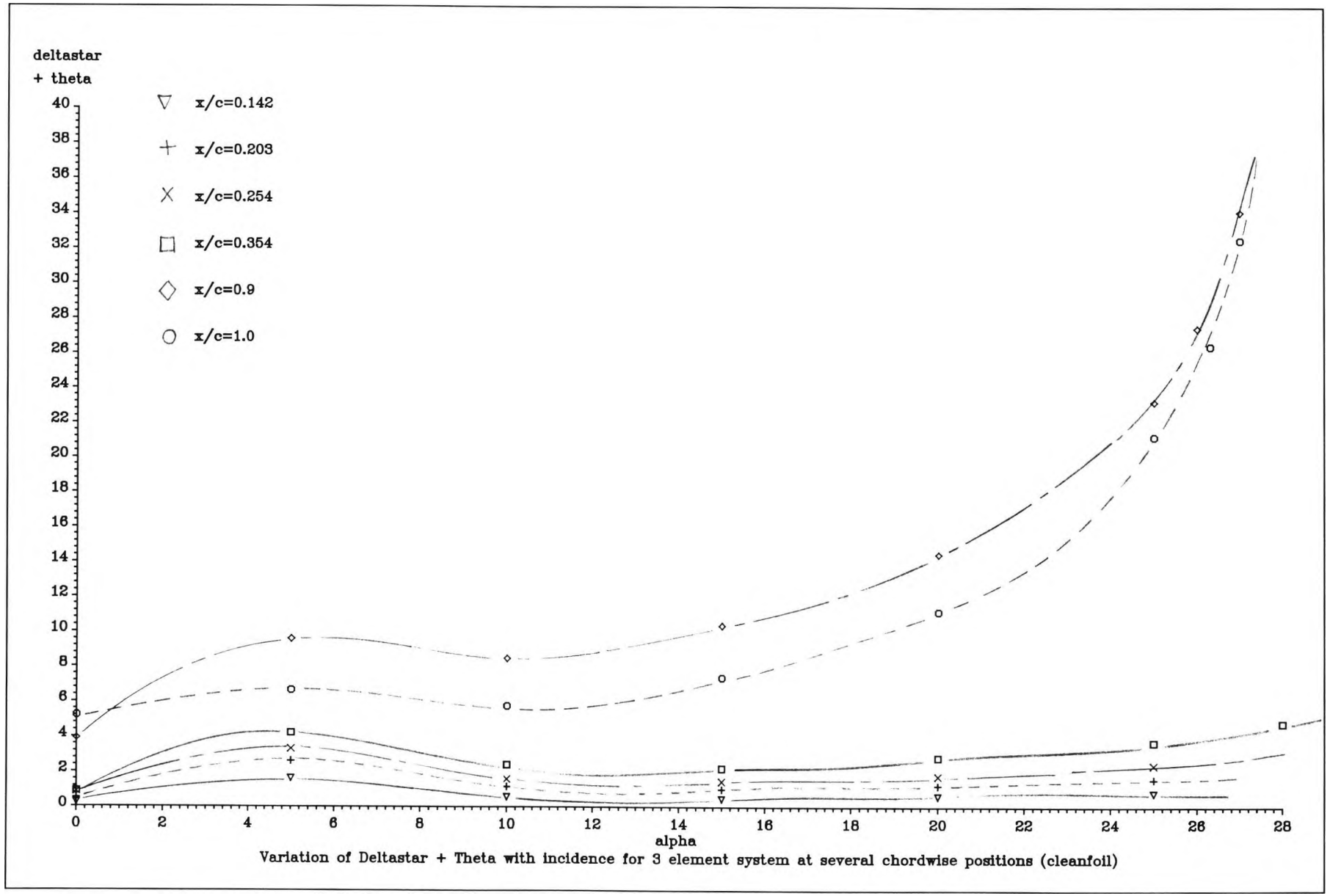

Figure 5.38 : Variation of ($\delta^* + \theta$) (in mm) with α for several chordwise positions on the cleanfoil

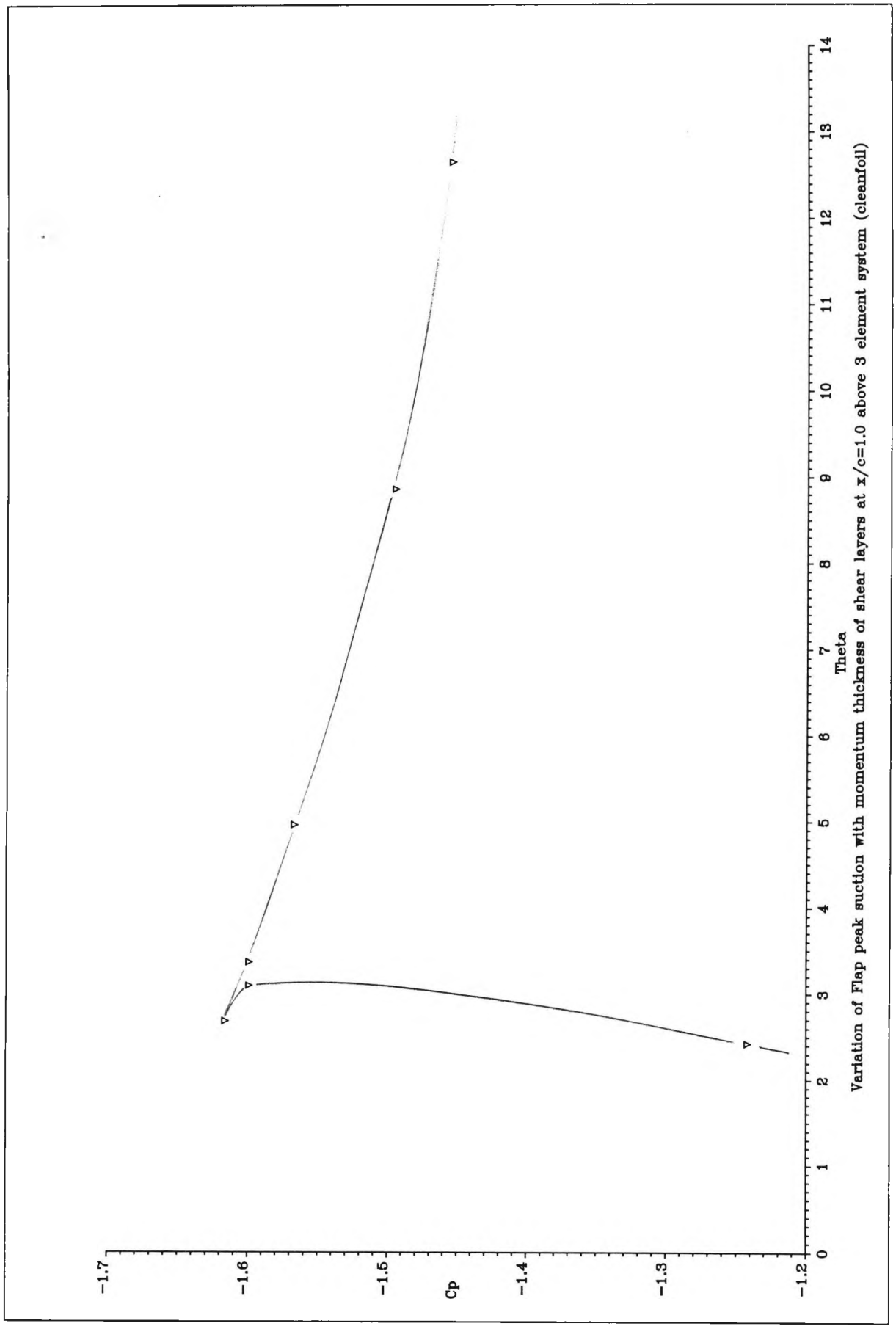

Figure 5.39 : Variation of Flap peak suction with θ (at x/c = 1.0) for the cleanfoil

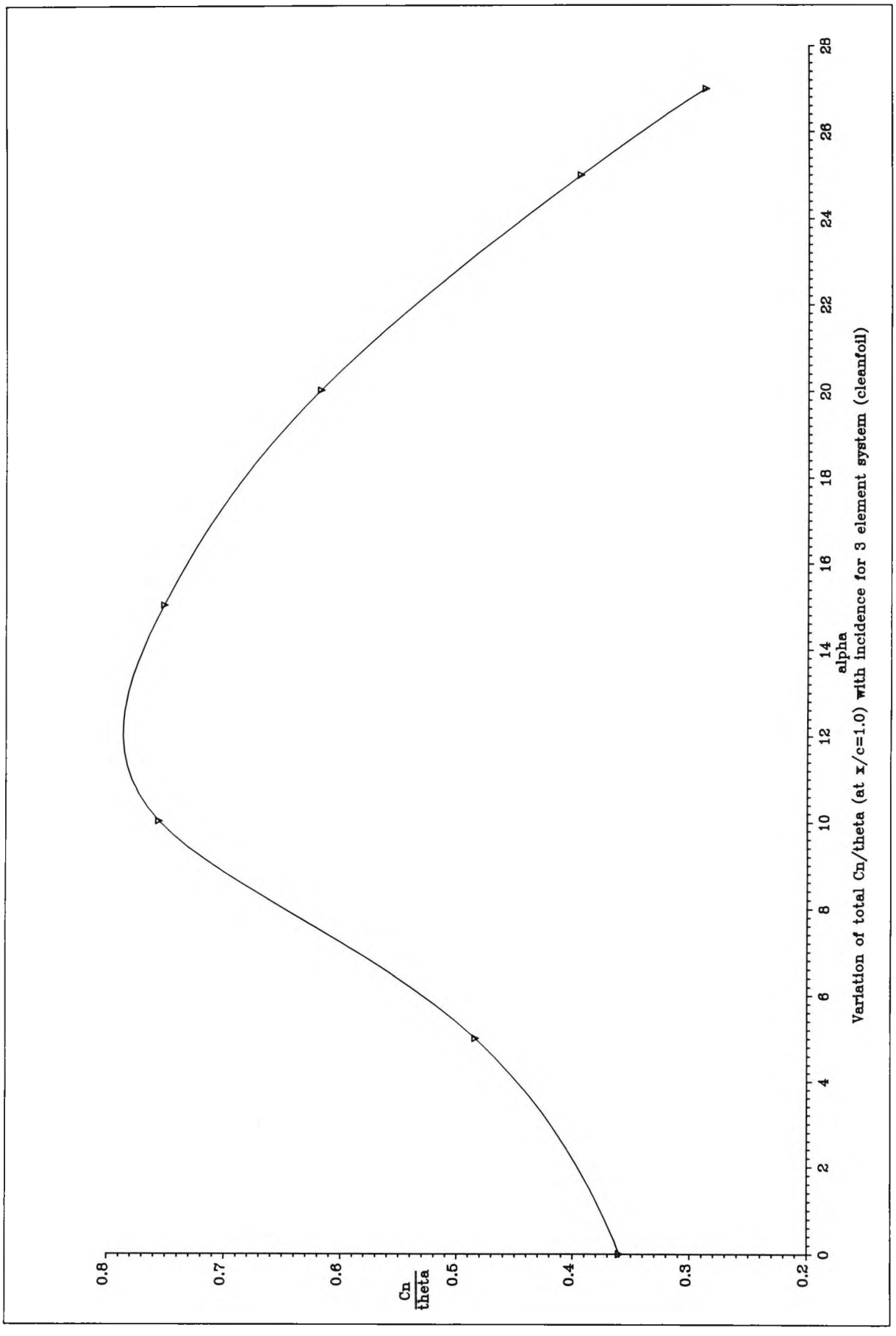

Figure 5.40 : Variation of total C_n/θ (at x/c = 1.0) with α for the cleanfoil

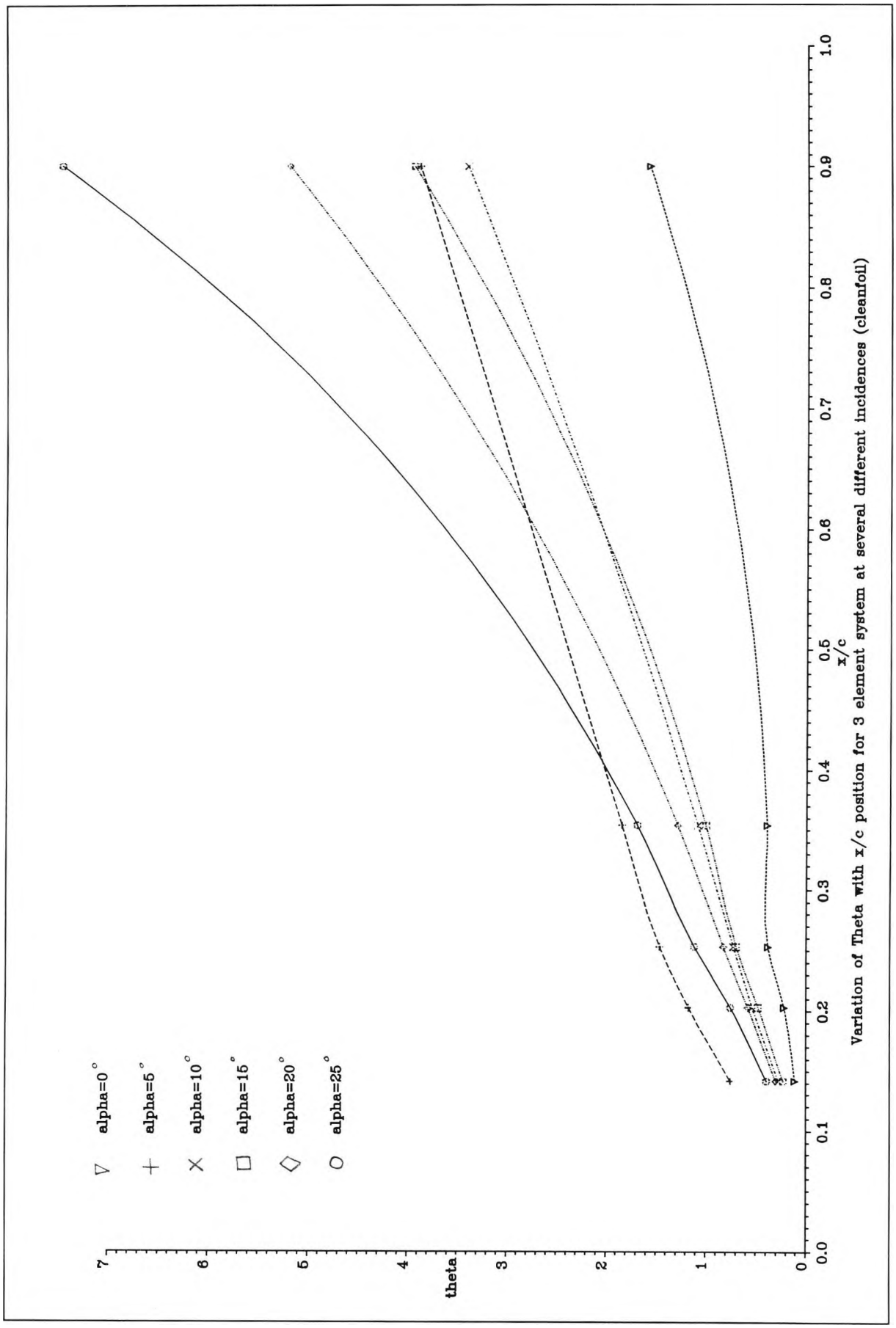

Figure 5.41 : Variation of θ (in mm) with x/c position on the main wing for several incidences

Appendix B - Windtunnel test results with vane vortex generators

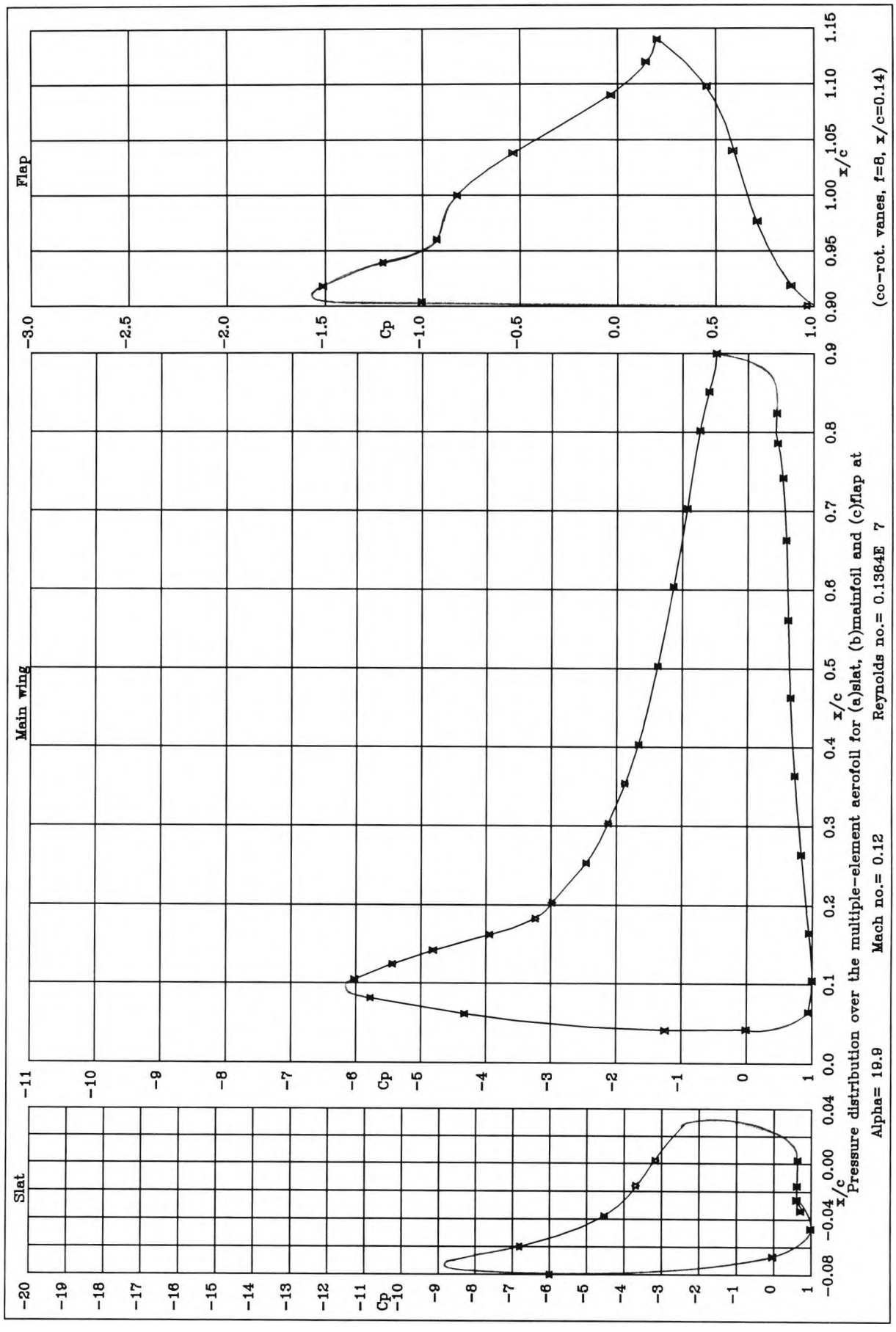

Figure 6.1 : Pressure distribution over the high lift system at 19.9° when co-rot. vvg's are at x/c = 0.14

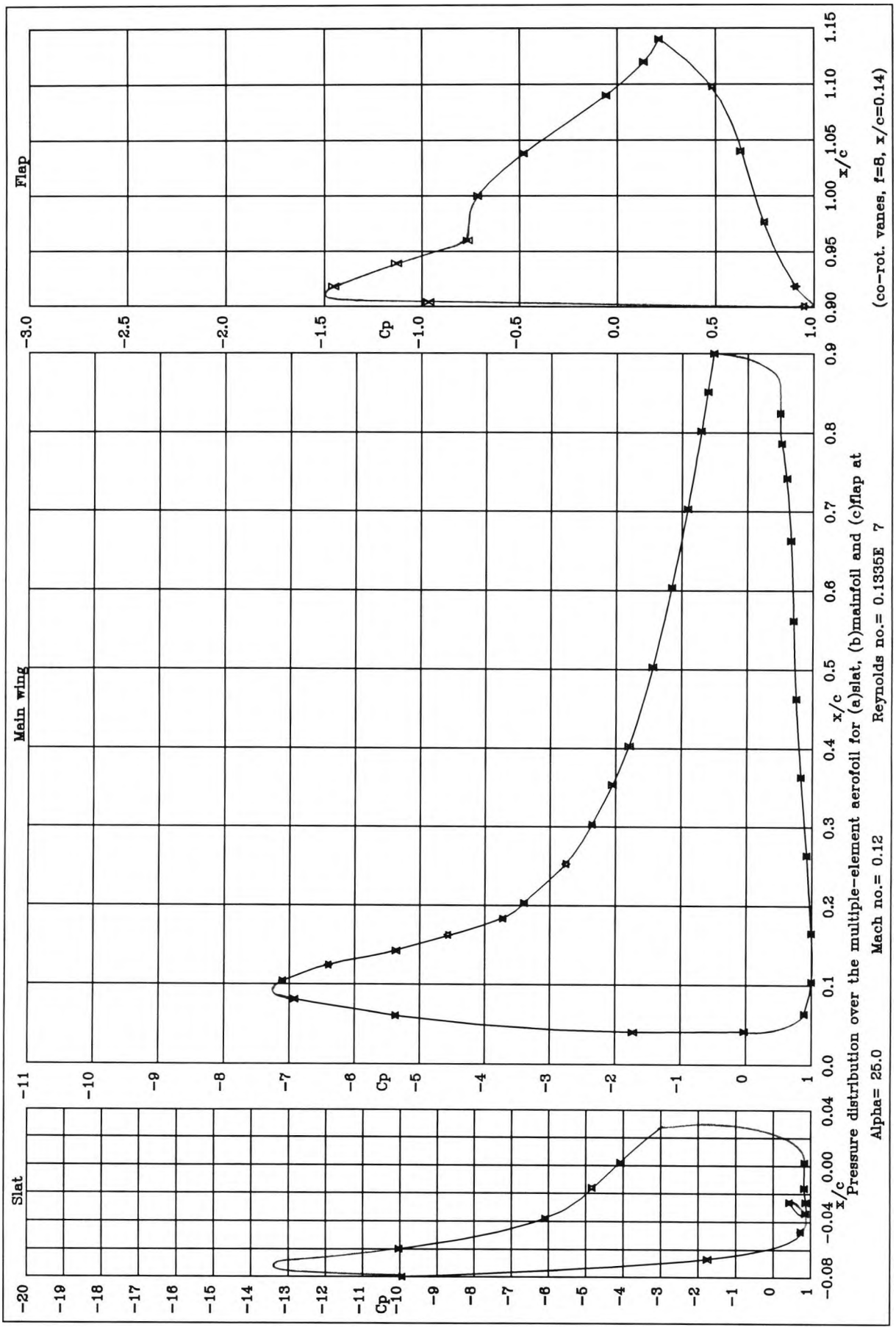

Figure 6.2 : Pressure distribution over the high lift system at 25° when co-rot. vvg's are at x/c = 0.14

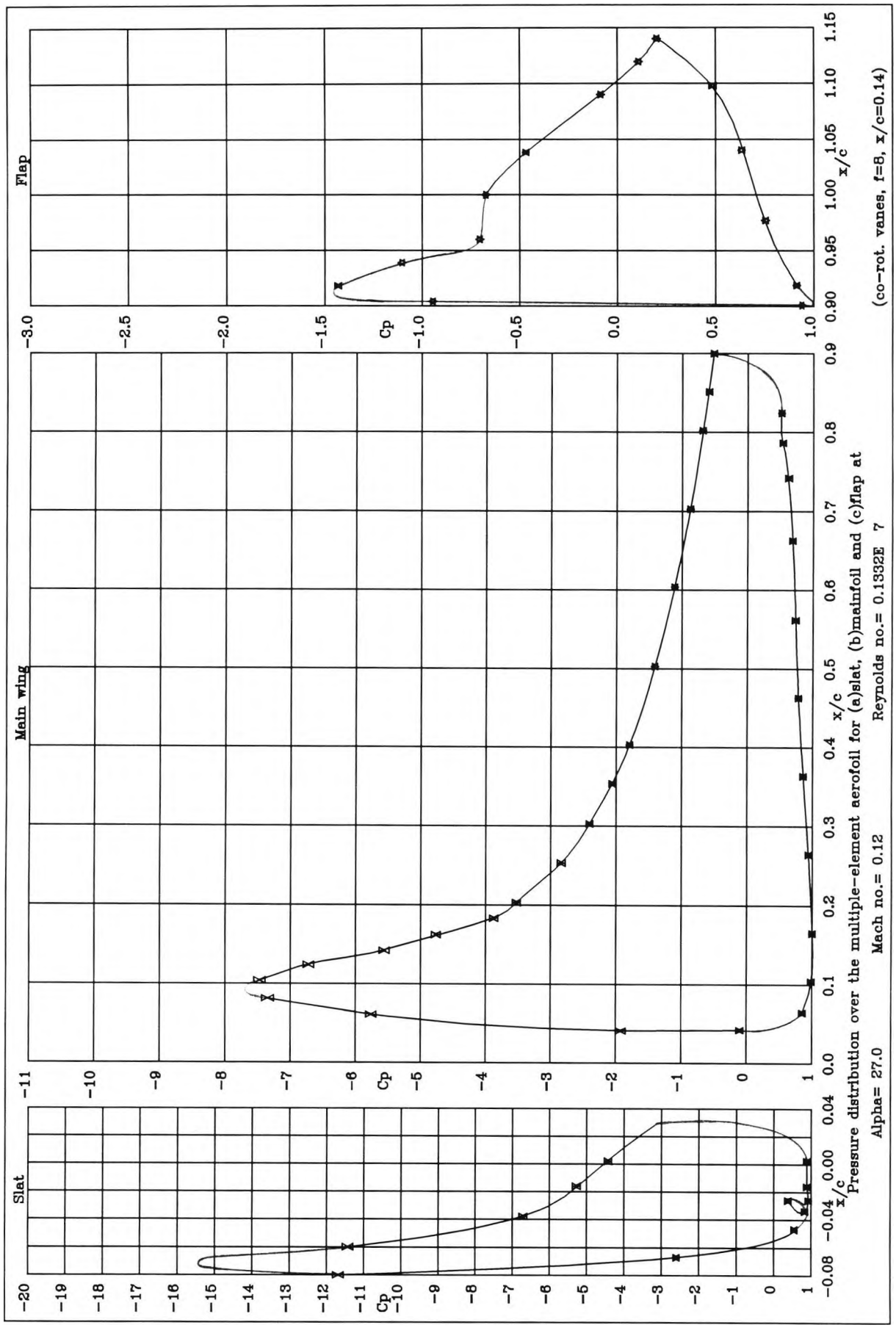

Figure 6.3 : Pressure distribution over the high lift system at 27° when co-rot. vvg's are at x/c = 0.14

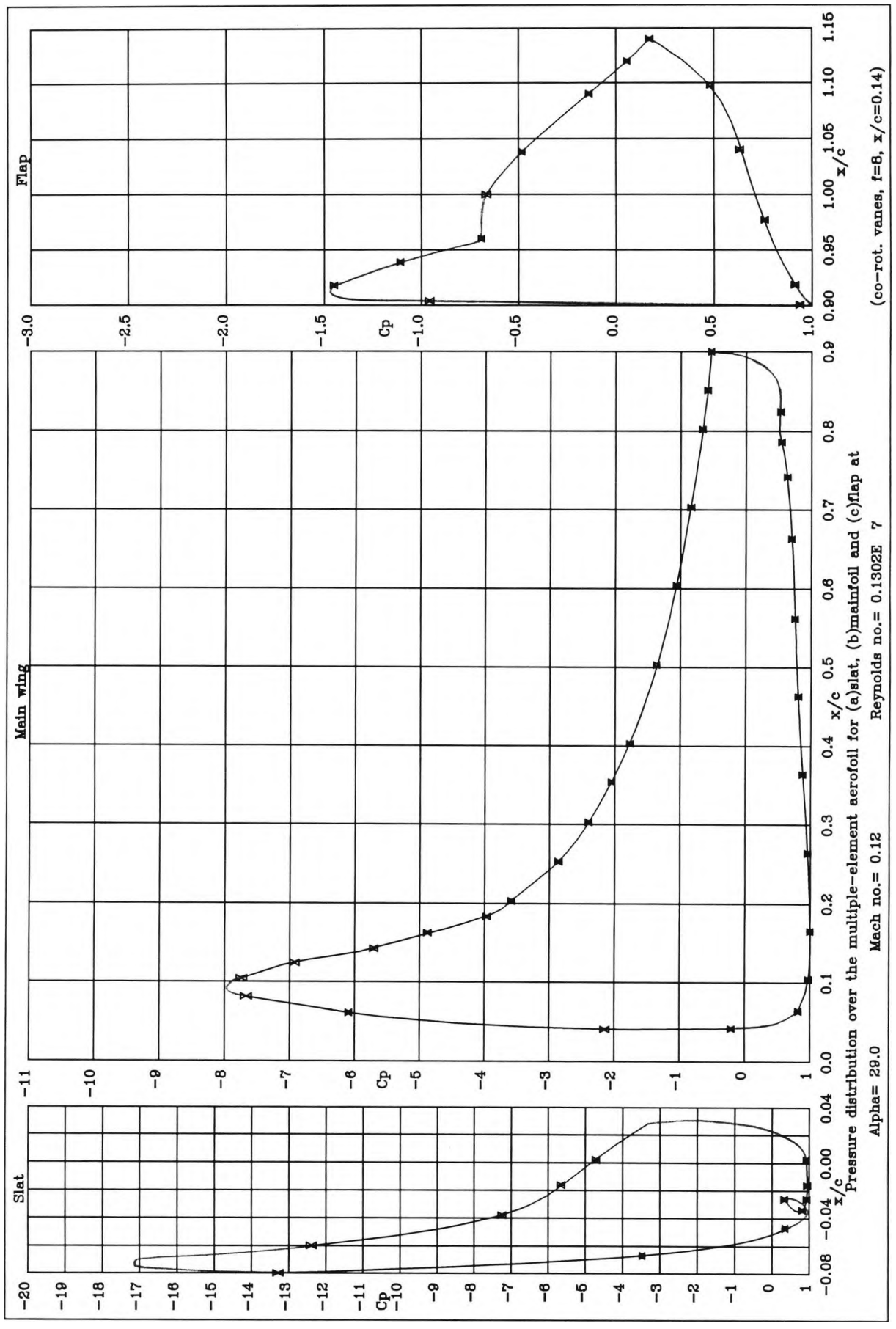

Figure 6.4 : Pressure distribution over the high lift system at 29° when co-rot. vvg's are at x/c = 0.14

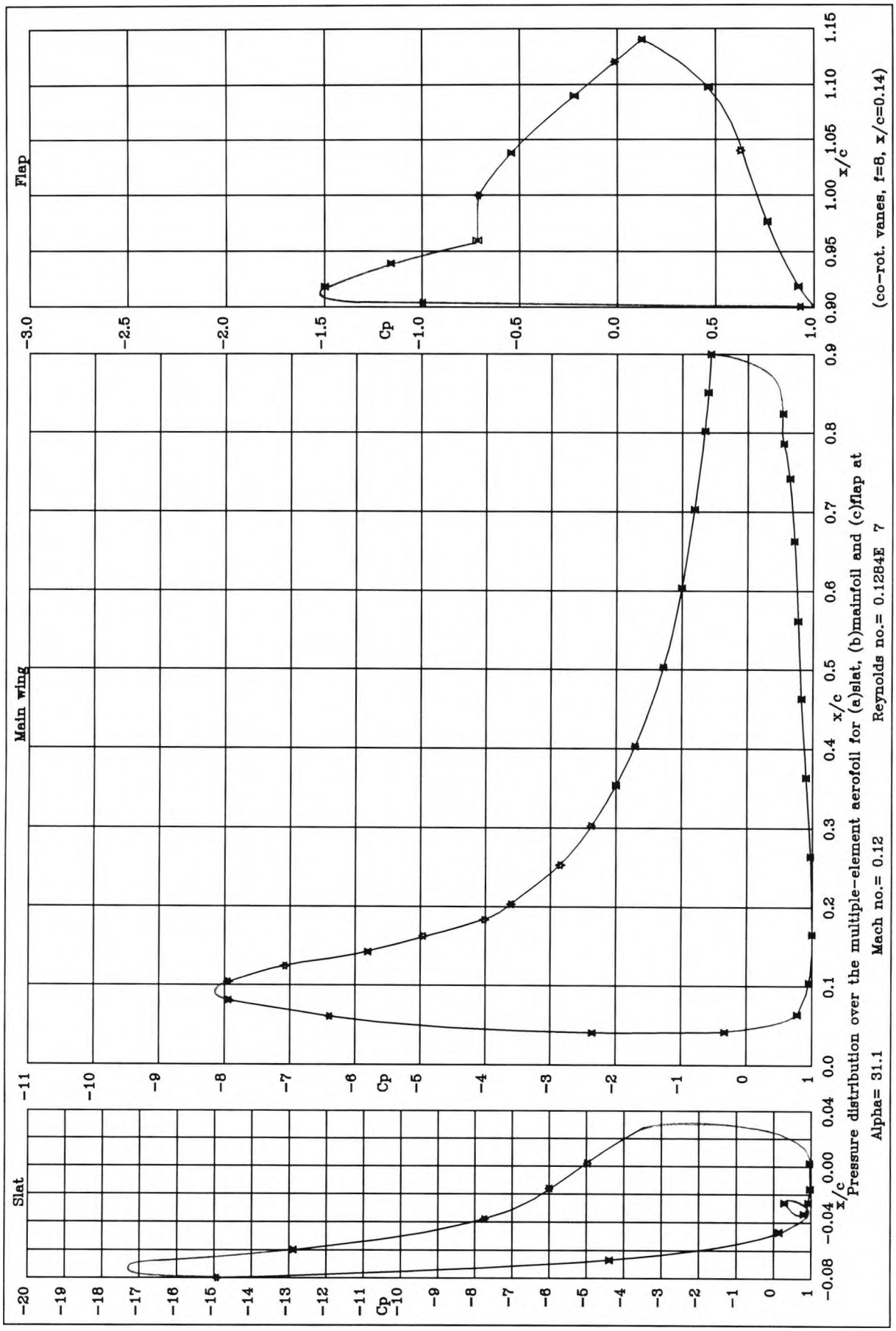

Figure 6.5 : Pressure distribution over the high lift system at 31.1° when co-rot. vvg's are at $x/c = 0.14$

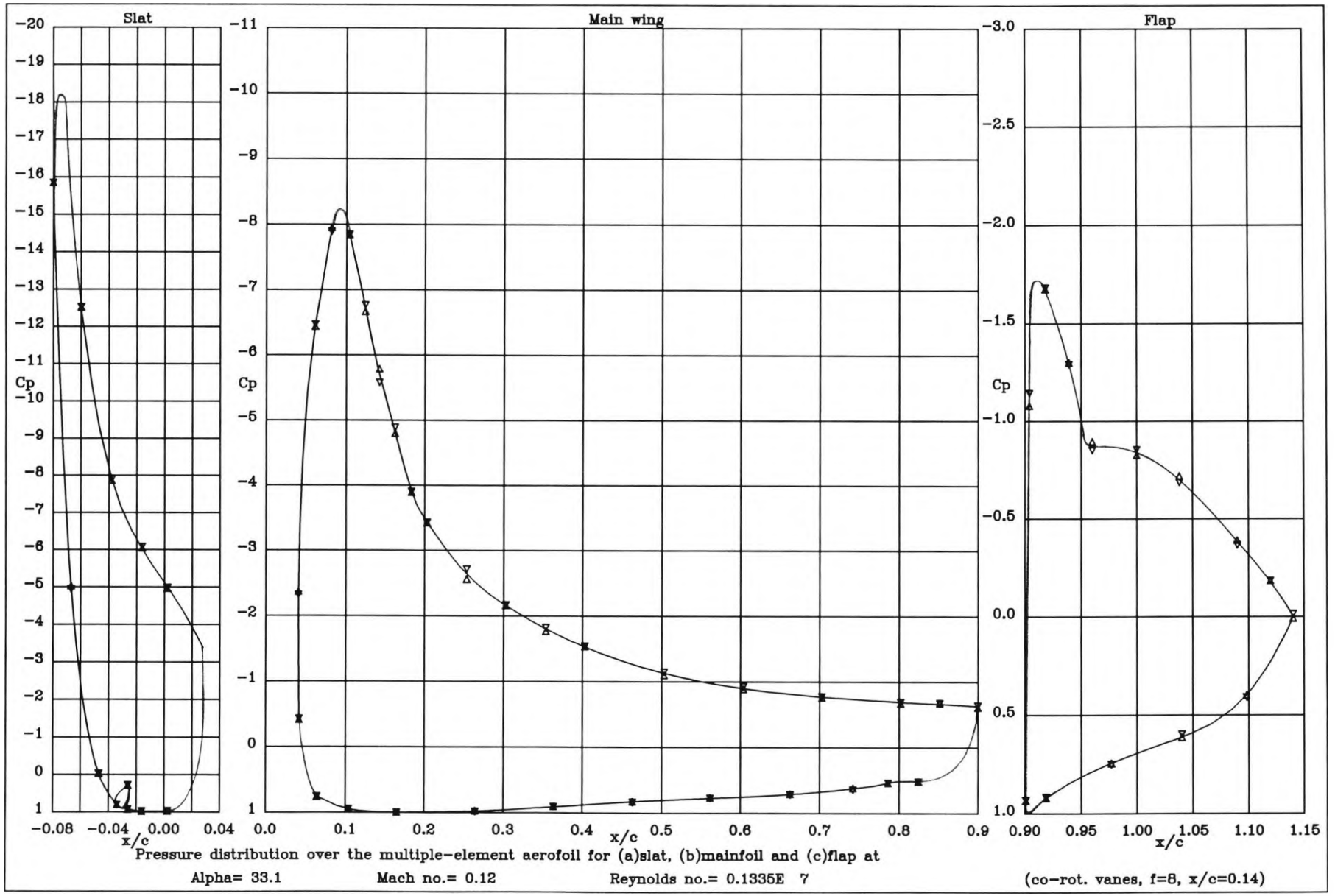

Figure 6.6 : Pressure distribution over the high lift system at 33.1° when co-rot. vvg's are at x/c = 0.14

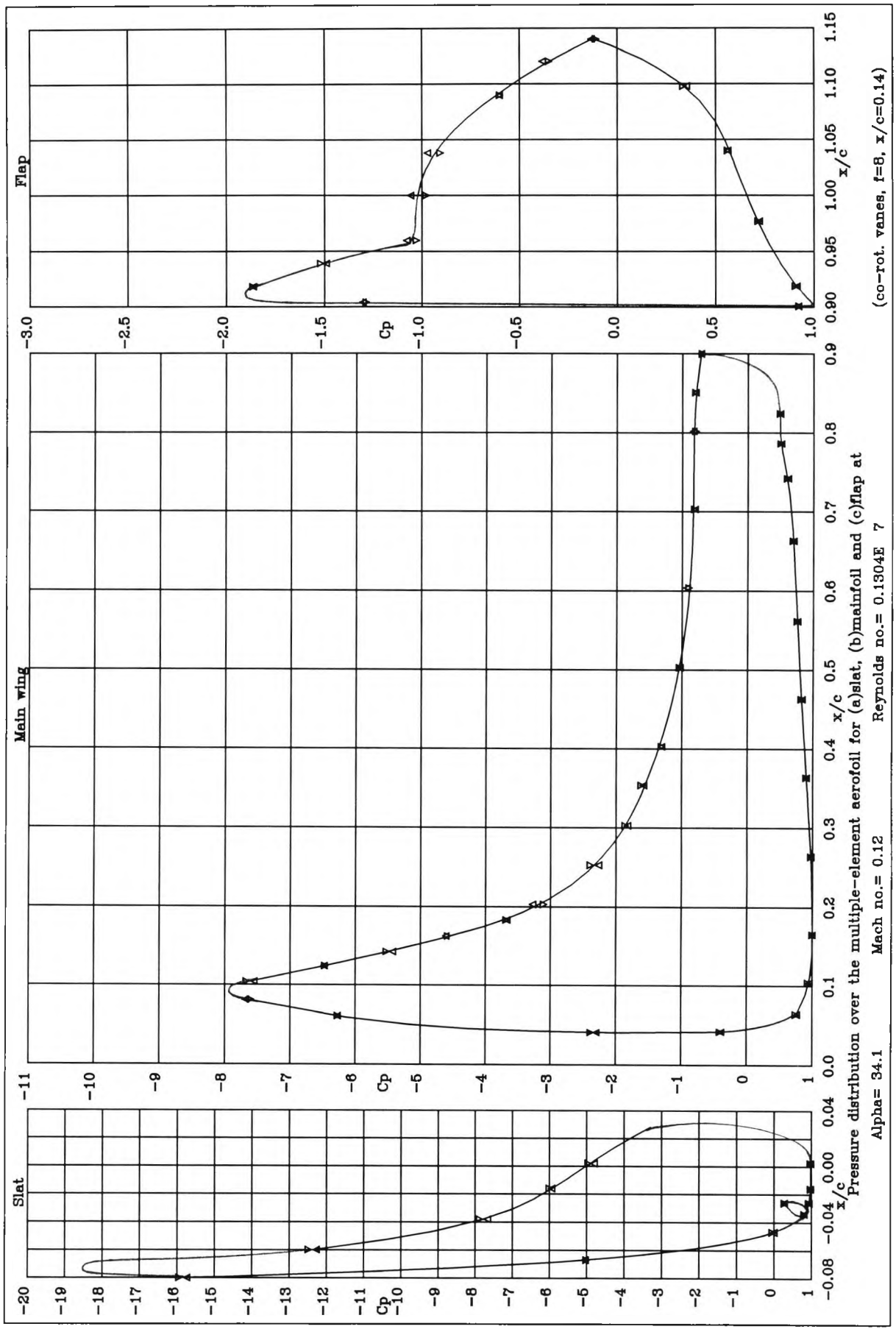

Figure 6.7 : Pressure distribution over the high lift system at 34° when co-rot. vvg's are at x/c = 0.14

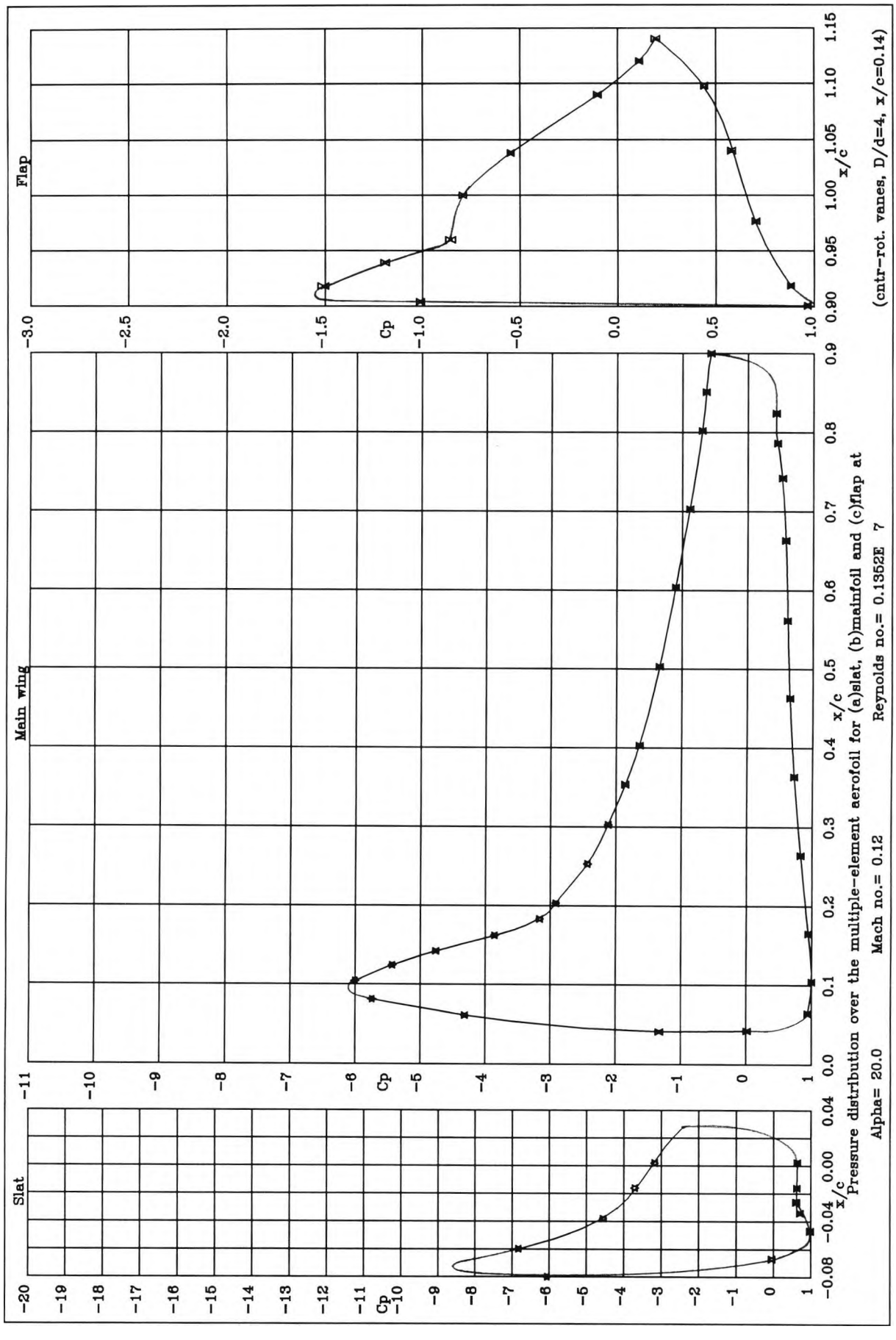

Figure 6.8 : Pressure distribution over the high lift system at 20° when cntr-rot. vvg's are at x/c = 0.14

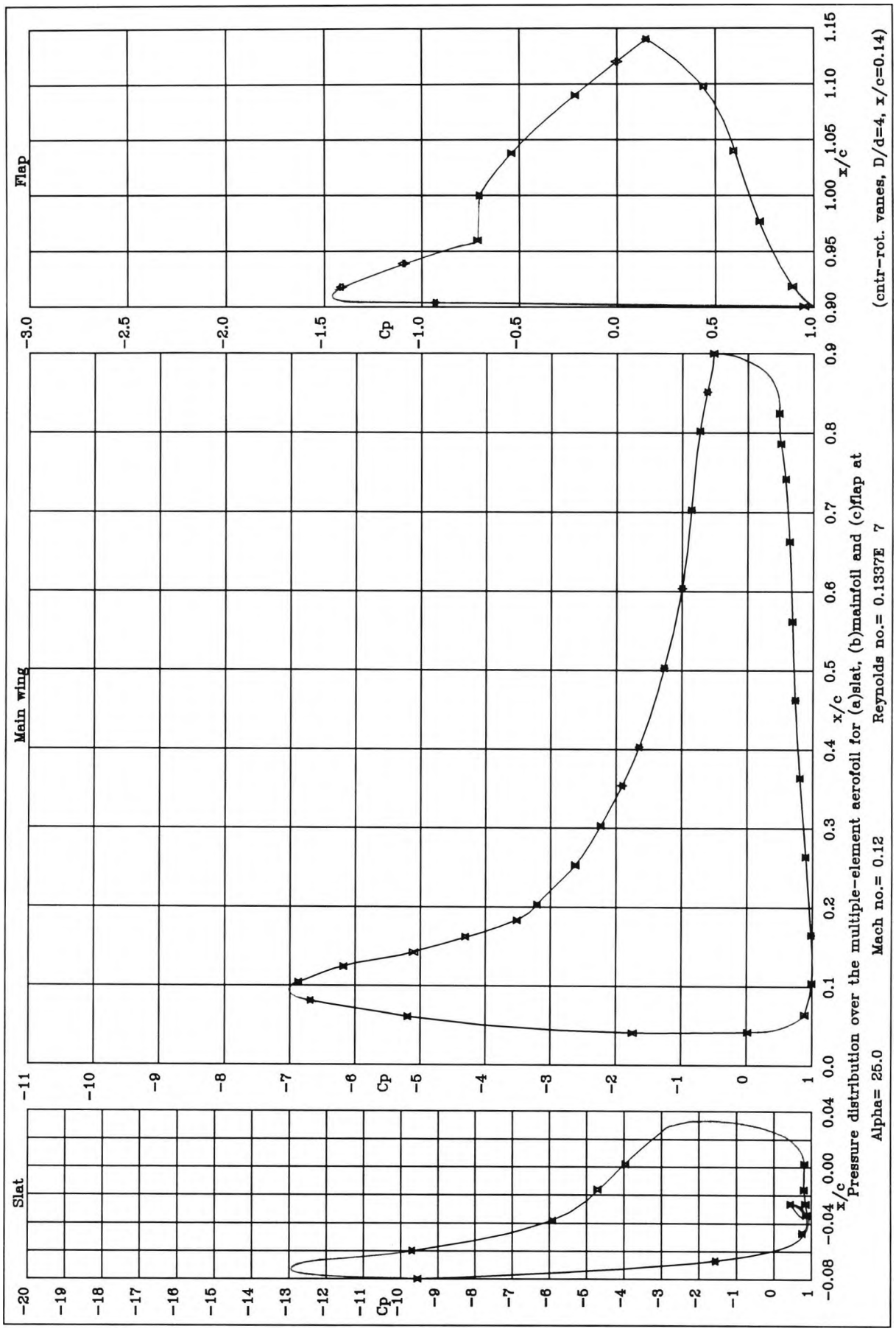

Figure 6.9 : Pressure distribution over the high lift system at 25° when cntr-rot. vvg's are at x/c = 0.14

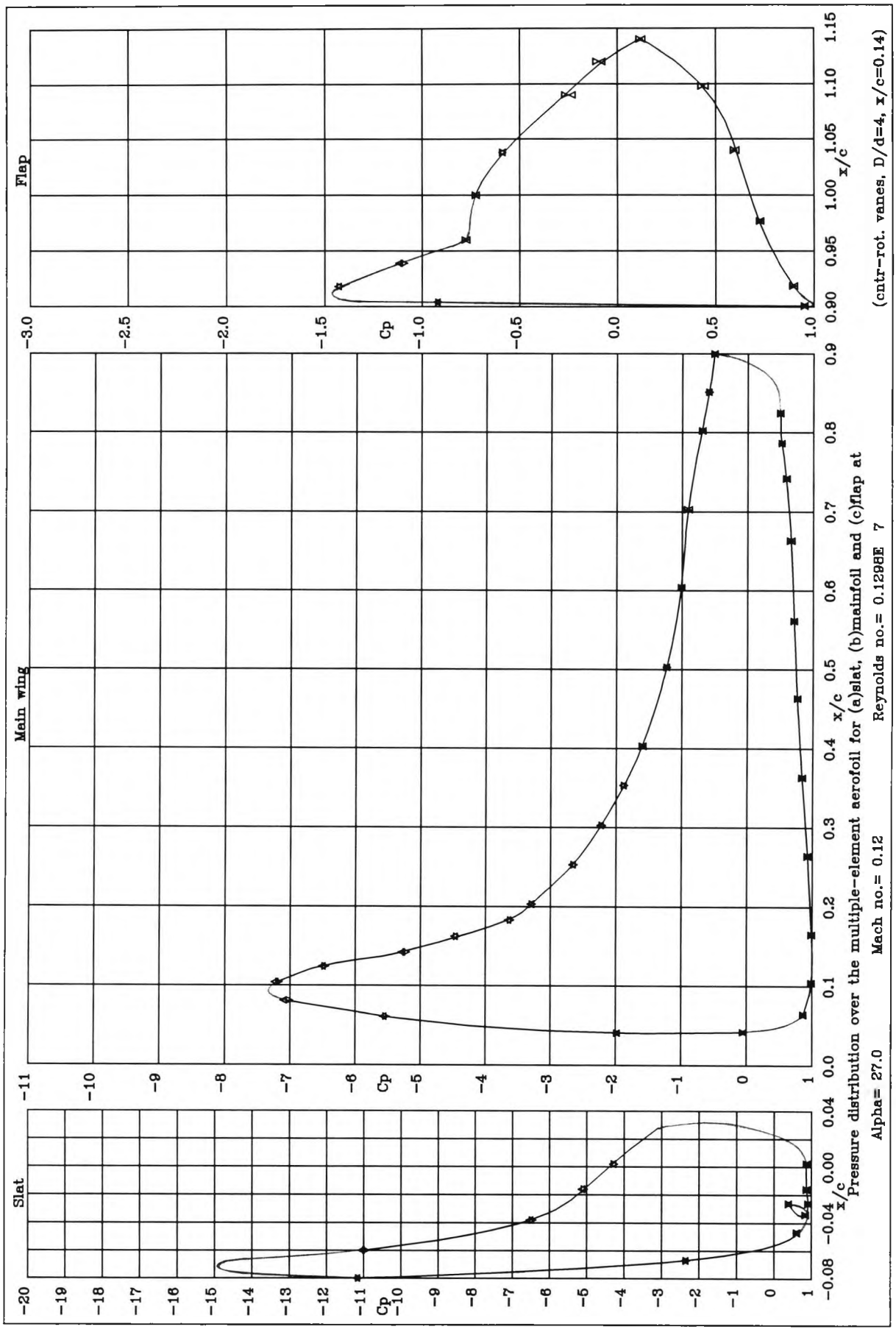

Figure 6.10 : Pressure distribution over the high lift system at 27° when cntr-rot. vvg's are at x/c = 0.14

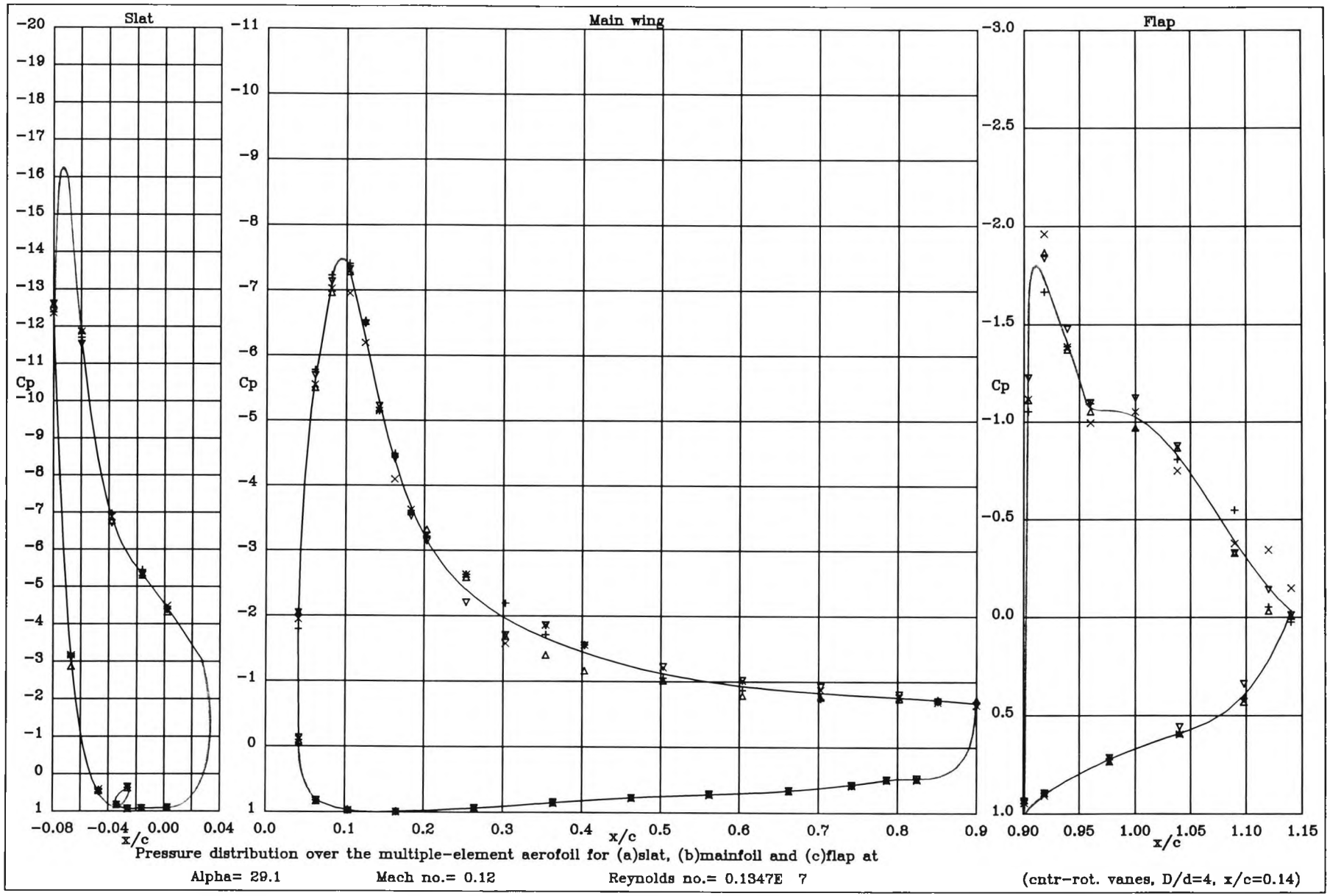

Figure 6.11 : Pressure distribution over the high lift system at 29° when cntr-rot. vvg's are at x/c = 0.14

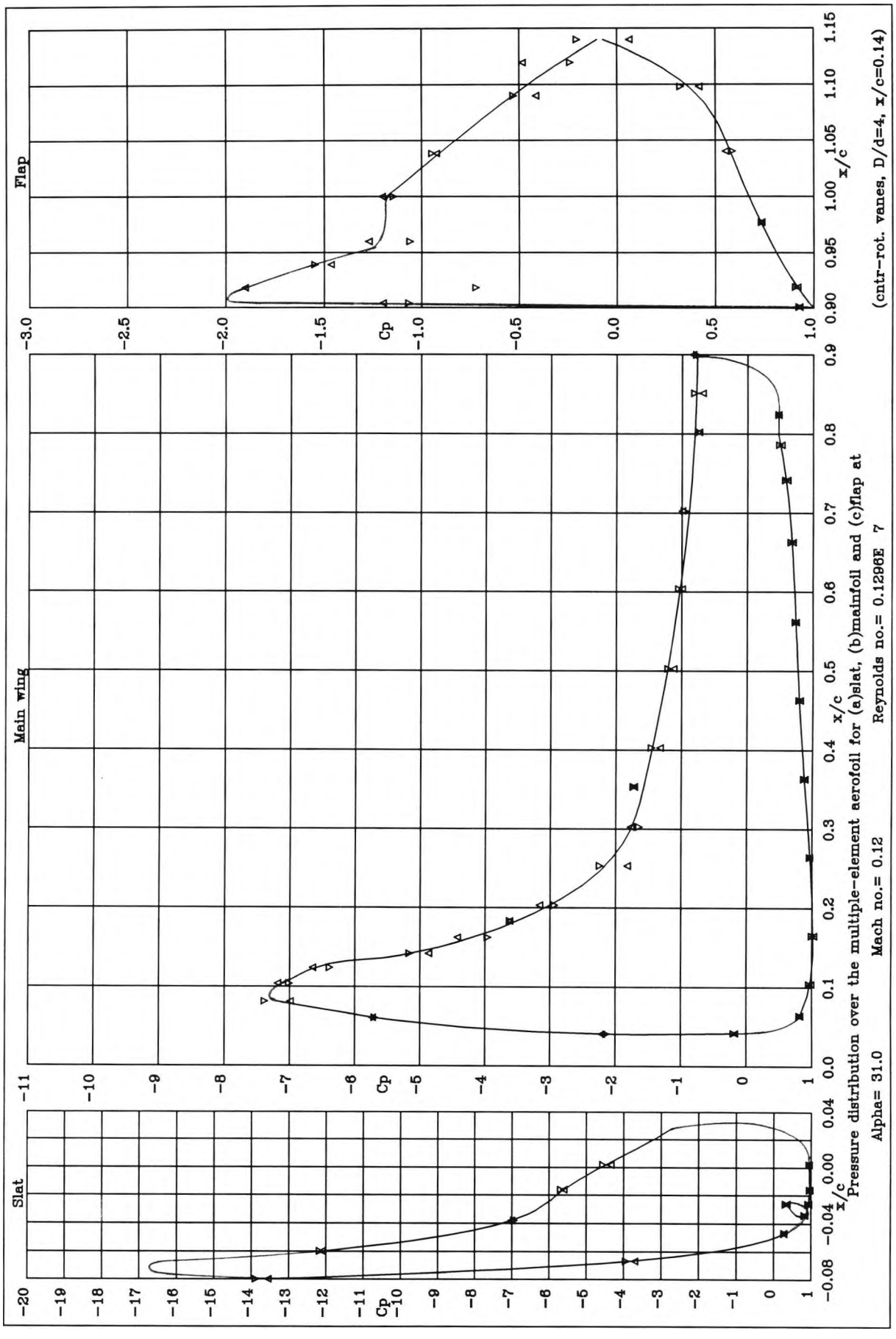

Figure 6.12 : Pressure distribution over the high lift system at 31° when cntr-rot. vvg's are at x/c = 0.14

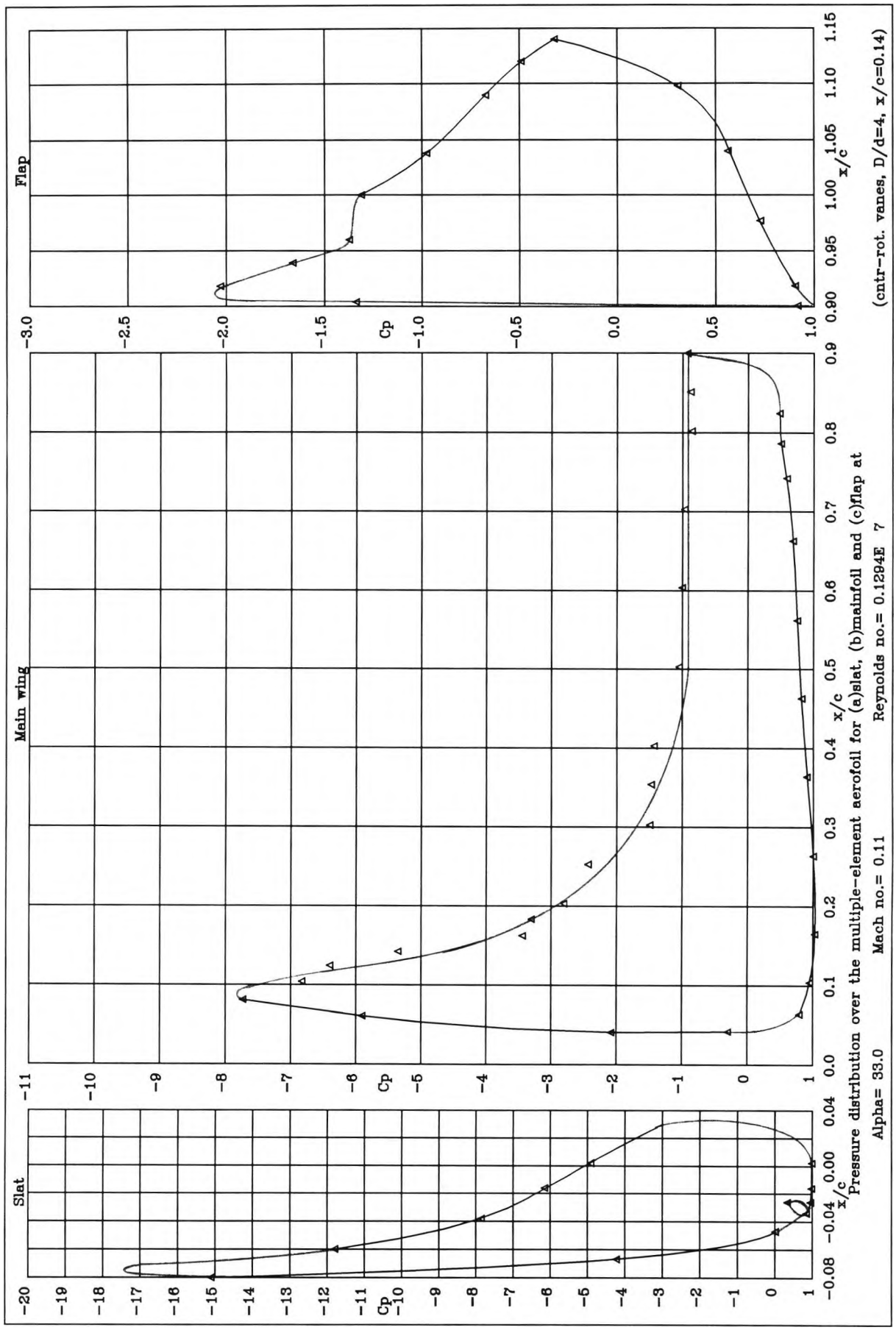

Figure 6.13 : Pressure distribution over the high lift system at 33° when cntr-rot. vvg's are at x/c = 0.14

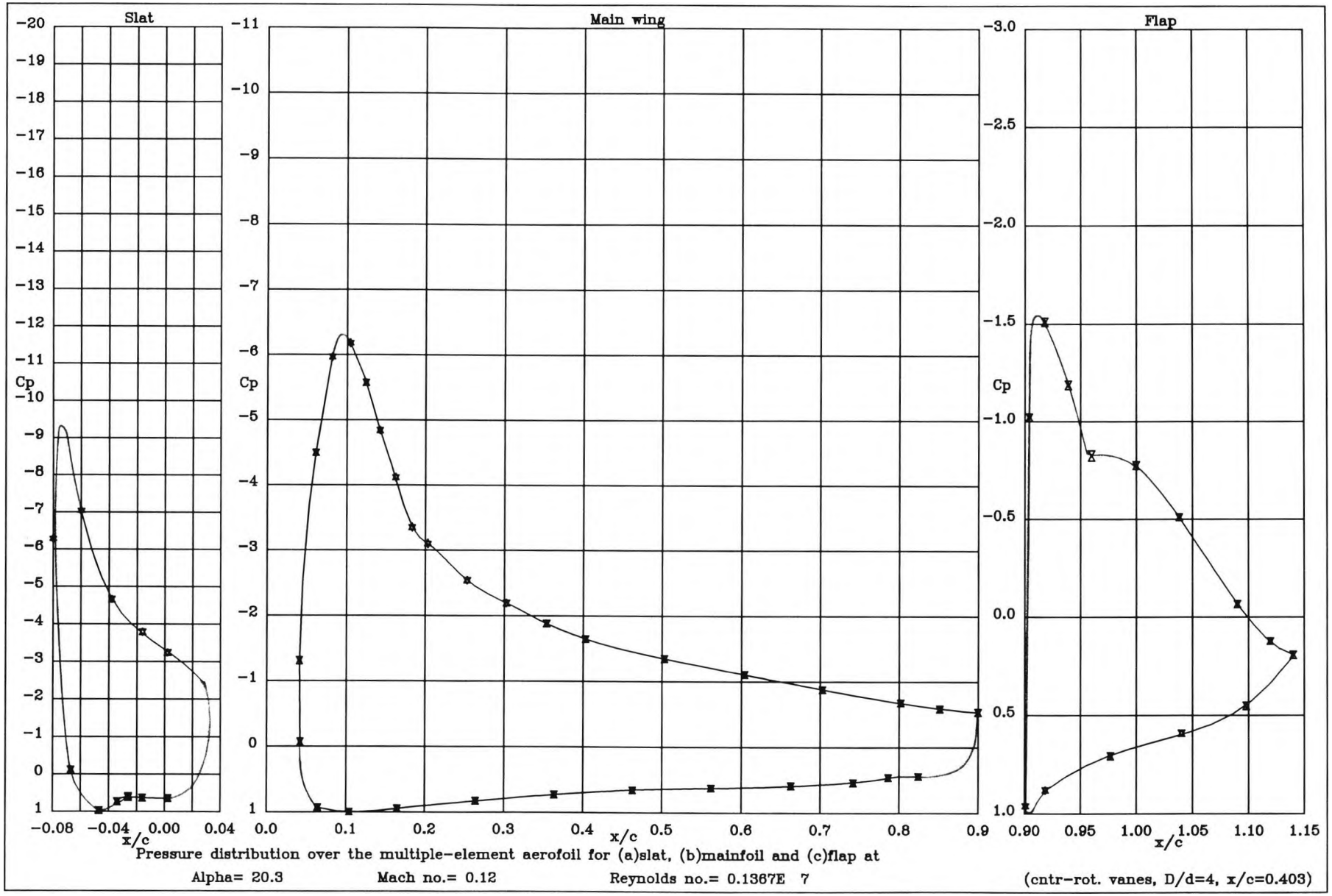

Figure 6.14 : Pressure distribution over the high lift system at 20.3° when cntr-rot. vvg's are at x/c = 0.403

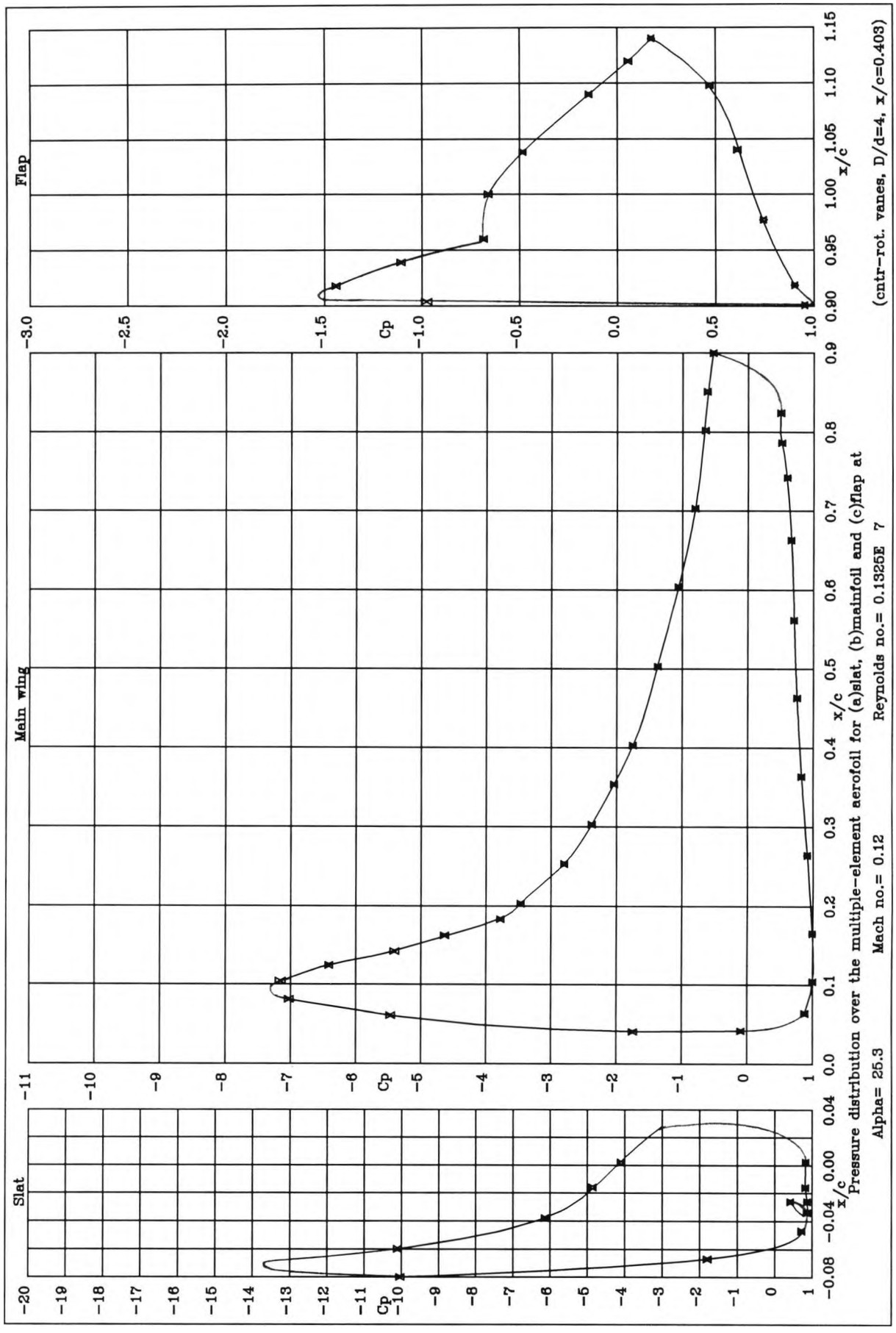

Figure 6.15 : Pressure distribution over the high lift system at 25.3° when cntr-rot. vvg's are at x/c = 0.403

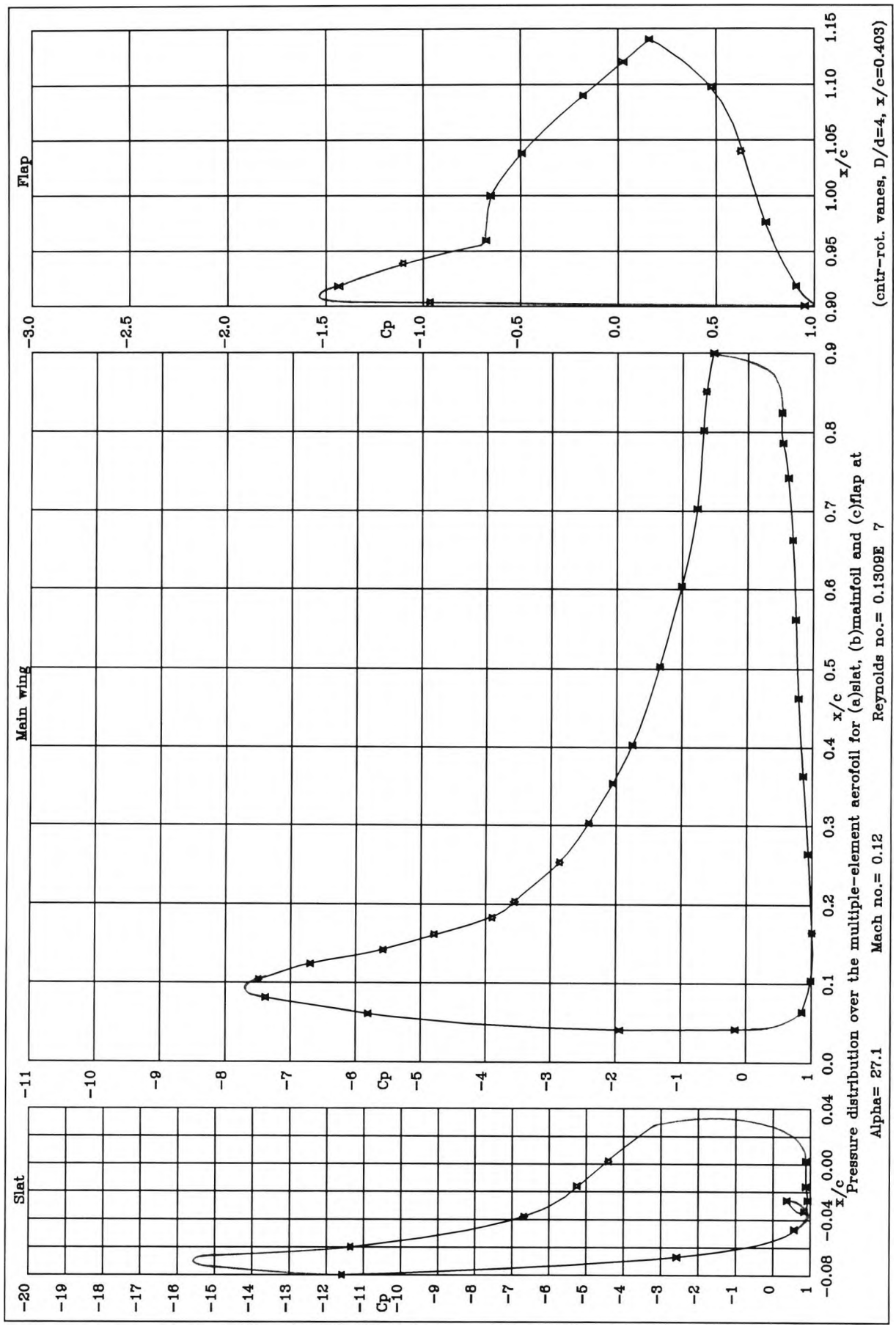

Figure 6.16 : Pressure distribution over the high lift system at 27.1° when cntr-rot. vvg's are at x/c = 0.403

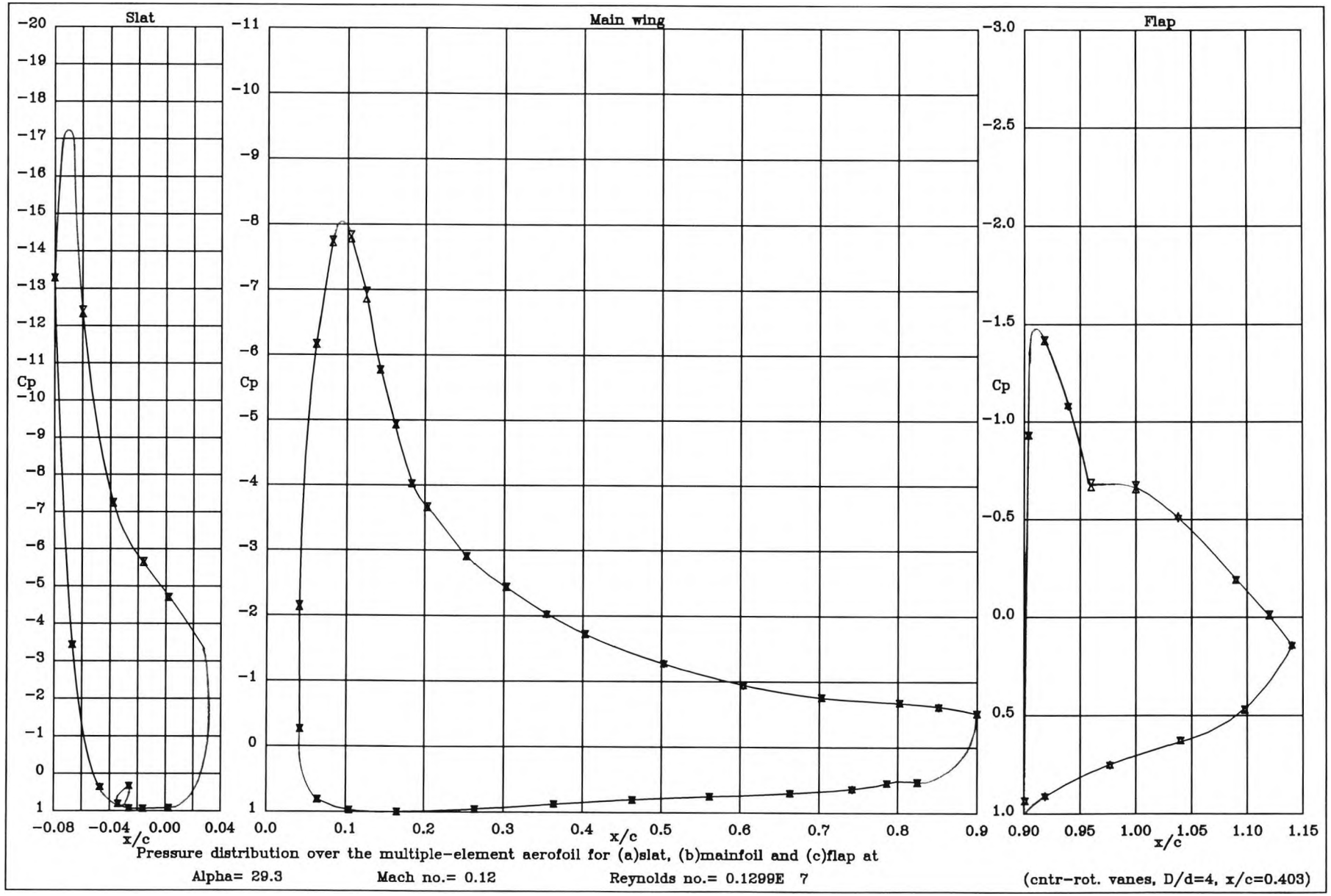

Figure 6.17 : Pressure distribution over the high lift system at 29.3° when cntr-rot. vvg's are at x/c = 0.403

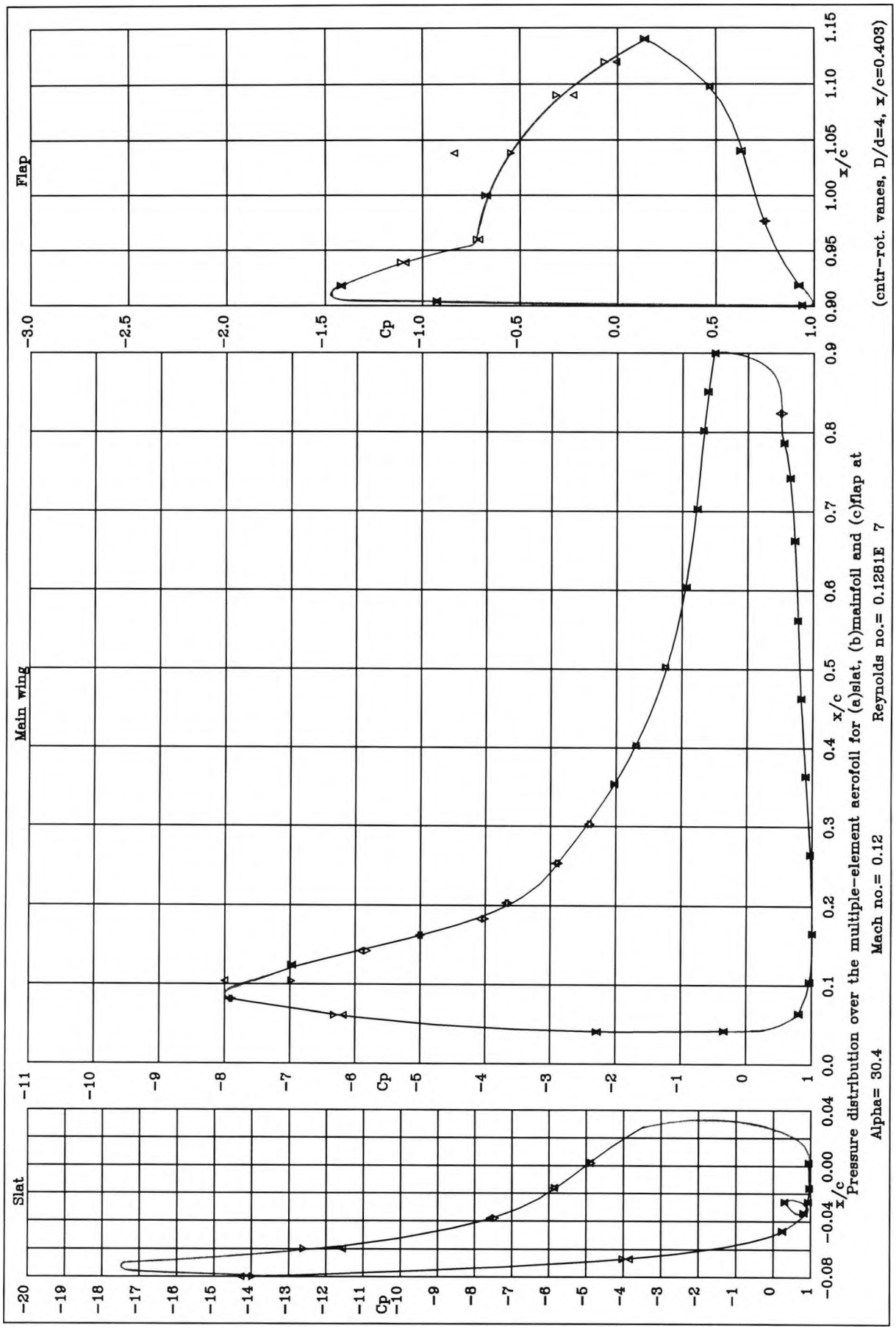

Figure 6.18 : Pressure distribution over the high lift system at 30.5° when cntr-rot. vvg's are at x/c = 0.403

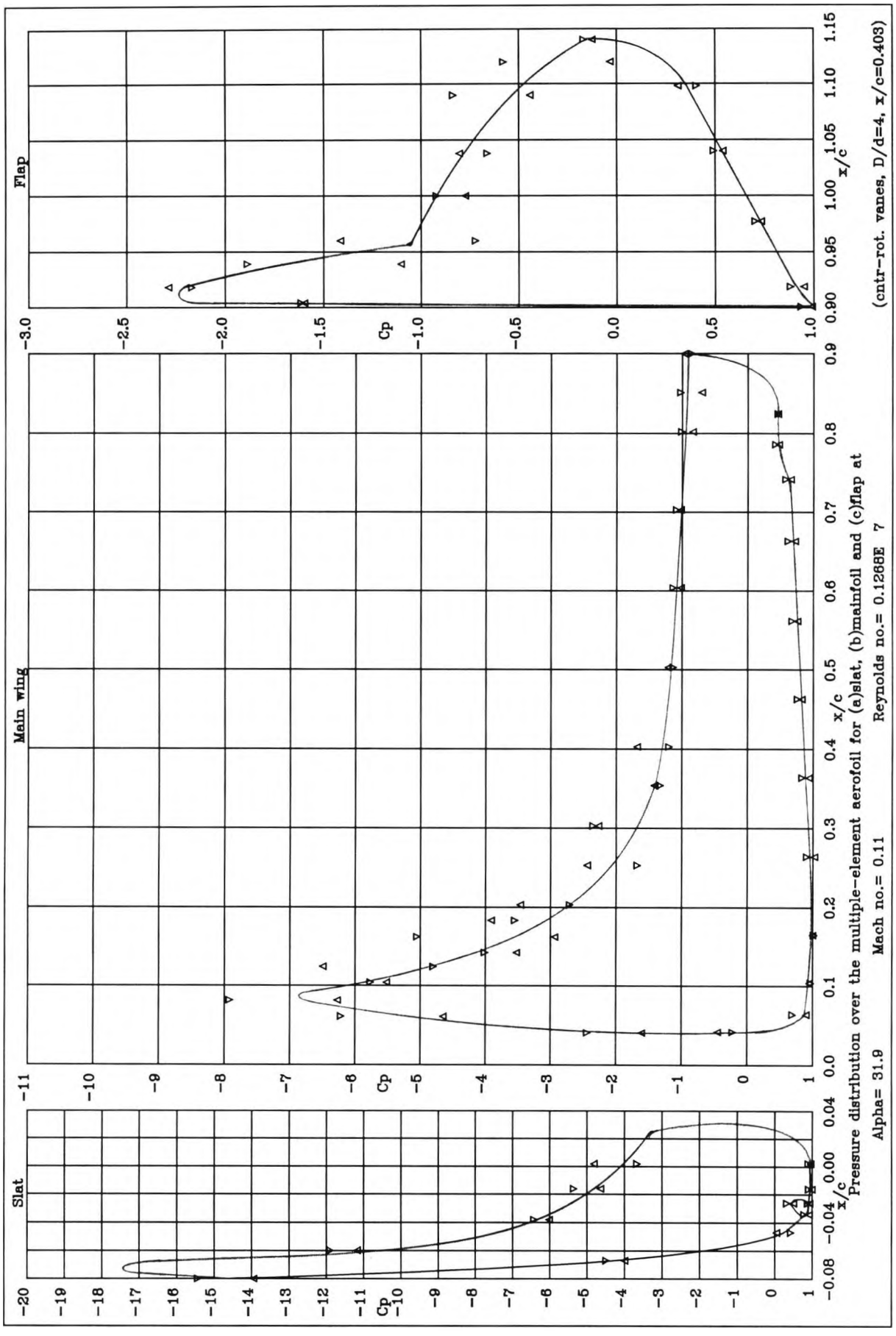

Figure 6.19 : Pressure distribution over the high lift system at 32° when cntr-rot. vvg's are at x/c = 0.403

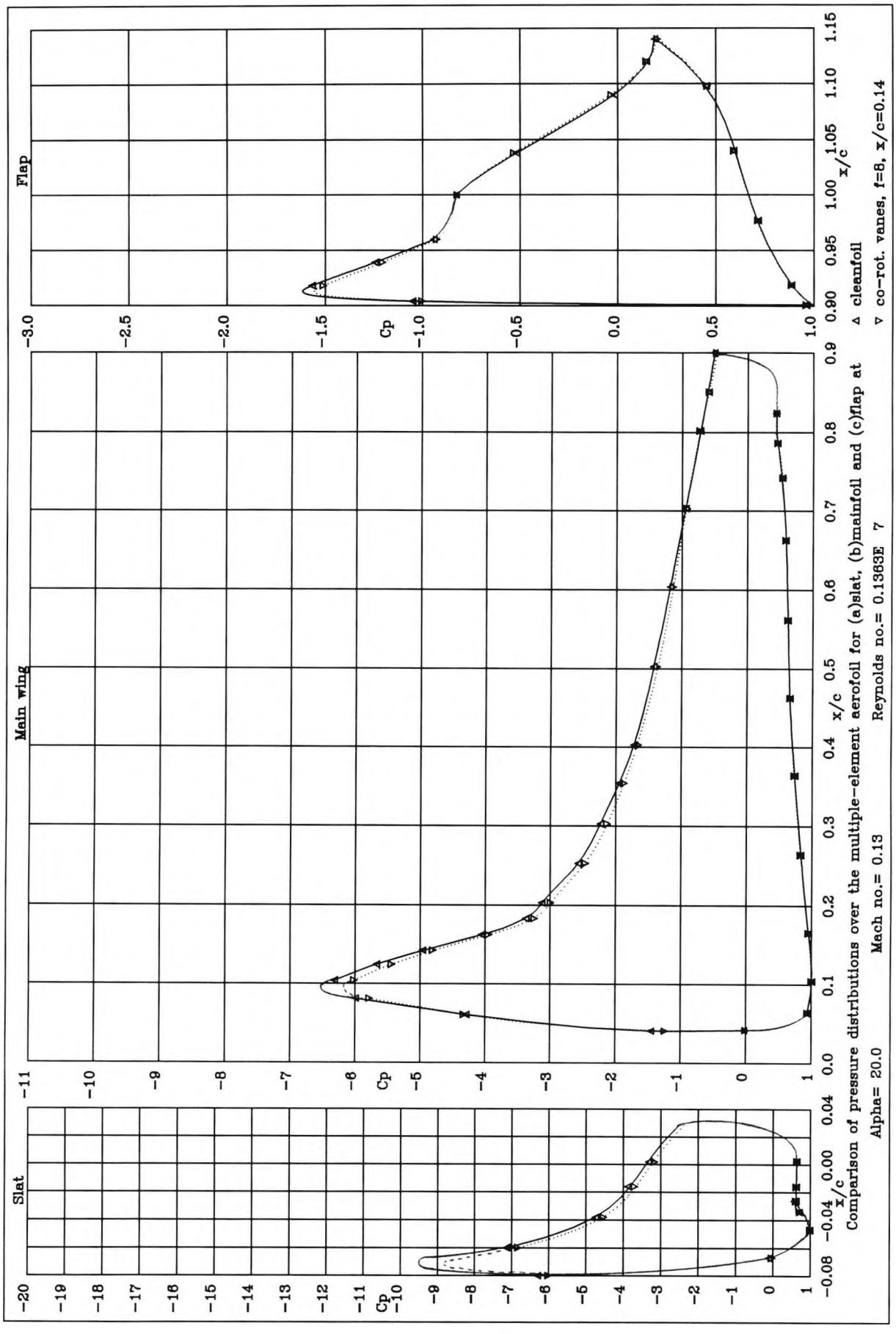

Figure 6.20 : Comparison of pressure distributions at $\alpha = 20°$ obtained with and without co-rot. vanes at x/c = 0.14

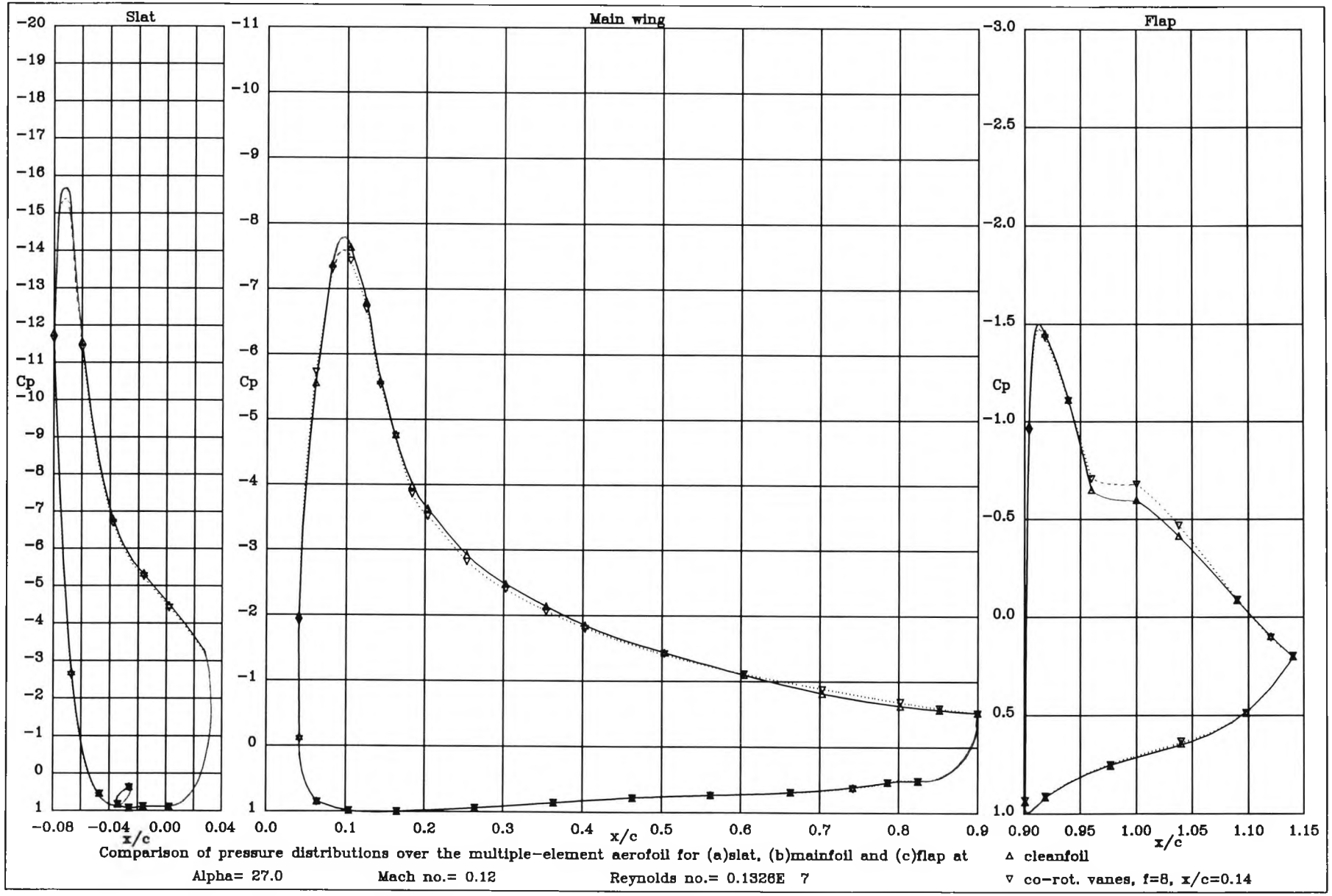

Figure 6.21 : Comparison of pressure distributions at $\alpha = 27°$ obtained with and without co-rot. vanes at x/c=0.14

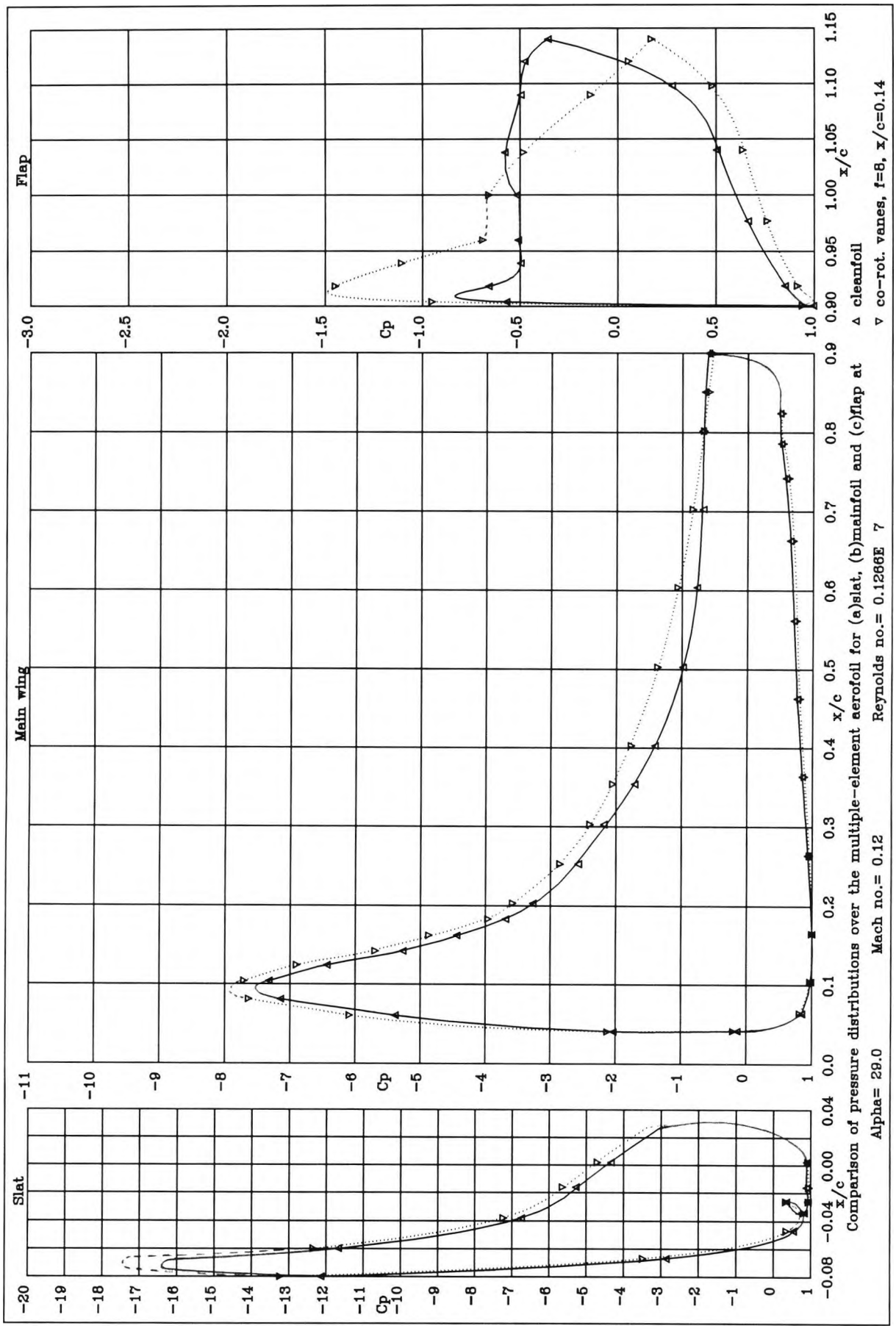

Figure 6.22 : Comparison of pressure distributions at $\alpha = 29°$ obtained with and without co-rot. vanes at x/c = 0.14

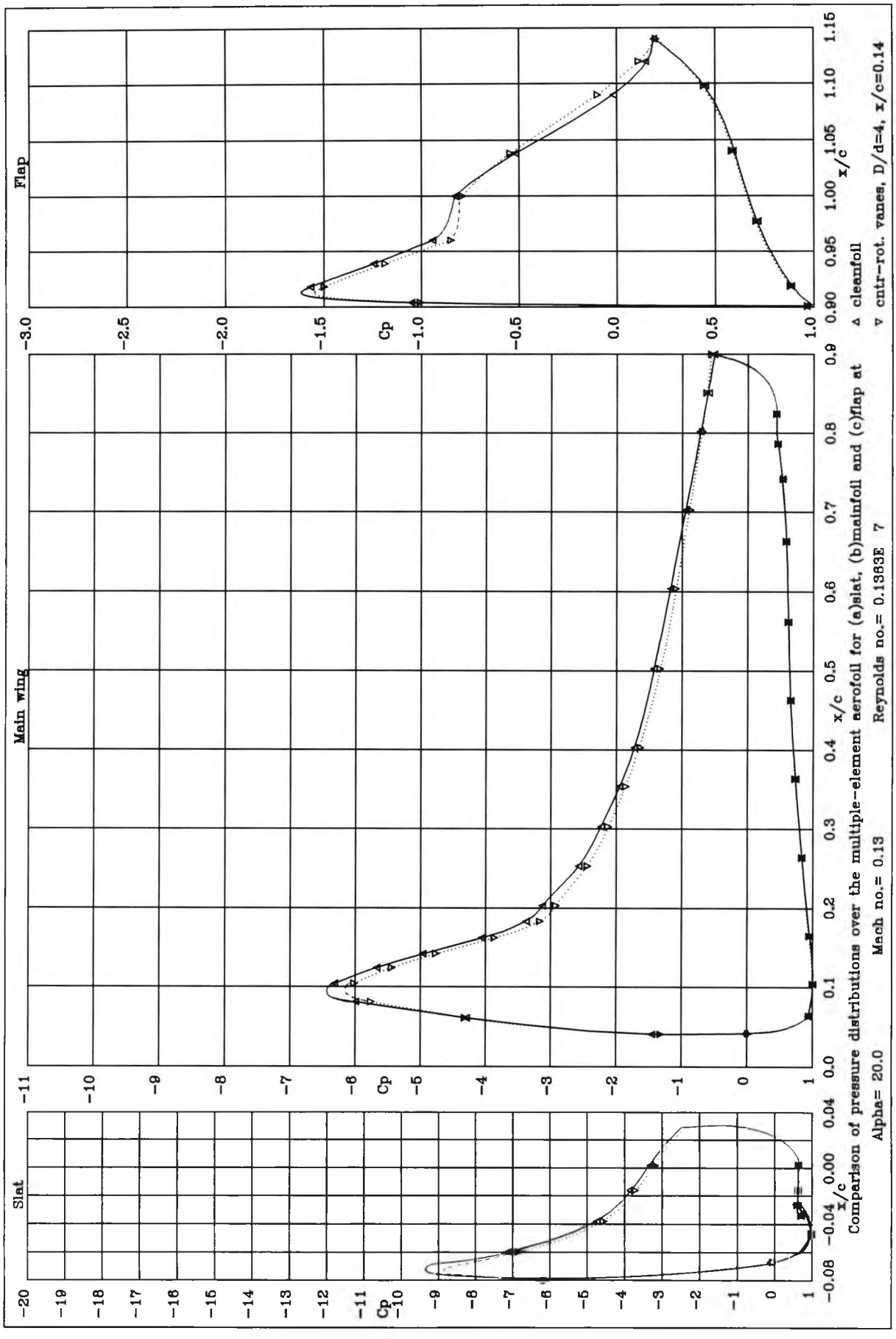

Figure 6.23 : Comparison of pressure distributions at $\alpha = 20°$ obtained with and without counter-rotating vane vortex generators at x/c = 0.14

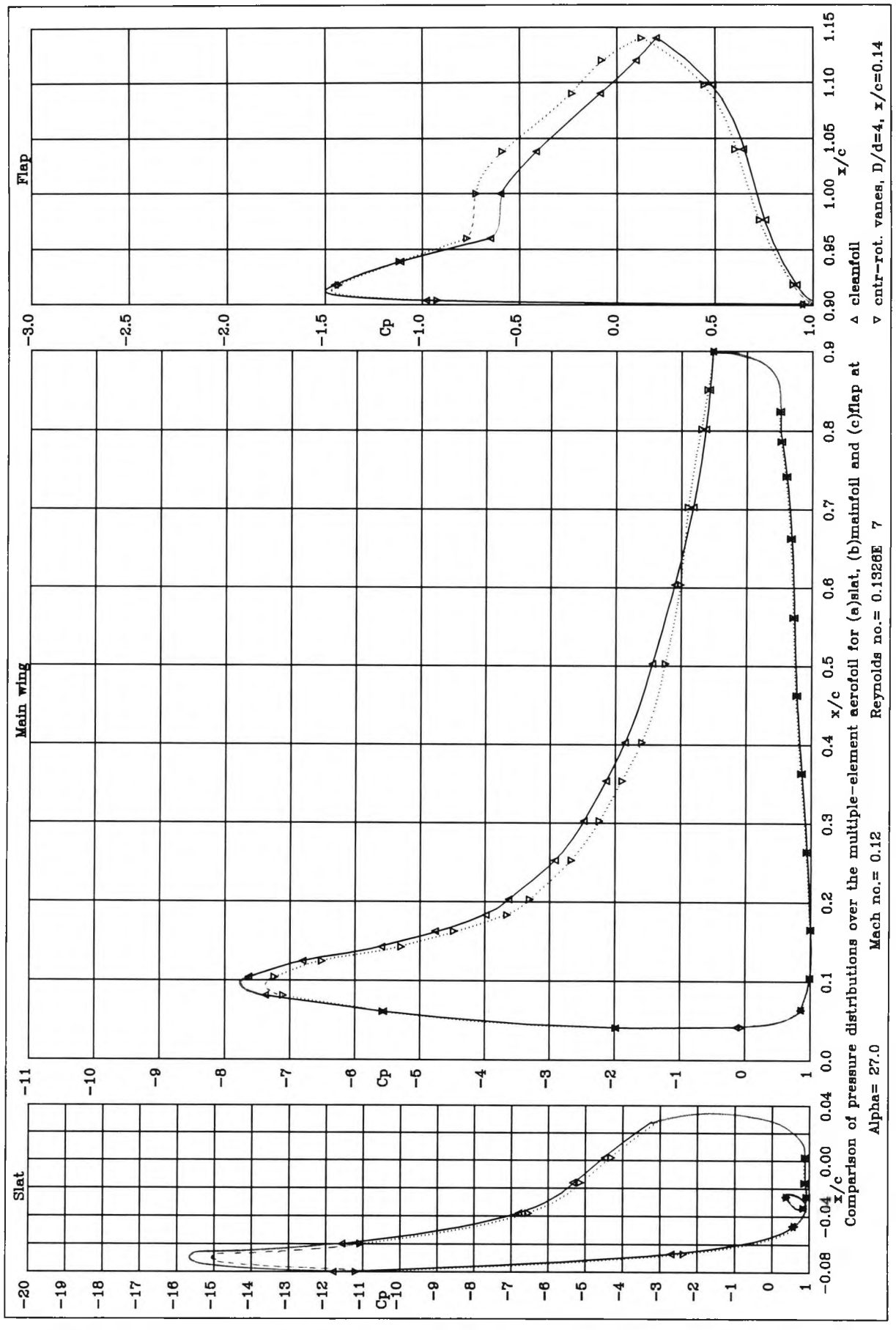

Figure 6.24 : Comparison of pressure distributions at $\alpha = 27°$ obtained with and without counter- rotating vane vortex generators at x/c = 0.14

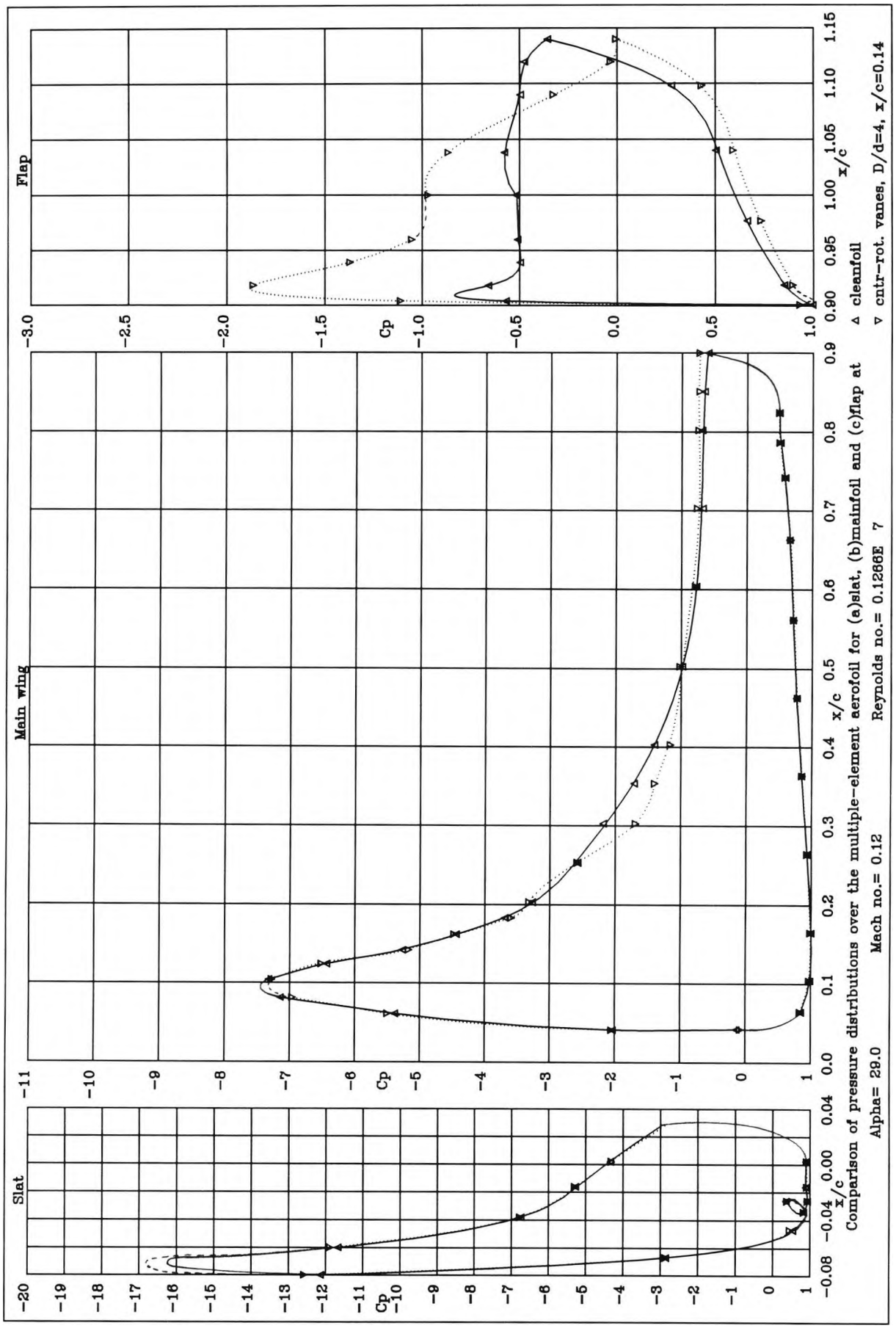

Figure 6.25 : Comparison of pressure distributions at $\alpha = 29°$ obtained with and without counter-rotating vane vortex generators at x/c = 0.14

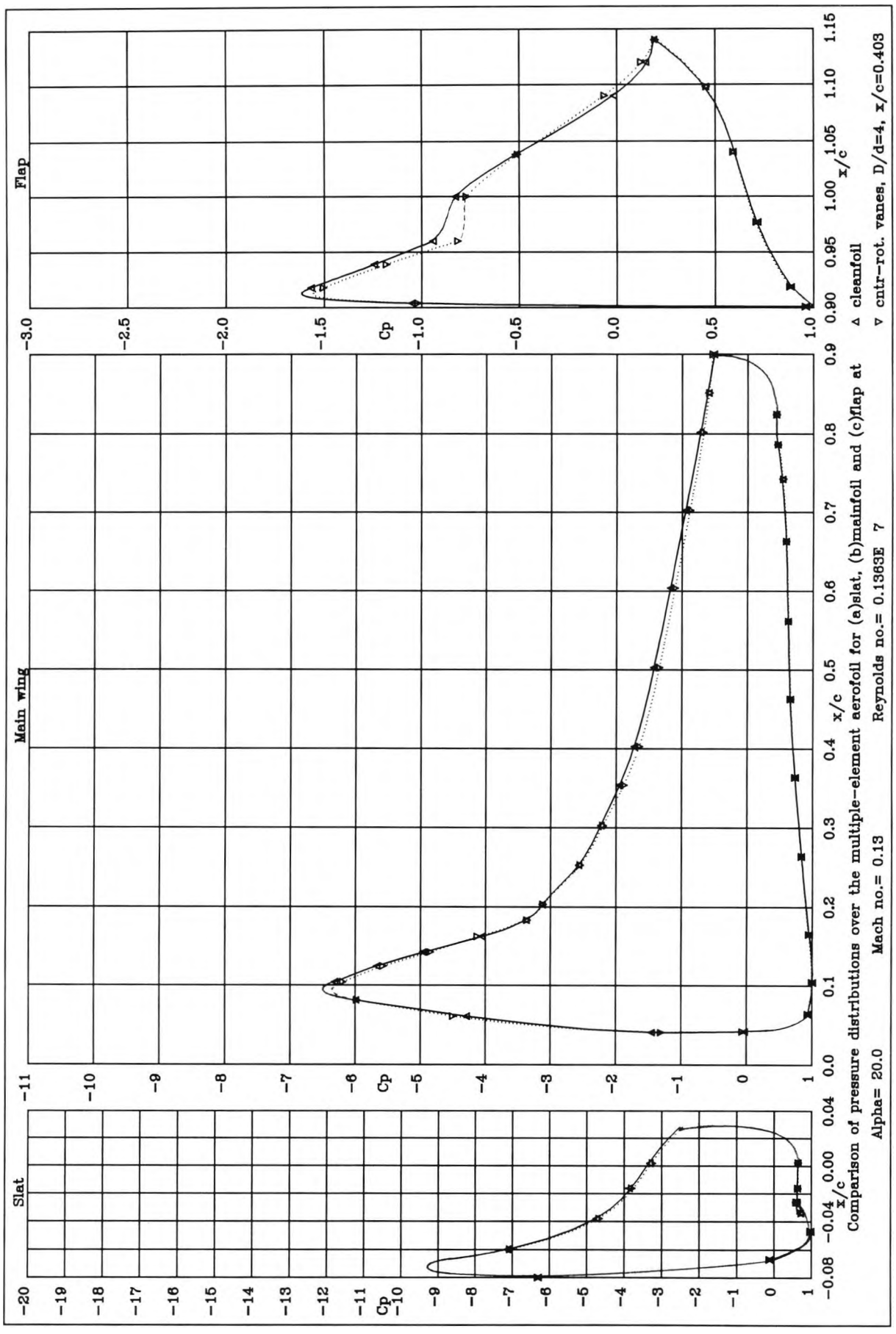

Figure 6.26 : Comparison of pressure distributions at $\alpha = 20°$ obtained with and without counter-rotating vane vortex generators at x/c = 0.403

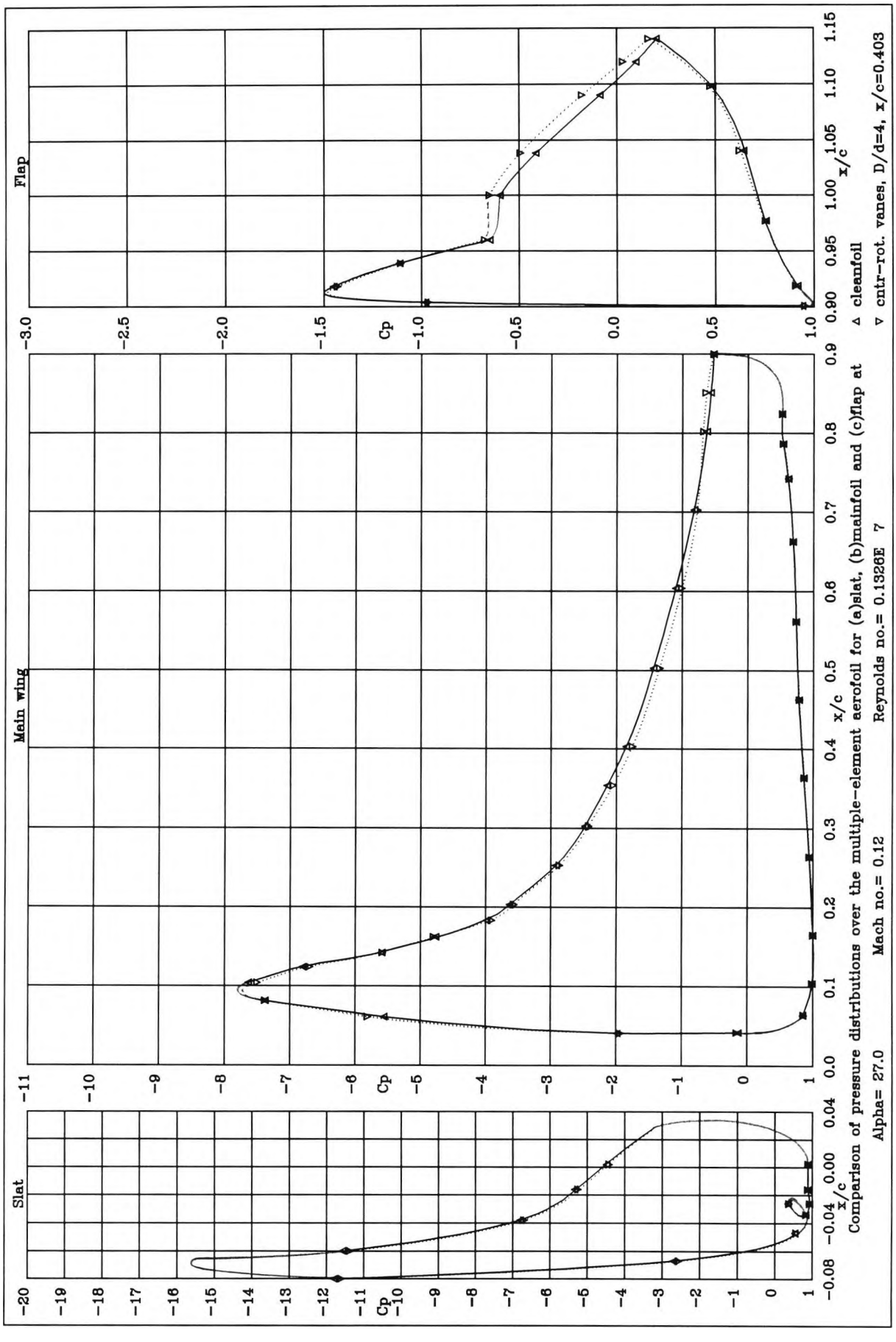

Figure 6.27 : Comparison of pressure distributions at $\alpha = 27°$ obtained with and without counter-rotating vane vortex generators at $x/c = 0.403$

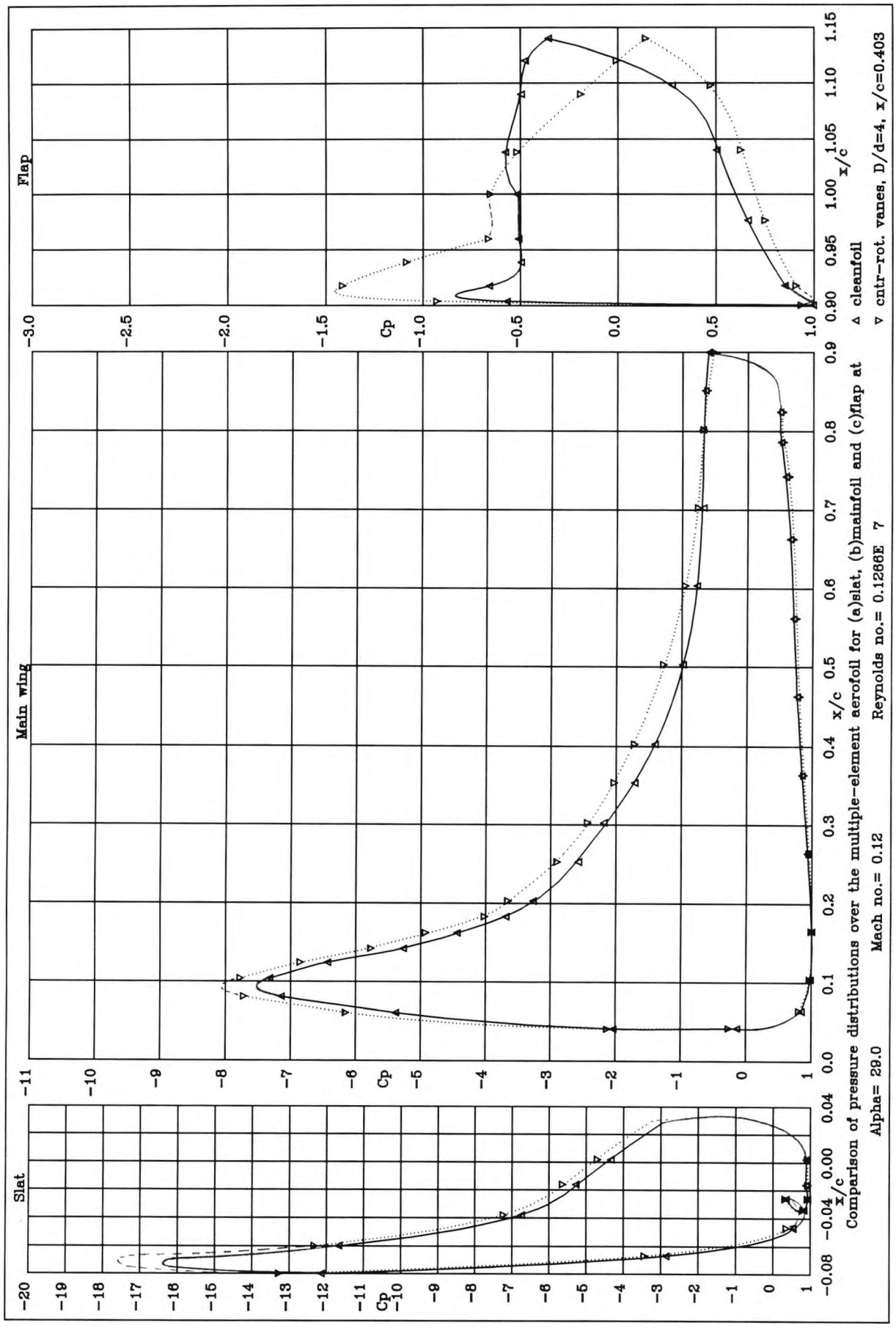

Figure 6.28 : Comparison of pressure distributions at $\alpha = 29°$ obtained with and without counter-rotating vane vortex generators at x/c = 0.403

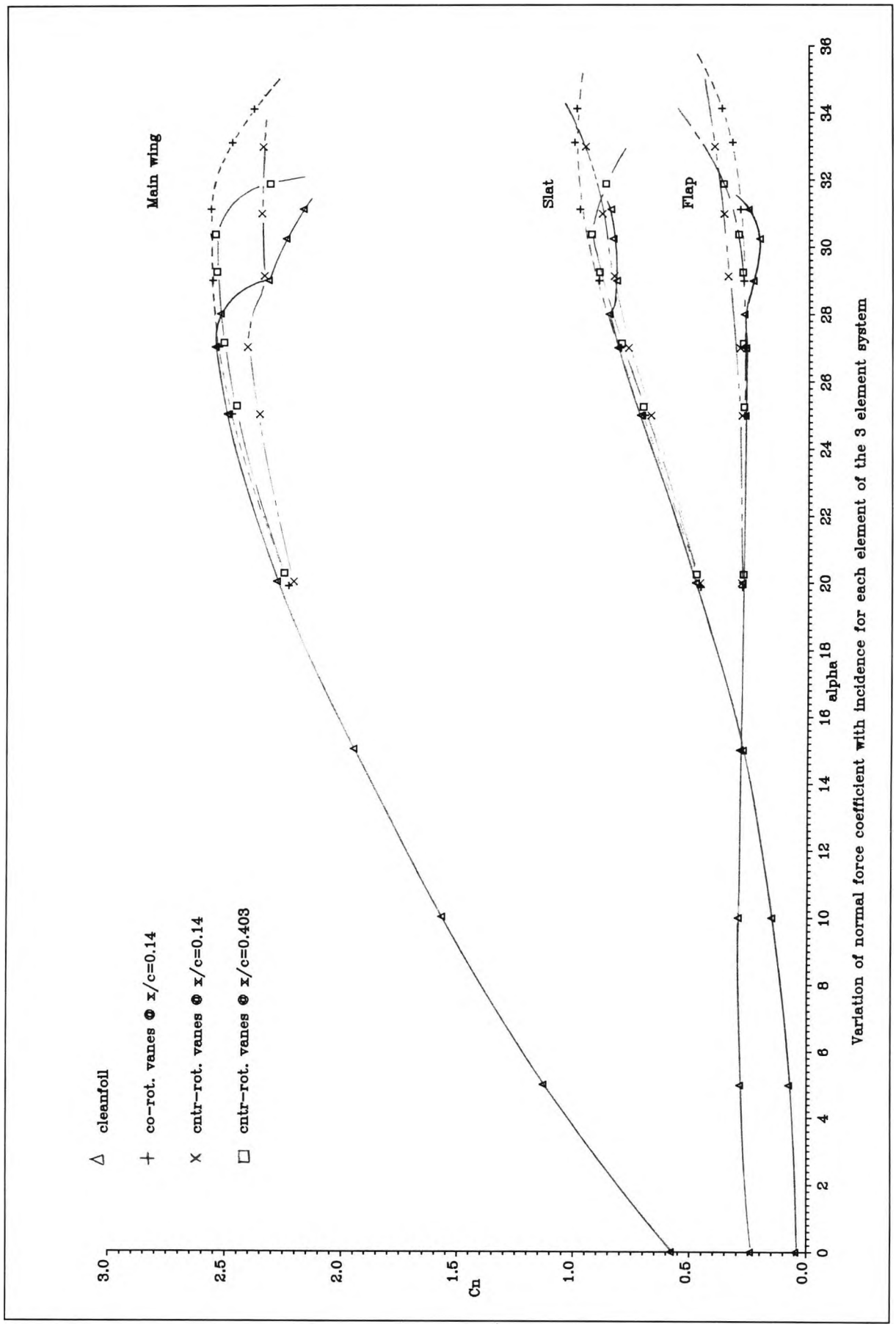

Figure 6.29 : Variation of C_n with α for each element of the 3 element system with and without vane vortex generators

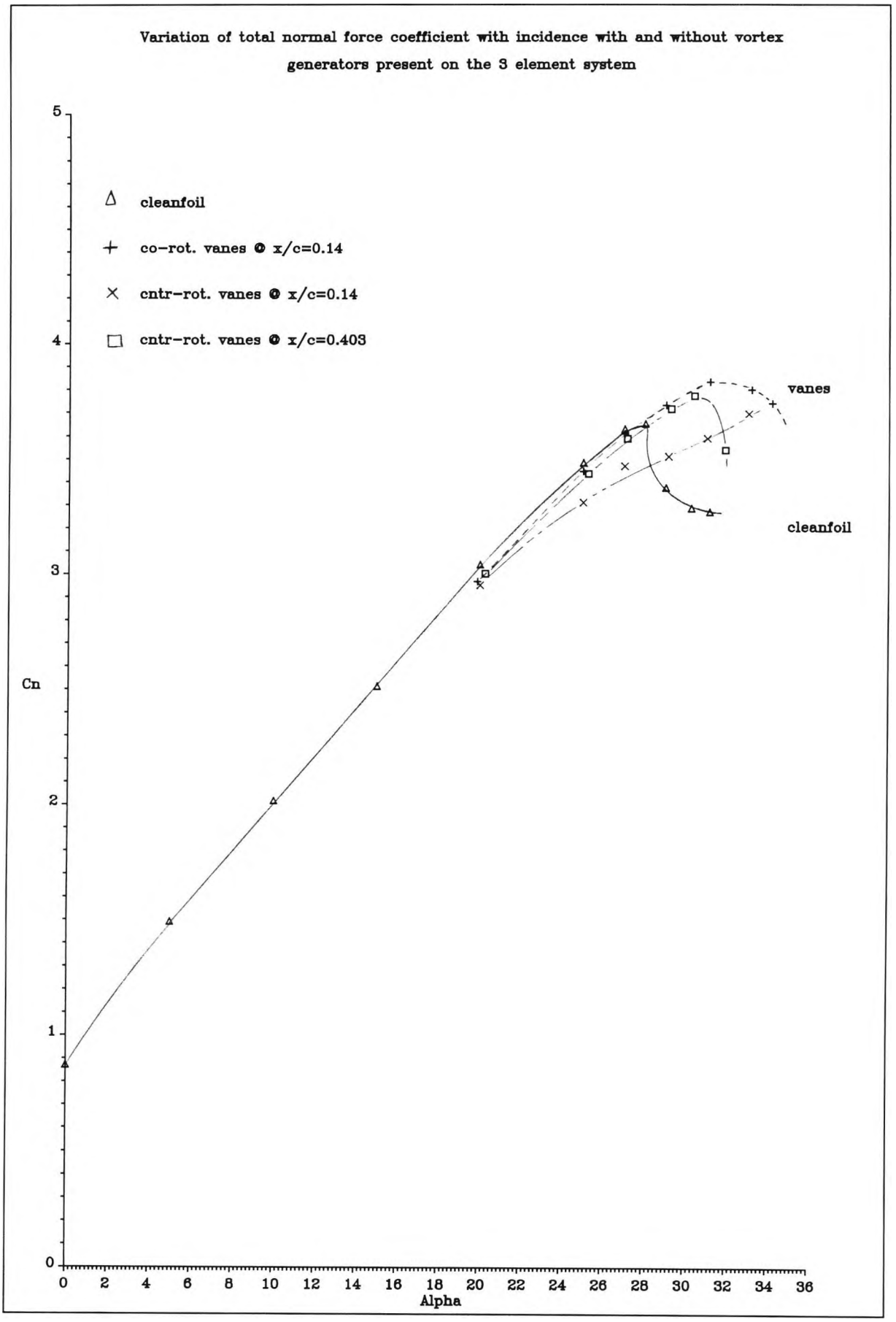

Figure 6.30 : Variation of total C_n with α with and without vane vortex generators present on the 3 element system

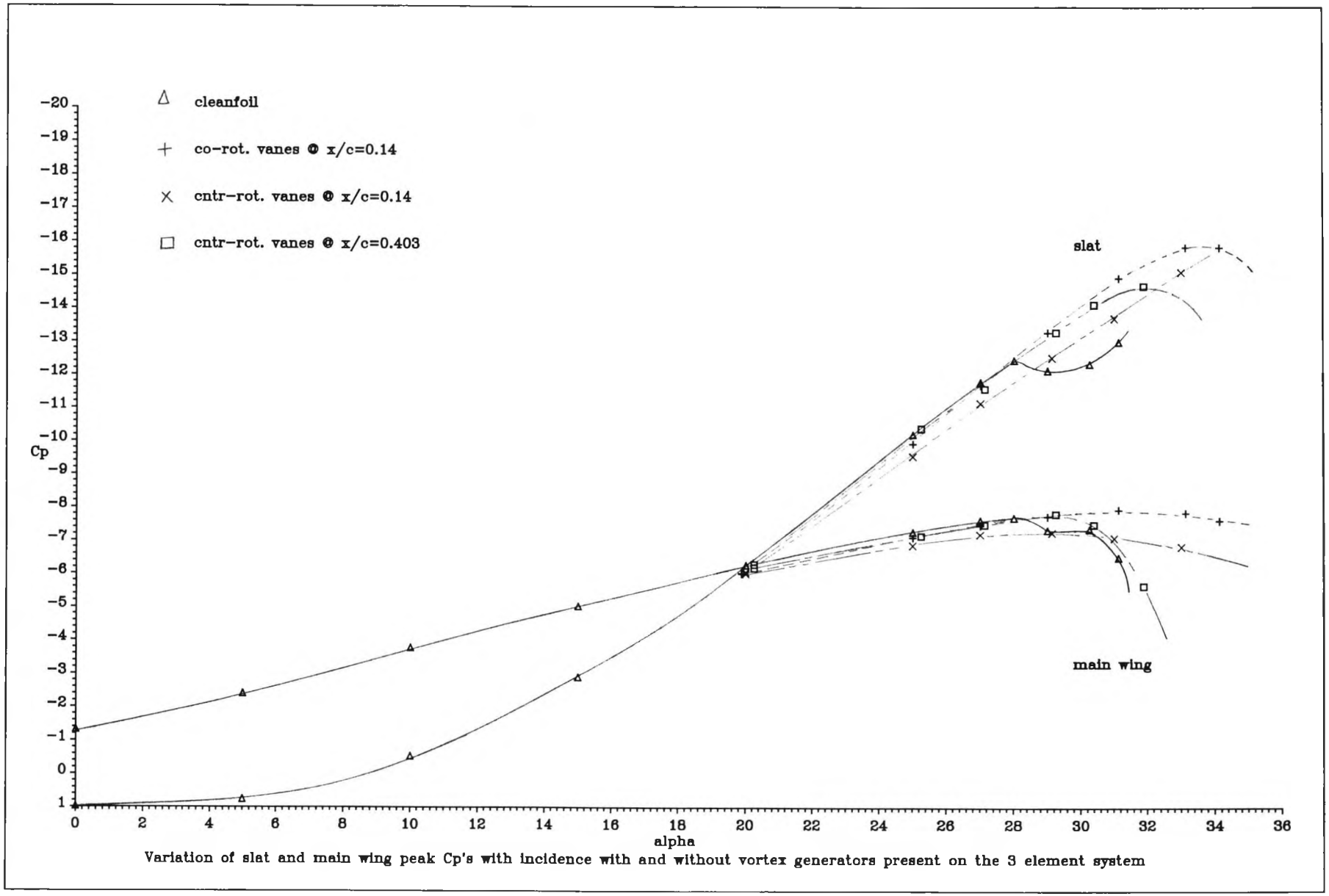

Figure 6.31 : Variation of slat & main wing peak C_p's with α with and without vane vortex generators present on the 3 element system

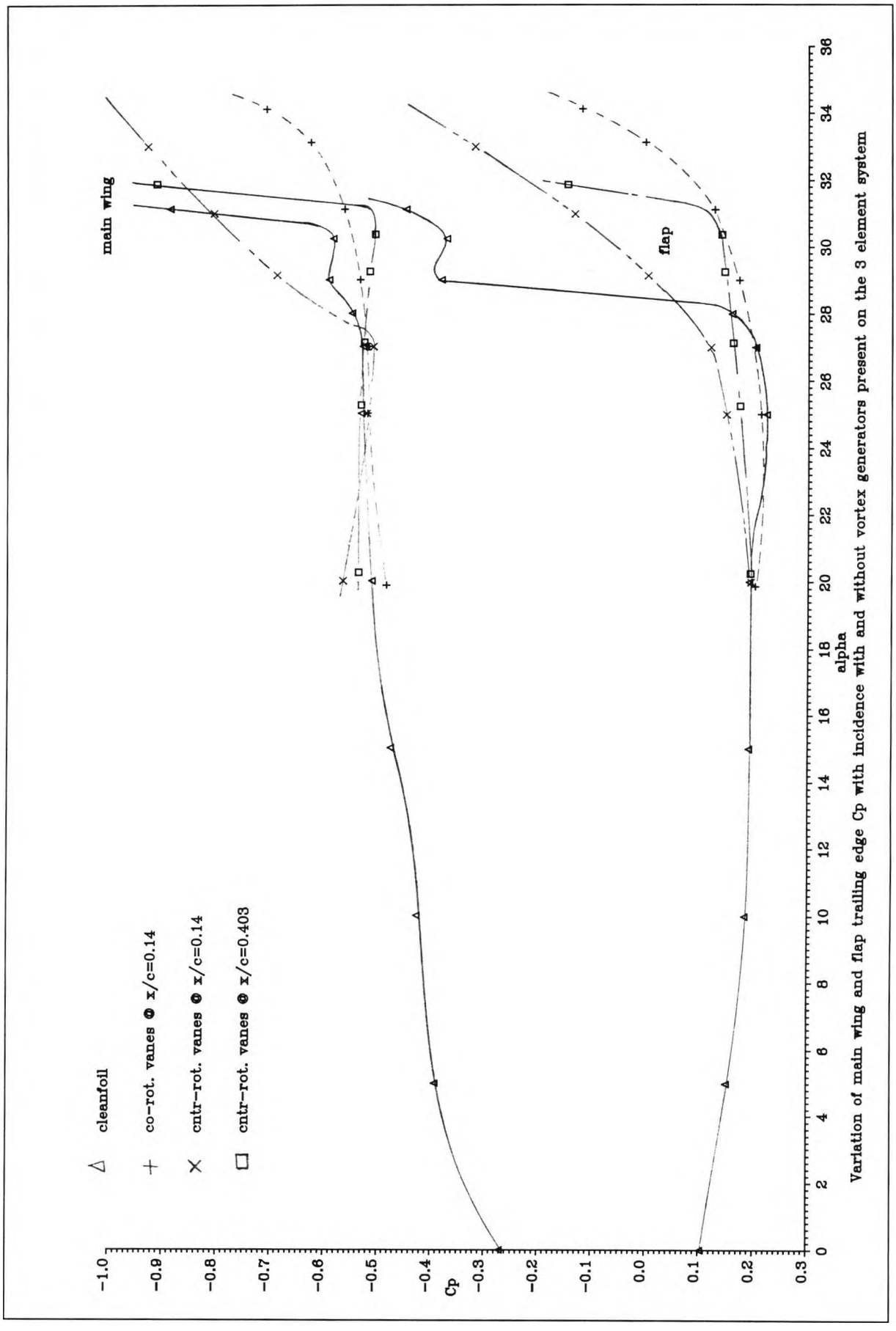

Figure 6.32 : Variation of main wing & flap trailing edge C_p's with α with and without vane vortex generators present on the 3 element system

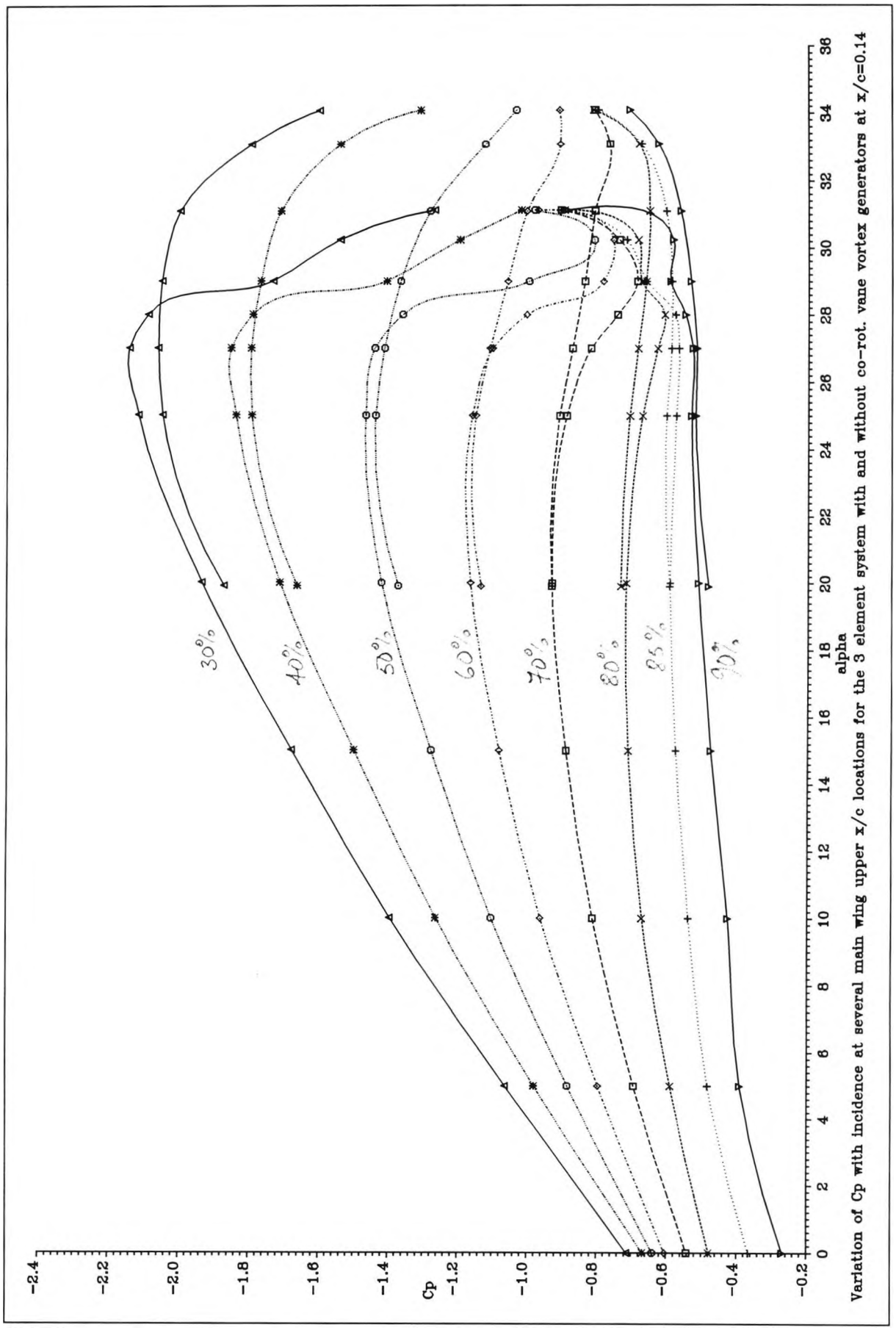

Figure 6.33 : Variation of static C_p with incidence at several x/c positions on the main wing upper surface with and without co-rot. vane vortex generators at x/c = 0.14

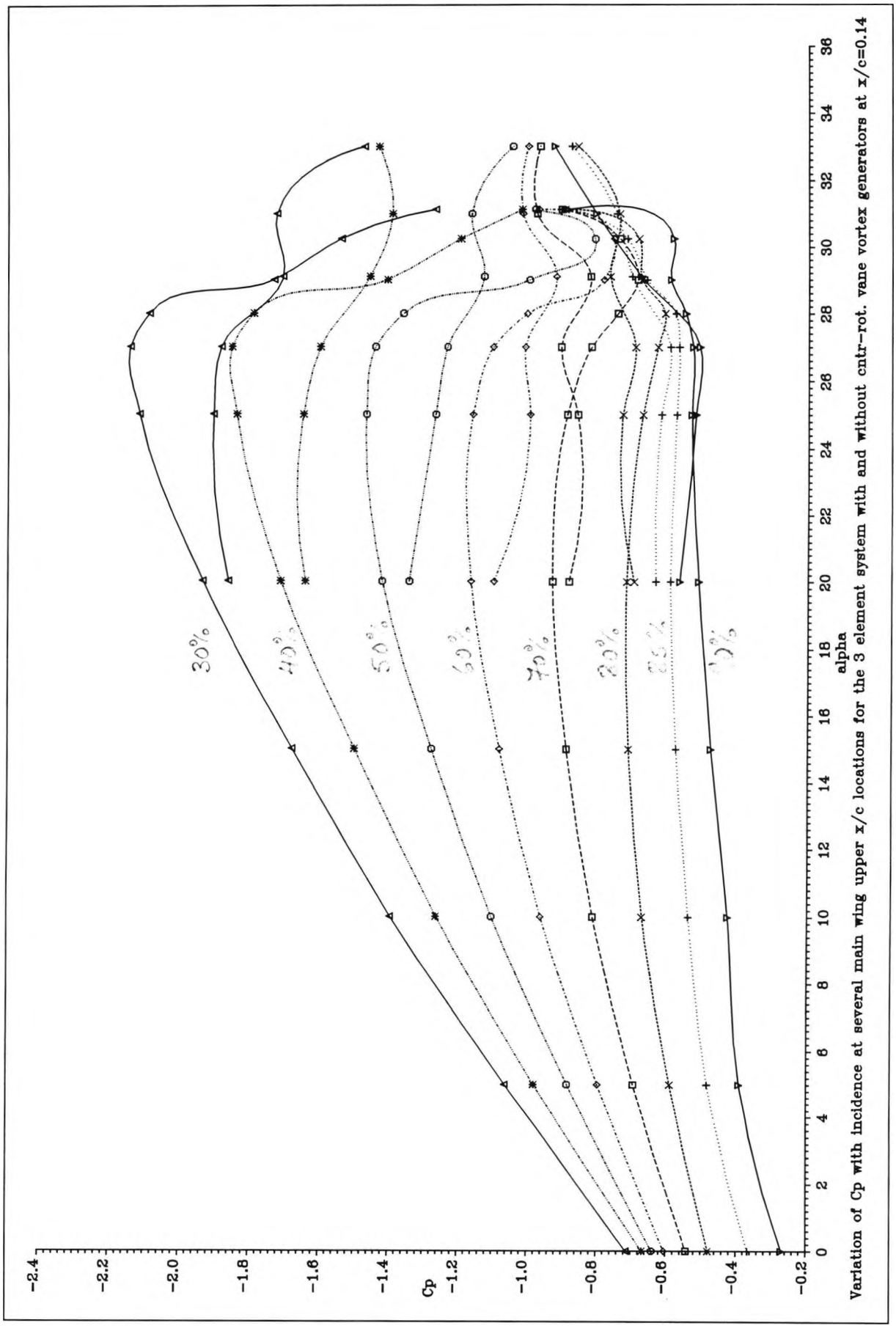

Figure 6.34 : Variation of static C_p with incidence at several x/c positions on the main wing upper surface with and without cntr-rot. vane vortex generators at x/c = 0.14

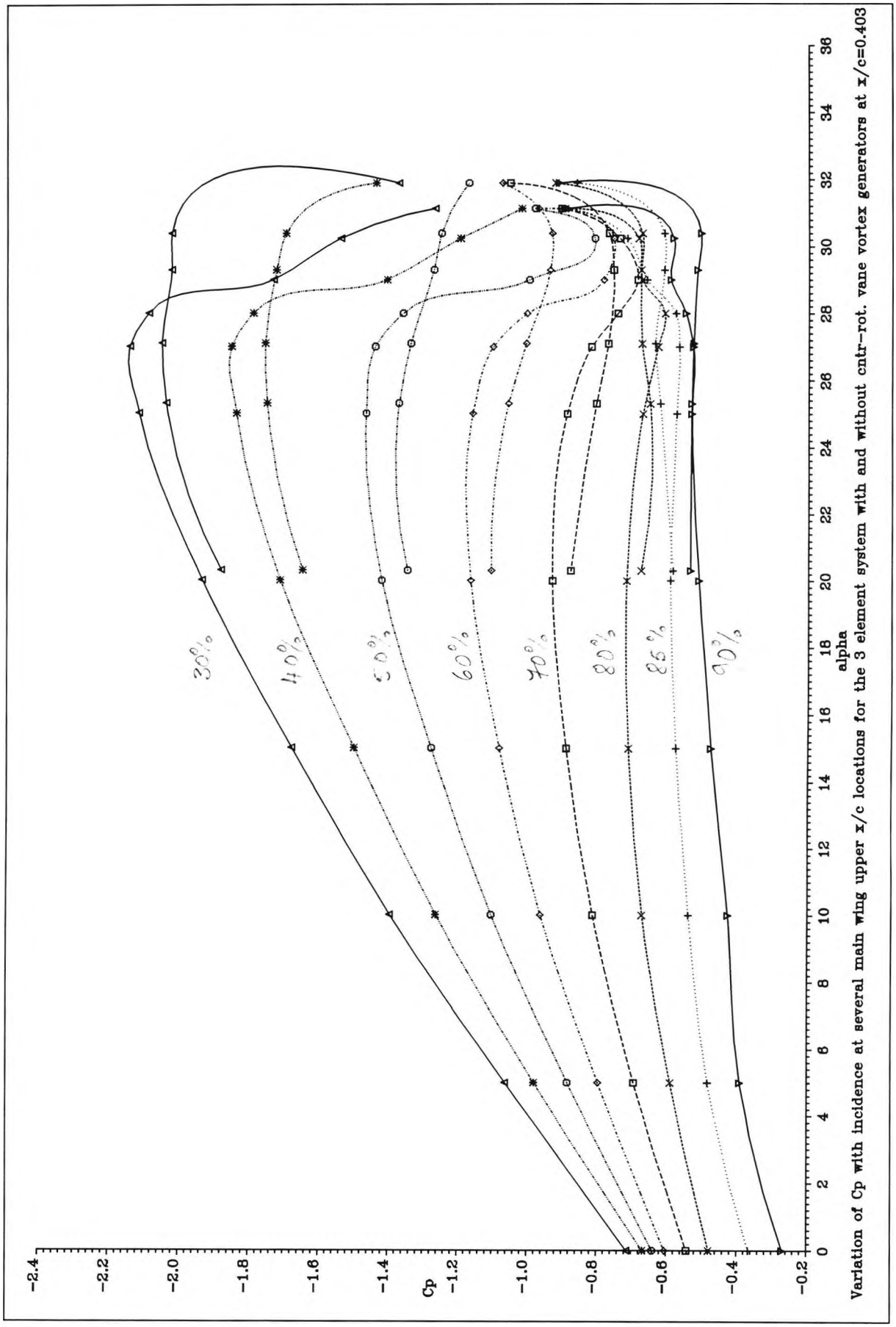

Figure 6.35 : Variation of static C_p with incidence at several x/c positions on the main wing upper surface with and without cntr-rot. vane vortex generators at x/c = 0.403

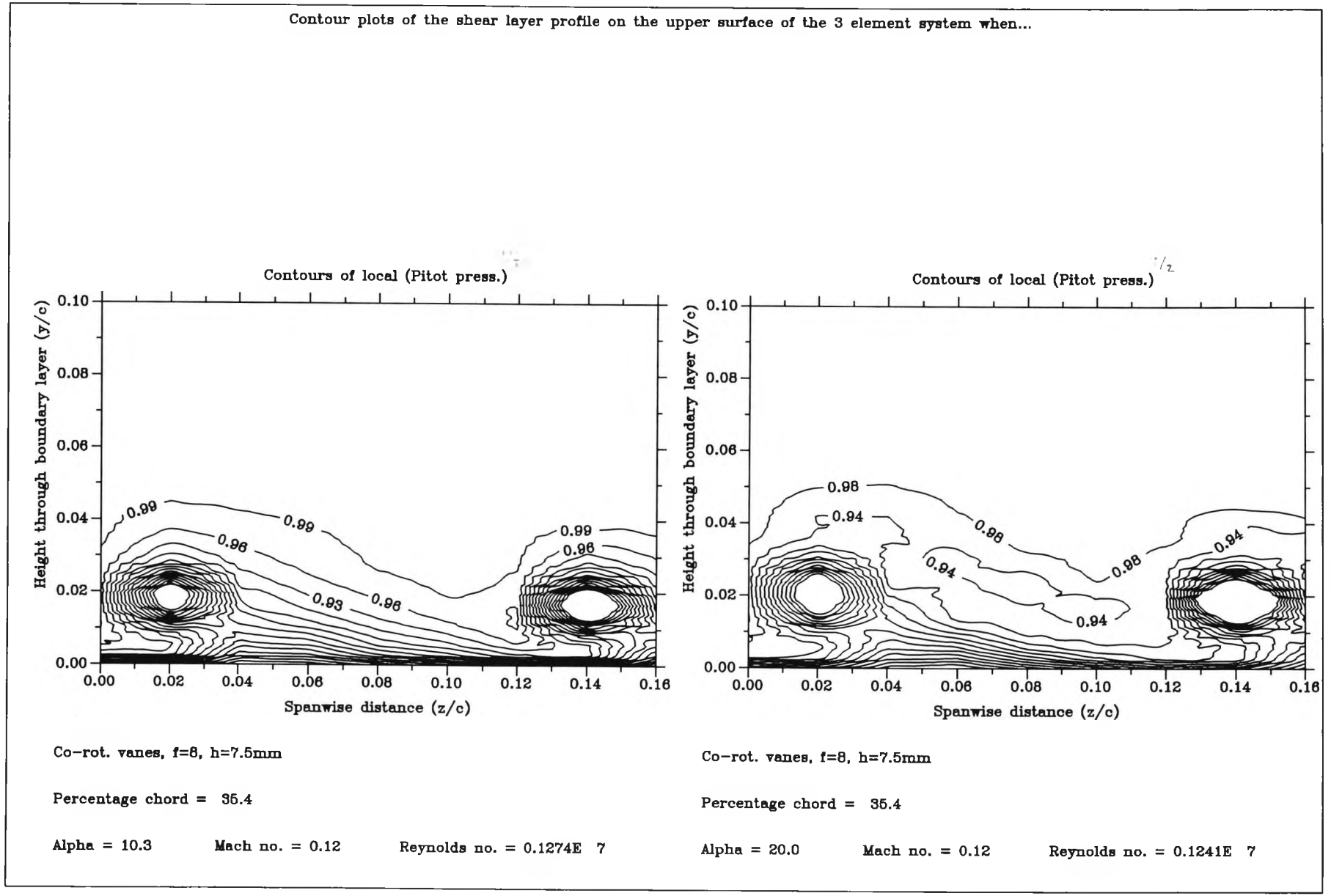

Figure 6.36 : Contour plots of the shear layer structure above the main wing at x/c = 0.354 for $\alpha = 10^{\circ}$ & 20° when co-rot. vvg's are at x/c = 0.14

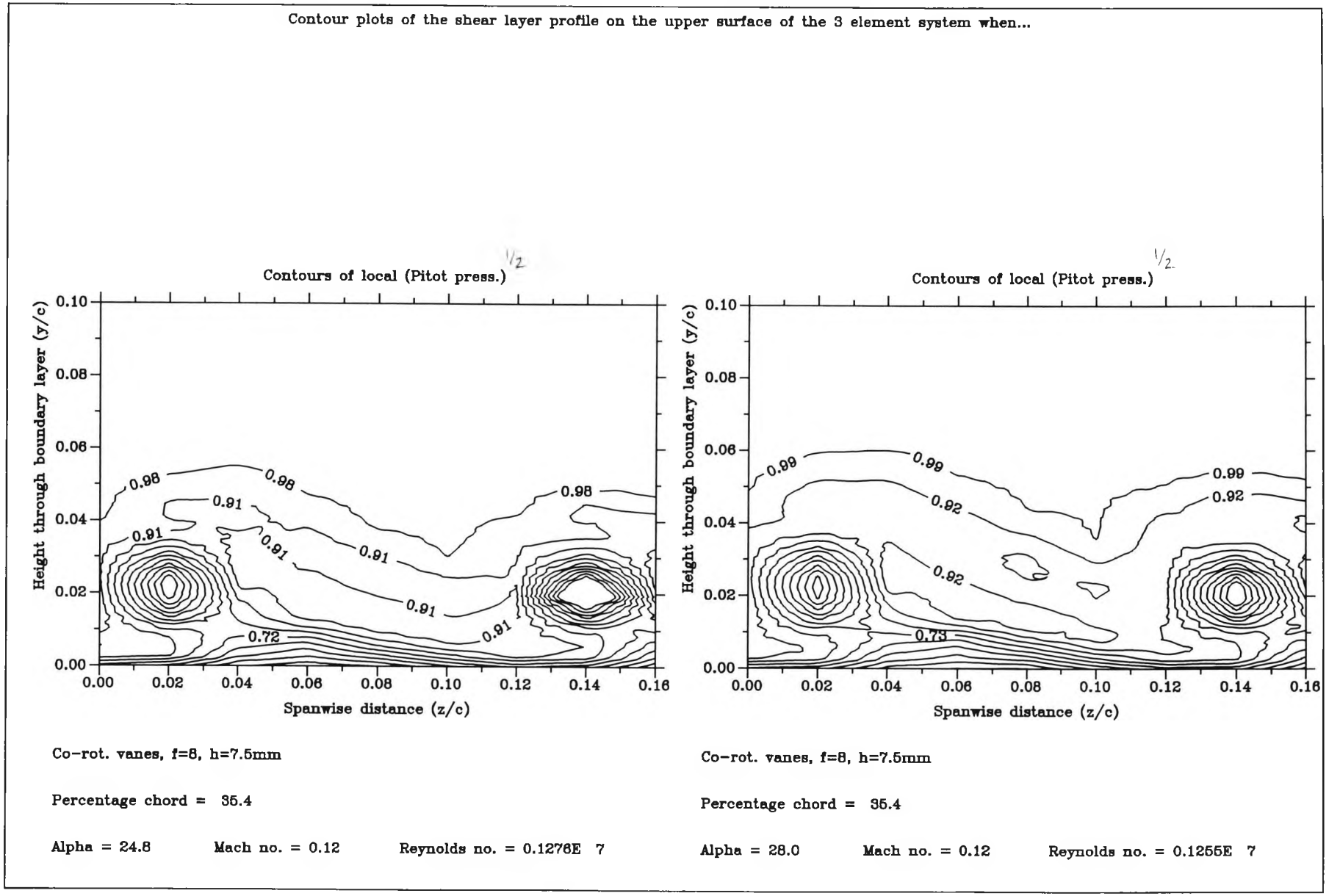

Figure 6.37 : Contour plots of the shear layer structure above the main wing at x/c = 0.354 for $\alpha = 25°$ & $28°$ when co-rot. vvg's are at x/c = 0.14

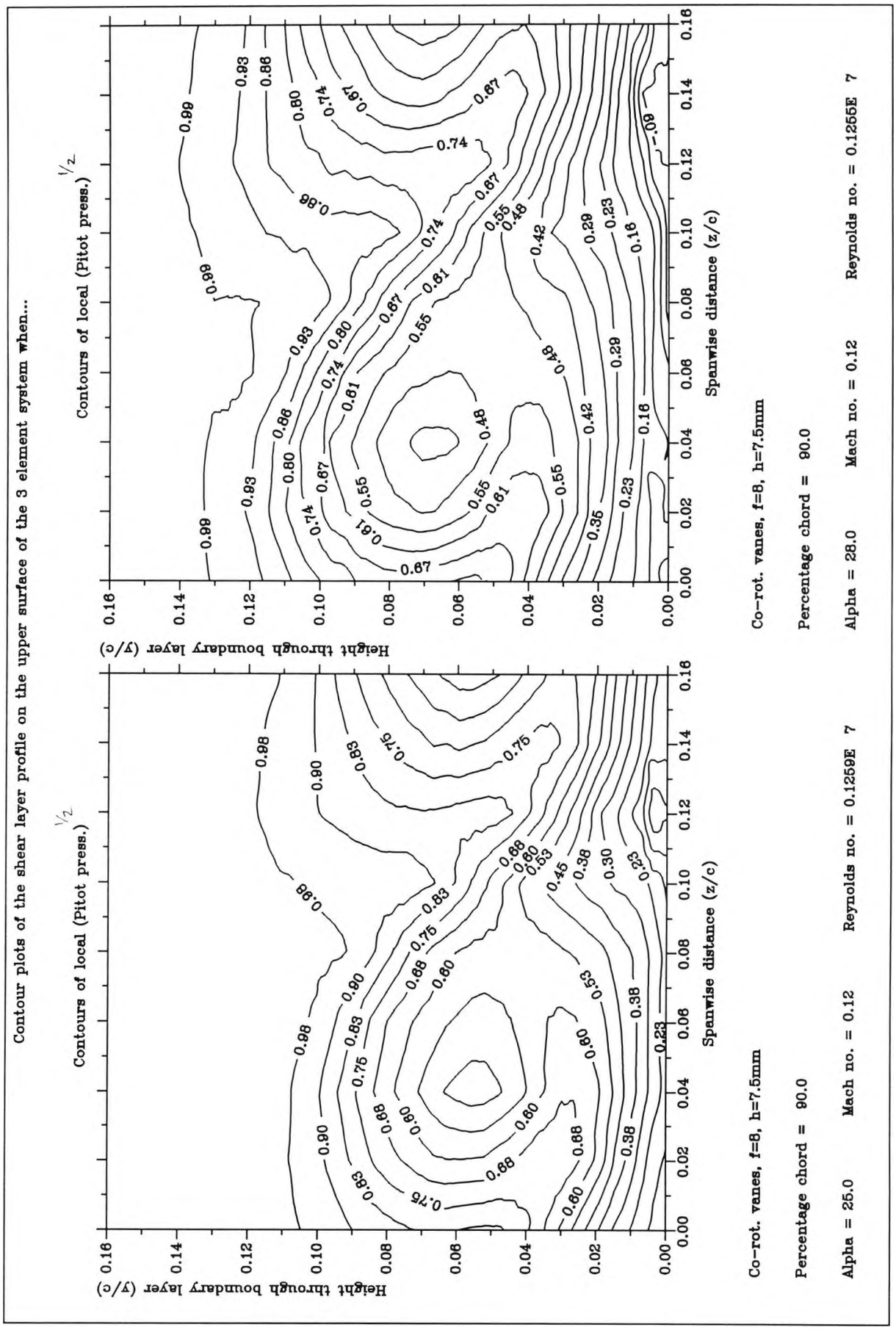

Figure 6.38 : Contour plots of the shear layer structure above the main wing at x/c = 0.9 for $\alpha = 25°$ & 28° when co-rot. vvg's are at x/c = 0.14

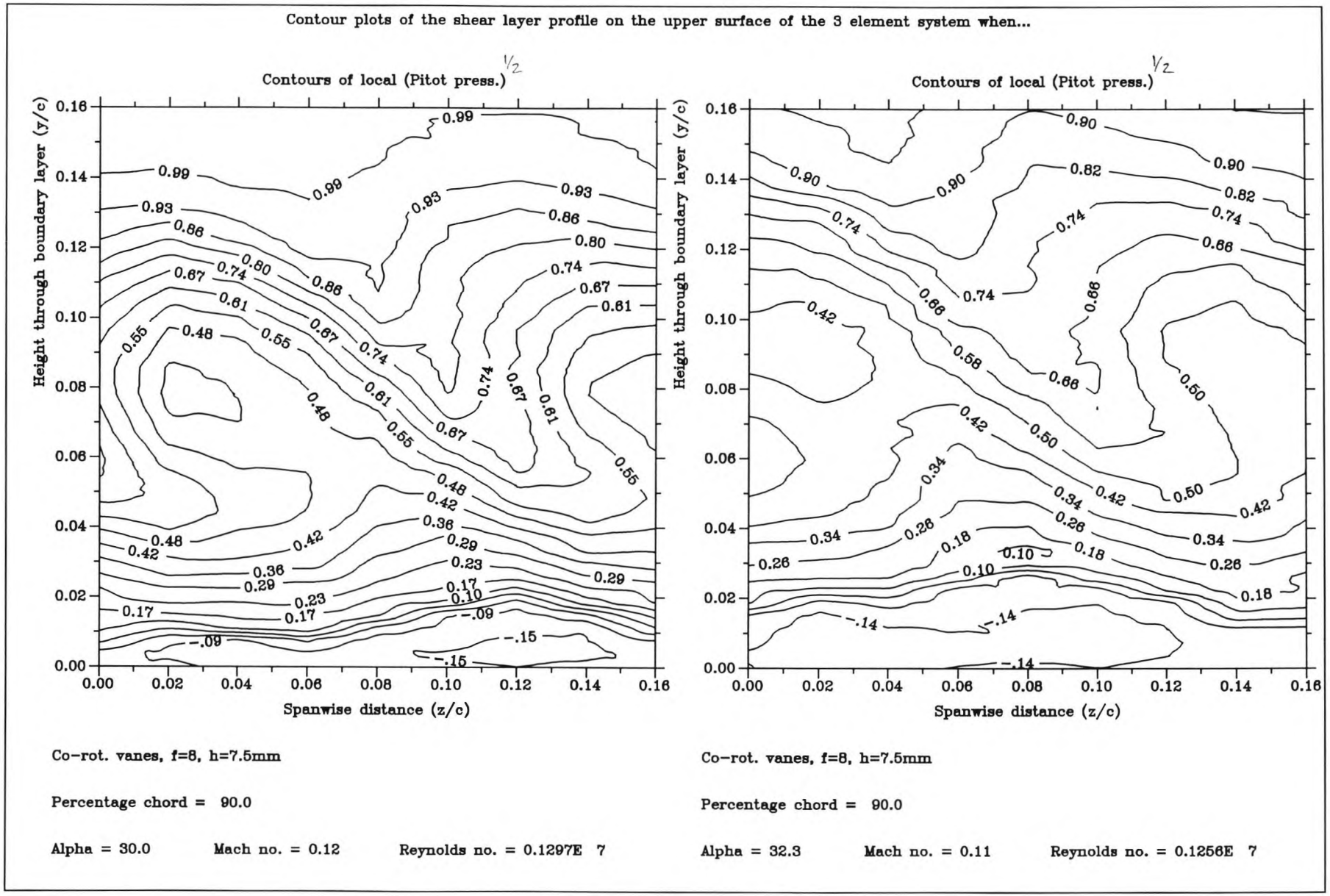

Figure 6.39 : Contour plots of the shear layer structure above the main wing at x/c = 0.9 for $\alpha = 30°$ & 32° when co-rot. vvg's are at x/c = 0.14

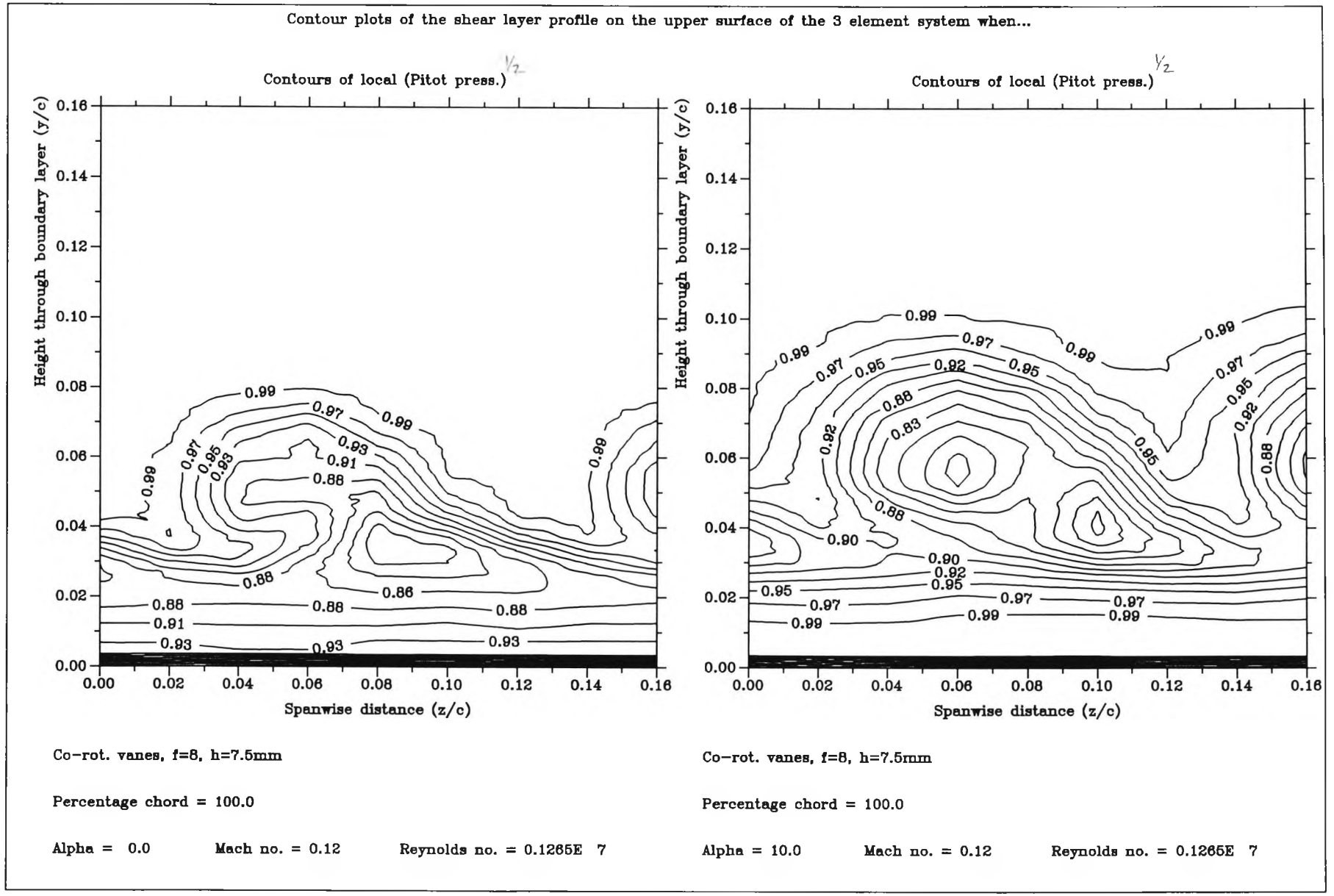

Figure 6.40 : Contour plots of the shear layer structure above the flap at x/c = 1.0 for $\alpha = 0°$ & 10° when co-rot. vvg's are at x/c = 0.14

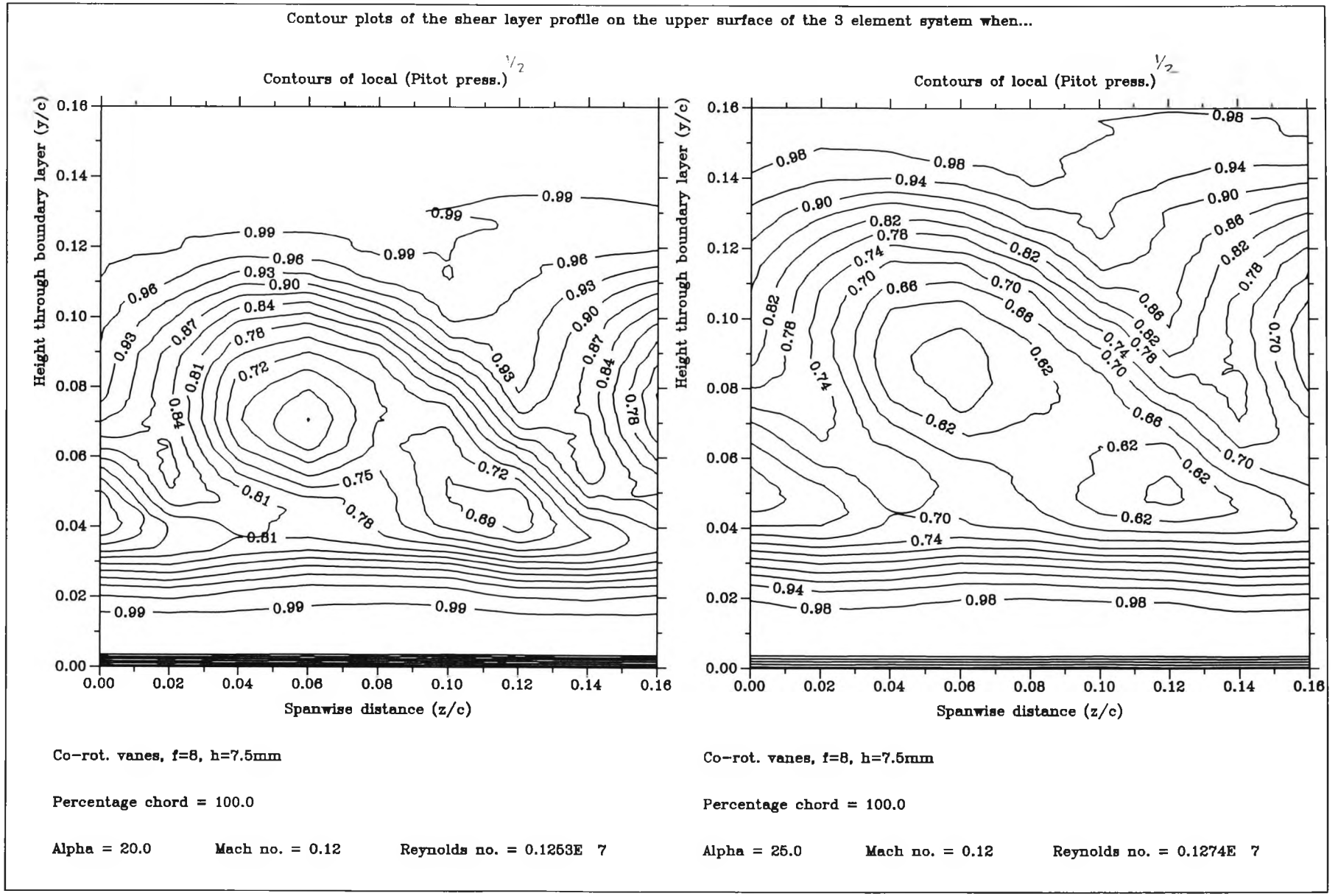

Figure 6.41 : Contour plots of the shear layer structure above the flap at x/c = 1.0 for $\alpha = 20°$ & 25° when co-rot. vvg's are at x/c = 0.14

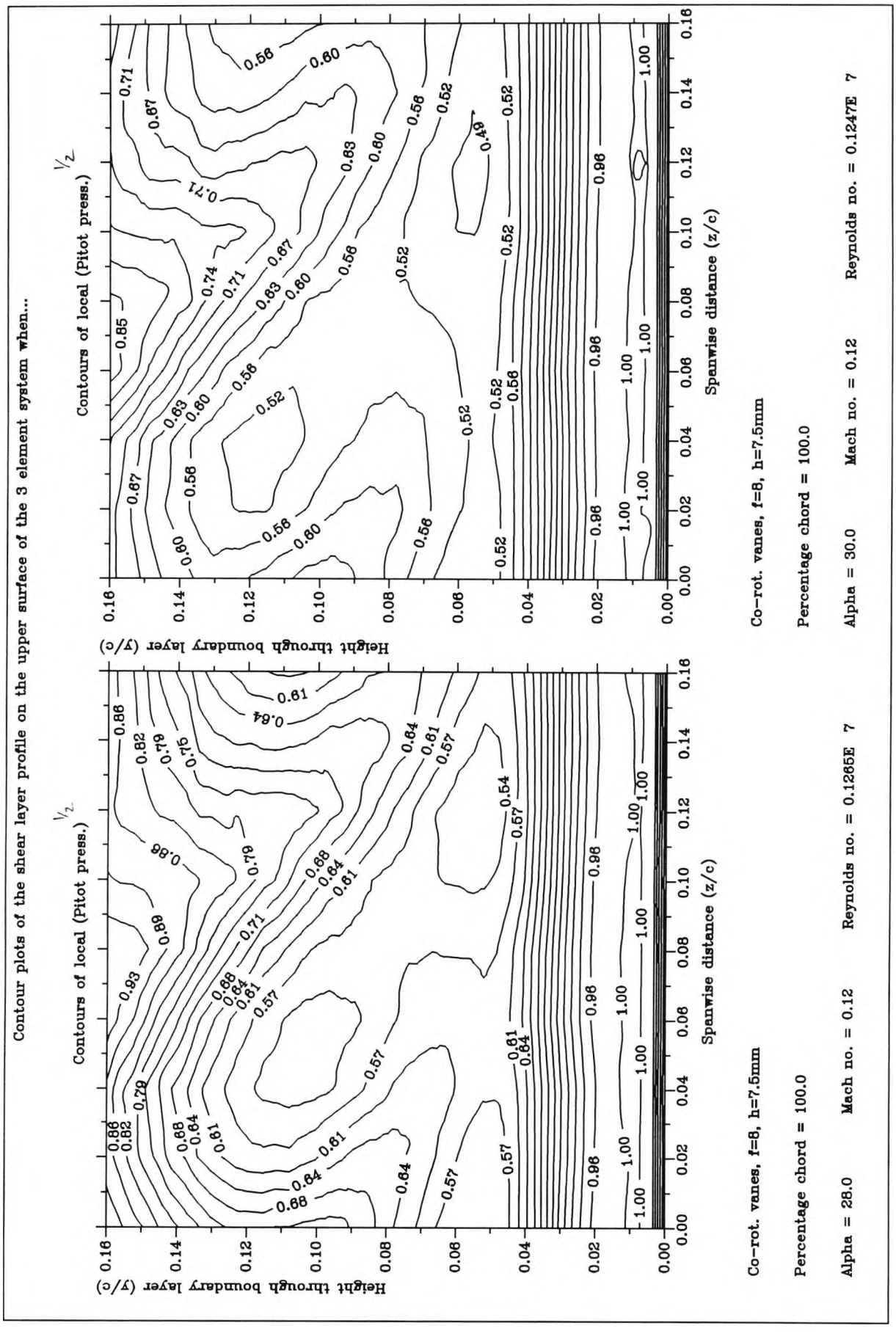

Figure 6.42 : Contour plots of the shear layer structure above the flap at x/c = 1.0 for $\alpha = 28°$ & 30° when co-rot. vvg's are at x/c = 0.14

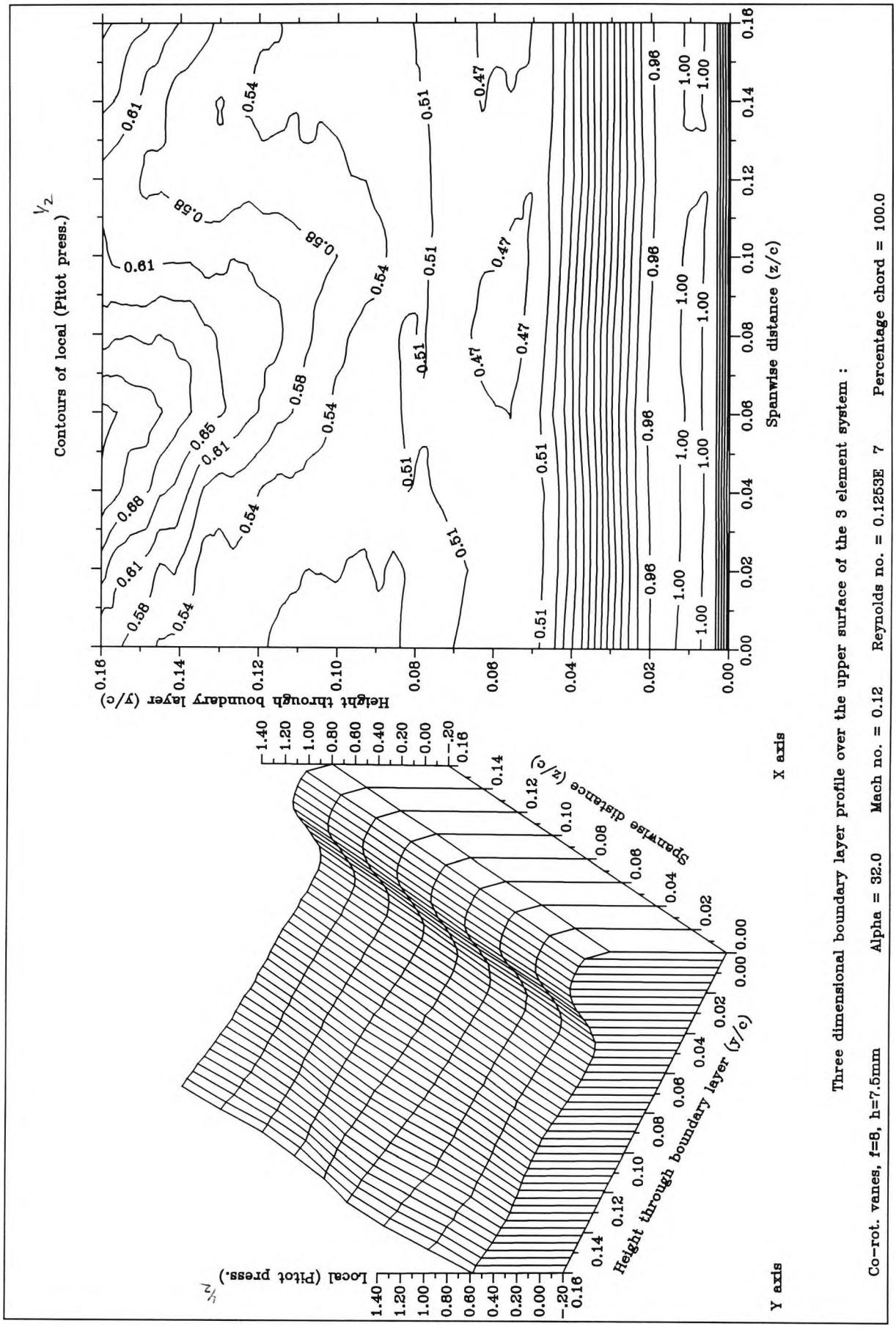

Figure 6.43 : Contour plot of the shear layer structure above the flap at x/c = 1.0 for $\alpha = 32°$ when co-rot. vvg's are at x/c = 0.14

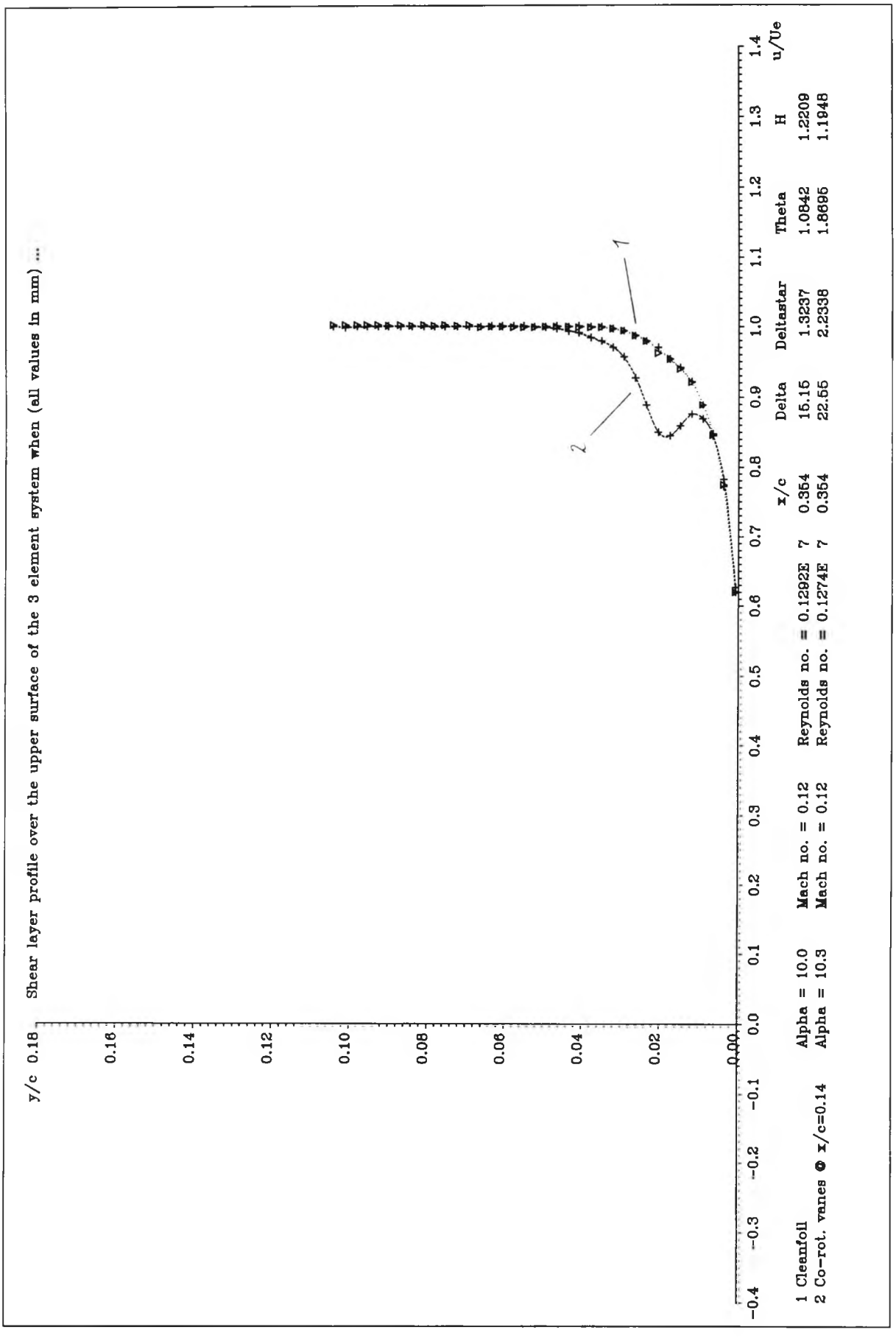

Figure 6.44 : Comparison of mean shear layer profiles at x/c = 0.354, $\alpha = 10°$, obtained with and without co-rot. vanes at x/c = 0.14

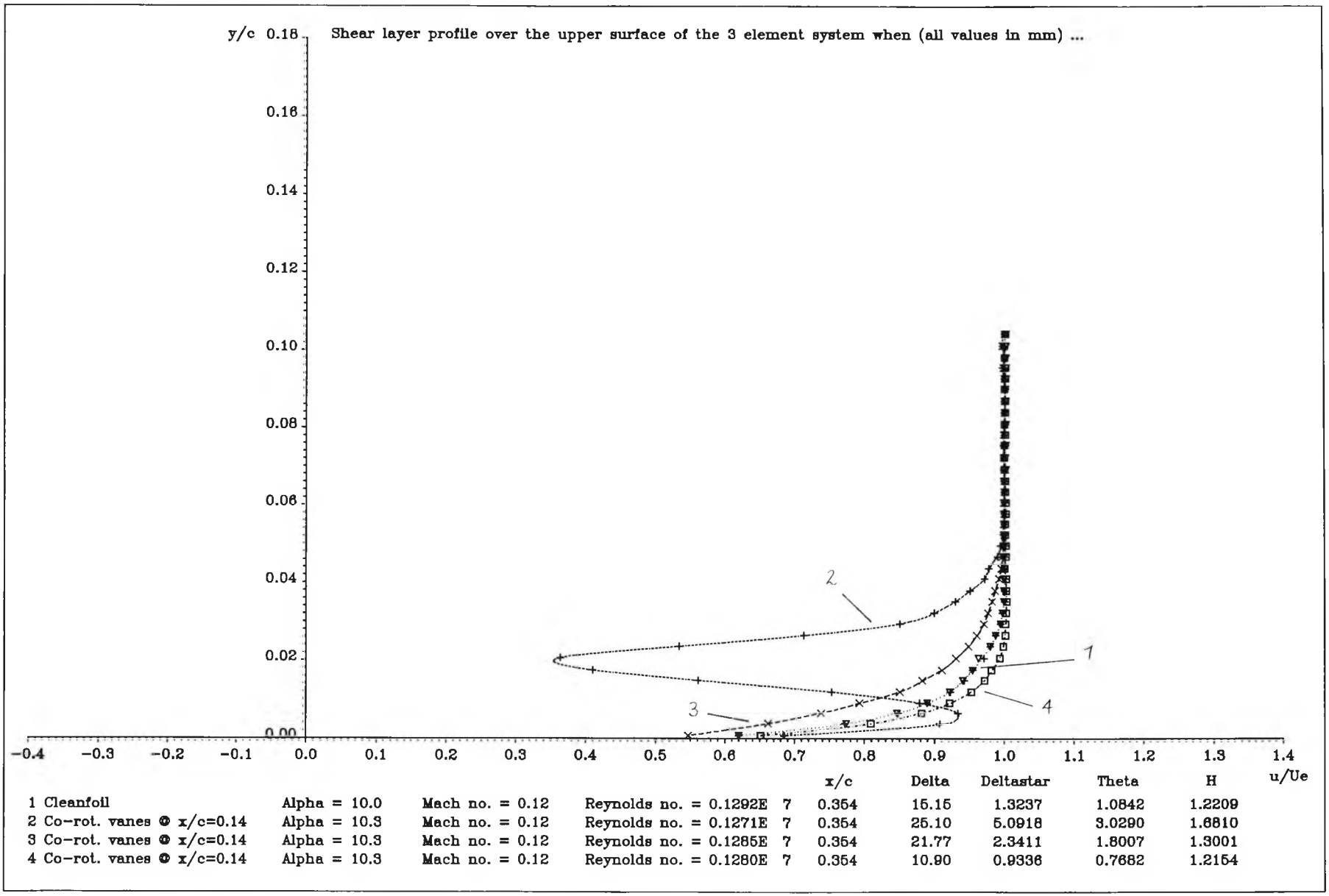

Figure 6.45 : Spanwise variation of shear layer profile at $x/c = 0.354$, $\alpha = 10°$, obtained when co-rot. vanes are at $x/c = 0.14$

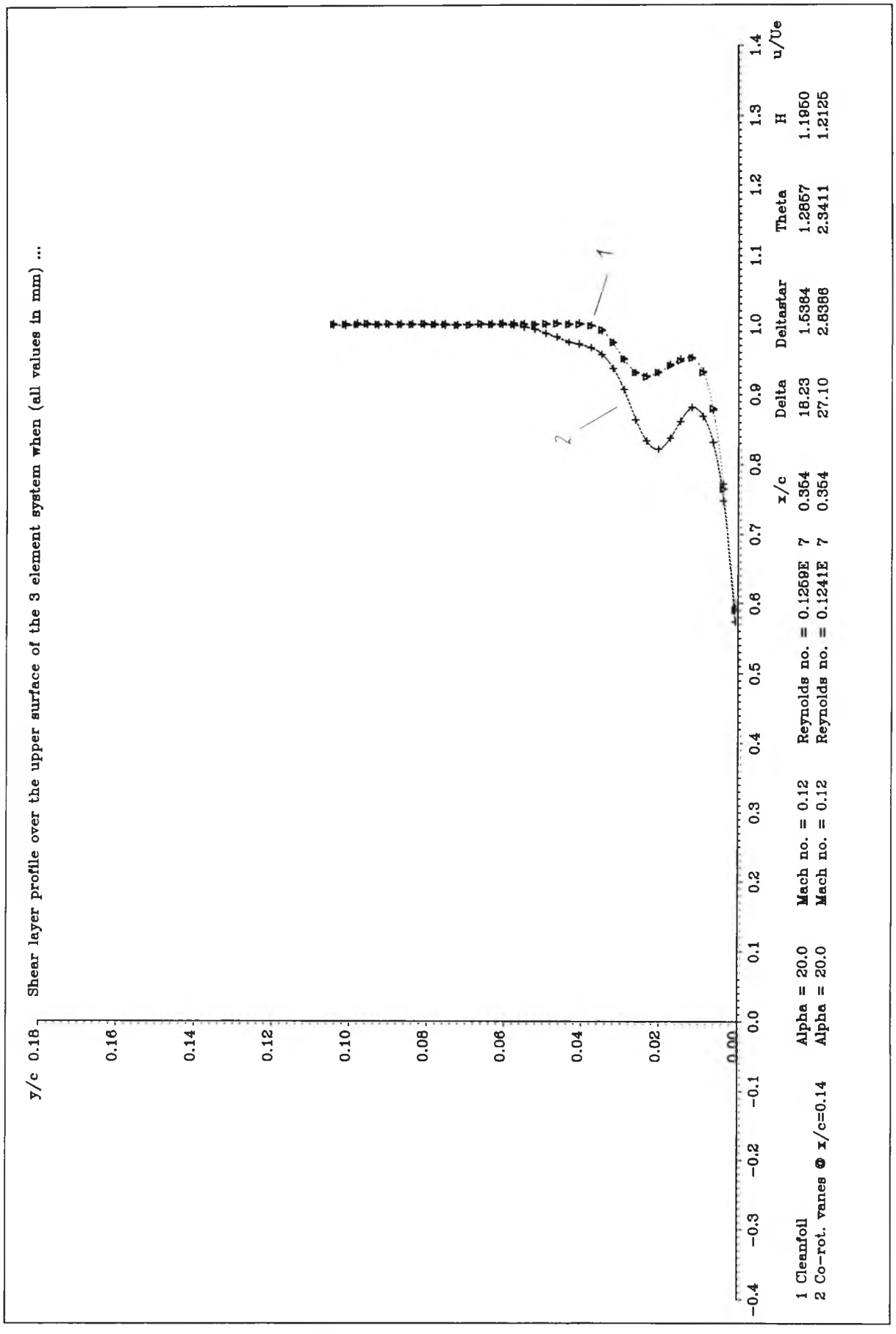

Figure 6.46 : Comparison of mean shear layer profiles at x/c = 0.354, $\alpha = 20°$, obtained with and without co-rot. vanes at x/c = 0.14

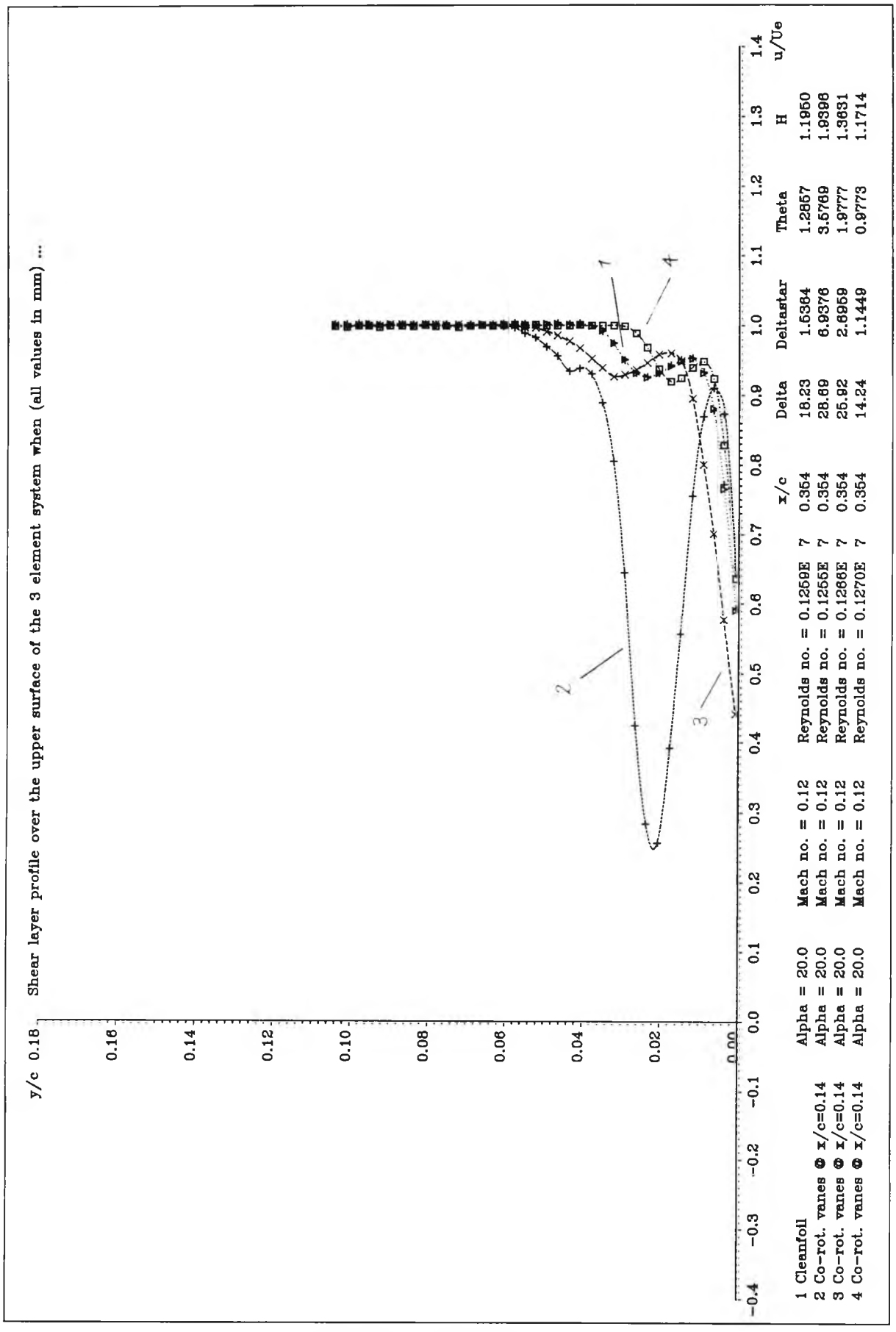

Figure 6.47 : Spanwise variation of shear layer profile at x/c = 0.354, $\alpha = 20°$, obtained when co-rot. vanes are at x/c = 0.14

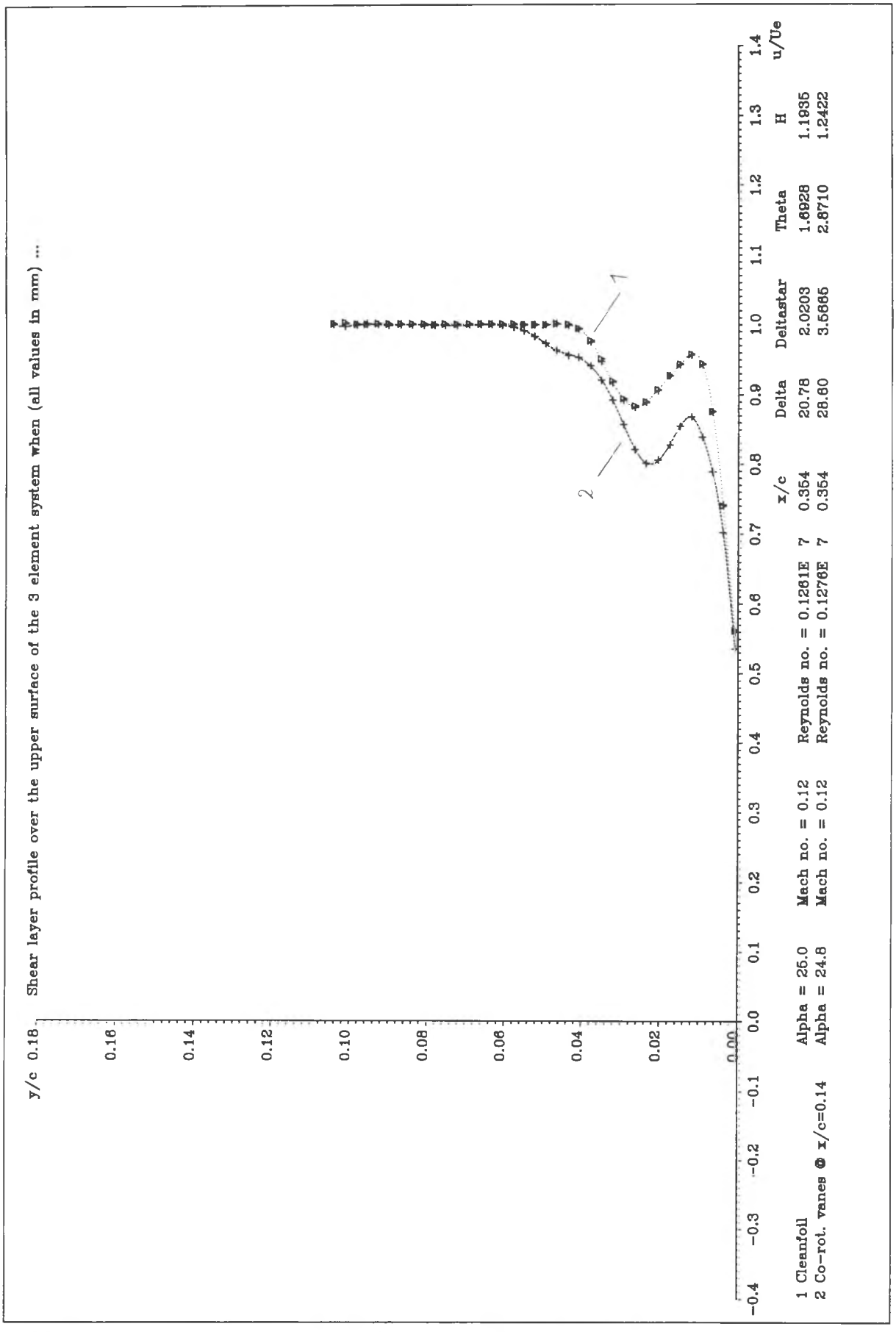

Figure 6.48 : Comparison of mean shear layer profiles at x/c = 0.354, $\alpha = 25°$, obtained with and without co-rot. vanes at x/c = 0.14

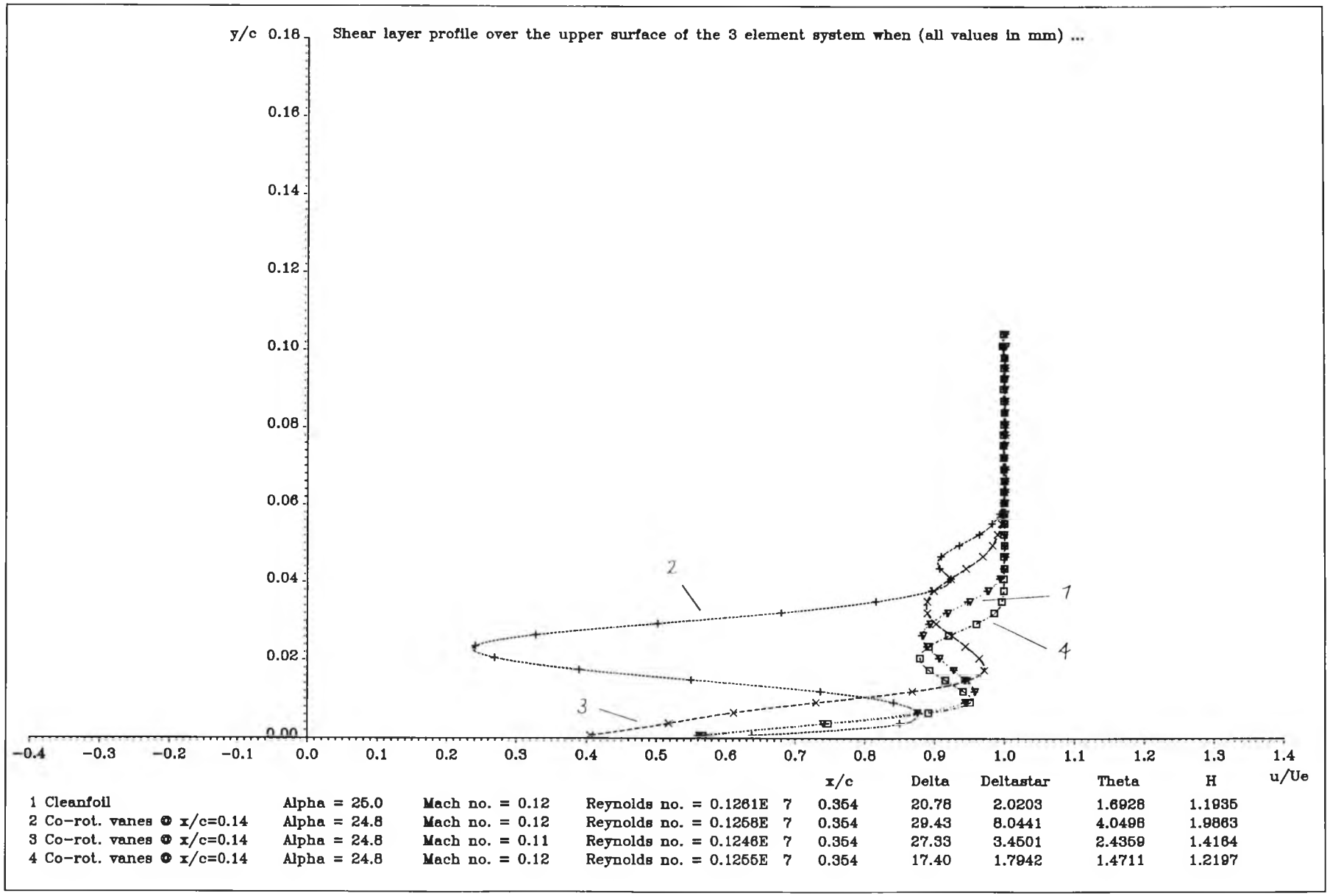

Figure 6.49 : Spanwise variation of shear layer profile at x/c=0.354, α=25°, obtained when co-rot. vanes are at x/c=0.14

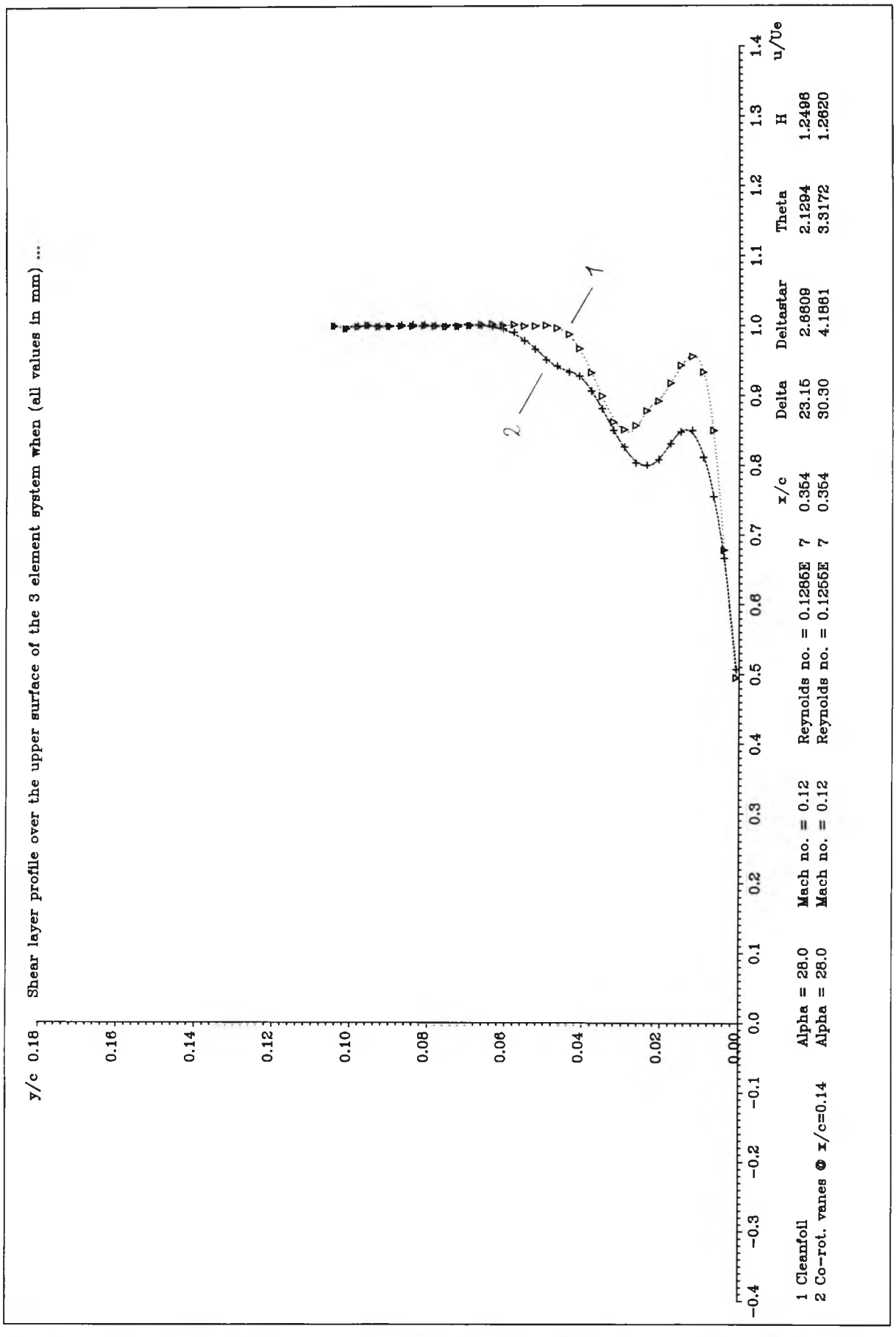

Figure 6.50 : Comparison of mean shear layer profiles at x/c = 0.354, $\alpha = 28°$, obtained with and without co-rot. vanes at x/c = 0.14

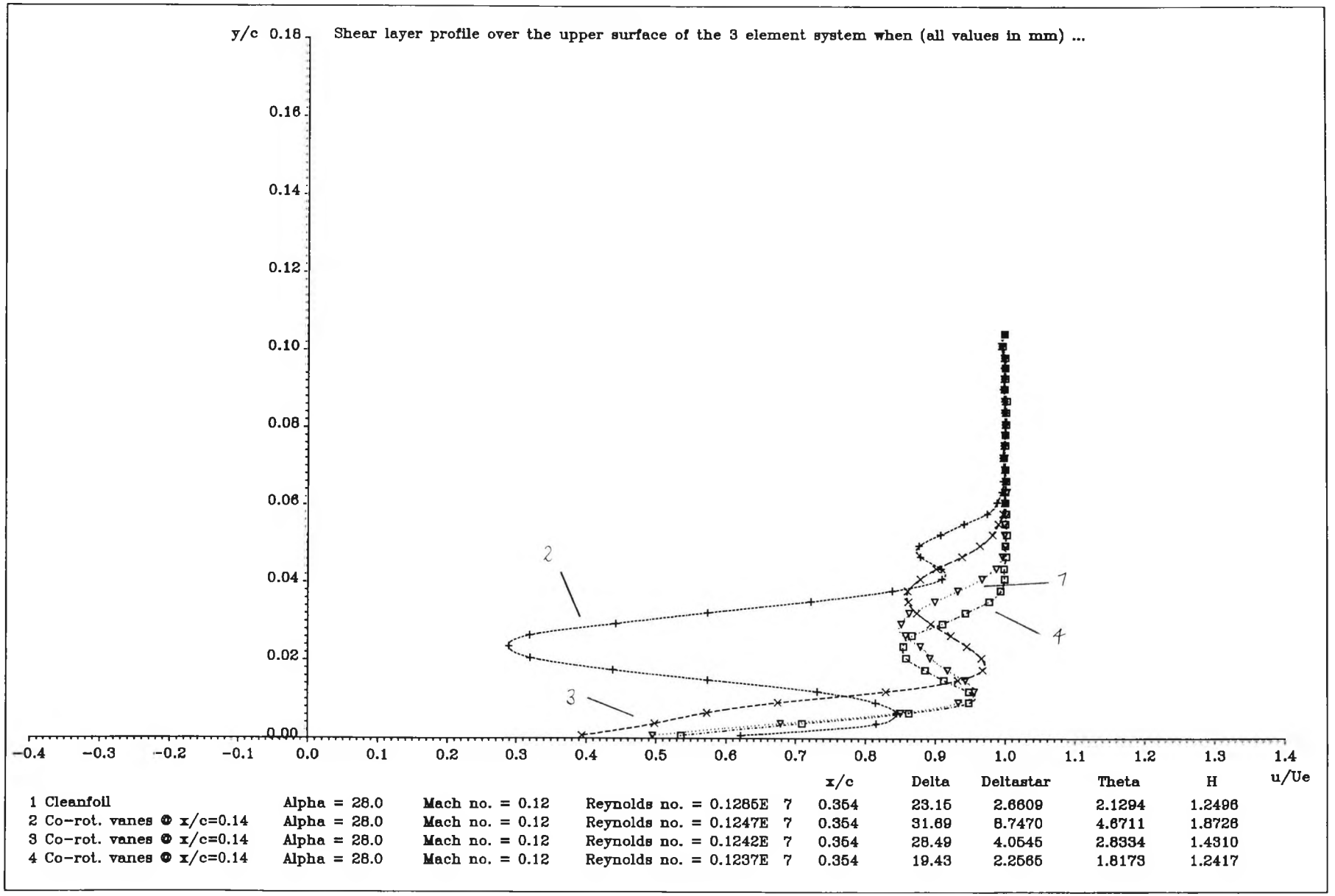

Figure 6.51 : Spanwise variation of shear layer profile at $x/c = 0.354$, $\alpha = 28°$, obtained when co-rot. vanes are at $x/c = 0.14$

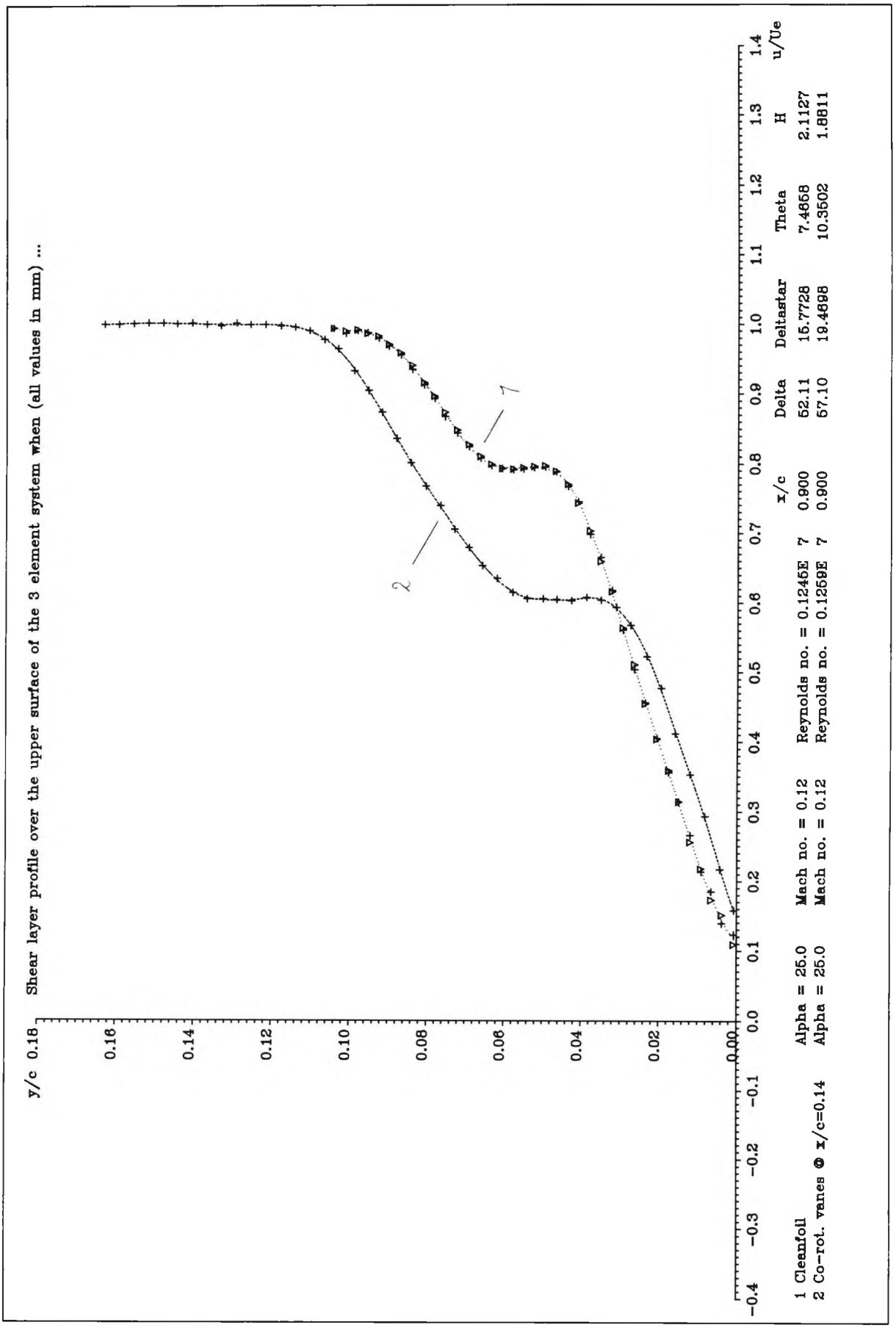

Figure 6.52 : Comparison of mean shear layer profiles at x/c = 0.9, $\alpha = 25°$, obtained with and without co-rot. vanes at x/c = 0.14

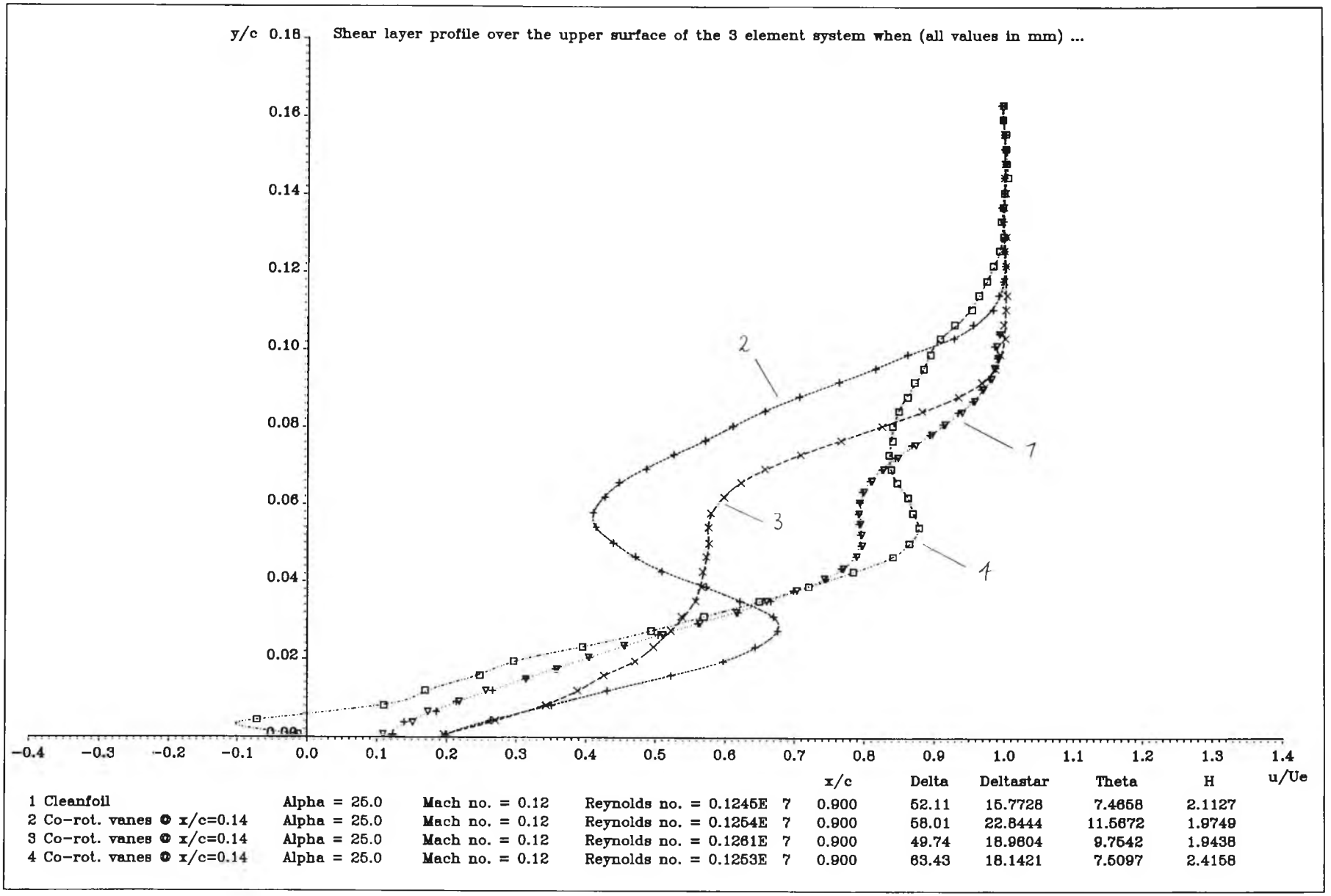

Figure 6.53 : Spanwise variation of shear layer profile at $x/c = 0.9$, $\alpha = 25°$, obtained when co-rot. vanes are at $x/c = 0.14$

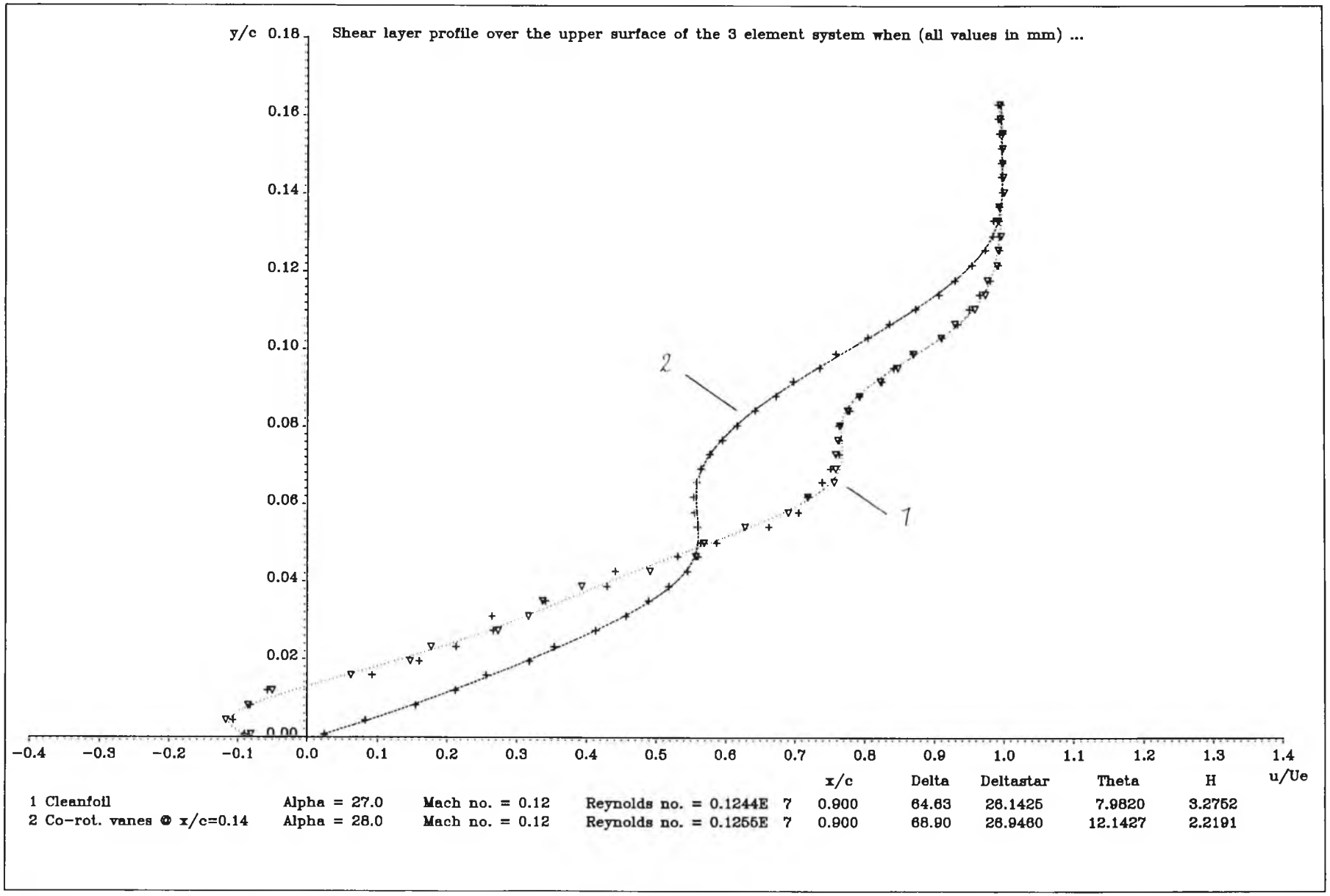

Figure 6.54 : Comparison of mean shear layer profiles at $x/c = 0.9$, $\alpha = 27°$ (cleanfoil) and $\alpha = 28°$ (co-rot. vanes at $x/c = 0.14$)

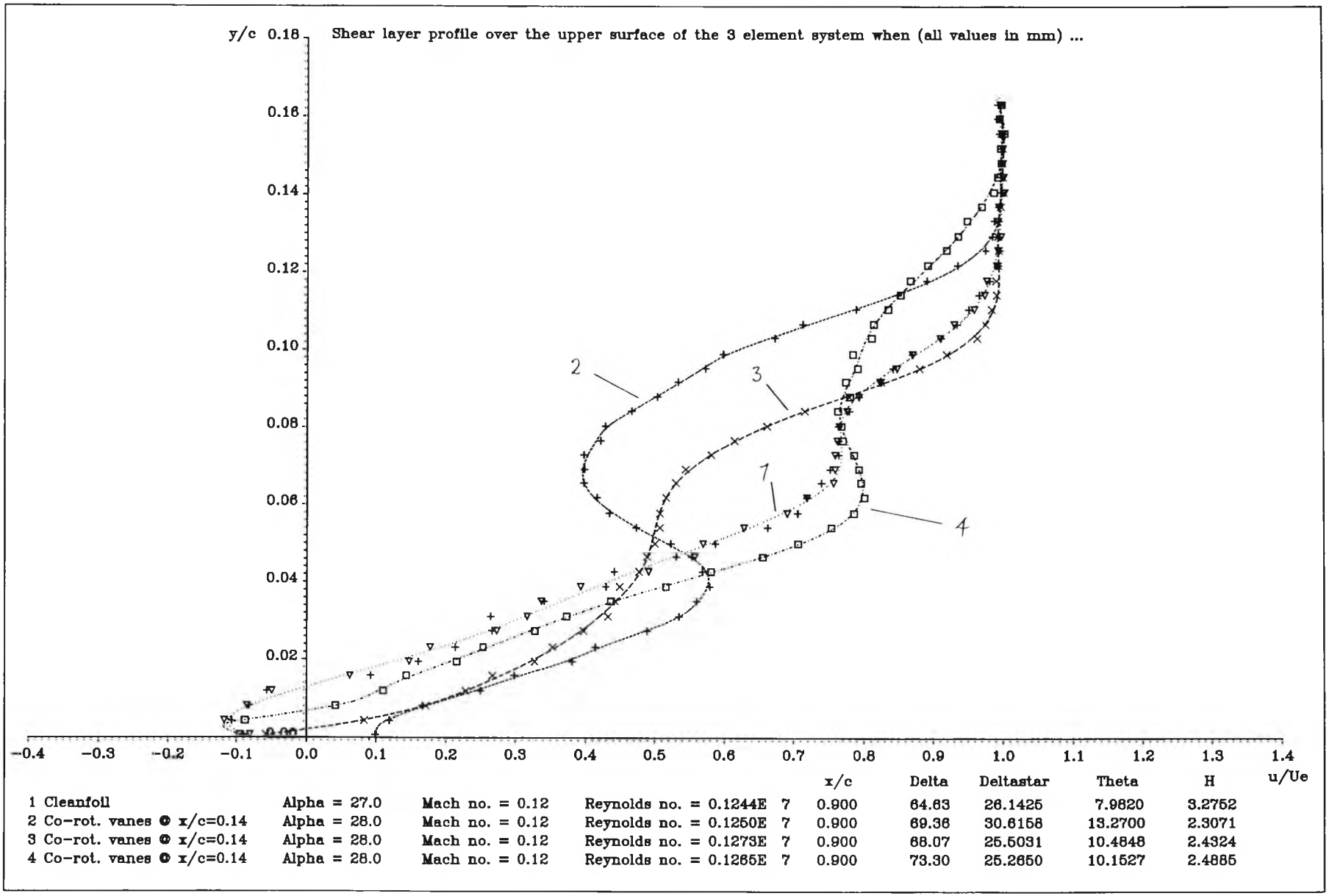

Figure 6.55 : Spanwise variation of shear layer profile at $x/c = 0.9$, $\alpha = 28°$, obtained when co-rot. vanes are at $x/c = 0.14$

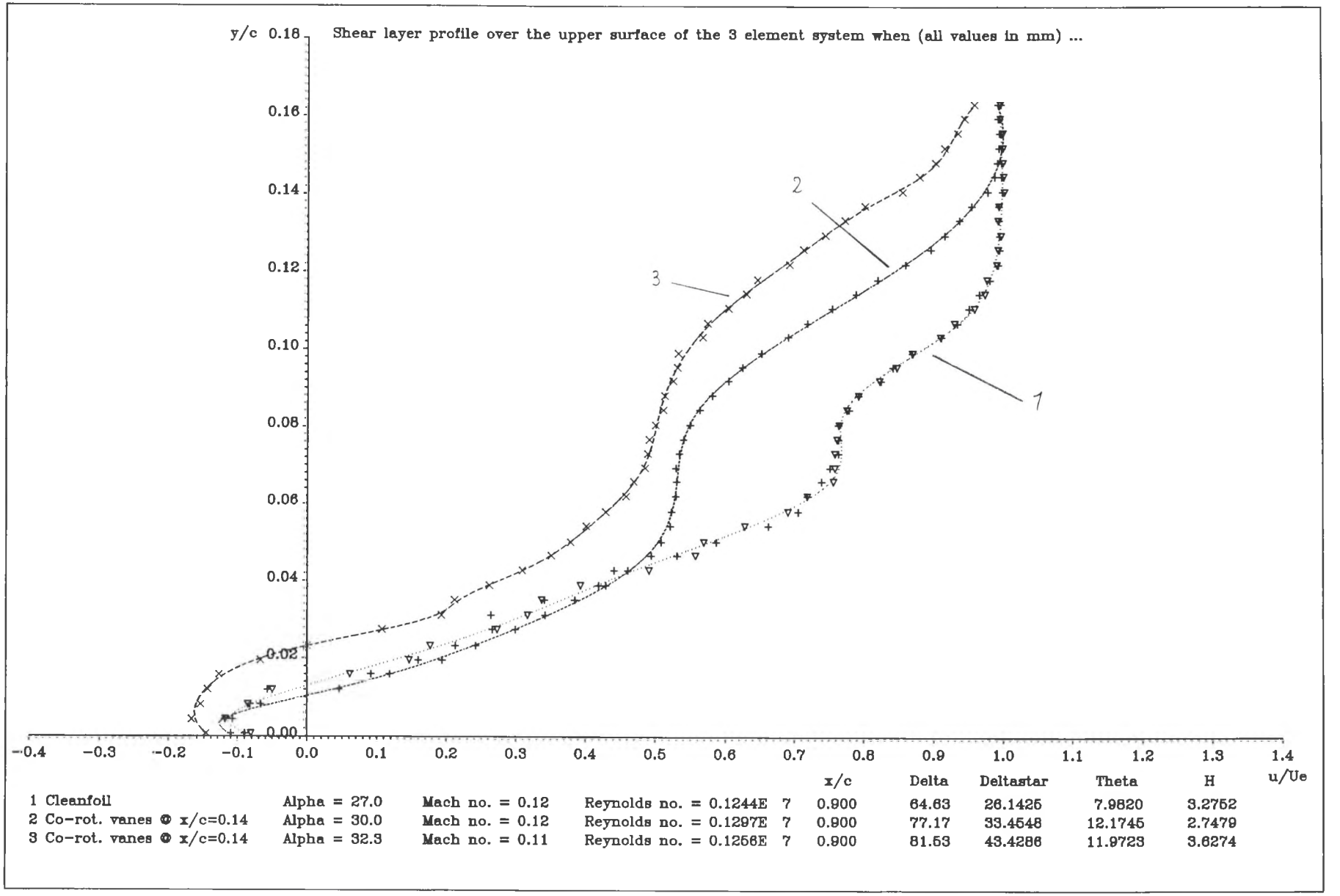

Figure 6.56 : Comparison of mean shear layer profiles at $x/c = 0.9$, $\alpha = 27°$ (cleanfoil), 30° & 32.3° (co-rot. vanes at $x/c = 0.14$)

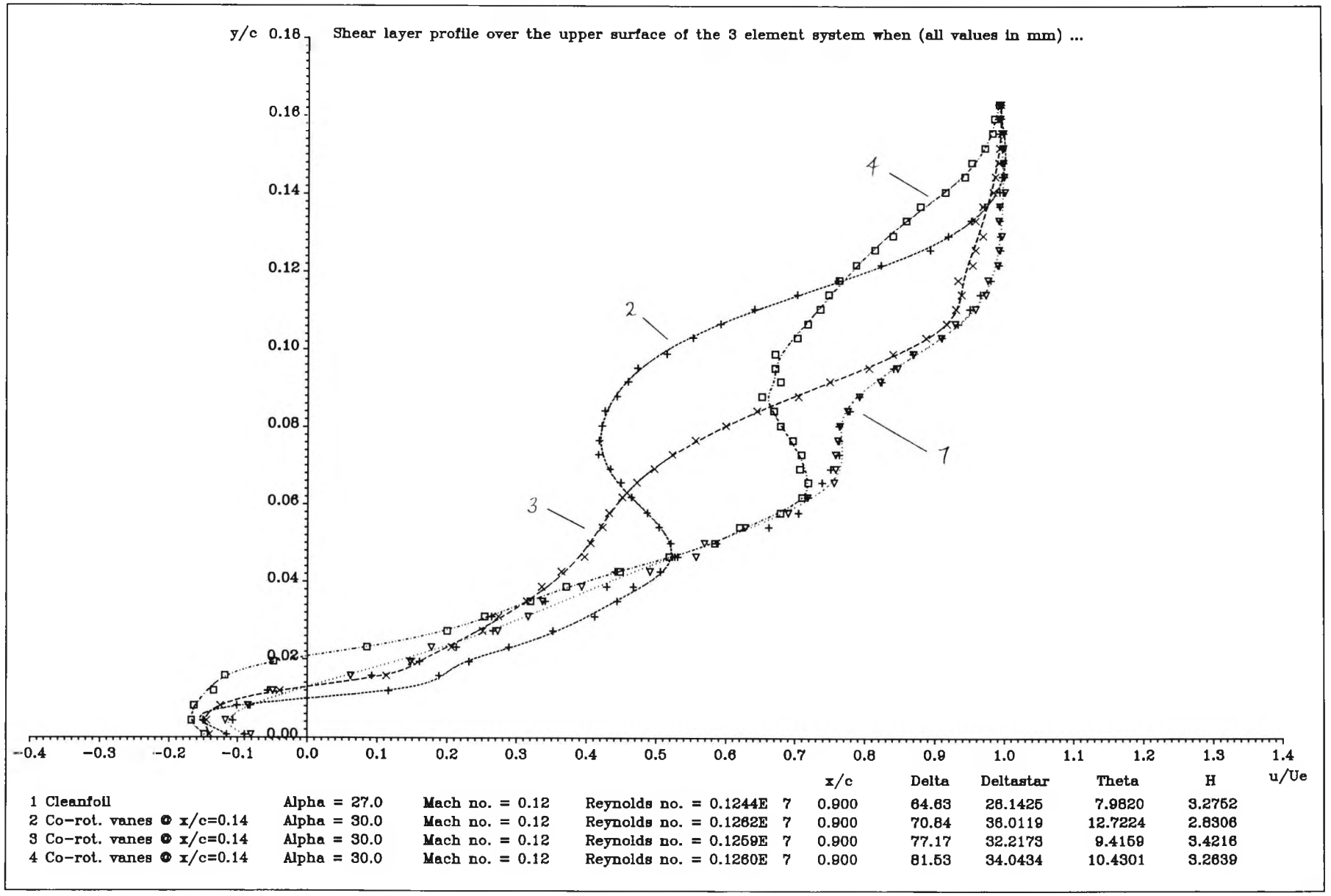

Figure 6.57 : Spanwise variation of shear layer profile at $x/c = 0.9$, $\alpha = 30°$, obtained when co-rot. vanes are at $x/c = 0.14$

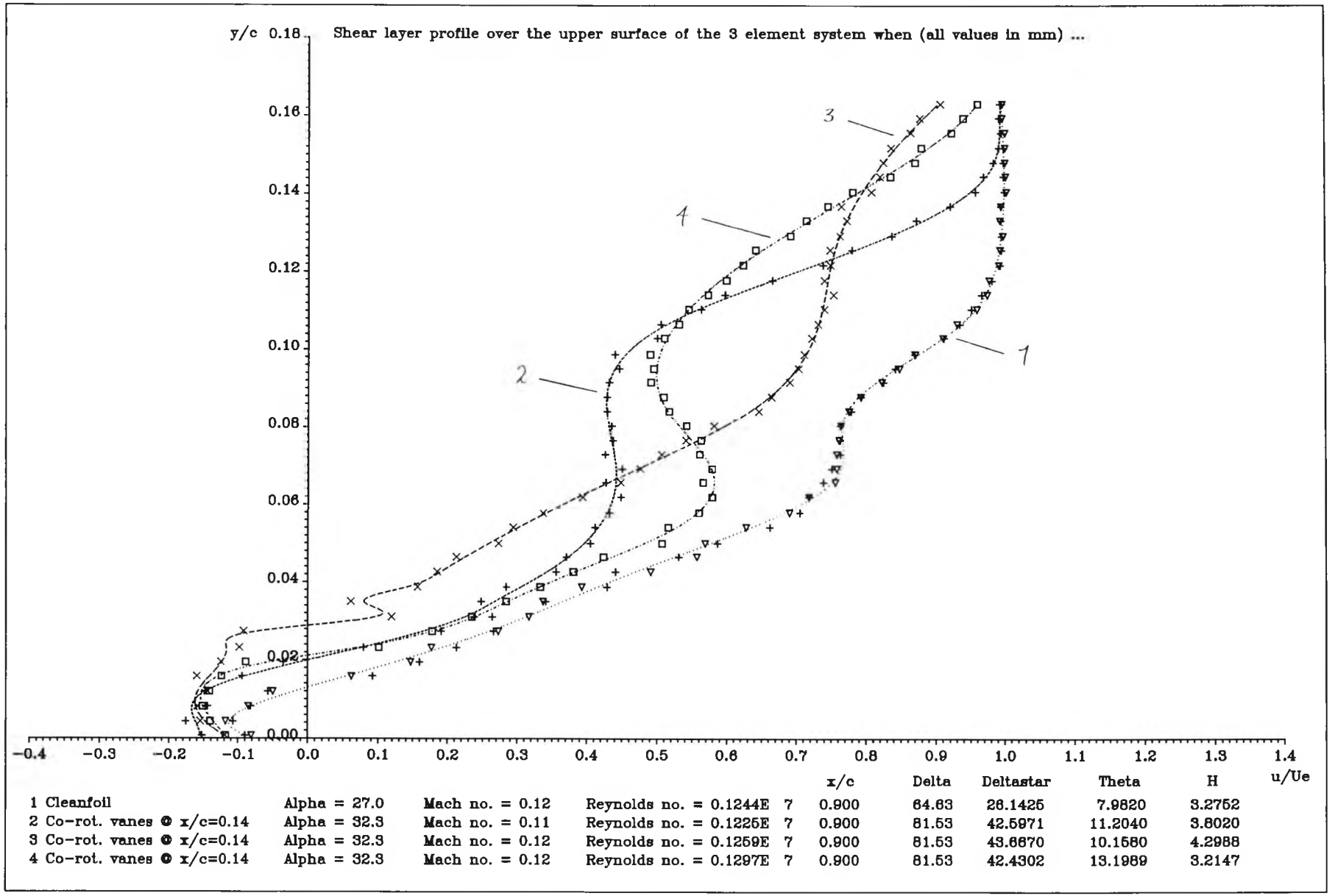

Figure 6.58 : Spanwise variation of shear layer profile at $x/c = 0.9$, $\alpha = 32.3°$, obtained when co-rot. vanes are at $x/c = 0.14$

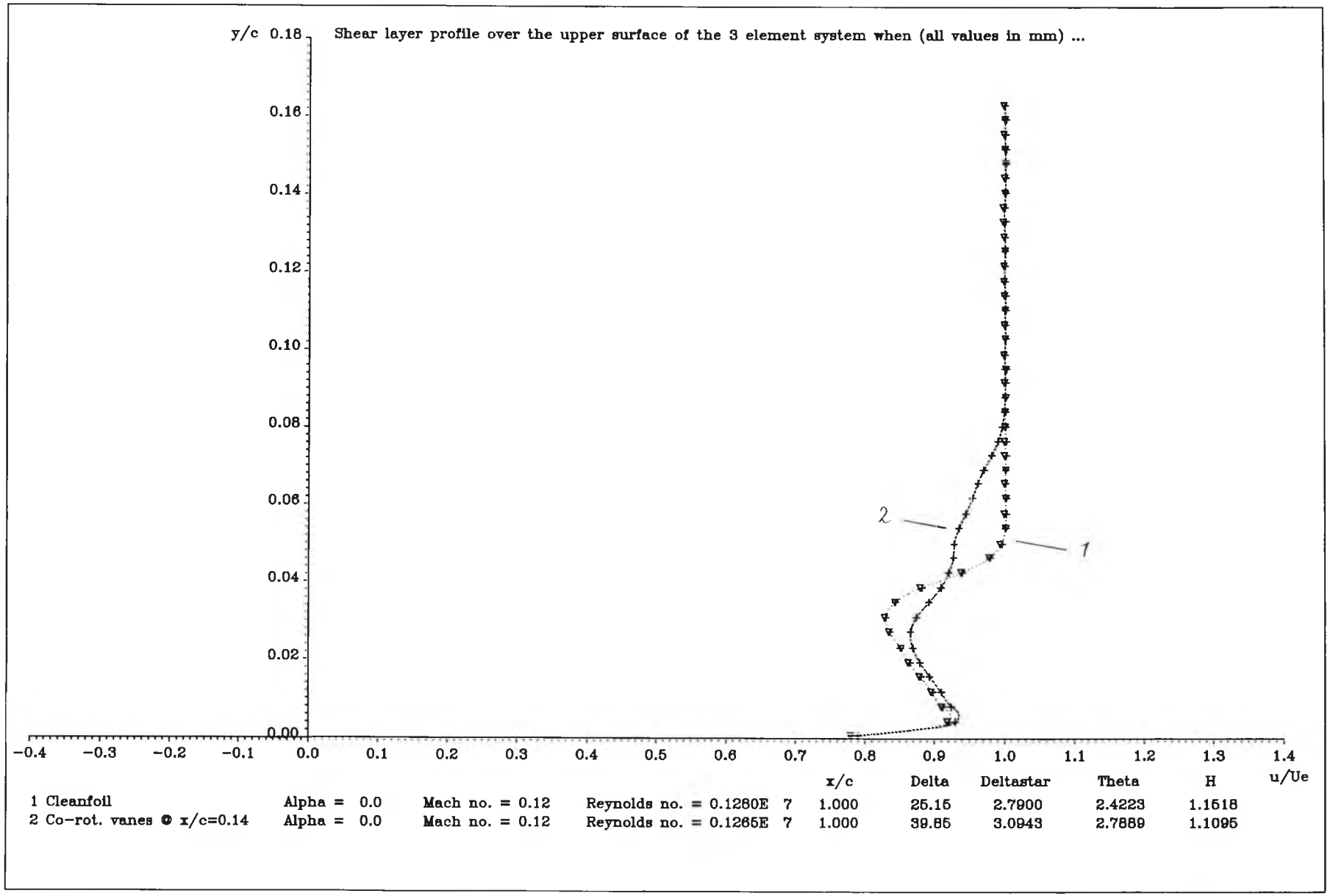

Figure 6.59 : Comparison of mean shear layer profiles at x/c = 1.0, $\alpha = 0°$, obtained with and without co-rot. vanes at x/c = 0.14

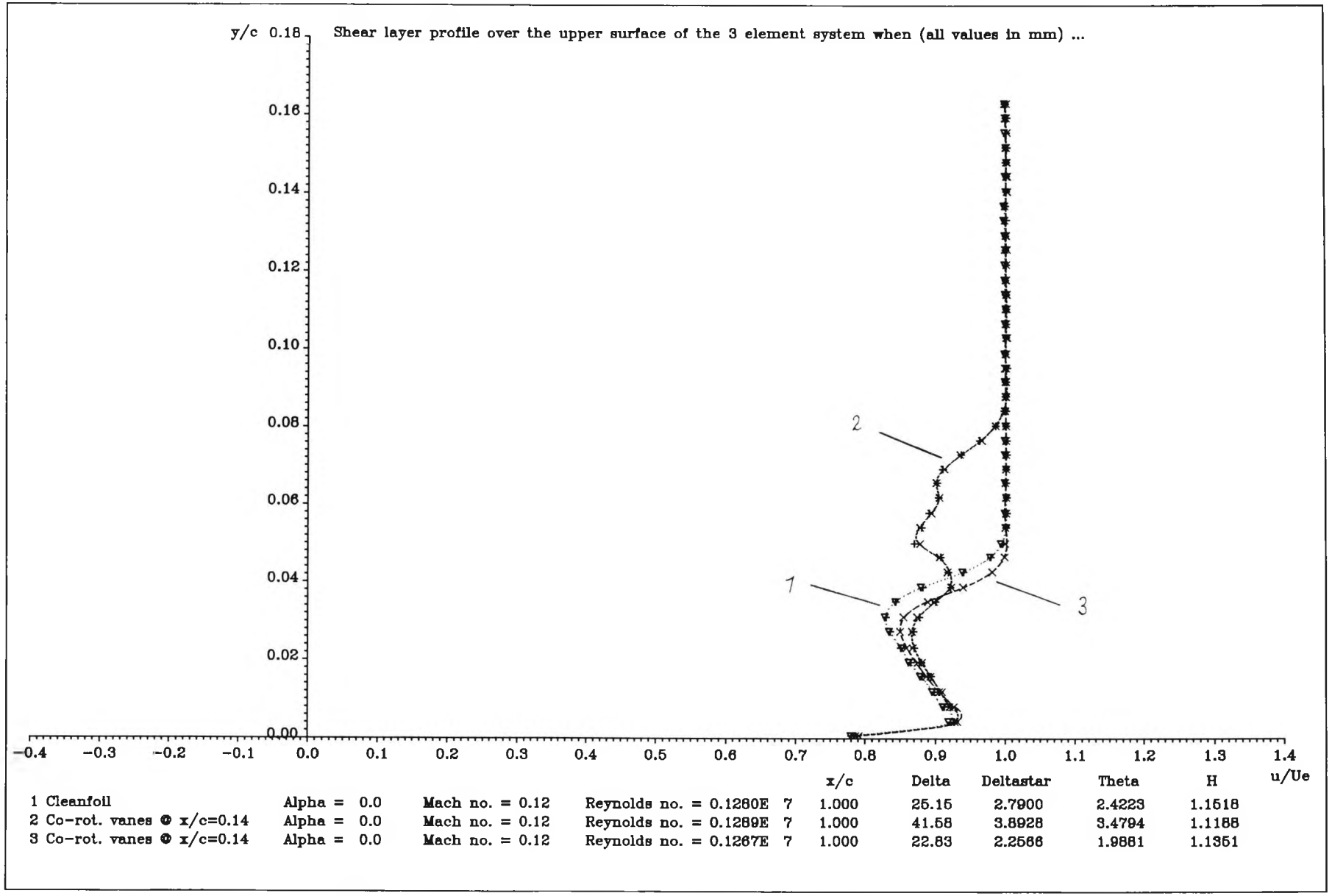

Figure 6.60 : Spanwise variation of shear layer profile at x/c = 1.0, $\alpha = 0°$, obtained when co-rot. vanes are at x/c = 0.14

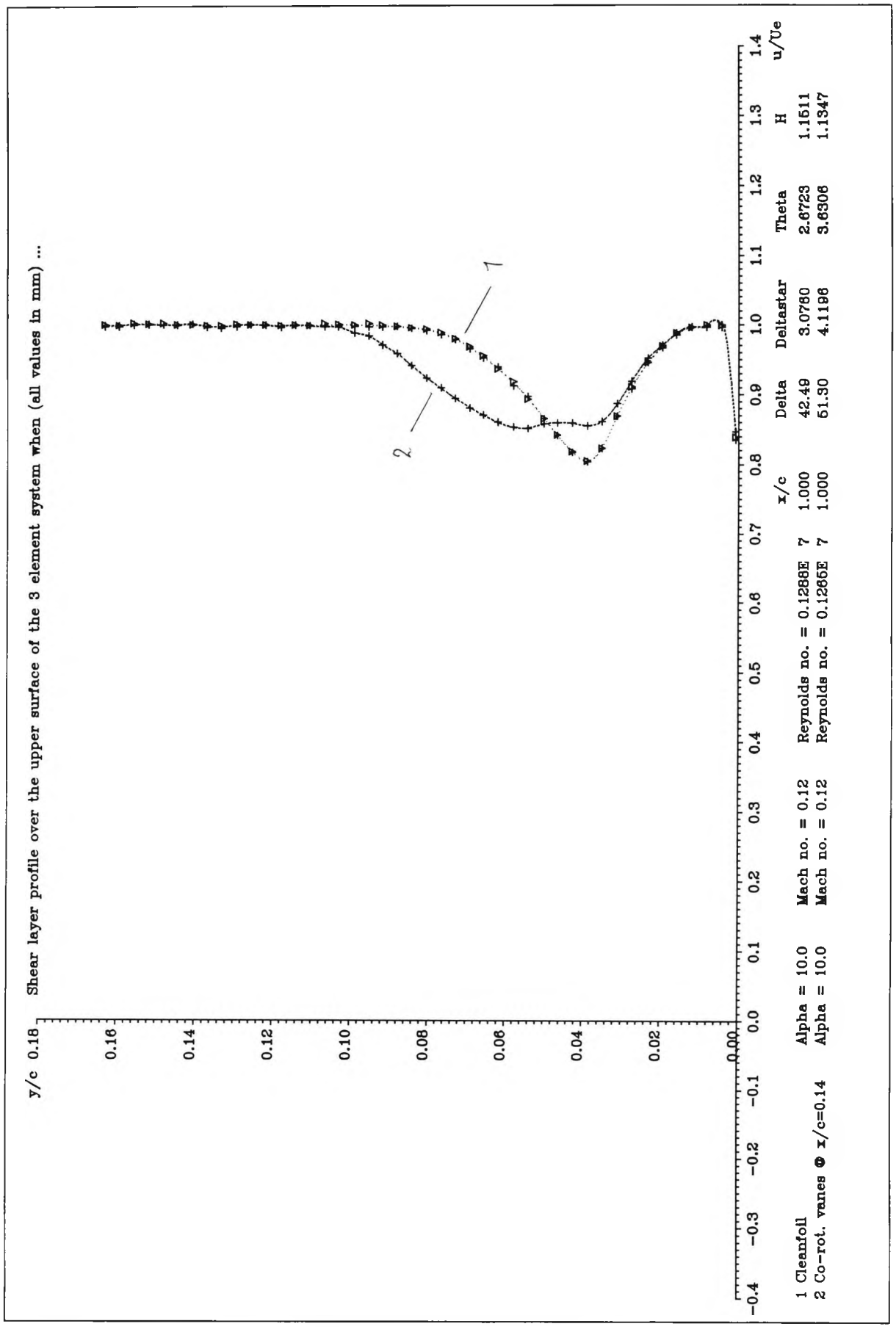

Figure 6.61 : Comparison of mean shear layer profiles at x/c = 1.0, $\alpha = 10°$, obtained with and without co-rot. vanes at x/c = 0.14

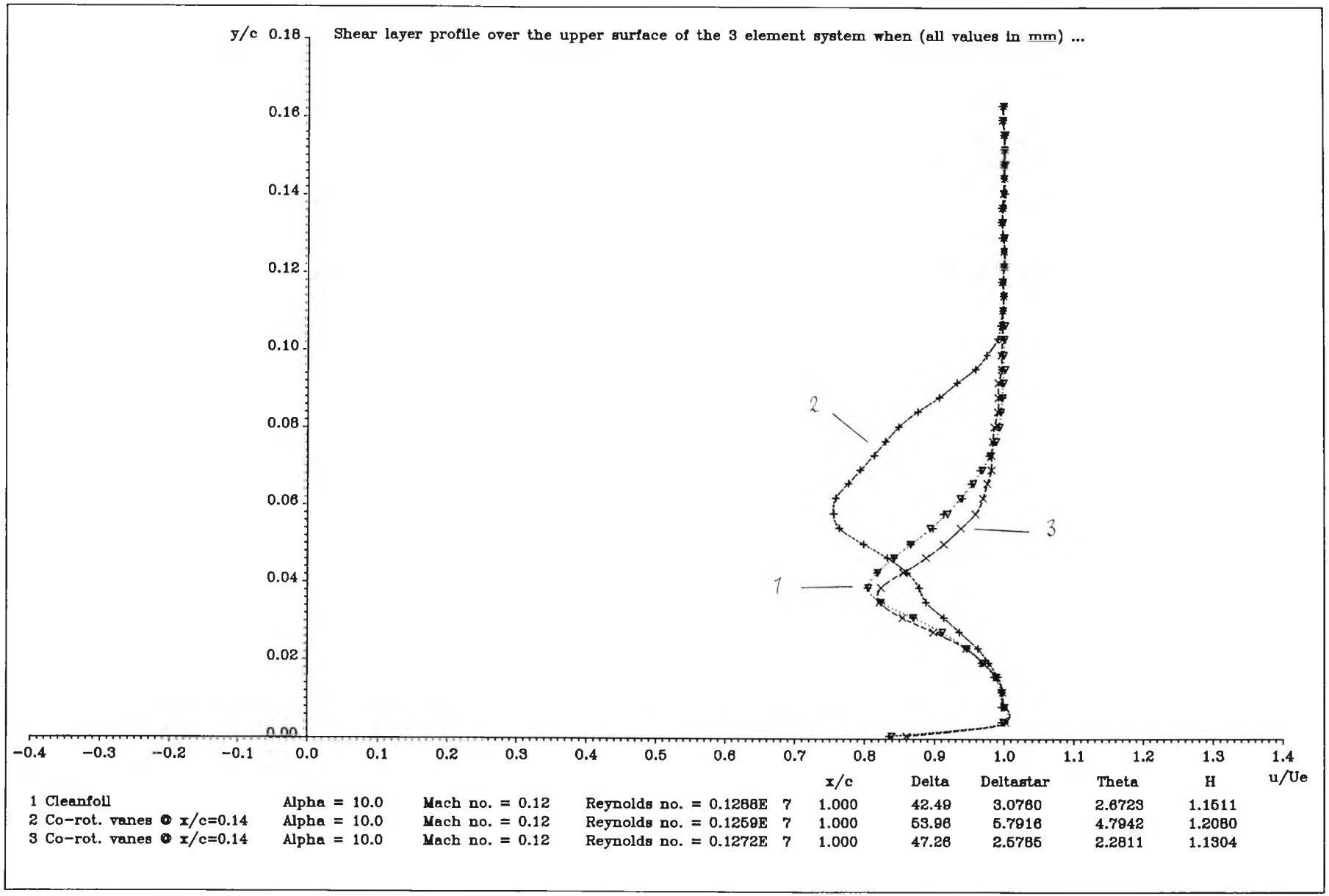

Figure 6.62 : Spanwise variation of shear layer profile at $x/c = 1.0$, $\alpha = 10°$, obtained when co-rot. vanes are at $x/c = 0.14$

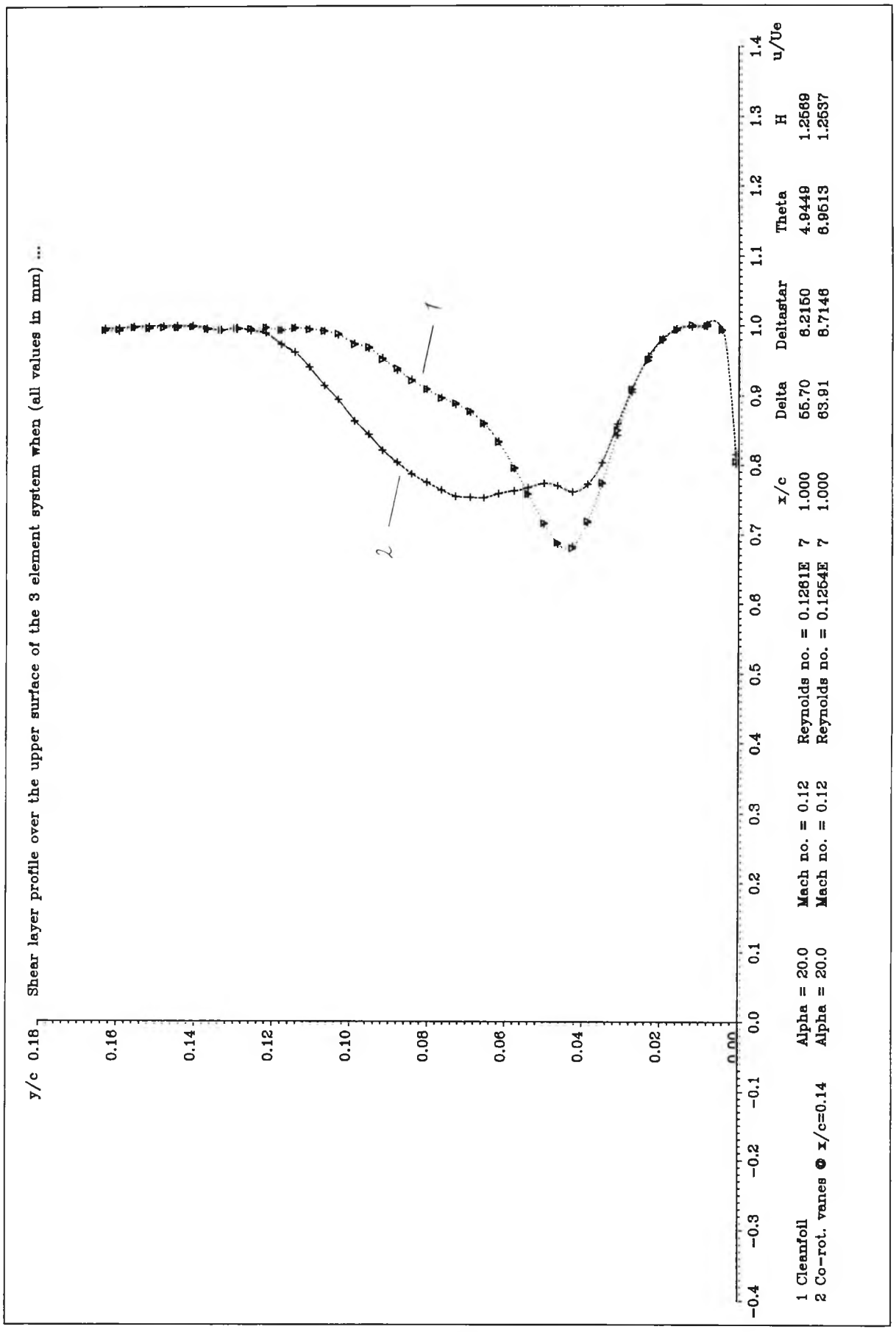

Figure 6.63 : Comparison of mean shear layer profiles at x/c = 1.0, $\alpha = 20°$, obtained with and without co-rot. vanes at x/c = 0.14

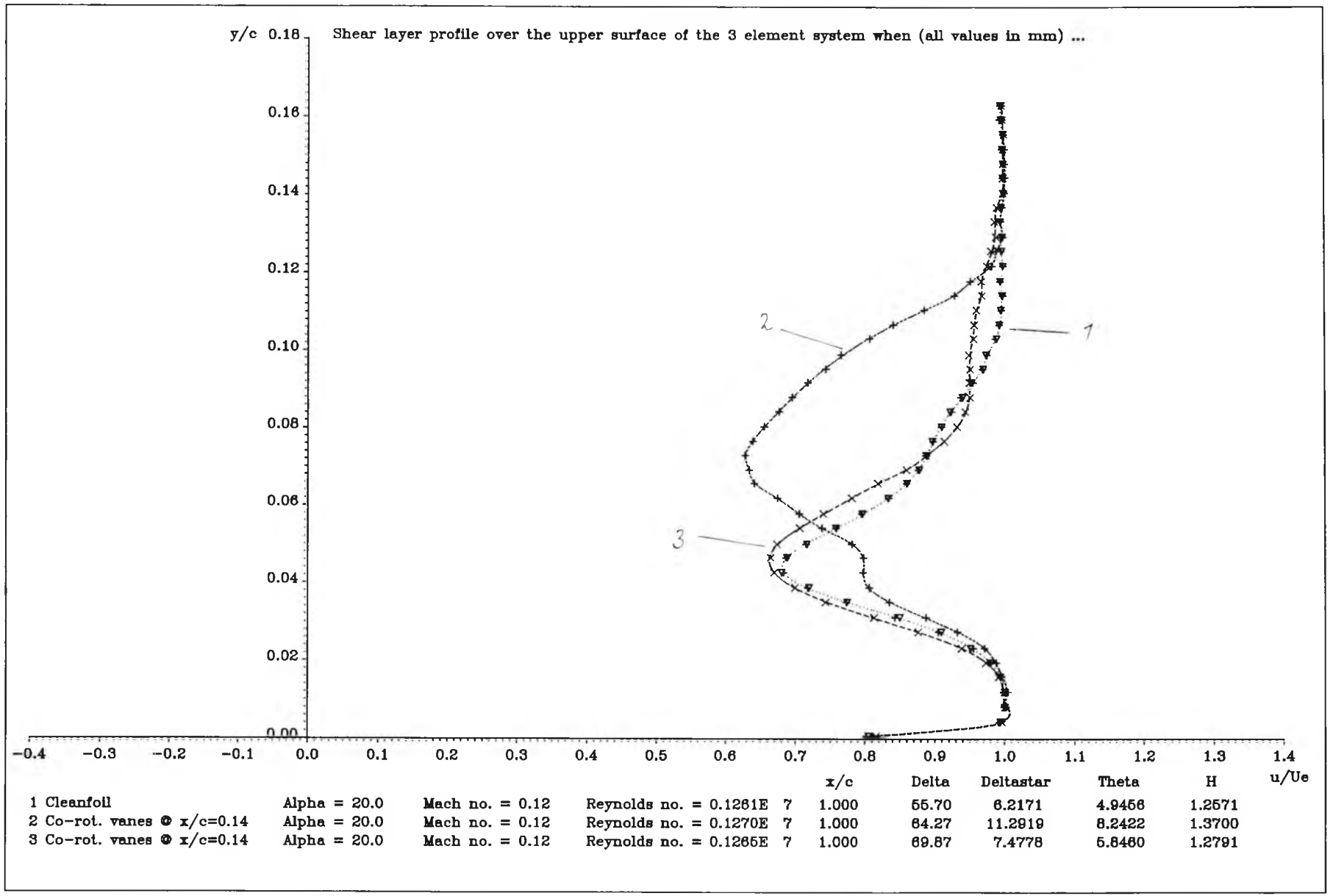

Figure 6.64 : Spanwise variation of shear layer profile at x/c = 1.0, $\alpha = 20°$, obtained when co-rot. vanes are at x/c = 0.14

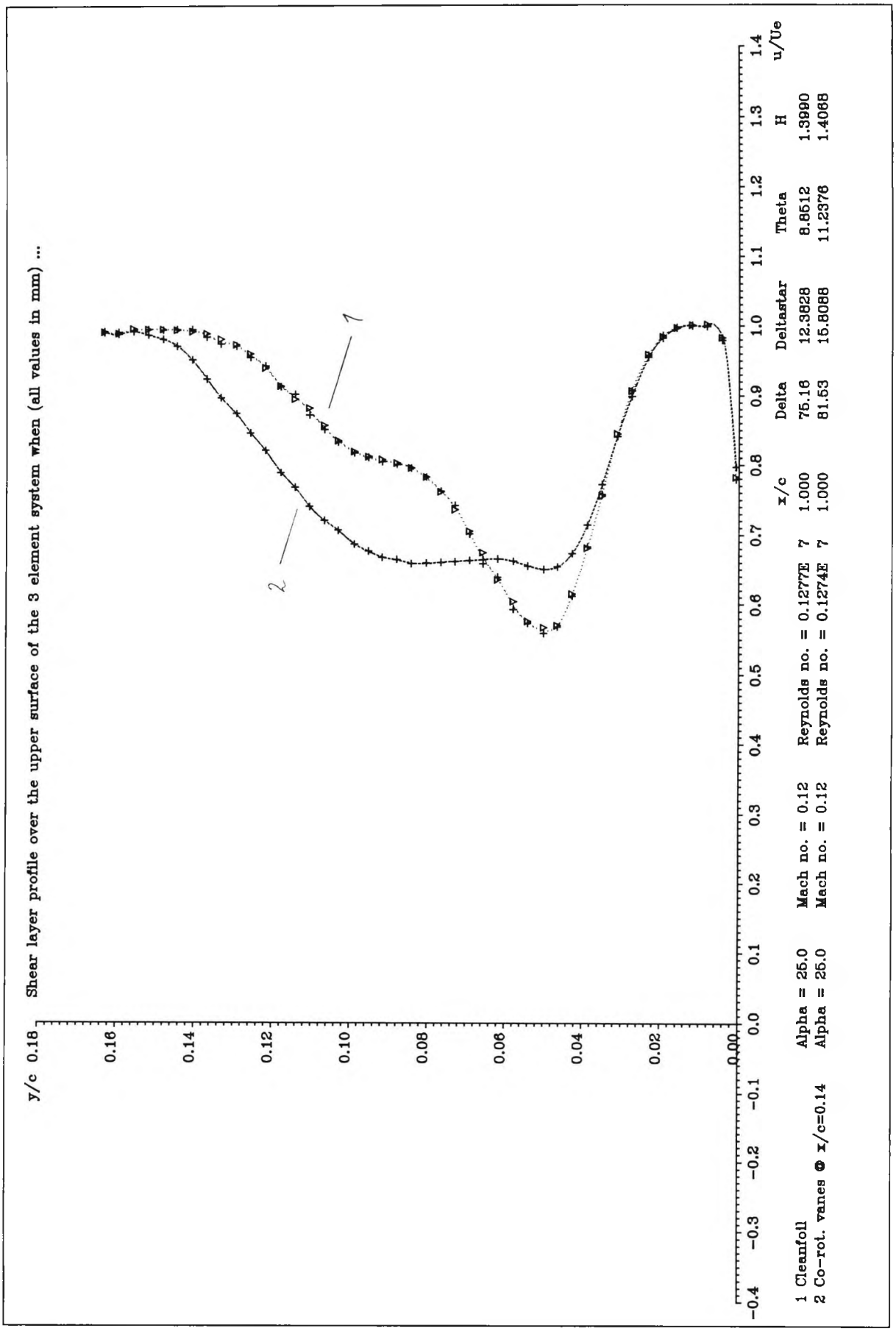

Figure 6.65 : Comparison of mean shear layer profiles at x/c = 1.0, $\alpha = 25°$, obtained with and without co-rot. vanes at x/c = 0.14

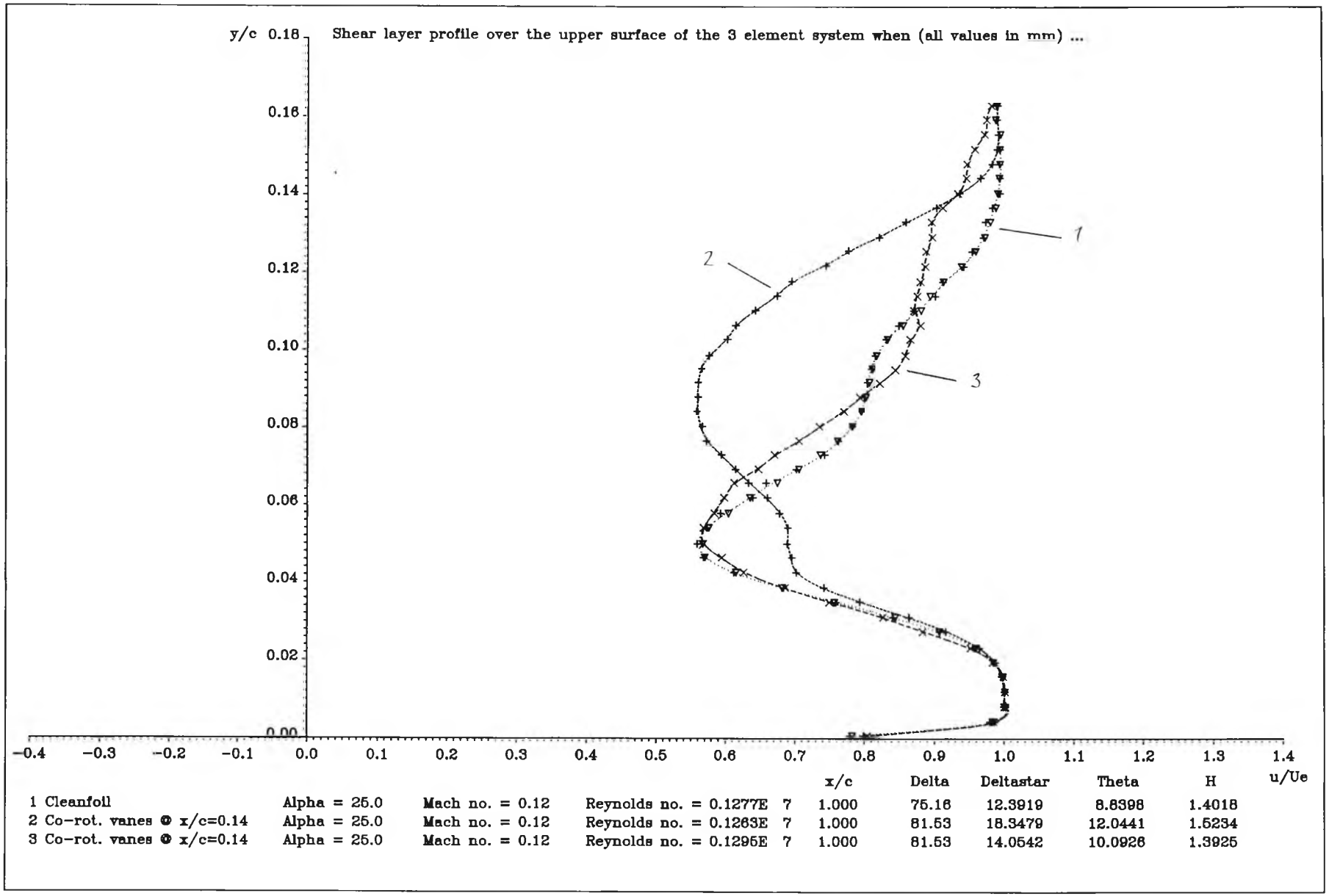

Figure 6.66 : Spanwise variation of mean shear layer profiles at x/c = 1.0, $\alpha = 25°$, obtained when co-rot. vanes are at x/c = 0.14

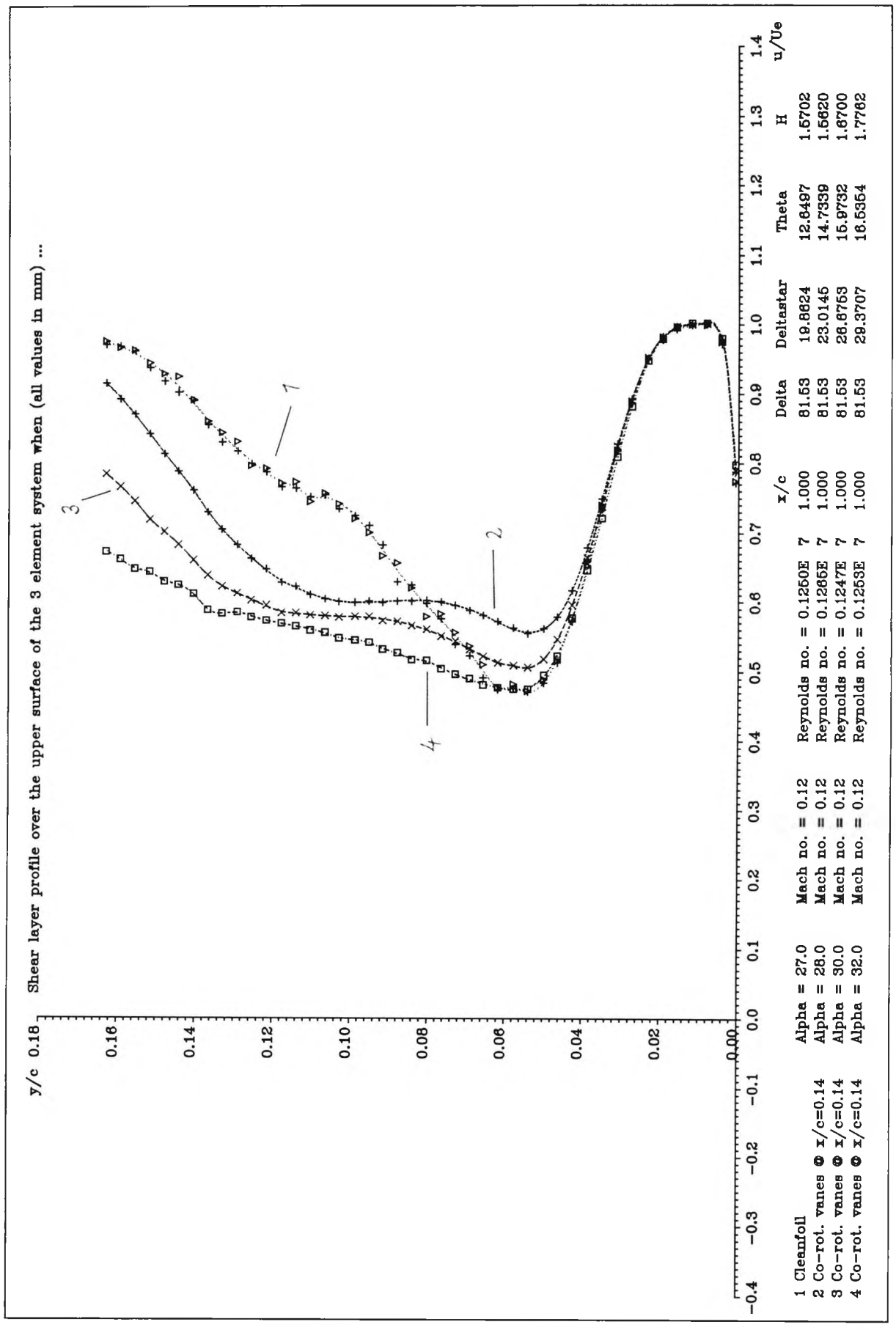

Figure 6.67 : Comparison of mean shear layer profiles at x/c = 1.0, $\alpha = 27°$ (cleanfoil), 28°, 30° & 32° (co-rot. vanes at x/c = 0.14)

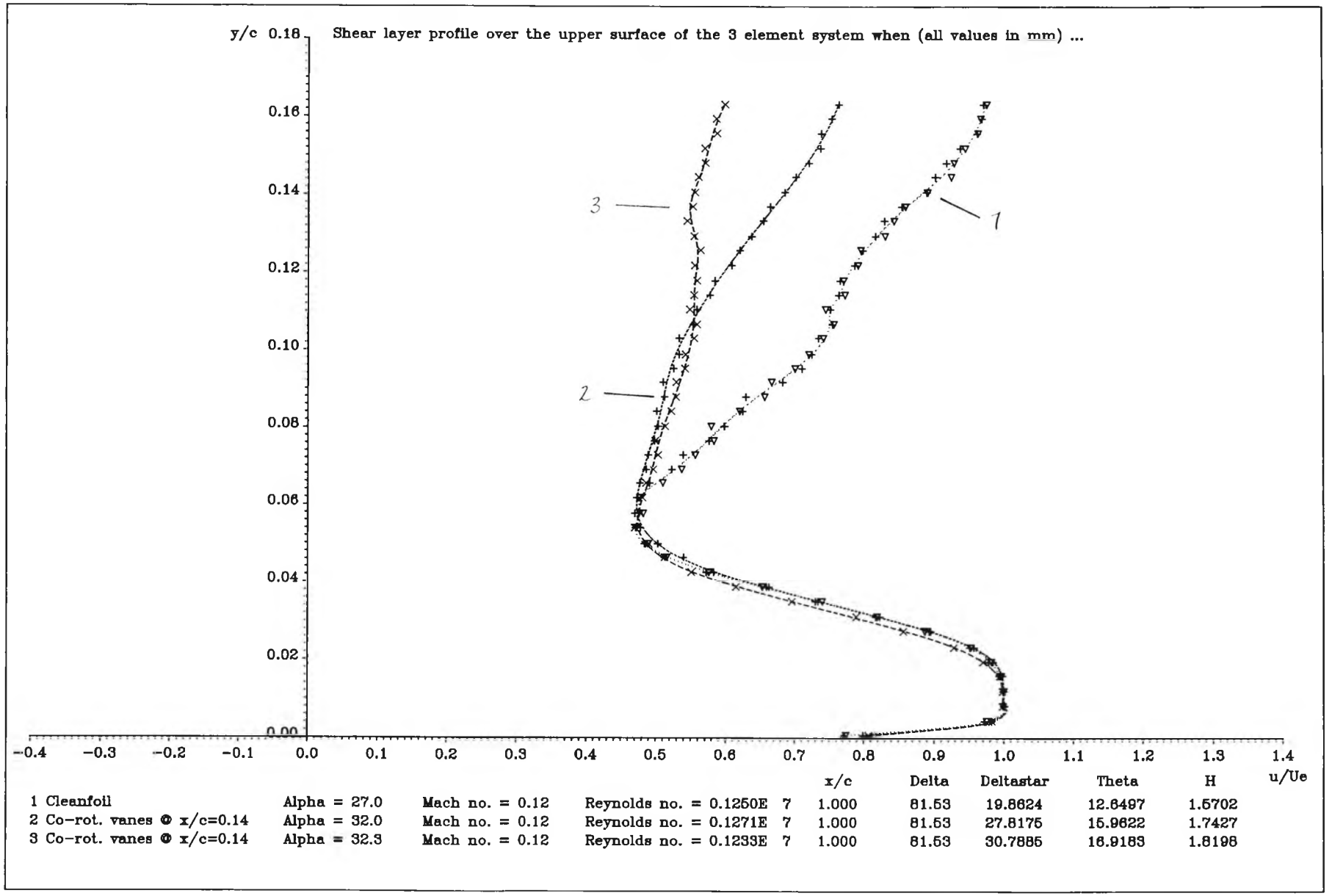

Figure 6.68 : Spanwise variation of shear layer profile at x/c = 1.0, $\alpha = 32°$, obtained when co-rot. vanes are at x/c = 0.14

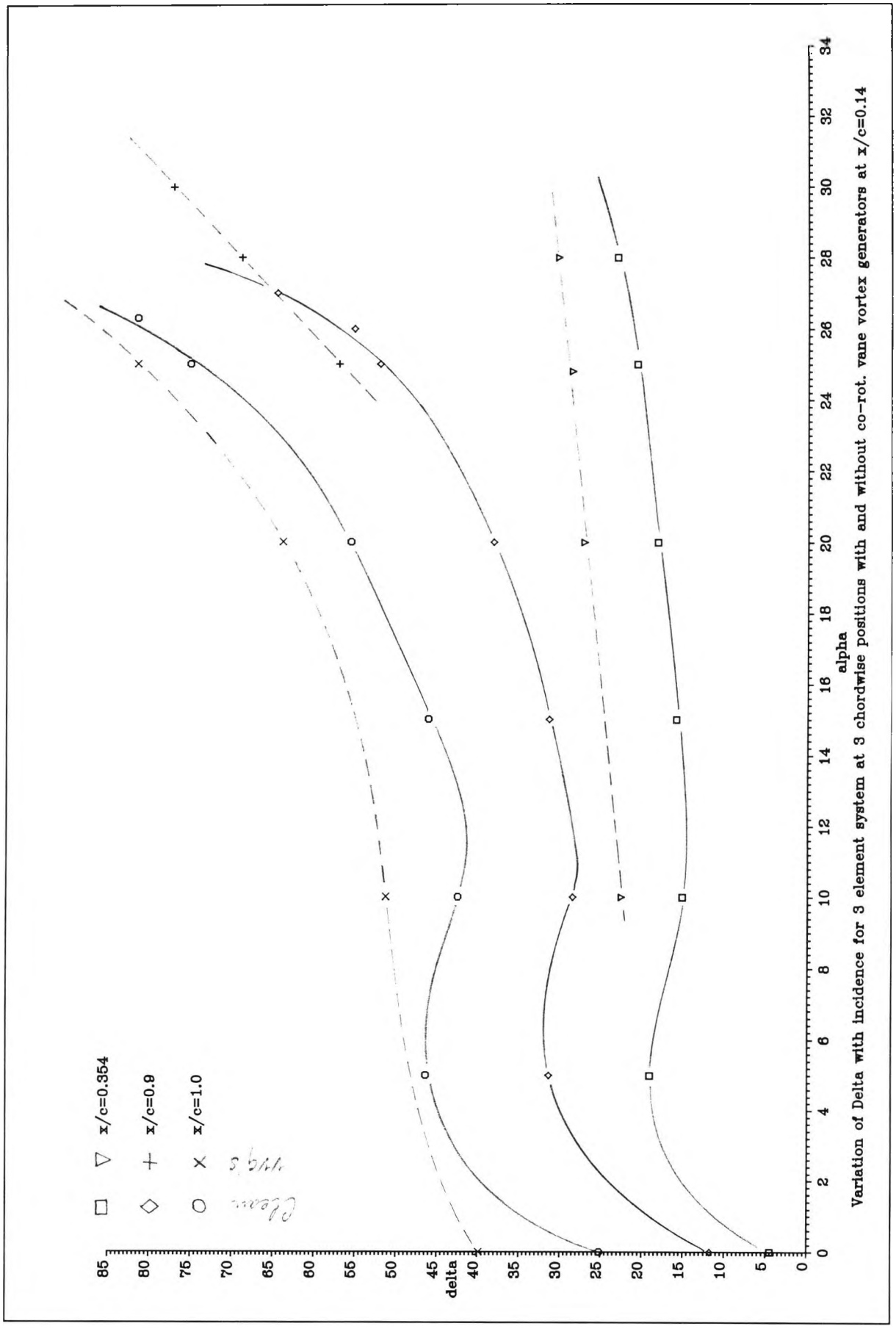

Figure 6.69 : Variation of δ (in mm) with α at 3 chordwise locations, with and without co-rot. vane vortex generators at x/c = 0.14

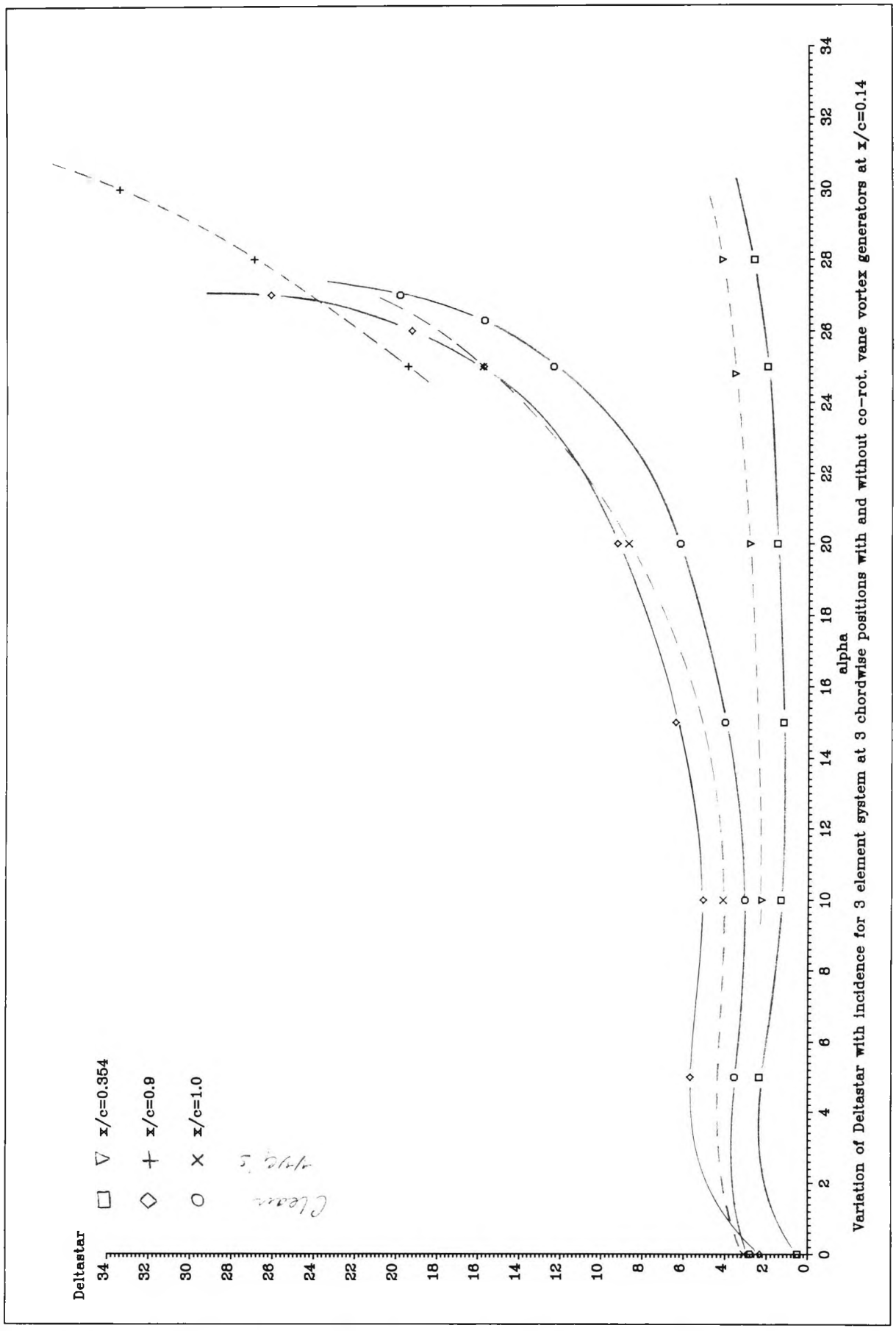

Figure 6.70 : Variation of δ^* (in mm) with α at 3 chordwise locations, with and without co-rot. vane vortex generators at x/c = 0.14

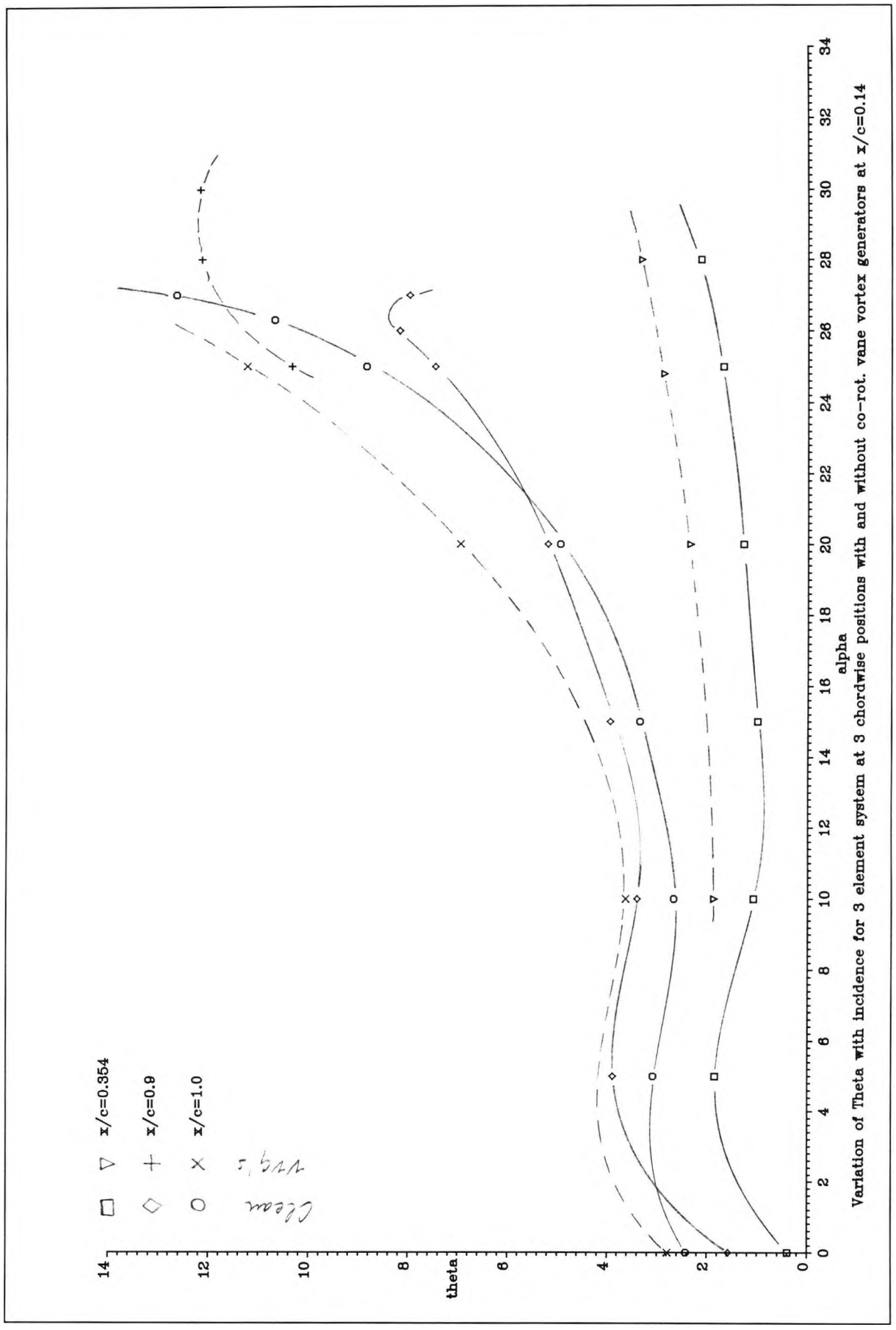

Figure 6.71 : Variation of θ (in mm) with α at 3 chordwise locations, with and without co-rot. vane vortex generators at x/c = 0.14

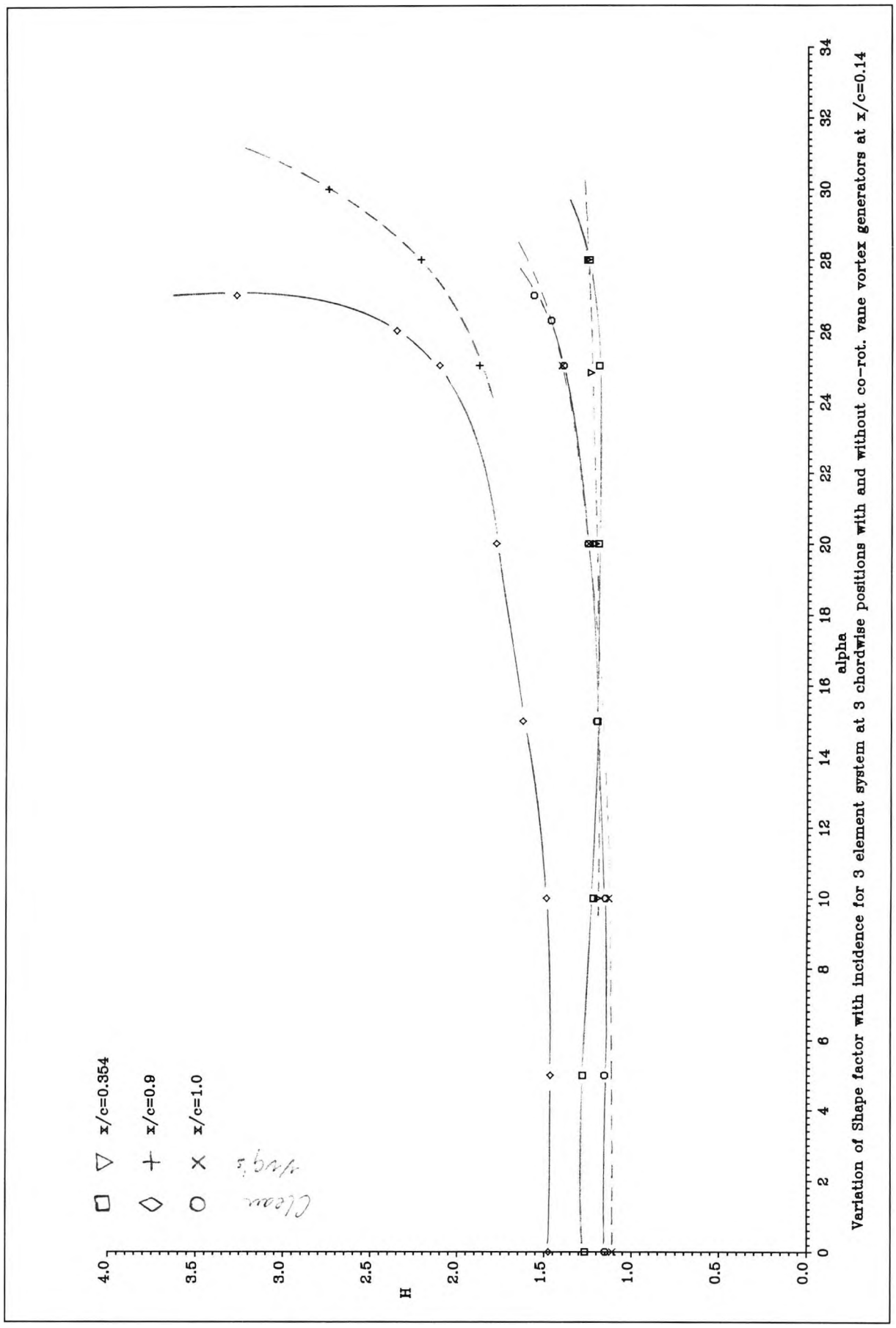

Figure 6.72 : Variation of H (in mm) with α at 3 chordwise locations, with and without co-rot. vane vortex generators at x/c = 0.14

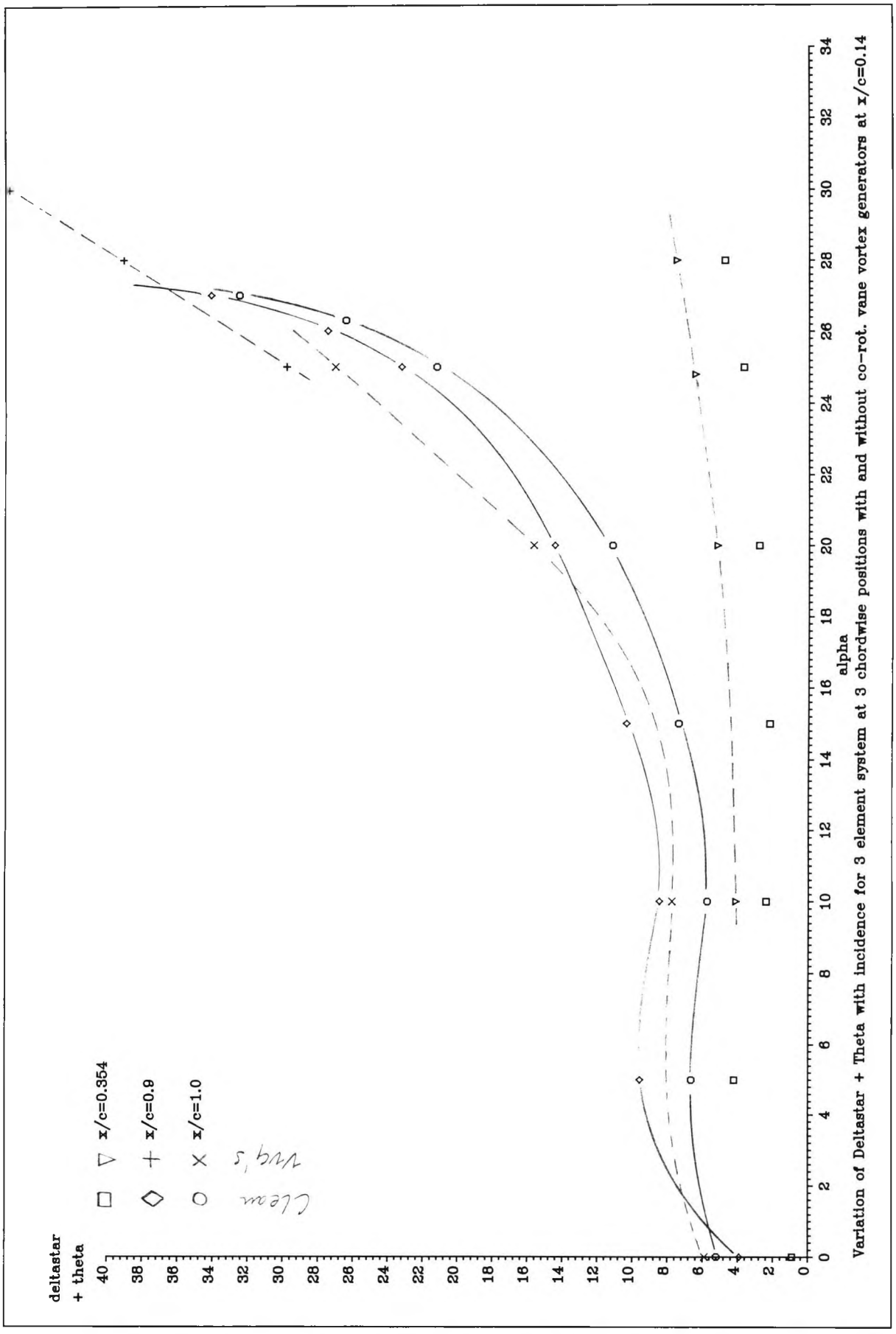

Figure 6.73 : Variation of $(\delta^* + \theta)$ (in mm) with α at 3 chordwise locations, with and without co-rot. vane vortex generators at x/c = 0.14

Appendix C - Windtunnel tests results with airjet vortex generators

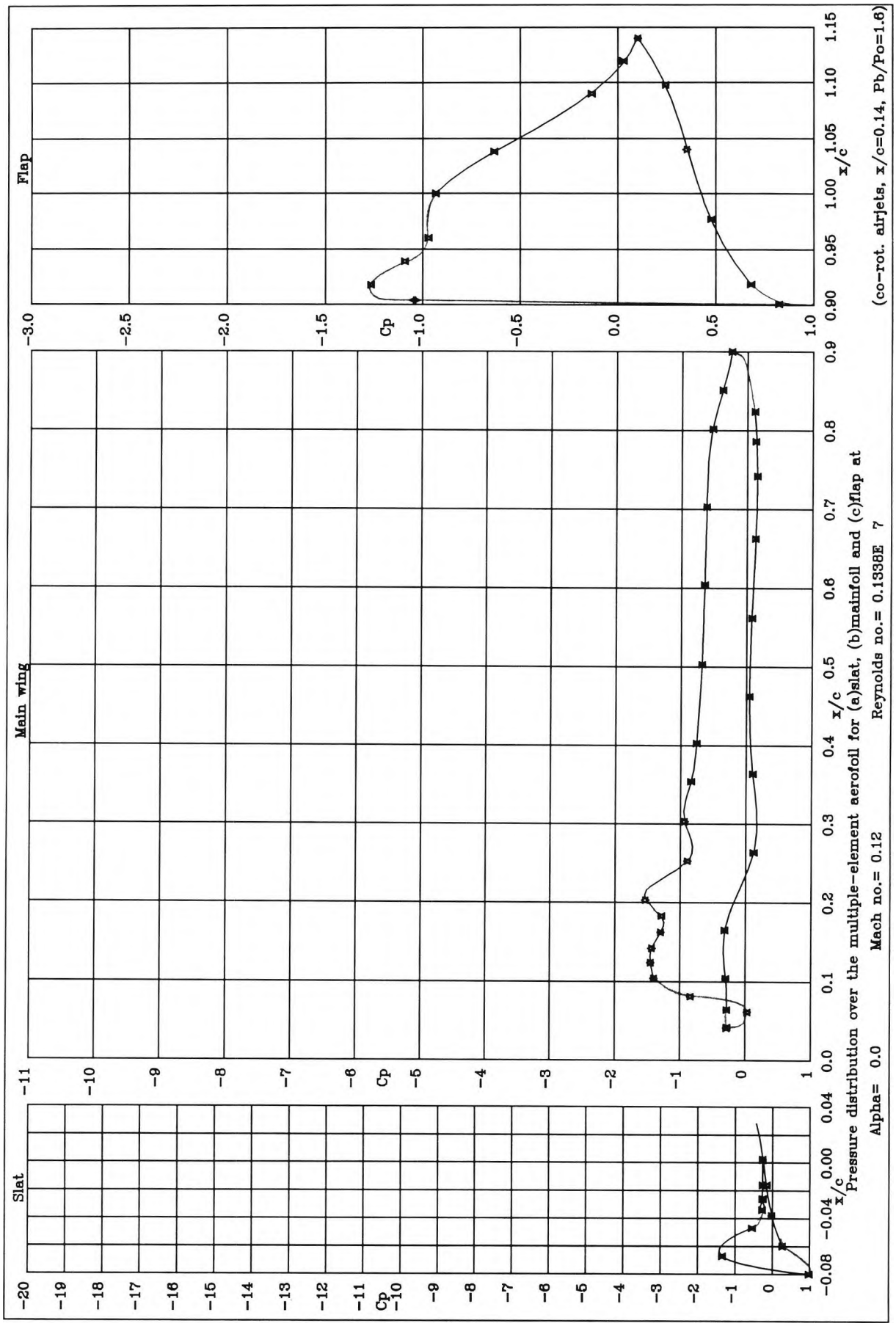

Figure 7.1 : Pressure distribution over the high lift system at 0° when co-rot. ajvg's are at x/c = 0.14

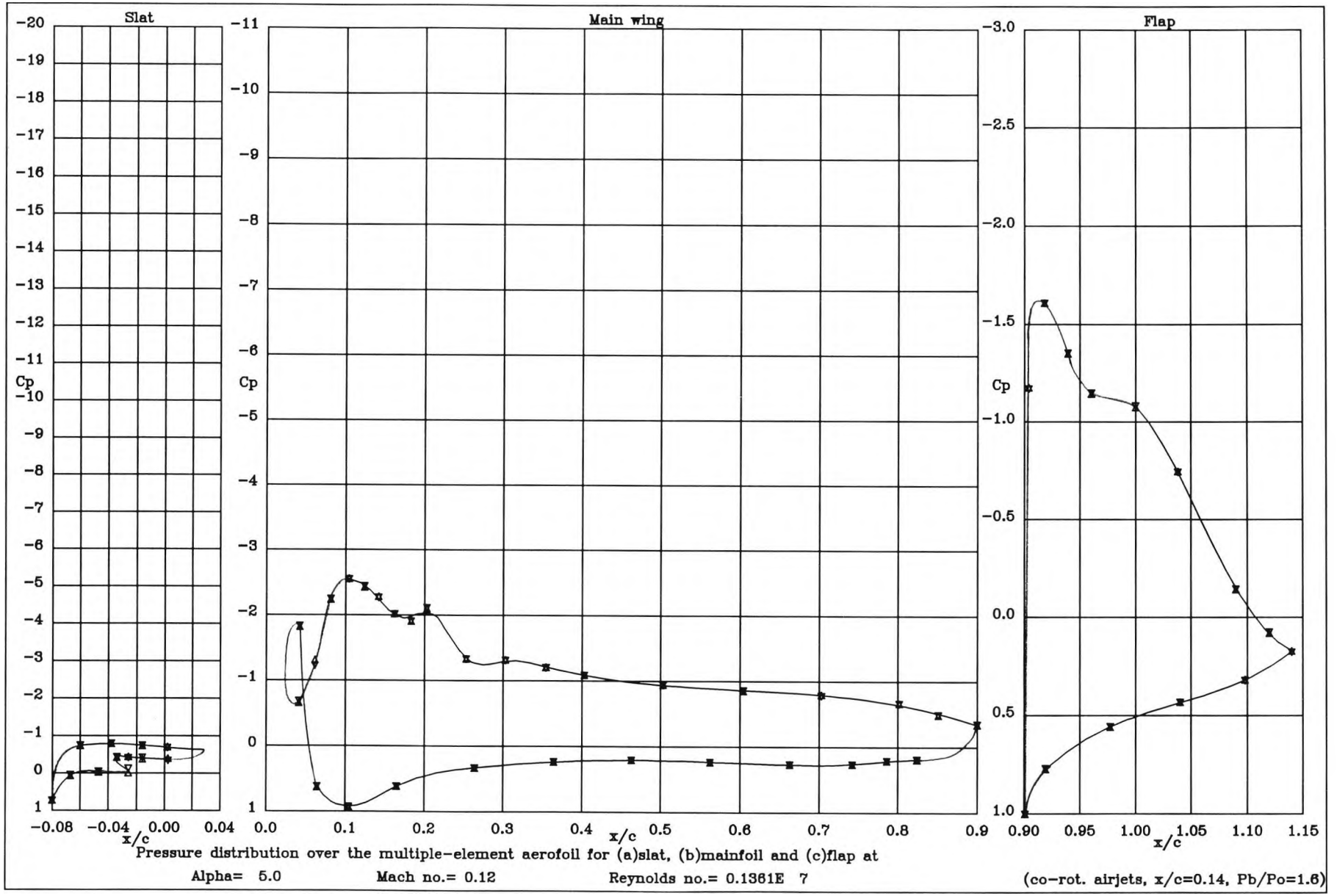

Figure 7.2 : Pressure distribution over the high lift system at 5° when co-rot. ajyg's are at x/c = 0.14

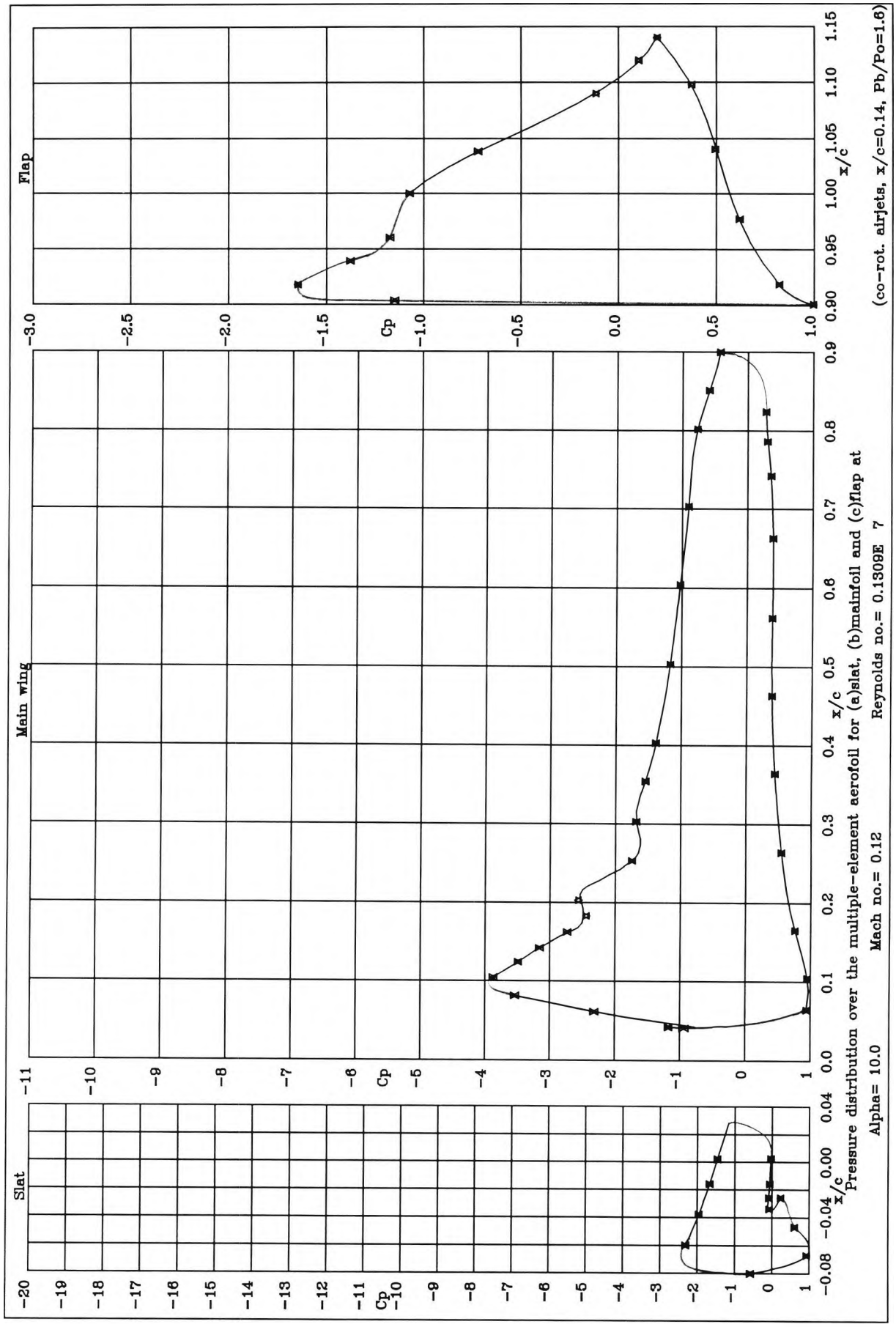

Figure 7.3 : Pressure distribution over the high lift system at 10° when co-rot. ajvg's are at x/c = 0.14

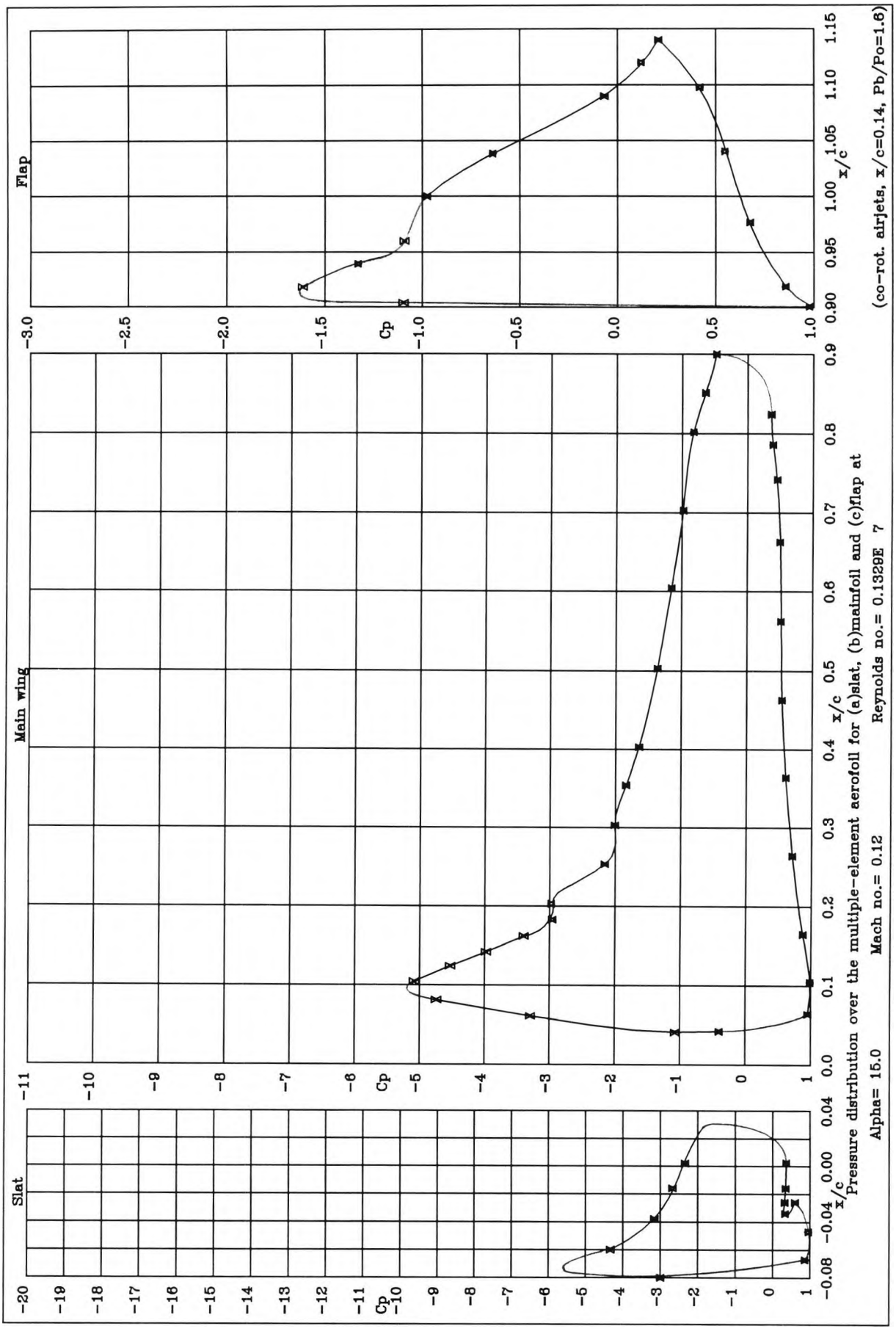

Figure 7.4 : Pressure distribution over the high lift system at 15° when co-rot. ajvg's are at x/c = 0.14

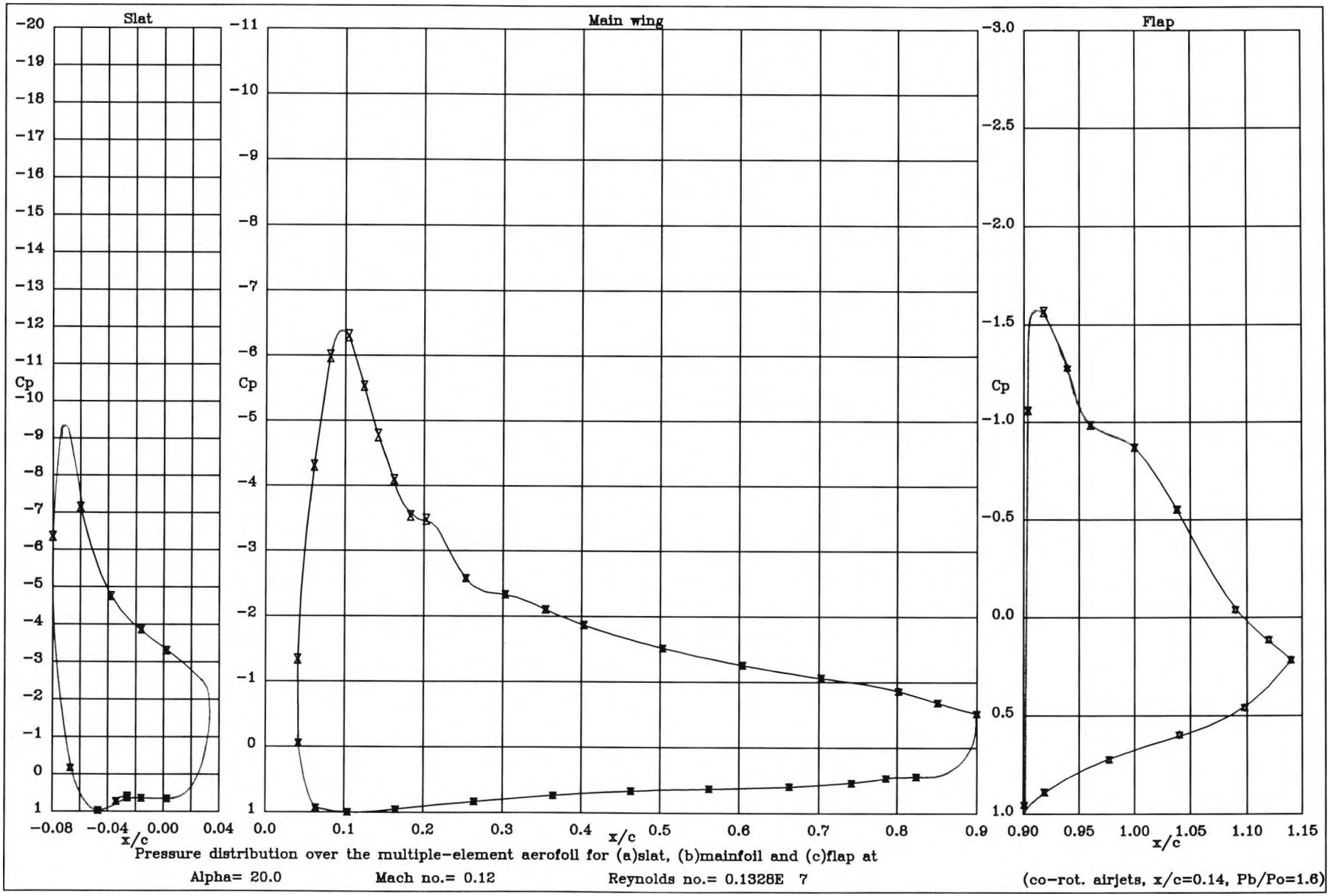

Figure 7.5 : Pressure distribution over the high lift system at 20° when co-rot. ajyg's are at x/c = 0.14

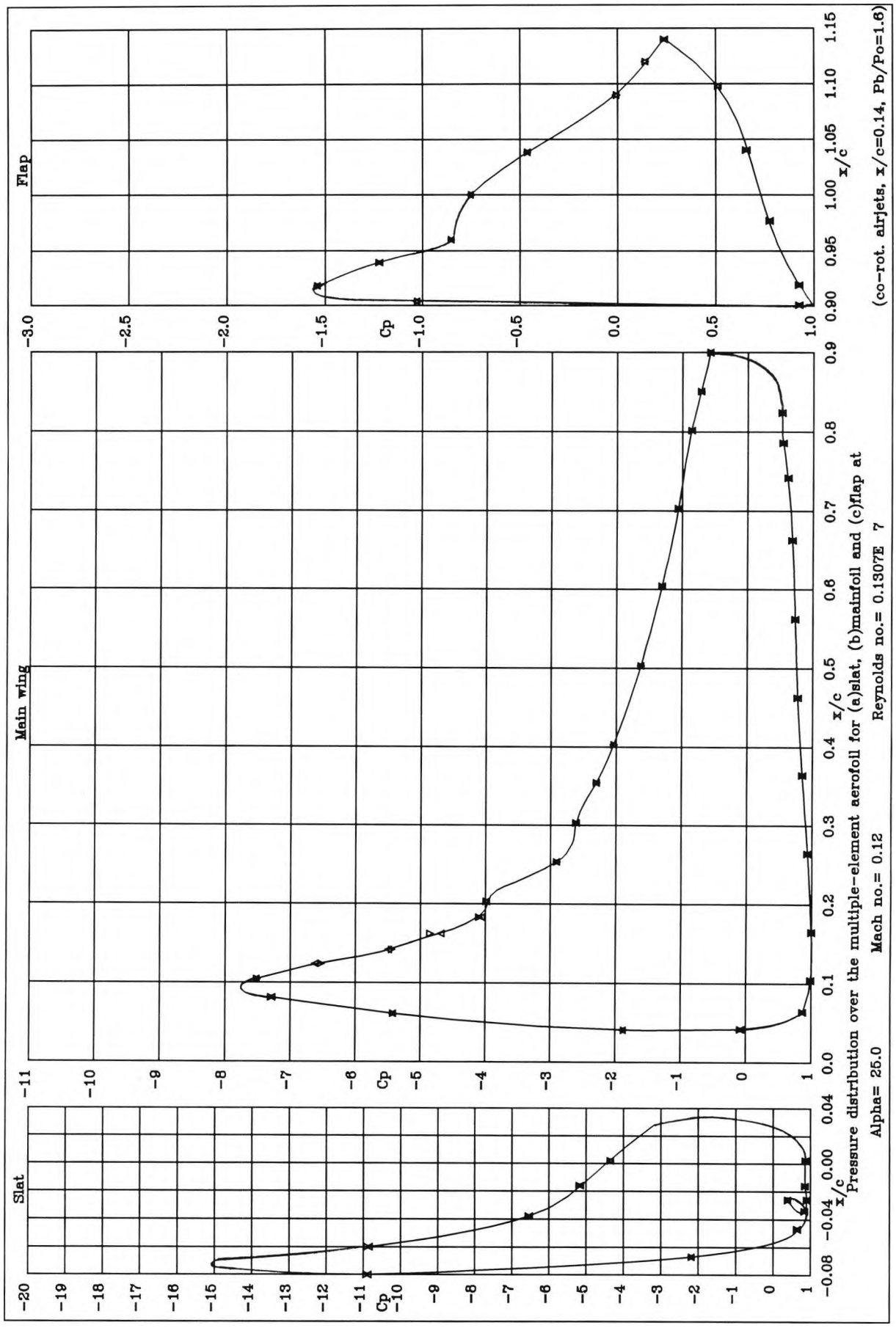

Figure 7.6 : Pressure distribution over the high lift system at 25° when co-rot. ajvg's are at x/c = 0.14

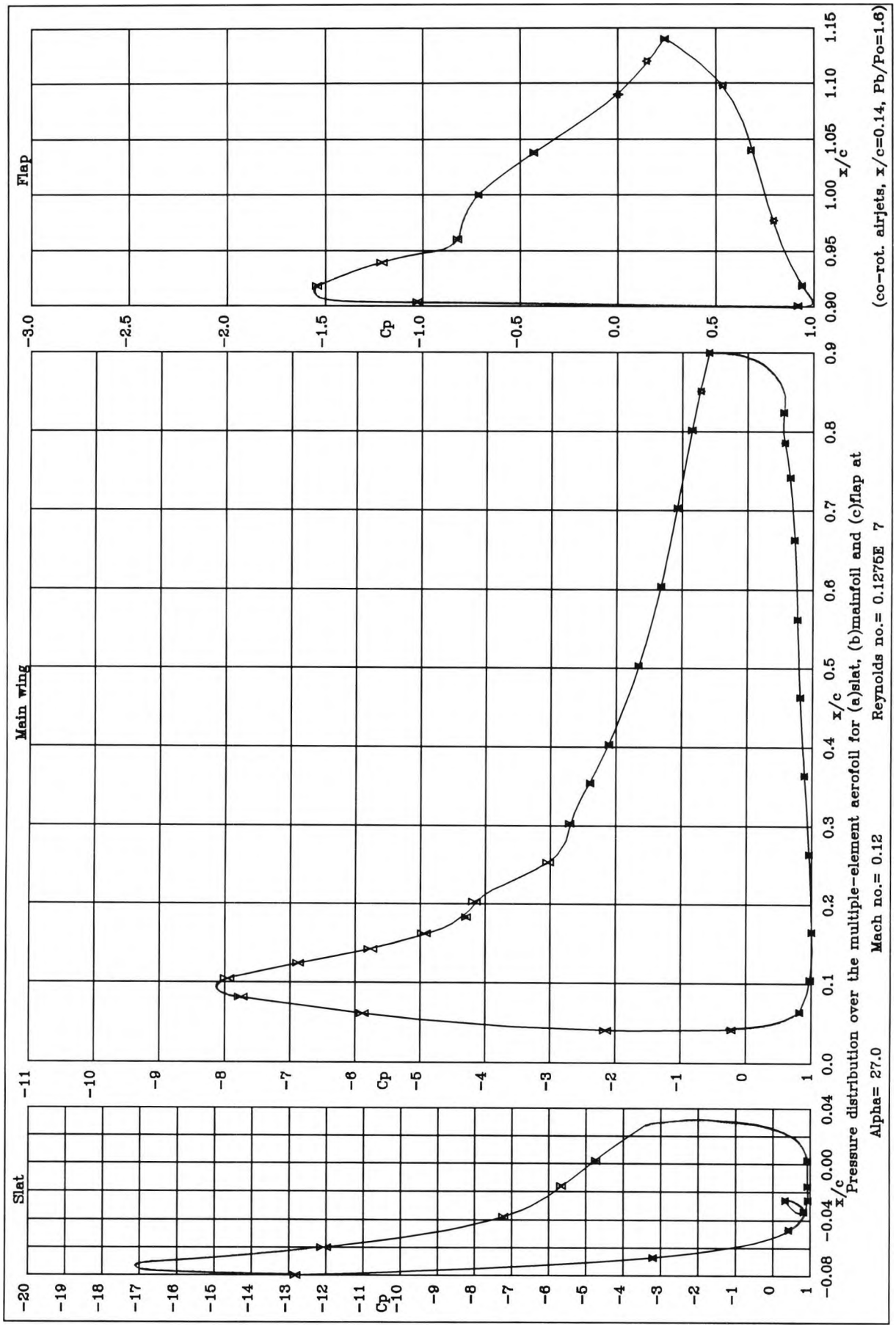

Figure 7.7 : Pressure distribution over the high lift system at 27° when co-rot. ajvg's are at x/c = 0.14

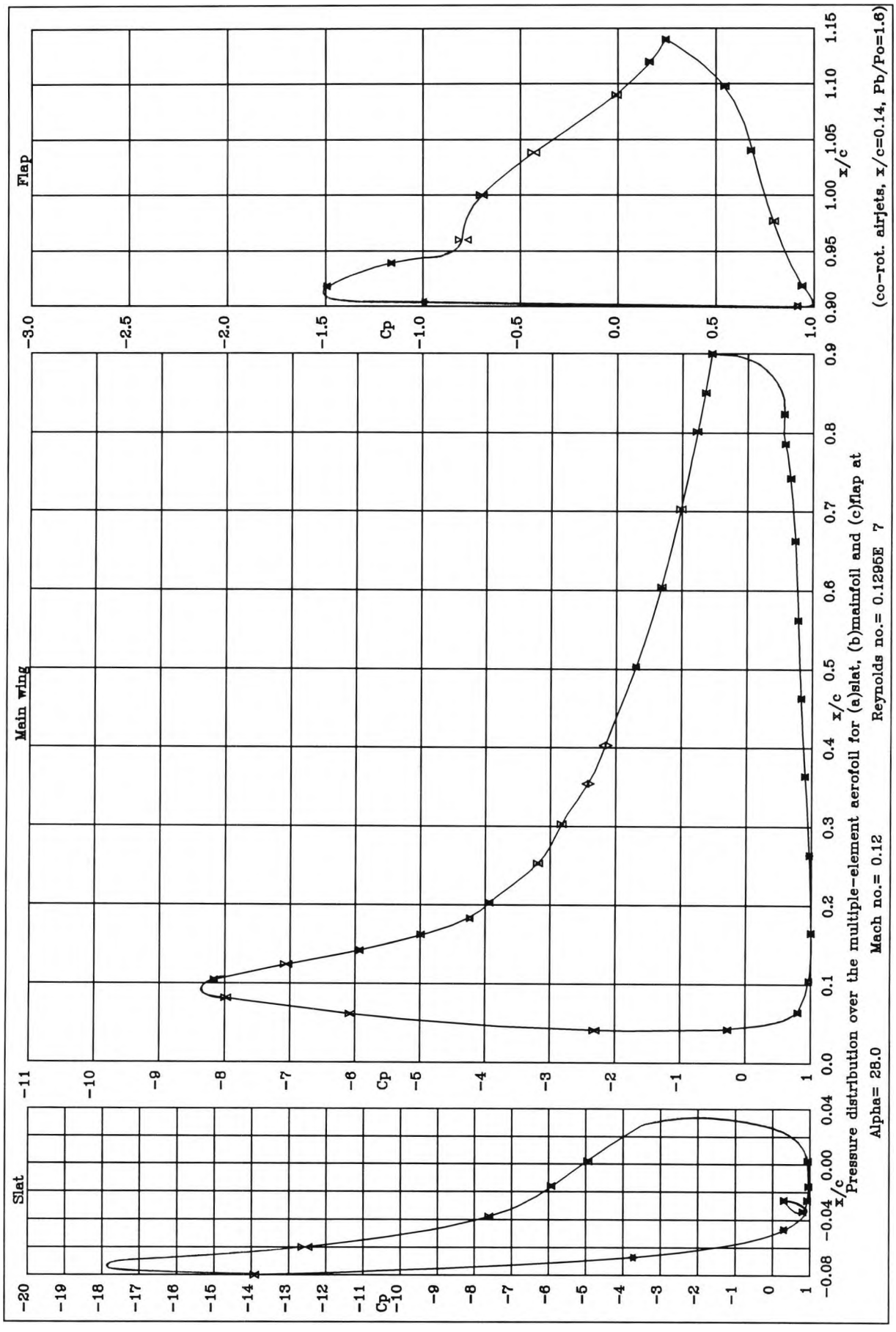

Figure 7.8 : Pressure distribution over the high lift system at 28° when co-rot. ajvg's are at x/c = 0.14

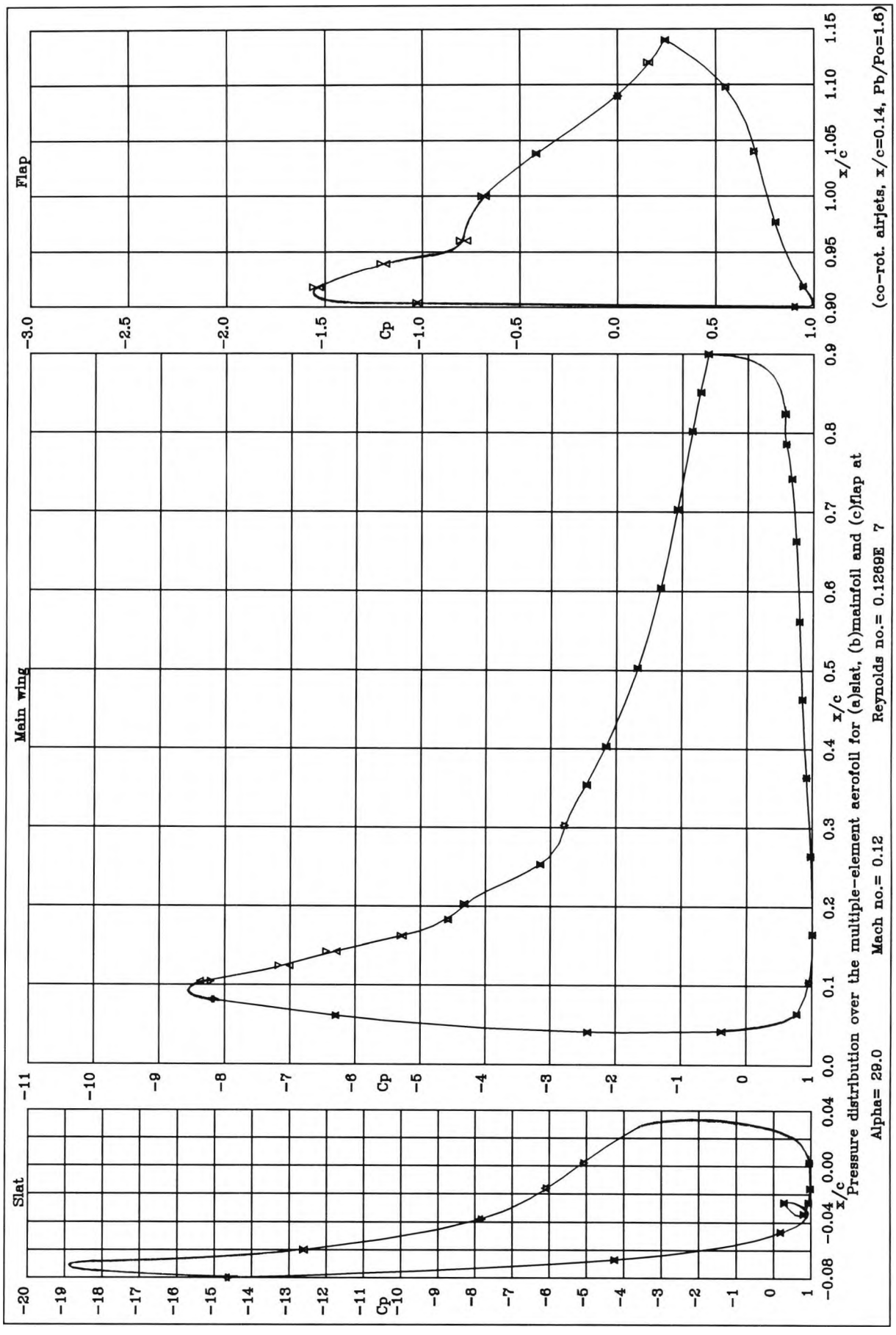

Figure 7.9 : Pressure distribution over the high lift system at 29° when co-rot. ajvg's are at x/c = 0.14

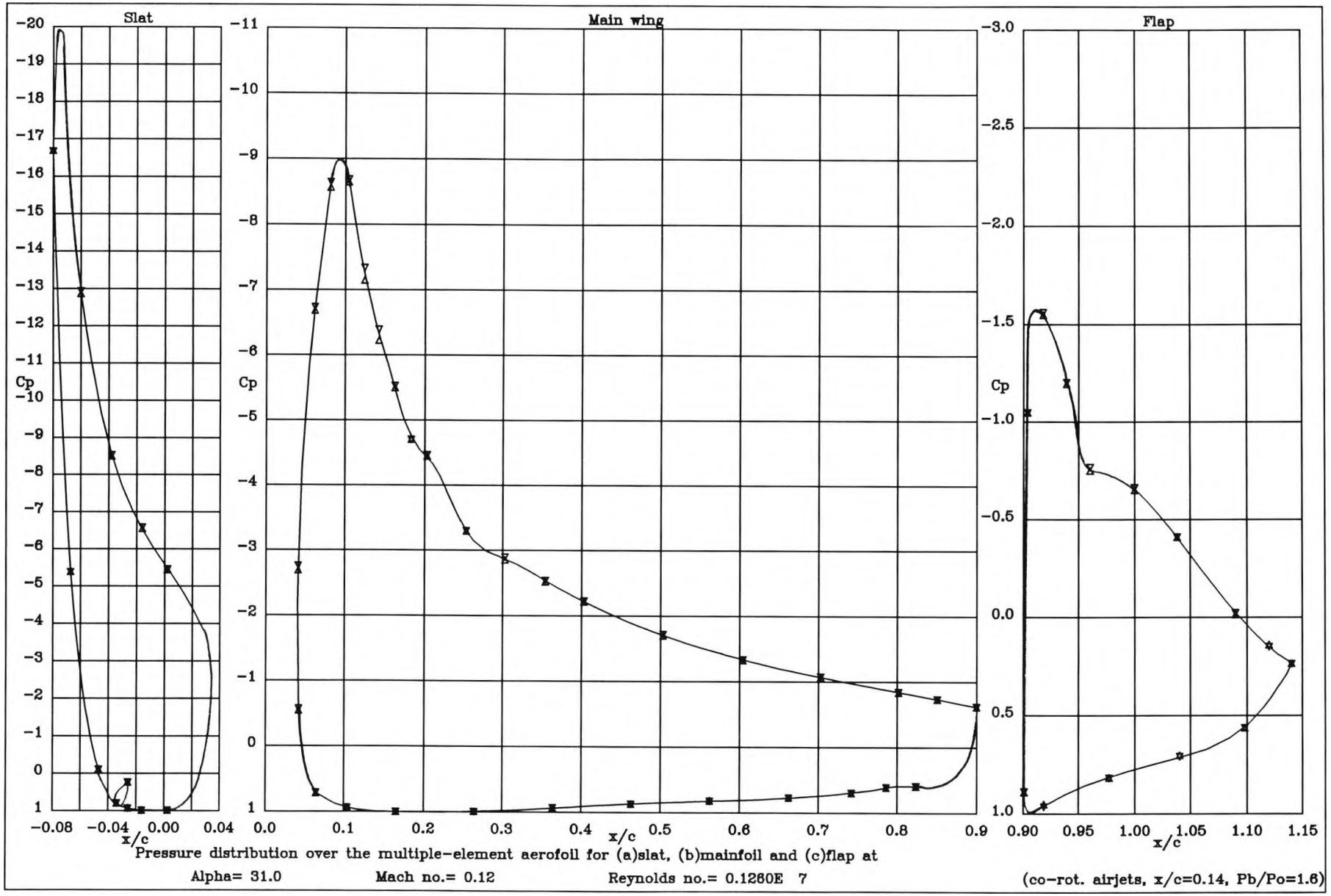

Figure 7.10 : Pressure distribution over the high lift system at 31° when co-rot. ajvg's are at x/c=0.14

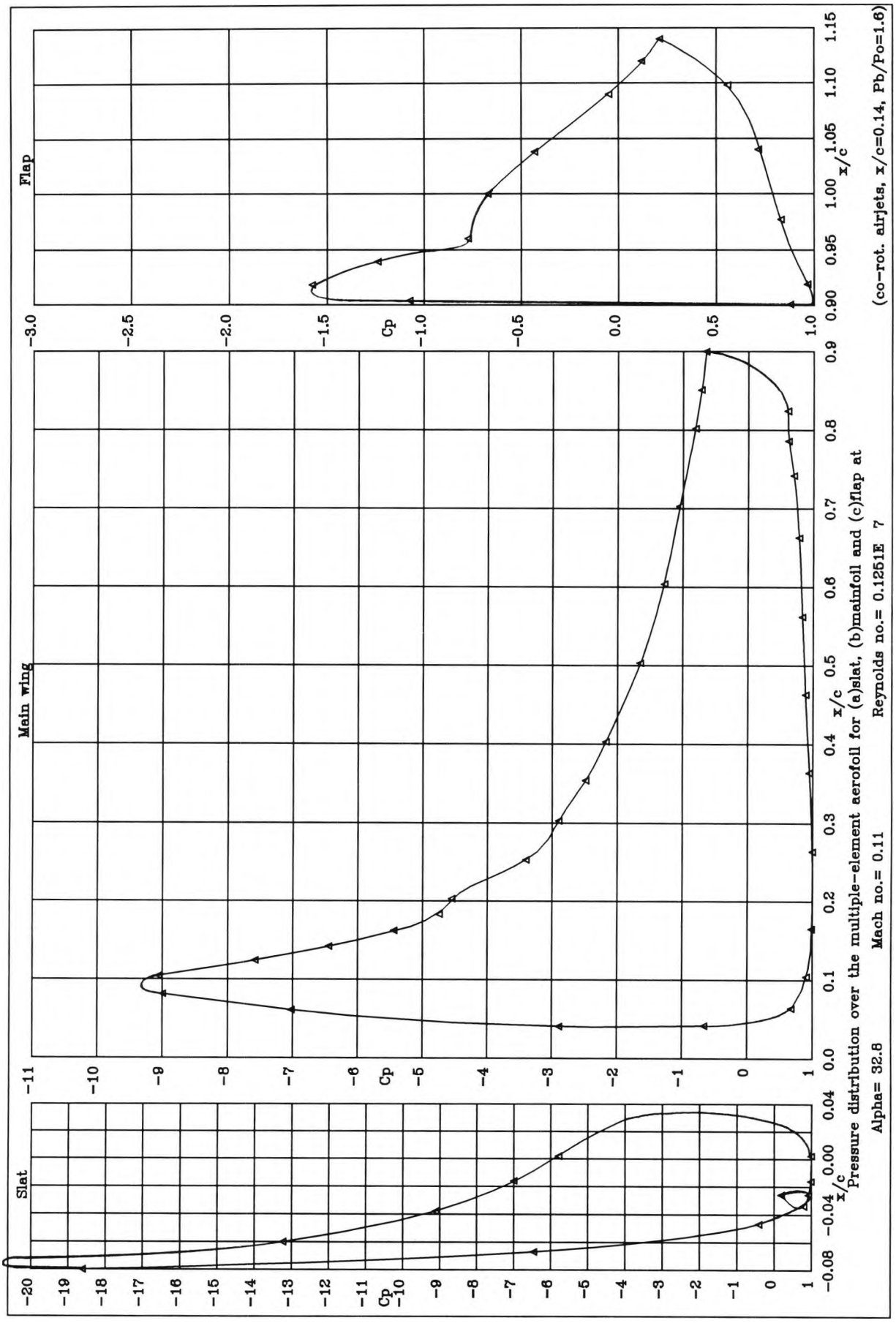

Figure 7.11 : Pressure distribution over the high lift system at 33° when co-rot. ajvg's are at x/c = 0.14

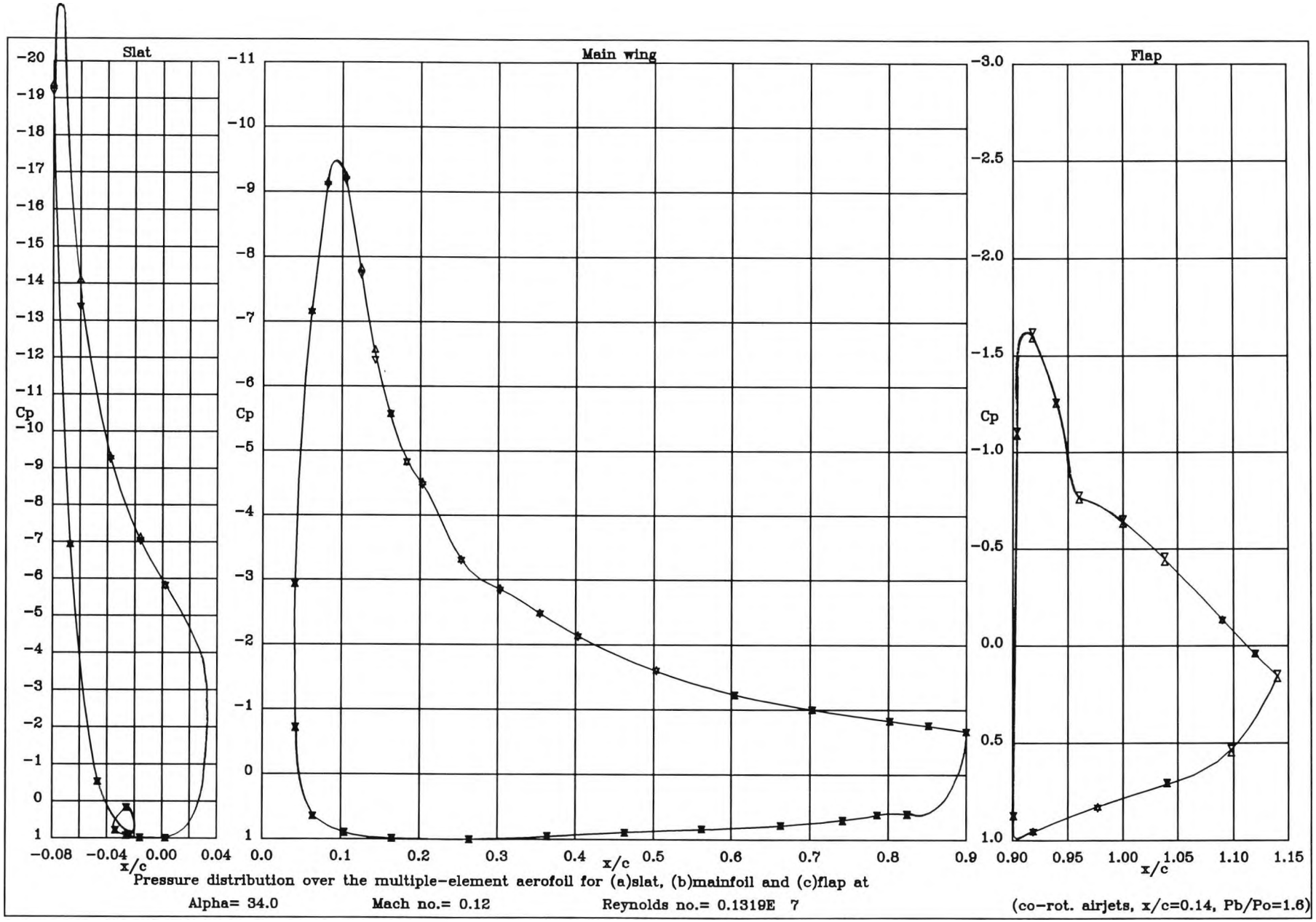

Figure 7.12 : Pressure distribution over the high lift system at 34° when co-rot. ajvg's are at x/c = 0.14

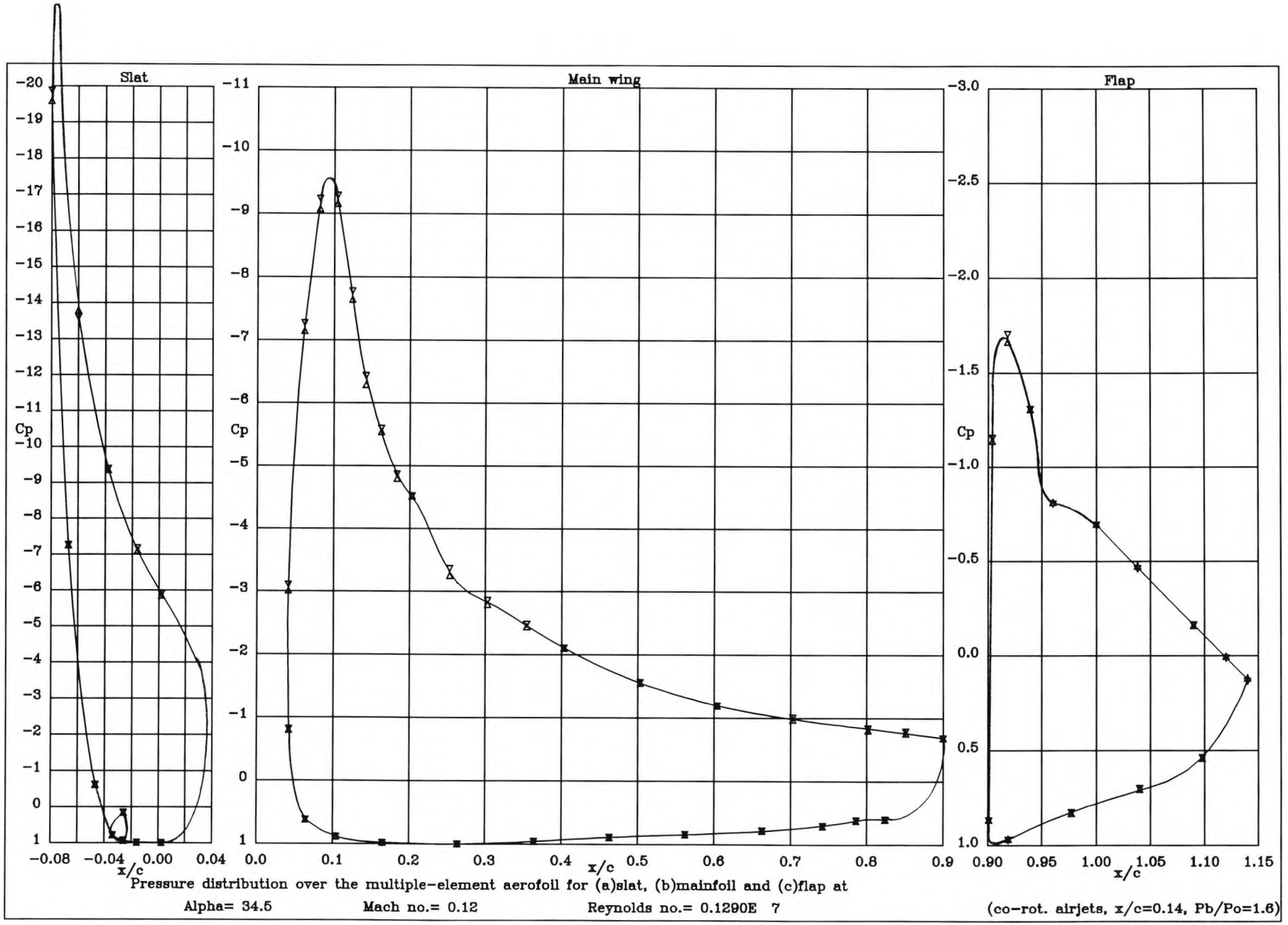

Figure 7.13 : Pressure distribution over the high lift system at 34.5° when co-rot. ajvg's are at x/c=0.14

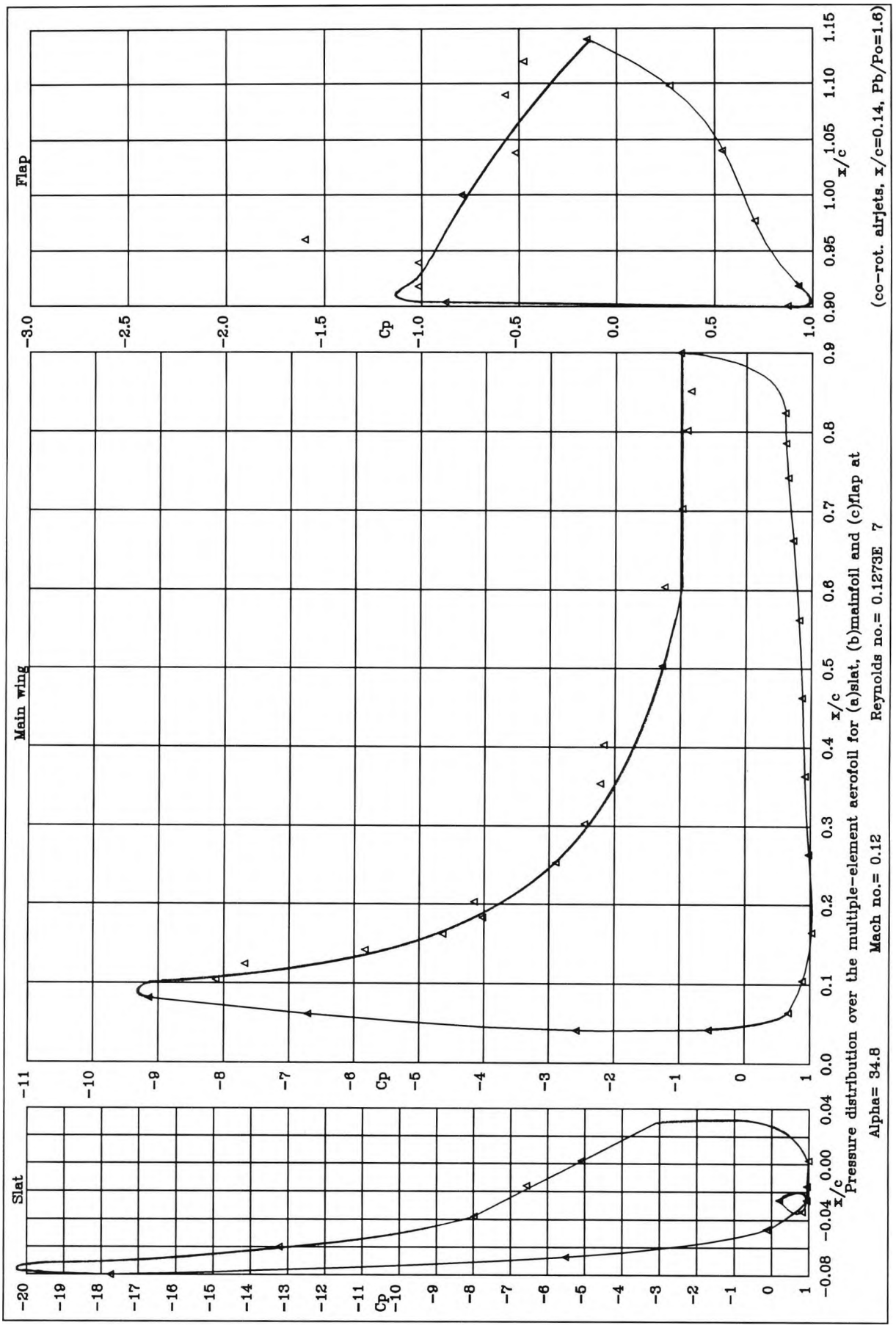

Figure 7.14 : Pressure distribution over the high lift system at 34.8° when co-rot. ajvg's are at x/c = 0.14

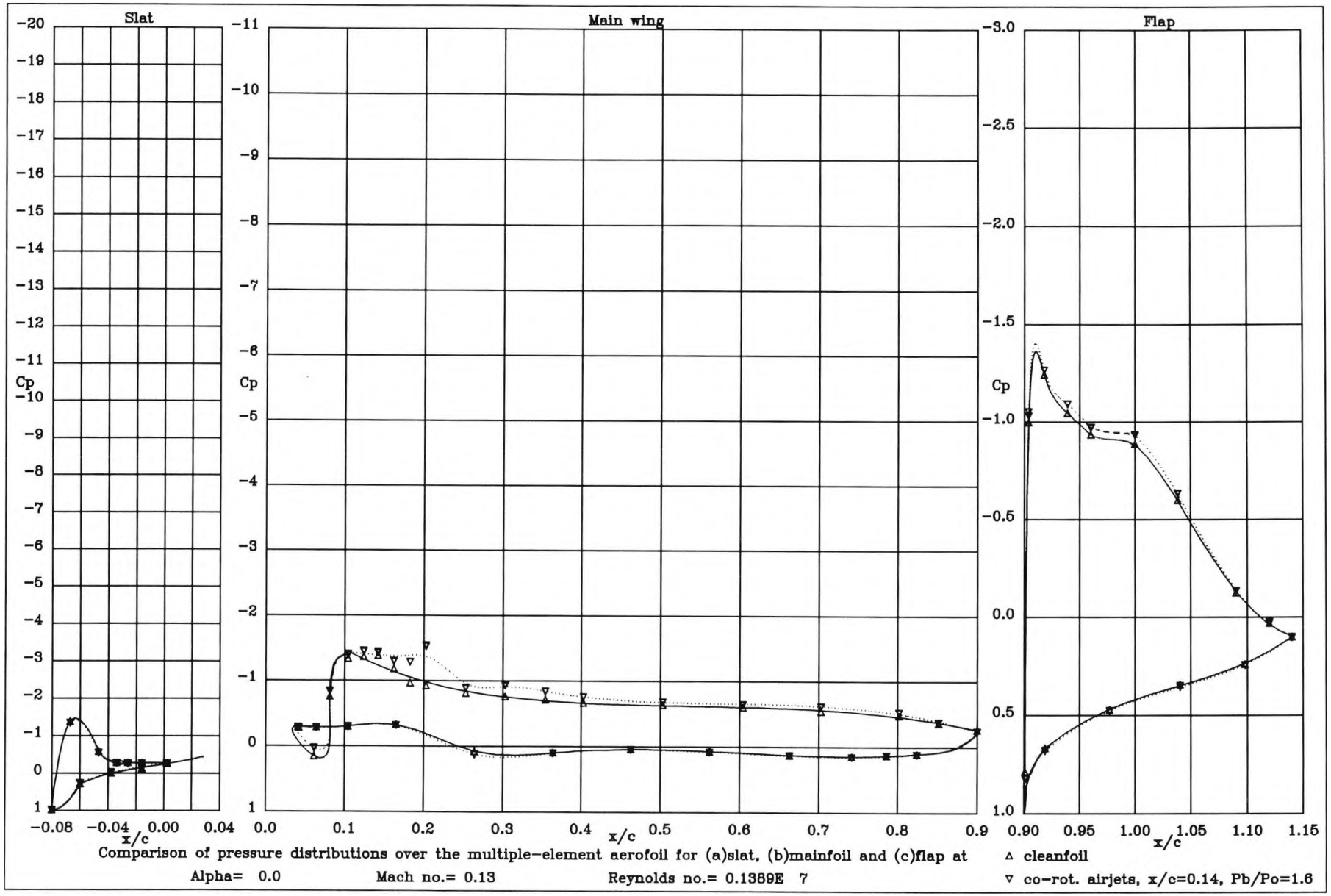

Figure 7.15 : Comparison of pressure distributions at $\alpha = 0°$ obtained with and without co-rot. airjets at x/c = 0.14

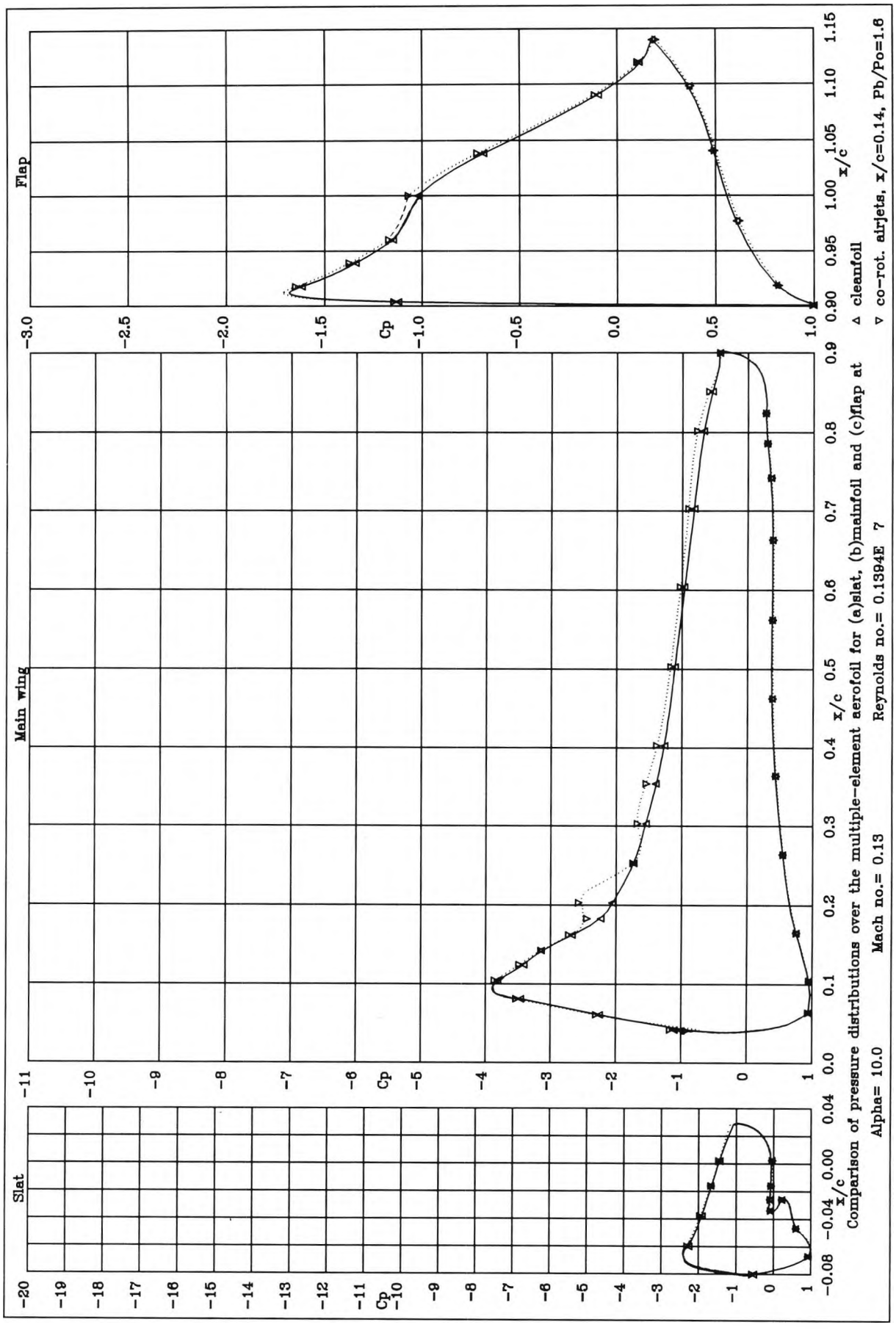

Figure 7.16 : Comparison of pressure distributions at $\alpha = 10°$ obtained with and without co-rot. airjets at x/c = 0.14

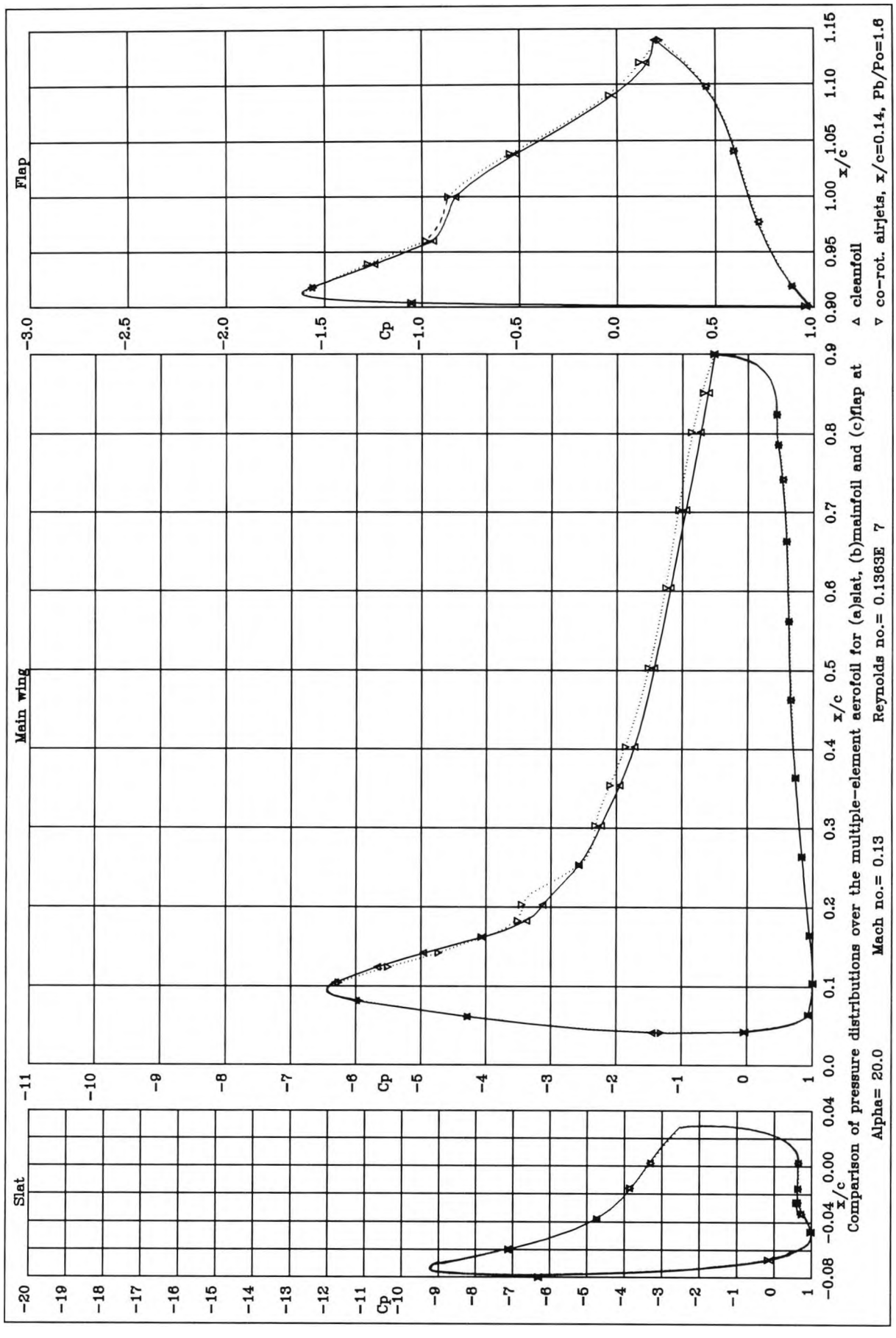

Figure 7.17 : Comparison of pressure distributions at $\alpha = 20°$ obtained with and without co-rot. airjets at x/c = 0.14

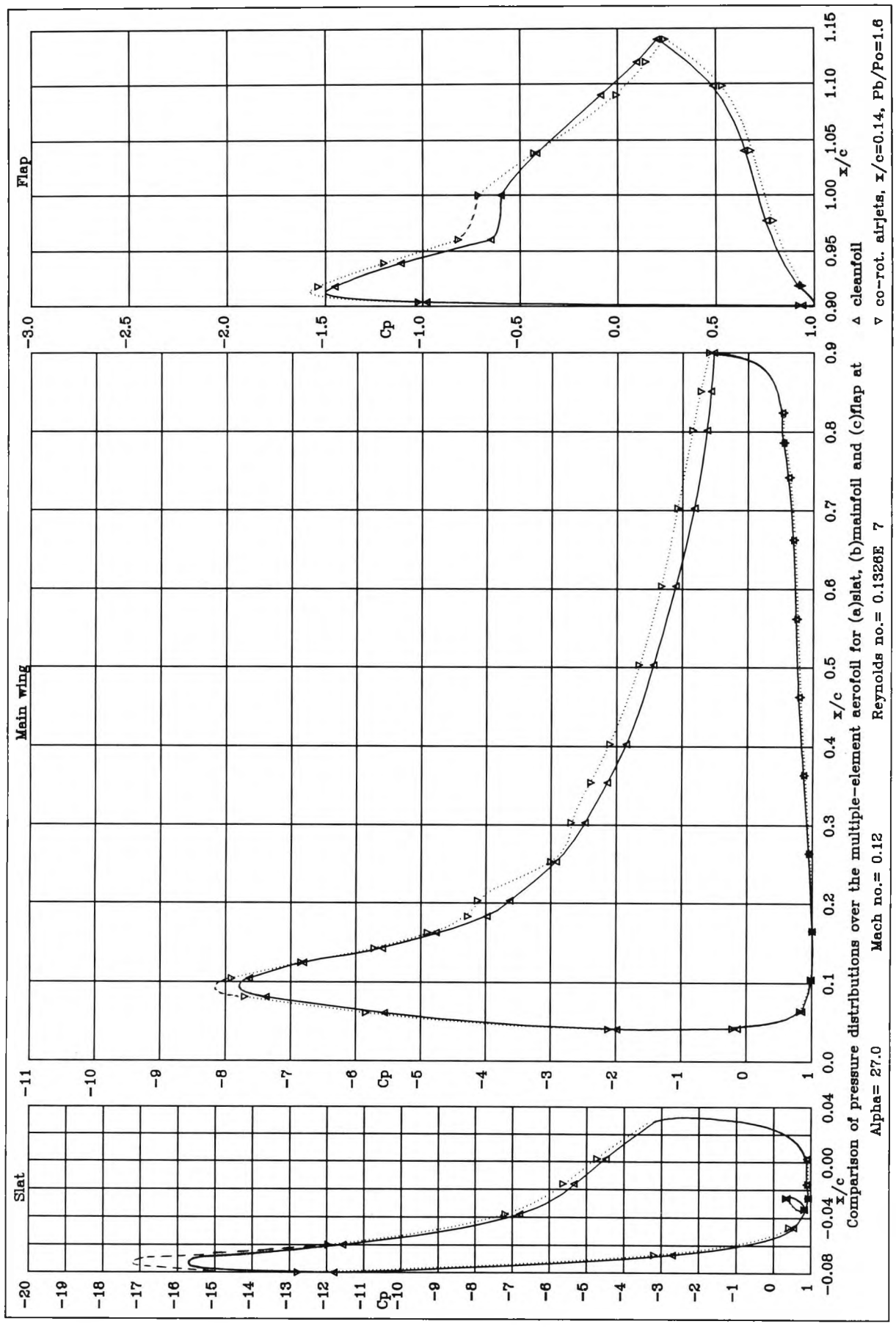

Figure 7.18 : Comparison of pressure distributions at $\alpha = 27°$ obtained with and without co-rot. airjets at x/c = 0.14

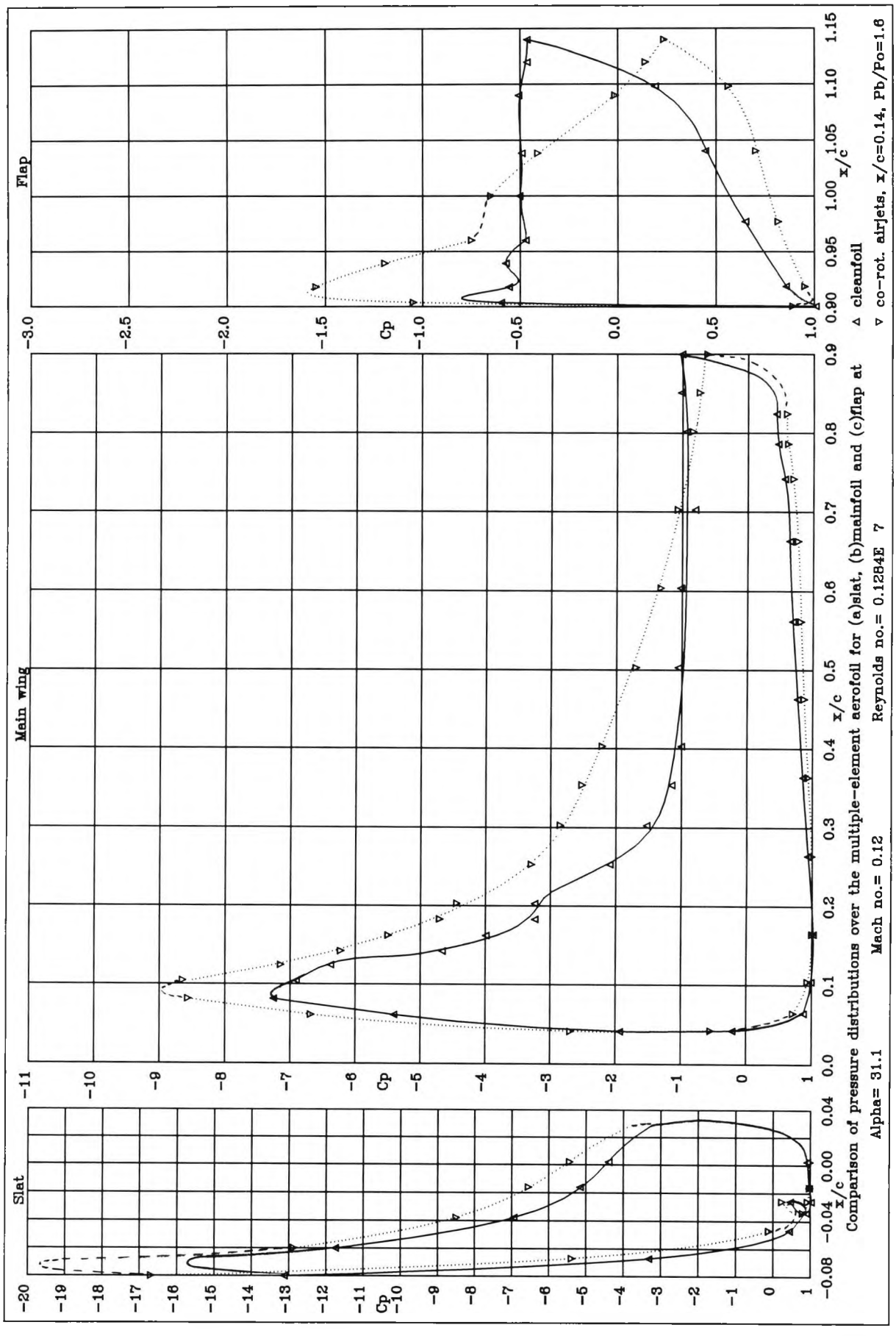

Figure 7.19 : Comparison of pressure distributions at $\alpha = 31°$ obtained with and without co-rot. airjets at x/c = 0.14

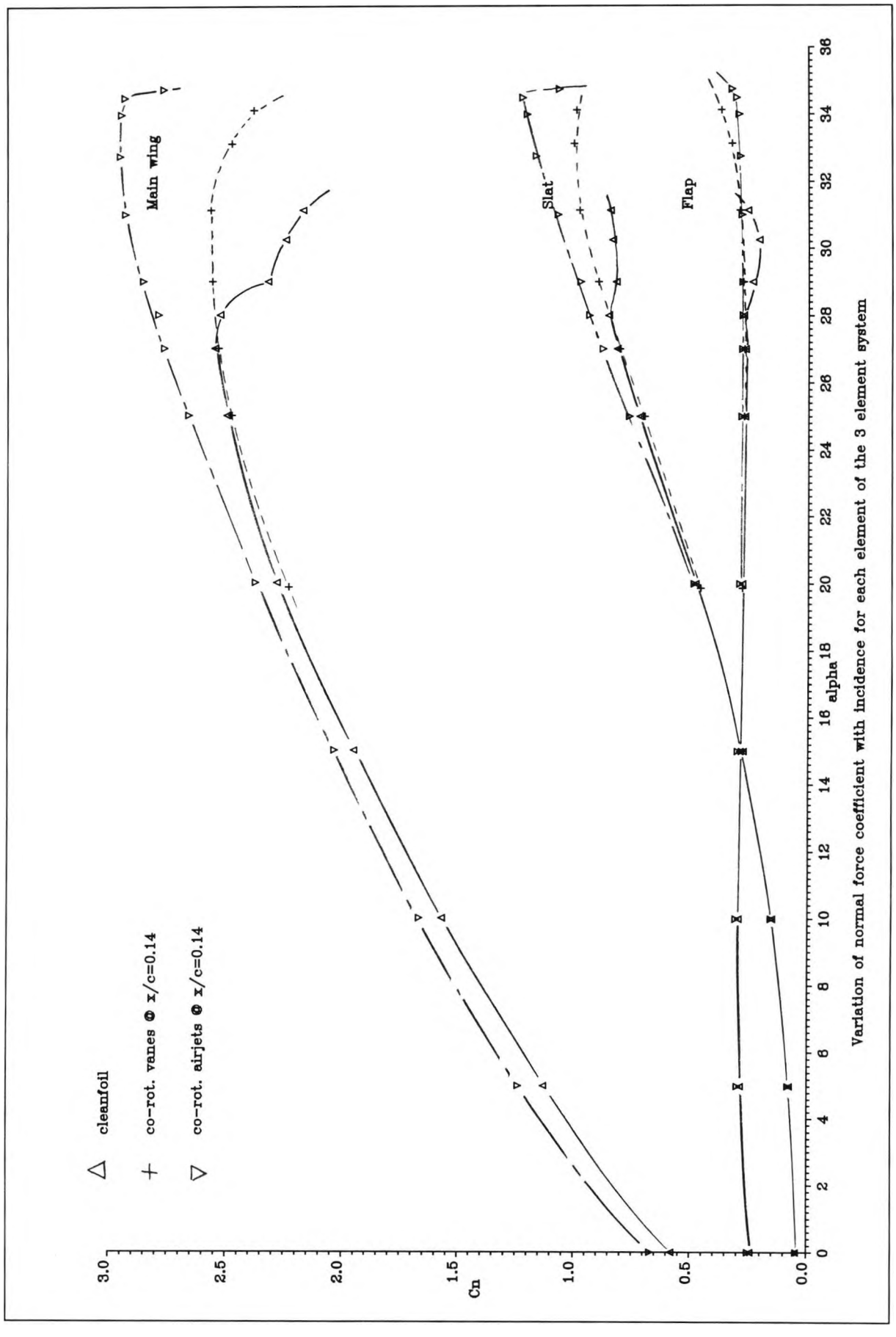

Figure 7.20 : Variation of C_n with α for each element of the high lift system when co-rot. airjet vortex generators are at x/c = 0.14

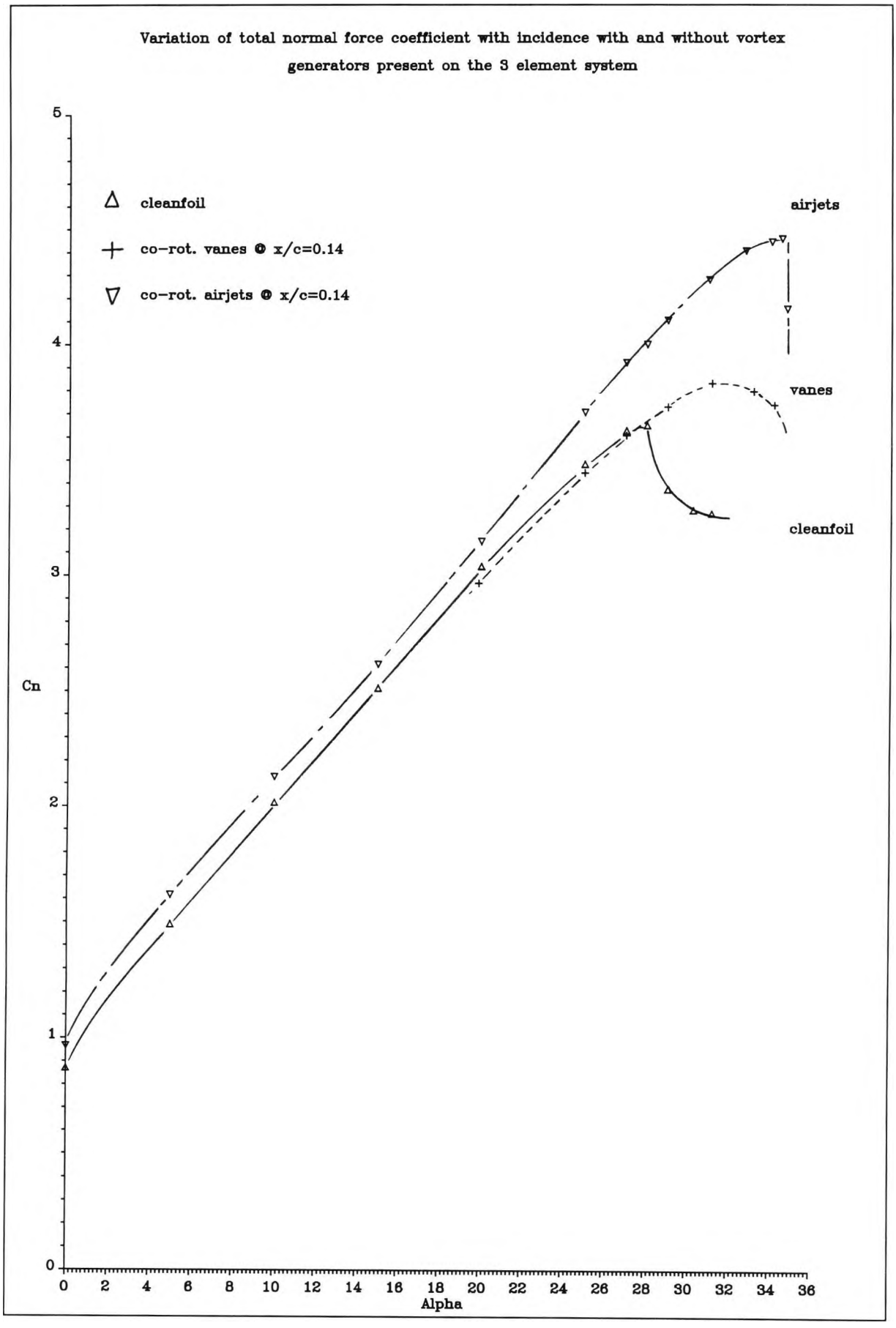

Figure 7.21 : Variation of total C_n with α for the high lift system when co-rot. airjet vortex generators are at x/c = 0.14

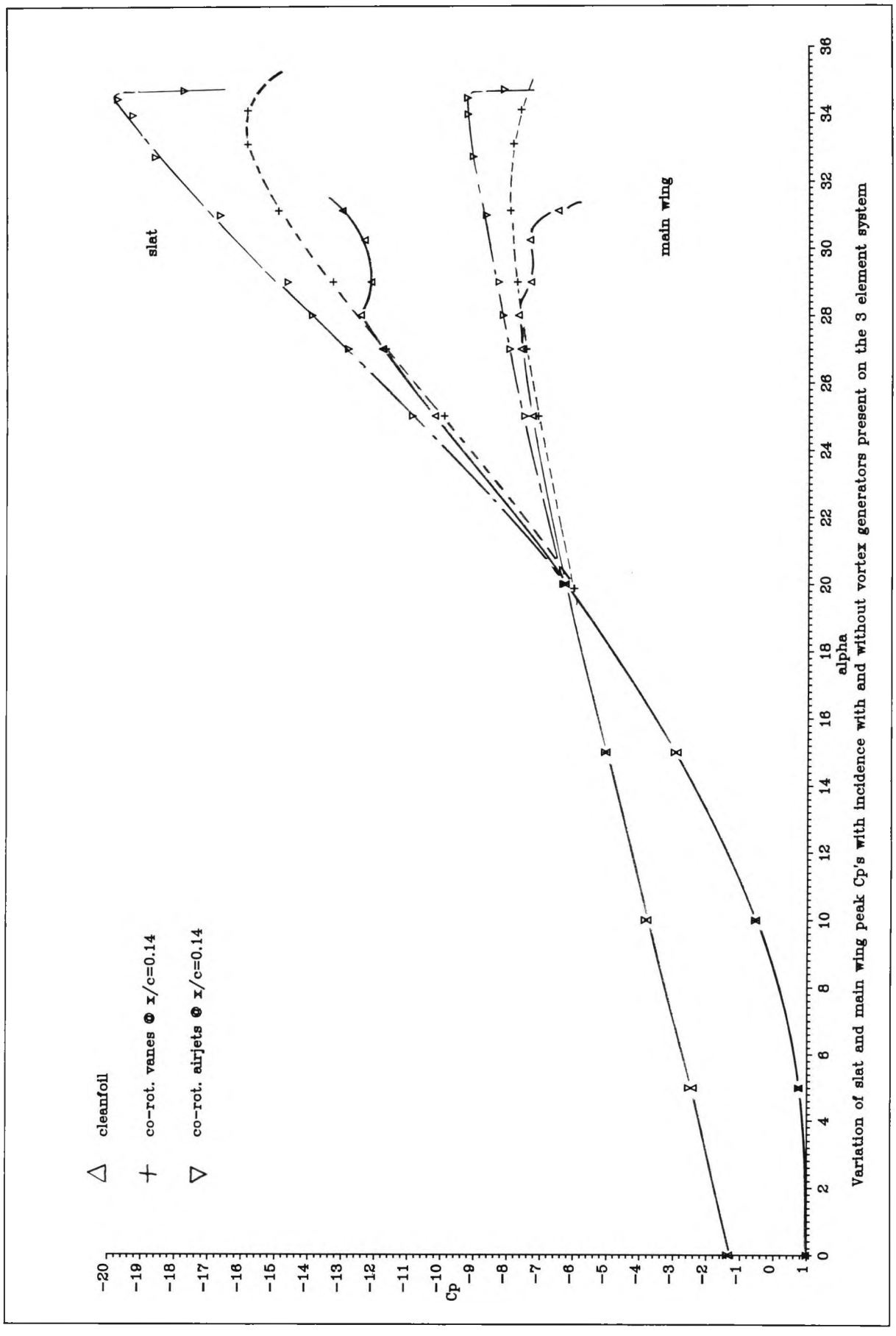

Figure 7.22 : Variation of slat and main wing peak C_p's with α when co-rot. airjet vortex generators are at x/c = 0.14

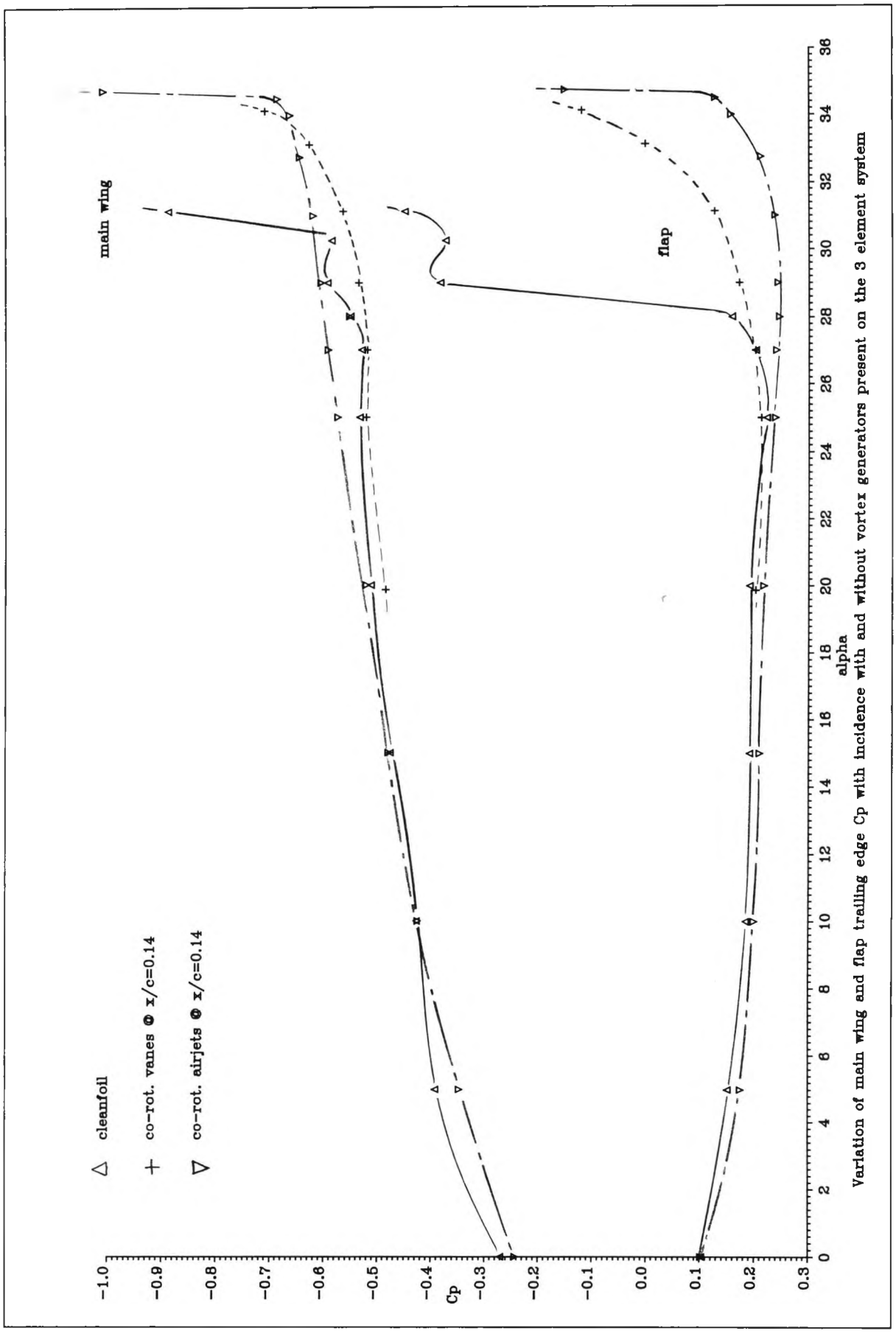

Figure 7.23 : Variation of main wing and flap trailing edge C_p's with α when co-rot. airjet vortex generators are at x/c = 0.14

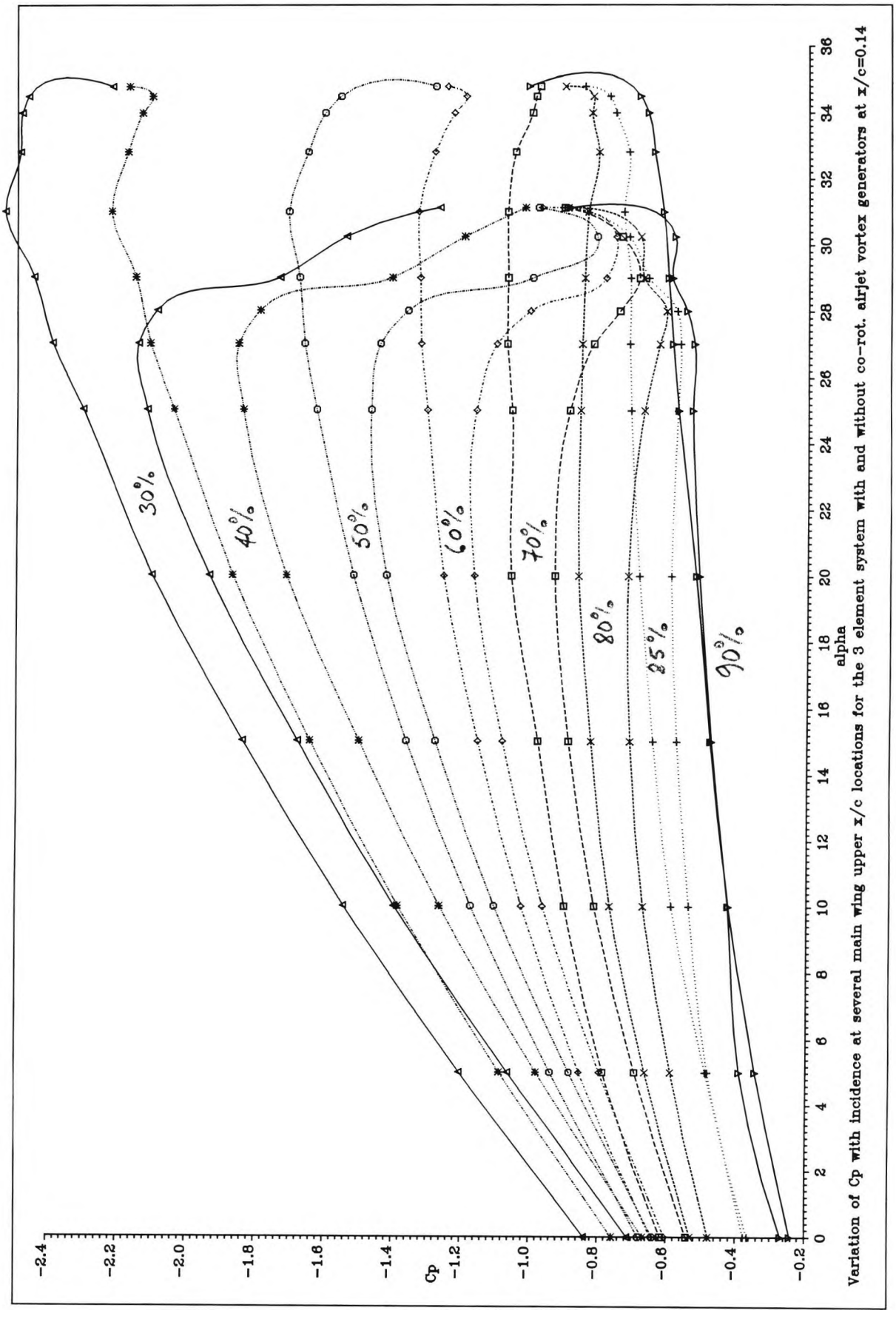

Figure 7.24 : Variation of static C_p with incidence at several x/c positions on the main wing upper surface with and without co-rot. airjet vortex generators at x/c = 0.14

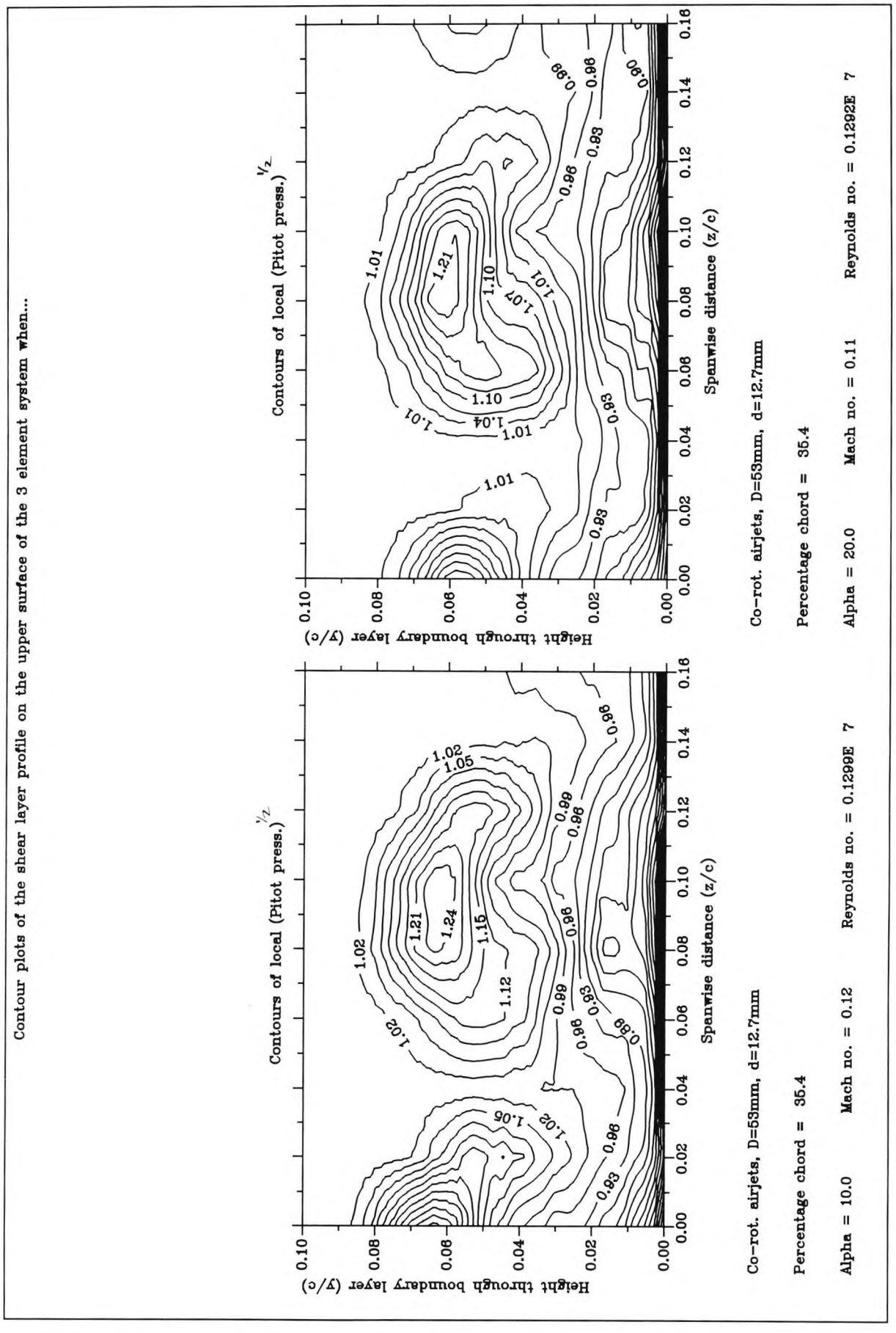

Figure 7.25 : Contour plots of the shear layer structure above the main wing at x/c = 0.354 for $\alpha = 10°$ & $20°$ when co-rot. ajvg's are at x/c = 0.14

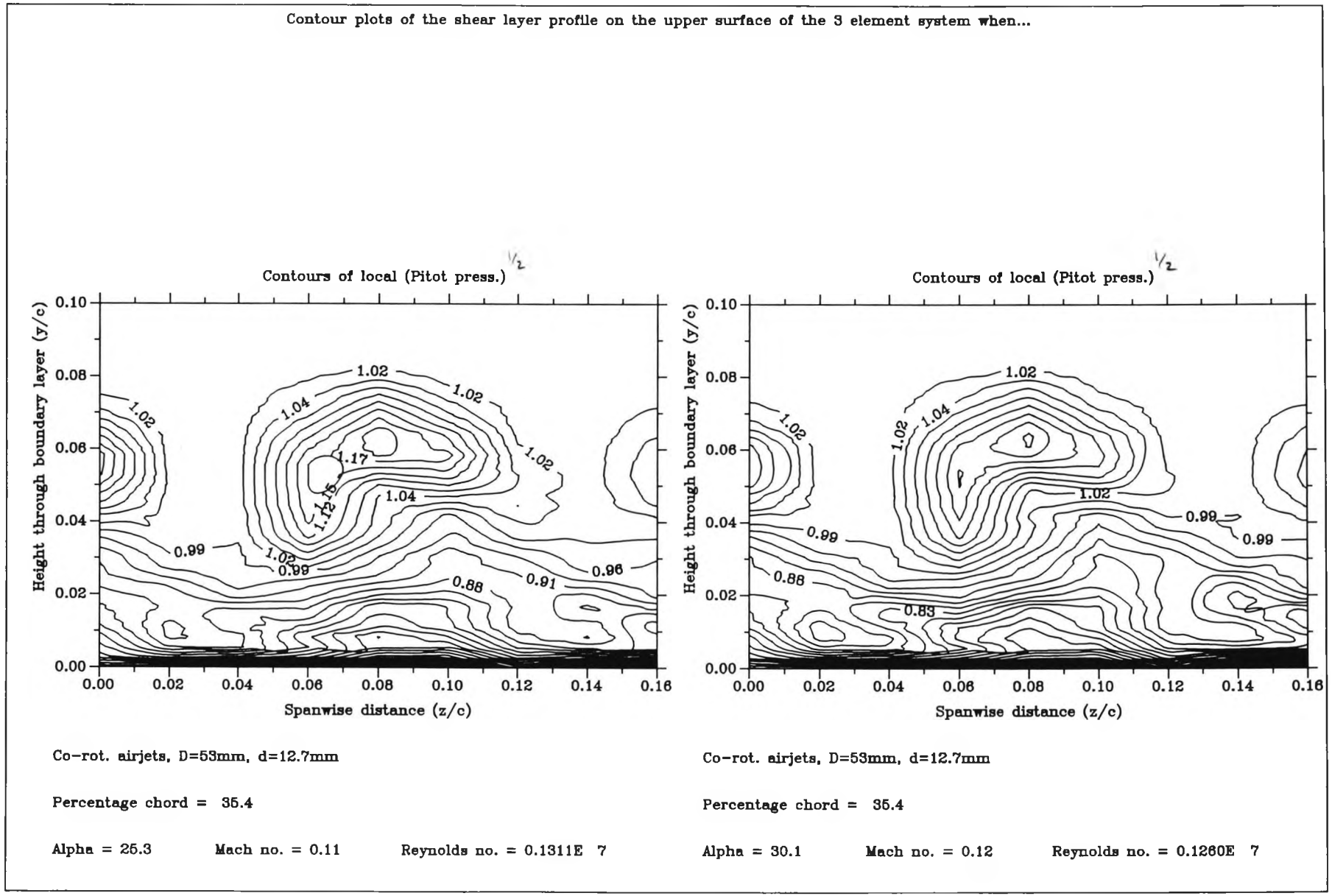

Figure 7.26 : Contour plots of the shear layer structure above the main wing at x/c = 0.354 for $\alpha = 25°$ & $30°$ when co-rot. ajvg's are at x/c = 0.14

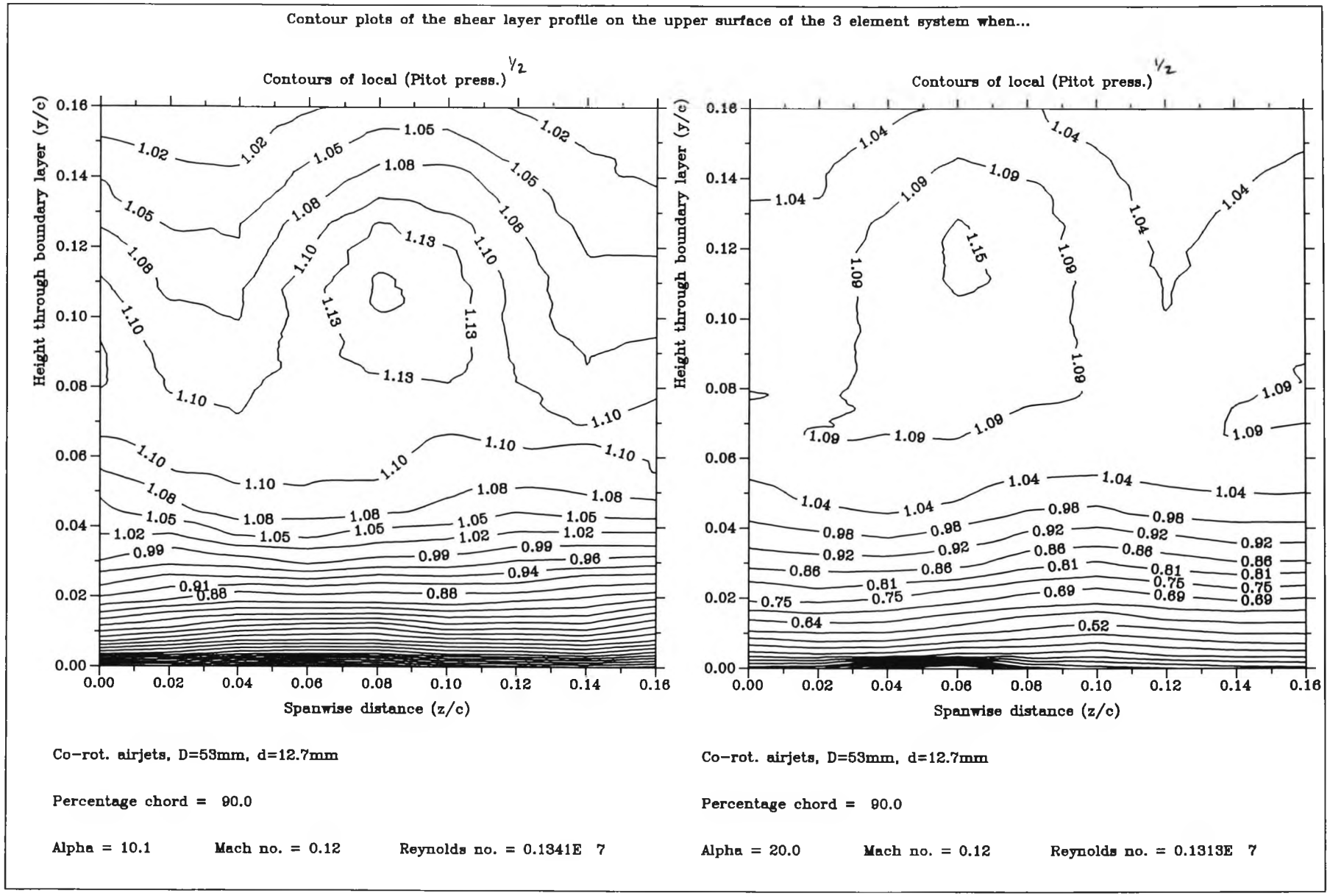

Figure 7.27 : Contour plots of the shear layer structure above the main wing at x/c = 0.9 for $\alpha = 10°$ & $20°$ when co-rot. ajvg's are at x/c = 0.14

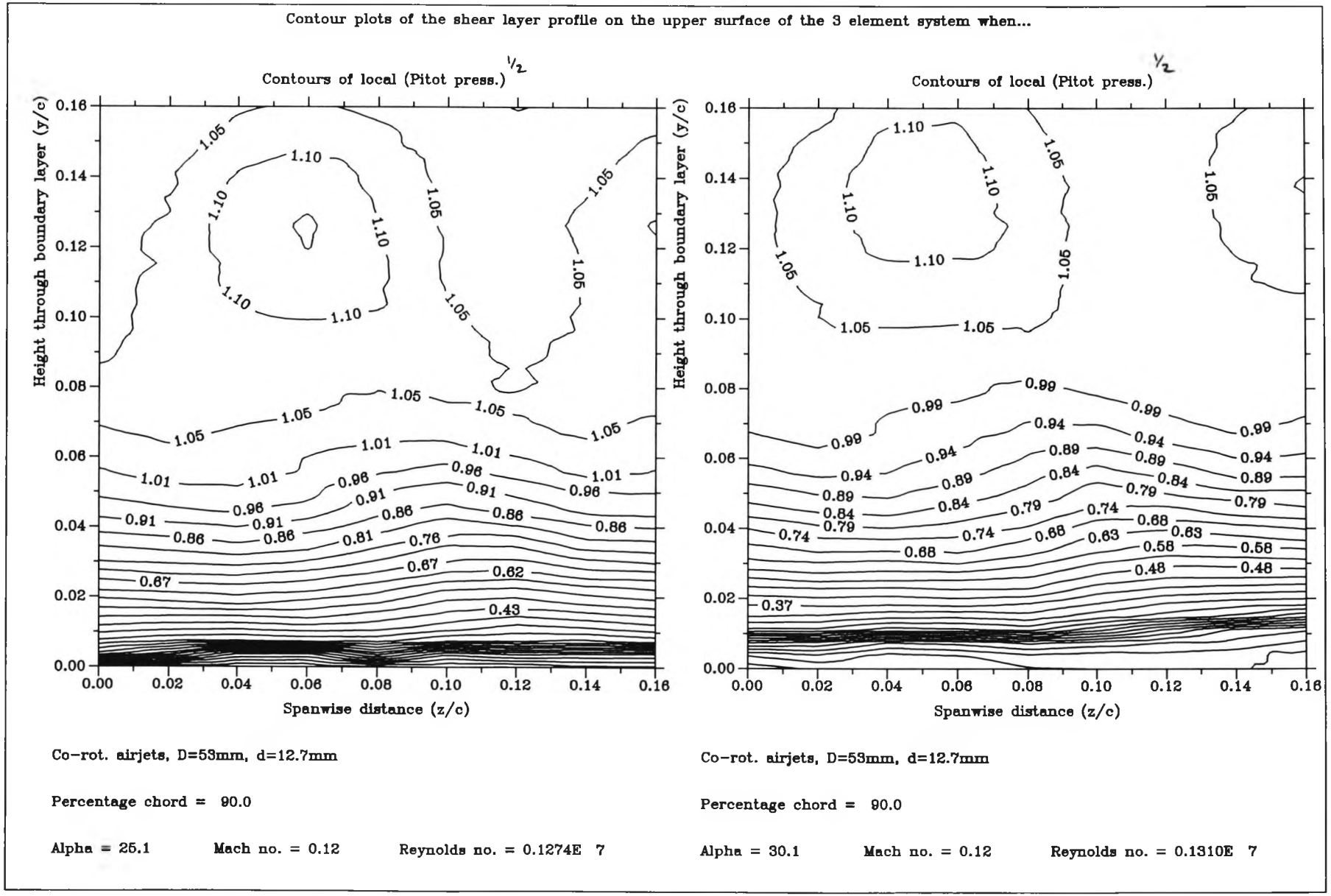

Figure 7.28 : Contour plots of the shear layer structure above the main wing at x/c = 0.9 for $\alpha = 25°$ & 30° when co-rot. ajvg's are at x/c = 0.14

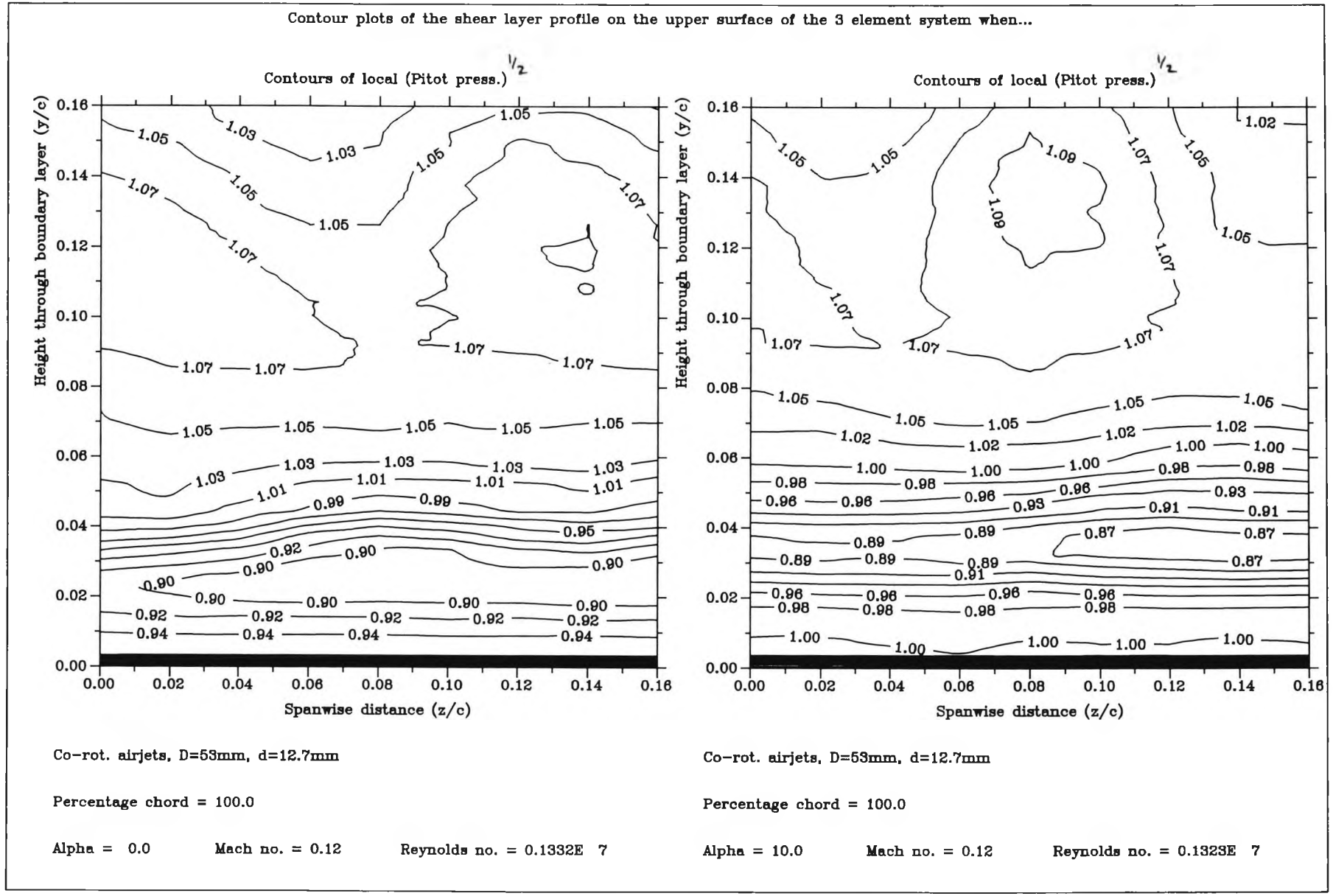

Figure 7.29 : Contour plots of the shear layer structure above the flap at x/c = 1.0 for $\alpha = 0°$ & 10° when co-rot. ajvg's are at x/c = 0.14

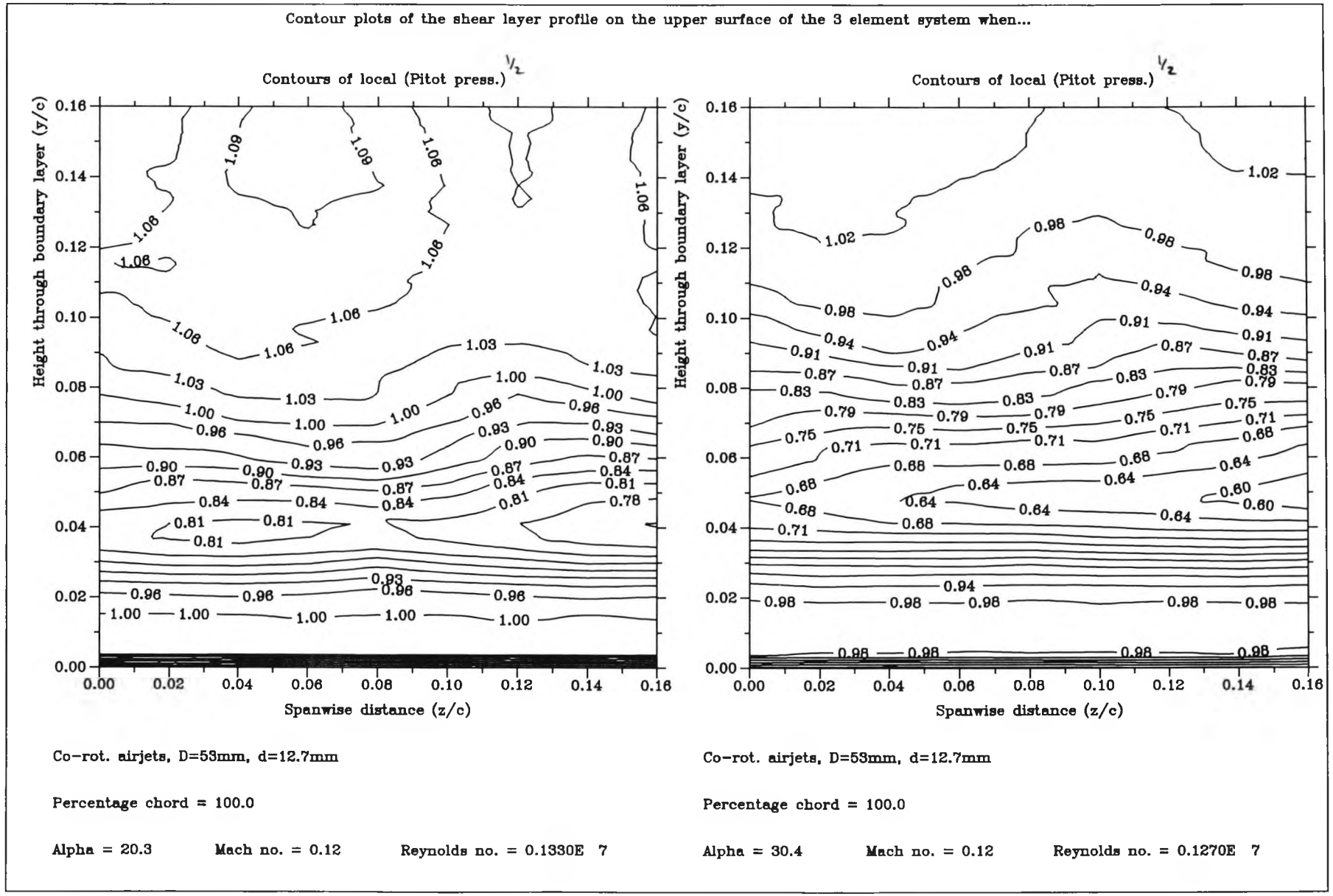

Figure 7.30 : Contour plots of the shear layer structure above the flap at x/c = 1.0 for $\alpha = 20°$ & $30°$ when co-rot. ajvg's are at x/c = 0.14

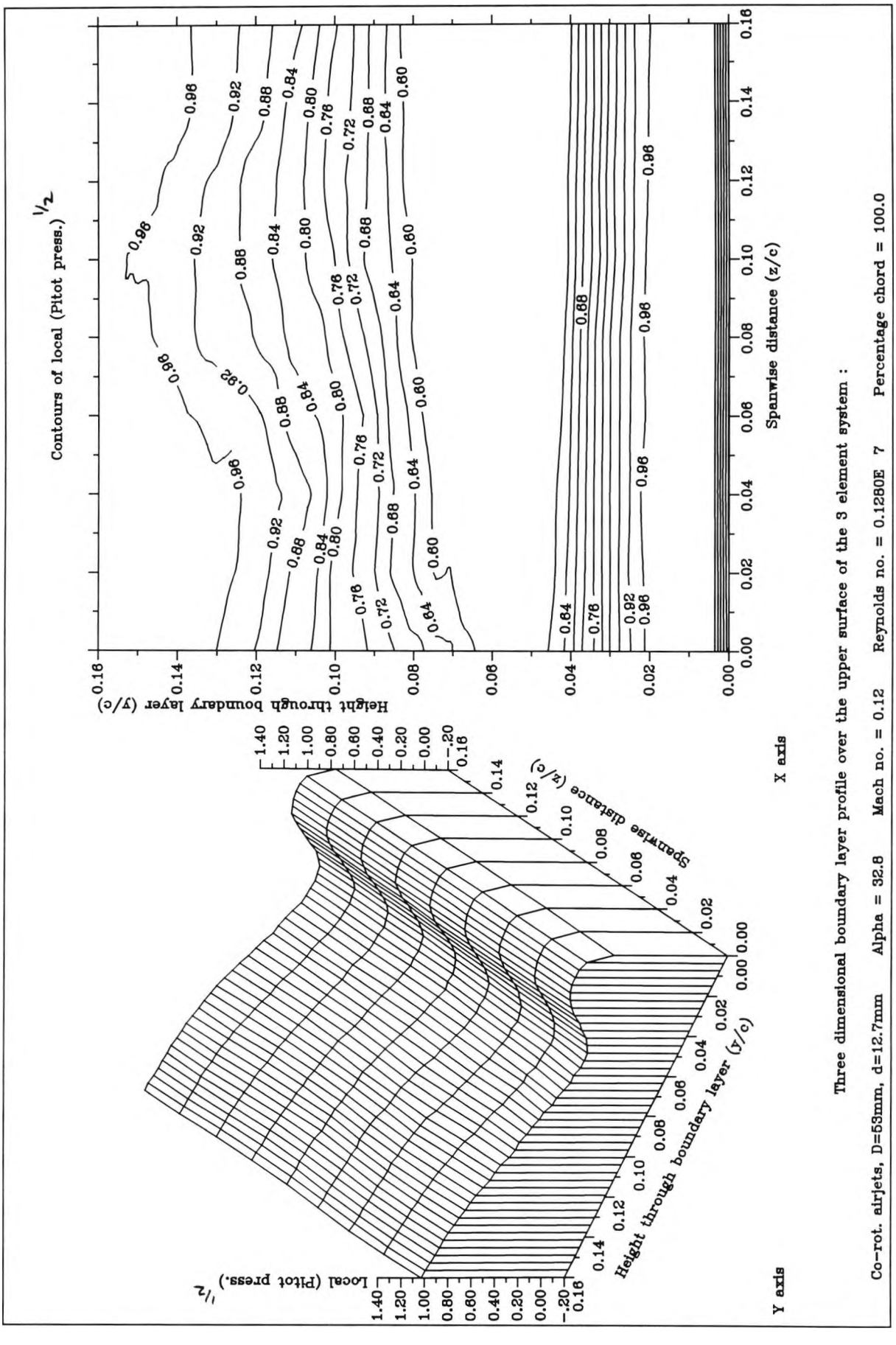

Figure 7.31 : Contour plot and surface plot of the shear layer structure above the flap at x/c = 1.0 for $\alpha = 32.8°$ when co-rot. ajvg's are at x/c = 0.14

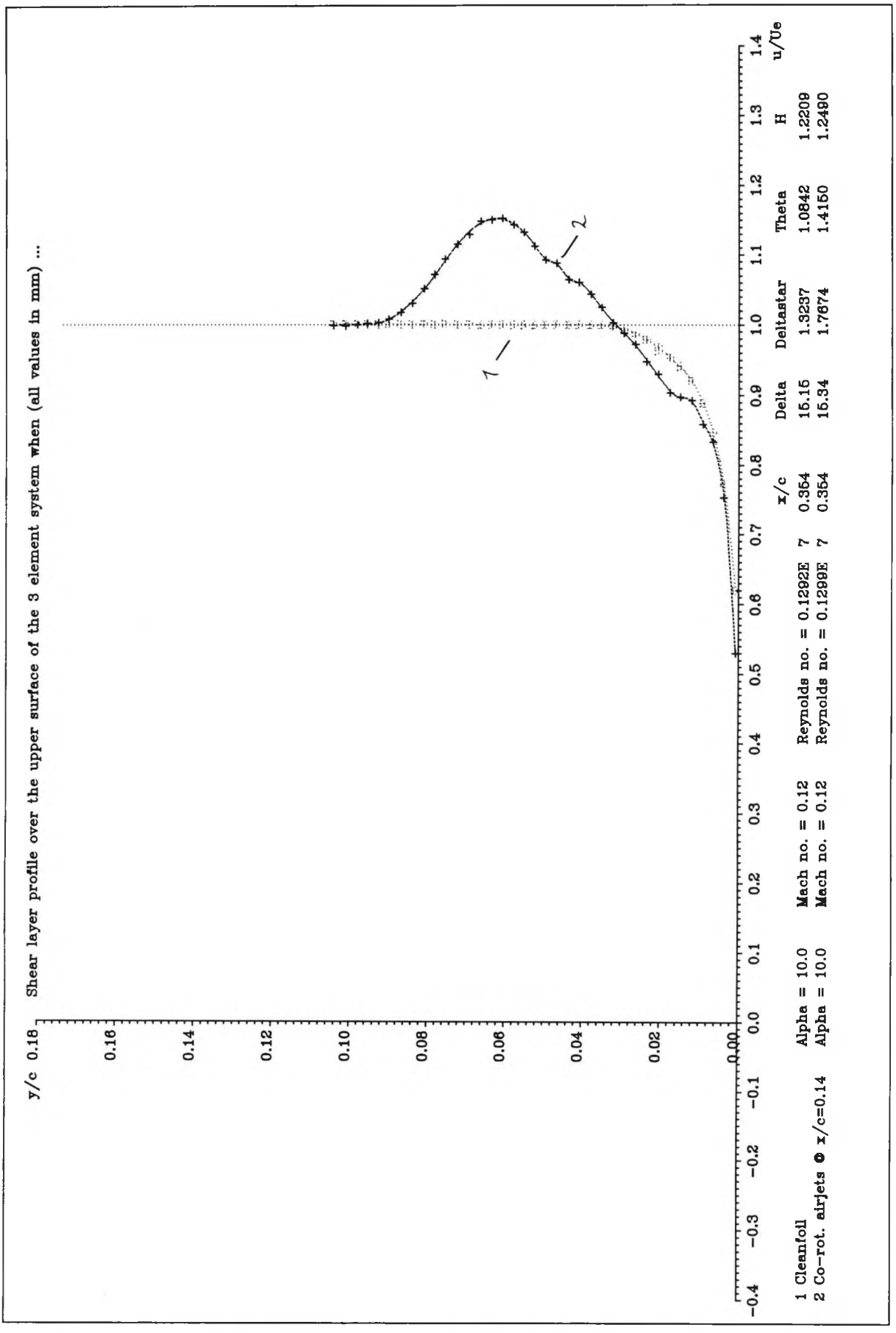

Figure 7.32 : Comparison of mean shear layer profiles at x/c = 0.354, $\alpha = 10°$; obtained with and without co-rot. airjets at x/c = 0.14

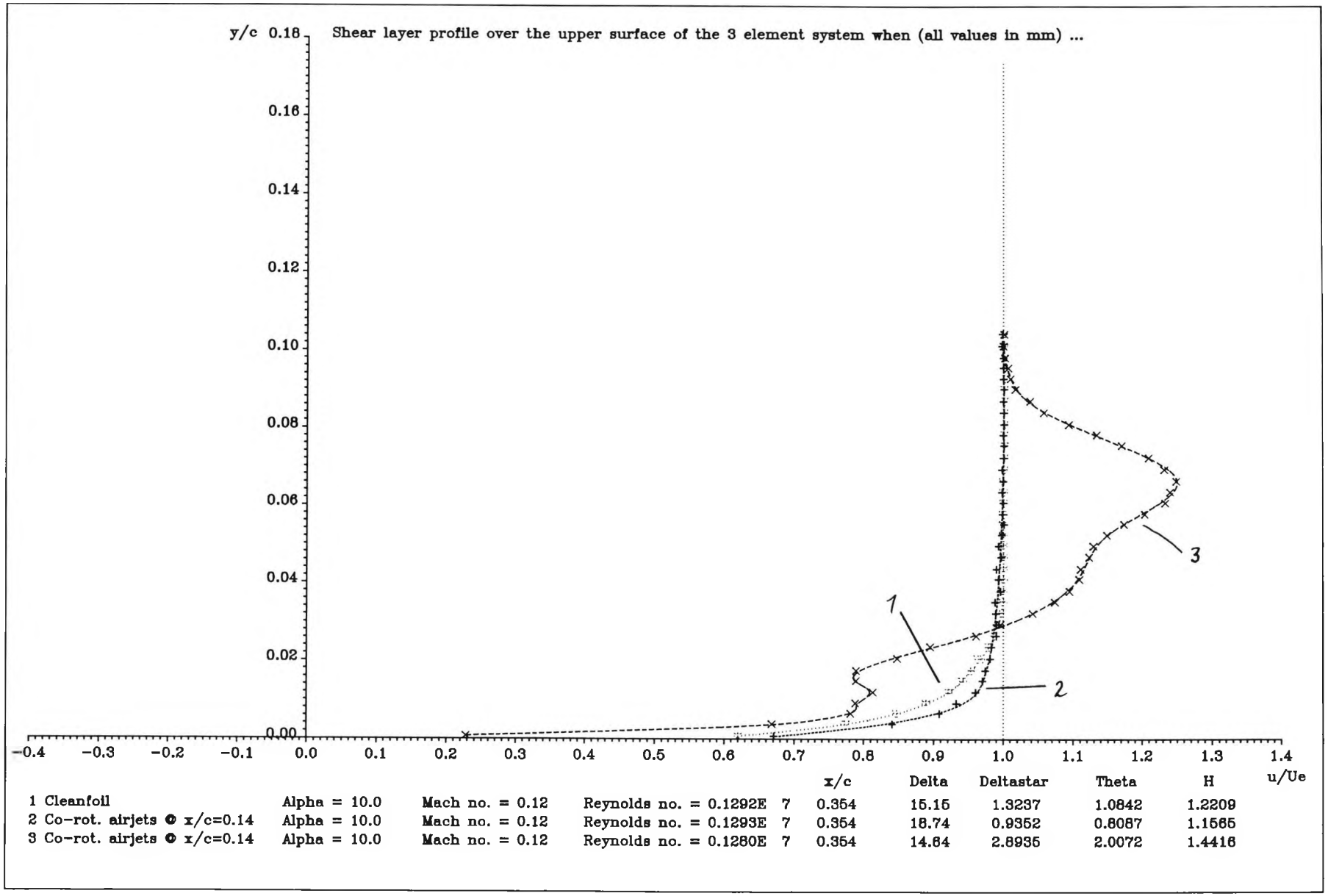

Figure 7.33 : Spanwise variation of shear layer profile at $x/c = 0.354$, $\alpha = 10°$, obtained when co-rot. airjets are at $x/c = 0.14$

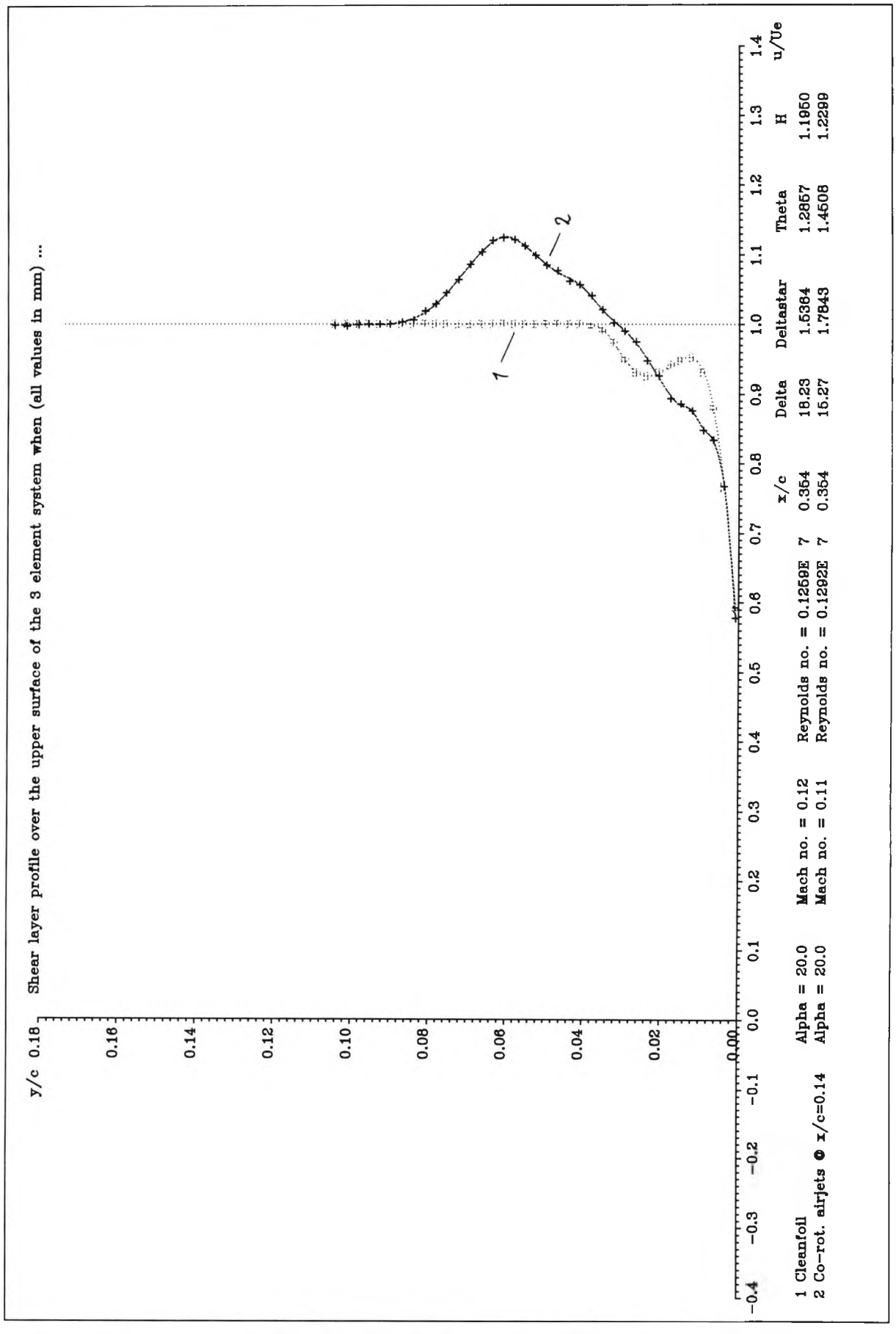

Figure 7.34 : Comparison of mean shear layer profiles at x/c = 0.354, $\alpha = 20°$; obtained with and without co-rot. airjets at x/c = 0.14

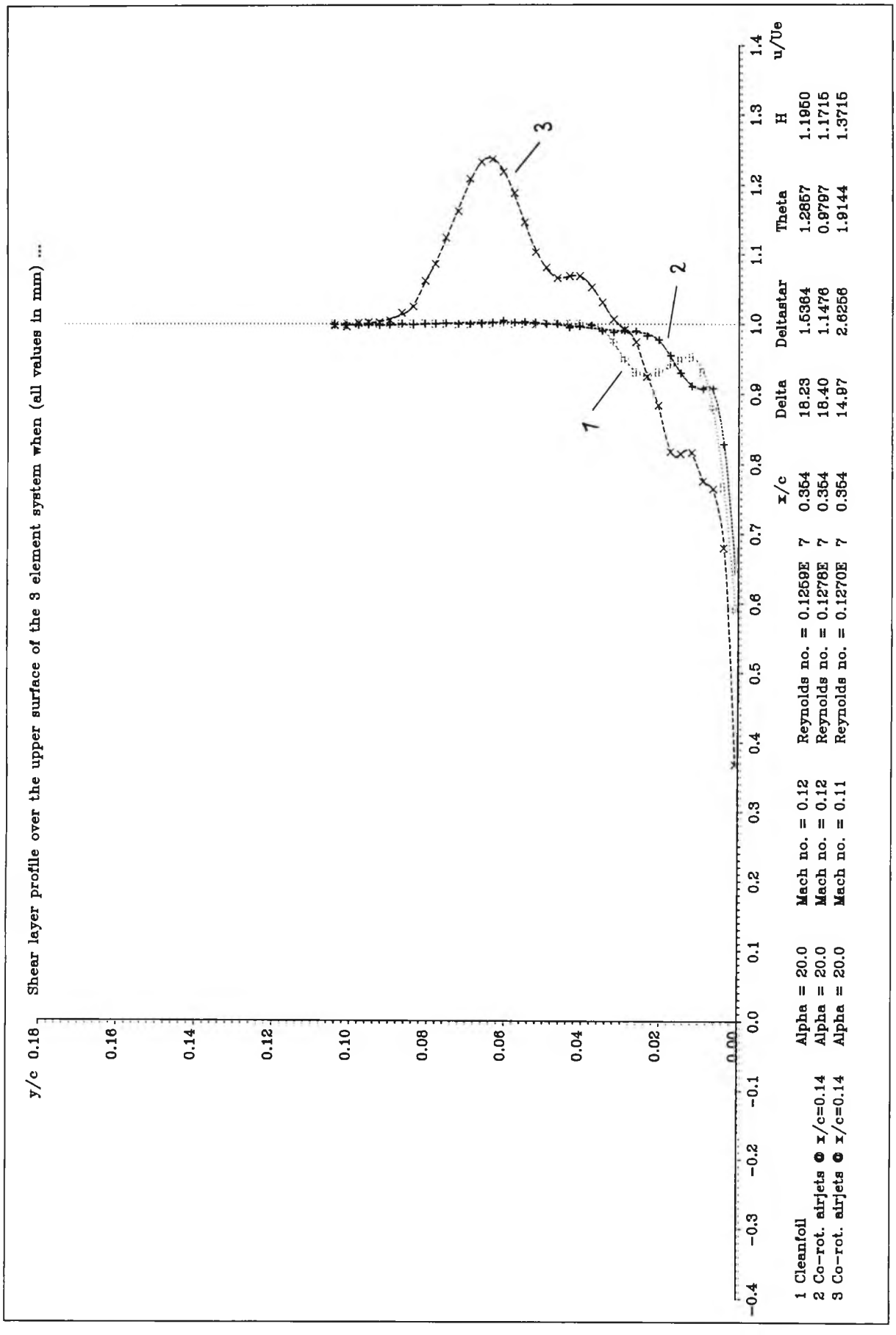

Figure 7.35 : Spanwise variation of shear layer profile at x/c = 0.354, $\alpha = 20°$, obtained when co-rot. airjets are at x/c = 0.14

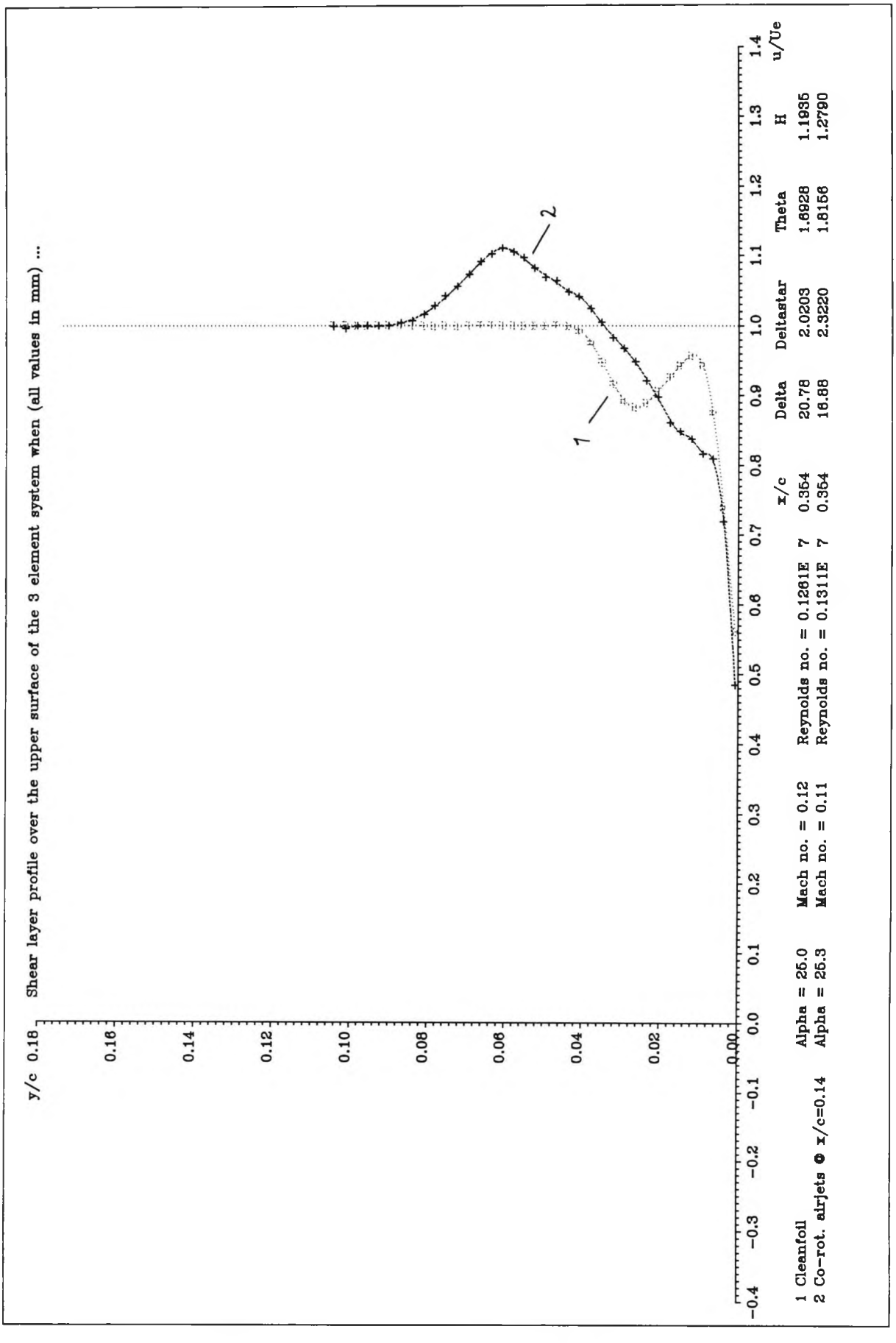

Figure 7.36 : Comparison of mean shear layer profiles at x/c = 0.354, $\alpha = 25°$; obtained with and without co-rot. airjets at x/c = 0.14

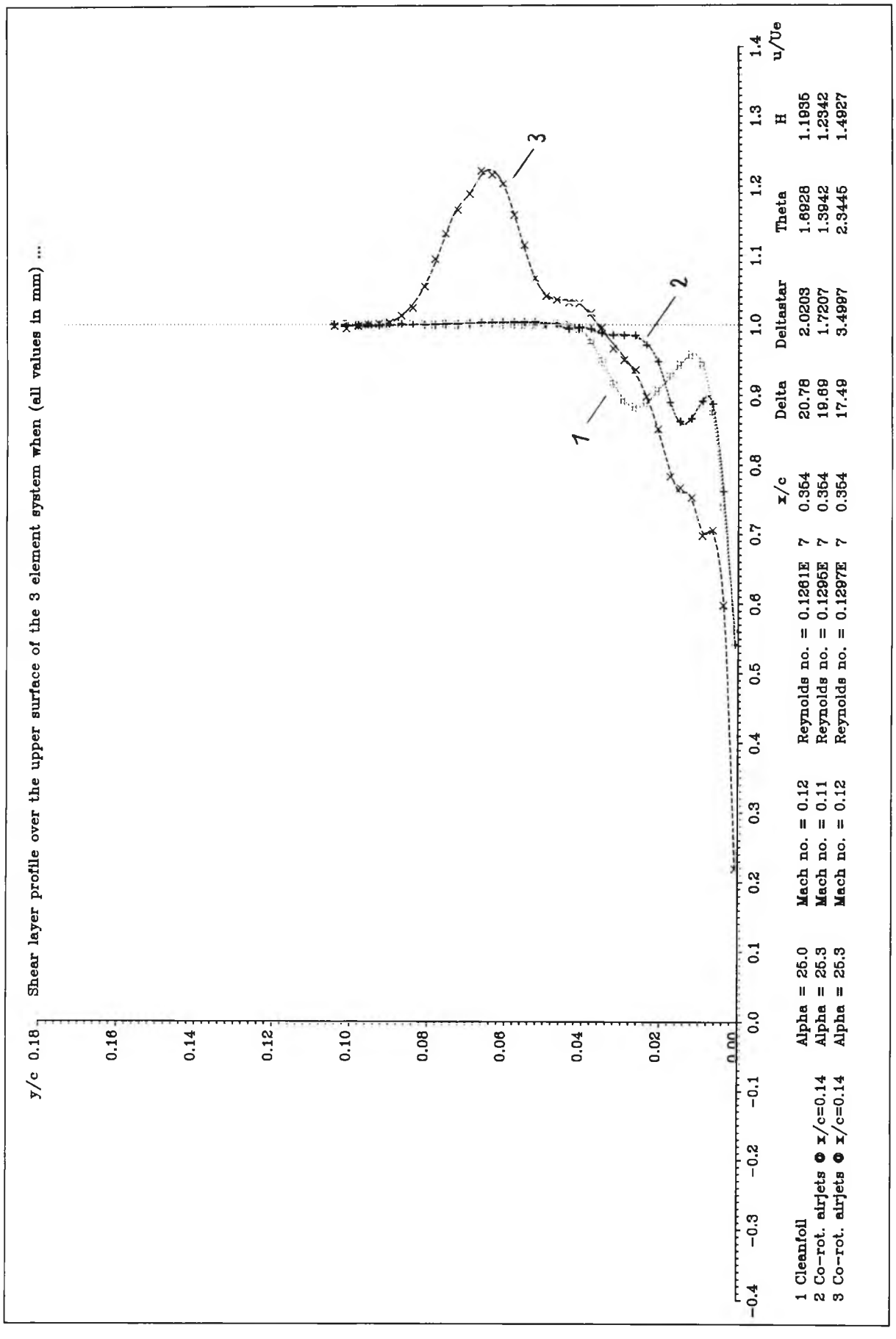

Figure 7.37 : Spanwise variation of shear layer profile at x/c = 0.354, $\alpha = 25°$, obtained when co-rot. airjets are at x/c = 0.14

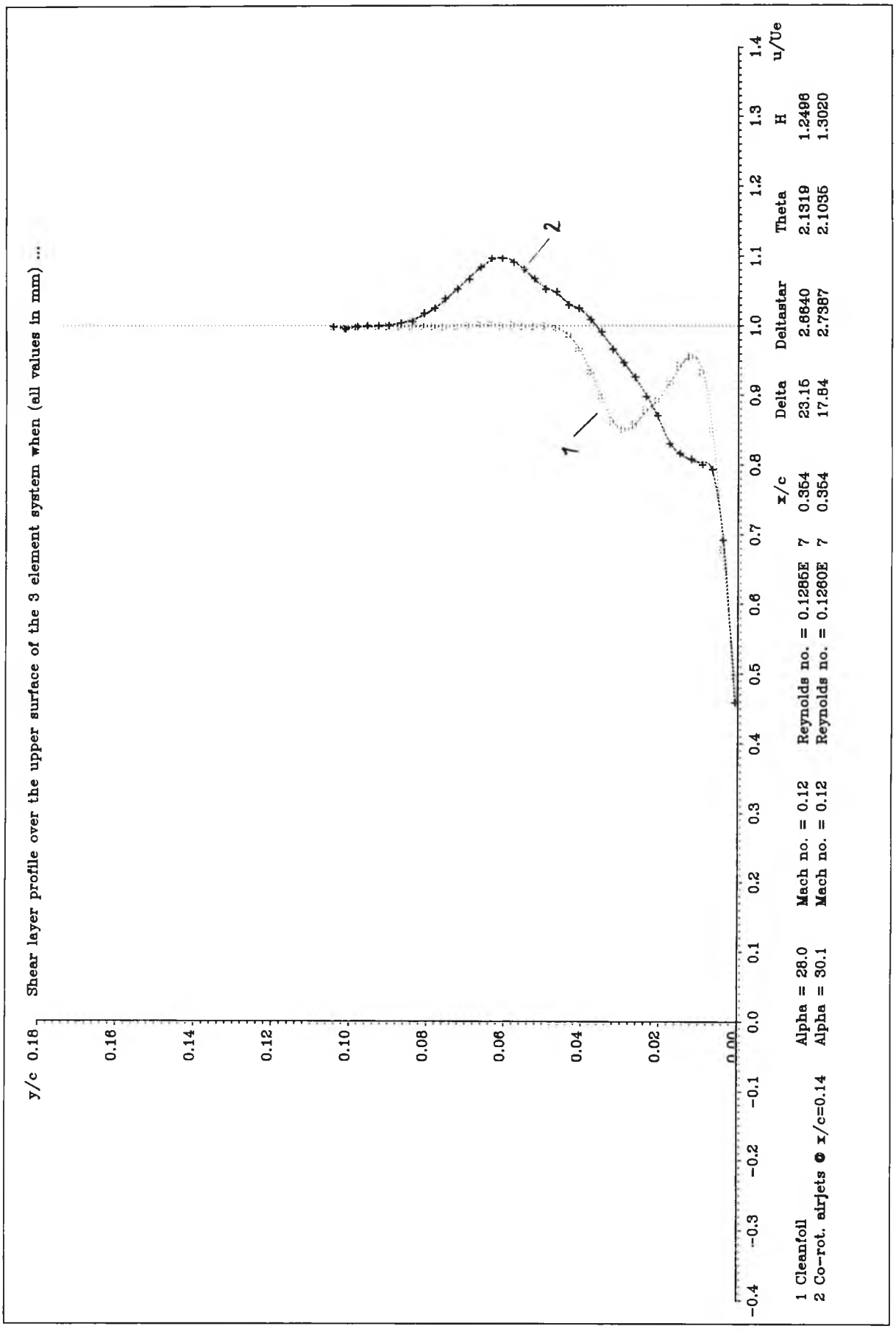

Figure 7.38 : Comparison of mean shear layer profiles at x/c = 0.354, $\alpha = 28°$ (cleanfoil) and 30° (co-rot. airjets at x/c = 0.14)

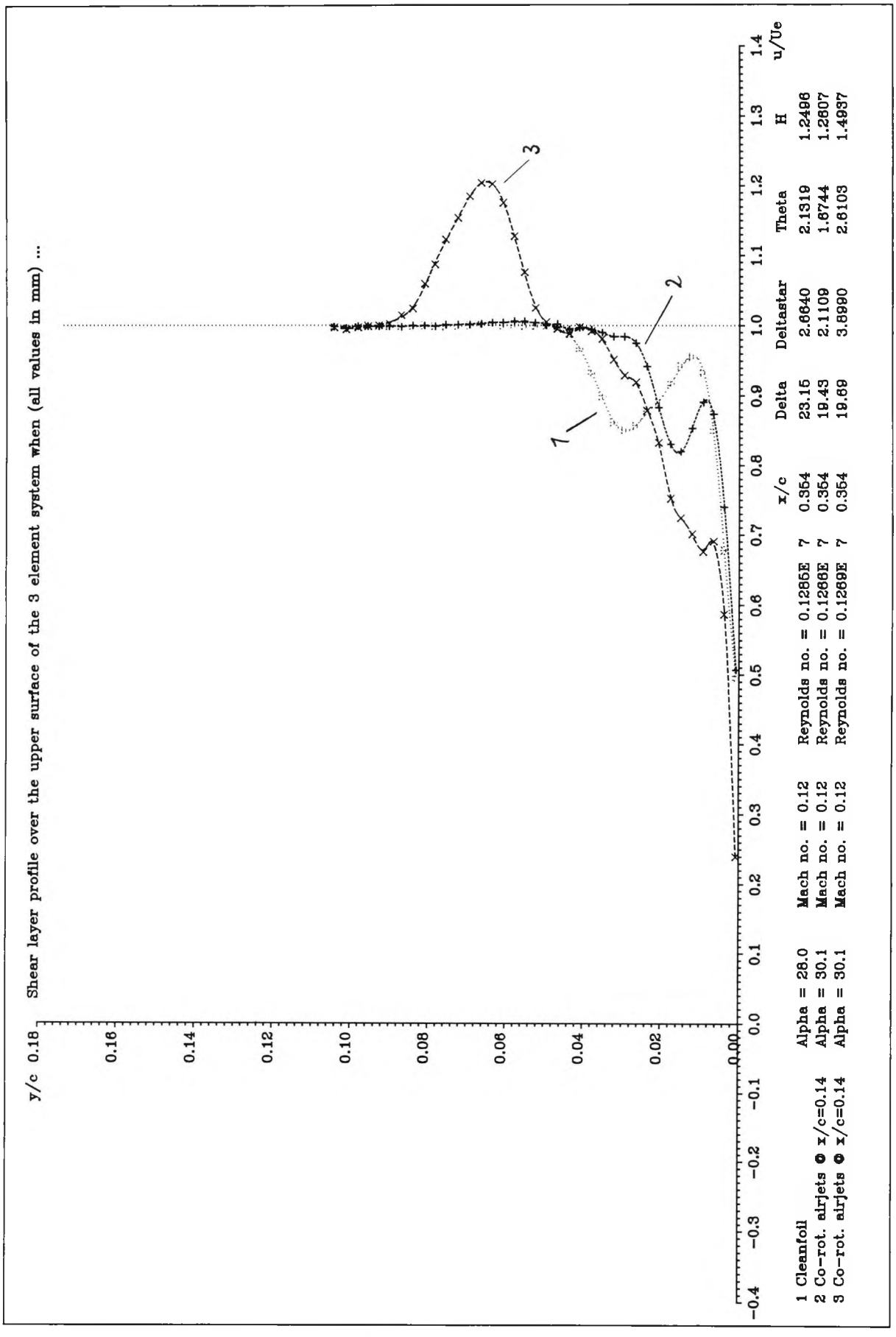

Figure 7.39 : Spanwise variation of shear layer profile at x/c = 0.354, $\alpha = 30°$, obtained when co-rot. airjets are at x/c = 0.14

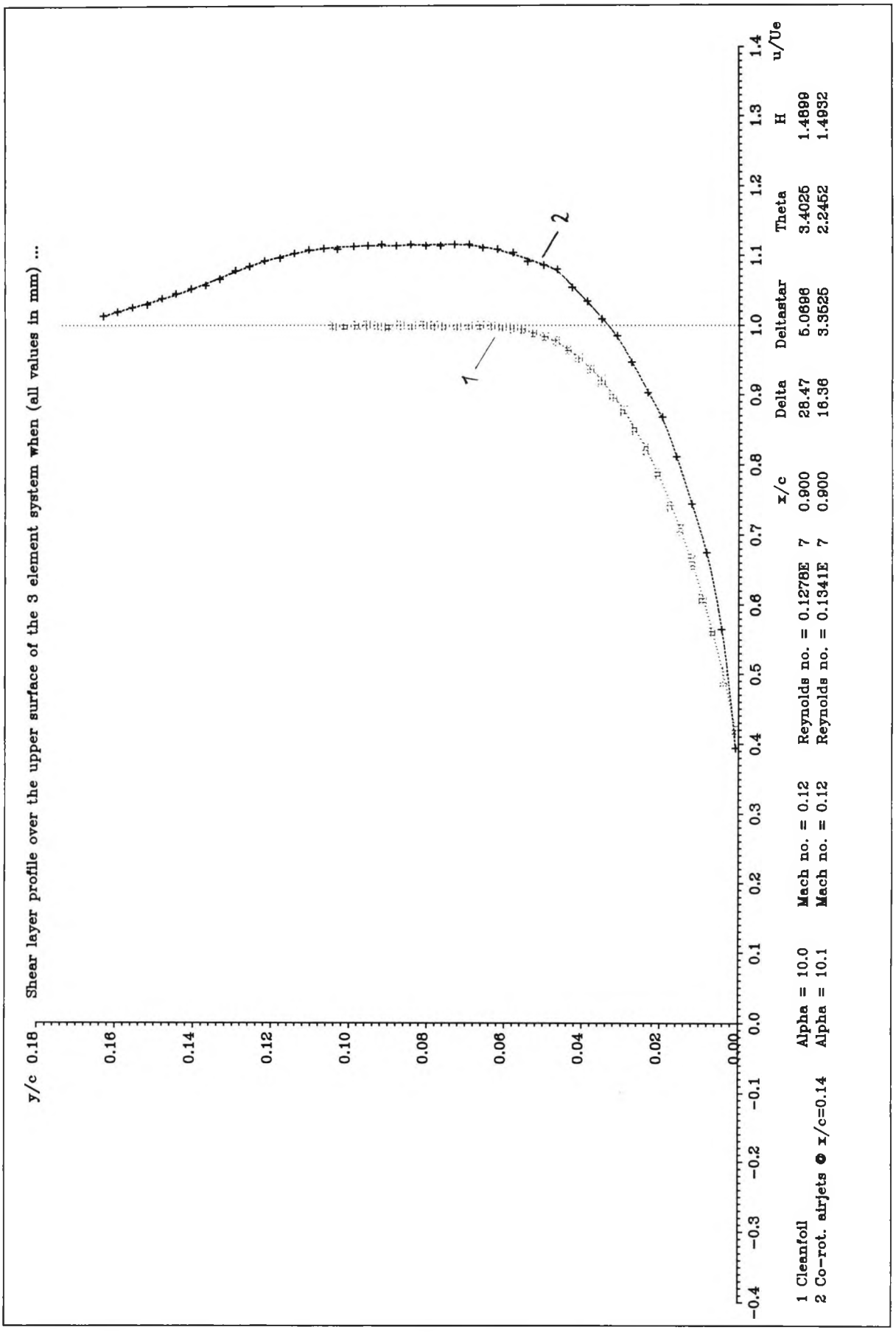

Figure 7.40 : Comparison of mean shear layer profiles at x/c = 0.9, $\alpha = 10°$; obtained with and without co-rot. airjets at x/c = 0.14

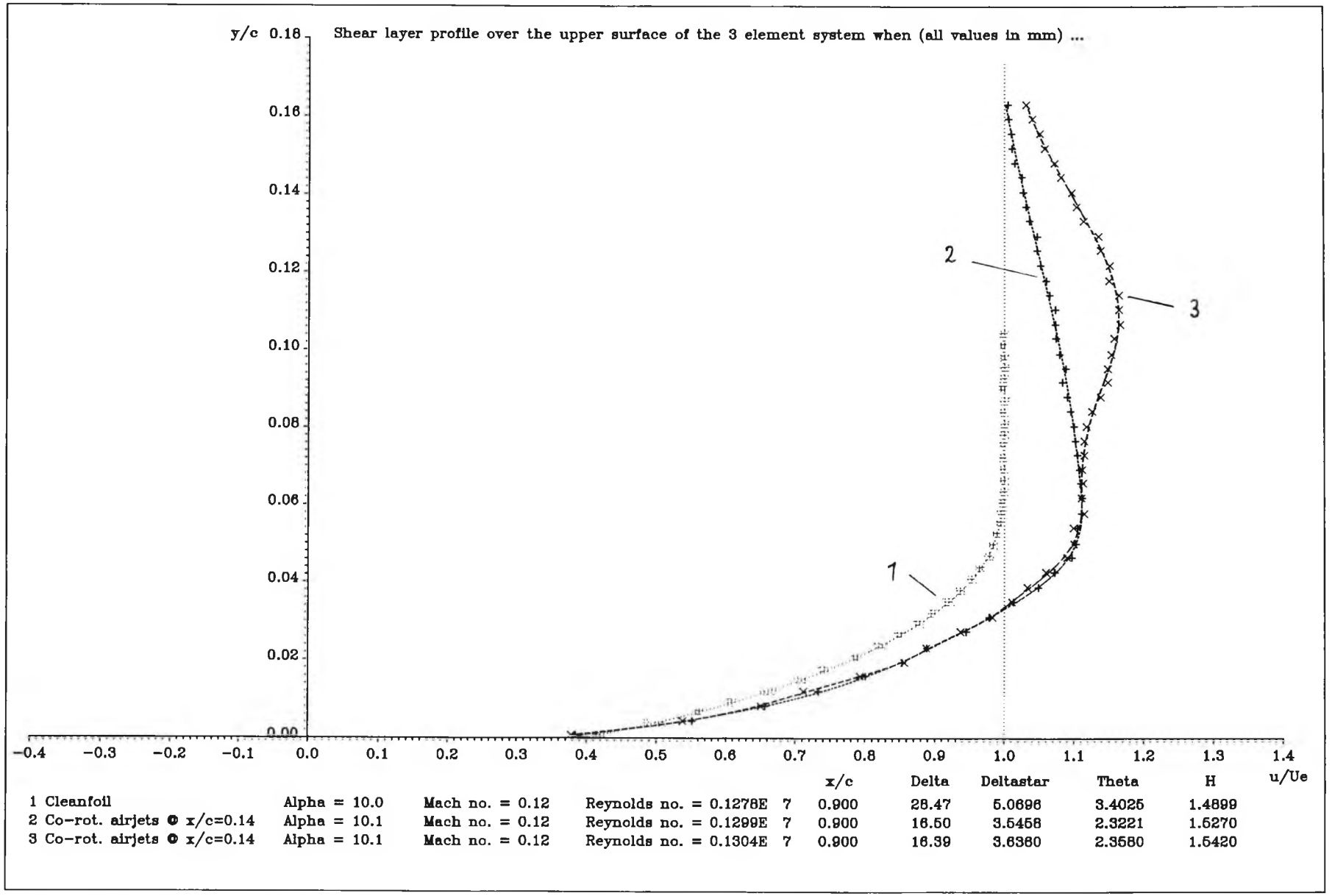

Figure 7.41 : Spanwise variation of shear layer profile at $x/c = 0.9$, $\alpha = 10°$, obtained when co-rot. airjets are at $x/c = 0.14$

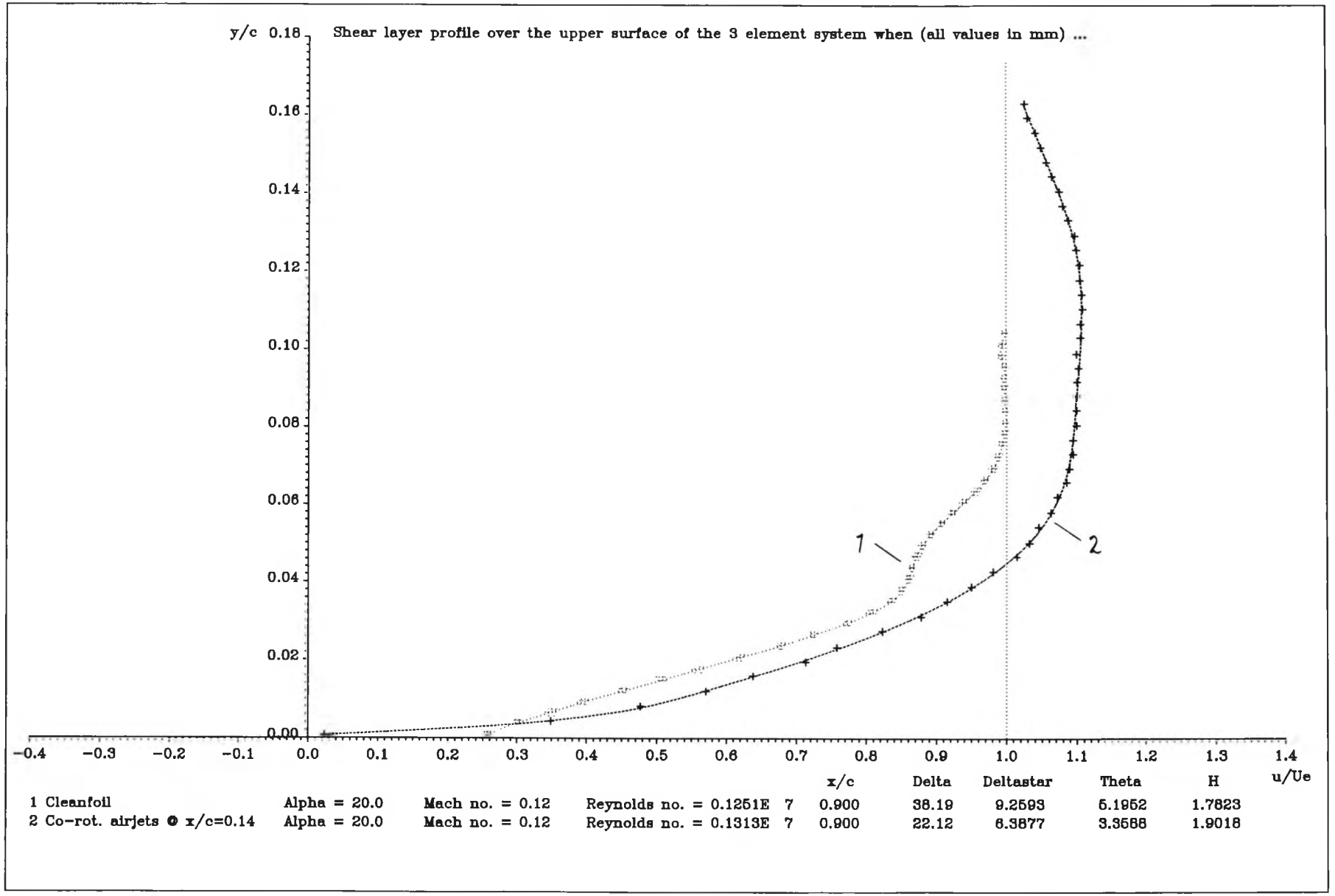

Figure 7.42 : Comparison of mean shear layer profiles at $x/c = 0.9$, $\alpha = 20°$; obtained with and without co-rot. airjets at $x/c = 0.14$

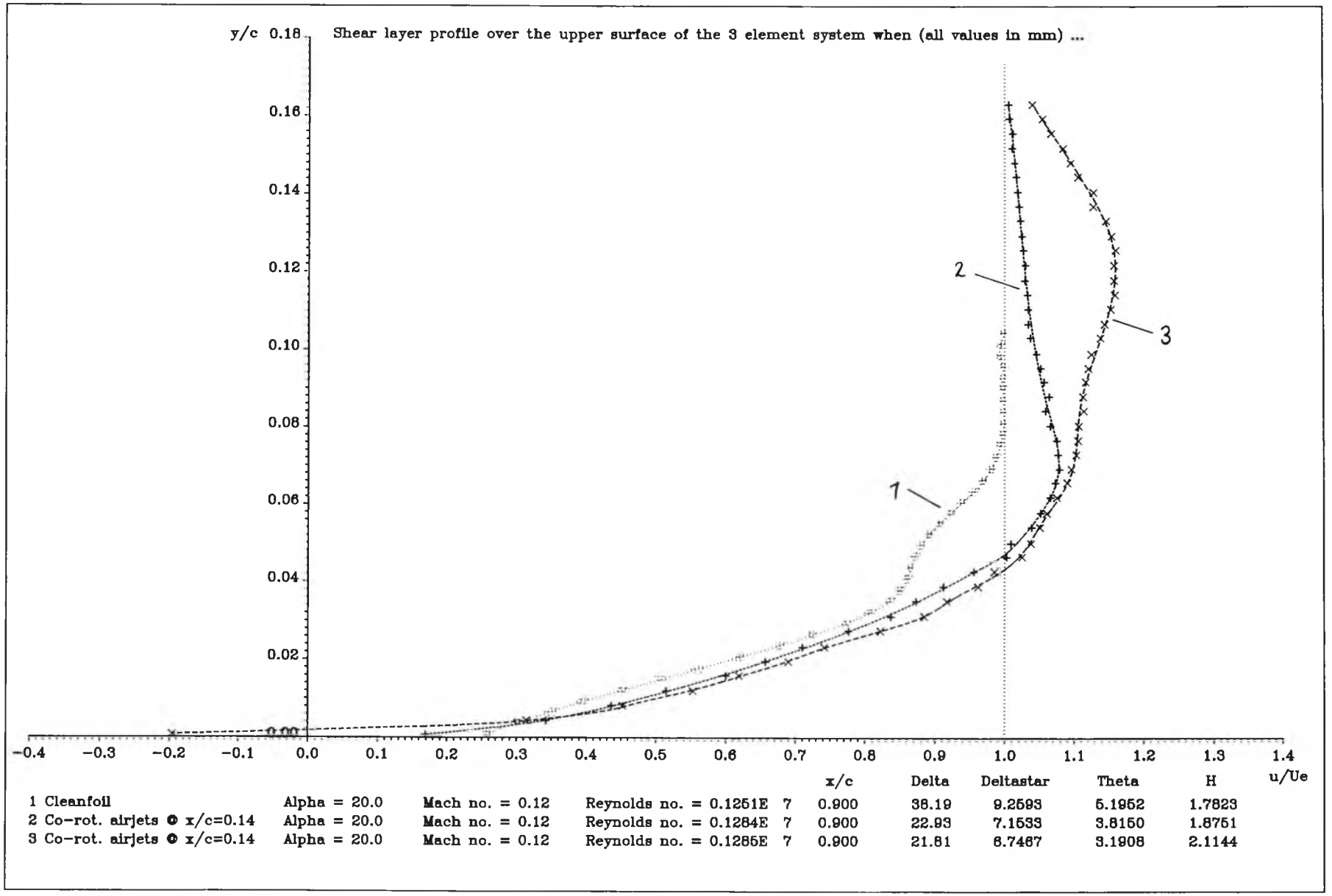

Figure 7.43 : Spanwise variation of shear layer profile at $x/c = 0.9$, $\alpha = 20°$, obtained when co-rot. airjets are at $x/c = 0.14$

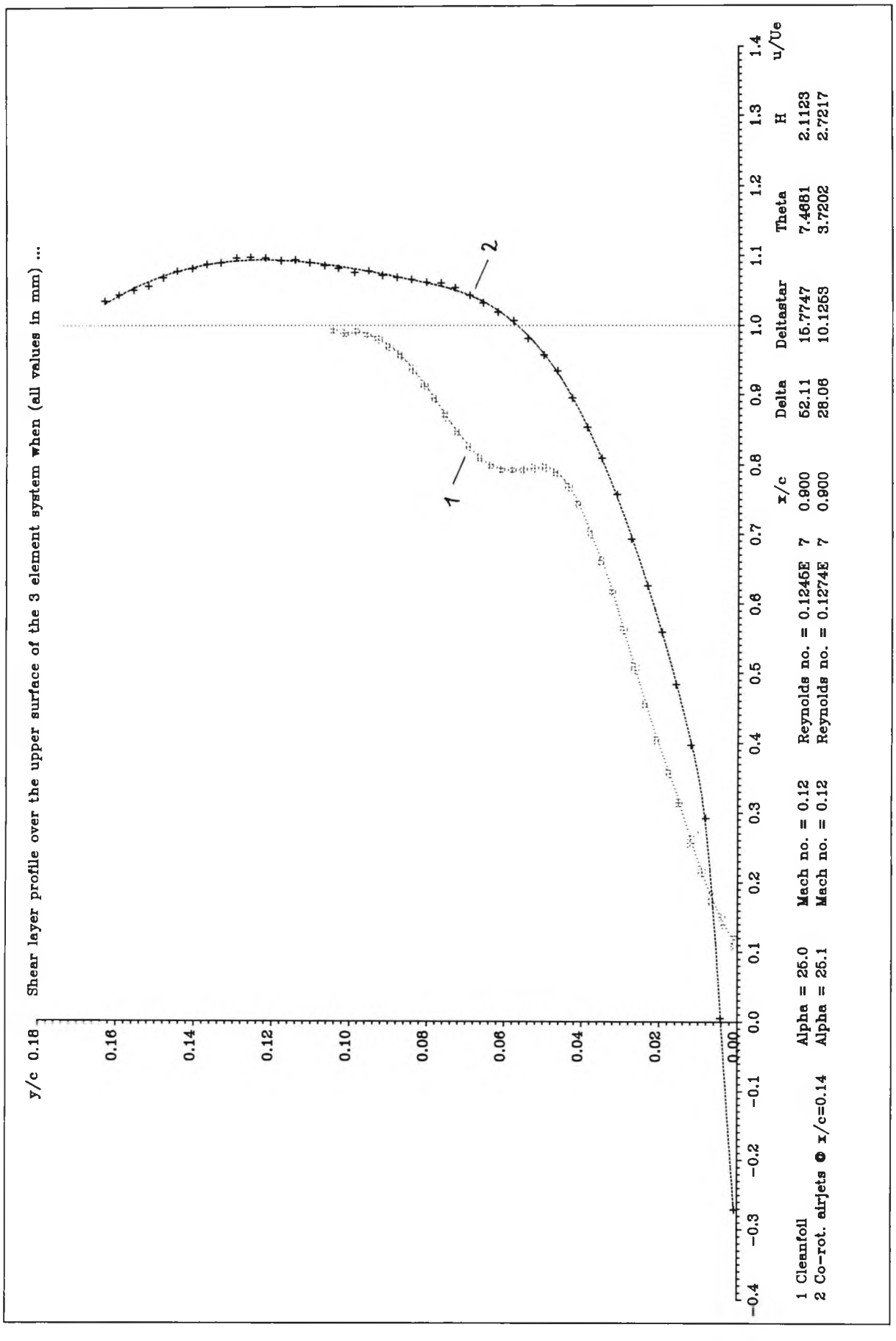

Figure 7.44 : Comparison of mean shear layer profiles at x/c = 0.9, $\alpha = 25°$; obtained with and without co-rot. airjets at x/c = 0.14

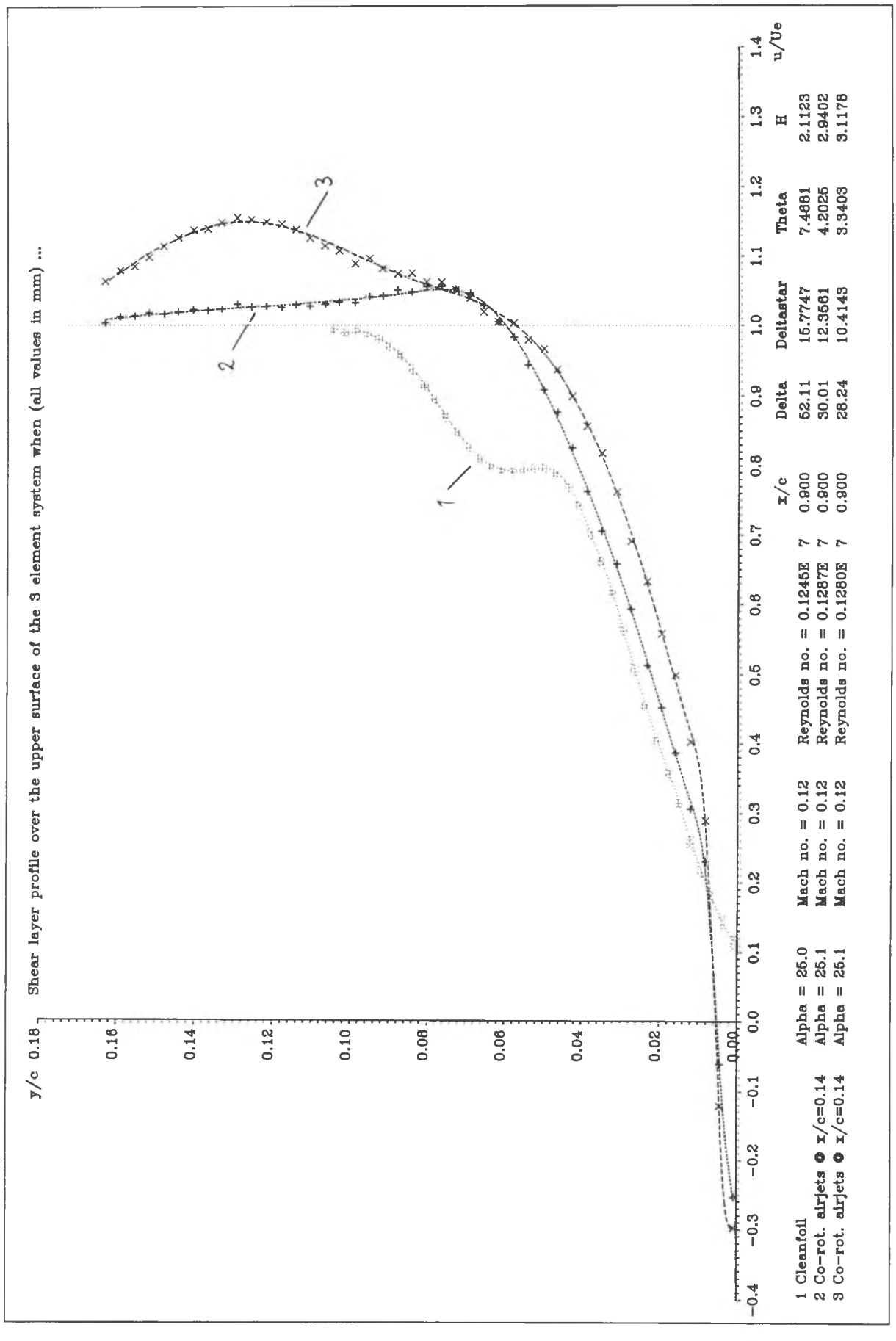

Figure 7.45 : Spanwise variation of shear layer profile at x/c = 0.9, $\alpha = 25°$, obtained when co-rot. airjets are at x/c = 0.14

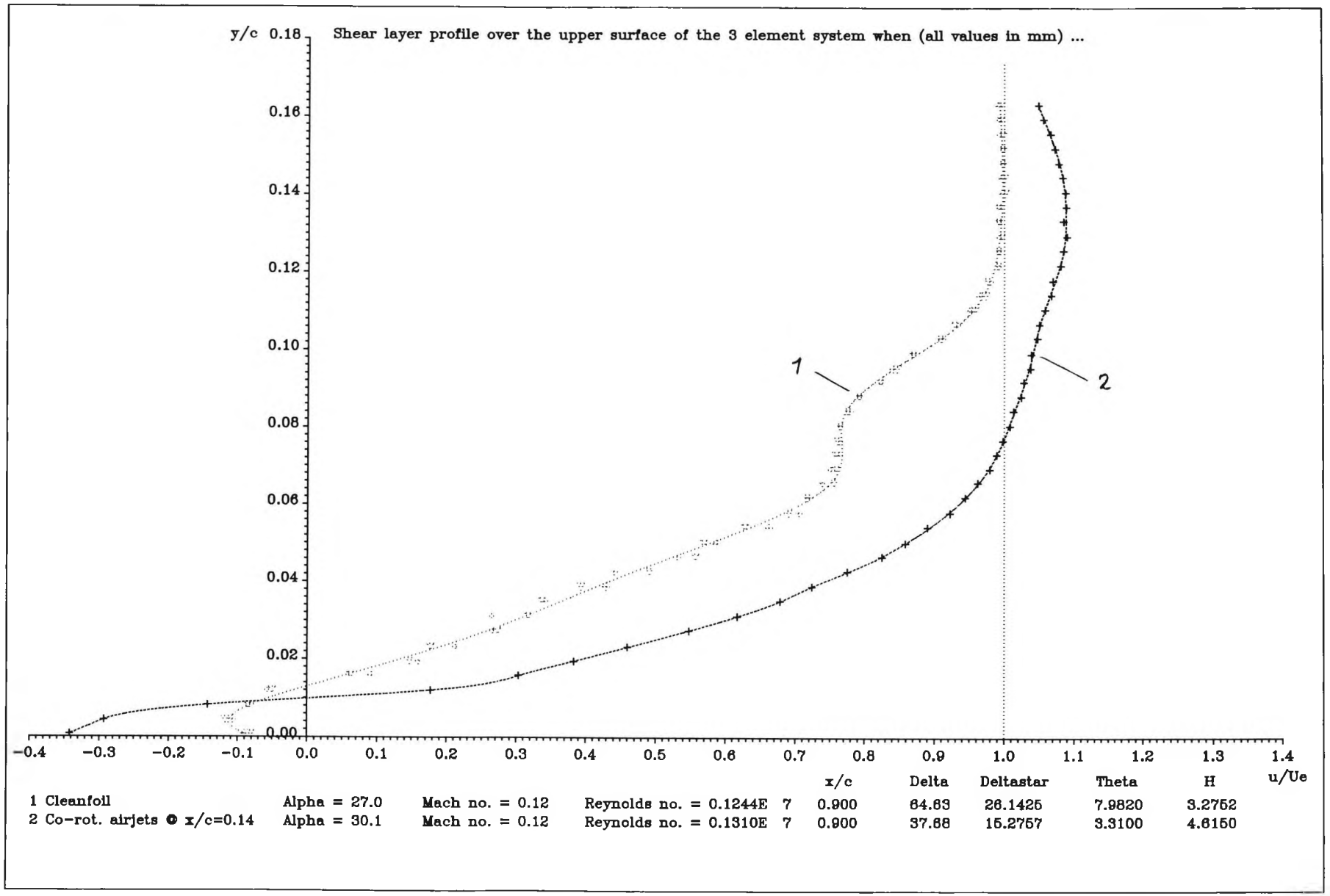

Figure 7.46 : Comparison of mean shear layer profiles at x/c = 0.9, $\alpha = 27°$ (cleanfoil) and 30° (co-rot. airjets at x/c = 0.14)

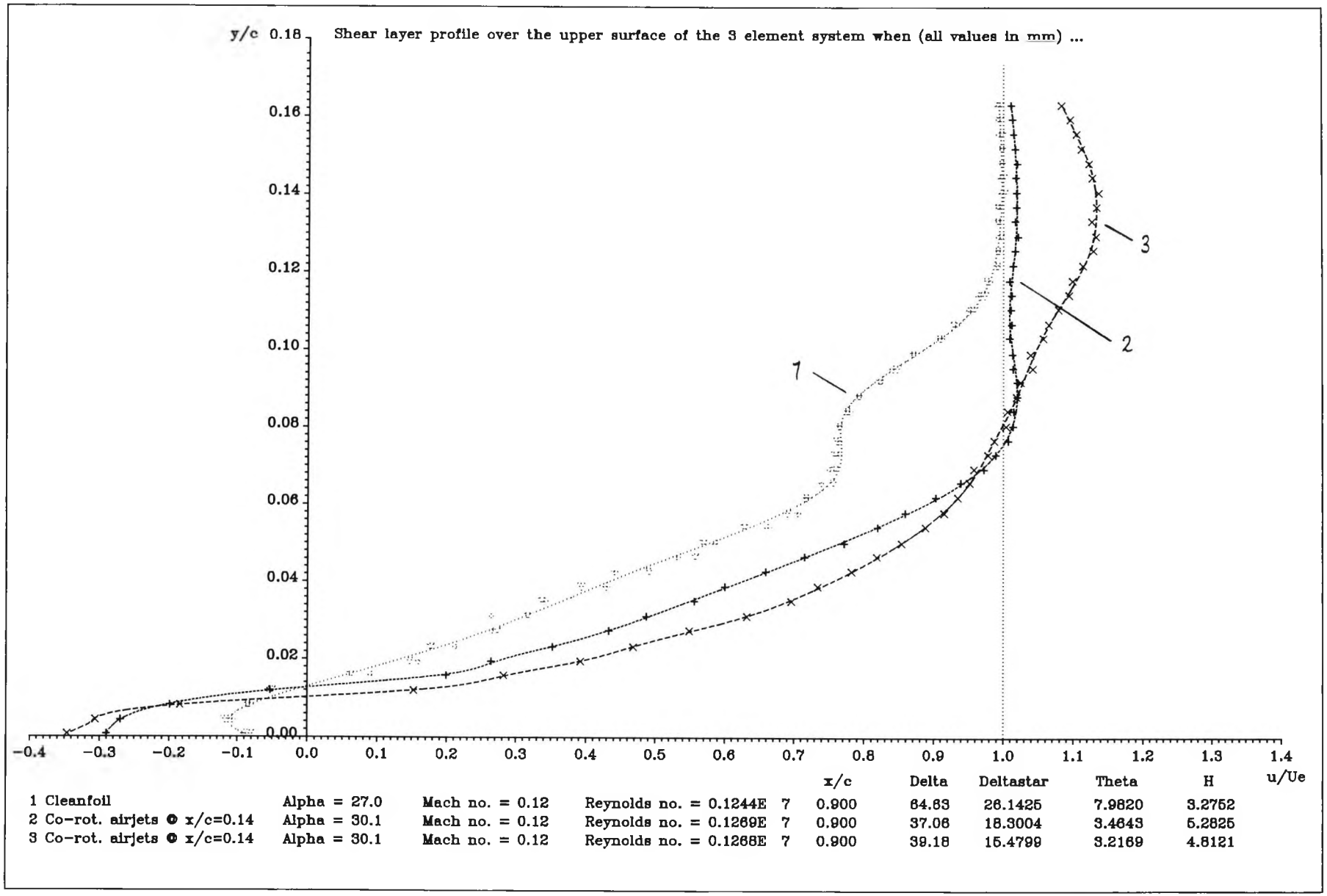

Figure 7.47 : Spanwise variation of shear layer profile at $x/c = 0.9$, $\alpha = 30°$, obtained when co-rot. airjets are at $x/c = 0.14$

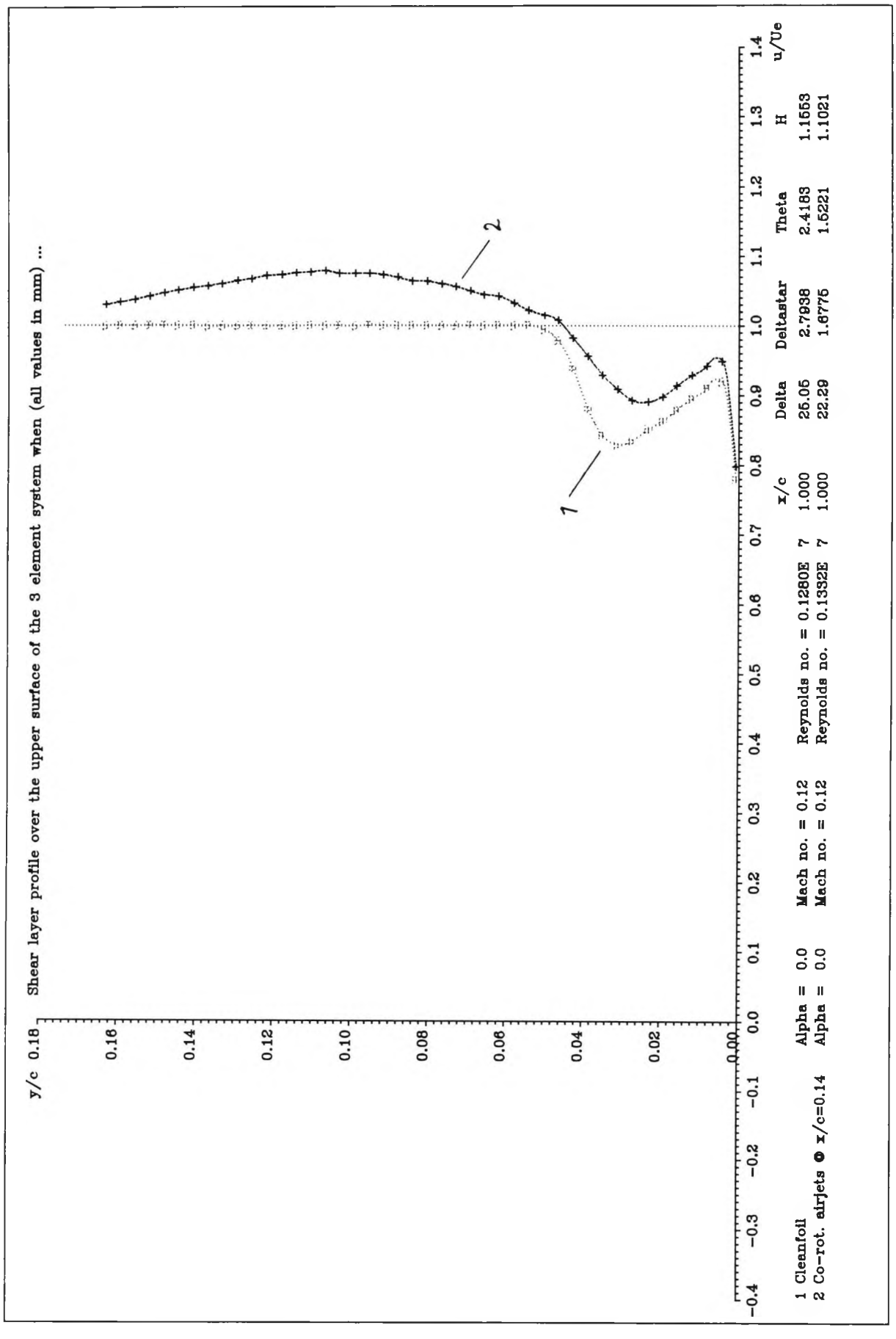

Figure 7.48 : Comparison of mean shear layer profiles at x/c = 1.0, $\alpha = 0°$; obtained with and without co-rot. airjets at x/c = 0.14

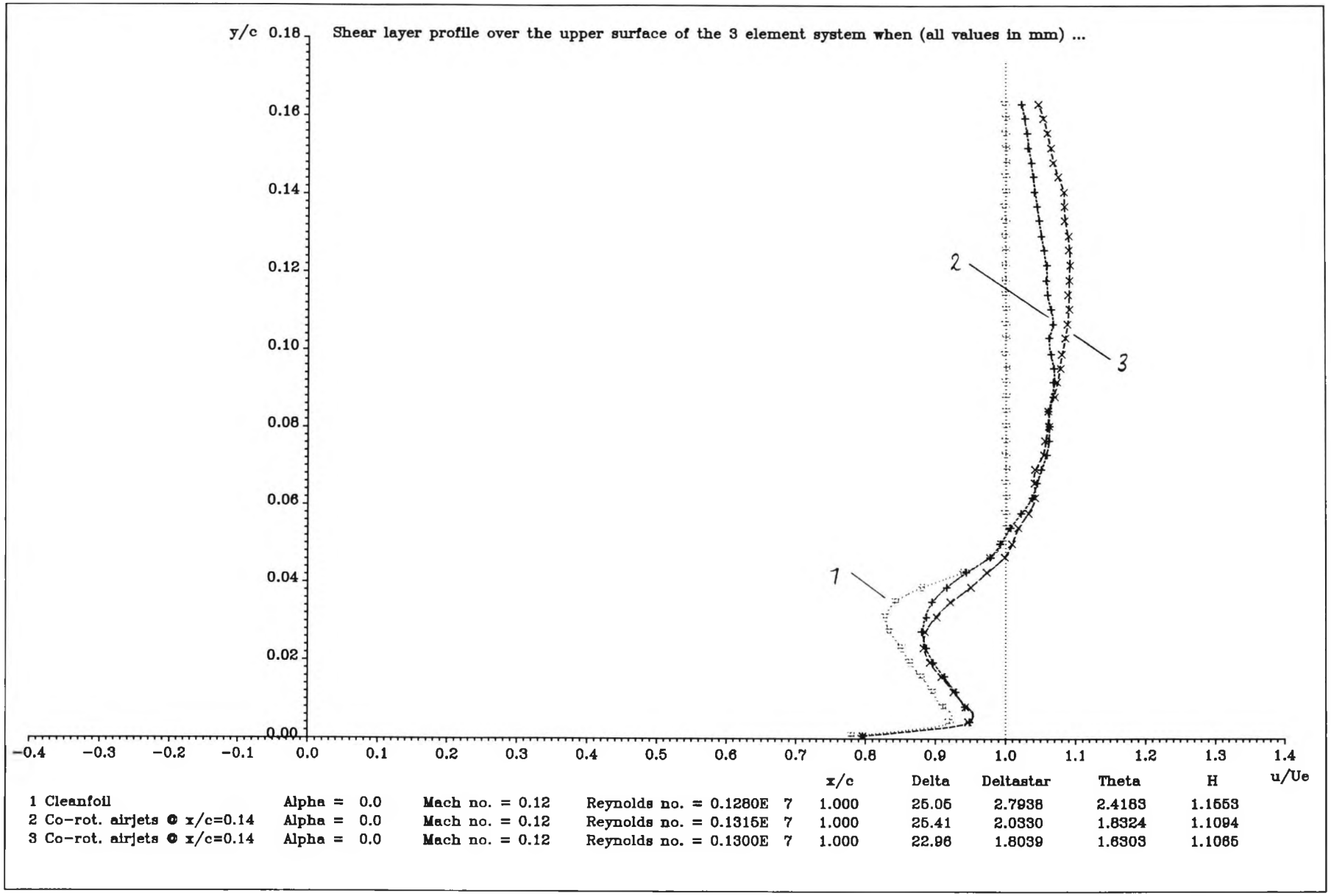

Figure 7.49 : Spanwise variation of shear layer profile at x/c = 1.0, $\alpha = 0°$, obtained when co-rot. airjets are at x/c = 0.14

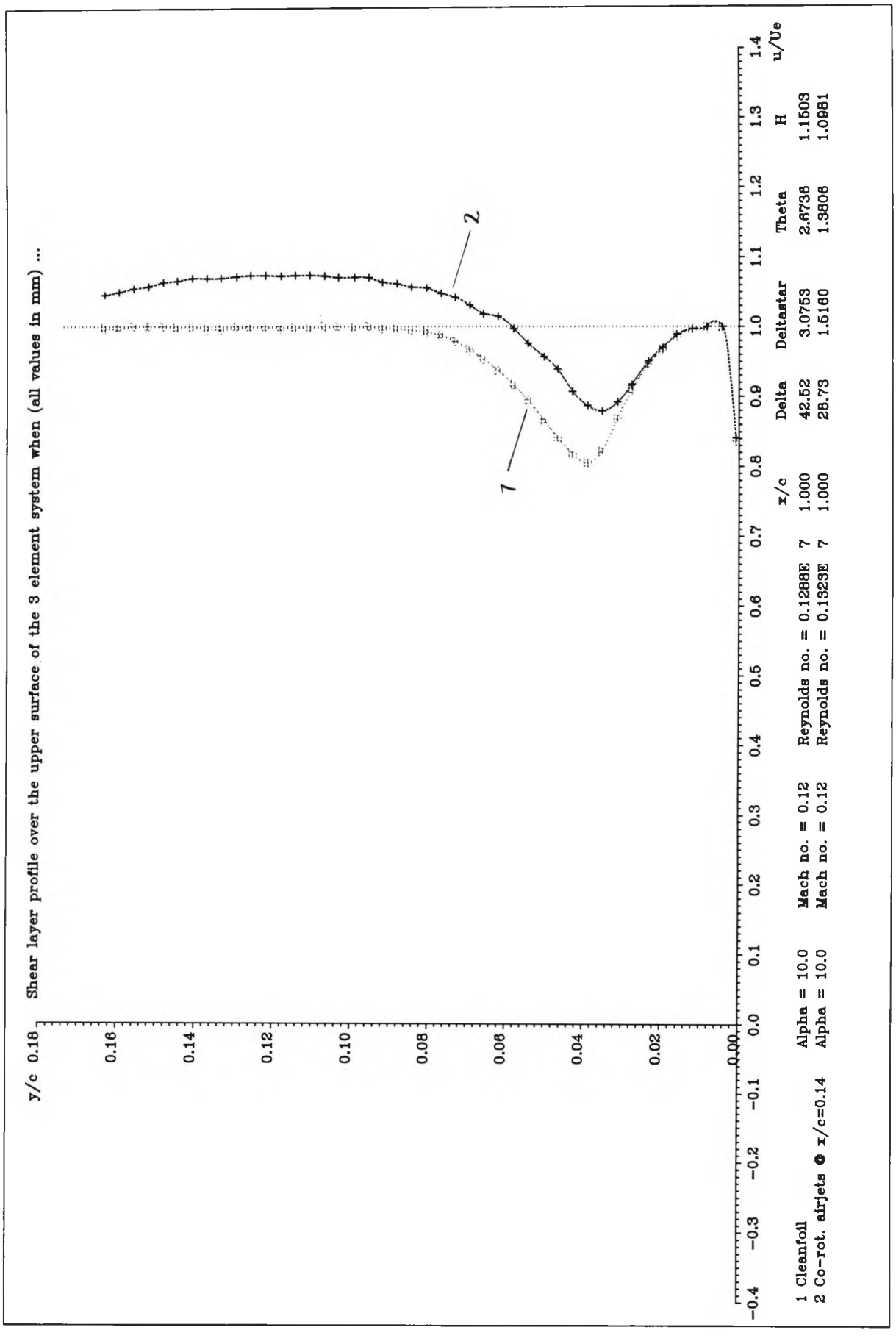

Figure 7.50 : Comparison of mean shear layer profiles at x/c = 1.0, $\alpha = 10°$; obtained with and without co-rot. airjets at x/c = 0.14

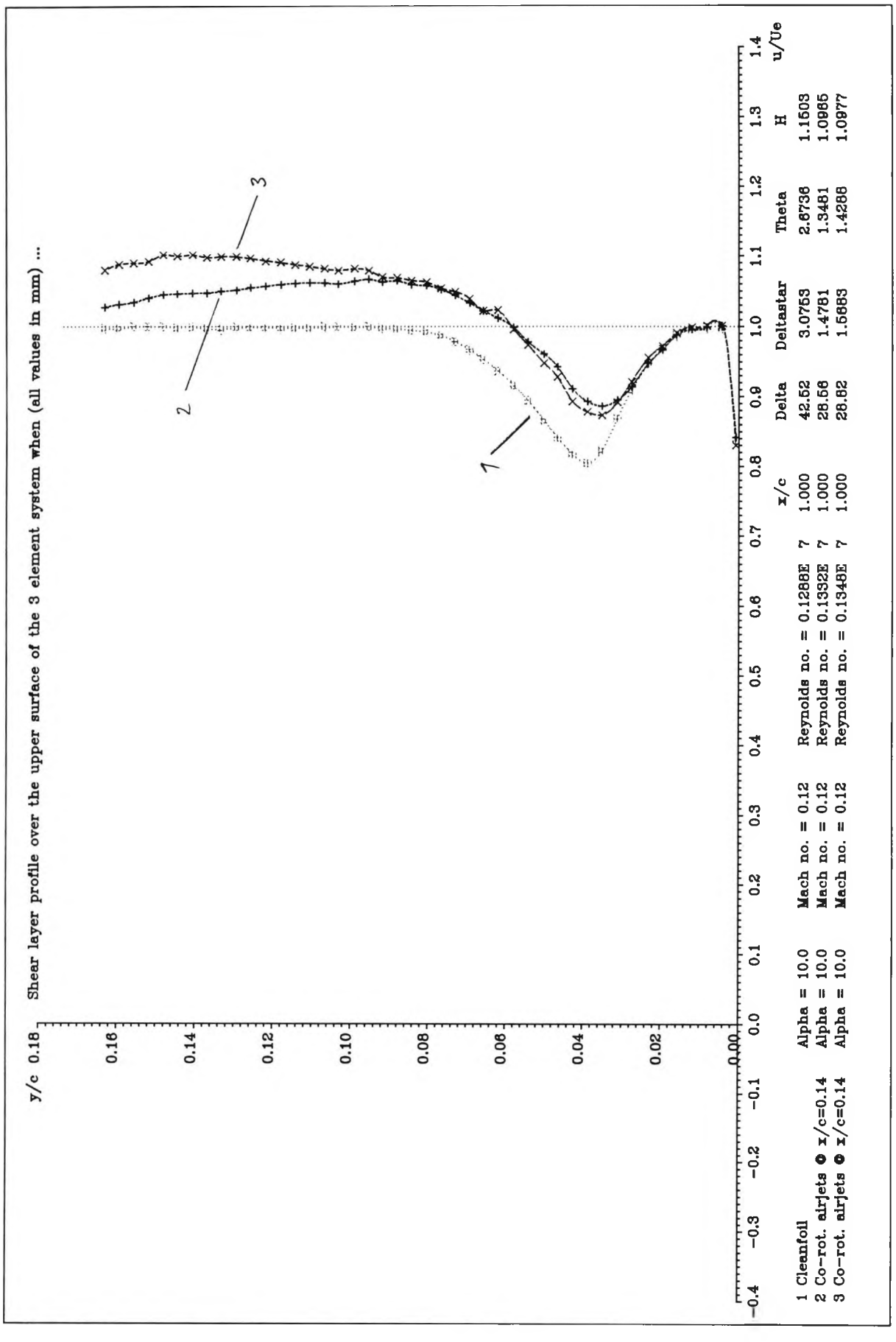

Figure 7.51 : Spanwise variation of shear layer profile at x/c = 1.0, $\alpha = 10°$, obtained when co-rot. airjets are at x/c = 0.14

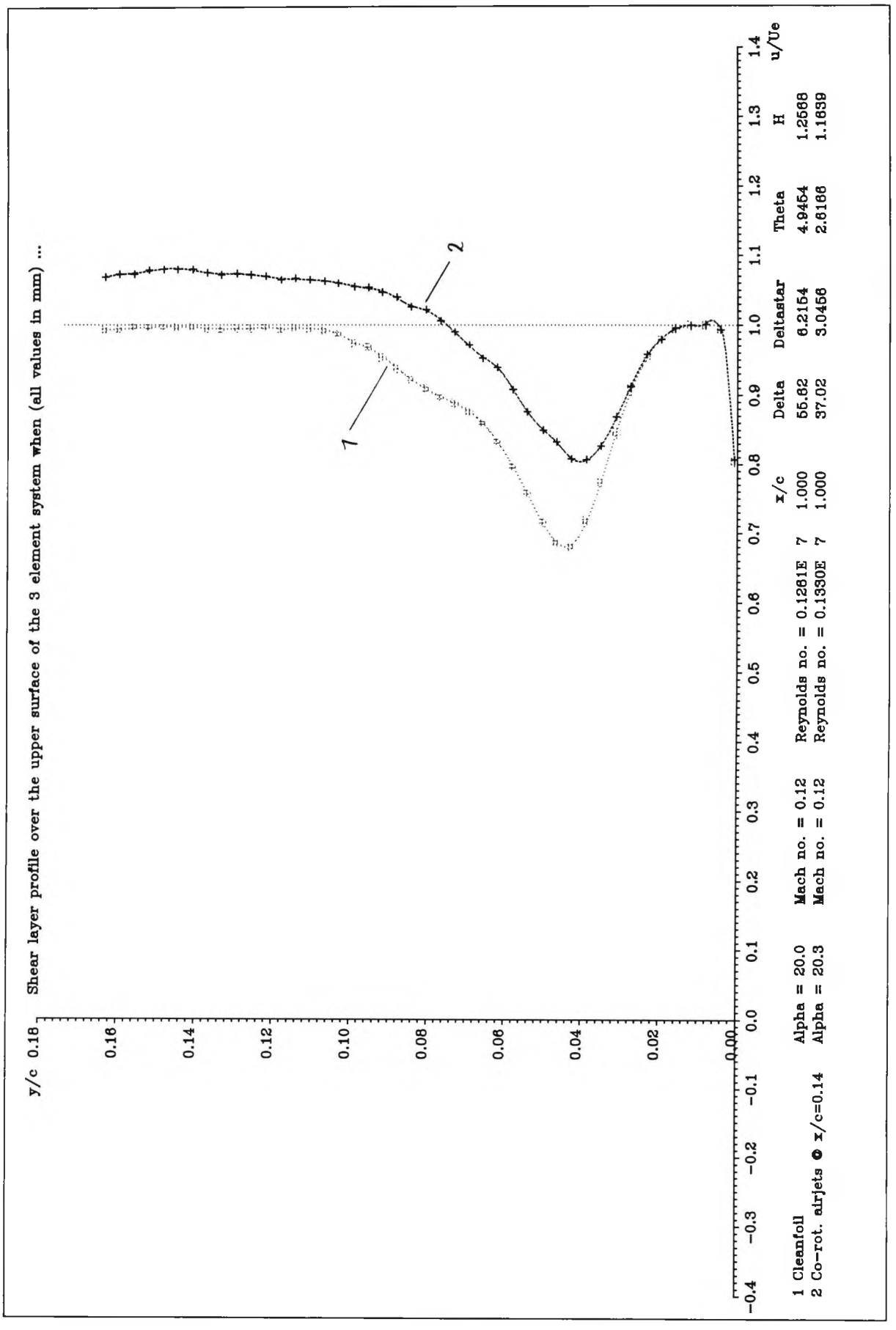

Figure 7.52 : Comparison of mean shear layer profiles at x/c = 1.0, $\alpha = 20°$; obtained with and without co-rot. airjets at x/c = 0.14

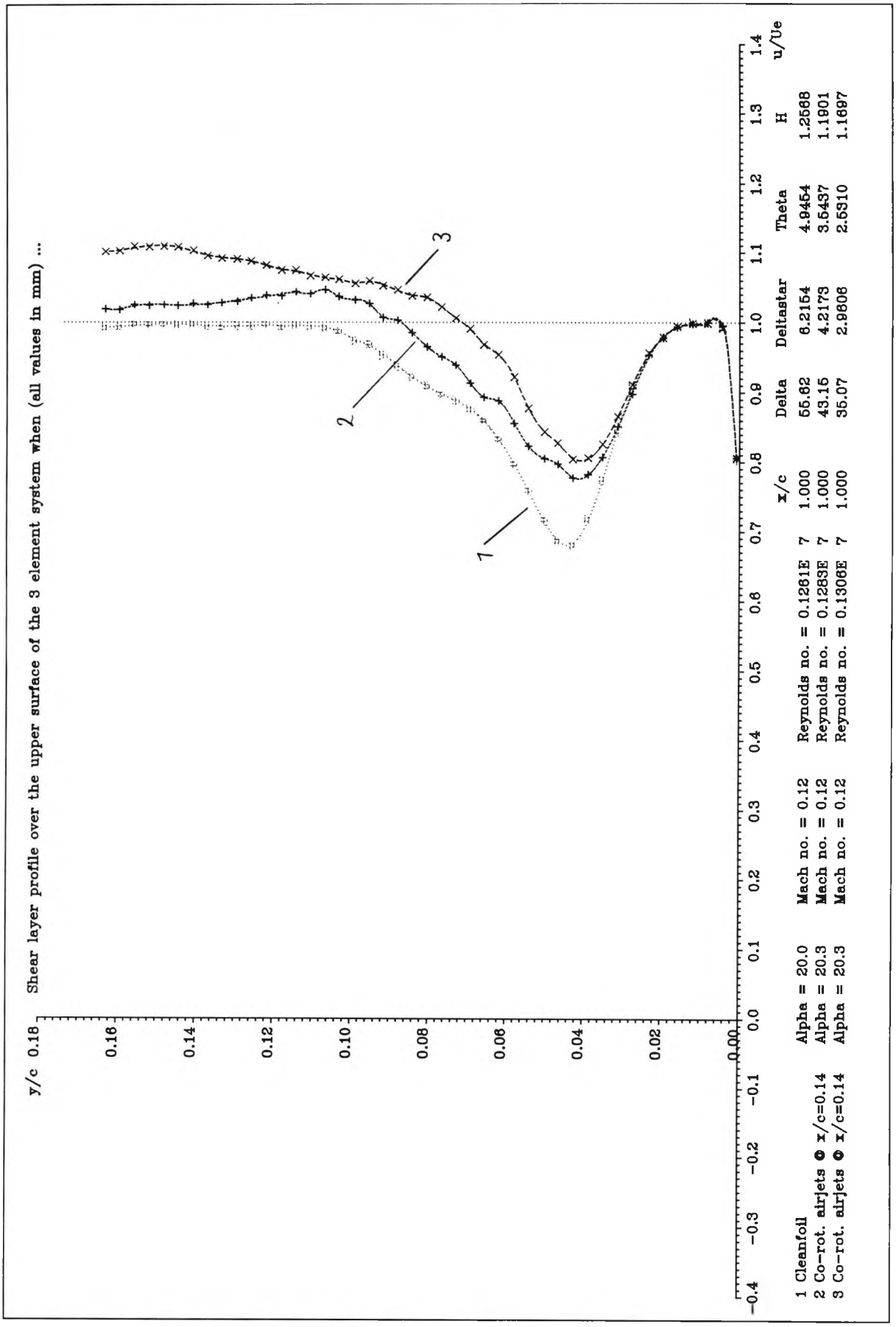

Figure 7.53 : Spanwise variation of shear layer profile at x/c = 1.0, $\alpha = 20°$, obtained when co-rot. airjets are at x/c = 0.14

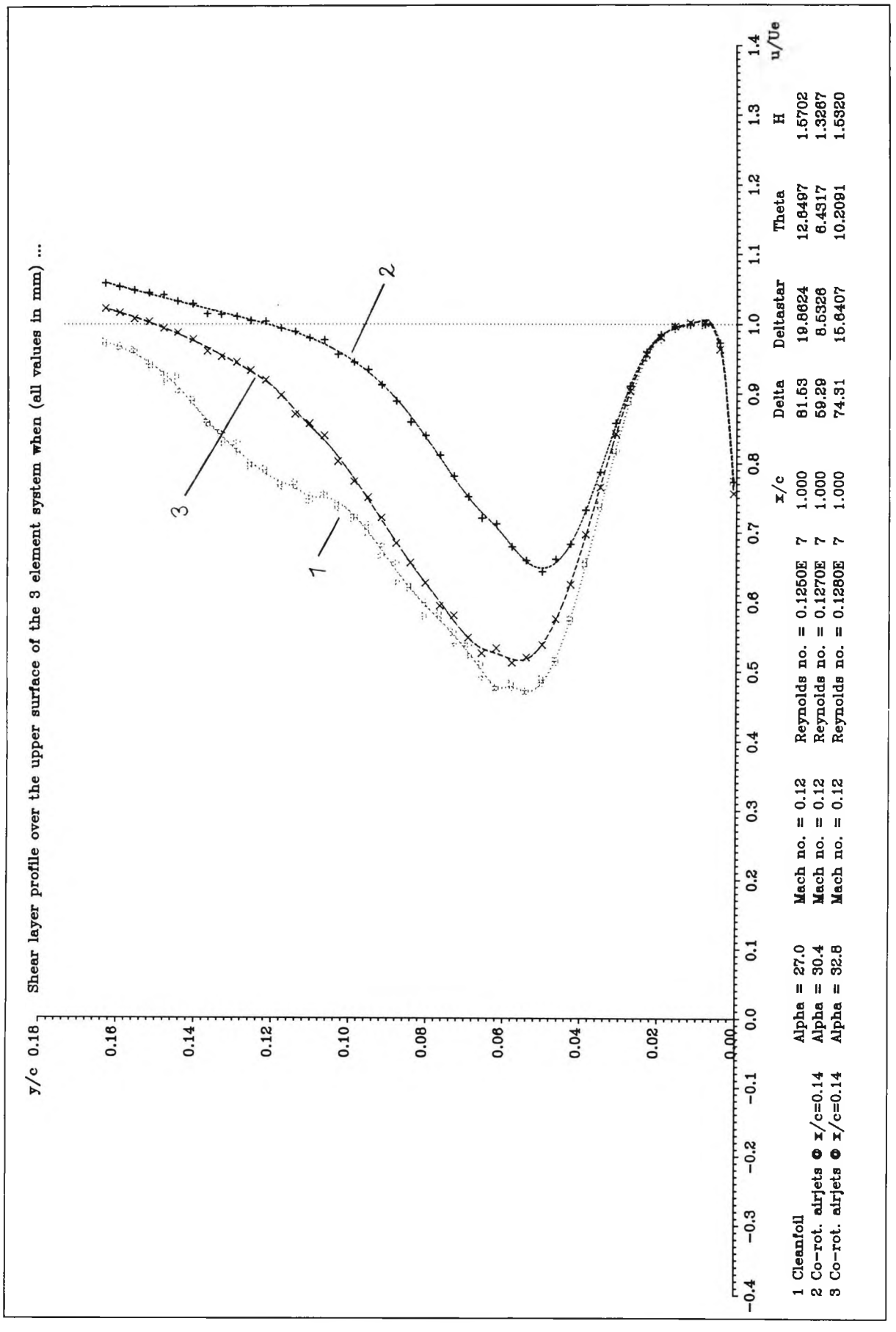

Figure 7.54 : Comparison of mean shear layer profiles at x/c = 1.0, $\alpha = 27°$ (cleanfoil), 30° and 32.8° (co-rot. airjets at x/c = 0.14)

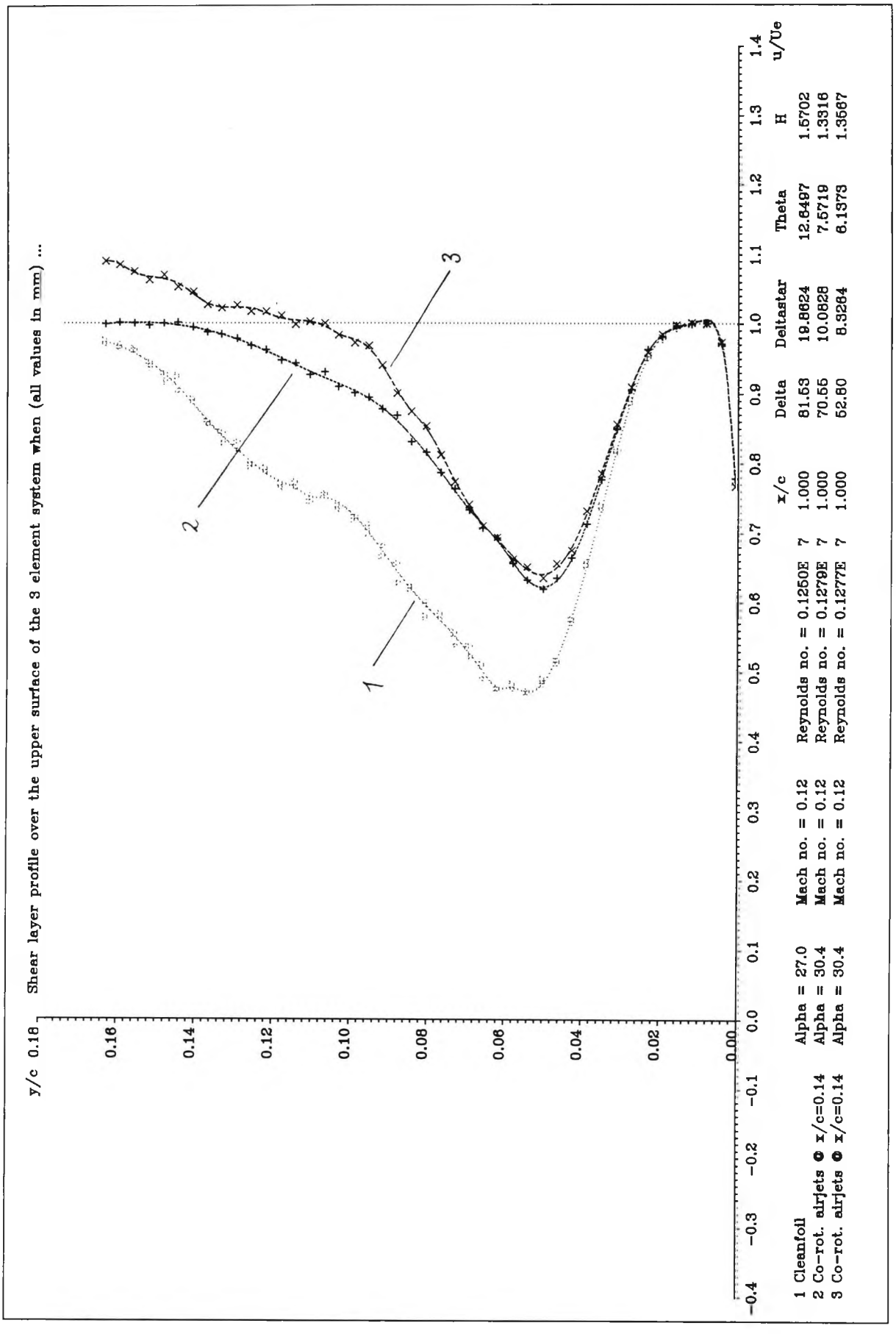

Figure 7.55 : Spanwise variation of shear layer profile at x/c = 1.0, $\alpha = 30°$, obtained when co-rot. airjets are at x/c = 0.14

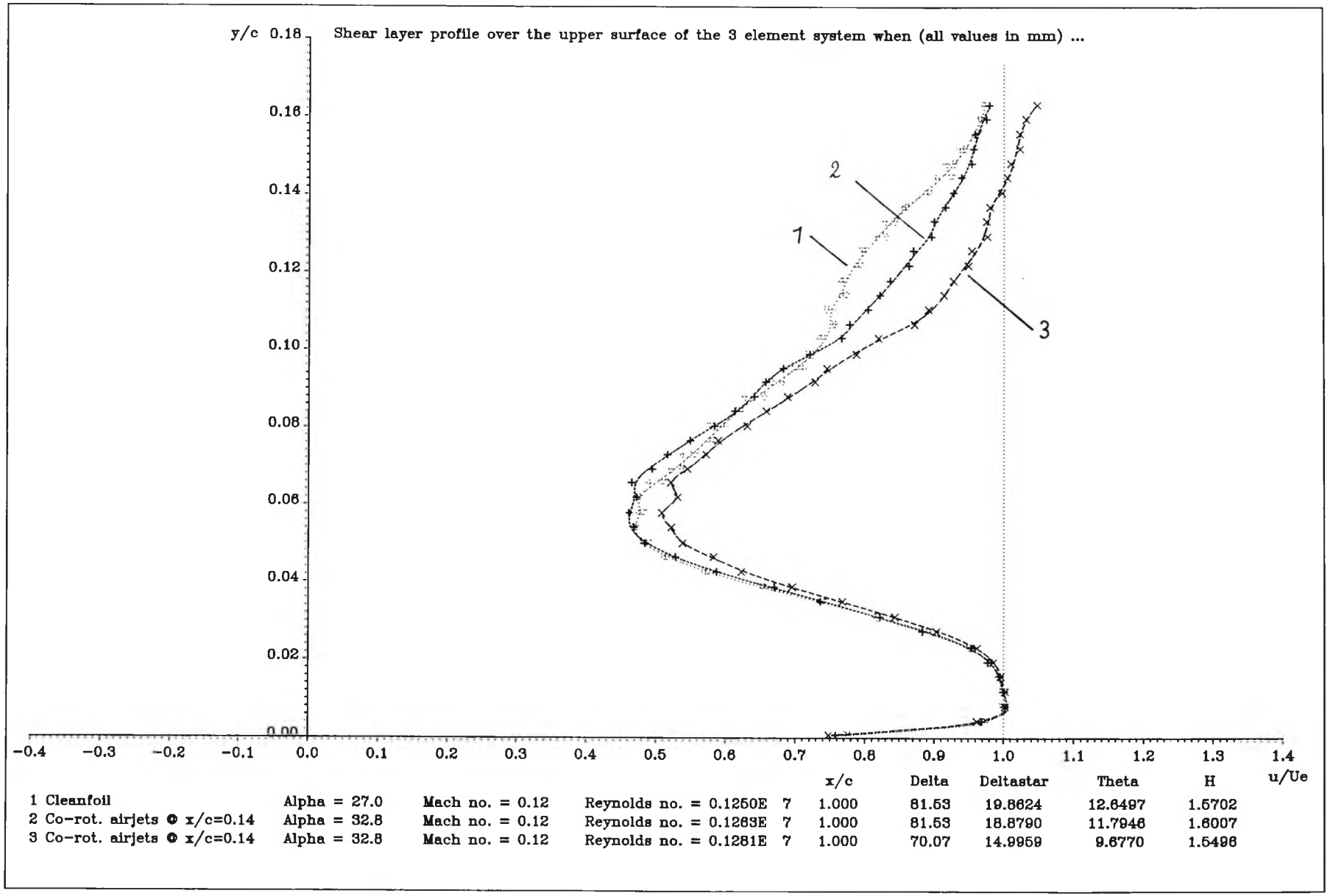

Figure 7.56 : Spanwise variation of shear layer profile at x/c = 1.0, $\alpha = 32°$, obtained when co-rot. airjets are at x/c = 0.14

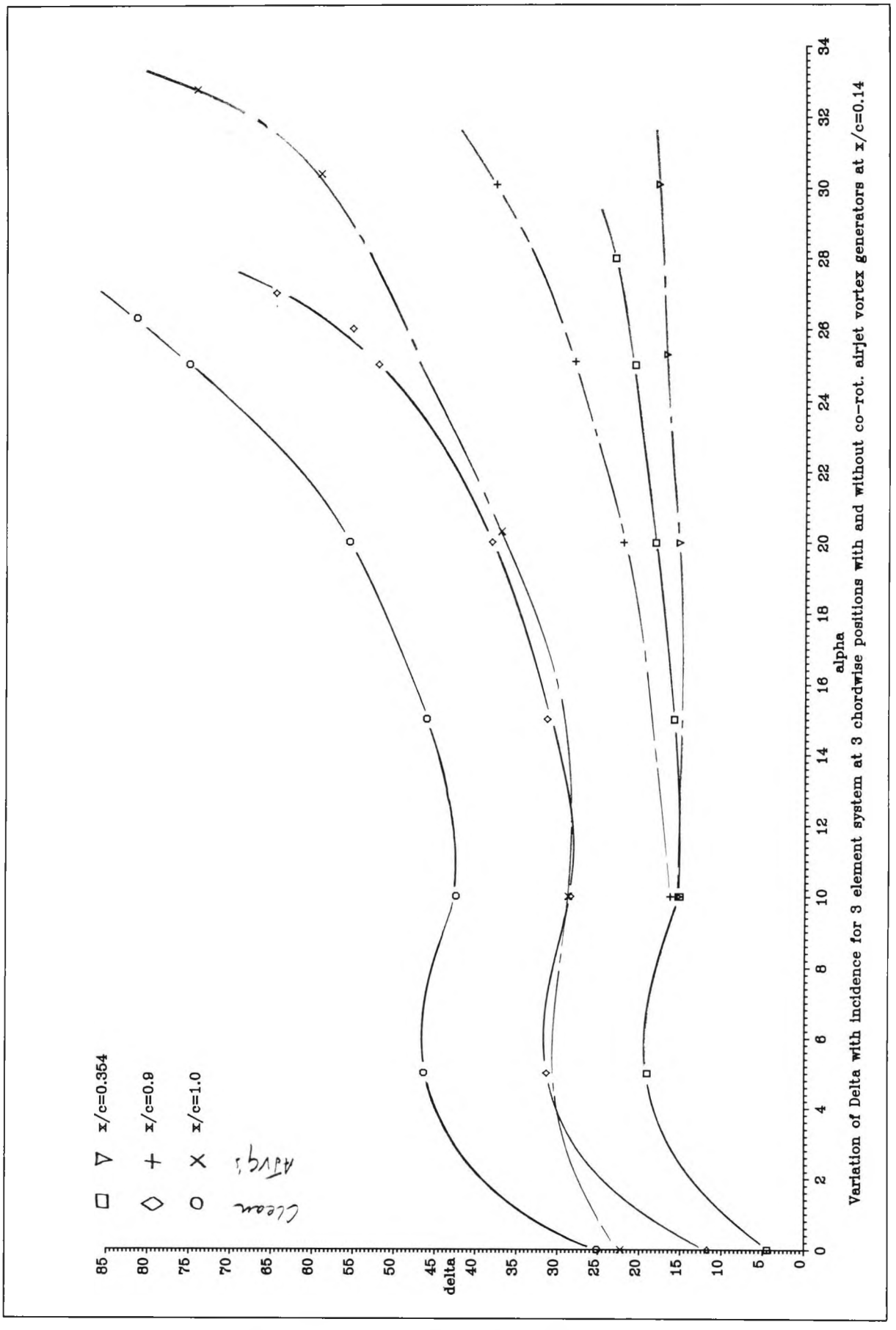

Figure 7.57 : Variation of δ (in mm) with α at 3 chordwise locations, with and without co-rot. airjet vortex generators at x/c = 0.14

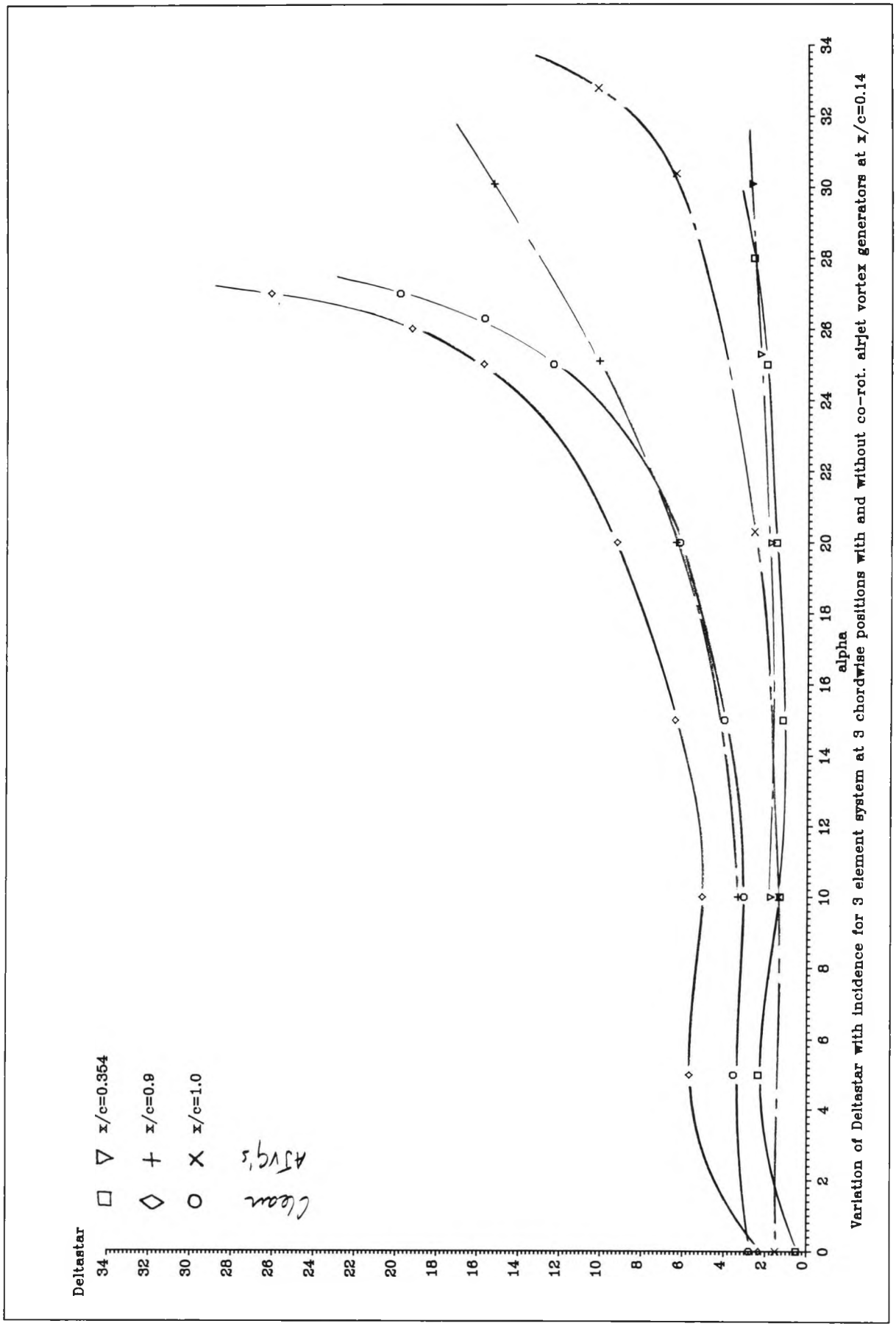

Figure 7.58 : Variation of δ^* (in mm) with α at 3 chordwise locations, with and without co-rot. airjet vortex generators at x/c = 0.14

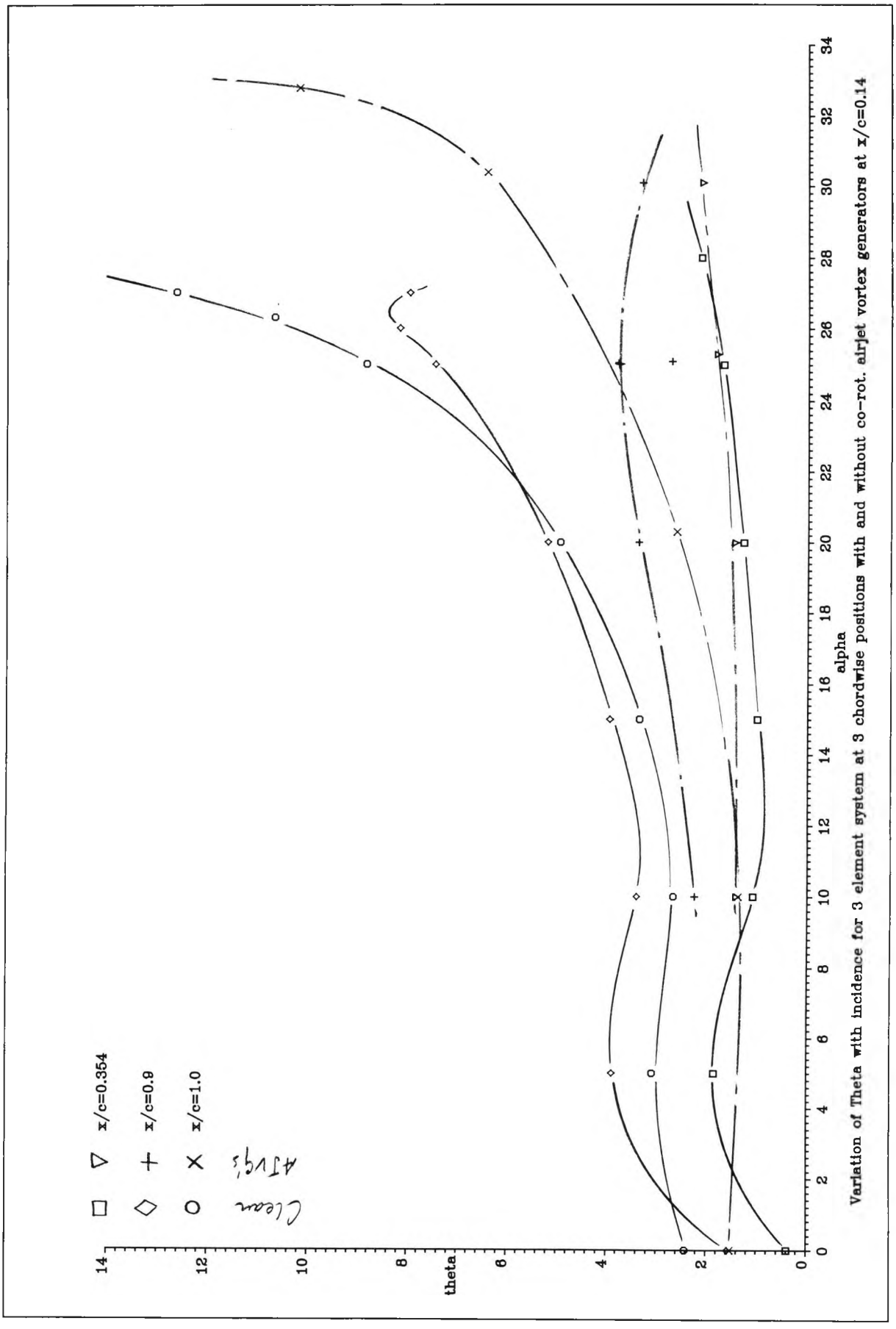

Figure 7.59 : Variation of θ (in mm) with α at 3 chordwise locations, with and without co-rot. airjet vortex generators at x/c = 0.14

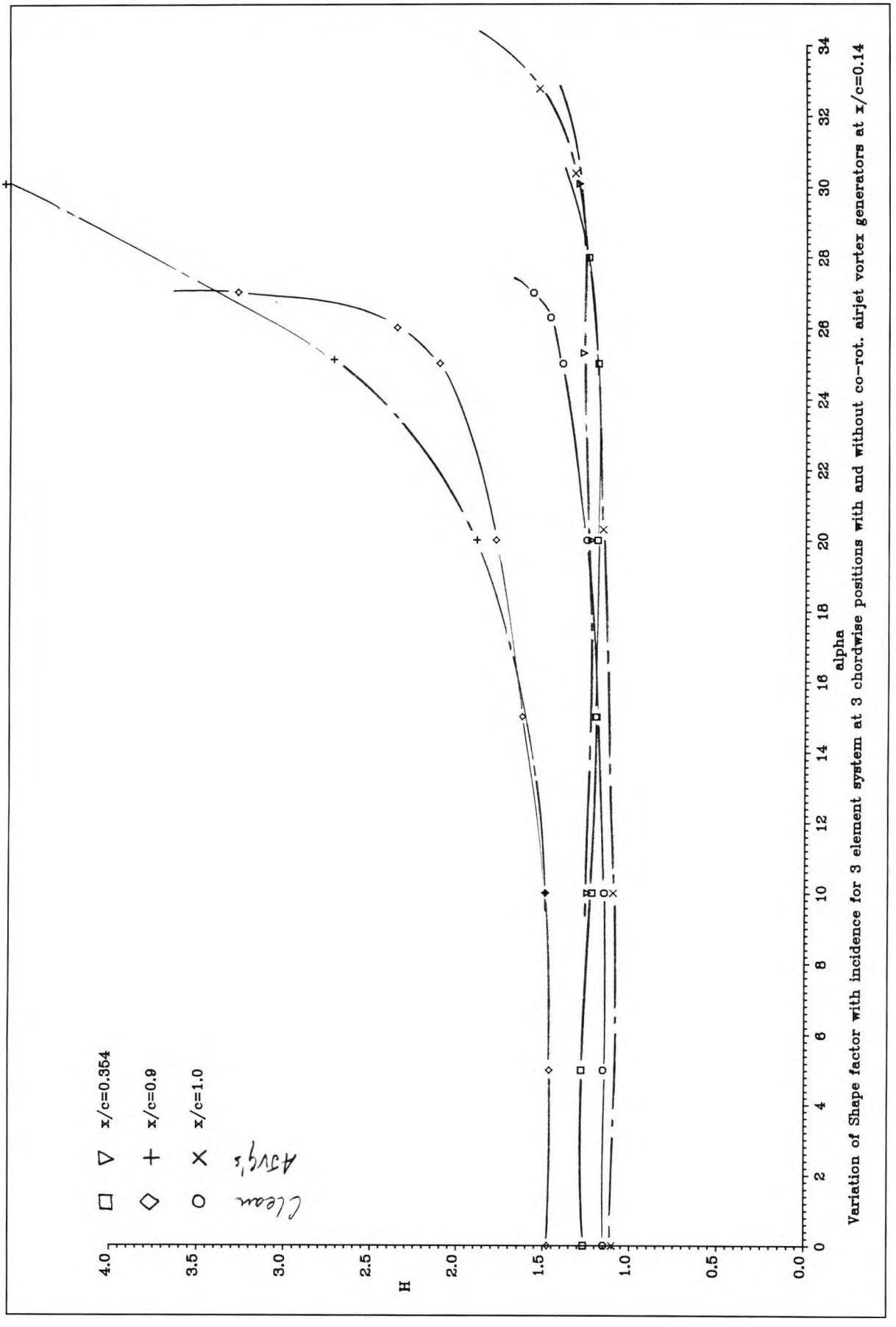

Figure 7.60 : Variation of H (in mm) with α for 3 chordwise locations, with and without co-rot. airjet vortex generators at x/c = 0.14

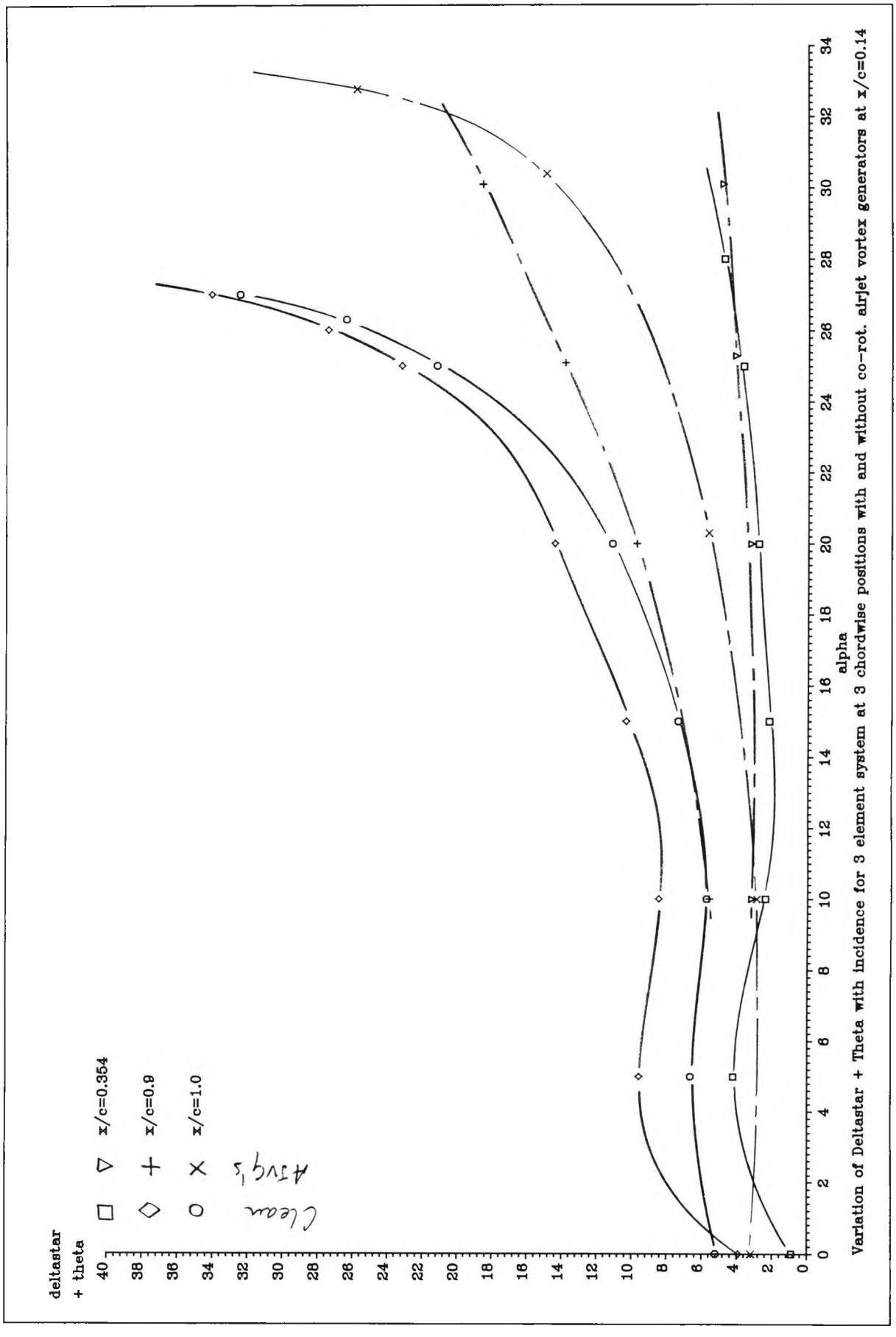

Figure 7.61 : Variation of ($\delta^* + \theta$) (in mm) with α at 3 chordwise locations, with and without co-rot. airjet vortex generators at x/c = 0.14

Appendix D - Data Acquisition Software

```
c Data Aquisition Software, March 1992
c Definition of variables

      integer*2 nmb,yawadc,rnmb,prstadc(4),manoadc
      integer*2 chan,stepchan,mp(4,0:47),dynh(4,0:47)
      integer*2 i,j,k,l,m,n,counter
      integer*2 LabGo
      integer*2 channel
      integer*2 step(4),home(4),stprt(4)
      real press,temp,alpha,inivolts,finvolts,yawzero,inimano
      real iniprst(4),cp(4,0:47)
      real finalpha,finmano,finprst(4),veas,vtas
      real avmano,avprst(4),cptemp(4,0:47),dynhtemp(4,0:47)
      real rhoatm,rhotun,tstag,tstatic,mu,re
      real Poody,cpatm,pstatic,pstag,pblow,blwpres
      real sum,average,total
      real locmach(4,0:47), P1T, P1, comp
      real locvel,cplocal(4,0:47)
      character*1 ans,filename*12,drive*2,path*14,title*12
      character*18 path1,suffix*4

c Introductory Screen

      call clrscrn
      write(6,'(20x,''BAe High Lift Data Aquisition Software'')')
      write(6,'(/10x,''This program enables an IBM compatible and CED
     +1401 Data Aquisition'',/,'' peripheral to be used at the heart of
     +a system to monitor and record pressures'',/,'' acting within the
     +vicinity of an aerofoil.'')')

c Setting up I/O parameters

      call clrscrn
      write(6,'(/1x,''When replying to subsequent prompts use of the''
     +,'' characters Y,N or Z (abort)''/1x,''is sufficient!'')')
      write(6,'(/1x,''Toggle Ctrl P to activate printer!'')')
      write(6,'(/1x,''Title for run? '')')
      read(5,'(a12)') title
      write(6,'(/30x,a12)') title
```

```
      write(6,'(/1x,''Are the results of the following run to be stored
     +on disc? '')')
      call answer(ans,i)
      if(i)10,20,30
20    write(6,'(/1x,''Filename required for data file? '')')
      read(5,'(a12)') filename
      write(6,'(/1x,''Drive to be accessed (include colon)? '')')
      read(5,'(a2)') drive
      path=drive//filename
      suffix='.raw'
      path1=path//suffix
      if(drive.eq.'c:') goto 10
40    write(6,'(/1x,''Is floppy present in drive? '')')
      call answer(ans,i)
      if(i)40,10,30

c Specifying Scanivalve parameters

10    write(6,'(/1x,''How many scanivalves are to be used for the curren
     +t run (max.=4)? '')')
      read(5,'(i1)') nmb
      call scanval(nmb,step,home)
      write(6,'(/1x,''Essentials are that port 0 = Patm, port 24 = Puc
     +and port 25 = Plc'')')

c Initialising CED1401 communication

      open(1,file='Labo')
      i=LabGo()
      write(6,'(/1x,''Open return code for 1401 was '',i8)') i

c Recording current laboratory conditions

      write(6,'(/1x,''What is the present atmos. press. (in mbar)? '')')
      read(5,'(f7.2)') press
      write(6,'(/1x,''What is the current lab temp. (in celcius)? '')')
      read(5,'(f4.1)') temp
      write(6,'(/1x,''Incidence setting of model? '')')
      read(5,'(f5.2)') finalpha
```

```
c Determining scanning rate

      call homescan(home,nmb)
      write(6,'(/1x,''Counter for timing loop (any +ve integer is adequa
     +te ,the larger the no. the'',/,'' slower the scan) = '')')
      read(5,'(i1)') counter

c Determination of flexible wiring parameters

      write(6,'(/1x,''What ADC channel(s) are connected to press. transd
     +ucers? '')')
      do 140 k=1,nmb
  140 read(5,'(i1)') prstadc(k)
      write(6,'(/1x,''What ADC channel is connected to the manometer? ''
     +)')
      read(5,'(i1)') manoadc

c Collecting current run parameters

  999 write(6,'(/1x,''Run number? '')')
      read(5,'(i2)') rnmb
  160 write(6,'(/1x,''Are we ready to take wind off values? '')')
      call answer(ans,i)
      if(i) 160,170,30
  170 continue
      call mean(manoadc,inimano)
      do 180 i=1,nmb
       call mean(prstadc(i),iniprst(i))
  180 continue
      write(6,'(/1x,''Manometer windoff voltage = '',f6.3)') inimano
      do 190 i=1,nmb
  190 write(6,'(/1x,''Windoff voltage for ADC channel '',i1,'' = '',
     +f6.3)') prstadc(i),iniprst(i)
      call strtscan(nmb,stprt,step,counter)
      write(6,'(/1x,''Tunnel stagnation temp. = '')')
      read(5,'(f4.1)') tstag

c Scanning

  230 write(6,'(/1x,''Are we ready to scan remaining ports? '')')
      call answer(ans,i)
```

```
      if(i) 230,240,30
240   call stepscan(home,nmb,stprt,step,prstadc,manoadc,
     +finmano,finprst,mp,dynh,counter,cptemp,dynhtemp,Poody)

c Pressure calculations and Printing routines

      call cpcalc(press,temp,inimano,finmano,iniprst,finprst,
     +nmb,stprt,cp,veas,vtas,re,tstag,tstatic,cptemp,avprst,dynhtemp,
     +rhotun,mach,Poody,cpatm,pstatic,pstag,pblow,blwpres,ans,locmach,
     +P1T,P1,comp,cplocal,locvel)
      call cpprint(cp,rnmb,finalpha,veas,vtas,re,tstatic,nmb,mach,path,
     +blwpres,locmach)

c Raw data storage

270   call rawdata(press,temp,finalpha,tstag,inimano,finmano,prstadc,
     +iniprst,finprst,cptemp,dynhtemp,nmb,rnmb,path1)
      write(1,'(''clear'')')
      do 997 m=1,nmb
            do 997 n=0,47
             cp(m,n)= 0.
997   locmach(m,n)= 0.
      write(6,'(/1x,''Do you want to continue running? '')')
      call answer(ans,i)
      if(i) 30,999,30
30    call labend
      close(2,status='keep')
      stop
      end

c CED1401 voltage calibration
      subroutine convert(int,res)
      integer*2 int
      real res
      res= (9.9976/65520) * (int+32768) - 5.0
      return
      end
      subroutine clrscrn
      write(6,'(7(/))')
      return
      end
```

```
      subroutine answer(ans,i)
      integer*2 i
      character*1 ans
      read(5,'(a1)') ans
      i=ichar(ans)-121
      return
      end

      subroutine clock(counter)
      integer*2 i,counter
      do 205 i=1,counter
       call timwaste()
205   continue
      return
      end

      subroutine timwaste()
      integer*2 j
      do 206 j=1,10
      write(3,*)
206   continue
      return
      end

c Channel definitions for relays
      subroutine scanval(nmb,step,home)
      integer*2 nmb,step(nmb),home(nmb),i
      do 150 i=1,nmb
       step(i)=2*i-1
150   home(i)=2*i
      write(6,'(/1x,''Scanivalve step channel(s) are = '',4(i2,4x))')
     +(step(i),i=1,nmb)
      write(6,'(/1x,''Scanivalve home channel(s) are = '',4(i2,4x))')
     +(home(i),i=1,nmb)
      return
      end

c Mean voltage calculation
      subroutine mean(channel,average)
      integer*2 channel
      real sum,average,total
```

```
      sum = 0.0
      do 141 i=1,20
       write(1,'(''adc,'',i1)') channel
       rewind(1)
       call labnum(1,l)
       call convert(l,total)
141   sum = sum + total
      average = sum/20.0
      return
      end

c Homing routine for scanivalves
      subroutine homescan(home,nmb)
      integer*2 nmb,home(nmb),chan,i,j
      character*1 ans
      do 155 i=8,15
155   write(1,'(''dig,o,0,'',i2)') i
      rewind(1)
      write(6,'(/1x,''Homing scanivalves!'')')
      do 110 i=1,nmb
       chan=home(i) + 7
110   write(1,'(''dig,o,1,'',i2)') chan
      write(6,'(/1x,''Once homed, press any key to continue....'')')
      call answer(ans,j)
      if(j)120,120,120
120   continue
      do 130 i=1,nmb
       chan=home(i) + 7
130   write(1,'(''dig,o,0,'',i2)') chan
      rewind(1)
      return
      end

c Routine to locate scanivalve at a particular port
      subroutine strtscan(nmb,stprt,step,counter)
      integer*2 nmb,stprt(nmb),step(nmb),stepchan,counter
      do 200 i=1,nmb
       write(6,'(/1x,''Required starting port for scanivalve '',i1,'' (
     +0-47)? '')') i
200   read(5,'(i2)') stprt(i)
      write(1,'(''dig,s,255'')')
```

```
      do 210 i=1,nmb
       stepchan=step(i) + 7
              do 220 j=1,stprt(i)
               write(1,'(''';dig,o,1,'',i2)') stepchan
               rewind(1)
               call clock(1)
               write(1,'(''';dig,o,0,'',i2)') stepchan
               rewind(1)
220    call clock(1)
210    write(6,'(/1x,''Scanivalve '',i1,'' located at port '',i2)') i,stp
      +rt(i)
      return
      end

c Scanning
      subroutine stepscan(home,nmb,stprt,step,prstadc,manoadc
      +,finmano,finprst,mp,dynh,counter,cptemp,dynhtemp,Poody)
      integer*2 nmb,stprt(nmb),step(nmb),prstadc(nmb),manoadc,chan,
      +mp(nmb,0:47),dynh(nmb,0:47),home(nmb),stepchan,i,j,k,l,m,n
      integer*2 i1,i2,channel,counter
      real finmano,finprst(nmb)
      real sm1,sm2
      real cptemp(nmb,0:47),dynhtemp(nmb,0:47),Poody,pounds
      character*1 ans
      Poody = 0.0
      do 250 i=1,nmb
       stepchan=step(i) + 7
       write(6,'(/1x,''Airjet blowing pressure (lb/in²)? '')')
       read(5,'(f6.3)') pounds
       Poody = Poody + pounds
       write(6,'(/)')
              do 250 j=stprt(i),47
               write(6,'(''+Scanning port number '',i2)') j
               call clock(counter*5)
               sm1 = 0.0
               sm2 = 0.0
                      do 251 k=1,50
                       write(1,'(''';adc,'',i1,'' '',i1)') prstadc(i),manoadc
                       rewind(1)
                       call labnum(2,mp(i,j),dynh(i,j))
                       call convert(mp(i,j),cptemp(i,j))
```

```
                        call convert(dynh(i,j),dynhtemp(i,j))
                        sm1 = sm1 + cptemp(i,j)
251                     sm2 = sm2 + dynhtemp(i,j)
                cptemp(i,j) = sm1/50.0
                dynhtemp(i,j) = sm2/50.0
                write(1,'(''dig,o,1,'',i2)') stepchan
                rewind(1)
                call clock(1)
                write(1,'(''dig,o,0,'',i2)') stepchan
                rewind(1)
250     call clock(1)
260     write(6,'(/1x,''Is the manometer reading windoff? '')')
        call answer(ans,m)
        if(m) 260,270,260
270     call homescan(home,nmb)
        call mean(manoadc,finmano)
        do 280 I = 1,nmb
         call mean(prstadc(I),finprst(I))
280     continue
        return
        end

c Print format parameters
        subroutine cpprint(cp,rnmb,finalpha,veas,vtas,re,tstatic,nmb,mach
       +,path,blwpres,locmach)
        character c
        integer*2 rnmb,nmb
        real mach,veas,vtas,re,tstatic,finalpha,cp(nmb,0:47)
        real locmach(nmb,0:47),blwpres
        character*14 path
        write(6,'(/1x,''Results for current run are as follows:'')')
        write(6,'(/1x,''Run no. ='',i2,10x,''Incidence = '',f5.2)') rnmb,
       + finalpha
        write(6,'(/1x,''Mach no. = '',f5.3,10x,''TAS = '',f5.2,10x,''EAS = ''
       +,f5.2)') mach,vtas,veas
        write(6,'(/1x,''Reynolds no. = '',e9.2,6x,''Tunnel static temp. = ''
       +,f4.1)') re,tstatic
        write(6,'(/1x,''Airjet blowing pressure Pb/Po = '',f5.3)') blwpres
        do 290 i = 1,nmb
         write(6,'(//1x,''Press. coeff. as measured by scanivalve '',i1
       +)') i
```

```
                do 290 j=0,5
                 write(6,'(/1x,''Port no.'',8(3x,i2,3x))') ((k+8*j),k=0,7)
                 write(6,'(/9x,8(f7.3,1x))') (cp(i,l+8*j),l=0,7)
290     write(6,'(/9x,8(f7.3,1x))') (locmach(i,l+8*j),l=0,7)
        if(path.le.' ') goto 998
        open(2,file=path,status='unknown')
5       continue
        read(2,101,end=6) c
        goto 5
6       continue
        backspace 2
        write(2,*) finalpha,re,vtas,tstatic,rnmb
        write(2,'(6(/4x,8(f7.3,1x)))') ((cp(i,j),j=0,47),i=1,nmb)
        write(2,'(6(/4x,8(f7.3,1x)))') ((locmach(i,j),j=0,47),i=1,nmb)
998     return
101     format(a)
        end

c Calculation of Cp's
        subroutine cpcalc(press,temp,inimano,finmano,iniprst,
       +finprst,nmb,stprt,cp,veas,vtas,re,tstag,tstatic,cptemp,avprst
       +,dynhtemp,rhotun,mach,Poody,cpatm,pstatic,pstag,pblow,blwpres
       +,ans,locmach,P1T,P1,comp,cplocal,locvel)
        integer*2 i,j,k,l,m,n,nmb,stprt(nmb)
        real press,temp,cp(nmb,0:47),mach
        real inimano,finmano,iniprst(nmb),finprst(nmb)
        real avmano,avprst(nmb)
        real cptemp(nmb,0:47),dynhtemp(nmb,0:47)
        real veas,vtas,rhoatm,rhotun,mu,re,tstag,tstatic
        real Poody,cpatm,pstatic,pstag,pblow,blwpres
        real locmach(nmb,0:47),P1T,P1,comp
        real cplocal(nmb,0:47),locvel
        character*1 ans
        avmano = 0.5*(inimano+finmano)
        do 354 i=1,nmb
354     avprst(i) = 0.5*(iniprst(i)+finprst(i))
        do 355 m=1,nmb
                do 355 n=stprt(m),47
                 cptemp(m,n)=cptemp(m,n)-avprst(m)
355              dynhtemp(m,n)=dynhtemp(m,n)-avmano
        do 360 k=1,nmb
```

```
                do 360 l=stprt(k),47
 360             cp(k,l)=(cptemp(k,l)-(cptemp(k,25)*dynhtemp(k,l)/dynhtemp(k,25)))
     + /(1.073*((cptemp(k,24)*dynhtemp(k,l)/dynhtemp(k,24))-
     + (cptemp(k,25)*dynhtemp(k,l)/dynhtemp(k,25)))) + .034
     veas=sqrt(.5*(dynhtemp(1,stprt(1))+dynhtemp(nmb,47))*1717.01)
     rhoatm=(press*100)/(287*(273+temp))
     rhotun=rhoatm*(temp+273)/(tstag+273)
     vtas=veas*sqrt((1.2256/rhotun))
     tstatic=(tstag+273)-((vtas**2)/2008)-273
     mu=1.714e-5*((tstatic+273)/273)**.75
     re=(rhotun*vtas*0.5)/mu
     mach=vtas/sqrt(1.4*287*(273+tstatic))
c    avcpbl=(cp(1,29)+cp(1,30))/2.
     cpatm=-cptemp(1,25)/(1.073*(cptemp(1,24)-cptemp(1,25))) + .034
     pstatic=(press*100)-(cpatm*.5*rhotun*vtas**2)
     pstag=pstatic+(.5*rhotun*vtas**2)
     write(6,'(/1x,''Has a b/l profile just been investigated? '')')
     call answer(ans,i)
     if(i) 450,460,430
 460 call bdlycalc(cp,nmb,stprt,mach,vtas,pstatic,rhotun,
     +locmach,P1T,P1,comp,cplocal,locvel)
     do 370 k=1,nmb
                do 370 l=stprt(k)+1,47
 370             cp(k,l)=cplocal(k,l)
c                pblow=(avcpbl*.5*rhotun*vtas**2)+pstatic
 450 pblow=(6894.76*Poody/nmb)+pstatic
     blwpres=pblow/pstag
 430 return
     end
c Rawdata storage routine
     subroutine rawdata(press,temp,finalpha,tstag,inimano,finmano,
     +prstadc,iniprst,finprst,cptemp,dynhtemp,nmb,rnmb,path1)
     character*1 c,path1*18
     integer*2 nmb,prstadc(nmb),rnmb
     real press,temp,finalpha,tstag,inimano,finmano,iniprst(nmb),
     +finprst(nmb),cptemp(nmb,0:47),dynhtemp(nmb,0:47)
     if(path1.le.' ') goto 997
     open(2,file=path1,status='unknown')
 7   continue
     read(2,102,end=8) c
     goto 7
```

```
 8      continue
        backspace 2
        write(2,'(/3x,i2,4x,4(f7.2,2x))') rnmb,press,temp,finalpha,tstag
        write(2,'(/4x,2(f6.3,4x))') inimano,finmano
        do 365 i=1,nmb
         write(2,'(/4x,i2,4x,2(f6.3,4x))') prstadc(i),iniprst(i)
       +,finprst(i)
         write(2,'(6(/4x,8(f7.3,1x)))') (cptemp(i,j),j=0,47)
 365    write(2,'(6(/4x,8(f7.3,1x)))') (dynhtemp(i,j),j=0,47)
 997    return
 102    format(a)
        end
c Boundary layer calculations
        subroutine bdlycalc(cp,nmb,stprt,mach,vtas,pstatic,rhotun,
       +locmach,P1T,P1,comp,cplocal,locvel)
        integer*2 nmb,stprt(nmb)
        real cp(nmb,0:47), mach, rhotun, pstatic, vtas
        real locmach(nmb,0:47), P1T, P1, comp
        real locvel, cplocal(nmb,0:47), dum
        do 380 i=1,nmb
         comp=(1 + (cp(i,stprt(i)) * 0.7 * (mach**2)))**.2857143
         locmach(i,stprt(i))=SQRT((((2+.4*(mach**2))/comp) -2) /0.4)
         P1=(cp(i,stprt(i))*0.5*rhotun*vtas**2)+pstatic
         locvel=vtas*SQRT(1-cp(i,stprt(i)))
                do 380 j=stprt(i)+1,47
                 P1T=(cp(i,j)*0.5*rhotun*vtas**2)+pstatic
                 dum=((P1T/P1)**0.2857143)-1
                if(dum.ge.0.0) then
                        locmach(i,j)=SQRT((((P1T/P1)**0.2857143)-1)/0.2)
                else
                        locmach(i,j)=-1.0*SQRT(ABS(dum)/0.2)
                endif
                cplocal(i,j)=((vtas/locvel)**2)*(cp(i,j)-cp(i,stprt(i)))
                if(cplocal(i,j).ge.0.0) then
                        cplocal(i,j)=SQRT(cplocal(i,j))
                else
                        cplocal(i,j)=-1.0*SQRT(ABS(cplocal(i,j)))
                endif
 380    continue
        return
        end
```

Table 1

Coordinates used in defining slat position

x	y
-4.525	-51.448
-7.412	-51.702
-11.781	-51.979
-15.783	-52.094
-19.420	-52.042
-22.690	-51.830
-25.604	-51.428
-28.185	-50.768
-30.439	-49.836
-32.368	-48.630
-34.002	-47.064
-35.388	-45.012
-36.542	-42.424
-37.449	-39.349
-37.907	-36.335
-37.915	-33.390
-37.486	-30.475
-36.617	-27.599
-35.298	-24.792
-33.535	-22.033
-31.336	-19.303
-28.707	-16.585
-25.661	-13.844
-22.211	-11.042
-18.356	-8.184
-14.096	-5.269
-9.431	-2.298
-4.364	0.738
1.104	3.842
6.976	7.007
13.250	10.233
13.908	10.564
14.113	10.000
9.827	7.115
5.845	4.234
2.199	1.265
-1.095	-1.832
-4.037	-5.059

Table 1 (cont)

Coordinates used in defining slat position

x	y
-6.635	-8.391
-8.905	-11.789
-10.863	-15.208
-12.525	-18.599
-13.908	-21.921
-15.025	-25.135
-15.887	-28.210
-16.503	-31.126
-16.878	-33.866
-17.015	-36.421
-16.917	-38.785
-16.584	-40.956
-16.017	-42.935
-14.959	-45.201
-13.483	-47.333
-11.620	-49.251
-9.447	-50.736
-7.076	-51.488
-4.525	-51.448

Table 2

Coordinates used in defining main wing position

x	y
385.000	-15.190
369.800	-17.395
352.800	-19.762
336.200	-21.949
320.000	-23.963
304.200	-25.807
288.800	-27.484
273.800	-28.995
259.200	-30.335
245.000	-31.507
231.200	-32.509
217.800	-33.327
204.800	-33.947
192.200	-34.363
180.000	-34.574
168.200	-34.587
156.800	-34.421
145.800	-34.100
135.200	-33.641
125.000	-33.054
115.200	-32.355
105.800	-31.563
96.800	-30.690
88.200	-29.751
80.000	-28.760
72.200	-27.731
64.800	-26.676
57.800	-25.598
51.200	-24.500
45.000	-23.380
39.200	-22.237
33.800	-21.072
28.800	-19.887
27.000	-19.430
24.590	-18.596
22.618	-17.077
21.085	-14.939
19.990	-12.499

Table 2 (cont)

Coordinates used in defining main wing position

x	y
19.332	-9.991
19.113	-7.500
19.257	-5.446
19.686	-3.292
20.402	-1.037
21.406	1.316
22.695	3.763
24.270	6.292
26.133	8.887
28.282	11.526
30.717	14.174
33.439	16.792
36.448	19.335
39.743	21.753
43.325	23.995
47.193	26.020
51.348	27.805
55.789	29.348
60.516	30.692
65.531	31.938
68.197	32.538
70.864	33.035
73.531	33.386
80.000	33.975
88.200	34.610
96.800	35.160
105.800	35.624
115.200	36.000
125.000	36.289
135.200	36.488
145.800	36.596
156.800	36.607
168.200	36.521
180.000	36.333
192.200	36.042
204.800	35.645
217.800	35.141
231.200	34.525

Table 2 (cont)

Coordinates used in defining main wing position

x	y
245.000	33.796
259.200	32.949
273.800	31.980
288.800	30.880
304.200	29.641
320.000	28.251
336.200	26.693
352.800	24.943
369.800	22.986
387.200	20.796
405.000	18.320
423.200	15.493
441.800	12.265
450.000	10.732
450.000	10.132
441.898	10.646
434.259	10.998
427.083	11.107
420.371	10.941
414.121	10.497
408.333	9.779
403.009	8.859
398.148	7.733
393.750	6.453
389.815	5.054
386.343	3.564
383.333	2.010
380.787	0.410
378.704	-1.226
377.083	-2.887
375.926	-4.571
375.231	-6.275
375.000	-8.000
375.278	-9.889
376.111	-11.743
377.500	-13.469
379.445	-14.816

381.945 -15.425 and 385.000 -15.190

Table 3

Coordinates used in defining flap position

x	y
570.452	-45.160
551.098	-40.443
532.097	-35.926
513.432	-31.655
495.100	-27.641
477.113	-23.846
459.499	-20.195
457.322	-19.743
454.370	-18.920
452.230	-17.492
450.863	-15.562
450.149	-13.464
450.000	-11.437
450.385	-9.567
451.192	-8.026
452.428	-6.661
454.091	-5.475
456.182	-4.468
458.699	-3.644
461.639	-3.011
464.998	-2.580
468.771	-2.489
472.947	-2.458
477.518	-2.700
482.471	-3.305
487.793	-4.248
493.472	-5.566
499.497	-7.286
505.862	-9.426
512.567	-11.979
519.626	-14.926
527.063	-18.180
529.195	-19.143
531.309	-20.160
533.382	-21.285
536.696	-23.289
553.564	-33.667
570.712	-44.444 and 570.452	-45.160